Karlsruhe Institute of Technology

A Phenomenological Theory of KATRIN Source Potential Systematics and its Application in Krypton-83m Calibration Measurements

Zur Erlangung des akademischen Grades eines
Doktors der Naturwissenschaften (Dr. rer. nat.)
von der KIT-Fakultät für Physik des
Karlsruher Instituts für Technologie (KIT)
genehmigte
Dissertation

von

Moritz Benedikt Machatschek, M. Sc.

aus Erlangen

Referentin:	Prof. Dr. Kathrin Valerius Institut für Astroteilchenphysik, KIT
Korreferent:	Prof. Dr. Ulrich Husemann Institut für Experimentelle Teilchenphysik, KIT

Tag der mündlichen Prüfung: 11.12.2020

Erklärung zur Selbstständigkeit

Ich versichere, dass ich diese Arbeit selbstständig verfasst habe und keine anderen als die angegebenen Quellen und Hilfsmittel benutzt habe, die wörtlich oder inhaltlich übernommenen Stellen anderer als solche kenntlich gemacht und die Satzung des KIT zur Sicherung guter wissenschaftlicher Praxis in der gültigen Fassung vom 24.05.2018 beachtet habe.

Karlsruhe, den 18.04.2021, _____

Moritz Machatschek

Introduction

Although the postulation of neutrinos by Wolfang Pauli in 1930 [Pau30] dates back 90 years and since then many experiments have been devoted to the study of these particles, not all their properties are known to this day. The measurement of neutrinos is challenging and involves a great deal of effort; for example, the first direct experimental proof of the existence of neutrinos in the Savannah River Experiment was only provided 26 years after their postulation [Cow+56]. Through the observation of the solar neutrino deficit and the discovery and experimental confirmation of neutrino flavour oscillations in many experiments [Suz95; SNO+02; Fuk+01; Ham+99; Abd+94] it has been proven today that neutrinos have a non-vanishing mass. The undisputed evidence of the experimental data thus exposes a clear shortcoming of the Standard Model of elementary particle physics, in which neutrinos are massless. Despite the overwhelming success of the Standard Model in describing the interaction of particles and thus fundamental physics on the smallest length scales, it is undisputed that its description of neutrinos is incomplete. The experimental study of neutrinos, including the determination of their mass, is an essential step to understand the necessary extension of the Standard Model and thus physics on the smallest length scales.

Neutrinos are not only relevant on the smallest but also on the largest length scales: According to the ΛCDM model, the "Standard Model" of cosmology, they are the most abundant massive particles in the universe. Their mass is one of the parameters that influences how structures in the early universe evolved, leading to the distribution of galaxies, voids and galaxy clusters observed today. Extensions of the ΛCDM model can be used to derive an upper limit on the size of the neutrino mass, however, the most sensitive results rely on the combination of several different observational data sets [CH20]. For this reason, although precision cosmology has become a sensitive probe for the sum of neutrino masses, direct laboratory measurements are indispensable to corroborate and test the interpretation in the cosmological framework.

Two experimental approaches have been established to determine the neutrino mass in the laboratory, both of which use a form of beta decay. The neutrinoless double beta decay ($0\nu\beta\beta$) assumes that neutrinos are Majorana particles, i.e. their own antiparticles, and is prohibited in the Standard Model as a lepton number violating process. The exchange of virtual Majorana neutrinos is a mediator of the hypothetical double beta decay. The Majorana neutrino mass thus impacts the decay rate of $0\nu\beta\beta$. Therefore, experiments that can detect this type of decay and measure its half-life could indeed prove that neutrinos are Majorana particles and contribute to an extension of the Standard Model. However, if neutrinos are not their own antiparticles, these experiments cannot determine the neutrino mass. Very long half-life times well in excess of ordinary first-order weak interactions

are expected for $0\nu\beta\beta$ and if it takes place at all, then only so rarely that it has not been observed until today [Ni+19].

The second established laboratory method is the precise measurement of the single beta decay spectrum. The most advanced current-generation experiment targeted at determining the neutrino mass in this way is the KArlsruhe TRItium Neutrino (KATRIN) experiment. It builds on the experience of the predecessor experiments in Mainz and Troitsk, but will exceed those in its sensitivity to the determination of the neutrino mass by a factor of 10. This is only possible with enormous technical efforts and numerous innovations, so that many components of KATRIN have set the limits of what is technically feasible at the moment. This work aims to contribute to the equally complex and extensive data analysis and modelling of the measurements.

The KATRIN experiment performs a kinematic measurement of the electron neutrino mass m_ν by precision spectroscopy of the tritium β decay spectrum at its kinematic endpoint with and energy of 18.6 keV. KATRIN's first published result of $m_\nu < 1.1\,\mathrm{eV}$ (90 % C.L.) [Ake+19] of the KNM1 campaign is the current most stringent limit from laboratory neutrino mass measurements. Future measurement campaigns will successively bring down the statistical uncertainty. In order to push for the target sensitivity of 200 meV (90 % C. L.) [KAT04b], though, a detailed understanding of the systematic uncertainties is needed, as well.

The topic of the thesis at hand is the development of a theory to characterise source potential systematics of the KATRIN experiment, which are critical systematic effects. This theory describes both the observables of the potential, which are obtained in $^{83\mathrm{m}}$Kr calibration measurements and, given estimates of these observables, the expected systematics in tritium measurements. While the main focus of this work is on the detailed understanding of the theoretical framework, the developed method is also applied to the KATRIN KNM1 and KNM2 measurement campaigns carried out in 2019.

One of the major systematic uncertainties stems from energy calibration, i.e. from the precise determination of the difference of the electric potential between source and spectrometer. The β decay takes place in the Windowless Gaseous Tritium Source (WGTS), where the gaseous tritium is continuously cycled. Inelastic scattering of the decay electrons off the gas molecules leads to two effects of relevance for this thesis: on the one hand, it leads to charge generation by ionisation of the gas, which entails the formation of a low-density plasma. This plasma can lead to a spatially non-homogeneous source potential and thus contributes to an uncertainty of the energy calibration. On the other hand, inelastic scattering provides spatial resolution on the source potential, due to the following reasoning: Scattering is more likely to occur for those electrons, which have to traverse a larger portion of the 10 m long source tube, such that electrons of higher scattering multiplicities are more likely to originate further from the rear part of the source. In addition, the inelastic scattering is quantum mechanically forbidden for incident electron energies smaller than $\approx$ 13 eV, so that the overall recorded electron spectrum consists of a summation of spectra for the different scattering multiplicities, starting from unscattered electrons. In combination, this provides a mechanism for sensitivity on the longitudinal starting position of the observed electrons: In mono-energetic spectra the

electrons of different scattering multiplicity, which stem from different parts of the source, appear in different energy ranges. In continuous spectra like the tritium β spectrum the scattering contributions overlap, which partly obscures this connection. Nevertheless, this mechanism still leads to spatial sensitivity on the source potential. The consequences of this observation are manifold and constitute the main part of this thesis.

The first consequence affects the description of energy calibration systematics. In the KATRIN systematic budget an accuracy on the order of 10 mV on the difference of the potentials of the main spectrometer and the tritium source is required. The exact quantitative specification of this requirement depends on the shift of the observable squared neutrino mass Δm_ν^2 resulting from inhomogeneities of the energy scale. For the latter there are different measures. In the simplest description of the β spectrum the shift of the squared neutrino mass is given by the standard deviation σ of an unaccounted distribution of the β-electron energy, caused by a systematic effect. In this case the relation [RK88]

$$\Delta m_\nu^2 = -2\sigma^2 \tag{1}$$

holds in leading order, for which the KATRIN design reports states a requirement of $\sigma < 60$ meV [KAT04b] for all energy scale systematics. However, inelastic scattering is one of the reasons why this simple case is not always realised at KATRIN and why in some situations equation 1 needs to be modified. The mechanism leading to this modification is sketched in the following.

The use of an overall energy distribution to describe systematic influences as opposed to detailed modelling of the physical effects involved makes this description phenomenological. As a consequence, this type of theory for the neutrino mass shift has some formal similarities with the theory of phase transitions. One of them is the relevance of symmetries and symmetry breaking. Equation 1 uses only a single distribution of the β-electron energy, which assumes that the measured β spectrum does not depend on spatial or temporal coordinates. In this sense the energy scale is fully symmetrical. However, as shown in this thesis, for certain experimental conditions more than one energy scale distribution must be considered, rendering σ not well defined. The emergence of more than one energy scale distribution is caused by physical effects that break certain symmetries. Consequently, additional degrees of freedom are required to fully specify the neutrino mass shift. Two of these effects are investigated in this thesis:

One is the mentioned inelastic electron scattering in the source, breaking the longitudinal symmetry of the source energy scale. As a consequence, electrons of different scattering multiplicity have different starting potential distributions. In leading order this is accounted for by a measure of the difference of their means Δ_ρ, in addition to the standard deviation for the unscattered electrons σ_0.

The other is energy scale fluctuations on run time scale, breaking the temporal symmetry of the energy scale. Energy fluctuations with periods much smaller than the usual measurement are averaged, such that no information on the fluctuation phase is contained in the recorded electron spectrum. However, comparable time scales of fluctuation and measurement lead to a predictable relation between fluctuation phase and energy of the

electrons. The occurrence of this effect is quantified by the size of the *Root Mean Square* value of the energy fluctuation σ_{RMS} on the time scale of the measurement.

As shown in this work, those additional degrees of freedom lead to the modification of equation 1 to

$$\Delta m_\nu^2 = \underbrace{-2\sigma_0^2 - \epsilon\Delta_\rho}_{\text{Longidutinal distribution}} + \underbrace{\epsilon'\sigma_{\mathrm{RMS}} + a\sigma_{\mathrm{RMS}}^2}_{\text{Temporal distribution}} . \tag{2}$$

The coefficients ϵ, ϵ' and a are order parameters which vanish for full symmetry. Their determination as a function of the relevant operating parameters, such as the tritium column density in the source or the time sequence used in the energy spectroscopy, is one of the topics of this thesis.

One tool for the energy calibration and the determination of σ_0, Δ_ρ and σ_{RMS} is the $^{83\mathrm{m}}$Kr mode of the gaseous source. In this mode, gaseous, mesomeric krypton-83m is dispersed along with the tritium gas inside the tritium source. Krypton-83m exhibits several electron conversion lines in a range measurable by KATRIN, such that it can be used as a nuclear standard. It approximately follows the tritium distribution in the source tube volume, such that the conversion electrons suffer from comparable source potential systematics as the β spectrum. However, due to the mono-energetic lines, the effect of inelastic scattering is directly visible in the krypton spectrum. In particular, the unscattered portion of the investigated line is directly related to the longitudinal plasma inhomogeneity σ_0, by an additional broadening on top of the intrinsic width. A line of one-time scattered electrons is observed approximately 13 eV below the unscattered electrons. From the difference of those two lines Δ_ρ can be determined. Temporal fluctuations lead to an additional broadening of the line, such that it can also be used to constrain σ_{RMS}.

As discussed, the parameters σ_0 and Δ_ρ are given by the central moments of the starting potential distributions for different scattering multiplicities. The expansion of the distributions in moments is a perturbative approach, which reveals the essential observables of the krypton-83m and the tritium measurement. This is particularly noticeable when examining the predictive power of the krypton-83m measurement on the actual potential. It can be shown that the ratio of the measured moments is given by the correlation of the potential with a certain longitudinal potential shape. In particular, potentials which are antisymmetric in relation to the gas injection point in the centre of the 10 m long source tube lead to extreme values of $\frac{\Delta_\rho}{\sigma_0}$ for typical KATRIN measurement conditions, while Δ_ρ vanishes for symmetric potentials.

Finding exact, model-independent relations like these is a focus of this work: The measurements of the KNM1 and KNM2 campaigns at KATRIN have shown that the determination of the plasma potential systematics is very difficult, since also the krypton-83m calibration measurement and other methods suffer from systematics. In addition, many dimensions like temporal drifts, radial dependencies of the observables and the multitude of the available methods lead to complicated discussions, such that additional model dependencies need to be avoided. This goal is fully achieved in this work, which rigorously relates symmetries of the potential to all observables of the krypton measurement and gives a

comprehensive description of the neutrino mass systematics resulting from those potential symmetries.

This rigour comes at the expense of a well founded mathematical approach of the developed formalism. As it turns out, there are many subtleties like for example differences in the longitudinal gas profiles for krypton and tritium, which lead to different moments for the two gas species. While such details are not relevant to understand the overall picture of the developed theory, they are relevant for the full KATRIN measurement. For this reason, the main part of this work starts with a short summary, which skips the mathematical details and derivations. The goal is to facilitate the understanding of the general picture, before the details are studied in the individual chapters.

This thesis is structured as follows:

Chapter 1 gives a short overview of the basic components of the KATRIN experiment as well as its analysis and simulation framework. It also includes descriptions of the KATRIN ^{83m}Kr mode modelling and of basic plasma physics.

Chapter 2 provides the short summary of the following three chapters without mathematical detail. It also lists the nomenclature used in the later chapters.

In chapter 3 the general formalism fitting to describe source plasma potential systematics is derived. Since all relevant relations are deduced here, it is the basis of the following chapters. The fundamental krypton-83m observables are identified and a general ansatz for the potential induced neutrino mass and endpoint shift is given. While in essence the used formalism is standard (Gaussian) statistics of the starting potential distribution, due to inelastic scattering several of those distributions and their relations need to be considered.

Chapter 4 describes the potential models deducible from the krypton-83m measurement. In an exact, analytical approach, all observables are related to symmetries of the potential and the remaining, model dependent portion of the potential is identified. To illustrate this abstract discussion by a concrete example, the potential moments resulting from a polynomial potential model are calculated.

In chapter 5 the coefficients of the equations derived in chapter 3 are simulated for conditions comparable to the KNM1, KNM2 and KNM3 measurements. Here all plots for the calculation of the plasma potential systematic from the potential observables measured with krypton-83 are found.

In chapter 6 the KNM1 and KNM2 krypton-83m measurements are described. A short discussion is dedicated to modelling, systematics and complementary measurements. However, the main focus is on the application of the previously derived methods, which for example includes model-independent constraints of the peak-to-peak value of the measured potential. The discussion on plasma potential systematics from longitudinal inhomogeneity is concluded with the calculation of the expected systematics in the KNM2 neutrino mass measurement.

In chapter 7 systematics stemming from time dependent energy scale perturbations are discussed. While this topic is not covered by the theoretical framework of the previous

discussion, time dependencies of the plasma potential are still one possible candidate to cause energy scale perturbations. Quantitative relations are found for the neutrino mass shift for different perturbation frequency regimes and time sequences of the measurement. The size of the systematic is constrained from the KNM2 krypton-83m measurement, both for the respective neutrino mass campaign, and for full KATRIN.

The thesis concludes with a summary and an outlook in chapter 8.

Contents

List of Figures

List of Tables

1. The KATRIN Experiment

The KArlsruhe TRItium Neutrino (KATRIN) experiment performs a kinematic measurement of the neutrino mass by precision spectroscopy of the tritium beta decay electron spectrum at the endpoint of 18.6 keV. By the time of writing of this thesis, three neutrino mass campaigns (KNM1-3) were successfully finished at KATRIN. The first published result from KNM1 is [Ake+19]

$$m_\nu < 1.1\,\mathrm{eV}\ (90\ \%\ \mathrm{C.L.})\ . \tag{1.1}$$

Although only using roughly four weeks of measurement time at reduced source strength, this improves the results of the predecessor experiments in Mainz and Troitsk [Kra+05; Ase+11] by almost a factor of two. The targeted total sensitivity of 200 meV (90 % C. L.) for 1000 days of data taking exceeds the sensitivity of the predecessor experiments even by one order of magnitude [KAT04b]. Reaching this goal can only be achieved by increasing the statistical sensitivity of the measurement, while keeping stringent limits on the systematic uncertainty budget. This chapter summarises which methods are used at KATRIN to do so and discusses the plasma systematics, which are at the focus of this thesis.

Section 1.1 discusses the measurement principle and setup of the experiment. In section 1.2 the simulation and data analysis framework of KATRIN is explained [1].

Section 1.3 describes the $^{83\mathrm{m}}$Kr mode of the gaseous source, which is a calibration mode used for the study of systematic effects.

Finally, in section 1.4 the source plasma potential systematics is explained, which is studied using the $^{83\mathrm{m}}$Kr mode and is the main concern of this thesis.

1.1. Measurement Principle and Setup

KATRIN performs a high-precision spectroscopy of the tritium β-electron spectrum close to the endpoint. The used molecular tritium T_2 decays mainly by the β reaction

$$T_2 \rightarrow HeT^+ + e^- + \bar{\nu}_e\ . \tag{1.2}$$

The electron antineutrinos $\bar{\nu}_e$ are not detected. However, using energy momentum conservation their mass can be inferred from the energy spectrum of the electrons e^-. Neglecting the final states of the daughter molecule HeT^+ from the β decay the spectrum is obtained

[1] Those topics were already covered in many publications of the KATRIN collaboration. Here they are reduced to the necessary parts for this thesis. [Sei19] was found to be a good, much more comprehensive recent overview.

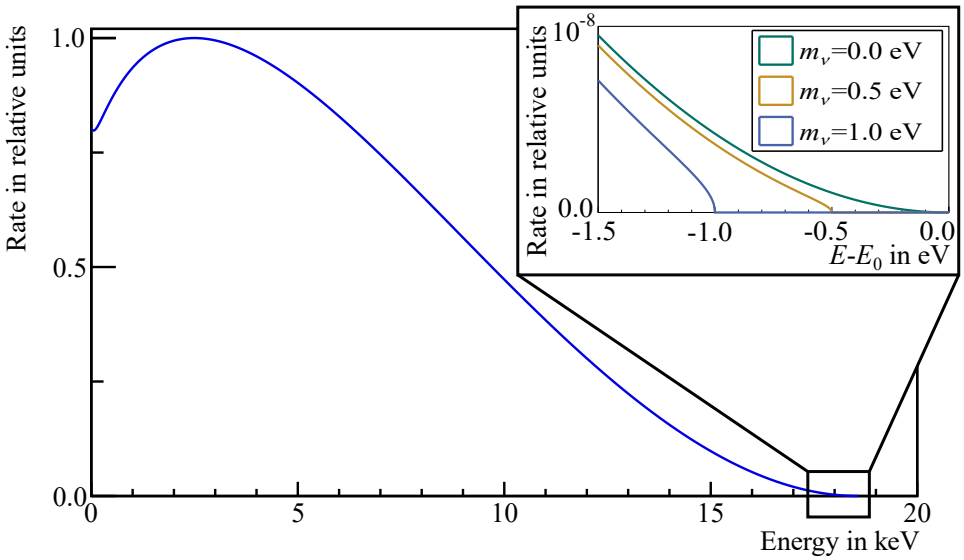

Figure 1.1.: Beta decay spectrum of tritium: Shown is the total energy spectrum of the electrons emitted in tritium beta decay normalised to the maximum. In the inset a close-up on the energy range 1.5 eV below the endpoint $E_0 \approx 18.6\,\mathrm{keV}$ is shown. Arbitrary effective electron antineutrino masses are included, which lead to a decrease of rate in comparison to the spectrum with zero mass. This rate decrease corresponds to the negative broadening expressed in equation 1.

by considering the phase space of the kinetic energy E and momentum p_e of the electrons and the corresponding quantities of the neutrino ν, leading to [OW08]

$$\frac{\mathrm{d}\dot{N}}{\mathrm{d}E} = A(E)\; p_\mathrm{e}\; E\; \underbrace{(E_0 - E)}_{E_\nu} \underbrace{\sum\nolimits_i |U_{ei}|^2 \sqrt{(E_0 - E)^2 - m_i^2}}_{p_\nu}\; \theta(E_0 - E - m_i)\;. \tag{1.3}$$

$A(E)$ is the amplitude, which depends on the matrix element of the transition and the coupling constant. The U_{ei} are elements of the Pontecorvo-Maki-Nakagawa-Sakata (PMNS) matrix, which specifies the mixing of the mass states m_i of the three neutrino flavours. The θ function ensures energy conservation. The energy of the endpoint E_0 is given by the released energy of the decay, corrected by the nuclear recoil of the daughter molecule.

The resulting electron spectrum is visible in figure 1.1. In the inset, one sees that the neutrino mass modifies the spectrum near the endpoint, most clearly visible in the lowering of the maximum electron energy. For each of the mass eigenstates m_i one expects a separate kink at its mass; however, KATRIN (and any other planned experiment) cannot resolve this substructure. The measured effective observable is the squared effective electron antineutrino mass [OW08]

$$m_\nu^2 = \sum_i^3 |U_{ei}|^2 m_i^2\;. \tag{1.4}$$

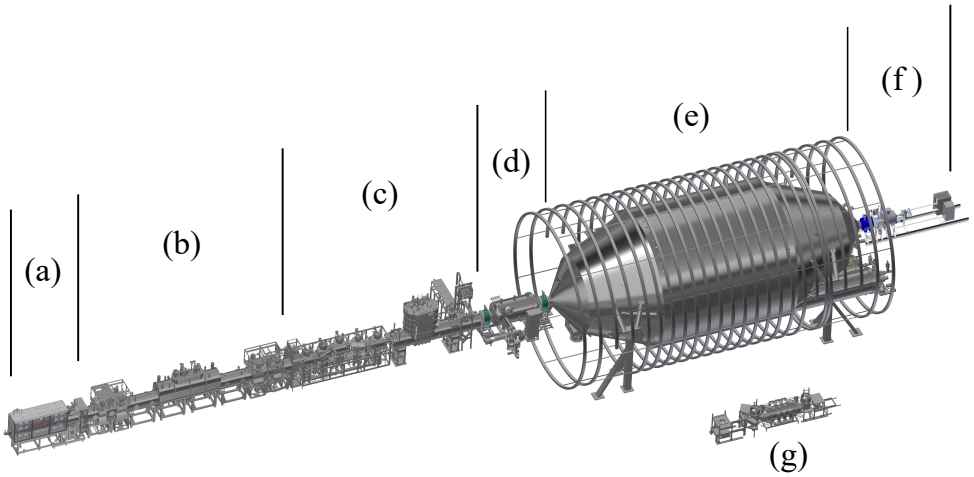

Figure 1.2.: The experimental setup of KATRIN, comprising:
(a) Rear Section, monitoring and calibration,
(b) Windowless Gaseous Tritium Source,
(c) Differential and Cryogenic Pumping Section, removal of the tritium,
(d) Pre Spectrometer, filtering of low energy electrons,
(e) Main Spectrometer, high resolution spectroscopy,
(f) Detector Section, position resolved electron counting,
(g) Monitor Spectrometer, precision high voltage monitoring.

To improve the sensitivity on m_ν by a factor of 10 compared to the predecessor experiments at Mainz and Troitsk [Kra+05; Ase+12], the sensitivity on m_ν^2 needs to be improved by a factor of 100. At KATRIN this is achieved by increasing the dimensions of the experiment and the source activity, while decreasing the systematic uncertainty budget.

The over 70 m long setup is shown in figure 1.2. The individual components are:

- *Rear Section*, figure 1.2(a): The rear section is used for calibration and monitoring.
- *Windowless Gaseous Tritium Source* (WGTS), figure 1.2(b): Here the decay of the molecular tritium takes place.
- *Transport Section*, figure 1.2(c): It prevents the gas inside the WGTS from reaching the spectrometers, while transporting the produced electrons adiabatically, using strong magnetic fields.
- *Spectrometer Section*, figure 1.2(d)+(e): Pre- and main spectrometer of the *Magnetic Adiabatic Collimation combined with Electrostatic* (MAC-E) filter type are used to block electrons with less energy than an applied retarding energy.
- *Detector*, figure 1.2(f): The detector counts the electrons which pass the retardation filter, thus producing an integral measurement of the tritium β spectrum.
- *Monitor Spectrometer*, figure 1.2(g): The monitor spectrometer is used for high voltage monitoring.

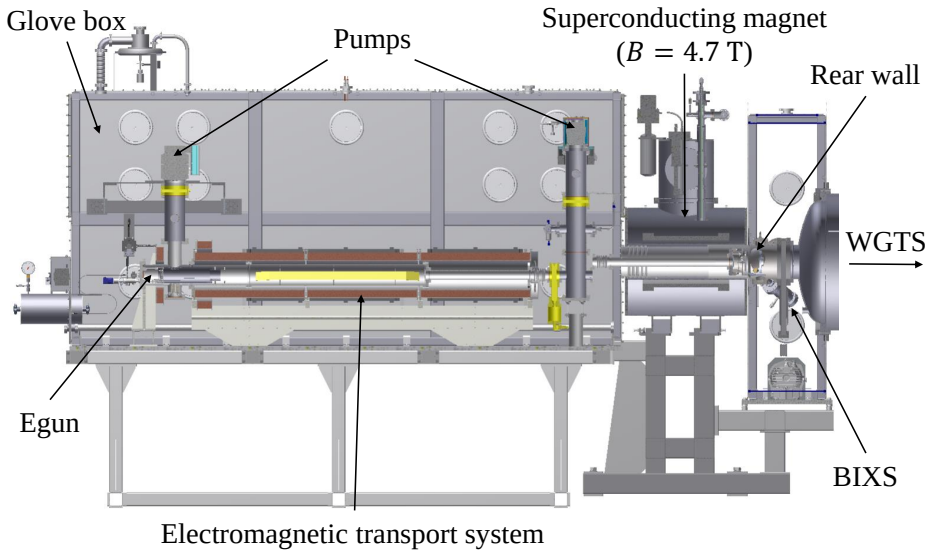

Figure 1.3.: The rear section: The rear section consists of three components; firstly the electron gun and its electromagnetic transport system, secondly a superconducting magnet focusing the flux to the rear wall disk, and thirdly the rear wall chamber, which includes the rear wall and the BIXS system for rate monitoring. The electron gun and rear wall chamber are surrounded by glove boxes which serve as second containment for tritium (after [Sei19]).

The isotropically generated electrons are guided from the source to the detector by a magnetic field in the range of a few tesla, which is created along the entire beam line by superconducting solenoids.

In the following the components and their significance for KATRIN and this work are explained in more detail.

1.1.1. The Rear Section

A detailed view of the rear section is shown in figure 1.3. It is placed at the upstream end of the WGTS and provides several calibration and monitoring devices:

Rear wall [Sch16]: The *rear wall* is used to define the electric potential of the source with a gold-coated stainless steel disk perpendicularly to the magnetic field lines. The gold-coating is used to guarantee that the inhomogeneity of the rear wall work function is smaller than 20 meV. Since the full magnetic flux hits the wall, the rear wall has significant influence on the low-density plasma forming in the WGTS. To influence the plasma conditions, a bias voltage can be applied, which is one of the key parameters of the studies presented in this work. Also, low energetic electrons can be created using the photoelectric effect by UV illumination of the rear wall [Ful20]. These electrons can be used to compensate or create space charges.

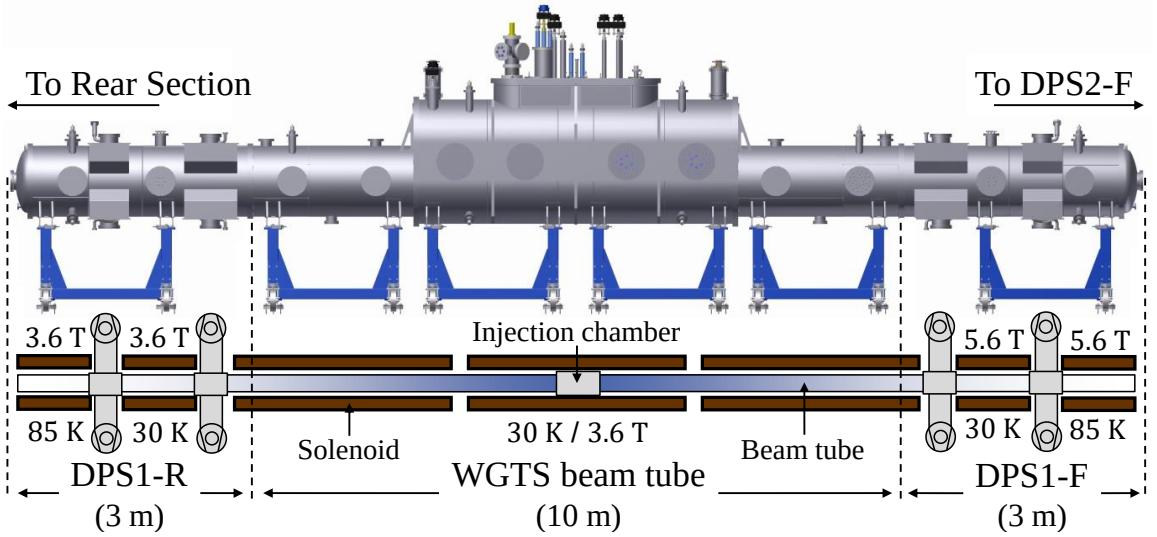

Figure 1.4.: Windowless gaseous tritium source: The central WGTS consists of the 10 m long, temperature-stabilised cryostat into which high-purity tritium is injected in the central chamber. The differential pumping sections (DPS1-R and DPS1-F) attached to each end of the central WGTS remove the gas from the beam line. The setup is connected to the rear and transport section on the left and right (after [Har15]).

Electron gun [Bab14; Sch16; Hei15]: The applications of the angular-resolved *electron gun* include the determination of the electron energy loss function discussed in section 1.2, continuous column density monitoring and alignment studies. 10^4 photo electrons are created per second using a UV illuminated cathode. Electrodes allow the acceleration of the electrons to keV energies, however the current hardware was designed to reach energies only up to 21 keV, whereas in this thesis the requirement to upgrade to 32 keV is shown. The energy width is approximately 0.2 eV. Before entering the WGTS through a hole in the center of the rear wall, the electrons pass through an aperture with a slight offset from the central axis. This prevents gas from the source from directly entering the rear wall chamber. The position of the electron beam can be controlled using dipole magnets in the WGTS, allowing to scan the whole flux tube.

BIXS [Röl15]: β *Induced X-ray Spectroscopy* (BIXS) is a method of rate monitoring of the source activity. It monitors the X-rays which are emitted from the rear wall due to electron impact. In KATRIN almost all of the 10^{11} electrons produced per second in the WGTS hit the rear wall, either directly or after being reflected at the spectrometer high voltage or magnetic fields. Thus, BIXS allows for rate monitoring on the 0.1 % level in 70 s measurement time.

1.1.2. The Windowless Gaseous Tritium Source

The *Windowless Gaseous Tritium Source* (WGTS), shown in figure 1.4, circulates the tritium for the β-spectrum measurement. It combines high luminosity with small systematic uncertainties. The tritium gas is provided by the Tritium Laboratory Karlsruhe (TLK) in a closed gas loop [Bor11]. Continuous filtering of the gas removes the daughter molecule HeT^+ as well as other impurities. Thereby an isotopic tritium purity inside the source of more than 95 % is ensured, which is monitored using a LAser RAman (LARA) system [Fis14].

Temperature: The central tube with a length of about 10 m and a diameter of 90 mm is embedded in a cryostat with a length of 16 m, a width of 1.5 m, a height of 4 m and a weight of 26 t [Gro+08]. Depending on the desired temperature it uses different coolants: For the nominal tritium measurement in the 30 K temperature range a two-phase neon cooling system is used, which reaches a temperature stability of ± 30 mK. The temperature stability directly affects the stability of the column density and thus the rate stability. For measurements involving krypton-83m the temperature needs to be raised to avoid freezing out of the krypton-83m at the walls. Accordingly, the neon is exchanged with coolants with more suitable vapour pressure. Temperature regimes of 80 K (nitrogen) and 100 K (argon) were used up to now.

The determination of the optimal temperature set point includes many factors: it is chosen to reduce the thermal Doppler effect leading to a broadening of the electron spectra and to ensure a high tritium density at low flow rate. On the other hand a low tritium pressure and small clustering of tritium molecules is required [KAT04b]. The KNM1 and KNM2 measurements were performed in the nominal 30 K mode. In KNM3a a focus was put on the study of systematics caused by the source plasma potential; to allow for equal source conditions in tritium and krypton-83m commissioning measurements, the temperature of 80 K was used also for the tritium measurement.

Column density [KAT04b]: The tritium or krypton gas is injected in the center of the central beam tube and pumped off by two *Differential Pumping Sections* at the rear and front sides (DPS-1-R/F-1 and DPS-1-R/F-2) with six Turbo-Molecular Pumps (TMP) each. They reduce the pressure from $p_{\mathrm{inj}} \approx 3 \cdot 10^{-3}$ mbar at the injection by around two orders of magnitude. The nominal value of the density is $\rho d \approx 5 \cdot 10^{21}\ \mathrm{m}^{-2}$, which is a compromise between a high signal rate and low probability of electrons to scatter off source gas. However, for co-circulation of tritium and krypton in $^{83\mathrm{m}}$Kr mode the tritium column density was limited to 30 − 40 % of the nominal value in the passed measurements, depending on the temperature. For a given column density, the increased temperature leads to a higher throughput of the gas, which has to be smaller than the pumping speed of the TMPs. Thus, while the column density could be increased from 22 % of nominal in the first neutrino mass measurement KNM1 to 84 % of nominal in KNM2, in KNM3a only 40 % of the nominal value was used to match the value of the KNM3 krypton measurement at 80 K.

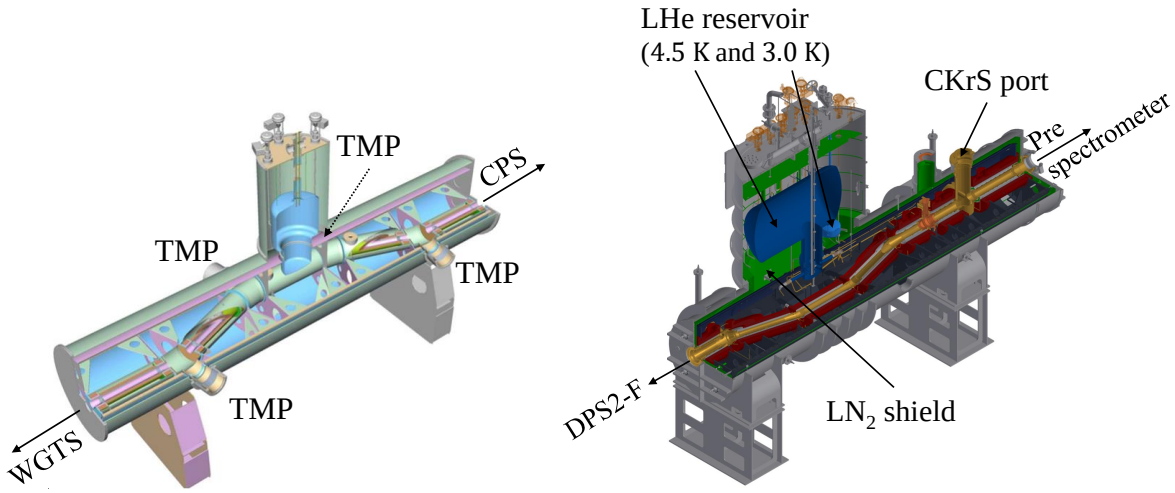

(a) DPS2-F (b) CPS

Figure 1.5.: Differential and cryogenic pumping section: In the DPS2-F the tritium gas throughput is reduced by five orders of magnitude using turbo molecular pumps. In the CPS an additional reduction by at least seven orders of magnitude is accomplished by using cryosorption. Both components use a chicanery of the beam tubes elements to block neutral particles (after [Höt12; Sei19]).

In forward direction (to the detector) the tritium gas cannot be contained within the source using a solid barrier, since the passing of the electrons through this barrier would lead to systematics. Consequently, the whole system from source to detector is a closely connected vacuum system, hence the term *windowless*. Regardless, it needs to be prevented that tritium gas reaches and contaminates the spectrometer section. This is achieved in a pumping section, which reduces the gas density, while ensuring adiabatic transport of the electrons.

1.1.3. The Transport and Pumping Section

The transport and pumping section is divided into the *Differential* and the *Cryogenic Pumping Sections* (DPS2-F and CPS), which reduce the partial pressure of tritium compounds to below 10^{-20} mbar and the overall gas pressure to below 10^{-11} mbar [KAT04b]. The first limit is necessary to prevent additional background created in the spectrometer by tritium decay, the second to prevent scattering of electrons on residual gas.

DPS2-F: As shown in figure 1.5a, the DPS2-F consists of five connected tubes. A tilt of 20° between the tubes ensures that neutral particles like tritium molecules cannot pass in direct line of sight to the spectrometer section. The four pump ports between the beam tube elements house TMPs, which reduce the tritium gas flow by five orders of magnitude. The electrons are transported adiabatically through the 7 m long unit by a magnetic field of up to 5.5 T, which is created using superconducting solenoids. In addition, the DPS2-F

is used for the analysis and blocking of ions such as T_n^+ or $^3(HeT)^+$, which are created in chemical and ionisation processes. Blocking and analysis are performed using ring- and dipole electrodes [Kle19].

CPS: Another reduction of the tritium flow is achieved by the CPS, which is visible in figure 1.5b. In a process called cryosorption gas particles get adsorbed on a 3 K cold argon frost layer. As the DPS2-F, the CPS uses a chicanery for neutral particles. Its overall reduction factor was demonstrated to be better than 10^{-10} [Eic+08; Jan15; Röt19].

CKrS: A measuring device for calibration and monitoring can be inserted in one of the pump ports of the CPS: The *Condensed Krypton-83m Source* (CKrS), which consists of a sub mono-layer of ^{83m}Kr on a highly oriented pyrolytic graphite (HOPG) substrate. It can be moved inside the flux tube to irradiate different pixels [Are+18]. In addition to measurements of the spectrometer transmission properties it also allows to determine parameters describing the ^{83m}Kr conversion electron lines. Compared to the measurements of the extended gaseous source described in section 1.3 it has the advantage that, due to its small dimensions, it does not suffer from the systematic of residual beam tube work function inhomogeneities. This is further discussed in chapter 6.

1.1.4. The Spectrometer Section

KATRIN uses a total of three MAC-E filters for the determination of the electron energy (pre- and main spectrometer) and for monitoring of the stability of the high voltage (monitor spectrometer).

The monitor spectrometer can be connected to the same voltage supply as the main spectrometer. It repeatedly measures the position of a ^{83m}Kr conversion electron line from an implanted ^{83}Rb/^{83m}Kr source, which functions as nuclear standard [Sle16].

The pre spectrometer is usually operated at a retarding voltage that allows only high-energy electrons a few 100 eV into the spectrum to pass on to the main energy filter. This reduces background creation by scattering processes in the large volume of the main spectrometer, which performs the precision spectroscopy of the remaining electrons.

Principle of the MAC-E filter: In the following the principle of the MAC-E filter is explained, which applies to all three spectrometers. This section is largely based on [Mac16].

An illustration of the MAC-E filter (based on the main spectrometer) is found in figure 1.6. The electric and magnetic fields are shown, as they are essential for the working principle of the MAC-E filter. Its magnetic field configuration is used to collimate the initial isotropic electron impulses. The energy spectroscopy is then carried out with an electrostatic retarding voltage U, which works as a high-pass filter. The details are as follows:

The electrons move in cyclotron motion around the magnetic field lines. In relation to the magnetic field their kinetic energy E_{kin} can be decomposed into a transverse $E_\perp$ and a

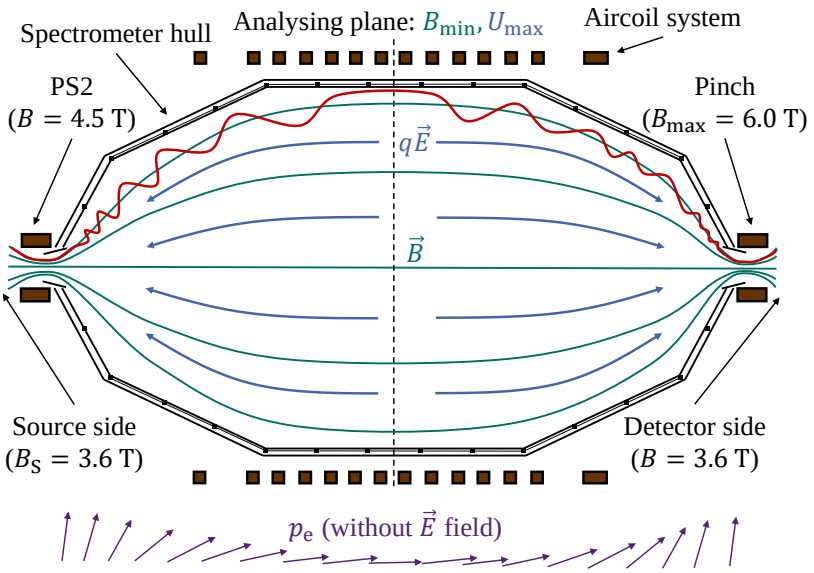

Figure 1.6.: Working principle of the MAC-E filter: Superconducting solenoids create the guiding magnetic field (green). The field strength is minimal in the middle of the spectrometer. Since the magnetic moment is conserved, the momentum of the electrons is collimated to be parallel to the magnetic field when the electrons reach the central analysis plane. As a consequence electrons with a total energy smaller than the retarding energy qU are reflected and only electrons of higher energies reach the detector (after [Sei19]).

parallel component $E_{\parallel}$

$$E_{\text{kin}} = E_{\perp} + E_{\parallel} \,. \tag{1.5}$$

The angle between the parallel component and the total momentum is called the polar angle θ.

For vanishing electric fields and low magnetic field B gradients, the movement of the electrons is adiabatic ($\delta E_{\text{kin}} = 0$)

$$\frac{\Delta B}{B} \ll 1 \,. \tag{1.6}$$

Since in this case the angular momentum $\vec{L}$ is conserved, the magnetic moment

$$\vec{\mu} = \frac{e}{2m_e}\vec{L} \tag{1.7}$$

is also a constant [Zub11]. Here e is the electric charge and m_e the mass of the electron. In non-relativistic approximation the transverse energy of the electron can be expressed as [Zub11]

$$E_{\perp} = -\vec{\mu}\vec{B} \,, \tag{1.8}$$

i.e. it is proportional to the magnetic field strength. This allows to express the transverse energy as function of the magnetic field strength

$$E_{\perp}(B) = E_{\perp}(B_S) \cdot \frac{B}{B_S} \,, \tag{1.9}$$

where B_S is the field at the point of the creation of the electrons. Due to the conservation of the total energy lowering the magnetic field transfers transverse energy to parallel energy.

In the spectrometer the electrons are slowed down by the retarding voltage U applied to the spectrometer vessel. They are reflected if their parallel energy in the analysing plane reaches zero, leading to the following condition:

$$\Rightarrow E_{\parallel} = E_{\text{kin}} - qU - \vec{\mu}\vec{B} \stackrel{!}{=} 0 \,. \tag{1.10}$$

If the magnetic field B_{min} in the analysing plane is small electrons with energies smaller than qU are reflected. Since all electrons of higher energies than qU can pass the spectrometer and are counted at the detector, MAC-E filters perform an integrated energy measurement.

Maximum acceptance angle: The larger the starting angle of the electrons, the larger is their pathway from the source to the detector. A larger pathway increases the probability of scattering off gas in the source and the loss of energy due to the emission of synchrotron radiation. It is therefore of advantage to exclude electrons with pitch angles larger than the maximum acceptance angle θ_{max} from the analysis. This is accomplished by inverse use of equation 1.9: For collimation the ratio B_{min}/B_S should be as small as possible, since this minimises the transverse component of the electron motion. Reversely, electrons can be reflected if they move into an increasing magnetic field $B_{\text{max}} > B_S$, since this can increase the transverse energy to a point, were the parallel energy vanishes. This is known as the magnetic mirror effect.

The maximum magnetic field is applied between spectrometer and detector. The resulting maximum acceptance angle is given by [KAT04b]

$$\theta_{\text{max}} = \arcsin \sqrt{\frac{B_S}{B_{\text{max}}}} \,. \tag{1.11}$$

Filtering width: The size of the vacuum vessel limits the minimum ratio of B_{min} and B_{max}: Due to the conservation of the magnetic flux a reduction of the magnetic field strength leads to an expansion of the field lines, which eventually intersect the walls of the vacuum vessel. The minimum ratio of B_{min} and B_{max} limits the possible energy resolution, which is explained considering the angular distribution of the electrons:

An electron starting in parallel to the magnetic field with an energy of $E = qU$ can just pass the retarding potential. Since the transverse component in the analysing plane is not vanishing due to the non-vanishing magnetic field, an electron starting with the maximal acceptance angle $\theta = \theta_{\text{max}}$ needs the additional (*surplus*) energy

$$\Delta E = E \cdot \frac{B_{\text{min}}}{B_{\text{max}}} \tag{1.12}$$

to be detected. Thus, ΔE is the width of the energy filter. It does not only depend on the ratio of the maximum and the minimum magnetic field, but also scales linearly with the energy of the electrons. The derivation only holds for isotropic electron sources; for focused sources like the electron gun, the reader is referred to [Zac15; Beh17].

Transmission function: The previous derivation of the filter width used the two extremal polar angles θ_{max} and zero, resulting in zero or one transmission probability. The transmission probability for polar angles in between those values and for general energies of the electrons is described by the transmission function $\mathcal{T}(E, qU)$. For isotropically generated electrons it holds in first order [KAT04b]

$$\mathcal{T}(E, qU) = \begin{cases} 0 & E - qU < 0 \\ \dfrac{1 - \sqrt{1 - \frac{E-qU}{E} \cdot \frac{B_S}{B_{\text{min}}}}}{1 - \sqrt{1 - \frac{B_S}{B_{\text{max}}}}} & 0 \leq E - qU \leq \Delta E \\ 1 & E - qU > \Delta E \end{cases} . \tag{1.13}$$

In higher orders the transmission function is modified by corrections for relativistic effects and synchrotron radiation, and by the modification of the angular distribution of the electrons due to inelastic scattering [Gro15]. While the former two are taken into account in all analyses of this work, the latter was neglected due to the unfeasible computation time.

Due to inelastic scattering of the electrons on the gas molecules inside the WGTS the transmission function needs to be convolved with the energy dependent probability of (multiple) energy losses, resulting in the response function. All three functions (transmission, energy loss and response function) are shown in section 1.2.2.

Field setting at KATRIN: KATRIN's design magnetic field values are $B_S = 3.6\,\text{T}$, $B_{\text{min}} = 3 \cdot 10^{-4}\,\text{T}$ and $B_{\text{max}} = 6\,\text{T}$ [KAT04b]. Consequently, the spectrometer vacuum vessel has a length of about 23 m and a maximum diameter of about 10 m. At the tritium endpoint of $E_0 \approx 18.6\,\text{keV}$ the resulting values of the maximum acceptance angle and filtering width are

$$\theta_{\text{max}} \approx 50.8^\circ \qquad \text{and} \qquad \Delta E \approx 0.93\,\text{eV} . \tag{1.14}$$

However, to guarantee safe and stable long-term operation of the superconducting magnets it was decided to reduce the magnetic fields to 70 % of nominal for all measurements [Hac17]. This does not affect the resolution or acceptance angle, since all fields are scaled uniformly.

The filtering width is much larger than the envisaged neutrino mass sensitivity of 200 meV. The latter is only achieved by the precise knowledge and modelling of the transmission function and its consideration in the modelling of the recorded spectrum. Thus, the lowering of the maximum electron energy by a non-vanishing neutrino mass (seen in figure 1.1) cannot be resolved by KATRIN, but it measures the rate decrease corresponding to the (negative) spectral broadening (see equation 1).

1.1.5. The Detector Section

Electrons that have passed the main spectrometer are directed to the *Focal Plane Detector* (FPD) system, visible in figure 1.7. Its main component is a 90 mm silicon PIN diode (i.e. a

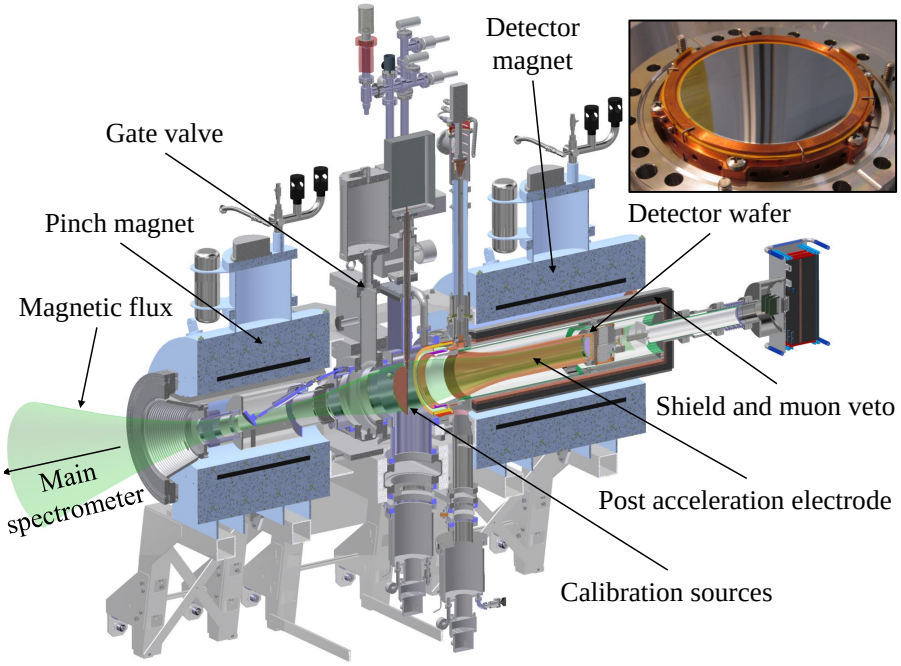

Figure 1.7.: Focal plane detector system: The setup of the detector section comprises two superconducting solenoids, calibration sources, the detector and the vacuum system and shielding. A post-acceleration can be applied to shift the electron energy to a region with a preferable signal-to-background ratio (after [Sei19]).

stack of a *p-type*, an undoped *intrinsic* and a *n-type* semiconductor) divided into 148 pixels, which allows radial analysis of the spectra. The energy resolution of the FPD of about 1-2 keV is used for background discrimination [Ams+15].

1.2. Neutrino Mass Analysis with KATRIN

This section gives a brief insight into simple analysis methods (section 1.2.1) and the analysis software used for this purpose (section 1.2.2). The final section 1.2.3 describes the prediction of the sensitivity of KATRIN in neutrino mass determination and gives an overview of the most important systematics.

1.2.1. KATRIN Likelihood Function

This section evaluates on the principle of maximum likelihood determination (or χ^2 minimisation), which allows the model parameters to be adapted to the measured data. It is largely based on [Kle14] and [Mac16]. Further literature on other, complementary methods can be found for example in [Kle14].

KATRIN measures the total number of integral counts $N_{\mathrm{obs},i}$ for i settings of the retarding energy qU_i and the respective measurement times t_i. For the extraction of the sought-after

neutrino mass m_ν the theoretically expected counts $N_{\mathrm{theo},i}(m_\nu^2)$ [2] for each set value of the retarding energy must be predicted precisely.

Nuisance parameters: Since the theoretical modelling is not complete in practice due to uncertainties and incomplete modelling, it is helpful to make $N_{\mathrm{theo},i}$ dependent on further free parameters $x \in X$, the so-called nuisance parameters. For the KATRIN neutrino mass measurements, the parameters used in the standard fit model are the tritium β-spectrum endpoint E_0, a constant background rate Bg and a spectrum intensity I.

Statistical fluctuations and likelihood: Since the observed counts are generated by a radioactive decay, they are Poisson distributed, which is also referred to as *statistical fluctuations*. Therefore, if the experiment is repeated several times, it gives a different result of the fit parameters X each time. Since the underlying Poisson distribution of the counts is known, the frequency distribution of X after an infinite number of measurements can be predicted. However, only one measurement can be performed. The probability distribution for the outcome of this measurement, given the statistical fluctuations, is called the likelihood $\mathcal{L}$.

For a number of signal events $\gtrsim 25$ the Poisson distribution of the measured counts can be approximated as a Gaussian distribution. Therefore, the likelihood is given as the product of the Gaussian distributions at each retarding energy or measurement point i

$$\mathcal{L}(N_{\mathrm{obs}}, N_{\mathrm{theo}}) = \prod_i \exp -\frac{1}{2}\left(\frac{N_{\mathrm{obs},i} - N_{\mathrm{theo},i}(X)}{\sigma_i}\right)^2 . \tag{1.15}$$

The quantity σ_i is the standard deviation of the counts. For the case of a Poisson distribution it is given by

$$\sigma_i = \sqrt{N_{\mathrm{theo},i}} . \tag{1.16}$$

Minimum χ^2: The goal of the analysis is to find the parameters X which lead to the maximum likelihood. However, for easier computation the likelihood is usually replaced by the double negative log likelihood, the χ^2 function

$$\chi^2 \equiv -2 \log \mathcal{L} = \sum_i \left(\frac{N_{\mathrm{obs},i} - N_{\mathrm{theo},i}(X)}{\sigma_i}\right)^2 , \tag{1.17}$$

and the best fit parameters of the X are obtained at the minimum of the χ^2. Due to the form of equation 1.17 the χ^2 minimisation is sometimes referred to as *weighted least squares* [Jam04].

The result of a measurement is then the set of parameters X which gives the minimum χ^2. Due to the erroneous nature of the measurement, caused both by the statistical fluctuations

[2] Since the theoretical modelling of the β spectrum depends only on the square of the neutrino mass, this is the actual observable.

and other, *systematic uncertainties*, this result is only as good as the determination of its uncertainty. Usually the latter is provided in the form of a *confidence interval* around X which, when the measurement could be repeated infinitely often, would cover the fraction of measurements specified by the *confidence level*. Thus, a small confidence interval at a large confidence level is a precise measurement. This confidence interval is related to the statistical $\sigma_{\text{stat}}(X)$ and systematic $\sigma_{\text{syst}}(X)$ uncertainties, which can both be inferred from the χ^2 function.

Determination of the statistical uncertainty: The size of the $\sigma_{\text{stat}}(X)$ is linked to the width of the χ^2 function near the minimum. If the χ^2 is interpreted as a function of one of the $x \in X$, it is a parabola around the minimum, if x enters the model $N_{\text{theo},i}$ linearly for its minimum value [Jam04]. The measured total counts are directly proportional to the total measurement time t_{tot}. Thus, it follows from equation 1.17 that the statistical uncertainty and the root of t_{tot} behave anti-proportional for Gaussian distributed variables and the Poisson distributed counts

$$\sigma_{\text{stat}}(X) \propto \frac{1}{\sqrt{t_{\text{tot}}}} \,. \tag{1.18}$$

The constant of proportionality is related to the second derivative of the χ^2 function.

Determination of systematic uncertainties: Different methods can be used to determine the size of the systematic uncertainties $\sigma_{\text{syst}}(X)$ caused by uncertainties of parameters P:

- **Pull method:** For parameters of mean P_{meas} with Gaussian uncertainty $\sigma(P)$ equation 1.17 can be amended with further terms of the form $\left(\frac{P_{\text{fit}}-P_{\text{meas}}}{\sigma(P)}\right)^2$ and by fitting P_{fit}. If the X are correlated to the P this changes the width of the χ^2 parabola in the direction of the X compared to the purely statistical width, which is interpreted as $\sigma_{\text{syst}}(X)$. Depending on the size of $\sigma(P)$ the change can be positive or negative. Thus, if $\sigma(P)$ is actually known from a more sensitive experiment, pull terms can also be used to decrease the uncertainty.
- **Shift method:** In the shift method, non-fitted parameters are deflected in the model by ΔP. If the X are correlated to the P this shifts the χ^2 parabola in the direction of the X, leading to a change of X by ΔX.

The pull method is used in this thesis to incorporate literature values of some of the krypton lines, as discussed in chapter 6. The shift method is used whenever systematic uncertainties are investigated in simulation studies, for example for all of chapter 5.

Asimov data: The determination of the uncertainties does not require an actual measurement. *Toy data* $N_{\text{obs},i}(X_{\text{toy}})$ can be generated by the model which is also used to predict $N_{\text{theo},i}(X_{\text{fit}})$. Also, this can be done without statistical fluctuations, such that $N_{\text{obs},i}(X_{\text{toy}}) = N_{\text{theo},i}(X_{\text{fit}})$, if $X_{\text{toy}} = X_{\text{fit}}$. This replaces the counts by their most representative values, i.e. without systematics the fit needs to recover the exact input values X_{toy}. This is referred to as using *Asimov data* [Cow+11].

Combined uncertainty: From the central limit theorem it follows that, given the combination of many systematic uncertainties, the total uncertainty can be considered as Gaussian uncertainty. Since uncorrelated Gaussian variances are added in quadrature and systematic and statistical uncertainties are by definition uncorrelated they can be combined like

$$\sigma_{\text{tot}} = \sqrt{\sigma^2_{\text{stat}} + \sigma^2_{\text{syst,tot}}} \,. \tag{1.19}$$

Confidence interval: In the case of Gaussian distributions, the confidence level is obtained by multiplying σ_{tot} by constant factors. A 1.645 σ_{tot} interval covers 90 % of the total area of a Gaussian, whereas a 1.0 σ_{tot} interval only covers 68.3 %.

In the following the spectrum simulation used to obtain the theoretical prediction $N_{\text{theo},i}$ is briefly discussed.

1.2.2. Fit and Spectrum Simulation

For all analyses carried out in this work the software framework of KaFit and *Source Spectrum Calculation* (SSC) is used. Booth are based on C++ and the ROOT library [Ant+09], but have various extensions to other languages like python or libraries like BOOST. Their connection and relation to the variety of KATRIN analysis tools is shown in figure 1.8.

KaFit: KaFit is a software package which can perform the likelihood calculation and χ^2 minimisation using different approaches. Only classical minimisers (based on ROOT::Minuit and ROOT::Minos uncertainty estimation [Jam04]) were used in this work in a frequentist method [Ken49].

The calculation of the expected counts $N_{\text{theo},i}$ is performed by SSC, which is explained briefly in the following. A comprehensive overview is found in [Kle+19].

Source spectrum calculation: Using SSC, the expected count rate $\dot{N}(qU)$ can be calculated for given retarding energy qU. The calculation can be done for each pixel individually, which is mapped to a radial starting position of the electrons in the source by the magnetic field. Furthermore, the source can be segmented longitudinally to take into account spatial dependencies of the source parameters. This calculation of many spectra for individual regions of the source, called voxelisation [Höt12], is shown in figure 1.9.

The total rate is thus given by the following summation over WGTS slices:

$$\dot{N}(qU) = \sum_{i}^{\text{slices}} \epsilon_{\text{det}} \frac{\Omega_i}{4\pi} \int_{-\infty}^{\infty} N_i \left(\frac{\mathrm{d}\dot{N}}{\mathrm{d}E} \right) R(E + qV_i, qU) \, \mathrm{d}E \,. \tag{1.20}$$

Thereby ϵ_{det} is the detector efficiency, $\frac{\Omega}{4\pi}$ the accepted solid angle, N_i the number of tritium atoms, $\frac{\mathrm{d}\dot{N}}{\mathrm{d}E}$ the differential tritium spectrum, $R(E, qU)$ the response function of the experiment and V_i the potential in each source slice. The response function is described

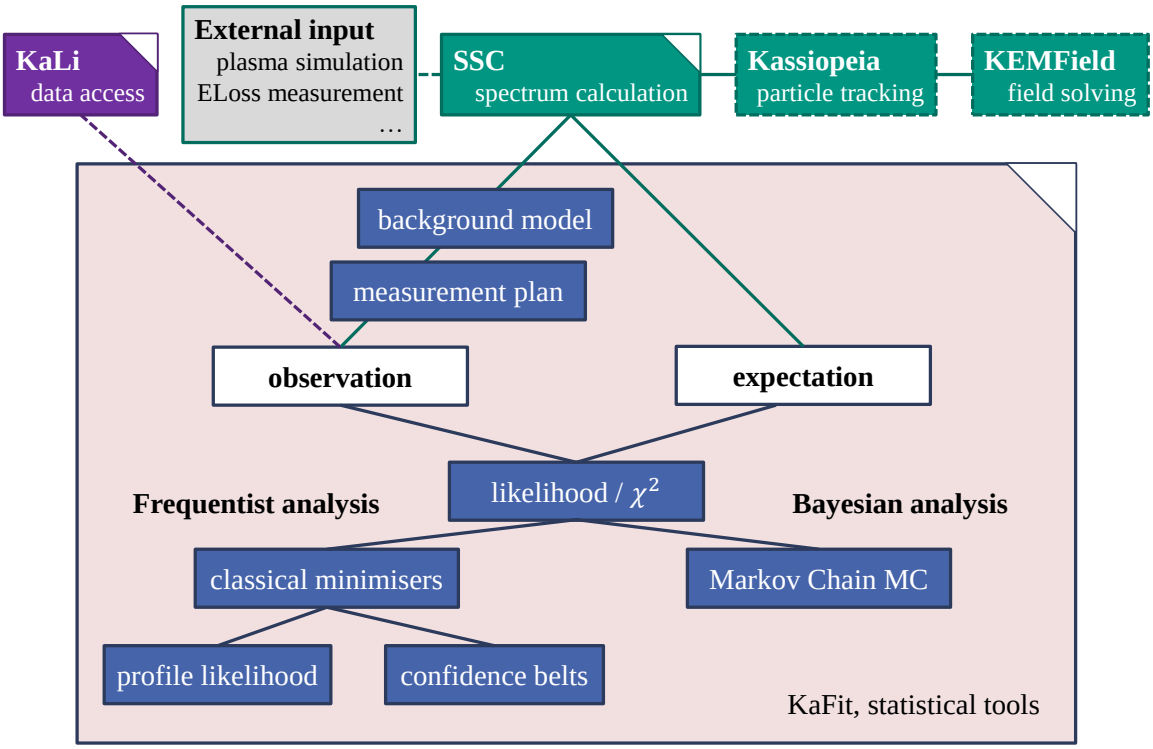

Figure 1.8.: Structure of the KATRIN analysis tools: KaFit can perform a χ^2 minimisation or maximum likelihood estimation using different methods. The spectrum calculation is performed by SSC, which comprises many tools or external inputs (for example plasma profiles like figure 1.19 or the energy loss function figure 1.10). SSC is also used to generate Asimov spectra (after [Kle14]).

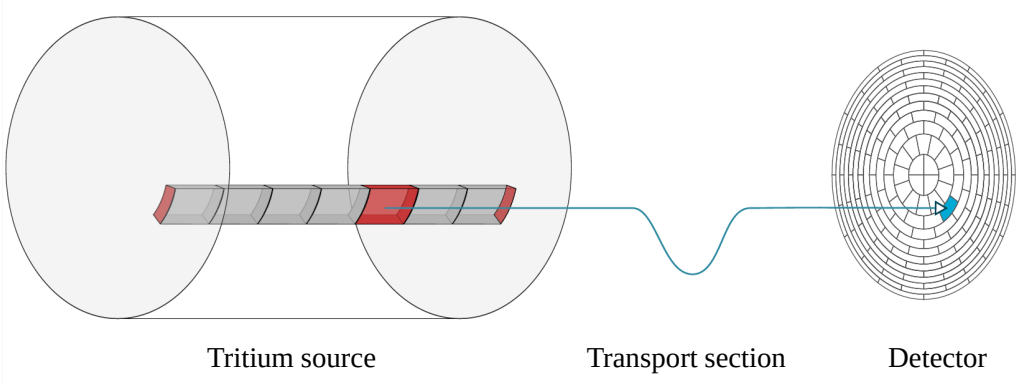

Figure 1.9.: Mapping of source regions to the detector and voxelisation: The electron origin in the source is mapped to detector pixels by the magnetic field lines. As a consequence the spectrum produced in each longitudinal intersection of the source with the magnetic field lines is mapped to distinct detector pixels (indicated in grey). Additionally, the longitudinal regions along this field line can be further divided into voxels, allowing to include longitudinal dependences of source quantities in the modelling (after [Kle14; Höt12; Mac16]).

below. Each quantity is obtained from models describing the physical process: The differential tritium spectrum is the decay spectrum as produced by the decay of the molecular tritium in the source. Its modelling includes the theoretical description of the β spectrum as well as nuclear recoil, excitations of the daughter molecule or a (relativistic) Doppler broadening. Quantities depending on the longitudinal coordinate z are taken from corresponding profiles, for example from gas dynamics simulations in the case of N_i.

Response function: The response function is used to convolve any other external influence on the electron spectrum from the point of creation of the electrons in the source to the detection at the focal plane detector. In addition to for example the transmission function of the spectrometer this also includes the inelastic scattering of the electrons on the gas in the source. Figure 1.10 shows the corresponding energy loss probability as function of the surplus energy of the incident electrons with regard to a gas particle. Multiple scatterings are considered by repeated convolutions of the energy loss function with itself, as shown in chapter 5. In total, this leads to the structure of the response function shown in figure 1.11.

1.2.3. Sensitivity of KATRIN on the Neutrino Mass

Following the considerations in section 1.2.1 the sensitivity of KATRIN on m_ν as defined in [KAT04b] is given by

$$S_{m_\nu}(90\%) = \sqrt{1.645 \cdot \sigma_{\text{tot}}(m_\nu^2)} = \sqrt{1.645 \cdot \sqrt{\sigma_{\text{stat}}^2(m_\nu^2) + \sigma_{\text{syst}}^2(m_\nu^2)}} \,. \tag{1.21}$$

A measured value of the neutrino mass of $S_{m_\nu}(90\%)$ allows to reject the null hypothesis of vanishing neutrino mass with 90 % confidence.

Statistical uncertainty: Many analyses have determined $\sigma_{\text{stat}}(m_\nu^2)$ and $\sigma_{\text{syst}}(m_\nu^2)$ in the recent years. It strongly depends on a variety of factors like the background rate, the used distribution of the measurement time to the energy bins of the spectrum (called *Measurement Time Distribution*, MTD) or the magnetic field setting determining the energy resolution. This list is by no means comprehensive and some effects which were not considered before were observed with the start of the first tritium measurement campaigns. Thus, these sensitivity analyses are subjected to constant changes and here only the one of [Kle14], which was performed prior to the first measurement, is discussed. It uses values from the design report [KAT04b] for the MTD, the total measurement time (three years net data taking) and background (10 mcps), yielding

$$\sigma_{\text{stat}}(m_\nu^2) = 0.0165\,\text{eV}^2 \,. \tag{1.22}$$

Systematic uncertainty: The list of relevant systematics identified in the design report are found in table 1.1. The total summation of the individual uncertainties is $\sigma_{\text{sys,tot}} = 0.01\,\text{eV}^2$. To leave room for unknown systematics the total systematic budget of KATRIN was chosen

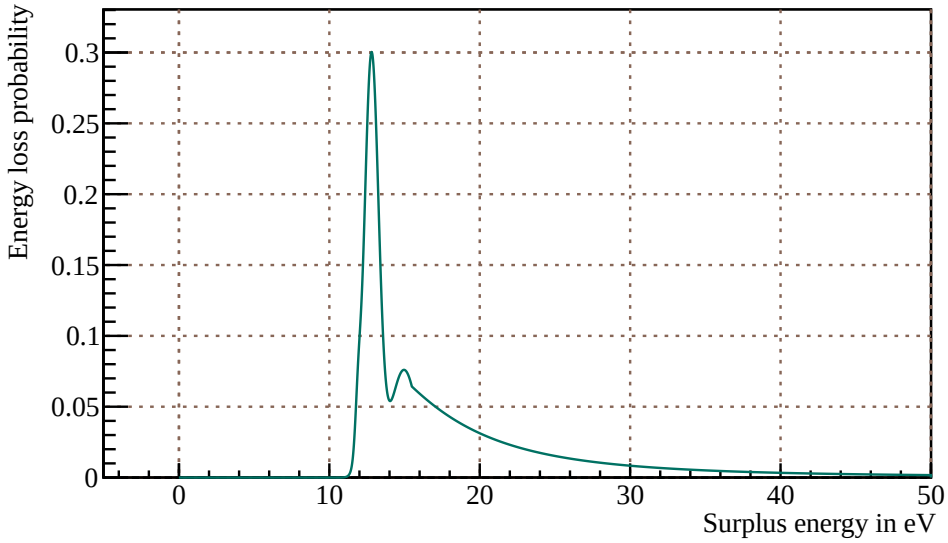

Figure 1.10.: Energy loss function: The energy loss function describes the inelastic energy loss of electrons due to scattering on tritium molecules. A key feature for the topic of this thesis is its gap of ≈ 13 eV. Thus, electrons need to loose at least ≈ 13 eV of energy upon single scattering. The function was measured by KATRIN during KNM2 [KATep]. Importantly, this measurement is only valid for electron energies close to the tritium β-spectrum endpoint, which leads to uncertainties in the analysis of the krypton-83m measurements. This is discussed in chapter 6.

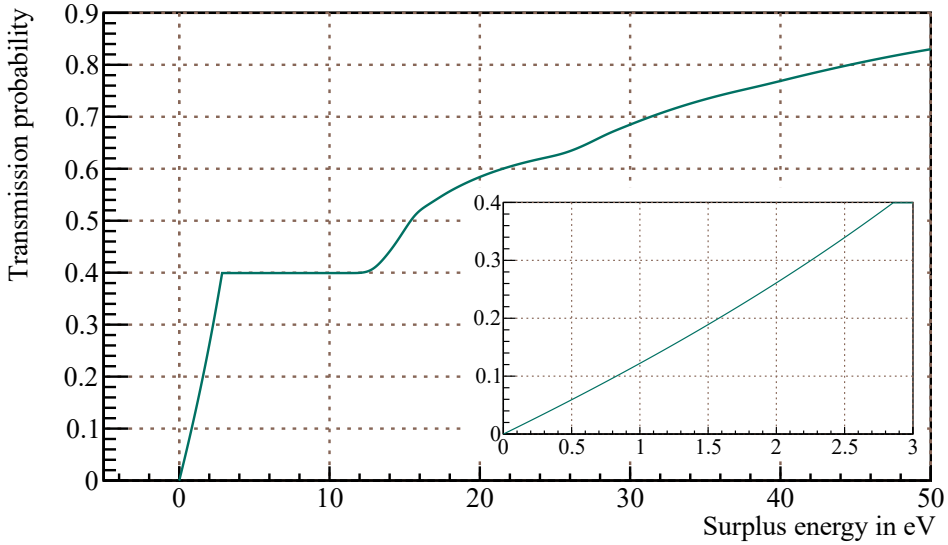

Figure 1.11.: Response function: The gap of the energy loss function is also visible in the response function, where multiple steps with a spacing of ≈ 13 eV are visible for the increasing scattering multiplicities. The first step starting from zero energy is given by the transmission function. A close-up can be seen in the inset. Due to the width of the energy loss function, increasing steps of higher scattering multiplicities get broadened.

Table 1.1.: **KATRIN systematic uncertainties.**
Sources of systematic uncertainties of the KATRIN experiment, as stated in the design report (from [KAT04b; Mac16]). For a recent, conclusive re-evaluation the reader is referred to [Sei19].

source of systematic shift	**achievable / projected accuracy**	**systematic shift** $\sigma_{\mathrm{syst}}(m_\nu^2)$ $(10^{-3}\,\mathrm{eV}^2)$
description of final states	$f < 1.01$	< 6
T^- ion concentration	$< 2 \cdot 10^{-8}$	< 0.1
unfolding of energy loss func. $f(\epsilon)$		< 6
monitoring of column density ρd	$\Delta T/T < 2 \cdot 10^{-3}$ $\Delta\Gamma/\Gamma < 2 \cdot 10^{-3}$ $\Delta\epsilon_T/\epsilon_T < 2 \cdot 10^{-3}$ $\Delta p_{\mathrm{inj}}/p_{\mathrm{inj}} < 2 \cdot 10^{-3}$ $\Delta p_{\mathrm{ex}}/p_{\mathrm{ex}} < 0.06$	$< \frac{\sqrt{5}\cdot 6.5}{10}$
background slope	$< 0.5\,\mathrm{mHz/keV}$ (Troitsk)	< 1.2
HV variations	$\Delta\mathrm{HV}/\mathrm{HV} < 3\,\mathrm{ppm}$	< 5
WGTS potential variations	$\Delta U < 10\,\mathrm{meV}$	< 0.2
WGTS mag. field variations	$\Delta B_S/B_S < 2 \cdot 10^{-3}$	< 2
elastic e^- - T_2 scattering		< 5
identified syst. uncertainties	$\sigma_{\mathrm{sys,tot}} = \sqrt{\sum \sigma_{\mathrm{sys}}^2} \approx 0.01\,\mathrm{eV}^2$	

slightly larger and equal to the statistical uncertainty after three years net data taking. This leads to

$$\sigma_{\mathrm{sys,tot}} \lesssim 0.017\,\mathrm{eV}^2\,. \tag{1.23}$$

Sensitivity: Plugging both values into equation 1.21 the following sensitivity of KATRIN is obtained

$$S_{m_\nu}(90\%) = 197\,\mathrm{meV}\,, \tag{1.24}$$

which is approximately the usually quoted value.

As discussed, it depends on many factors which were not known by the time of the analysis leading to this sensitivity. For example, the central topic of the thesis at hand is the investigation of source potential systematics, which is one of the systematic uncertainties which in the current analysis of the KNM2 neutrino mass campaign is much larger than predicted by the design report. The essential tool for the study of the source potential systematics is the $^{83\mathrm{m}}$Kr mode of the gaseous source which is discussed in the following section.

1.3. ^{83m}Kr Mode of the Gaseous Source for Investigation of Systematics

^{83m}Kr is commonly used as calibration standard in neutrino experiments [Rob+91; Wil+87; Pic+92; SD95; FP12] as well as in the search for dark matter [LUX+14]. At KATRIN in principle it allows for an in situ monitoring of the difference of the spectrometer and source electric potential. As discussed below, it is the only means to access the longitudinal inhomogeneity of the source potential. The basic idea is to inject a gaseous electron source with a well known electron spectrum into the WGTS and to monitor the distortion of the spectrum shape, caused by the presence of systematic effects [Wil03; Bon03]. Prior to the campaigns carried out in this work it has already been applied in several other measurement campaigns [Sei19; Sle+19] which are described in more detail in chapter 6.

Requirements on calibration source for source potential systematics: The energy spectroscopy at KATRIN relies on the precise knowledge of the difference of the starting and analysing plane electric potential. The calibration and monitoring of this potential difference has to meet three main requirements:

- **Small energy width:** The potential difference of WGTS and spectrometer must be calibrated with a precision in the 10 mV range [KAT04b], which is more easily achieved by using a quasi mono-energetic calibration source.
- **Gaseous source:** Since the WGTS is an extended source, the calibration electron source must be dispersed together with the tritium gas within the WGTS to be sensitive to the spatially extended electric source potential.
- **No contamination:** KATRIN is a low background experiment. Accordingly, the calibration source needs to have a small half-life such that it does not contaminate the experiment, leading to interference with the tritium measurement.

Gaseous ^{83m}Kr fulfils all three requirements. Quasi mono-energetic electrons in the 5-35 keV energy range are created in the process of inner conversion. The conversion lines have widths in the few eV range. The energy scale of the krypton electrons is comparable to the tritium endpoint of $E_0 \approx 18.6$ keV and therefore fits to the KATRIN hardware. The half-life $T_{1/2} = 1.83$ h [McC15] of ^{83m}Kr is short enough that it does not interfere with the tritium measurements or leads to contamination. Most importantly, it is gaseous under operating temperatures and pressures feasible for KATRIN operation. Therefore it can be mixed with the tritium gas within the WGTS which allows for the determination of source potential systematics.

Generation and activity of the krypton-83m: Since the width of the krypton-83m conversion electron lines in question is on the order of 1 eV a several mV sensitivity on the source potential can only be achieved in a high-statistics measurement, which allows for the precise determination of the spectrum shape. Consequently, the activity of the krypton-producing source nuclide rubidium-83 is several 100 MBq [Vén+14], and in the future even 10 GBq. The half-life of $T_{1/2} = 86.2$ d [McC15] of rubidium-83 is sufficiently long that a

once prepared krypton generator can continuously supply mesomeric krypton-83m during a measurement campaign of a few weeks.

Although krypton-83m is the most suitable gaseous calibration source for the needs of KATRIN, it has one disadvantage, namely that the source has to be operated at an elevated temperature compared to the nominal tritium mode in order to avoid freezing of the krypton. This and other details of the ^{83m}Kr mode operation are discussed in section 1.3.1.

The modelling of the krypton-83m conversion electron spectrum is described in section 1.3.2.

The application of the ^{83m}Kr mode to study the systematics related to the plasma potential is discussed along with the plasma creating processes in section 1.4.

1.3.1. ^{83m}Kr Mode Operation at KATRIN

In the following the key parameters of the ^{83m}Kr mode operation at KATRIN are reviewed briefly. This includes a discussion of the different source temperatures in ^{83m}Kr and nominal tritium mode and the consequences for the achievable column densities. Furthermore, it is outlined how the differences in the modes affect the pressure stabilisation and purification of the gas. All differences in ^{83m}Kr and tritium mode operation can lead to systematics in the translation of the calibration results from the krypton to the tritium measurement.

Temperature in ^{83m}Kr and tritium mode: The Troitsk neutrino mass experiment used a temperature of 30 K for regular operation and 110 K for ^{83m}Kr mode [Bel+08]. The elevated temperature in the krypton measurements had to be chosen to avoid freeze out of the krypton-83m in the vacuum system. The krypton reduction in the gas system downstream of the krypton generator depends on several factors like the conductivity of the pipes (scaling linearly with pressure and temperature [Pfe09]) or freeze out on the walls (depending on temperature and vapour pressure [Mar20]). These factors are of course different for the different experiments. Prior to the first gaseous krypton measurements at KATRIN the exact quantification of these effects was still pending, and for the first campaigns the experience of the Troitsk experiment was drawn upon. Thus, the temperature of 100 K was used in the krypton measurements of July17, STS3a, KNM1 and KNM2. In KNM3 it was shown that the temperature can be reduced to 80 K without losing the krypton-83m rate.

Gas dynamics and column density: In the central WGTS the gas dynamics is dominated by the laminar flow regime, where the pressure scales linearly with temperature. Thus, at elevated temperatures a higher pressure has to be maintained to reach the nominal tritium column density of $\rho d_{T_2} = 5 \cdot 10^{21} \frac{1}{m^2}$. However, the pressure is limited by the suction capacity of the turbomolecular pumps [Mar20]. Up to KNM2 krypton, for 100 K operation only 30 % of the nominal tritium column density could be obtained, which was increased to around 40 % for the 80 K operation of KNM3 krypton.

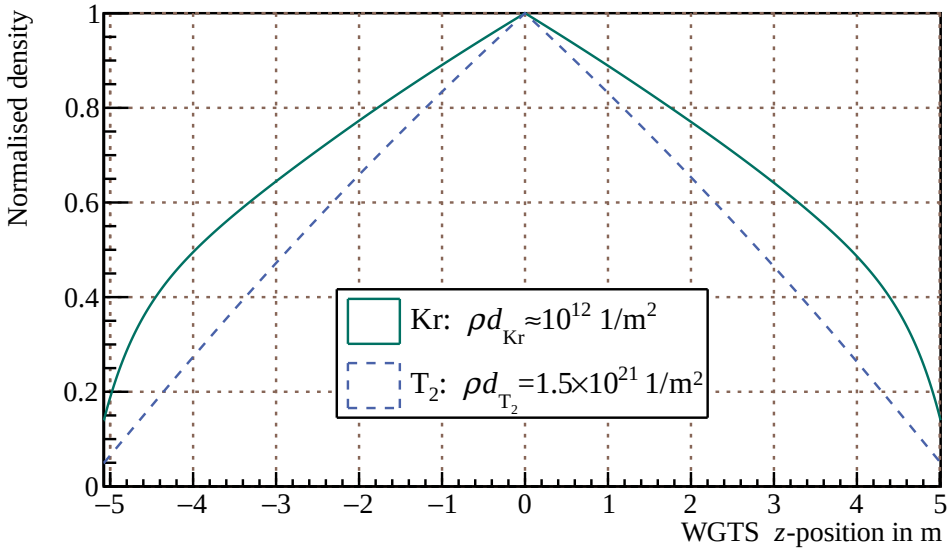

Figure 1.12.: Tritium and krypton gas profiles for KNM2 krypton conditions, normalised to injection density: Due to the difference in mass, the relative concentration of krypton is increased towards the WGTS ends. The krypton column density leads to the range of observed rates in the old krypton mode, the tritium column density holds for KNM2. The gas dynamics calculations leading to this plot are described in [Mac16].

Differences of the ^{83m}Kr and tritium mode temperature affect the energy spectrum of the thermalised particles in the WGTS and thus directly impact the plasma formation, as discussed in section 1.4.1. The latter also holds for differences in the tritium column densities between the modes. Since the study of the source plasma is the main goal of the ^{83m}Kr mode, differences in the plasma potential between the modes need to be avoided. As a consequence, efforts to create a mode with identical properties were intensified: From KNM4 on, both the krypton-83m measurements and the tritium measurements are carried out at 75 % nominal column density and 80 K. However, this is accompanied by a significant reduction in the available krypton-83m conversion electron rate, so that the old 40 % nominal column density operation must still be used in part. With regard to the tritium measurement, it could be shown that the reduction of the nominal column density by 25 % does not seriously affect the achievable sensitivity of the KATRIN experiment.

Demixing of the gas species: Identical source properties for both modes circumvent systematics from changes in the plasma potential. However, as shown in figure 1.12, even for identical experimental properties of the source the shapes of the density profiles of krypton and tritium differ slightly. The visible demixing of the two gas species is related to the different masses, which causes the aggregation of the krypton at the ends of the WGTS [KS10]. This leads to an unavoidable systematic, since the krypton signal electrons probe a different portion of the WGTS than the tritium electrons. Methods to calculate this

systematic are derived in chapter 3 and the associated uncertainties for typical KATRIN measurements are calculated in chapter 5.

Krypton low density limit: The column densities printed in figure 1.12 from the KNM2 krypton measurement are comparable for all krypton measurement campaigns prior to KNM4 (in the new krypton mode, the krypton column density will be even smaller). Due to the difference of 9 orders of magnitude between krypton and tritium, the effect of interactions of krypton atoms (with the walls, tritium or other krypton atoms) is negligible with regard to the tritium gas dynamics. Thus, the tritium gas profile is not affected when krypton is present. Also, the krypton gas profile is completely dominated by tritium krypton interactions [KS10]. As a result, the krypton column density is a mere scaling factor with the practical consequence, that its precise value is insignificant in the modelling. It is fully correlated with the overall intensity of the krypton conversion electron spectrum.

Impurities and pressure stabilisation: In tritium operation permeators are used for a continuous purification of the gas mixture. Since this would filter out the krypton, up to KNM3 krypton a gas circulation loop was chosen for the krypton measurements which bypasses the permeators. This inevitably also bypasses the buffer vessel used to stabilise the pressure, such that the tritium column density showed measurable drifts. Also, without gas purification, dirt that outgasses from the pumps accumulates over time. As discussed in chapter 6, systematics from the drift can be controlled. How the increasing impurities affect the measurement is currently under investigation [Rodep], but it is believed, that it is a small effect. Both effects are eliminated with the 75 % nominal column density krypton mode, which does not bypass the permeators. The latter is also the reason for the reduction of the krypton column density.

1.3.2. ^{83m}Kr Conversion Electron Spectrum

In the following the modelling of the integrated krypton-83m conversion electrons rate is described. The model used in this work was largely implemented into the analysis software SSC in [Mac16] and here only a short summary of [Mac16] is given.

The calculation of the integrated β spectrum by SSC was described in section 1.2.2. For the modelling of the krypton mode, equation 1.20 is extended with the krypton-83m conversion electron spectrum and the krypton gas profile, leading to

$$\dot{N}(qU) = \sum_{i}^{\text{slices}} \epsilon_{\text{det}} \frac{\Omega_i}{4\pi} \int_{-\infty}^{\infty} \left\{ N_i^{\text{Kr}} \left(\frac{\mathrm{d}\dot{N}}{\mathrm{d}E} \right)_{\text{Kr}} + N_i^{\text{T}_2} \left(\frac{\mathrm{d}\dot{N}}{\mathrm{d}E} \right)_{\text{T}_2} \right\} R(E, qU + V_i)\, \mathrm{d}E \,. \tag{1.25}$$

The number N_i^{Kr} of krypton-83m atoms in each slice i of the source is taken from density profiles like figure 1.12. The modelling of the differential krypton-83m conversion spectrum $\left(\frac{\mathrm{d}\dot{N}}{\mathrm{d}E}\right)_{\text{Kr}}$ is discussed in the following.

The krypton-83m electrons are produced by the process of inner conversion. Several lines exist, corresponding to the binding states of the emitted electrons. Further lines are created

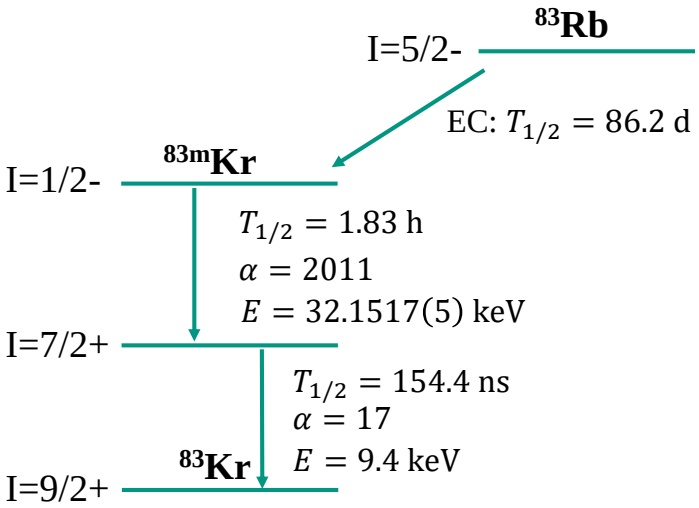

Figure 1.13.: Creation of the ^{83m}Kr isomer and its deexcitation: ^{83m}Kr is created by the electron capture decay of its mother isotope ^{83}Rb. The ^{83m}Kr deexcitates to the ground state by γ emission or inner conversion via the intermediate state of angular momentum $I = 7/2+$. α is the conversion coefficient, which specifies the relative activity of the transition (after [Ost08]).

by secondary *shake up/off* effects, which account for the change of the atomic potential upon electron emission.

Process of inner conversion: A simplified decay scheme is shown in figure 1.13 (an extensive scheme if found for example in [McC15]). Rubidium-83 decays by electron capture to the mesomeric krypton-83m, which deexcitates to the ground state via an intermediate state. Thus, the total excitation energy of $E_{\mathrm{exc}} \approx 41$ keV is split into a transition of $E^{32}_{\mathrm{exc}} \approx 32.2\,\mathrm{keV}$ and $E^{9.4}_{\mathrm{exc}} \approx 9.4\,\mathrm{keV}$. The transitions t either occur by direct γ emission or by inner conversion, where the excitation energy is transferred to one or more shell electrons through Coulomb interaction. When the excitation energy of the transition E^t_{exc} is larger than the binding energy E^s_{B} of the electron in shell $s \in \{\mathrm{K}, \mathrm{L}_{l_1}, \mathrm{M}_{l_2}, \mathrm{N}_{l_3}, \ldots\}$ with sub shells l_i, it is emitted with a net kinetic energy of

$$E^{t,s}_{\mathrm{kin}} = E^t_{\mathrm{exc}} - E^s_{\mathrm{B}} \,. \tag{1.26}$$

As a consequence, line groups corresponding to the transition energies with subgroups corresponding to the shells are observed in the conversion electron spectrum. This is denoted as: $\mathrm{Shell}_{\mathrm{subshell}}$-Transition (i.e. K-32, L_1-9.4, …).

For the specification of the intensity, the conversion coefficient $\alpha^{t,s}$ is used. It is the ratio of the emitted electron rate to the emitted photon rate

$$\alpha^{t,s} = \dot{N}^{t,s}_{\mathrm{e}^-} / \dot{N}^t_{\gamma} \,. \tag{1.27}$$

Using the law of radioactive decay, the decay rate $\dot{N}^t_{\mathrm{Kr}}$ of the excited krypton-83m can be expressed in terms of the half-life $T^t_{1/2}$ and the number of krypton atoms N^t_{Kr} as

$$\dot{N}^t_{\mathrm{Kr}} = \frac{\ln 2}{T^t_{1/2}} \cdot N^t_{\mathrm{Kr}} = \sum\nolimits_s \dot{N}^{t,s}_{\mathrm{e}^-} + \dot{N}^t_\gamma = \left(\sum\nolimits_s \alpha^{t,s} + 1\right) \dot{N}^t_\gamma \,. \tag{1.28}$$

Due to the production of the krypton-83m in rubidium-83 decay, the observed rate of the krypton-83m conversion electrons is given by the decay law of two chained decays. However, since the half-life of the mother isotope rubidium-83 of 86.2 d [McC15] is much larger than the half-life of krypton-83m of 1.83 h [McC15], the measurement is quasi stationary and the overall time dependence is only given by the decay of rubidium-83. This time dependence is not included in the model, but accounted for by a phenomenological intensity I, which is constant in each fit.

Combining equation 1.27 and equation 1.28 allows the electron activity per krypton-83m atom to be expressed by the conversion coefficient and the half-life

$$A^{t,s} \equiv \frac{\dot{N}^{t,s}_{\mathrm{e}^-}}{N^t_{\mathrm{Kr}}} = \frac{\ln 2}{T^t_{1/2}} \frac{\alpha^{t,s}}{\sum_s \alpha^{t,s} + 1} \,. \tag{1.29}$$

As indicated by Heisenberg's uncertainty principle the lines obey a finite width $\Gamma^{t,s}$. Their energy distribution function $F(E, E^{t,s}_{\mathrm{mean}}, \Gamma^{t,s})$ with mean energy $E^{t,s}_{\mathrm{mean}}$ is specified below in equation 1.33.

Differential krypton spectrum: Combining the previous considerations the total electron conversion rate per krypton-83m atom and energy is obtained as

$$\left(\frac{\mathrm{d}\dot{N}}{\mathrm{d}E}\right)_{\mathrm{Kr}} (E) = I \sum_{t,s}^{\substack{\text{transitions} \\ \text{shells}}} A^{t,s}\, F(E, E^{t,s}_{\mathrm{mean}}, \Gamma^{t,s}) \,. \tag{1.30}$$

Accordingly, krypton-83m conversion electron lines are characterised by their mean energy, their line width and the intensity.

Experimental data: Many experiments have determined the parameters of the krypton-83m spectrum using different experimental techniques [Sev79; BB67; Des+03]. From KATRIN results can be found in [Sei19; Sle+19]. For all analyses carried out in this work the parameters of the relevant lines are self-measured. Only for the following plots of the total spectrum the recent literature values from [Vén+18] are taken. They can be found in table 1.2. The line intensities are corrected with a probability p for shake up/off (discussed below) effects to occur.

Usage of the 9.4 keV transition: For the determination of KATRIN systematics the 9.4 keV transition cannot be used: Its energy is smaller than the tritium endpoint energy, such that it is either completely covered in the tritium β spectrum or suffers from a large background

in combined tritium and krypton measurements. Since the first tritium exposure, this kind of background would also exist in krypton only measurements, due to residual tritium on the surfaces. Since the krypton measurement is very sensitive to energy dependent backgrounds, as discussed in section 6.1, this leads to systematics in 9.4 keV measurements.

Furthermore, the 9.4 keV conversion lines are further split into several lines, as reported in [DS90]: If the primary 32 keV transition occurs via electron emission, the krypton ends up in an ionised state of charge +1. Successive Auger emissions can lead to a state of multiple ionisations. Due to the low density in the WGTS the neutralisation time is longer than the live time of the intermediate state, such that the secondary 9.4 keV transition is sensitive to the electronic state of the krypton. The resulting line splitting was studied at KATRIN in [Sei19], which was performed prior to the first tritium exposure of the source.

Thus, only lines of the 32 keV transition are used in this work. In the following, indices specifying the transition and the "32" are left out for the sake of readability.

Shake up/off effect: The deexcitation of the krypton-83m atom under electron emission leads to a change of the potential of the atom. In *sudden approximation* successive emissions and potential change are described separately [War+91]. Since the potential change affects the energy levels of the electrons, additional lines can appear in the spectrum:

- **Shake up:** If an outer shell electron ends up in a higher state, the energy difference is taken from the primary particle. This does not affect the line shape and leads to a satellite line at lower energies.
- **Shake off:** If the electron from the outer shell ends up in the continuum its energy is not quantised. This produces a low-energy tail of the satellite and thus a different line shape than that of the main line.

Due to lacking better knowledge, in this thesis all satellites are modelled with the same shape as the main lines. Also, in this work and in [Sei19] some shake lines were measured, where this approximation in most, but not all cases, fitted to the data. The mean shake energies and shake probabilities p are shown in table 1.3.

Modelling of the line shape: Electrons created in the process of inner conversion have a Lorentzian energy distribution $L(E, E_{\text{mean}}, \Gamma)$ [BW36; WW30]

$$L(E, E_{\text{mean}}, \Gamma) = \frac{1}{\pi} \frac{\Gamma/2}{(\Gamma/2)^2 + (E - E_{\text{mean}})^2} \,. \tag{1.31}$$

E_{mean} is the line mean and Γ the intrinsic line width. The leading order effect of inhomogeneities of the energy scale is considered by convolving the Lorentzian with a Gaussian kernel $G(E, \sigma_{\text{g}})$ of width σ_{g} [3]

$$G(E, \sigma_{\text{g}}) = \frac{1}{\sqrt{2\pi}\sigma_{\text{g}}} \mathrm{e}^{-\frac{E^2}{2{\sigma_{\text{g}}}^2}} \,. \tag{1.32}$$

[3] Since σ_{g} enters the Gaussian convolution kernel quadratically σ_{g}^2 is a normal-distributed fit parameter. A continuation to the regime of negative squares is performed using the method of [Bel+08].

Table 1.2.: **^{83m}Kr conversion spectrum - main lines.**
Shown is the ≈ 32 keV transition. The different energies of the lines are related to the shells from which the respective electrons originate, which are given by the character in the symbol. The probability p is that for shake up/off effects (values from [Vén+18; CN73]).

Symbol	E_{mean}/eV	Γ/eV	α	p in percent
K	17824.2(5)	2.71(2)	478.0(50)	79.5
L_1	30226.8(9)	3.75(93)	31.7(3)	100.0
L_2	30419.5(5)	1.25(25)	492.0(50)	82.2
L_3	30472.2(5)	1.19(24)	766.0(77)	82.3
M_1	31858.7(6)	3.5(4)	5.19(5)	100.0
M_2	31929.3(5)	1.6(2)	83.7(8)	92.0
M_3	31936.9(5)	1.1(1)	130.0(13)	93.4
M_4	32056.4(5)	0.07(2)	1.31(1)	91
M_5	32057.6(5)	0.07(2)	1.84(2)	91
N_1	32123.9(5)	0.40(4)	0.643(6)	100.0
N_2	32136.7(5)	0.03	7.54(8)	93
N_3	32137.4(5)	0.03	11.5(1)	93

Table 1.3.: **^{83m}Kr conversion spectrum - satellite lines.**
In case of the M and N lines the values were calculated by subtracting the relative positions of the satellites from [CN73; Eri+87] from the main lines. The denotation with S1, S2, S3 is phenomenological (values from [CN73; Eri+87; War+91]). Only the strongest satellites are shown here. Rich photoelectron spectra are found in [Kik+96; Cal+06].

Symbol	E_{mean}/eV | p in percent					
	S1		S2		S3	
K	17664.18	3.56	17781.00	1.80	17805.12	13.45
L_2	30262.58	3.56	30379.40	1.53	30403.52	11.99
L_3	30314.88	3.53	30431.70	1.52	30455.82	11.94
M_2	31904.3	2	31909.3	6		
M_3	31911.9	0.6	31916.9	6		
$M_{4,5}$	32024	1	32037	8		
$N_{2,3}$	32116	5	32118	2		

The inhomogeneity of the energy scale is composed both of source and spectrometer potential inhomogeneities. Inhomogeneities can be spatial or temporal and in all cases the widths of the contributions add quadratically.

The resulting line shape is given by the so-called Voigt profile

$$V(E, E_{\text{mean}}, \Gamma, \sigma_{\text{g}}) = \int_{-\infty}^{\infty} G(\tau, \sigma_{\text{g}}) L(E - \tau, E_{\text{mean}}, \Gamma)\, \mathrm{d}\tau\ . \tag{1.33}$$

Differential spectrum model: Summing up the previous paragraphs, the differential krypton-83m conversion electron spectrum is modelled as [Mac16]

$$\left(\frac{\mathrm{d}\dot{N}}{\mathrm{d}E}\right)_{\text{Kr}}(E) = I \cdot A^{32} \sum_{l}^{\substack{\text{satellites} \\ \text{shells}}} \frac{\alpha^l}{\sum_s \alpha^{32,s} + 1} \frac{p^l}{100} V(E, E^l_{\text{mean}}, \Gamma^l, \sigma_{\text{g}})\ . \tag{1.34}$$

The total rate of the 32 keV-transition is $A^{32} = \frac{\ln 2}{1.83\,\text{h}} = 1.05 \cdot 10^{-4}\,\frac{1}{\text{s}}$ per krypton atom. I is a fit parameter for the total intensity. For the fits performed in this thesis only the L_3 and the L_3^{S3} line were included in the modelling. As discussed in section 6.2 their intrinsic parameters were determined in krypton only measurements and replace the above literature values in the analysis carried out in this thesis.

Figure 1.14 shows the conversion lines of the 32 keV transition in the region of 30 – 32 keV. The corresponding integrated spectrum is shown in figure 1.15. As visible in the close-up of the integrated spectrum at the L_2 and the L_3 line region, figure 1.16, due to energy loss by inelastic scattering of the electrons off the gas inside the WGTS additional steps can be observed. This observation is essential, since it leads to longitudinal sensitivity to the source potential, which is described in section 1.4.2.

Distortion of the krypton-83m spectrum: The mean unaccounted potential difference of spectrometer and source potential is parametrised by a line shift ΔE_{main}. Together with the Gaussian broadening squared σ_{g}^2 this makes for the first and second moment of the distribution of possible energy scale systematics. Those moments can be obtained from the distortion of the krypton-83m spectrum. Notably, the usage of a Gaussian broadening to model this distortion is a deliberate choice, which has two main motivations: Firstly, the shift of the squared neutrino mass (equation 1)

$$\Delta m_\nu^2 = -2\sigma^2$$

is governed by the standard deviation σ of the distribution of the energy scale systematic. As shown in [Sle16] this does not mean that this distribution needs to be a Gaussian. The fact that a Gaussian is used in krypton-83m is only the conscious choice to be able to calculate the systematics of the neutrino mass measurement according to equation 1. Secondly, using the first few moments of the distribution simply is the natural expansion in the magnitude of the systematic.

In the following the focus is put on systematics related to the source plasma. The rigorous definition of these moments and their relation to the plasma potential is the topic of chapter 3. The plasma-creating processes are described in the next section.

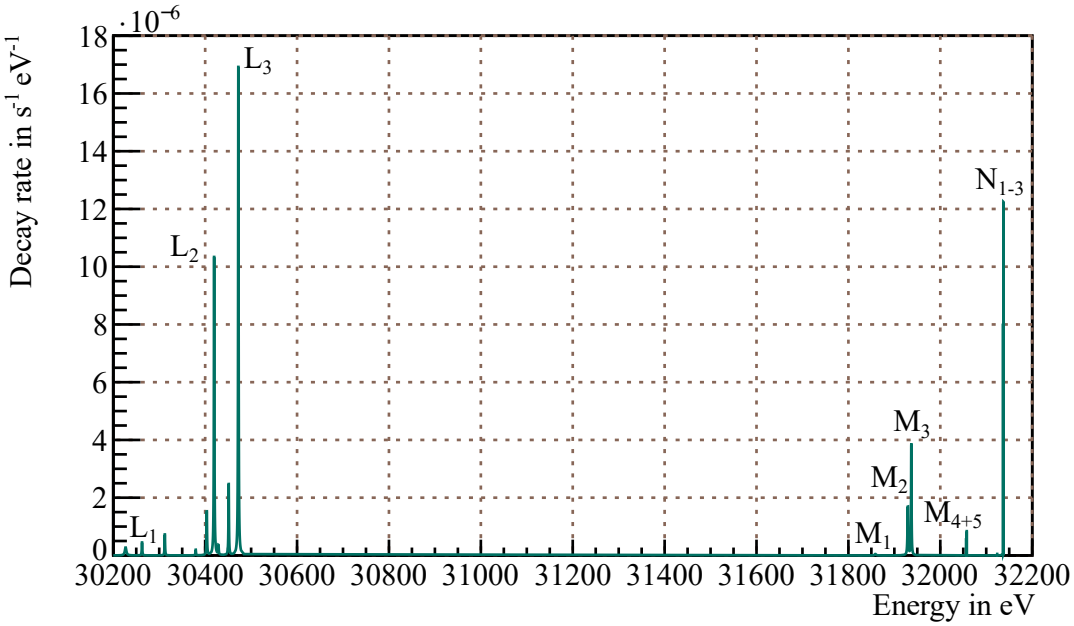

Figure 1.14.: Differential krypton-83m conversion electron spectrum: The differential rate per atom of the L, M and N conversion lines and the corresponding shake off/up lines is shown. At its mean it is inversely proportional to the line width. This is why the N transition seems large, although its total intensity is one magnitude smaller than that of the L and M transition.

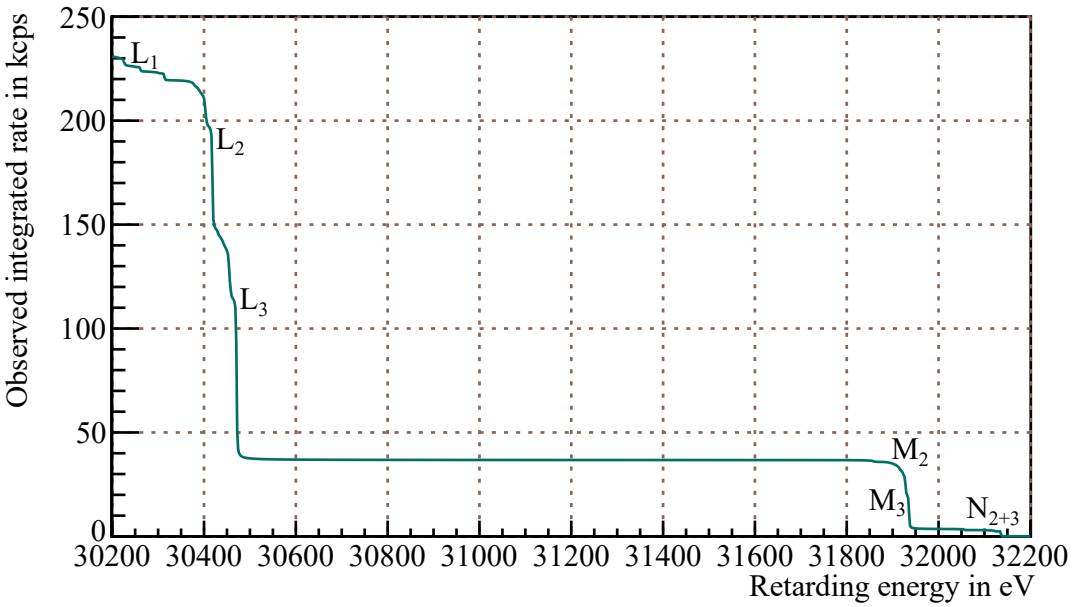

Figure 1.15.: Integrated krypton-83m conversion electron spectrum: The krypton column density on the order of $10^{12} \frac{1}{m^2}$ leads to the range of observed count rates. The M_1, M_4, M_5 and N_1 krypton-83m conversion lines are not visible on this scale and the tiny additional steps stem from shake up/off electrons.

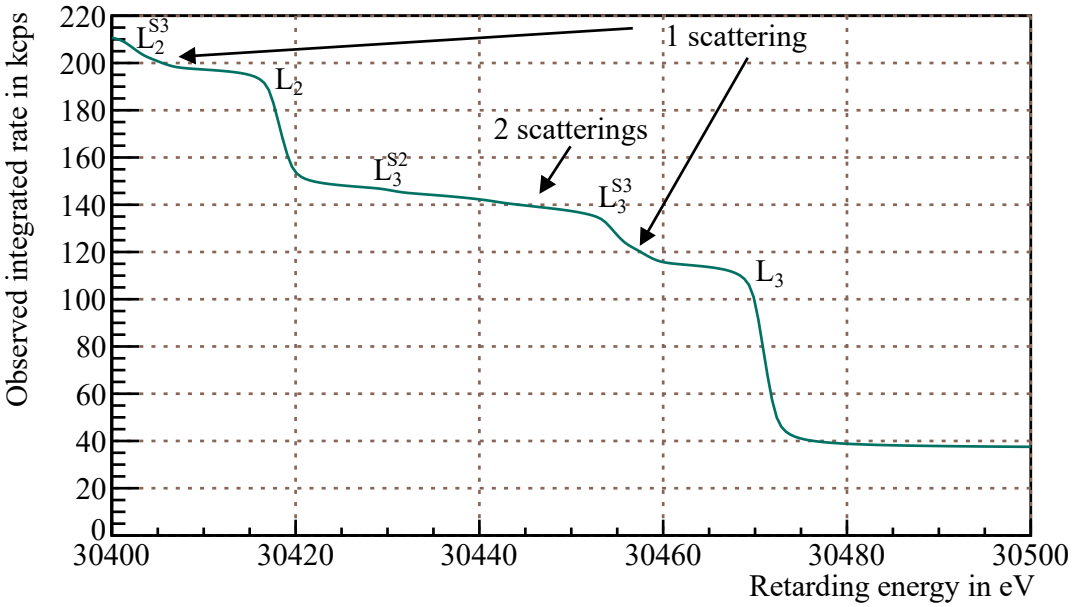

Figure 1.16.: Close-up on a region of interest around the integrated krypton-83m L_2 and L_3 conversion electron lines: Due to the gap of the energy loss function of about 13 eV (see figure 1.10) steps of different scattering multiplicities appear with a spacing of about 13 eV below each line of the integrated krypton-83m spectrum.

1.4. Source Potential Systematic

In this section the effect of source potential systematics on the tritium β and krypton-83m conversion spectrum is described. The shape distortion of the spectra is fully characterised by the spatially and time dependent source potential V. In this work only spatial dependencies are considered. The potential is determined by the low density plasma of the source, the formation of which is described in section 1.4.1.

The radial and angular segmentation of the KATRIN focal plane detector in 148 pixels allows to search for radial inhomogeneities of the source potential. In principle radial inhomogeneities lead to different endpoint and line position shifts for each pixel, but do not affect the neutrino mass estimate of a single pixel. However, the shape distortion of the tritium β spectrum caused by longitudinal inhomogeneities of the potential $V(z)$ along the source cannot be distinguished from the physical imprint of a non-vanishing neutrino mass. While the full potential $V(z)$ for each pixel in principle fully characterises the shape distortion of the spectra and thus the resulting systematics, in a perturbative approach the distortion can be characterised by a few scalar estimates of $V(z)$. Previous to [Mac16], it was believed that the only necessary quantity is the variance of the potential $\sigma^2[V]$, leading to (equation 1) [4]

$$\Delta m_\nu^2[V] = -2\sigma^2[V] \ .$$

However, as shown in this work, one additional parameter needs to be introduced to characterise source potential systematics. The process leading to this result is longitudinal sensitivity to the potential by inelastic scattering, which was discovered in [Mac16]. It is described in section 1.4.2.

1.4.1. Plasma Potential of the Source

The three-dimensional potential of the WGTS volume is determined by the work functions of the surfaces (beam tube and rear wall) and the source plasma. The interplay of these components and the plasma formation are described in the following.

Plasma generation at KATRIN: The essential ingredient for a plasma to occur is net charges on a microscopic scale. In KATRIN the main charge generation process is the tritium β decay, which creates 10^{11} electrons and $^3(\mathrm{HeT})^+$ ions per second [KAT04b]. Due to inelastic scattering of the electrons on the gas on the order of 50 secondary electrons and ions are created per β electron [5]. Here it has to be considered that almost all electrons are reflected at the spectrometer potential and that the probability for backscattering on the rear wall is on the order of several ten percent [Bab14]. As a consequence, electrons on average traverse the WGTS multiple times, undergoing multiple scatterings, before they are eventually absorbed at the rear wall.

[4] Square brackets are used whenever functionals are treated. Most of the times the argument of the function is omitted in the expression and used implicitly. Here, for example, the shift of the squared neutrino mass is a functional of the z-dependent potential V.

[5] According to calculations by Ferenc Glück and Marco Röllig, personal communication.

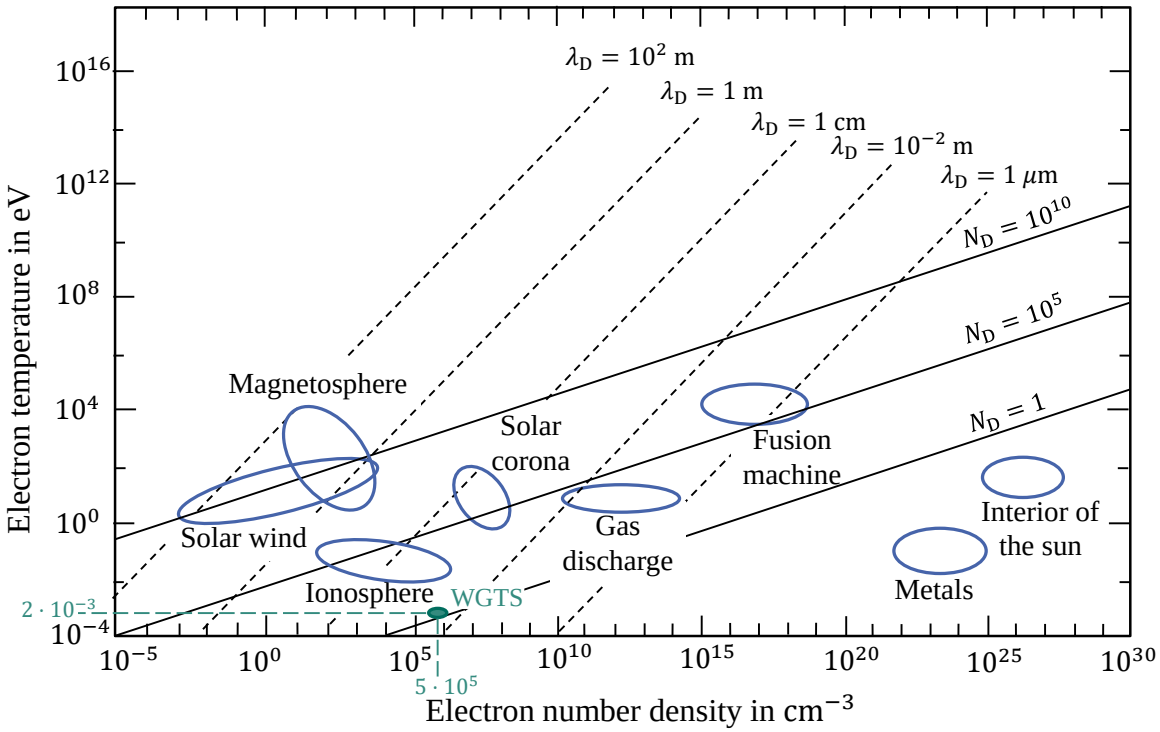

Figure 1.17.: Electron number density and temperature for common plasmas and the KATRIN source: The KATRIN source plasma is set apart from other plasmas by its very low electron temperature. As a consequence, its plasma parameter is rather small, such that it is on the edge of being an ideal plasma (figure recreated, found in [Gal12; Lab17], idea from [Kuc16], original source unknown).

Typical plasma parameters: Plasmas are characterised by collective behaviour [Din+05]. Accordingly, they are described by collective parameters like their electron temperature T_e or the electron number density n_e. Figure 1.17 shows those quantities for the KATRIN WGTS plasma compared to other plasmas. With its low electron density on the order of $n_e \approx 5 \cdot 10^{11} \frac{1}{m^3}$ [KAT04a] it is comparable to atmospheric plasmas, like in the solar corona or the ionosphere. However, its electron temperature $T_e = 29$ K ≈ 2.5 meV [KAT04b] is much lower than that of most other commonly studied plasmas.

The scale above which the microscopic charges are exponentially shielded is the *Debye length*

$$\lambda_D \propto \sqrt{\frac{n_e}{T_e}}\,, \tag{1.35}$$

which is between 0.3 mm and 1 mm for typical KATRIN source conditions [Kuc16]. At scales larger than the Debye length the plasma is quasi-neutral. The number of particles in the Debye sphere is called the *plasma parameter*

$$N_D = \frac{4}{3}\pi n_e \lambda_D^3\,. \tag{1.36}$$

If the plasma parameter is much larger than one, the plasma is called an *ideal plasma*. In this case, the collective behaviour of charges dominates over binary collisions and individual charges can be described as interacting with a smooth background field. As visible in figure 1.17, for the typical values of electron density and temperature at KATRIN this condition is overall just about fulfilled. However, the theoretical description and simulation of the KATRIN source plasma is complicated by further factors: The length-to-radius ratio of the WGTS is large ($r \approx 4.5$ mm, $L_{\mathrm{WGTS}} \approx 10$ m), such that boundary conditions are important, the gas densities along the axis of the WGTS are not constant, such that different gas dynamics regimes have to be considered, and the motion of charged particles is bound to a strong magnetic field, such that the quasi-neutrality due to the shielding of charges is hindered by a reduced mobility in radial direction.

Influence of the work function of rear wall and beam tube: Due to the confinement of the charges to the magnetic field lines, the rear wall dominates the overall plasma potential. However, work function differences between the stainless steel surface of the beam tube and the gold surface of the rear wall can contribute to inhomogeneities of the spatial plasma potential. To balance those differences, a bias voltage can be applied to the rear wall, which is the major input parameter for the measurements carried out in this work. It was expected, that for a certain choice of the rear wall voltage setting the work function differences of the beam tube walls and rear wall are compensated, resulting in minimum radial and longitudinal inhomogeneity [Kuc16]. This expectation is now partly confirmed by krypton-83m measurements, as shown in section 6.3 and in [Ost20]: The radial differences in the plasma potential are indeed found to be minimal at some optimum rear wall voltage. However, perfect compensation is not possible over all source radii at the same time. The longitudinal inhomogeneity is minimal, when the radial inhomogeneity is minimal, however the minimum has a width of several 100 mV with regard to the rear wall voltage setting. This might be related to systematics of the krypton-83m measurement, to temporal plasma instabilities, also leading to a shape distortion of the krypton-83m spectrum, or to a large capability of the plasma to compensate for local charges.

Plasma simulations: KATRIN uses two approaches to determine plasma systematics: The experimental determination of plasma parameters in krypton-83m and other calibration measurements, and the direct calculation of the spatial potential in simulation. Both approaches are complementary: While it is established in this work, that in principle the plasma estimates from the krypton-83m measurements are sufficient to fully characterise the plasma systematics, those estimates are affected by unavoidable uncertainties. Those stem both from the measurement itself and from the translation between the krypton-83m and the tritium β spectrum. Thus, in the best possible approach the krypton-83m measurements are used to verify plasma simulations, such that in combination plasma estimates for the tritium spectrum with small uncertainties can be obtained. Detailed simulations of the KATRIN source potential based on the drift-diffusion fluid-dynamical approach were carried out in [Kuc16]. Figure 1.18 shows a resulting 30 K source potential with an axially symmetric WGTS model. The potentials of the beam tube wall ($r = 4.5$ cm) and rear wall ($z = -5$ m) were set to the same value (here zero), which leads to the smallest

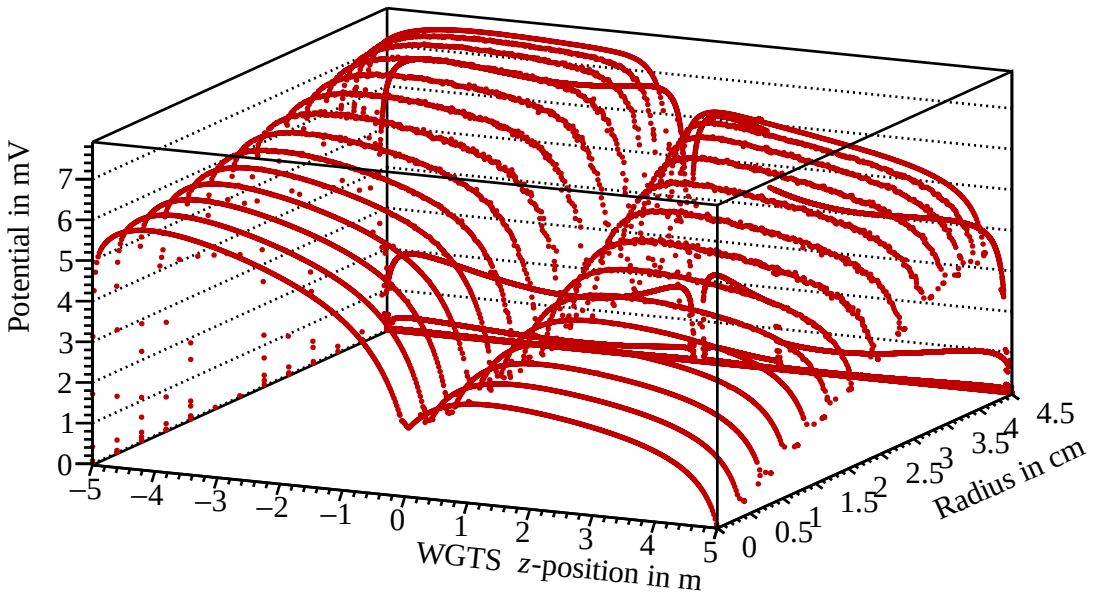

Figure 1.18.: Simulated plasma potential inside the WGTS for 30 K: Rear and tube walls are set to zero potential, which is visible as a steep drop of the plasma potential at the boundaries. The dip at $z = 0$ m is caused by the gas injection point of the WGTS. An axially symmetric model is assumed and the rear wall is placed directly at the WGTS rear termination at $z = -5$ m (data from [Kuc16]).

overall inhomogeneities. The central dip is caused by the gas injection, from where the gas flows into the two opposite directions towards detector or rear wall. The higher mobility of the electrons compared to the positive charges leads to the formation of the positively charged regions in front of the walls. The front side ($z = 5$ m) is not grounded, since the source is windowless, and accordingly here the potential differs from zero.

Currently new plasma simulations are performed in [Kelep] using microscopic particle-in-cell simulations. Among other factors, the behaviour of ions in the front side transport system is ongoing research and is already known to influence the krypton-83m plasma estimates. Thus, since the plasma simulations depicted here do not include such effects, in their current state they should only be taken as an example of the overall plasma behaviour. This is the approach of the work at hand, which uses the high temperature plasma simulation shown in figure 1.19 for all studies and examples.

Systematics from the plasma potential: The effect of radial dependencies of the plasma can be in principle observed directly in pixel wise analyses of the KATRIN measurements. Accordingly, radial inhomogeneities of the potential can be considered in a radial analysis.

However, the measurement of an individual pixel is a summation over all electron spectra gathered over the magnetic flux through the pixel, in particular over the ≈ 10 m long WGTS z-profile. If not taken into account in the model of the theoretical tritium β spectrum, the

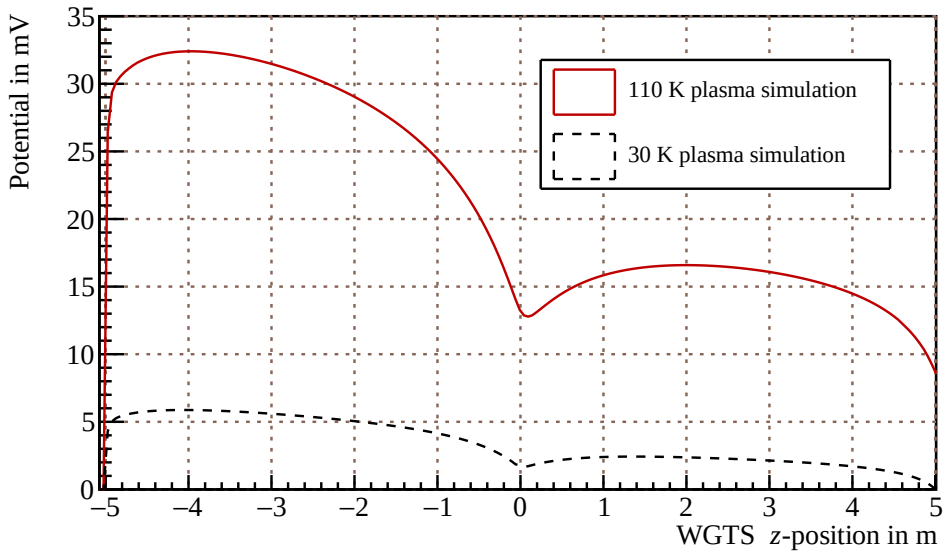

Figure 1.19.: Simulated z-profile of the central plasma potential inside the WGTS for 30 K (black) and 110 K (red): The peak-to-peak values are $\approx$ 5 mV and $\approx$ 20 mV. This is in agreement with the expectation from the KATRIN design report, which states a linear scaling of the inhomogeneity with temperature. The high temperature potential is used throughout this work as an example for the ^{83m}Kr mode potential (data from [Kuc16]).

longitudinal inhomogeneity of the potential along this line causes a neutrino mass shift. It is considered with $|\sigma_{\text{syst}}(m_\nu^2)| < 0.2 \cdot 10^{-3}$ eV^2 in the original KATRIN systematics budget from the design report (table 1.1).

For the 30 K simulation of the potential shown in figure 1.19 the resulting shift of the squared neutrino mass is $\sigma_{\text{syst}}(m_\nu^2) = -0.3 \cdot 10^{-3}$ eV^2 for nominal KATRIN measurement conditions, which does not stay in the projected limit. This is the case, even though the standard deviation of the potential is only a few mV, which would lead to only a small neutrino mass shift according to equation 1. The reason is the considerable rear-to-front asymmetry of the potential. It increases the systematics due to the longitudinal sensitivity on the potential in the presence of inelastic scattering, which is discussed in section 1.4.2.

Plasma measurements using ^{83m}Kr mode: Both the standard deviation and rear-to-front asymmetry of the potential can be obtained in the ^{83m}Kr mode of the gaseous source. While krypton-83m was used in the Troitsk neutrino mass experiment which also uses a gaseous source [Bel+08], previously only the standard deviation of the potential was considered. The connection of potential rear-to-front asymmetry and krypton-83m observables is rigorously established and applied in measurements in the context of this thesis.

The basic idea of the measurements is to compare krypton-83m conversion electron spectra of a krypton only source (called *reference measurement*) with a measurement of a mixture of krypton and tritium (called *plasma measurement*). Since the β decay is the driving force

for charge creation, in the krypton only measurement no plasma is present, such that these measurements serve as a reference [6]. Thus, compared to the reference, the krypton-83m lines are shifted and broadened according to mean and standard deviation of the potential. The exact relations of krypton-83m estimates and potential are established in chapter 3.

In the following the mechanism of longitudinal sensitivity by inelastic scattering is discussed, which leads to the sensitivity of the gaseous krypton-83m and tritium β measurements to the rear-to-front asymmetry of the potential.

1.4.2. Sensitivity to the Source Potential in the Presence of Inelastic Scattering

The effect of the source potential is not sufficiently described by using only its mean $\langle V \rangle$ and standard deviation $\sigma[V]$, but one additional parameter has to be considered. The reason is longitudinal sensitivity to the potential by inelastic scattering.

Due to the presence of scattering the measured electron spectrum has a dependence on the longitudinal starting position z of the electrons. Understanding this effect requires two steps, which are most easily explained for the krypton-83m spectrum:

1. **Energy separation of spectra of different scattering multiplicities:** Electrons of different scattering multiplicities are grouped into separate lines in the spectrum, since they are separated by the minimum energy loss of ≈ 13 eV. This is sketched in figure 1.20 for the L_3 line. Here the energy loss function from figure 1.10 is overlaid with the integrated spectrum. The main L_3 line is caused by the electron conversion electrons and contains only unscattered electrons. Electrons can scatter inelastically on the residual gas in the source, where they lose a minimum of ≈ 13 eV in the process. As a consequence, the spectra of different scattering multiplicities are shifted with respect to the unscattered one by multiples of ≈ 13 eV [7]. Notably, this also holds for the tritium β spectrum, although there the intervals of different scattering multiplicities are hidden by the continuous shape of the spectrum.
2. **Separation of the average longitudinal starting positions of electrons of different scattering multiplicities:** Electrons of different scattering multiplicities not only occur at different energies in the spectrum, but also on average stem from different regions of the source. This is shown in figure 1.21. Since the scattering probabilities are the higher, the further from the rear the electrons start, the average electron starting positions $\langle z \rangle_i$ are different for electrons of different scattering multiplicities i.

[6] As shown in the context of this thesis and in [Ost20], the WGTS potential of the reference measurements shows larger inhomogeneities than that of the plasma measurement, which is most likely caused by residual inhomogeneities of the beam tube work function. As a consequence, the determination of the reference estimates requires additional krypton measurements of the $N_{2,3}$ doublet. This is further discussed in chapter 6 and [Ost20].

[7] For completeness it should be mentioned that, due to the tail and width of the energy loss function, the scattered spectra are also broadened compared to the unscattered spectrum. However, this is not relevant to understand the mechanism leading to longitudinal sensitivity on the potential.

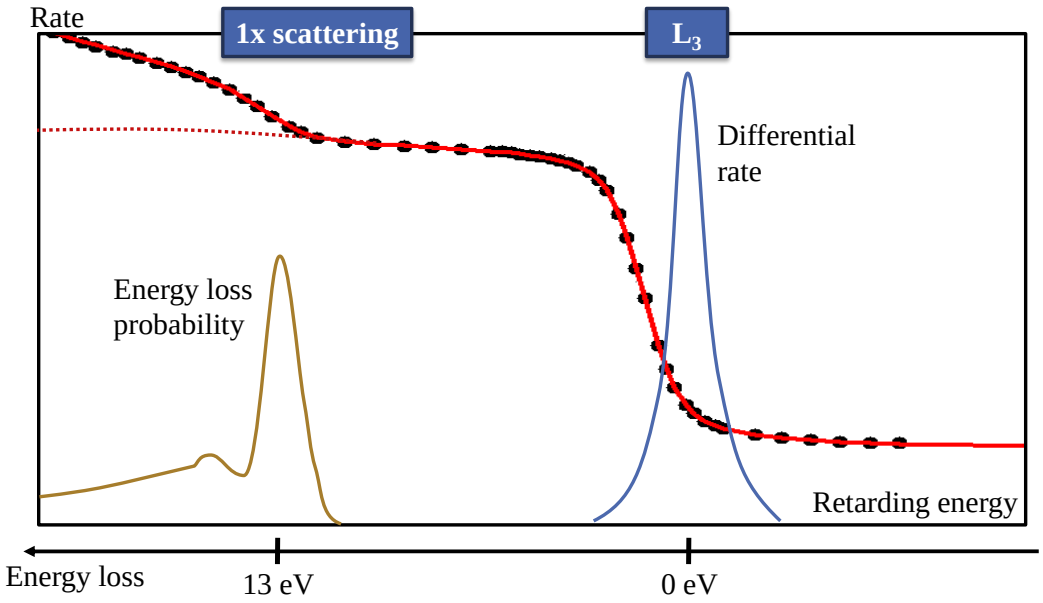

Figure 1.20.: Energy separation of spectra of different scattering multiplicities: The shown krypton-83m spectrum at the L_3 line is composed of distinct lines of different scattering multiplicities. The main L_3 line on the right only contains unscattered electrons. Approximately 13 eV below the main line an additional line of one-time scattered electrons is visible. The gap is caused by the fact that electrons need to lose at least $\approx$ 13 eV in inelastic scattering.

As a consequence, the electrons of different scattering multiplicities, visible as distinct lines in the krypton-83m spectrum, probe different potential means $\langle V \rangle_i$. While in the tritium β spectrum the different potential means are not directly measurable, still different regions of the spectrum are affected by different compositions of the $\langle V \rangle_i$.

For the analysis range of the krypton spectrum depicted in figures 1.20 and 1.21 only one-time scattered (mean potential $\langle V \rangle_1$) and unscattered (mean potential $\langle V \rangle_0$) electrons are relevant. The difference of their observed mean potentials

$$\Delta_{10}[V] \equiv \langle V \rangle_1 - \langle V \rangle_0 \tag{1.37}$$

is the change of the line distance with respect to the expectation of $\approx$ 13 eV. In a simplified view, the scattering probabilities shown in figure 1.21 allow to interpret $\langle V \rangle_1$ and $\langle V \rangle_0$ as the mean rear and front potential, such that the line distance $\Delta_{10}[V]$ is indeed a measure of the longitudinal *antisymmetry* of the potential with regard to the injection point. This dependence on the potential shape is depicted in figure 1.22:

- If the mean rear potential is larger than the mean front potential ($\Delta_{10}[V] > 0$), the distance of the one-time scattered and the unscattered line increases.
- If the mean rear potential is equal to the mean front potential ($\Delta_{10}[V] = 0$), the distance of the lines does not change.
- If the mean rear potential is smaller than the mean front potential ($\Delta_{10}[V] < 0$), the distance of the lines decreases.

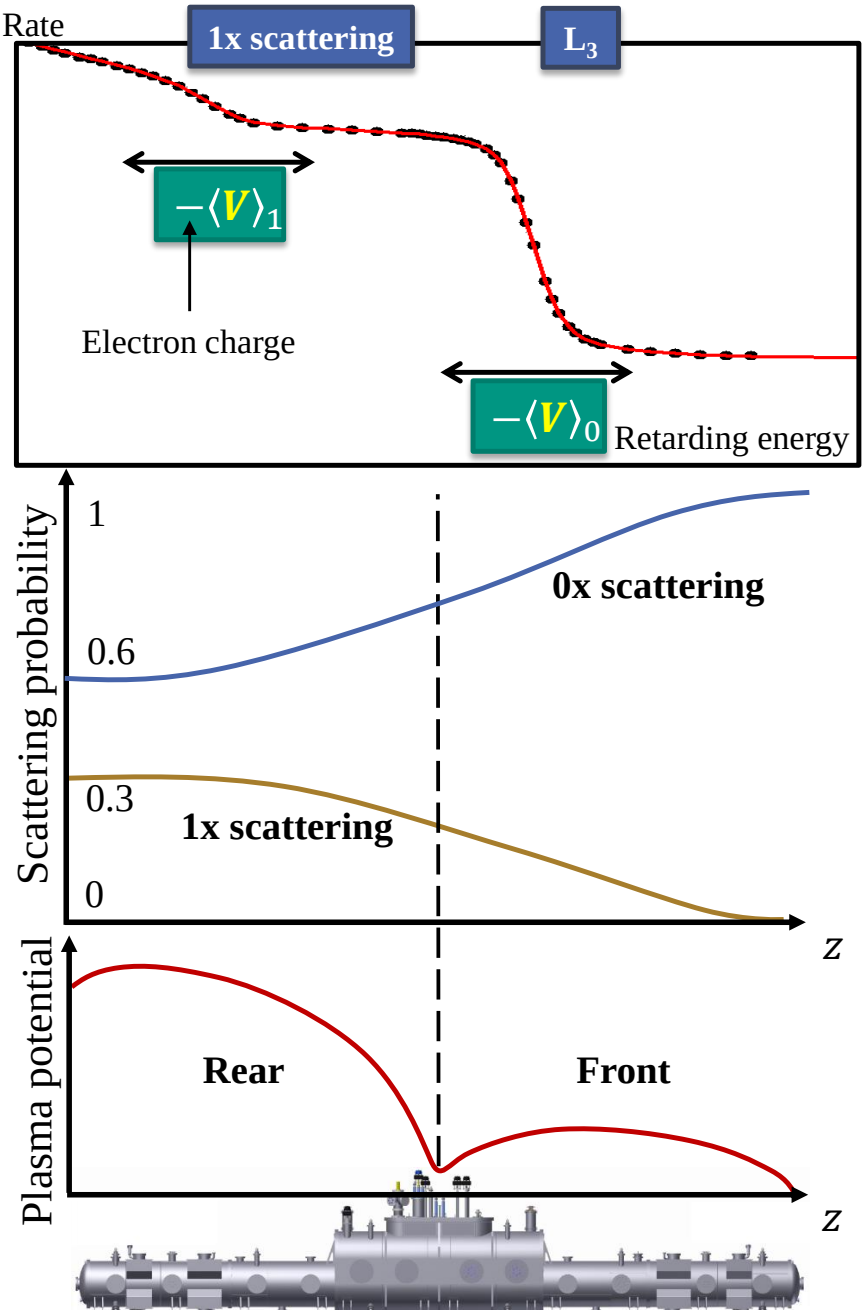

Figure 1.21.: Longitudinal sensitivity on the source potential in the presence of inelastic scattering: Since the probability that detected electrons have been scattered increases for starting positions towards the rear part of the source, on average scattered electrons start further towards the rear part than unscattered electrons. Consequently, electrons of different scattering multiplicities i see a different mean potential $\langle V \rangle_i$. The different mean potentials are directly measurable in the quasi mono-energetic krypton spectrum, where the lines of different scattering multiplicities are separated in energy. Due to the negative charge of the electrons, positive potentials lead to negative shifts of the line position and vice versa.

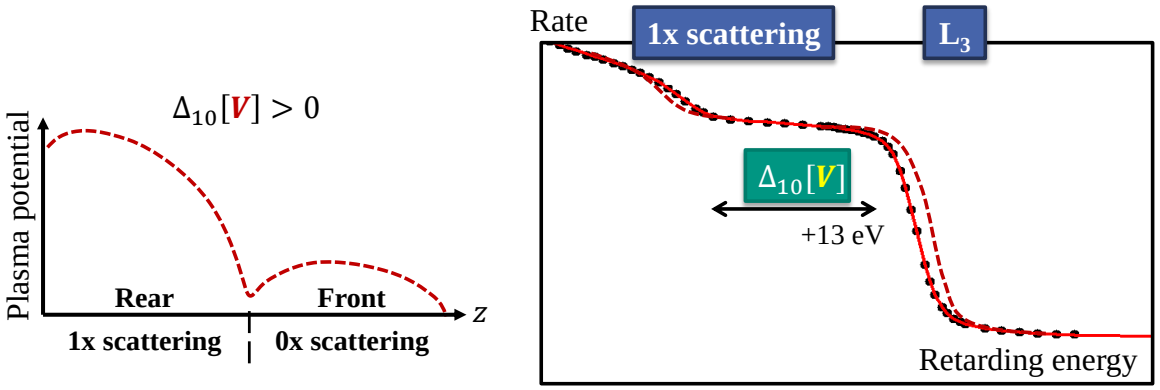

(a) Potential with positive antisymmetry

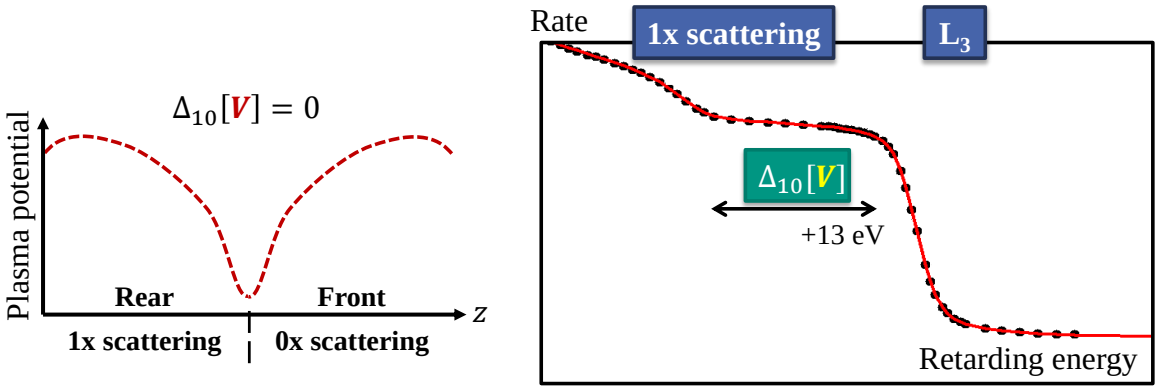

(b) Potential without antisymmetry

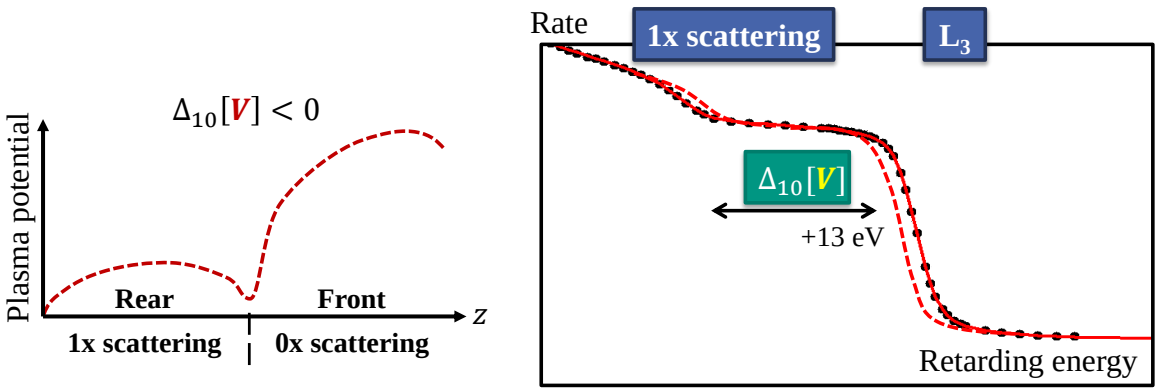

(c) Potential with negative antisymmetry

Figure 1.22.: Dependence of the krypton line distance on the potential antisymmetry: In a simplified picture the scattered electrons stem from the rear side of the source, while the unscattered electrons stem from the front. The distance $\Delta_{10}[V]$ of the krypton lines of one-time scattered and unscattered electrons thus is a measure of the potential *antisymmetry* with regard to the injection point (the sign is chosen opposite to the slope of the potential to fit the sign of $\Delta_{10}[V]$). The overall shift and the broadening of the spectrum due to some (weighted) mean and variance of the potential are neglected in this plot.

Thus, clearly the modelling of the electron spectra needs to consider $\Delta_{10}[V]$, which is why equation 1 is incomplete for this particular systematic. Deriving the correct equation for the neutrino mass shift is the topic of the following chapters.

Scattering weights and starting potential distributions: The rigorous definition of the $\langle V \rangle_i$ as functionals of the potential $V(z)$ not only requires the consideration of the z-dependent scattering probabilities, but also of all other z-dependent functions, most importantly the gas density. Clearly, the mean potentials measured by the krypton-83m or tritium β spectrum are dominated by the region of highest gas density, and the potential in regions without gas is irrelevant. The relationship of $\langle V \rangle_i$ and $V(z)$ was identified in [Mac16] (a more rigorous derivation is found in appendix A.1) and it boils down to a weighted average over z

$$\langle V \rangle_i = \langle P_i V \rangle = \int_z \frac{\mathrm{d}z}{L_{\mathrm{WGTS}}} P_i(z) V(z) \,, \tag{1.38}$$

with normalised weight functions $P_i(z)$. Throughout this work they are called *scattering weights*. Their calculation is defined in chapter 3 and they are plotted in chapter 5 for typical KATRIN measurement conditions modelled after the KNM1-3a measurement campaigns.

The scattering weights exactly define the longitudinal symmetry of the potential, which the measurements are sensitive on by the mechanism described here. For typcial KATRIN measurement conditions it is indeed given by a rear-to-front asymmetry, such that in a simple picture $\langle V \rangle_1$ is approximately the mean potential of the rear and $\langle V \rangle_0$ the mean potential of the front side of the source. However, this should only serve to simplify the understanding of the concept. The essential step is the realisation that the mean potentials $\langle V \rangle_i$ are in general different for different scattering multiplicities. The related symmetry of the potential is only a second step and the rear-to-front symmetry is a mere coincidence, given by the shape of the scattering weights for the respective measurement conditions. Also, the means $\langle V \rangle_i$ are only the first order expansion of the *Starting Potential Distributions* (SPD_i) for different scattering multiplicities. Equation 1.38 defines, how these distributions are weighted. Thus, numerically they can be calculated by sampling the value of the potential $V(z)$ over equally spaced z, weighting it with $P_i(z)$ and filling it into a histogram. Examples are shown in chapter 3. The rigorous derivation of both the SPD_i and the $P_i(z)$ is found in appendix A.1. There it is also shown that the spectral distortion from the starting potential is equivalent to a convolution of the SPD_i with the energy loss function for i-fold scattering, which is indeed how this systematic should be modelled.

The following chapter 2 is a summary over the detailed discussions carried out in chapters 3, 4 and 5. The overall goal of those chapters is to rigorously establish the connection between the source potential and the estimates of the krypton-83m and the tritium β measurements, given the discussed longitudinal sensitivity on the source potential due to inelastic scattering.

2. Summary of Source Systematics Theory and Nomenclature

In the following the nomenclature and the most important relations relevant for source potential systematics are compiled without derivations. This is intended to provide an abbreviated, but comprehensive picture of the following work, with the aim to facilitate the understanding of the mathematically detailed description to follow in chapter 3. Reading section 1.4.2 can further facilitate the introduction to the complex topic. The nomenclature is found in table 2.1 in the form of a glossary.

Convolution of energy scale systematics: The theory discussed in this thesis uses a convolution approach. In this approach, Starting Potential Distributions (SPD) are used to describe systematics of the energy scale E, rather than a full z-dependent inclusion of the actual source potential $V(z)$. This ansatz is not new, but forms an essential part of the modelling of the measurable integrated count rate $\dot{N}(qU)$ at retarding energy qU

$$\dot{N}(qU) \propto \int_{-\infty}^{\infty} \frac{\mathrm{d}\dot{N}}{\mathrm{d}E}(E) R(E, qU)\, \mathrm{d}E\,, \quad \text{(cf. section 1.2.2)}\,.$$

Therein, the complexity of the experiment (z-dependencies, fields, temperatures, ...) is condensed into the response function $R(E, qU)$, which is convolved with the differential rate $\frac{\mathrm{d}\dot{N}}{\mathrm{d}E}$ of the theoretical spectrum. A different example is the shift of the squared neutrino mass (equation 1) [RK88]

$$\Delta m_\nu^2 = -2\sigma^2\,,$$

which is derived by convolving the energy spectrum with the Probability Density Function (PDF) of an energy scale perturbation. It turns out that, in leading order, the standard deviation σ of the PDF predicts the neutrino mass shift, even if the PDF is not a Gaussian [Sle16]. Leading order here is in orders of the energy scale perturbation, i.e. in the moments of the considered distribution. Thus, equation 1 is the expansion of the shift of the squared neutrino mass up to the second moment σ^2. It was shown in [Sle16] that it does not depend on the third moment and it can be expected, that even higher moments are only small corrections. However, as shown in this work, in the case of source potential systematics there exists a first order term, which previously was not considered and which, depending on the shape of the potential, dominates the neutrino mass shift.

The essential deviation of this work to the derivation of equation 1 is the finding, that electrons of different scattering multiplicity i observe different spatial regions of the plasma potential and thus have different starting potential distributions SPD_i (see section 1.4.2).

Table 2.1.: **Nomenclature for quantities used in this work.**
Due to the weighting, all potential moments depend on the tritium or krypton spectrum, even if not stated explicitly. Usually the longitudinal coordinate z is omitted. Instead z often appears as index, which is not related to the coordinate.

quantity	description
P_i or $P_i(z)$	Longitudinal electron distribution for i scattering probability, normalised to 1. Used for weighting the longitudinal averages and derived quantities. In tritium this weighting is generalised to summations over the P_i, since contributions are mixed in the β spectrum.
Indices x, y, z	Generalised electron distribution, usually constructed from summations like $P_x = \frac{1}{\sum a_i} \sum a_i P_i$. Normalised to 1.
Negated indices $\bar{x}, \bar{y}, \bar{z}$	Generalised electron distribution, usually constructed from summations like $P_{\bar{x}} = \frac{1}{\sum a_i} \sum a_i (P_i - P_0)$. Normalised to 0.
Index ρ	Used to specify the special weight summation appropriate for the respective tritium measurement condition. For the standard 40 eV analysis interval, $P_\rho \approx P_1 - P_0$. For increasing analysis interval, P_ρ contains a summation over higher orders of $P_i - P_0$.
$\langle ... \rangle_x$	z-integrated average, weighted with P_x (i.e. $\langle V \rangle_x = \int_z \frac{\mathrm{d}z}{L_{\mathrm{WGTS}}} P_x(z) V(z)$).
V or $V(z)$	Plasma potential in the WGTS.
SPD_i	*Starting potential distribution* of scattering multiplicity i (i.e. frequency distribution of the plasma potential weighted with P_i).
$\sigma_i[V]$	*Standard deviation* of the potential, weighted with P_i (i.e. $\sigma_i^2[V] = \langle V^2 \rangle_i - \langle V \rangle_i^2$). Only σ_0 is relevant at nominal KATRIN.
$\Delta_{ij}[V]$	*Mean difference* of SPD_i and SPD_j (i.e. $\Delta_{ij}[V] = \langle V \rangle_i - \langle V \rangle_j$).
$\Delta_{10}[V]$ and $\Delta_\rho[V]$	Relevant mean differences for krypton and tritium.
$\kappa_{\bar{x},z}$ and $\kappa_{\bar{x}\bar{y},z}$	Weight standard deviation and covariance, $\kappa_{\bar{x},z} = \sigma_z \left[\frac{P_{\bar{x}}}{P_z}\right]$, $\kappa_{\bar{x}\bar{y},z} = \mathrm{Cov}_z \left[\frac{P_{\bar{x}}}{P_z}, \frac{P_{\bar{y}}}{P_z}\right]$. Fully quantify relations between different observables.
$\rho_{\bar{x}\bar{y},z}$	Weight correlation, $\lvert\rho_{\bar{x}\bar{y},z}\rvert \leq 1$. Given by the ratio $\rho_{\bar{x}\bar{y},z} = \frac{\kappa_{\bar{x}\bar{y},z}}{\kappa_{\bar{x},z}\kappa_{\bar{y},z}}$.
$\hat{\rho}_{\bar{x},z}[V]$	Correlation operator, $\lvert\hat{\rho}_{\bar{x},z}[V]\rvert \leq 1$. Given by the ratio $\hat{\rho}_{\bar{x},z}[V] = \frac{1}{\kappa_{\bar{x},z}} \frac{\Delta_{\bar{x}}}{\sigma_z}[V]$. Specifies the correlation of the measured potential to the longitudinal shape defined by $\frac{P_{\bar{x}}}{P_z}$.
$\hat{\rho}[V]$	*Antisymmetry operator*, which is the correlation operator of the relevant krypton and tritium observables ($\frac{\Delta_{10}}{\sigma_0}[V]$ for krypton, $\frac{\Delta_\rho}{\sigma_0}[V]$ for tritium). The corresponding longitudinal shape is antisymmetrical (≈linear) for typical KATRIN.
ϵ_i and a_i	*Susceptibility* of neutrino mass and endpoint to mean differences (i.e. $\epsilon_i = -\frac{\mathrm{d}m_\nu^2}{\mathrm{d}\Delta_{i0}}$ and $a_i = -\frac{\mathrm{d}E_0}{\mathrm{d}\Delta_{i0}}$).
ϵ and a	Absolute total susceptibilities (i.e. $\epsilon = \lvert\sum_i \epsilon_i\rvert$ and $a = \lvert\sum_i a_i\rvert$). Give tritium shifts by simultaneous shift of all scatterings, i.e. by $\Delta_{i0} = \Delta_{j0}$.
ϵ_ρ	*Shape energy*, $\epsilon_\rho = -\frac{1}{2} \frac{\mathrm{d}m_\nu^2}{\mathrm{d}\sigma_0 \mathrm{d}\hat{\rho}} = \frac{1}{2}\kappa_{\rho,0}\epsilon > 0$. Quantifies the neutrino mass shift for the potential shape that produces the maximum shift, respecting the correlation of Δ_ρ and σ_0. a_ρ equivalently for the endpoint.

As a consequence, plasma potential systematics cannot be considered with only one convolution, but instead the β spectrum obtained for each scattering multiplicity needs to be convolved with its own SPD_i. As in equation 1, in a perturbative theory the resulting neutrino mass shift is determined by a few scalar moments of these distributions, namely $\sigma_0[V]$, the standard deviation of the unscattered distribution, and $\Delta_{10}[V]$, the difference of the mean of the one-time scattered to the unscattered distribution. In general those moments are derived from longitudinal averages over the WGTS length L_{WGTS} of the form

$$\langle V \rangle_i = \int_z \frac{\mathrm{d}z}{L_{\mathrm{WGTS}}} P_i(z) V(z) \ ,$$

where the weighting with the longitudinal distributions $P_i(z)$ of the signal electrons for the scattering multiplicity i needs to be considered. Throughout this thesis square brackets (for the means $\langle V \rangle_i$ rectangular brackets) are used for functional dependencies in contrast to round brackets, which are used for scalar dependencies. Thus, all quantities in rectangular brackets are z-dependent functions.

The resulting shift of the squared neutrino mass reads

$$\Delta m_\nu^2[V] = -\epsilon_1 \Delta_{10}[V] - 2\sigma_0^2[V] \ .$$

ϵ_1 depends on the fraction of scattered electrons in the measurement time distribution for the respective column density. It is determined from simulation in chapter 5 and is around 1 eV for the typical KATRIN measurement conditions. Notably, this additional term is in fact dominant for usual plasma potential inhomogeneities $\sigma_0[V]$ on the order of 100 mV.

Determination of $\sigma_0[V]$ and $\Delta_{10}[V]$: Fortunately, it turns out that both $\sigma_0[V]$ and $\Delta_{10}[V]$ are in principle observables of the krypton-83m measurement. They are obtained by measuring a broadening of the unscattered line ($\sigma_0[V]$), and the difference of the position of the one-time scattered line to the unscattered line ($\Delta_{10}[V]$). The latter requires the precise knowledge of the expected mean energy loss on a level of 10 meV, i.e. the precise knowledge of the energy loss function. Leaving such uncertainties aside, in principle $(\sigma_0[V], \Delta_{10}[V])$ could be obtained from the krypton-83m measurement, and they could be put into the tritium spectrum modelling to compensate for the source plasma induced neutrino mass shift. While this is the result of a phenomenological ansatz, there is no fundamental difference to already included physical effects like for example the Doppler effect, which is also included in the spectrum model via a broadening of the energy scale.

Real-life complications: While the previous discussion covers the essential picture, many details have been skipped. One of the problems is that the estimates $(\sigma_0[V], \Delta_{10}[V])$ depend on the gas species and measurement conditions, since the electron distributions $P_i(z)$ of tritium and krypton are not the same and up to the 2020 measurement phase KNM4 also the operating conditions of the source modes of krypton-83m and tritium were not the same. Differences in the respective potential estimates are related to the different weighting with the signal electrons from either krypton-83m or tritium and even appear if the plasma potential is exactly the same in both measurements. Notably, all

differences in measurement modes and gas species can be condensed into differences of the $P_i(z)$ and the cause is irrelevant. Moreover, it is not even relevant whether the different $P_i(z)$ are the result of different scattering multiplicities, or have some other origin. An example is the question how a measurement of $\sigma_0[V]$ in krypton can constrain $\sigma_1[V]$ in krypton or $\sigma_0[V]$ in tritium. The only difference is in the shape of the $P_i(z)$, regardless of whether it is a difference in the scattering multiplicity in one case or a difference in gas species in the other. In order to cover all cases in an efficient formalism, the scattering index i is generalised to indices x, y, z for normalisation of the weight to 1, and to negated indices $\bar{x}, \bar{y}, \bar{z}$ for normalisation to 0. The use of general indices also takes into account the fact that the weights can be composed of several scattering weights, as discussed below. These indices translate to the indices of all derived quantities like the σ_z and $\Delta_{\bar{x}}$. How the measurement $(\sigma_0[V], \Delta_{10}[V])$ from krypton-83m constrains quantities with different weights, for example the same observables seen from the tritium spectrum, boils down to a correlation analysis of the involved weights. Deriving the respective equations is a large part of the discussion in chapter 3.

Relation of $\sigma_0[V]$ and $\Delta_{10}[V]$: This discussion also has some welcome by-products. Namely, it allows to establish relations between quantities like $\sigma_z[V], \Delta_{\bar{x}}[V]$ or also the peak-to-peak value of the potential. One is especially helpful, since $\Delta_{10}[V]$ can currently not be obtained with sufficient precision from the krypton-83m measurement. The key insight here is that it is given by the covariance

$$\Delta_{10}[V] = \mathrm{Cov}_0\left[\frac{P_1 - P_0}{P_0}, V\right] ,$$

which follows straightforward from its definition. Dividing by the standard deviations of the arguments leads to the correlation

$$\hat{\rho}[V] = \frac{\mathrm{Cov}_0\left[\frac{P_1-P_0}{P_0}, V\right]}{\sigma_0\left[\frac{P_1-P_0}{P_0}\right]\sigma_0[V]} = \frac{1}{\kappa_{\overline{10},0}}\frac{\Delta_{10}}{\sigma_0}[V] .$$

$\kappa_{\overline{10},0}$ is the standard deviation of the involved weights, which is of the order of 0.77 for typical KATRIN conditions. Since $\hat{\rho}[V]$ by definition is a correlation, $|\hat{\rho}[V]| \leq 1$ holds. Thus, if only $\sigma_0[V]$ can be measured, $\Delta_{10}[V]$ can still be constrained in a meaningful way.

Relation of $\Delta_{10}[V]$ and $\hat{\rho}[V]$ to the potential shape: A second important conclusion is that $\Delta_{10}[V]$ measures the covariance of the potential to the longitudinal shape $\frac{P_1-P_0}{P_0}(z)$. For typical KATRIN conditions this shape is approximately antisymmetrical (in very good approximation even linear) to the injection point, i.e. such potentials produce the largest $\Delta_{10}[V]$ for a given $\sigma_0[V]$. This coincides with the simple understanding that scattered electrons are more likely to stem from the rear of the WGTS and unscattered electrons from the front, such that the largest difference of their starting potential distributions is observed if the potential inhomogeneity is mainly given by a rear-to-front asymmetry (see section 1.4.2).

Following the above reasoning, $\hat{\rho}[V]$ is called the antisymmetry operator. Using it instead of $\Delta_{10}[V]$ has the advantage that σ_0 and $\hat{\rho}$ are independent quantities (such that their dependence on V can be omitted), whereas $\sigma_0[V]$ is an upper limit to $\Delta_{10}[V]$, as described above. Also, since $\hat{\rho}$ is a measure of a certain potential shape and σ_0 for inhomogeneity magnitude, using those to parametrise the potential $V(z)$ reveals the fundamental connection of the krypton-83m observables to the symmetries of the potential in a model-independent way. This is the topic of chapter 4.

Relation of neutrino mass shift and potential shape: Reformulating the neutrino mass shift equation in terms of $\hat{\rho}$ leads to an equation for which a simple analytical curve sketching can be performed. However, one generalisation should be mentioned before, namely, that in the above discussion terms proportional to Δ_{i0} with scatterings larger than $i = 1$ have been neglected. Of course, if the measurement time distribution of the β spectrum includes significant portions of electrons of higher scattering multiplicity, those terms are also relevant. It turns out that this in general only affects the $\Delta_{i0}[V]$ term, and that standard deviations $\sigma_i[V]$ with $i > 0$ are negligible. For the KNM2 measurement campaign with a tritium column density of 84 % of nominal, 0.6 % of two times scattered electrons are included in the standard analysis interval of 40 eV. These details are considered by using generalised weights $P_{\tilde{x}}(z)$, which are weighted summations over all relevant scattering contributions. To specify the concrete weighting, which is relevant for the respective tritium measurement condition, the index ρ is used. Thus, formally equivalent equations as before are obtained, when replacing indices "10" with ρ. Notably, this generalisation has no fundamental impact on the predictive power of the krypton measurement. Still correlations between $\Delta_{10}[V]$ from krypton and $\Delta_\rho[V]$ in tritium can be studied, and it turns out that the resulting uncertainties are acceptable. This correlation analysis is also necessary in the case where higher scatterings are negligible: As discussed, $\Delta_{10}[V]$ from krypton-83m and $\Delta_{10}[V]$ from tritium are in general two different quantities, since the gas profiles of the gas species are different.

Thus, the shift of the squared neutrino mass reads

$$\begin{aligned} \Delta m_\nu^2[V] &= -\epsilon \Delta_\rho[V] - 2\sigma_0^2[V]\,, \\ \Rightarrow \Delta m_\nu^2(\hat{\rho}, \sigma_0) &= -\underbrace{\epsilon \kappa_{\rho,0}}_{\equiv 2\epsilon_\rho}\, \sigma_0 \hat{\rho} - 2\sigma_0^2\,, \\ &= -2\sigma_0 \Big(\underbrace{\epsilon_\rho \hat{\rho}}_{\text{shape}} + \underbrace{\sigma_0}_{\text{variance}} \Big)\,. \end{aligned}$$

The newly introduced quantity ϵ_ρ is the shape energy. It represents the penalty neutrino mass shift with regard to the worst possible potential shape. Since $\hat{\rho}$ specifies the correlation to this shape, the term is extremal for antisymmetrical potentials with $\hat{\rho} = \pm 1$ and vanishes for symmetrical potentials with $\hat{\rho} = 0$. For typical KATRIN conditions ϵ_ρ is of the order of 500 meV, such that it is relevant even for small $|\hat{\rho}|$ on the order of 0.1.

In the following this theory is studied in all necessary detail.

3. Observables of the WGTS Plasma Potential in the Presence of Inelastic Scattering

In this chapter the general properties of observables of the z-dependent source plasma potential are studied. As first observed in [Mac16], due to the presence of inelastic scattering the usual simple linear connection between the shift of the squared neutrino mass and the energy scale variance does not hold for the source potential. While deriving the correct equation is the overall goal of this chapter, many steps on the way are necessary to understand the implications on the tritium β plasma potential systematics and the krypton-83m commissioning measurements. Reading section 1.4.2, which provides a more qualitative introduction, is recommended before studying this chapter.

The chapter starts with the definition of the fundamental moments of the potential for each scattering multiplicity and their related starting potential distributions in section 3.1. These moments are the observables in krypton-83m conversion electron measurements.

Section 3.2 studies the connection of injectivity and surjectivity of the measurement to the potential shape. The dependence of both the krypton-83m and the tritium β observables on a certain symmetry of the potential shape is the essential addition to the description without inelastic scattering.

The moments depend on the distribution of signal electrons in the source. In section 3.3 it is analysed how moments obtained with differing electron distributions constrain each others and which potential shapes produce the maximum differences.

Section 3.4 studies the compositions of moments of different scattering multiplicities, which are observables in the tritium β neutrino mass measurement.

In section 3.5 it is shown how these general observables are constrained by measurements of the fundamental moments, i.e. how the observables obtained in krypton-83m measurements constrain the neutrino mass shift.

Finally, section 3.6 discusses how the potential shape influences the neutrino mass shift and concludes the chapter with a curve sketching of the derived neutrino mass shift equation.

3.1. Starting Potential Distributions at fixed Scattering Multiplicity and their Moments

All quantities in the WGTS which are observed by the focal plane detector undergo a z-dependent, longitudinal averaging and only estimates which are functions of the following *first moments* (or *means*) can be measured [Mac16] (rigorous derivation in appendix A.1):

$$\langle V \rangle_i = \frac{\int_z \mathrm{d}z\ \Omega(z) N^{\mathrm{Kr,T_2}}(z) p_i(z) V(z)}{\int_z \mathrm{d}z\ \Omega(z) N^{\mathrm{Kr,T_2}}(z) p_i(z)} \equiv \int_z \frac{\mathrm{d}z}{L_{\mathrm{WGTS}}} P_i(z) V(z) = \langle P_i V \rangle \ . \tag{3.1}$$

V is the plasma potential, the weights are the products of all z-dependent functions (densities $N^{\mathrm{Kr,T_2}}$, scattering probabilities p_i for scattering multiplicity i, maximum pitch angle Ω). The normalised weights $P_i(z)$ have been introduced, such that the following normalisations hold:

$$\left\langle P_i^{-1} \right\rangle_i = \int_z \frac{\mathrm{d}z}{L_{\mathrm{WGTS}}} = 1 \ , \tag{3.2}$$

$$\langle 1 \rangle_i = \int_z \frac{\mathrm{d}z}{L_{\mathrm{WGTS}}} P_i(z) = 1 \ . \tag{3.3}$$

These normalisations are enough to derive all the relations in this chapter. In particular, no knowledge of the shape of the $P_i(z)$ is necessary. This means that all relations are true, even if the modelling of the P_i in reality is erroneous and it allows to generalise the obtained relations to weights which are not a composition of functions characterising the WGTS. Even so, weights for krypton-83m conversion electron or tritium β spectra are naturally used for examples or sketches, as they represent the use case. Still sketches are preferred over showing plots for specific measurements, since the latter depend on many parameters innate to the respective measurement conditions. Plots for the KNM1-3a measurement campaigns are found in chapter 5. A sketch of typical weights is shown in figure 3.1.

Typically the weights vanish for $z \longrightarrow \pm\infty$, leading to unproblematic boundary conditions and simple numeric integration. In practice, the following discussion is restricted to the non-zero region in the central WGTS.

Here and in the following lower indices i, j, k are always indicative of the corresponding scattering multiplicities. To represent general weights, indices x, y, z are used, indicating that weights can also differ in operating conditions or gas profiles or that they can be composed of several scattering weights. Brackets around upper or lower indices of operators mean "up to". Small letters a, b (sometimes with indices) are always real numbers, capital letters F, G are integrable test functions (in L^1 or L^2) from $\mathbb{R} \longrightarrow \mathbb{R}$. To indicate scalars with units of energy ϵ is used, sometimes with indices.

Equation 3.1 is a functional of the potential, which can be interpreted as an integral operator [1]. This interpretation allows to study the properties of the first moments and

[1] The dimensionless line element $\frac{\mathrm{d}z}{L_{\mathrm{WGTS}}}$ is used, but the coordinates are not transformed. That means, that only the respective integrals are normalised and functional derivatives or integrals (i.e. the area in plots over z) using dimensional $\mathrm{d}z$ are scaled by L_{WGTS}. For this reason usually a normalised z-axis is shown.

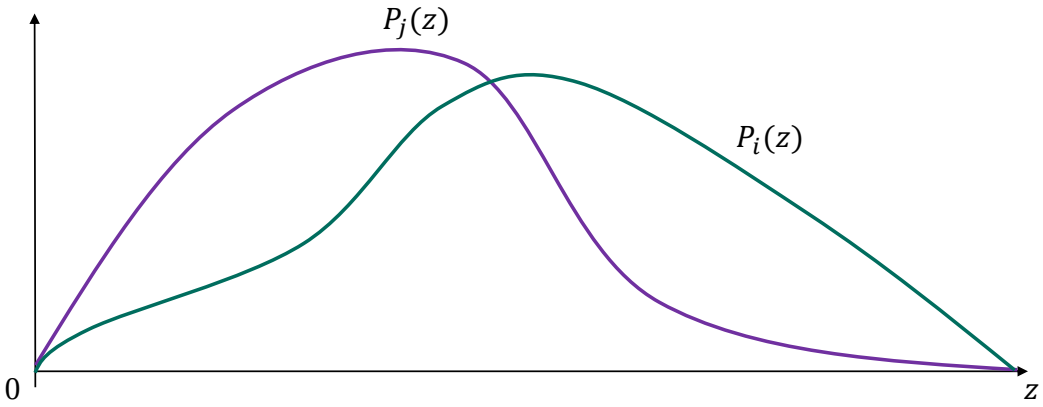

Figure 3.1.: Sketch of normalised weights in WGTS: The area of the weights is normalised to 1, but their maximum can be larger. They are positive and vanish at the longitudinal boundaries of the WGTS. Since they usually overlap, they have at least one point of intersect. The sketch follows common shapes for $i = 0$ and $j = 1$.

derived operators using functional derivatives. Since the moments do not depend on the derivative of the potential $\partial_z V$ it follows from the Euler-Lagrange equation, that the functional derivative is identical to the partial derivative of the integrand with respect to V. $L_{\mathrm{WGTS}} = 1$ is used in all derivatives, since it cancels anyway in all use cases. Also writing out the argument z is, in most cases, omitted for brevity. Square and angular brackets are used to indicate the functional nature of the operators in contrast to round brackets for scalar dependencies.

3.1.1. Potential Moments

As sketched in figure 3.2, in the quasi mono-energetic krypton-83m conversion electron spectrum the scattering effects are separated in energy by the minimum inelastic energy loss, such that the moments of the form 3.1 can be observed separately for each scattering multiplicity. Thus, expansions of general operators O_i in the order l of the potential read

$$O_i[V] = \sum_{m+n=l} a_{mn} \langle V^m \rangle_i \langle V \rangle_i^n \ . \tag{3.4}$$

The potential is a perturbation of the spectrum, such that higher orders decrease in magnitude and can be discussed separately. The zeroth order is a constant shift of the measurement and is set to zero. The first order observables are the means $\langle V \rangle_i$. Expanding up to second order,

$$O_i^{(2)}[V] = \epsilon \langle V \rangle_i + a \langle V^2 \rangle_i + b \langle V \rangle_i^2 \tag{3.5}$$

is obtained. Usually it is demanded that the expectation value vanishes for constant potentials $V \equiv v_0$

$$O_i^{(2)}[v_0] = \epsilon v_0 + (a+b) v_0^2 = 0 \quad \forall v_0 \in \mathbb{R} \,, \tag{3.6}$$

$$\Rightarrow \epsilon = 0 \,, \quad a = -b \,, \tag{3.7}$$

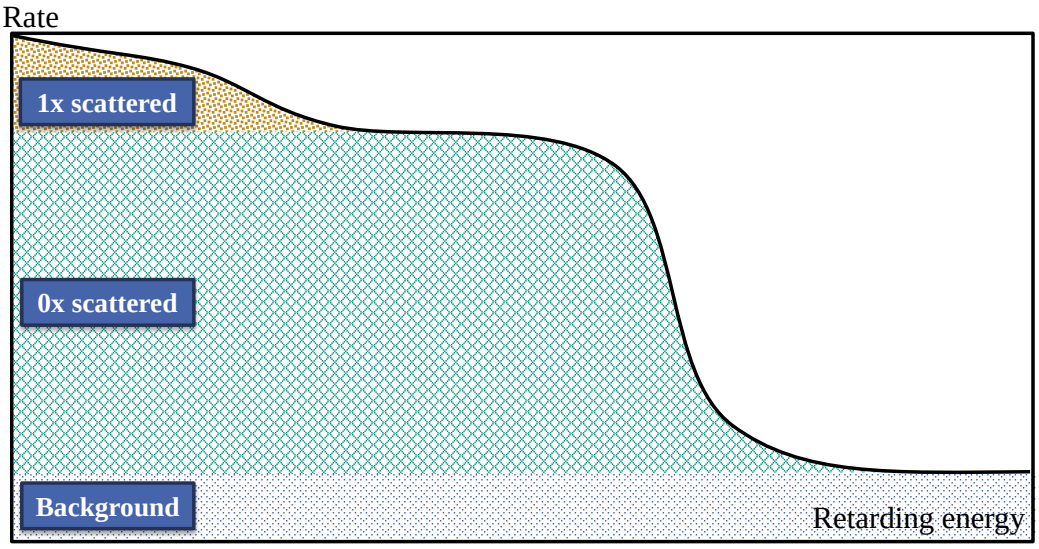

Figure 3.2.: Separation of scattering effects in mono-energetic spectra: In quasi mono-energetic spectra like the krypton-83m spectrum, the non-constant rate contributions are well separated in energy. Since only the non-constant contributions are affected by the potential, observations of the potential can be separated in scattering multiplicity.

$$\Rightarrow O_i^{(2)} = a\left(\langle V^2\rangle_i - \langle V\rangle_i^2\right) \ . \tag{3.8}$$

The operator $\sigma_i^2[V] \equiv \left\langle V^2\right\rangle_i - \langle V\rangle_i^2$ is the *central variance* or *second central moment* and its square root is commonly known as the *standard deviation*

$$\sigma_i[V] \equiv \sqrt{\mathrm{Var}_i[V]} = \sqrt{\langle V^2\rangle_i - \langle V\rangle_i^2} \ . \tag{3.9}$$

Thus, different means $\langle V\rangle_i$ and standard deviations $\sigma_i[V]$ of the potential can be obtained at the krypton lines of i scattering multiplicity. In practice this is implemented by convolving a different Gaussian $G(\langle V\rangle_i, \sigma_i)$ [2] with each of the i times convoluted energy loss functions (cf. appendix A.1). Higher orders in the potential are not obtainable in a feasible measurement time and are not discussed further.

To characterise potential-induced differences in the means $\langle V\rangle_i$, the *first moment differences* (or *mean differences*)

$$\Delta_{ij}[V] \equiv \langle V\rangle_i - \langle V\rangle_j \tag{3.10}$$

are defined.

3.1.2. Starting Potential Distributions

In figure 3.3 the unweighted frequency distribution of the krypton condition plasma potential obtained in plasma simulations (figure 1.19) is shown. This unweighted distribution

[2] The constant a in equation 3.8 depends on the observable that is used for the measure of inhomogeneity. If the measure is a Gaussian variance, $a = 1$ by definition. This is not the case if for example a total Lorentzian width Γ is fitted, where $a \approx 0.085$ is expected, as shown in section 6.2.1.

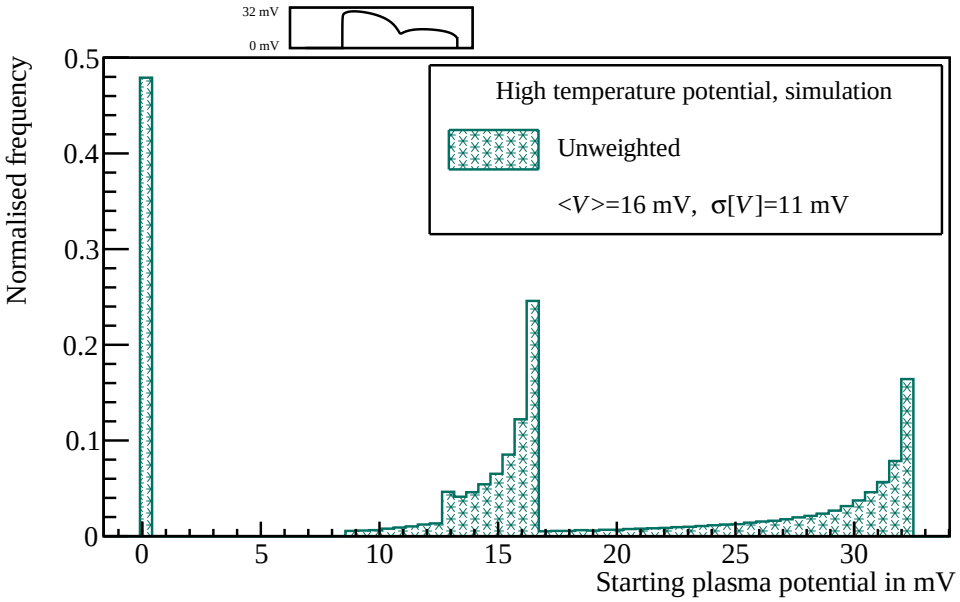

Figure 3.3.: Unweighted starting potential distribution: The potential is shown in the sketch above the plot, where the non-zero region is the central WGTS and the zero region extends to the rear wall. Thus, the distribution includes sizeable zero contribution, which is a boundary effect of the simulation.

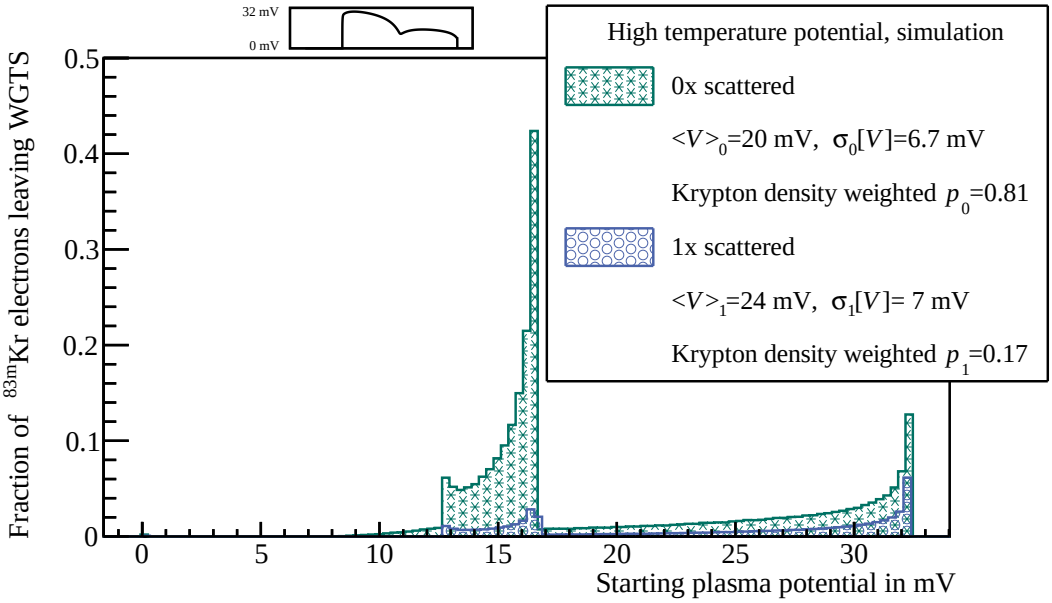

Figure 3.4.: Scattering weighted starting potential distribution: If the potential is weighted with the scattering weights, several distributions are obtained. Here, it is obvious that the boundary conditions of the simulation are indeed irrelevant, since they are cut by the vanishing weights outside the central WGTS. Thus, also the first moments displayed in the legend are considerably higher than without weighting. In contrast, the standard deviations are smaller, since the large variance at the boundaries is cut.

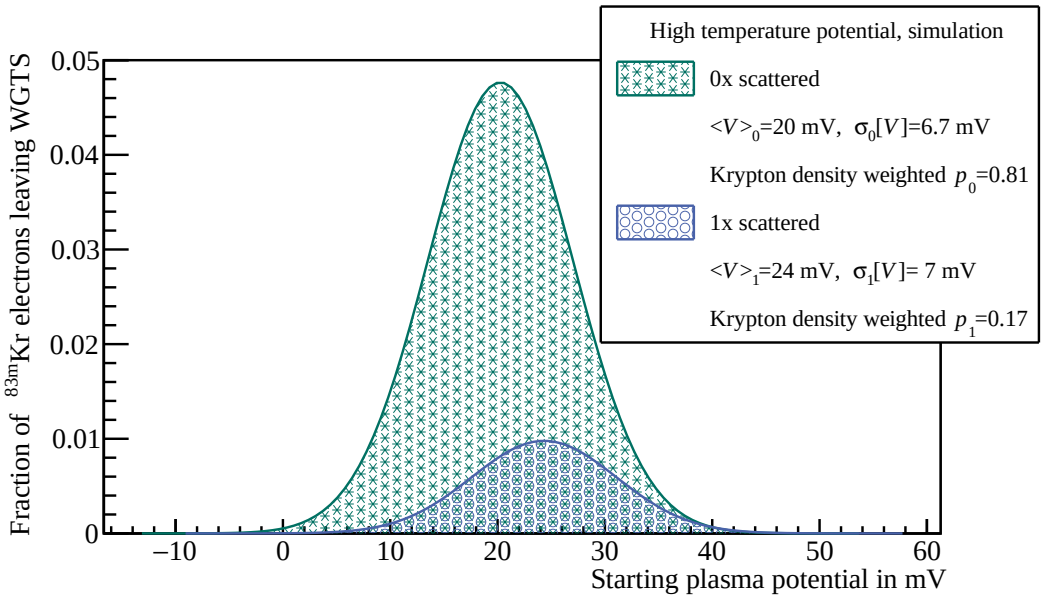

Figure 3.5.: Approximated starting potential distribution: If the full distributions are approximated with their means and variances, they can be represented by Gaussians, which are directly obtained in krypton-83m measurements by fitting Voigt profiles to lines of different scattering multiplicities. Thus, there is no systematic related to this approximation and it is shown in [Sle16] that the higher potential orders are also irrelevant for tritium β systematics.

is of little physical relevance, which is evident from the fact that a sizeable portion of the distribution is at zero potential. Zero was the boundary condition of the simulation, which assumed that the particle densities are dominated from the central WGTS. The sensitive region of the distribution, however, was picked to include the region up to the rear wall, as visible in the sketch. Thus, the term unweighted in this case refers to a piecewise constant weight which is one for z in this sketch and zero elsewhere. Without the specification of the weight, neither the distributions nor the moments are well defined, and both only give reasonable insight on the measurement, if they are weighted with electron densities that fit to the experiment.

Thus, if the same potential is weighted according to equation 3.1, several distributions are obtained for the different scattering multiplicities, which is shown in figure 3.4. These are the distributions of relevance for the measurements and if they are known, they can be convolved with the spectra of the according scattering multiplicity to fully account for the plasma effects (cf. appendix A.1) [3].

However, only the three moments $\langle V\rangle_0$, $\langle V\rangle_1$ and $\sigma_0[V]$ are obtainable in krypton-83m measurements in practice. Thus, conceptually the exact distributions are replaced with

[3] Figure 3.4 also illustrates the connection of the average electron starting position to the average starting potential, which is visible in the different peak heights: More one-time scattered electrons start in high potential than in low potential, which indicates a dominant starting position towards the rear, as visible in the sketched potential. The unscattered electrons show the opposite behaviour.

Table 3.1.: **Overview of plasma potential-related quantities in krypton-83m measurements.**
The expectation values of the three operators are the true values. The krypton observables are subject to systematics which are not related to the potential. The negative signs are due to the negative charge of the electrons.

operator	expectation value	krypton observable	name
$\langle ... \rangle_0$	$\langle V \rangle_0$	$-\Delta E_{\text{Main}}$	Line position shift
$\sigma_0[...]$	$\sigma_0[V]$	σ_{g}	Gaussian broadening
$\Delta_{10}[...]$	$\Delta_{10}[V]$	$-\Delta\epsilon_{\text{Eloss}}$	Eloss shift

Gaussians with the same moments, depicted in figure 3.5. Since $\sigma_1[V]$ cannot be obtained, $\sigma_0[V] = \sigma_1[V]$ is assumed. As shown in section 5.1, this does not lead to sizeable systematics due to the intrinsic width of the energy loss function. Also, disregarding the higher potential order moments is not a systematic in krypton-83m measurements, since the remaining moments are the direct observables.

Krypton spectrum observables: Since the effect of the potential is now condensed to three parameters, doing two full convolutions of the starting potential distributions with the spectra of the respective scattering multiplicities becomes unnecessary:

- The mean value $\langle V \rangle_0$ is the measurable *line position shift* $-\Delta E_{\text{Main}}$ in krypton measurements.
- The standard deviation $\sigma_0[V]$ is the *Gaussian broadening* σ_{g} fitted in krypton measurements. In practice, a Voigt profile is used, however $\sigma_0^2[V]$ can also be added to already existing variances like the spectral broadening caused by the Doppler effect.
- The mean difference $\Delta_{10}[V]$ is implemented as a shift of the energy loss function [4] $-\Delta\epsilon_{\text{Eloss}}$, shown in chapter 5. This is referred to as *eloss shift*.

The negative signs on the linear quantities are due the electric charge of the electrons. In relations between the moments of the potential and those of the energy spectrum an elementary charge $e = 1$ is used. Measured estimate and expectation value of the operator are only equal if all systematic effects are understood, this is why distinct names are kept. This leads to the definitions in table 3.1.

With these definitions the effect of the plasma potential on the krypton-83m conversion electron spectrum is sufficiently described in up to second order in the potential. However, more can be learned about the relations of moments to the potential shape as well as

[4] The shift should be applied to each i times convoluted energy loss function $f_i(\epsilon)$ separately. This assumes $\Delta_{i0} = -\Delta\epsilon_{\text{Eloss}}$ $(\forall i > 0)$, which is physically likely due to the weight degeneracy discussed in section 3.2.2. If the energy loss function $f_1(\epsilon)$ (see figure 1.10) is shifted, the shift of each spectrum is multiplied with the scattering multiplicity $\Delta_{i0} = -i\Delta\epsilon_{\text{Eloss}}$. For tritium both cases differ in normalisation, which is further discussed in chapter 5. For krypton only one scattering is relevant such that shifting each $f_i(\epsilon)$ or $f_1(\epsilon)$ is equivalent.

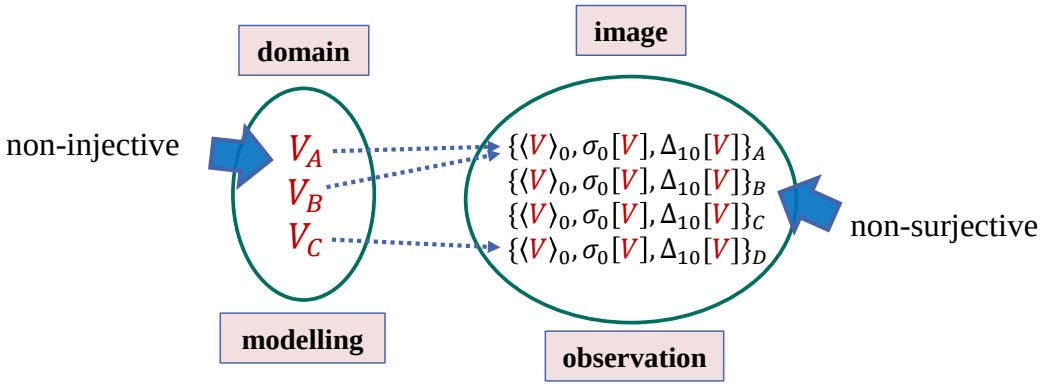

Figure 3.6.: Non-surjectivity and non-injectivity of plasma measurements: Since multiple potentials V_A, V_B can lead to the same observables, measurements of the WGTS plasma are in principle non-injective. It is shown in the sections below that they are also non-surjective, i.e. that some combinations of observables can never be obtained.

systematics in the krypton measurements by studying general properties of the involved operators.

3.1.3. Generalised Potential Moments and their Algebraic Properties

In the following sections some of the algebraic properties of the defined operators are studied. Some focus will be put on their surjectivity, injectivity and their kernels. The benefit is sketched in figure 3.6:

- Surjectivity→Data integrity: It turns out that the obtainable set of expectation values is not surjective, i.e. the image is bounded. This offers an assumption-free possibility to perform data integrity checks and constraints, i.e. observations have to be in the image of the operators, otherwise there are unaccounted systematics.
- Injectivity→Potential determination: Since the means are not injective, none of the operators is injective. Thus, while in general the measurement $(\langle V\rangle_0, \Delta_{10}[V], \sigma_0[V])$ cannot determine the full potential $V(z)$, it turns out that a certain potential leads to a unique measurement. In essence this is related to the non-trivial kernel of the $\Delta_{ij}[...]$, which measure only a very specific form of inhomogeneity.

Lastly, the question of injectivity is relevant for plasma modelling, which is discussed in chapter 4. Naturally, if the potential model is expanded as function of the weights P_i, algebraic relations following from their normalisations (equations 3.2 and 3.3) can be used to calculate the expectation values of the operators analytically. Some relations are obtained in the following, which will prove useful later on.

Mean potentials: The means $\langle ...\rangle_i$ are linear operators

$$\langle aF + bG\rangle_i = a\langle F\rangle_i + b\langle G\rangle_i \ . \tag{3.11}$$

The linearity is apparent from the functional derivative

$$\frac{\delta \langle V \rangle_i}{\delta V} = P_i \,, \tag{3.12}$$

which is constant in V.

Orthogonal potentials in different scattering means can be constructed using expansions like

$$\left\langle \frac{\sum_k a_k (P_k - 1)}{P_j} \right\rangle_i \propto (1 - \delta_{ij}) \,, \tag{3.13}$$

where δ_{ij} is the Kronecker delta. More specifically, for $i = j$ equation 3.13 describes a subset of z-dependent functions in the kernel of $\langle ... \rangle_i$. This is achieved by subtraction of the respective expectation value (1 in this case), which works in general due the linearity of the means.

The $\langle ... \rangle_i$ are surjective, which follows from their linearity.

Potential mean differences: The mean differences $\Delta_{ij}[V] = \langle V \rangle_i - \langle V \rangle_j$ are linear operators, which follows from the linearity of the means, equation 3.11.

Thus, their derivative

$$\frac{\delta \Delta_{ij}[V]}{\delta V} = P_i - P_j \,, \tag{3.14}$$

is constant in V.

They are antisymmetric in their weights

$$\Delta_{ij}[...] = -\Delta_{ji}[...] \,. \tag{3.15}$$

The kernel is non-trivial. An example for expansions of functions in their kernel is

$$\Delta_{ij} \left[\frac{\sum_k a_k (P_k - 1)}{P_{i'} - P_{j'}} \right] \propto (1 - \delta_{ii'} \delta_{jj'}) \,. \tag{3.16}$$

The mean differences are a measure of longitudinal inhomogeneity

$$\Delta_{ij}[b] = b \left(\langle 1 \rangle_i - \langle 1 \rangle_j \right) = 0 \,. \tag{3.17}$$

From this property it follows:

$$\begin{aligned} 0 &= \Delta_{ij}[1] \,, \\ &= \Delta_{ij}[\Theta(P_i - P_j) + \Theta(P_j - P_i)] \,, \\ &= \Delta_{ij}[\Theta(P_i - P_j)] + \Delta_{ij}[\Theta(P_j - P_i)] \,, \\ \Rightarrow \Delta_{ij}[\Theta(P_i - P_j)] &= -\Delta_{ij}[\Theta(P_j - P_i)] \,, \end{aligned} \tag{3.18}$$

i.e. the positive and negative parts of their weights cover the same area, which is shown in figure 3.7.

Like the $\langle ... \rangle_i$, the $\Delta_{ij}[...]$ are surjective and non-injective.

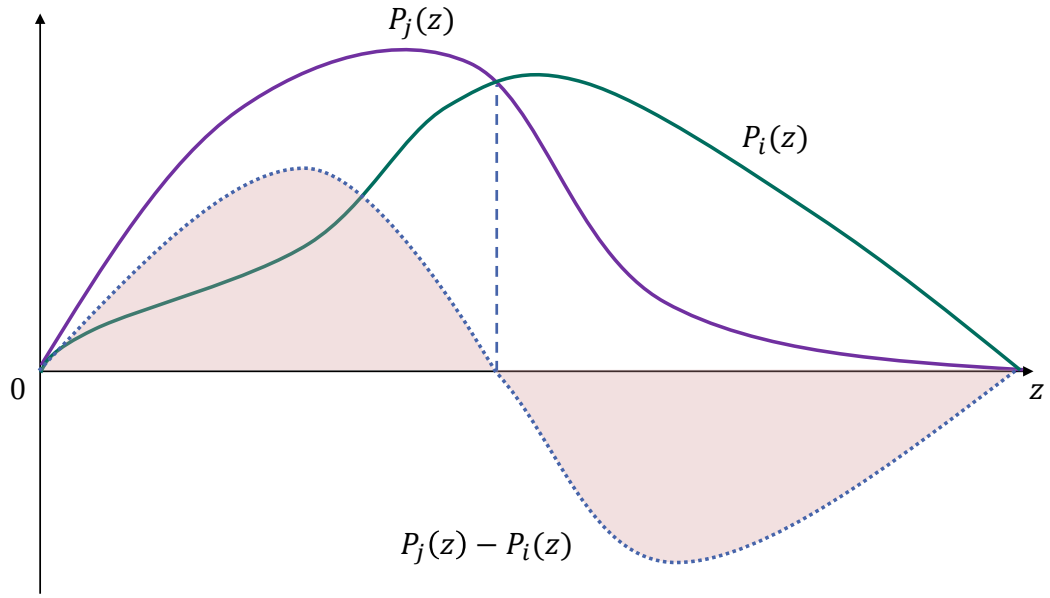

Figure 3.7.: Sketch of differences of normalised weights in the WGTS: Due to the normalisation of the weights, their differences have at least one zero crossing. At this position their corresponding operators are not sensitive to the potential. Furthermore, they cover the same positive and negative area.

Generalised indices: Equation 3.18 is the defining property of generalised mean differences:

$$\frac{\delta \Delta_{\bar{x}}[V]}{\delta V} = P_{\bar{x}} \,, \quad \langle 1 \rangle_{\bar{x}} \equiv 0 \,. \tag{3.19}$$

Thus, negated indices $\bar{x}, \bar{y}, \bar{z}$ are used as abbreviated notation for weights that are normalised to 0. Here the weight $P_{\bar{x}}$ usually is constructed from compositions of scattering weights P_i like

$$P_{\bar{x}} \equiv \frac{1}{\sum_i a_i} \sum_i a_i (P_i - P_0) \,. \tag{3.20}$$

The coefficients a_i specify the scattering contribution. As shown in section 3.4.3, such composed operators are relevant to describe the tritium β-spectrum systematics. Analogously, indices x, y, z without negation are used for weights like

$$P_z \equiv \frac{1}{\sum_i a_i} \sum_i a_i P_i \,, \tag{3.21}$$

which are normalised to 1. All equations derived in this chapter only depend on the normalisation conditions of the weights, such that they hold for the pure operators $\langle ... \rangle_i$, $\Delta_{ij}[...]$, $\sigma_i[...]$ as well as for the composed operators $\langle ... \rangle_z$, $\Delta_{\bar{x}}[...]$, $\sigma_z[...]$. Since the latter is the more general case, in the following indices for composed operators are used.

Longitudinal standard deviations of the potential: The derivative of the standard deviations $\sigma_z[...]$ is

$$\frac{\delta \sigma_z^r[V]}{\delta V} = r \sigma_z^{r-2}[V] P_z \left(V - \langle V \rangle_z \right) , \quad r \in \mathbb{R} \,, \tag{3.22}$$

which is linear in V for $r = 2$. Thus, the $\sigma_z^2[...]$ are quadratic operators, leading to the usual rules

$$\begin{aligned}\sigma_z^2[aF + bG] &= \langle (aF + bG)^2 \rangle_z - \langle aF + bG \rangle_z^2 \\ &= a^2 \langle F^2 \rangle_z + 2ab \langle FG \rangle_z + b^2 \langle G^2 \rangle_z - a^2 \langle F \rangle_z^2 - 2ab \langle F \rangle_z \langle G \rangle_z - b^2 \langle G \rangle_z^2 \\ &= a^2(\langle F^2 \rangle_z - \langle F \rangle_z^2) + b^2(\langle G^2 \rangle_z - \langle G \rangle_z^2) + 2ab(\langle FG \rangle_z - \langle F \rangle_z \langle G \rangle_z) \\ &= a^2\sigma_z^2[F] + b^2\sigma_z^2[G] + 2ab\mathrm{Cov}_z[F, G] \,, \end{aligned} \tag{3.23}$$

with the covariance

$$\mathrm{Cov}_z[F, G] \equiv \langle FG \rangle_z - \langle F \rangle_z \langle G \rangle_z \,. \tag{3.24}$$

Using the covariance, the variance can be expressed as

$$\sigma_z^2[aF] = \mathrm{Cov}_z[aF, aF] \,. \tag{3.25}$$

Like the $\Delta_{\bar{x}}[...]$, the $\mathrm{Cov}_z[...]$ and $\sigma_z[...]$ by construction only measure non-constant expansions of the potential

$$\begin{aligned}\mathrm{Cov}_z[aF, bG + c] &= \langle aF(bG + c) \rangle_z - \langle aF \rangle_z \langle bG + c \rangle_z \,, \\ &= ab \langle FG \rangle_z + ac \langle F \rangle_z - ab \langle F \rangle_z \langle G \rangle_z - ac \langle F \rangle_z \,, \\ &= \langle aFbG \rangle_z - \langle aF \rangle_z \langle bG \rangle_z \,, \\ &= \mathrm{Cov}_z[aF, bG] \,. \end{aligned} \tag{3.26}$$

The $\sigma_z[...]$ are not surjective, which can be proven by calculating stationary solutions. Requiring the variation equation 3.22 to vanish leads to the integral equation

$$V(z) = \langle V \rangle_z \,,$$

which is the definition of a constant potential. Thus, constant potentials minimise $\sigma_z[...]$, and since it was shown in equation 3.26 that the expectation value of constant potentials vanishes, it follows that

$$\sigma_z[V] \geq 0 \tag{3.27}$$

holds. Therefore, positiveness can be demanded of the broadening σ_g of the krypton spectrum, which allows to constrain systematics.

3.1.4. Connection of Mean Difference and Covariance

An important conclusion of the previous discussion is that

$$\ker(\sigma_z) = \{V(z) = b, b \in \mathbb{R}\} \tag{3.28}$$

is the complete kernel of the $\sigma_z[...]$ and that consequently it holds

$$\ker(\sigma_z) \subset \ker(\Delta_{\bar{x}}) \,. \tag{3.29}$$

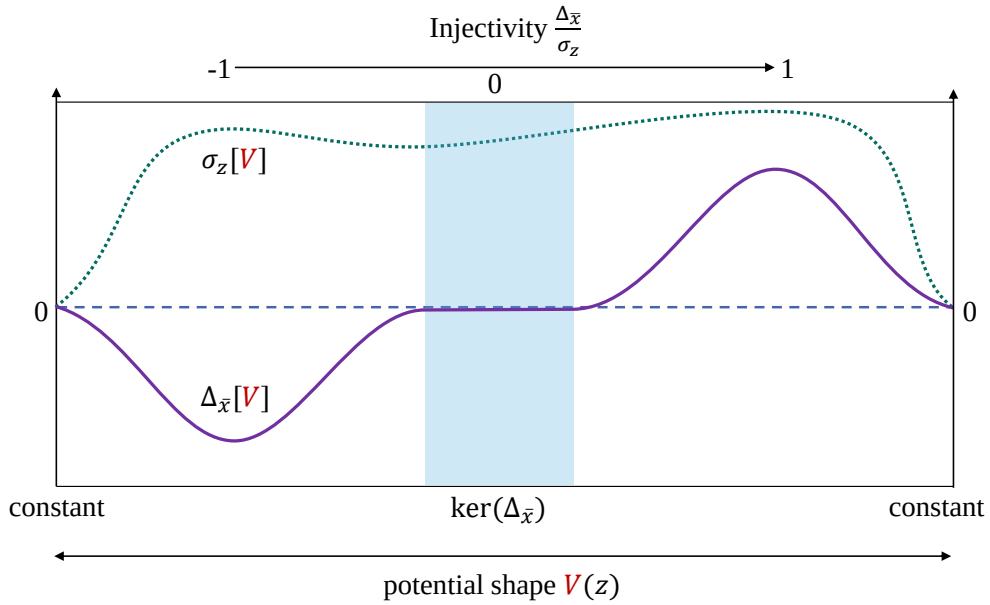

Figure 3.8.: Image of mean differences and standard deviations: All non-constant potentials V can be normalised such that they have the same standard deviation $\sigma_z[V]$. For potentials with given $\sigma_z[V]$ the image of $\Delta_{\bar{x}}[...]$ is bounded, such that $|\Delta_{\bar{x}}[V]|$ is maximal for a certain potential shape. Potential shapes are represented by the ratio $\frac{\Delta_{\bar{x}}[V]}{\sigma_z[V]}$ and since the shape that produces the maximum is unique, this ratio is a measure of the injectivity of the measurement $(\Delta_{\bar{x}}[V], \sigma_z[V])$.

Thus, standard deviations measure all inhomogeneities, mean differences only a special kind. The resulting images of $\Delta_{\bar{x}}$ and σ_z are sketched in figure 3.8. The inhomogeneity which $\Delta_{\bar{x}}$ is sensitive on is specified by the following fundamental relation:

$$\Delta_{\bar{x}}[V] = \langle P_{\bar{x}} V \rangle = \left\langle \frac{P_{\bar{x}}}{P_z} V \right\rangle_z = \mathrm{Cov}_z \left[\frac{P_{\bar{x}}}{P_z}, V \right] , \tag{3.30}$$

where $\langle P_{\bar{x}} \rangle = 0$ was used. Accordingly, the $\Delta_{\bar{x}}[V]$ measure the P_z-weighted covariance of the potential V along the symmetry axis $\frac{P_{\bar{x}}}{P_z}$. Here the choice of P_z is arbitrary, since it cancels. However, it is necessary to normalise equation 3.30 by measurable observables, as shown in the next section.

3.2. Measures of Injectivity and Surjectivity

Naturally, measurements like the krypton-83m measurement, which obtain a few scalar estimates of the potential and its inhomogeneity, suffer from non-injectivity, i.e. it is not possible to reconstruct the full z-dependent potential. However, inversely this means that the influence of the z-dependent potential on the krypton-83m spectrum can perturbatively be described with only a few observables, and while those can depend on the potential shape, no actual knowledge of the latter is required. The same is true for the modelling of the tritium β spectrum: in a perturbative description the systematics of the tritium β

measurement is determined by only a few scalar observables of the potential, independent of its actual shape.

Standard deviations only allow the classification in constant ($\sigma_z[V] = 0$) and non-constant ($\sigma_z[V] > 0$) potentials. In contrast, the mean differences depend on the potential shape, as shown by equation 3.30. Normalising it allows to quantify the injectivity of the measurement (σ_0, Δ_{10}), such that for each measurement there exists a *shape operator* which constrains the potentials that could have led to these estimates. This is discussed in section 3.2.1.

Inversely, it is possible to quantify the surjectivity of any operator of the potential by studying the *weight covariances* of the moments, which is discussed in section 3.2.2. This allows to constrain all moments of longitudinal inhomogeneity of the potential $\Delta_{\bar{x}}, \sigma_y$ with only one measured estimate of the total inhomogeneity scale $\sigma_{\bar{z}}$, and more tightened constraints for parameters obtained additionally. This is the topic of the subsequent section 3.3.

3.2.1. Potential Shape and Injectivity

Following from equation 3.30 the *shape operators* (or *correlation operators*) are defined as

$$\hat{\rho}_{\bar{x},z}[...] \equiv \frac{\mathrm{Cov}_z\left[\frac{P_{\bar{x}}}{P_z}, ...\right]}{\sigma_z\left[\frac{P_{\bar{x}}}{P_z}\right]\sigma_z[...]} = \frac{1}{\kappa_{\bar{x},z}}\frac{\Delta_{\bar{x}}}{\sigma_z}[...] \,. \tag{3.31}$$

$\bar{x}, z$ represent generalised weights normalised to 0 and 1, respectively. The $\kappa_{\bar{x},z} \equiv \sigma_z\left[\frac{P_{\bar{x}}}{P_z}\right]$ are positive normalisation constants. Since the $\hat{\rho}_{\bar{x},z}$ are correlations their image is bounded

$$-1 \leq \hat{\rho}_{\bar{x},z}[V] \leq 1 \quad \forall V \in L^2 \,, \tag{3.32}$$

which is proven in section 3.3. For a given test potential shape $\frac{1}{\kappa_{\bar{x},z}}\frac{P_{\bar{x}}}{P_z}$, $\hat{\rho}_{\bar{x},z}[V]$ quantifies how similar the true potential V is to the shape observed in the weighted region specified by P_z.

Potential shapes: The term similarity is defined by considering how test potential shapes are constructed from arbitrary given test potentials V_{test} and given P_z. The natural representation of V_{test}, if only its shape is of interest, is to subtract its mean and to normalise it to its standard deviation

$$\frac{1}{\kappa_{\bar{x},z}}\frac{P_{\bar{x}}}{P_z} \equiv \frac{1}{\sigma_z[V_{\mathrm{test}}]}\left(V_{\mathrm{test}} - \langle V_{\mathrm{test}}\rangle_z\right) \,. \tag{3.33}$$

For given P_z and V_{test} this equation defines $P_{\bar{x}}$. The ratio $\frac{P_{\bar{x}}}{P_z}$ is a formalised way to indicate that the first moment vanishes

$$\frac{1}{\kappa_{\bar{x},z}}\left\langle\frac{P_{\bar{x}}}{P_z}\right\rangle_z = \frac{1}{\sigma_z[V_{\mathrm{test}}]}\left\langle V_{\mathrm{test}} - \langle V_{\mathrm{test}}\rangle_z\right\rangle_z = 0 \,. \tag{3.34}$$

Thus, the statement of V being similar to $\frac{1}{\kappa_{\bar{x},z}}\frac{P_{\bar{x}}}{P_z}$ (i.e. $\hat{\rho}_{\bar{x},z}[V] = \pm 1$) means that V (or the reflected $-V$) fulfils equation 3.33. In this case the measurement $\left(\sigma_z[V], \hat{\rho}_{\bar{x},z}[V] = \pm 1, \langle V \rangle_z\right)$ is injective and the exact potential is given by

$$V - \langle V \rangle_z = \pm \frac{\sigma_z[V]}{\kappa_{\bar{x},z}} \frac{P_{\bar{x}}}{P_z} \,. \tag{3.35}$$

Also, due to this exact relation in the case $\hat{\rho}_{\bar{x},z} = \pm 1$ it is convenient to say that $\hat{\rho}_{\bar{x},z}$ is the (reflected) potential shape. The smaller the absolute $\hat{\rho}_{\bar{x},z}$ is, the less injective is the measurement and the less similar are the potential and test potential shape. While no exact relation like 3.35 can be given for non-extremal correlations, a measurement of $\hat{\rho}_{\bar{x},z}[V]$ with given $P_{\bar{x}}$ and P_z can still be used to test the *possibility*, that the true potential shape is $\hat{\rho}_{\bar{y},z}$ (which can be derived from any test potential by equation 3.33), which is discussed in section 3.3.1.

Antisymmetry operator: For the weights related to observables of the krypton-83m measurement this operator reads

$$\hat{\rho}[\ldots] \equiv \frac{1}{\kappa_{\overline{10},0}} \frac{\Delta_{10}}{\sigma_0}[\ldots] \,. \tag{3.36}$$

It is called the *antisymmetry operator*, since for usual weights P_0, P_1 it quantifies the prevalence of an antisymmetrical shape of the potential $V(z)$.

This connection to the potential shape can also be understood as a consequence of scale invariance, which is sketched in figure 3.9: The Δ_{10} and σ_0 are different measures of longitudinal inhomogeneity, such that their scale invariant ratio is a measure only of potential shape.

The normalisations $\kappa_{\bar{x},z}$ are a measure of surjectivity. They are given by the covariances of the involved weights, which is discussed in the following section.

3.2.2. Weight Covariances and Surjectivity

Using the boundedness $|\hat{\rho}_{\bar{x},z}| \leq 1$ it follows

$$\kappa_{\bar{x},z} \geq \frac{|\Delta_{\bar{x}}|}{\sigma_z} \,. \tag{3.37}$$

Thus, σ_z is an upper limit to $\Delta_{\bar{x}}$ and $\Delta_{\bar{x}}$ is a lower limit to σ_z, which is sketched in figure 3.10. The magnitude of this constraint is given by $\kappa_{\bar{x},z}$, which is a measure of surjectivity, i.e. the size of the image of $\frac{\Delta_{\bar{x}}}{\sigma_z}[L^2]$:

$$\underset{\text{surjectivity}}{0 \xrightarrow{\qquad\qquad \kappa_{\bar{x},z} \qquad\qquad}} \infty$$

$$\underset{\text{fully constrained}}{\text{Max}\left(\frac{|\Delta_{\bar{x}}|}{\sigma_z}\right) = 0} \qquad \underset{\text{not constrained}}{\text{Max}\left(\frac{|\Delta_{\bar{x}}|}{\sigma_z}\right) = \infty} \,. \tag{3.38}$$

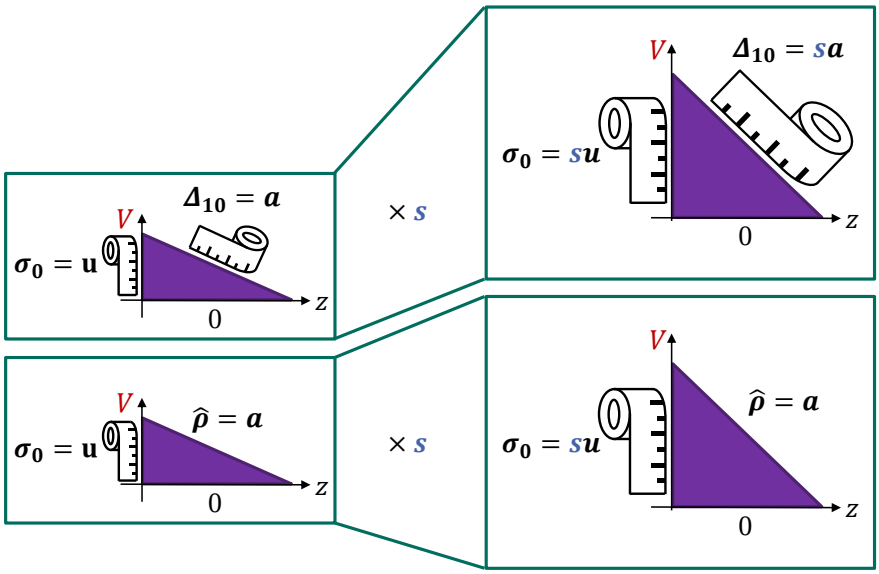

Figure 3.9.: Antisymmetry and scaling: Measuring the potential using σ_0 and Δ_{10} resembles the usage of two different tape measures, both scaling proportional to the overall magnitude of the potential, represented by the scale factor s. In contrast, the antisymmetry $\hat{\rho}$ is scale invariant, quantifying the prevalence of a certain symmetry of the potential shape. Thus, σ_0 is used to quantify the potential magnitude and other estimates like Δ_{10} and the derived $\hat{\rho}$ are estimates of prevalence of symmetries. This is true for all potentials, not only the sketched antisymmetrical shape.

A 2D-representation of the image is sketched in figure 3.11. For all potentials and for any given measurement of $\Delta_{\bar{x}}$ and σ_z their ratio has to stay inside the circle of radius $\kappa_{\bar{x},z}$.

The constant $\kappa^2_{\bar{x},z}$ is the variance of the ratio of the involved weights

$$\kappa^2_{\bar{x},z} \equiv \sigma_z^2 \left[\frac{P_{\bar{x}}}{P_z}\right] \overset{3.30}{=} \Delta_{\bar{x}} \left[\frac{P_{\bar{x}}}{P_z}\right], \tag{3.39}$$

and its relation to the sensitive (i.e. non-vanishing) regions of the weights is sketched in figure 3.12. Spatial regions where both weights are sensitive increase $\kappa_{\bar{x},z}$. Regions where only σ_z is sensitive do not change $\kappa_{\bar{x},z}$, since increasing σ_z always stays inside the circle in figure 3.11. Finally, regions where only $\Delta_{\bar{x}}$ is sensitive lead to an unconstrained image, since in this case $\Delta_{\bar{x}}$ can be increased independently from σ_z.

Accordingly, these variances quantify the variation of the operator $\Delta_{\bar{x}}$ observed on the scale σ_z. $\kappa_{\bar{x},z} \simeq 1$ indicates that $\Delta_{\bar{x}}$ varies on the same scale and spatial region as σ_z. In this case every observation of potential inhomogeneity where $\sigma_z[V]$ is relevant must also include $\Delta_{\bar{x}}[V]$.

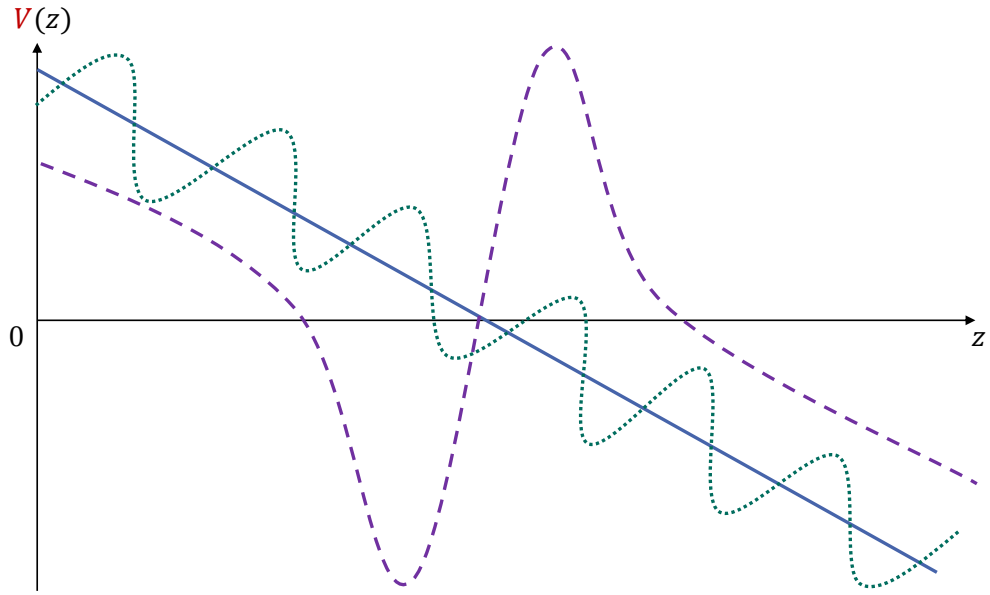

Figure 3.10.: Constraints of mean differences by the standard deviation: All three sketched potentials have the same overall symmetry. Thus, depending on the weights, the potentials can lead to the same expectation value of the $\Delta_{\bar{x}}$, since the latter are a linear measure of the potential inhomogeneity, i.e. positive and negative components can cancel. In contrast, the σ_z^2 are a measure of total longitudinal inhomogeneity, such that by adding oscillatory patterns or antisymmetrical poles, the σ_z^2 can be increased, while keeping the $\Delta_{\bar{x}}$ constant.

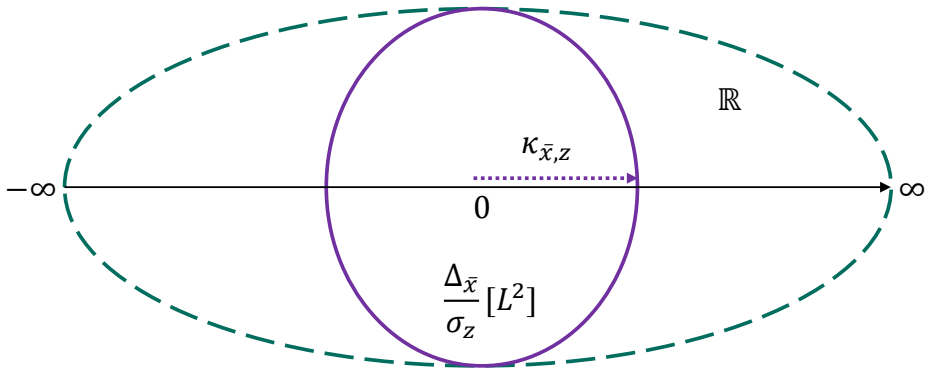

Figure 3.11.: Surjectivity of the ratio of $\Delta_{\bar{x}}$ and σ_z: The image of all square-integrable functions is bounded by $\kappa_{\bar{x},z}$. To better visualise the corresponding interval $[-\kappa_{\bar{x},z}, \kappa_{\bar{x},z}]$ in this 2D-representation $\kappa_{\bar{x},z}$ is the radius of the circular image, which is centred at 0 on the line of the real numbers $\mathbb{R}$.

This has two subtleties:

- Possible *prefactors* have to be included in the weights. In the example where $P_{\bar{x}}$ is composed of scattering weight differences $P_i - P_j$ which are normalised, the $\kappa_{\overline{ij},k}$ quantify sheer spatial overlap. They do not quantify how likely it is to observe electrons of different scattering multiplicities in the first place.
- The $\kappa_{\bar{x},z}$ do not quantify how different $\Delta_{\bar{x}}$ is from other $\Delta_{\bar{y}}$. The possible *degeneracy* is sketched in figure 3.13 for typical scattering weights. Observations of differences between expectation values of $\Delta_{i0}[V]$ and $\Delta_{j0}[V]$ ($i \neq j \neq 0$) on the scale of $\sigma_0[V]$ require fine tuning of V. The difference of two operators can be quantified by calculating the covariance of their weights.

Generalisation to covariances: The z-weighted covariances of weights are defined as

$$\kappa_{\bar{x}\bar{y},z} \equiv \mathrm{Cov}_z\left[\frac{P_{\bar{x}}}{P_z}, \frac{P_{\bar{y}}}{P_z}\right] = \Delta_{\bar{x}}\left[\frac{P_{\bar{y}}}{P_z}\right] , \tag{3.40}$$

where

$$\kappa_{\bar{x}\bar{x},z} \equiv \kappa^2_{\bar{x},z} . \tag{3.41}$$

In contrast to the usual notation of covariances $\sigma_{\bar{x}\bar{y}}$, $\kappa_{\bar{x}\bar{y}}$ is used here to better distinguish from the operator $\sigma_z[\ldots]$. Also, the $\kappa_{\bar{x}\bar{y}}$ are dimensionless, whereas $\sigma_z[V]$ has the dimension of V, which usually is energy.

Since the $\kappa_{\bar{x}\bar{y},z}$ are covariances, they are symmetrical in their first two indices

$$\kappa_{\bar{x}\bar{y},z} = \kappa_{\bar{y}\bar{x},z} , \tag{3.42}$$

such that the covariance matrices are given by

$$\kappa_{\bar{x}\bar{y},z} \simeq \begin{pmatrix} \kappa_{\bar{x}\bar{x}} & \kappa_{\bar{x}\bar{y}} \\ \kappa_{\bar{y}\bar{x}} & \kappa_{\bar{y}\bar{y}} \end{pmatrix}_z \equiv \begin{pmatrix} \kappa^2_{\bar{x}} & \kappa_{\bar{x}\bar{y}} \\ \kappa_{\bar{x}\bar{y}} & \kappa^2_{\bar{y}} \end{pmatrix}_z . \tag{3.43}$$

The correlation coefficient has the usual form

$$\rho_{\bar{x}\bar{y},z} \equiv \frac{\kappa_{\bar{x}\bar{y},z}}{\sqrt{\kappa_{\bar{x}\bar{x},z}\kappa_{\bar{y}\bar{y},z}}} = \frac{\kappa_{\bar{x}\bar{y},z}}{\kappa_{\bar{x},z}\kappa_{\bar{y},z}} , \tag{3.44}$$

and from the Cauchy-Schwarz inequality it follows that

$$|\rho_{\bar{x}\bar{y},z}| \leq 1 . \tag{3.45}$$

With these definitions all the tools are ready to study general covariances between potential moments. In the case of KATRIN, estimates of $\Delta_{10}[V]$ and $\sigma_0[V]$ derived in krypton-83m measurements constrain all other generalised moments up to second order in the potential.

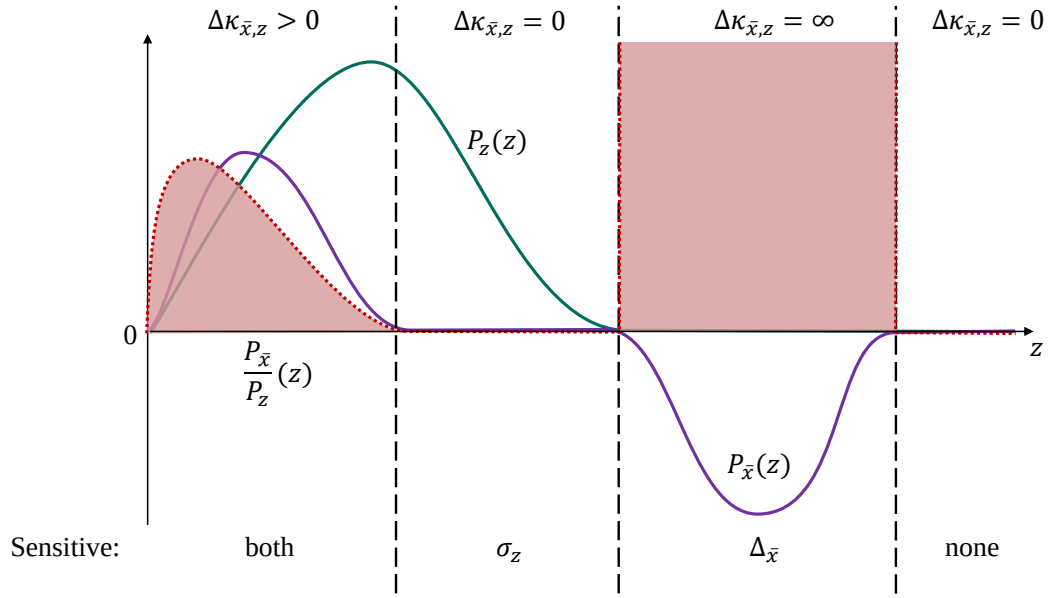

Figure 3.12.: Variance of weights: The sensitivity provided by weights of general $\Delta_{\bar{x}}$ and σ_z can be divided into four possible regions, where either both, one, or none are sensitive. Thus, the variance of their ratio, which is related to the coloured areas, is either positive, vanishing or infinite.

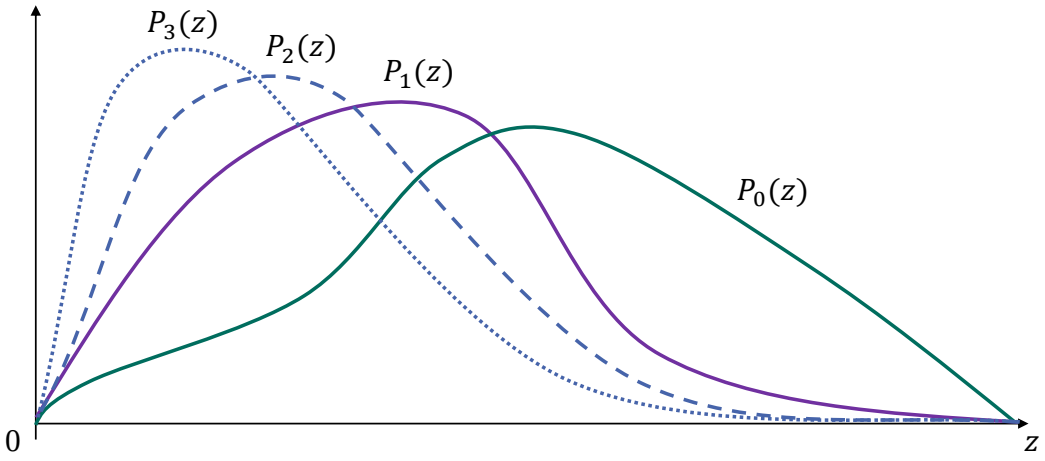

Figure 3.13.: Degeneracy of weights: Sketched are typical weights for increasing scattering multiplicities. The main asymmetry is between the weights P_0 and $P_{\geq 1}$. Thus, observing differences in estimates from operators composed of weights $P_{>1}$ requires increasing fine tuning of the potential.

3.3. Constraints for Potential Moments

In the krypton-83m measurements estimates of $\Delta_{10}[V]$ and $\sigma_0[V]$ can be obtained. Since the weights $P_0,\ P_1$ depend on operating conditions, uncertainties arise if these estimates are required in other operating conditions or if the weights are not known well enough in the first place.

The question how obtained estimates $\Delta_{\bar{y}}$, σ_z^2 constrain measurements of general operators $O[V]$ can be studied by using variational calculus on constrained Lagrangians. In a first step this is done by considering constraints of the fixed order potential moments $\Delta_{\bar{x}}[V]$ and $\sigma_x^2[V]$. The more general approach of studying mixed operators of up to second order in the potential is presented in section 3.5.

Constraints are derived by finding stationary solutions of Lagrangians $\mathcal{L}$ constrained with Lagrange multipliers λ_Δ, λ_σ

$$\mathcal{L}_\Delta = \Delta_{\bar{x}}[V] + \lambda_\Delta \Delta_{\bar{y}}[V] + \lambda_\sigma \sigma_z^2[V]\ , \tag{3.46}$$

$$\mathcal{L}_\sigma = \sigma_x^2[V]\ + \lambda_\Delta \Delta_{\bar{y}}[V] + \lambda_\sigma \sigma_z^2[V]\ . \tag{3.47}$$

The operators $\Delta_{\bar{x}}$ and σ_x are representations of general purely linear $O^1_{\bar{x}}[...]$ and quadratic $O^2_x[...]$ operators with derivatives

$$\frac{\delta O^1_{\bar{x}}[V]}{\delta V} = P_{\bar{x}}\ , \tag{3.48}$$

$$\frac{\delta O^2_x[V]}{\delta V} = 2(V - \langle V\rangle_x)P_x\ , \tag{3.49}$$

and the only necessary conditions are the normalisations of the weights

$$\langle 1\rangle_x = 1\ , \quad \langle 1\rangle_{\bar{x}} = 0\ . \tag{3.50}$$

3.3.1. Constraints for Linear Measures of Inhomogeneity and Potential Shape

Stationary solutions of equation 3.46 are obtained by requiring a vanishing derivative

$$\frac{\mathrm{d}\mathcal{L}_\Delta}{\mathrm{d}V} = P_{\bar{x}} + \lambda_\Delta P_{\bar{y}} + 2\lambda_\sigma (V - \langle V\rangle_z) P_z = 0\ . \tag{3.51}$$

In the following, the different cases of vanishing λ_Δ or λ_σ are considered separately.

Measured only $\Delta_{\bar{y}}$ ($\lambda_\sigma = 0, \lambda_\Delta \neq 0$): In this case the obtained $\Delta_{\bar{y}}[V]$ constrains $\Delta_{\bar{x}}[V]$ solely if the operators differ only by a constant scaling $\Delta_{\bar{x}} = \lambda \Delta_{\bar{y}}$. The potential shape is unknown.

Measured only σ_z ($\lambda_\sigma \neq 0, \lambda_\Delta = 0$): In this case the solution reads

$$V - \langle V \rangle_z = -\frac{1}{2\lambda_\sigma} \frac{P_{\bar{x}}}{P_z} \,. \tag{3.52}$$

λ_σ is determined by calculating the expectation value of the known $\sigma_z[...]$

$$\sigma_z^2[V] = \frac{1}{4\lambda_\sigma^2} \sigma_z^2 \left[\frac{P_{\bar{x}}}{P_z}\right] \,, \tag{3.53}$$

$$= \frac{1}{4\lambda_\sigma^2} \kappa_{\bar{x},z}^2 \,, \tag{3.54}$$

such that the stationary solutions are

$$V - \langle V \rangle_z = \pm \frac{\sigma_z}{\kappa_{\bar{x},z}} \frac{P_{\bar{x}}}{P_z} \,. \tag{3.55}$$

The expectation value of $\Delta_{\bar{x}}[...]$ reads

$$\Delta_{\bar{x}}[V] = \pm \frac{\sigma_z}{\kappa_{\bar{x},z}} \Delta_{\bar{x}} \left[\frac{P_{\bar{x}}}{P_z}\right] \,, \tag{3.56}$$

$$= \pm \frac{\sigma_z}{\kappa_{\bar{x},z}} \kappa_{\bar{x},z}^2 \,, \tag{3.57}$$

$$= \pm \sigma_z \kappa_{\bar{x},z} \,. \tag{3.58}$$

Since the kernel of $\Delta_{\bar{x}}$ is not empty, such that there exist expectation values in between these two extrema ($\pm$), the image of $\Delta_{\bar{x}}[V]$ for all potentials with given $\sigma_z[V]$ is bounded. Another way of writing this equation is

$$-1 \leq \hat{\rho}_{\bar{x},z}[V] = \frac{1}{\kappa_{\bar{x},z}} \frac{\Delta_{\bar{x}}}{\sigma_z}[V] \leq 1 \quad \forall V \in L^2 \,, \tag{3.59}$$

which is exactly the boundedness of the shape operators. The extremal solutions 3.55 define the symmetry which these operators measure. At the extrema the symmetry is fully prevalent and the measurement is injective.

Measured both σ_z and $\Delta_{\bar{y}}$ ($\lambda_\sigma \neq 0, \lambda_\Delta \neq 0$): The following definitions of $a, b \in \mathbb{R}$ are used for brevity:

$$V - \langle V \rangle_z = -\frac{1}{2} \frac{\lambda_\Delta}{\lambda_\sigma} \frac{P_{\bar{y}}}{P_z} - \frac{1}{2\lambda_\sigma} \frac{P_{\bar{x}}}{P_z} \,, \tag{3.60}$$

$$\equiv a \frac{P_{\bar{y}}}{P_z} + b \frac{P_{\bar{x}}}{P_z} \,. \tag{3.61}$$

They are found by calculating the expectation values of the known $\Delta_{\bar{y}}[...]$ and $\sigma_z^2[...]$, yielding

$$\Delta_{\bar{y}}[V] = a\Delta_{\bar{y}}\left[\frac{P_{\bar{y}}}{P_z}\right] + b\Delta_{\bar{y}}\left[\frac{P_{\bar{x}}}{P_z}\right] , \tag{3.62}$$

$$= a\kappa^2_{\bar{y},z} + b\kappa_{\bar{x}\bar{y},z} , \tag{3.63}$$

$$\sigma_z^2[V] = a^2\sigma_z^2\left[\frac{P_{\bar{y}}}{P_z}\right] + b^2\sigma_z^2\left[\frac{P_{\bar{x}}}{P_z}\right] + 2ab\mathrm{Cov}_z\left[\frac{P_{\bar{y}}}{P_z}, \frac{P_{\bar{x}}}{P_z}\right] , \tag{3.64}$$

$$= a^2\kappa^2_{\bar{y},z} + b^2\kappa^2_{\bar{x},z} + 2ab\kappa_{\bar{x}\bar{y},z} . \tag{3.65}$$

If the first equation is solved for b and plugged into the second, a quadratic equation for a is obtained. It has the solutions

$$a_\pm = \frac{\sigma_z}{\kappa_{\bar{y},z}}\left[\hat{\rho}_{\bar{y},z} \pm \rho_{\bar{x}\bar{y},z}\frac{\sqrt{1-\hat{\rho}^2_{\bar{y},z}}}{\sqrt{1-\rho^2_{\bar{x}\bar{y},z}}}\right] , \tag{3.66}$$

where $\hat{\rho}_{\bar{y},z}$ is the shape operator (equation 3.31) and $\rho_{\bar{x}\bar{y},z}$ is the correlation coefficient (equation 3.44).

The solutions for b now read

$$b_\pm = \mp\frac{\sigma_z}{\kappa_{\bar{x},z}}\frac{\sqrt{1-\hat{\rho}^2_{\bar{y},z}}}{\sqrt{1-\rho^2_{\bar{x}\bar{y},z}}} . \tag{3.67}$$

Solutions and elliptic constraints: Summarising, stationary potentials are of the form

$$V - \langle V\rangle_z = \sigma_z\left[\left(\hat{\rho}_{\bar{y},z} \pm \rho_{\bar{x}\bar{y},z}\frac{\sqrt{1-\hat{\rho}^2_{\bar{y},z}}}{\sqrt{1-\rho^2_{\bar{x}\bar{y},z}}}\right)\frac{P_{\bar{y}}}{P_z}\frac{1}{\kappa_{\bar{y},z}} \mp \frac{\sqrt{1-\hat{\rho}^2_{\bar{y},z}}}{\sqrt{1-\rho^2_{\bar{x}\bar{y},z}}}\frac{P_{\bar{x}}}{P_z}\frac{1}{\kappa_{\bar{x},z}}\right] . \tag{3.68}$$

The expectation value of the operator $\Delta_{\bar{x}}[...]$ is found to be

$$\Delta_{\bar{x}}(\sigma_z, \hat{\rho}_{\bar{y},z}) = \sigma_z\kappa_{\bar{x},z}\left(\rho_{\bar{x}\bar{y},z}\hat{\rho}_{\bar{y},z} \pm \sqrt{1-\hat{\rho}^2_{\bar{y},z}}\sqrt{1-\rho^2_{\bar{x}\bar{y},z}}\right) , \tag{3.69}$$

$$\Rightarrow \hat{\rho}_{\bar{x},z}(\hat{\rho}_{\bar{y},z}) = \rho_{\bar{x}\bar{y},z}\hat{\rho}_{\bar{y},z} \pm \sqrt{1-\hat{\rho}^2_{\bar{y},z}}\sqrt{1-\rho^2_{\bar{x}\bar{y},z}} , \tag{3.70}$$

which is a parametrisation of an ellipse, as shown in figure 3.14. The ± give the maximum and minimum solutions.

The solution for the shape operator $\hat{\rho}_{\bar{x},z}$ depends only on the weight correlation $\rho_{\bar{x}\bar{y},z}$. Thus, for a given estimate of $\hat{\rho}_{\bar{y},z}$ the central value μ and half sided maximum uncertainty Δ of $\hat{\rho}_{\bar{x},z}$ are given by

$$\mu(\hat{\rho}_{\bar{x},z}) = \rho_{\bar{x}\bar{y},z}\hat{\rho}_{\bar{y},z} , \tag{3.71}$$

$$\Delta(\hat{\rho}_{\bar{x},z}) = \sqrt{1-\rho^2_{\bar{x}\bar{y},z}}\sqrt{1-\hat{\rho}^2_{\bar{y},z}} . \tag{3.72}$$

These should not be understood as moments of a Gaussian distribution, since a priori all estimates in the allowed interval are of equal probability.

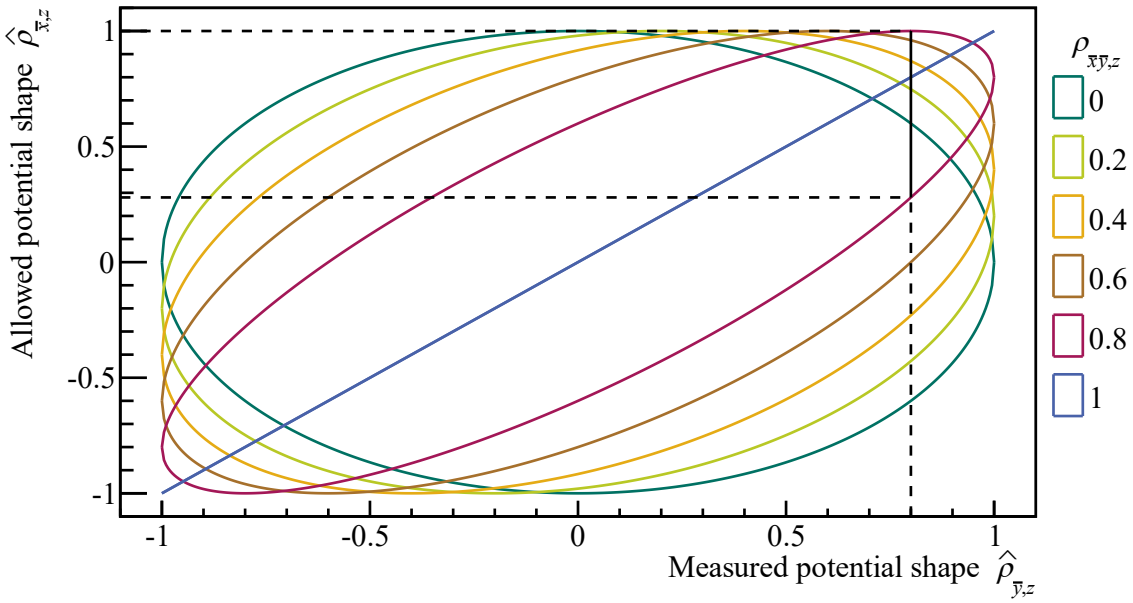

Figure 3.14.: Constraints of potential shapes: The shape operator $\hat{\rho}_{\bar{x},z}$ is constrained by the measured shape $\hat{\rho}_{\bar{y},z}$. The allowed image is fully described by the correlation $\rho_{\bar{x}\bar{y},z}$ of the involved weights. Here the example of $\hat{\rho}_{\bar{y},z} = 0.8$ is depicted. Inversely, if $\hat{\rho}_{\bar{x},z}$ is the true potential shape, i.e. $\hat{\rho}_{\bar{x},z} = 1$, it is visible that the only possible ellipse is given by $\rho_{\bar{x}\bar{y},z} = \hat{\rho}_{\bar{y},z}$.

Possibility and shape testing: Using the concept of possibility, an intuitive interpretation can be obtained when using $\hat{\rho}_{\bar{x},z}$ as a test potential shape: A required condition for $\hat{\rho}_{\bar{x},z}$ to be the true shape, i.e. $\hat{\rho}_{\bar{x},z} = 1$, is $\rho_{\bar{x}\bar{y},z} = \hat{\rho}_{\bar{y},z}$. This can be seen from the position of the maxima in figure 3.14. Using this condition, the necessity that it is the true potential shape is obtained from equation 3.71, such that it holds [5]

$$\mathrm{pos}(\hat{\rho}_{\bar{x},z} = 1) = \delta(\rho_{\bar{x}\bar{y},z} - \hat{\rho}_{\bar{y},z}) \,, \tag{3.73}$$

$$\mathrm{nec}(\hat{\rho}_{\bar{x},z} = 1) = \hat{\rho}^2_{\bar{y},z} \,. \tag{3.74}$$

In this case the shape constraints are given by

$$V^+ - \langle V \rangle_z = \sigma_z \frac{P_{\bar{x}}}{P_z} \frac{1}{\kappa_{\bar{x},z}} \,, \tag{3.75}$$

$$V^- - \langle V \rangle_z = \sigma_z \left[2\hat{\rho}_{\bar{y},z} \frac{P_{\bar{y}}}{P_z} \frac{1}{\kappa_{\bar{y},z}} - \frac{P_{\bar{x}}}{P_z} \frac{1}{\kappa_{\bar{x},z}} \right] \,. \tag{3.76}$$

[5] This definition of necessity uses the size of the image of $\hat{\rho}_{\bar{x},z}$, i.e. the length $2(1 - \hat{\rho}^2_{\bar{y},z})$ of the allowed vertical black line in figure 3.14. This length intuitively quantifies the cardinality of its inverse image, i.e. of the set of potential shapes, that can lead to the given measurement of $\hat{\rho}_{\bar{y},z}$. In order to define the probability that a given potential shape is the true shape, the cardinality of the inverse image and not that of the image would have to be used. In all cases except $\hat{\rho}_{\bar{y},z} = \pm 1$ this cardinality is infinite, so probabilities cannot be normalised. Further reading about possibility theory for example in [DP91].

V^+ is the test shape. Together with V^- it limits an error band of transformations of the shape, which also produce the given $\hat{\rho}_{\bar{y},z}$. This is illustrated in figures 3.15 and 3.16 for the case of the krypton measurement. If the test potential shape and measurement show large antisymmetry, the necessity that the test potential shape is the true potential shape is large. In contrast, if the test potential shape and measurement show small antisymmetry, the test potential shape can be the true potential shape, but the necessity is small. Thus, the krypton measurement can confirm or dismiss antisymmetrical potentials, but it cannot confirm symmetrical potentials. The shown potential shape transformations go along a vertical line of fixed $\hat{\rho}_{\bar{y},z}$ in the ellipse with $\rho_{\bar{x}\bar{y},z} = \hat{\rho}_{\bar{y},z}$ in figure 3.14, for example the solid black line, if $\hat{\rho}_{\bar{y},z} = 0.8$. In both figures 3.15 and 3.16 the obtained error band depends on the used test shape and only the total quadratic area of the band $\sigma_z[V^+ - V^-] = 2\sigma_z\sqrt{1-\hat{\rho}^2_{\bar{y},z}}$ is known.

3.3.2. Constraints of Quadratic Operators and Inhomogeneity Localisation

The variational derivation for the constraints of quadratic operators is cumbersome, and therefore found in appendix A.2. The result is that the constraint depends on the localisation of the potential, which is sketched in figure 3.17. If the inhomogeneity is caused by a fully localised fluctuation at z_0, then the ratio of variances with different weights is given by the ratio of the weights at z_0. Vice versa, if the inhomogeneity is fully delocalised, all variances measure the same value. Thus, the constraint is

$$\text{Min}\left[\frac{P_{z'}}{P_z}\right] \leq \frac{\sigma^2_{z'}}{\sigma^2_z}[V] \leq \text{Max}\left[\frac{P_{z'}}{P_z}\right] . \tag{3.77}$$

In the following, this is made plausible using a simple potential model.

Localisation model: The following potential is a simple representation of strongly localised inhomogeneity at z_0

$$V(z) = \begin{cases} v & -\frac{b}{2} \leq z - z_0 < \frac{b}{2} , \\ 0 & \text{else} . \end{cases} \tag{3.78}$$

For small b the weights are constant on the scale of b, such that the potential moments are easily obtained from their defining integrals

$$\langle V\rangle_z = P_z(z_0)\frac{b}{L_{\text{WGTS}}}v , \tag{3.79}$$

$$\Delta_{\bar{x}}[V] = P_{\bar{x}}(z_0)\frac{b}{L_{\text{WGTS}}}v , \tag{3.80}$$

$$\sigma^2_z[V] = \frac{b}{L_{\text{WGTS}}}v^2\left(1 - P_z(z_0)\frac{b}{L_{\text{WGTS}}}\right) . \tag{3.81}$$

The equation for $\sigma^2_z[V]$ can be used to fix the relation between v and b in the limit $b \to 0$. However, if ratios are considered, v cancels and the expectation value of the shape operator

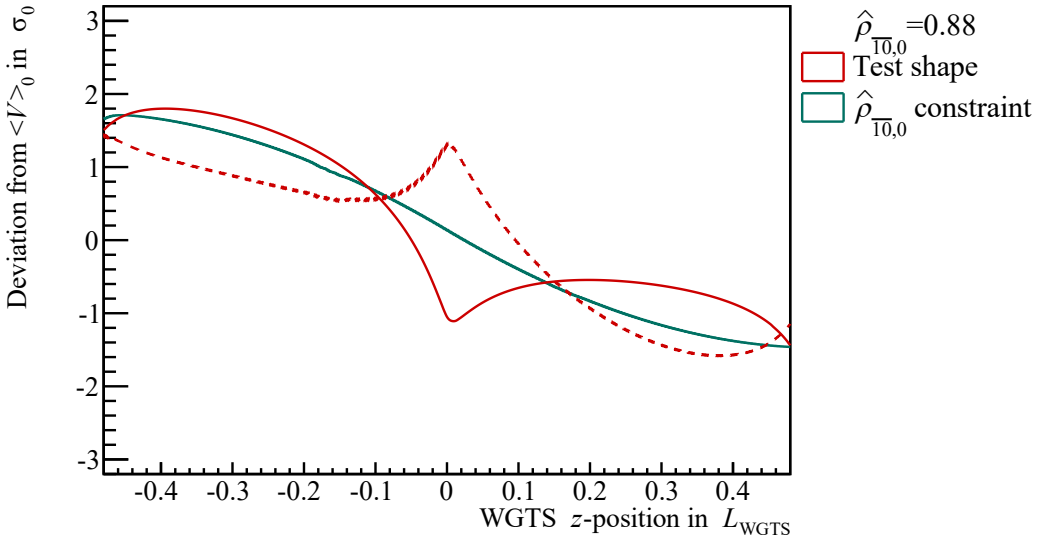

Figure 3.15.: Testing potential shapes, high correlation: The plasma potential simulation (red, from figure 1.19) has an antisymmetry $\hat{\rho}_{\overline{10},0} = 0.88$ (solid green). Thus, if a different value of antisymmetry is measured, the simulated shape is not the true shape. The continuous transformations from red to dashed red also would have produced the measured value, which can be interpreted as an error band. The red curves are the true shapes with a necessity of 0.88^2. Since the absolute measured value is not one, $\hat{\rho}_{\overline{10},0}$ is not the true shape and is not part of the transformations.

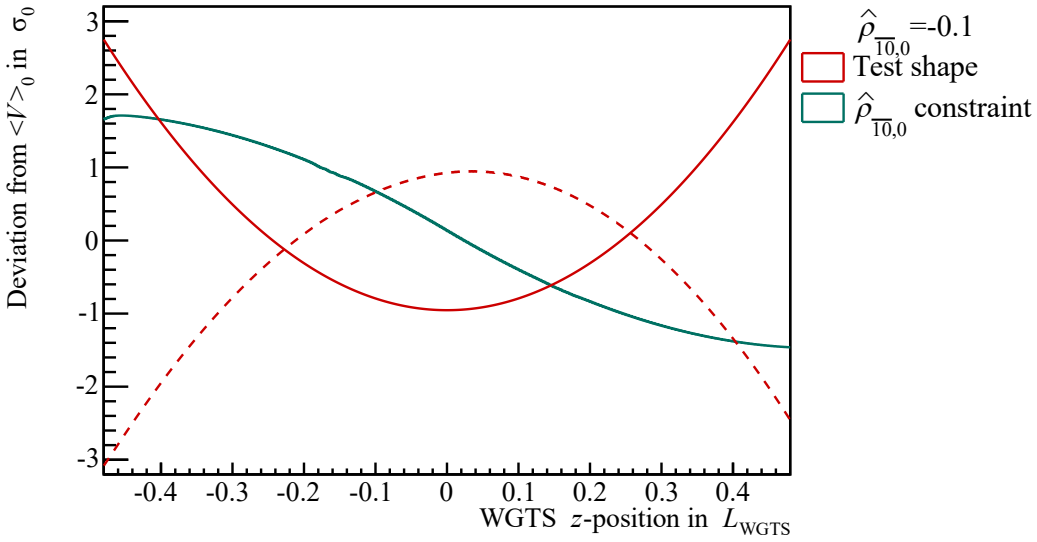

Figure 3.16.: Testing potential shapes, low correlation: For low correlation $\hat{\rho}_{\overline{10},0}$ and the assumed parabolic test shape (red) differ in symmetry, such that the obtained error band is distinct from $\hat{\rho}_{\overline{10},0}$. In addition, the transformations allow for large variance, such that the necessity $\hat{\rho}^2_{\overline{10},0}$ for the test shape to be the true shape is small. In both plots the distribution of the uncertainty depends on the used test shape.

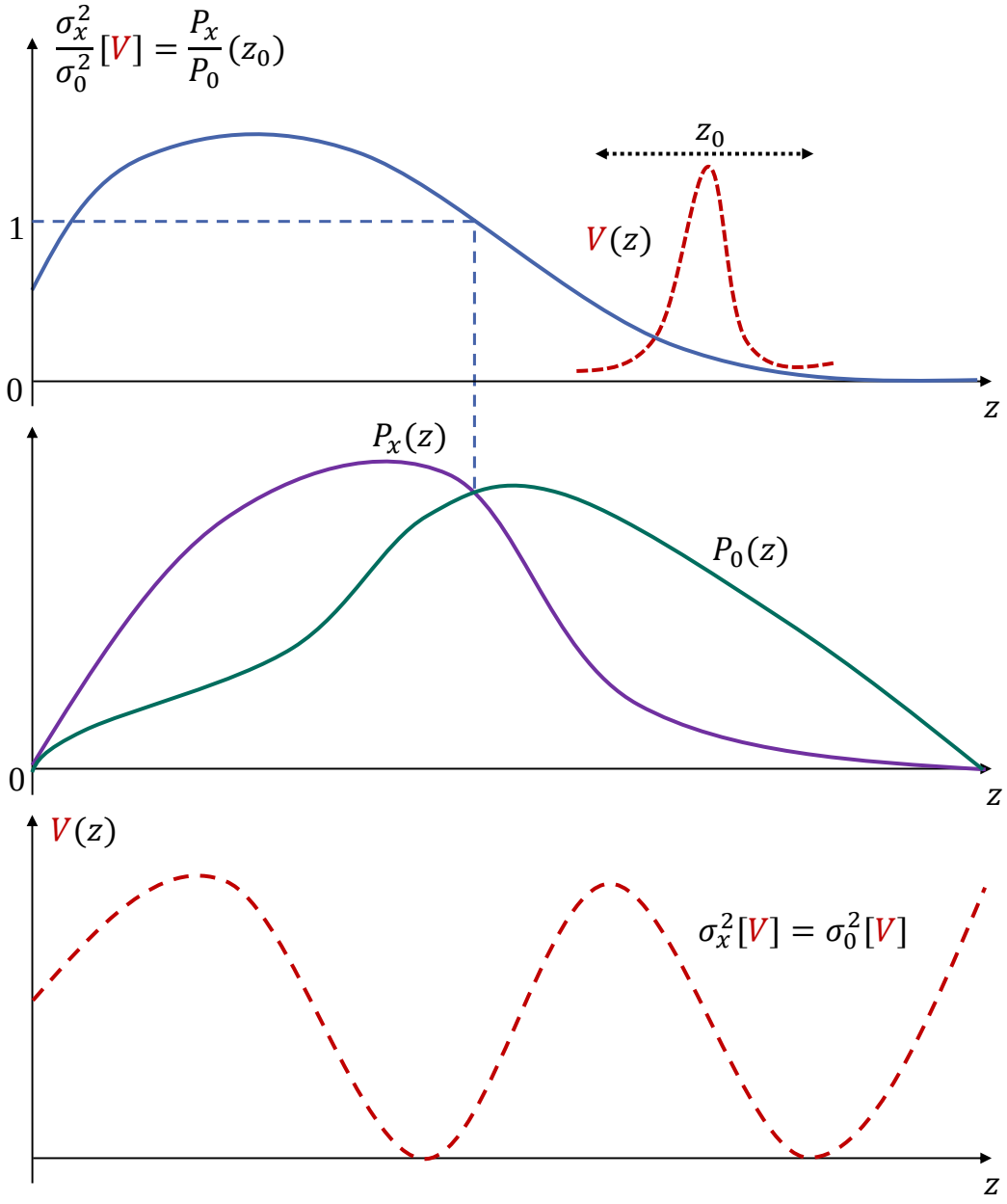

Figure 3.17.: Potential variance depending on inhomogeneity localisation: The middle graph shows sketched weights of two variances $\sigma_0^2[...]$ and $\sigma_x^2[...]$. The upper graph shows the ratio of their expectation values (blue) of a potential (red dashed) which is constant despite a localised fluctuation at position z_0. In this case, the ratio of their expectation values is given by the ratio of the weights at z_0. The inverse relation is also true, i.e. in the case of delocalised inhomogeneity the expectation values are identical, which is depicted by the sinusoidal potential in the lower graph.

as well as the ratio of the different variances can easily be calculated:

$$\frac{\sigma_{z'}^2}{\sigma_z^2}[V] = \frac{P_{z'}(z_0)}{P_z(z_0)} \frac{1 - P_{z'}(z_0)\frac{b}{L_{\mathrm{WGTS}}}}{1 - P_z(z_0)\frac{b}{L_{\mathrm{WGTS}}}} \overset{b \ll L_{\mathrm{WGTS}}}{\longrightarrow} \frac{P_{z'}(z_0)}{P_z(z_0)} , \tag{3.82}$$

$$\hat{\rho}_{\bar{x},z}[V] = \frac{1}{\kappa_{\bar{x},z}} \frac{P_{\bar{x}}(z_0)}{\sqrt{P_z(z_0)}} \sqrt{\frac{\frac{b}{L_{\mathrm{WGTS}}}}{1 - P_z(z_0)\frac{b}{L_{\mathrm{WGTS}}}}} \overset{b \ll L_{\mathrm{WGTS}}}{\longrightarrow} 0 . \tag{3.83}$$

Thus, maximally localised potentials are uncorrelated to any given shape which is not localised itself, and consequently also $\Delta_{\bar{x}}$ vanishes. In an approximate way, non-vanishing correlation to a shape and maximum localisation are opposites and the allowed $\frac{\sigma_{z'}}{\sigma_z}$ for given shape $\hat{\rho}_{\bar{x},z}$ is again approximately elliptic. This is shown in figure A.2 in the appendix.

3.3.3. Constraints of Unweighted Standard Deviation and Peak-to-Peak Value

For physics-driven potential models the relation of the weighted to the *unweighted first moment* (or *unweighted mean*)

$$\langle V \rangle = \frac{\int_z \mathrm{d}z\, V(z)}{\int_z \mathrm{d}z} = \int_z \frac{\mathrm{d}z}{L_{\mathrm{WGTS}}} V(z) \tag{3.84}$$

is of interest. Here, the integration is taken over the length of the WGTS, and the results do depend on these limits. This is in contrast to the weighted case, where the weights are vanishing outside the WGTS, due to the diluted particle densities.

Thus, the normalisation condition

$$\langle 1 \rangle = \int_z \frac{\mathrm{d}z}{L_{\mathrm{WGTS}}} = 1 \tag{3.85}$$

is obtained.

Unweighted standard deviation: The operator for the *unweighted standard deviation* now has the usual form

$$\sigma[V] \equiv \sqrt{\mathrm{Var}[V]} = \sqrt{\langle V^2 \rangle - \langle V \rangle^2} . \tag{3.86}$$

If these operators are interpreted as having weights that are constant in the region of interest in the central WGTS and vanish outside, constraints can be calculated using the equations from the previous sections.

However, these methods do not work if the operator cannot be defined in terms of weight functions or simple derivatives. One case of interest is the peak-to-peak value.

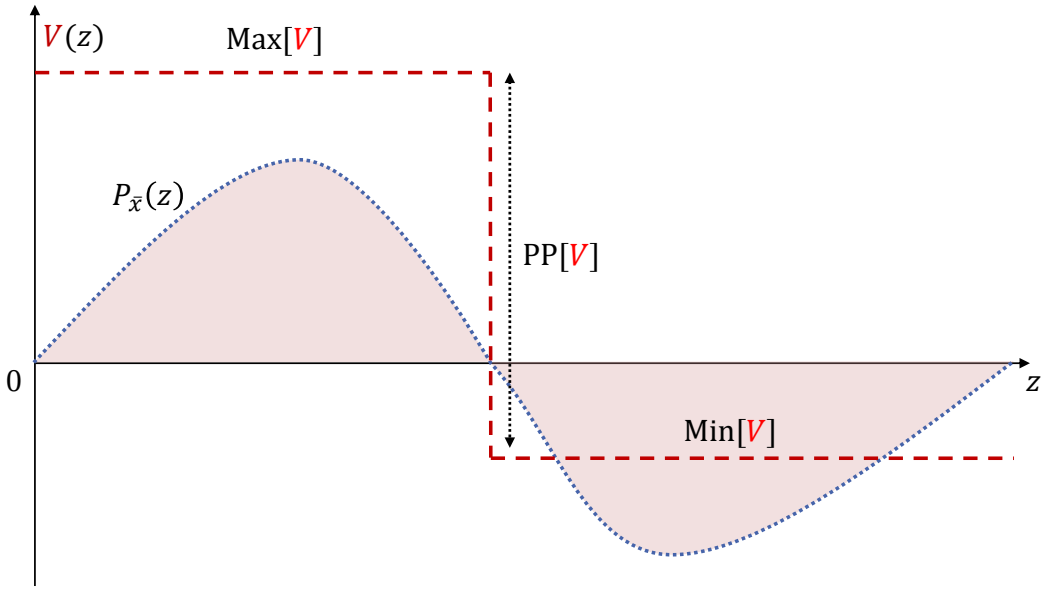

Figure 3.18.: Minimum peak-to-peak value for given $\Delta_{\bar{x}}$: If the potential V is equal to its maximum at positive weights and equal to its minimum at negative weights (or vice versa), the maximum $\Delta_{\bar{x}}[V]$ for given $\mathrm{PP}[V]$ is observed. However, such potentials have high derivatives at $P_{\bar{x}}(z) = 0$.

Peak-to-peak value for given $\Delta_{\bar{x}}$: For simple approximations the peak-to-peak value

$$\mathrm{PP}[V] = \mathrm{Max}[V] - \mathrm{Min}[V] \tag{3.87}$$

is of interest, with the definitions of the maximum and minimum

$$\begin{aligned} \mathrm{Max}[V] &= \text{maximum } \{V(z), z \in [-L_{\mathrm{WGTS}}, L_{\mathrm{WGTS}}]\} , \\ \mathrm{Min}[V] &= \text{minimum } \{V(z), z \in [-L_{\mathrm{WGTS}}, L_{\mathrm{WGTS}}]\} . \end{aligned}$$

Trivially, for given $\mathrm{Max}[V]$ and $\mathrm{Min}[V]$ a piecewise constant potential of the form

$$V(z) = \mathrm{Max}[V]\Theta(P_{\bar{x}}) + \mathrm{Min}[V]\Theta(-P_{\bar{x}}) \tag{3.88}$$

leads to extremal $\Delta_{\bar{x}}[...]$, which is sketched in figure 3.18. It follows:

$$\begin{aligned} \Delta_{\bar{x}}[V] &= \Delta_{\bar{x}} \left[\mathrm{Max}[V]\Theta(P_{\bar{x}}) + \mathrm{Min}[V]\Theta(-P_{\bar{x}})\right] , && (3.89) \\ &= \mathrm{Max}[V]\Delta_{\bar{x}}[\Theta(P_{\bar{x}})] + \mathrm{Min}[V]\Delta_{\bar{x}}[\Theta(-P_{\bar{x}})] , && (3.90) \\ &\overset{3.18}{=} \mathrm{Max}[V]\Delta_{\bar{x}}[\Theta(P_{\bar{x}})] - \mathrm{Min}[V]\Delta_{\bar{x}}[\Theta(P_{\bar{x}})] , && (3.91) \\ &= (\mathrm{Max}[V] - \mathrm{Min}[V])\, \Delta_{\bar{x}}[\Theta(P_{\bar{x}})] , && (3.92) \\ &= \mathrm{PP}[V]\Delta_{\bar{x}}[\Theta(P_{\bar{x}})] . && (3.93) \end{aligned}$$

Thus, the extremum does not depend on $\mathrm{Max}[V]$ or $\mathrm{Min}[V]$ individually, but only on the peak-to-peak value of the potential. Consequently, the potential

$$V_{\mathrm{PP}} - \langle V_{\mathrm{PP}} \rangle = \mathrm{PP}[V_{\mathrm{PP}}] \left(\Theta(P_{\bar{x}}) - \langle \Theta(P_{\bar{x}}) \rangle\right) \tag{3.94}$$

produces the extremal $\Delta_{\bar{x}}[V]$ for all potentials and given peak-to-peak value, the extremum being

$$\Delta_{\bar{x}}[V_{\mathrm{PP}}] = \mathrm{PP}[V_{\mathrm{PP}}]\Delta_{\bar{x}}[\Theta(P_{\bar{x}})] \ . \tag{3.95}$$

The other way around, this means that a given $\Delta_{\bar{x}}[V]$ requires a $\mathrm{PP}[V]$ satisfying

$$\begin{aligned} \frac{\mathrm{PP}[V]}{|\Delta_{\bar{x}}[V]|} &\geq \frac{\mathrm{PP}[V_{\mathrm{PP}}]}{\Delta_{\bar{x}}[V_{\mathrm{PP}}]} = \frac{1}{\Delta_{\bar{x}}[\Theta(P_{\bar{x}})]} \ , \\ \Rightarrow \mathrm{PP}[V] &\geq \frac{1}{\Delta_{\bar{x}}[\Theta(P_{\bar{x}})]} \, |\Delta_{\bar{x}}[V]| \ . \end{aligned} \tag{3.96}$$

This gives a lower limit of the peak-to-peak value if a measurement of $\Delta_{\bar{x}}[...]$ was obtained.

Physical approximations: The solutions of the form 3.94 or continuously differentiable approximations to it have physically unlikely high derivatives at z with $P_{\bar{x}}(z) = 0$. A more physical shape of potential is found analogous to section 3.2.1, i.e. by demanding that the potential leads to extremal values in

$$\hat{\rho}_{\bar{x},z}[V] \equiv \frac{1}{\kappa_{\bar{x},z}} \frac{\Delta_{\bar{x}}[V]}{\sigma_z[V]} \ . \tag{3.97}$$

Thus, the solutions are the most constant in terms of the chosen σ_z, while still producing the given $\Delta_{\bar{x}}$. By calculating the peak-to-peak value of the potential of equation 3.55, the approximate constraint

$$\mathrm{PP}[V] \gtrsim \frac{\mathrm{PP}\left[\frac{P_{\bar{x}}}{P_z}\right]}{\Delta_{\bar{x}}\left[\frac{P_{\bar{x}}}{P_z}\right]} \, |\Delta_{\bar{x}}[V]| \tag{3.98}$$

is obtained.

Peak-to-peak value for given σ_z: From the mean value theorem it follows

$$\mathrm{PP}[V] \leq \mathrm{Max}\left[\left|\frac{\mathrm{d}V(z)}{\mathrm{d}z}\right|\right] L_{\mathrm{WGTS}} \ , \tag{3.99}$$

i.e. a given peak-to-peak value requires a large enough derivative value at a certain point in the WGTS. Trivially, the linear potential

$$V(z) = \mathrm{PP}[V]\frac{z}{L_{\mathrm{WGTS}}} \tag{3.100}$$

has the smallest maximum derivative and all other potential shapes require a larger value. This is also visible in figure 3.18, where the linear connection of the maximum at the rear and the minimum at the front has the smallest possible derivative. The same potential also gives the minimum unweighted standard deviation

$$\sigma\left[\mathrm{PP}[V]\frac{z}{L_{\mathrm{WGTS}}}\right] \leq \sigma[V] \ , \tag{3.101}$$

$$\Leftrightarrow \mathrm{PP}[V] \leq \frac{L_{\mathrm{WGTS}}}{\sigma[z]}\sigma[V] \ , \tag{3.102}$$

for a given peak-to-peak value. The factor is calculated to be

$$\frac{L_{\mathrm{WGTS}}}{\sigma[z]} = L_{\mathrm{WGTS}} \left(\langle z^2\rangle - \underbrace{\langle z\rangle^2}_{=0}\right)^{-1/2} = \left(\frac{z^3}{3}\Big|_{-1/2}^{1/2}\right)^{-1/2} = \sqrt{12} \approx 3.46 \,. \tag{3.103}$$

Using equation 3.77 to derive an upper constraint of the unweighted standard deviation $\sigma[V]$ by a general standard deviation $\sigma_z[V]$ yields

$$\sigma[V] \leq \frac{1}{\sqrt{\mathrm{Min}[P_z]}} \sigma_z[V] \,. \tag{3.104}$$

As discussed in section 3.3.2 this constraint depends on the localisation of the inhomogeneity of the potential. Only if the inhomogeneity is fully localised at the position of the minimum of the weight P_z the left and right side of equation 3.104 are equal. If the inhomogeneity is delocalised, the standard deviations are the same. Also, a non-vanishing estimate of a shape $\hat{\rho}_{\bar{x},z}$ can improve this constraint, as discussed in section 3.3.2.

Summarising, it is possible to constrain the peak-to-peak value from the measurement of $\Delta_{\bar{x}}$ and σ_z from both sides

$$\frac{1}{\Delta_{\bar{x}}[\Theta(P_{\bar{x}})]} |\Delta_{\bar{x}}[V]| \leq \frac{\mathrm{PP}\left[\frac{P_{\bar{x}}}{P_z}\right]}{\Delta_{\bar{x}}\left[\frac{P_{\bar{x}}}{P_z}\right]} |\Delta_{\bar{x}}[V]| \lesssim \mathrm{PP}[V] \leq \frac{3.46}{\sqrt{\mathrm{Min}[P_z]}} \sigma_z[V] \,. \tag{3.105}$$

If the unweighted standard deviation is used ($\sigma_z = \sigma$) the weight is constant in the central WGTS, such that $\mathrm{Min}[P_z] = 1$. Also, for the unweighted standard deviation the upper constraint is obtained by linear potentials. Thus, potentials that include more structure (i.e. higher derivatives) produce a larger standard deviation for a given peak-to-peak value. If both the peak-to-peak value and σ (or as an approximation σ_z) are given this allows to make a prediction on the necessary derivatives of the potential, which is applied on KNM2 krypton data in section 6.3.1.

Since the constraints are derived from σ_z and $\Delta_{\bar{x}}$ which are only measured in the central WGTS, they only apply to the peak-to-peak value in this region. The lower constraints are plotted for different conditions in section 5.2.

3.4. Expansions of Operators of Mixed Scattering Multiplicity

In this section operators are studied which have mixed contributions from different scattering multiplicities. Those operators are relevant for continuous spectra which have overlapping rate contributions from electrons of different scattering multiplicities, like in the tritium β measurements at KATRIN. A sketch of a typical measurement can be seen in figure 3.19.

The expansion of general operators in the first moments up to second order in the potential reads

$$O^{(2)}[V] = -\sum_i \epsilon_i' \langle V\rangle_i + \sum_i \left(a_i \langle V^2\rangle_i + \sum_j a_{ij} \langle V\rangle_i \langle V\rangle_j\right) \,. \tag{3.106}$$

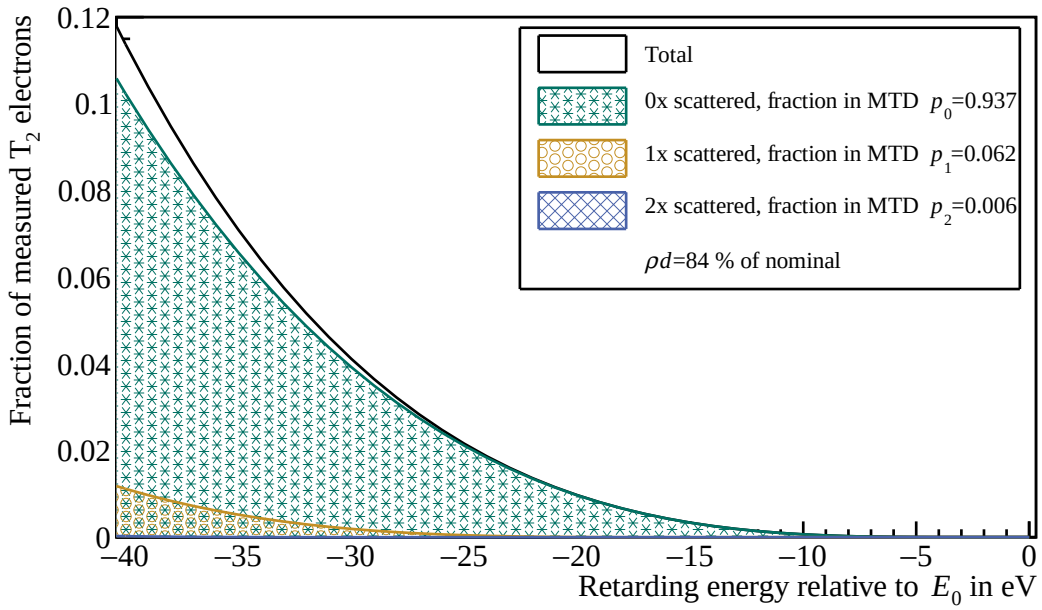

Figure 3.19.: Mixture of scattering effects in continuous spectra: In continuous spectra like the tritium β spectrum the rate contributions of the different scattering multiplicities overlap in energy. Thus, the observables of the plasma potential have contributions from plasma moments of different scattering weights.

The zeroth order in the potential is a constant shift and is set to zero. ϵ_i', a_i and a_{ij} are coefficients $\in \mathbb{R}$. The a_{ij} are symmetrical in their indices. The negative sign of the linear component is used to account for the fact that positive changes in the potential lead to negative changes in electron spectra due to the fact that electrons carry negative elementary charge. Square and angular brackets are used to indicate the functional nature of the operators in contrast to round brackets for scalar dependencies. The description can be limited to second order in the potential in all problems relevant to tritium β systematics, which follows from the fact that the neutrino mass is mathematically equivalent to the second order energy perturbation of the β spectrum [Sle16].

Perturbation approach in scattering and separability: In the usual KATRIN measurement the contribution from scatterings decreases with increasing scattering multiplicity, thus enabling a perturbative treatment.

Also, since the total spectrum is a summation over spectra of pure scattering multiplicity as visible in figure 3.19, observables of the total spectrum can only depend on sum of observables of the individual spectra. Thus, equation 3.106 can be simplified to

$$O^{(2)}[V] = \sum_i \left(-\epsilon_i' \langle V \rangle_i + a_i \sigma_i^2[V]\right) \ . \tag{3.107}$$

In the following, two classes of those operators are discussed:

- Measures of non-constant portions of the potential in section 3.4.1: Those quantify potential-induced changes of the observables of the non-uniformity of the energy scale, like the neutrino mass in the tritium β spectrum.
- Measures of a mean of the potential in section 3.4.2: Those quantify potential induced changes of observables of the total energy scale, like shifts of the tritium β-spectrum endpoint.

In the krypton-83m case this distinction was simply given by the first and second order in potential. However, due the mixed contributions of moments of different scattering multiplicity, this distinction is no longer given in the tritium β spectrum.

For simplicity, at the beginning the description is restricted to a maximum scattering multiplicity of one. In section 3.4.3 it is shown by using generalised potential moments that the approximated equations for one scattering and the exact equations for all scatterings are of the same form, if the scattering is a perturbation.

Since the derived operators are only composed of operators $\Delta_{\bar{x}}[V]$ and $\sigma_z^2[V]$ the longitudinal inhomogeneity can be constrained from the estimates obtainable in krypton-83m measurements, as presented in section 3.3. These constraints are calculated for operators of fixed potential order, i.e. they constrain $\Delta_{\bar{x}}[V]$ and $\sigma_z^2[V]$ separately, which neglects correlations. To avoid that, in section 3.5 it is shown how to constrain operators of mixed orders in potential like equation 3.107 or the neutrino mass shift derived thereof.

3.4.1. Operators of Longitudinal Inhomogeneity

Operators of longitudinal inhomogeneity need to vanish for constant potentials $V(z) \equiv v_0$. Since for constant potentials any mean is equivalent

$$\langle v_0 \rangle_i = v_0 \quad \forall i \in \mathbb{N}_0 \,, \tag{3.108}$$

it holds

$$O^{(2)}[v_0] = -v_0 \sum_i \epsilon_i' = 0 \quad \forall v_0 \in \mathbb{R} \,, \tag{3.109}$$

$$\Rightarrow \sum_i \epsilon_i' = 0 \,. \tag{3.110}$$

Using $\Delta_{ij}[V] = \Delta_{i0}[V] - \Delta_{j0}[V]$ to reformulate the first term of equation 3.107 fulfils this condition:

$$O^{(2)}[V] = \sum_i \left(-\epsilon_i \Delta_{i0}[V] + a_i \sigma_i^2[V]\right) \,. \tag{3.111}$$

The ϵ_i are free coefficients. Notably, since also the neglected higher central potential moments (skewness, kurtosis etc.) vanish for constant potentials the proportionality to $\Delta_{i0}[V]$ remains also in higher potential order and higher powers of $\Delta_{i0}[V]$ do not appear.

Zeroth order scattering: In zeroth order scattering

$$O^{(2)}_{(0)}[V] = a_0\sigma_0^2[V] \tag{3.112}$$

is obtained. Thus, in the no-scattering case second order measures of potential inhomogeneity are given by the variance which is weighted with zero-scattering weights. It is well known that $a_0 = -2$ in case of energy systematics on the tritium β spectrum as observed by shifts of the squared neutrino mass $O^{(2)}_{(0)}[V] = \Delta m_\nu^2[V]$ [RK88]. However, in case of the starting potential already the zero-scattering description is different from the previously known relation, since the necessary weighting with the zero-scattering weight was identified.

Up to first order scattering: In up to first order scattering the operator reads

$$O^{(2)}_{(1)}[V] = -\epsilon_1\Delta_{10}[V] + a_0\sigma_0^2[V] + a_1\sigma_1^2[V]\,, \tag{3.113}$$

i.e. a term proportional to the mean difference $\Delta_{10}[V]$ has to be considered, which is linear in the potential. Thus, $O^{(2)}_{(1)}[V]$ has mixed first and second order potential components and is no longer strictly parabolic. In case of the shift of the squared neutrino mass a_1 is small, which is shown in chapter 5, such that it reads

$$\Delta m_\nu^2[V] = -\epsilon_1\Delta_{10}[V] - 2\sigma_0^2[V]\,. \tag{3.114}$$

The fraction of scattered electrons in the measurement determines ϵ_1 and the magnitude of the potential thus determines which of the terms is dominant. The general curve sketching is found in section 3.6.1.

Susceptibility to mean differences: ϵ_i has units of energy. A more general way of defining it is

$$\epsilon_i \equiv -\frac{\partial O^{(2)}}{\partial \Delta_{i0}}\,, \tag{3.115}$$

i.e. it is the *susceptibility* of the measured observable with regard to perturbations in form of mean differences Δ_{i0}. In principle, the definition using the derivative accounts for the fact that it is only the linear approximation of a more complete theory. However, due to the separability of the spectra for different scattering multiplicities, leading to equation 3.111, no higher-order terms in Δ_{i0} are possible, such that a truely linear connection is expected.

The product $\epsilon_i\Delta_{i0}[V]$ accounts for the broken longitudinal symmetry of the source energy scale. Notably, the two ingredients are that the energy scale is actually inhomogeneous ($\Delta_{i0}[V] \neq 0$) and that scattering is present, which leads to longitudinal sensitivity on the potential ($\epsilon_i \neq 0$). In addition, since only one symmetry is affected, this leads to only one new degree of freedom. This is shown below by absorbing the summation in equation 3.111 into a new operator.

In the perturbative approach coefficients like ϵ_i and thus the expansion of the operator can be determined order by order in simulation. This is done by calculating the derivatives 3.115

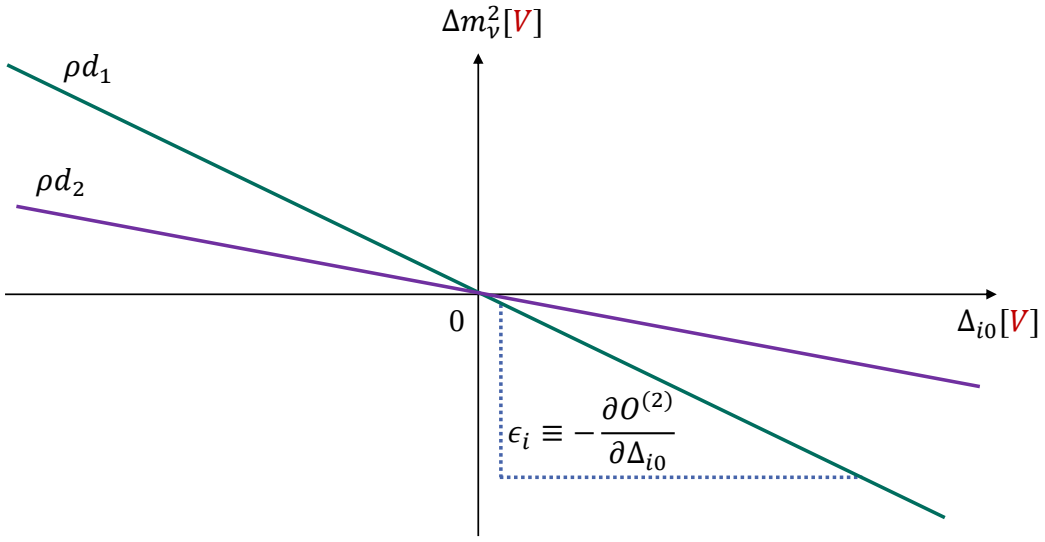

Figure 3.20.: Determination of coefficients in simulation: Due to the perturbative approach expansion coefficients for any operator can be determined in simulation by considering partial derivatives. Here the determination of the mean difference susceptibility of the neutrino mass for different tritium column densities is sketched. When repeated for many column densities, figure 3.21 can be constructed.

(i.e. by using the pull method, cf. section 1.2.1) which is sketched in figure 3.20 for $O^{(2)}[V] = \Delta m_\nu^2[V]$. Due to the dependence on scattering contribution, the susceptibilities depend on the operating conditions and the measurement time distribution. A sketch of ϵ_i in dependence of the tritium column density can be found in figure 3.21. The detailed analysis for typical KATRIN conditions is carried out in chapter 5.

3.4.2. Operators of Mean Potential

For operators measuring means, it is expected that they are of first order in the potential:

$$O^1[V] = -\sum_i a_i \langle V \rangle_i \ , \tag{3.116}$$

$$= -\langle V \rangle_0 \sum_i a_i - \sum_i a_i \Delta_{i0}[V] \ . \tag{3.117}$$

For constant potentials the scattering effects need to vanish, i.e.

$$\sum_i a_i \equiv a \tag{3.118}$$

is a constant, regardless of the amount of scattering. Usually $a = 1$ holds, as it is the case for the endpoint shift $\Delta E_0[V]$ of the tritium β spectrum.

Thus, the zeroth order reads

$$O^1_{(0)}[V] = -a \langle V \rangle_0 \ . \tag{3.119}$$

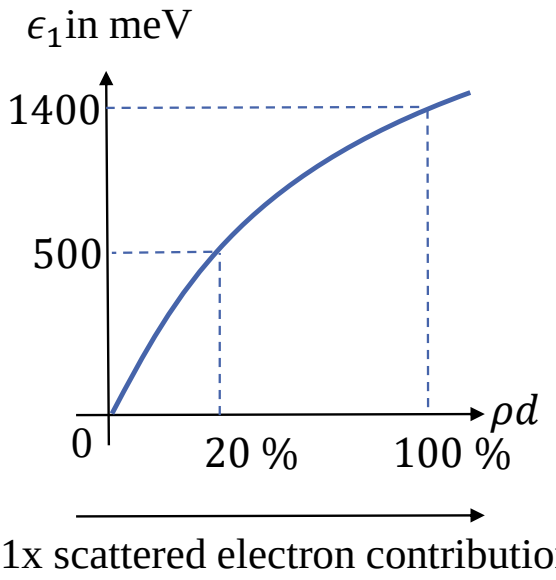

Figure 3.21.: Sketch of the mean difference susceptibility as function of scattering contribution: The larger the contribution of scattered electrons to the measurement, the larger ϵ_1 gets. Here, the measure of potential inhomogeneity is the shift of the squared neutrino mass $\Delta m_\nu^2[V]$ and the scattering contribution is given by the tritium column density ρd in percentage of nominal.

Again, the zero-scattering weighting is necessary even for situations where higher scattering orders are negligible.

In scattering up to first order the operator is

$$O^1_{(1)}[V] = -a_0 \langle V \rangle_0 - a_1 \langle V \rangle_1 \ , \tag{3.120}$$

$$= -a \langle V \rangle_0 - a_1 \Delta_{10}[V] \ , \tag{3.121}$$

which is

$$\Delta E_0[V] = - \langle V \rangle_0 - a_1 \Delta_{10}[V] \tag{3.122}$$

for the endpoint shift of the tritium β spectrum.

As before the coefficients can generally be defined as

$$a_i \equiv -\frac{\partial O}{\partial \langle V \rangle_i} \ , \tag{3.123}$$

$$\overset{i>0}{=} -\frac{\partial O}{\partial \Delta_{i0}} \ . \tag{3.124}$$

Since observables of mean and inhomogeneity like tritium endpoint and neutrino mass shift are usually fitted at the same time, the last step allows to find ϵ_i and a_i at the same time in dependence of Δ_{i0}. The plots of the a_i for different conditions are found in chapter 5.

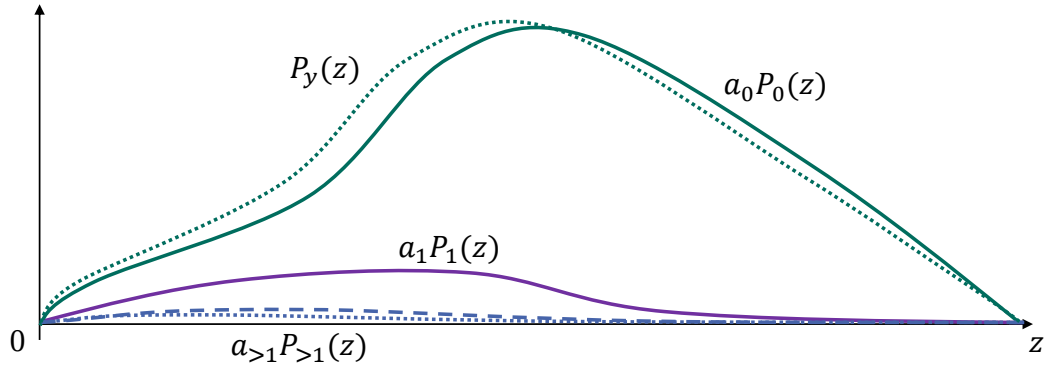

Figure 3.22.: Generalised weights for measures of means: For the relevant scattering contributions at KATRIN a_1 is in the region of up to 15 %, such that general measurements of mean potentials $\langle V \rangle_y$ (dotted green) look like measurements of mostly $\langle V \rangle_0$ (solid green) with a correction of $\langle V \rangle_1$ (purple), which shifts the sensitive region slightly to the back. Higher scattering orders (blue) are smaller.

3.4.3. Generalised Weights for Infinite Scattering Order

In this section it is investigated how the infinite summations over the scatterings can be condensed into new weight functions [6]. It is shown that even up to infinite scattering order the operators can be expanded in $\langle ... \rangle_y$, $\sigma_z^2[...]$ and $\Delta_{\bar{x}}[...]$ with generalised weights $P_{\bar{x}}$, P_y and P_z.

Operators of means: The trivial case is the measure of the mean

$$O_\infty^1[V] = -\sum_i a_i \langle V \rangle_i \ , \tag{3.125}$$

$$\equiv -a \langle V \rangle_y \ , \tag{3.126}$$

with

$$a \equiv \sum_i a_i \ , \quad P_y \equiv \frac{1}{a} \sum_i a_i P_i \ . \tag{3.127}$$

Due to the condition 3.118, $a \neq 0$ holds. P_y satisfies the usual normalisation condition 3.3. Thus, the exact expression for any operator measuring a mean potential in presence of scattering has the usual form of a longitudinal average. However, the scattering weight is replaced with a generalised weight function P_y, which depends on all scattering contributions. Figure 3.22 shows the typical KATRIN case. Notably, the different analysis methods in KATRIN (i.a. β-spectrum endpoint, krypton-83m, PRO-KATRIN, 300 V analysis [7]) effectively see different scattering contributions, such that they all measure different means.

[6] In practice the summation is always cut by the maximum multiplicity of scatterings which is actually observed in the chosen analysis range of the tritium β spectrum.

[7] A full description of the last two methods is found in [Fri20].

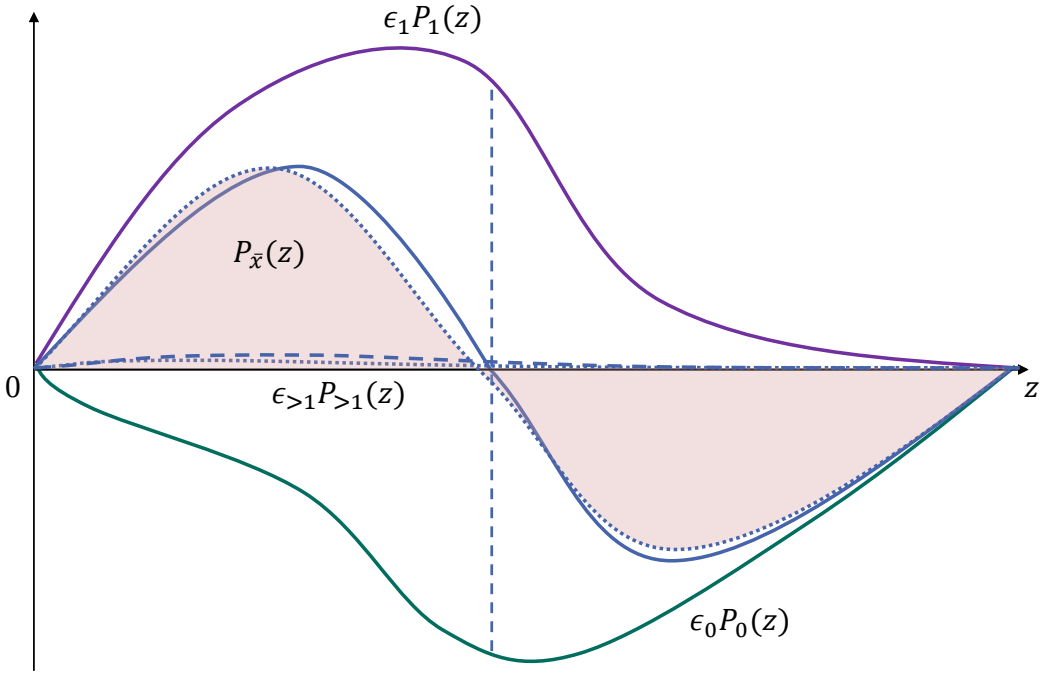

Figure 3.23.: Generalised weights for measures of mean differences: In the relevant regimes of scattering contributions ϵ_1 (purple) is dominant over higher terms $\epsilon_{>1}$, such that general measurements of $\Delta_{\bar{x}}[V]$ (dotted blue) look like measurements of mostly $\Delta_{10}[V]$ (solid blue) with some shift of sensitivity to the back.

Operators of longitudinal inhomogeneity: Similarly, in case of operators of longitudinal inhomogeneity, it holds for the linear terms

$$O_{\infty}^{(2),\text{linear}}[V] = -\sum_i \epsilon_i \Delta_{i0}[V] \,, \tag{3.128}$$

$$\equiv -\epsilon \Delta_{\bar{x}}[V] \,, \tag{3.129}$$

with [8]

$$\epsilon \equiv \left| \sum_i \epsilon_i \right| \,, \quad P_{\bar{x}} \equiv \frac{1}{\epsilon} \sum_i \epsilon_i (P_i - P_0) \,. \tag{3.130}$$

Thus, the exact expression for any linear measure of inhomogeneity of potential in presence of scattering has the form of a mean difference $\Delta_{\bar{x}}[V]$ with a generalised weight function $P_{\bar{x}}$. Figure 3.23 shows the typical KATRIN case.

Using the definitions

$$P_z \equiv \frac{1}{a} \sum_i a_i P_i \,, \quad a \equiv \sum_i a_i \,, \tag{3.131}$$

[8] The case $\epsilon = 0$, $\exists \epsilon_i \neq 0$ is possible, in this case a different normalisation needs to be chosen. The consequences are further discussed below and in chapter 5. The positive normalisation is chosen to avoid phase jumps of the operator at $\sum_i \epsilon_i = 0$.

the quadratic components can be written as

$$O_\infty^2[V] = \sum_i a_i \sigma_i^2[V] \,, \tag{3.132}$$

$$= \sum_i a_i \langle V^2 \rangle_i - \sum_i a_i \langle V \rangle_i^2 \,, \tag{3.133}$$

$$= a \langle V^2 \rangle_z - \sum_i a_i (\langle V \rangle_z - \Delta_{zi}[V])^2 \,, \tag{3.134}$$

$$= a \langle V^2 \rangle_z - a \langle V \rangle_z^2 + 2 \langle V \rangle_z \sum_i a_i \Delta_{zi}[V] - \sum_i a_i \Delta_{zi}^2[V] \,, \tag{3.135}$$

$$= a\sigma_z^2[V] - \sum_i a_i \Delta_{zi}^2[V] \,. \tag{3.136}$$

Using the shape operators 3.31 this becomes

$$O_\infty^2[V] = a\sigma_z^2[V] \left(1 - \sum_i \frac{a_i}{a} \hat{\rho}_{\overline{zi},z}^2[V] \kappa_{\overline{zi},z}^2 \right) \,, \tag{3.137}$$

$$\equiv a\sigma_z^2[V] \left(1 - \frac{\delta a[V]}{a} \right) \,. \tag{3.138}$$

Thus, the exact expression for any measure of potential variance in presence of scattering has the form of a variance $\sigma_z^2[V]$ with a generalised weight function P_z. In addition, the total amplitude of the variance term has a dependence on the potential shape. Figure 3.24 shows the typical KATRIN case.

Adding both terms, the exact form of separable operators of longitudinal inhomogeneity in the presence of scattering is

$$O_\infty^{(2)}[V] = -\epsilon \Delta_{\bar{x}}[V] + (a - \delta a[V]) \, \sigma_z^2[V] \,. \tag{3.139}$$

It consists of a generalised mean difference $\Delta_{\bar{x}}[V]$ and a generalised variance $\sigma_z^2[V]$ with amplitudes $-\epsilon$ and $a - \delta a[V]$.

3.4.4. Discussion

At KATRIN usually the scattering contributions decrease with scattering multiplicity and $\frac{\delta a[V]}{a} \ll 1$ holds. This leads to the final result of

$$O_\infty^{(2)}[V] = -\epsilon \Delta_{\bar{x}}[V] + a\sigma_z^2[V] \,. \tag{3.140}$$

The fundamental difference to the non-scattering case is given by the energy scale ϵ. It is the susceptibility of $O_\infty^{(2)}[V]$ to the potential shape defined by $P_{\bar{x}}$. Here it should be recalled that $\Delta_{\bar{x}}[V]$ equals the covariance of the potential with $P_{\bar{x}}$.

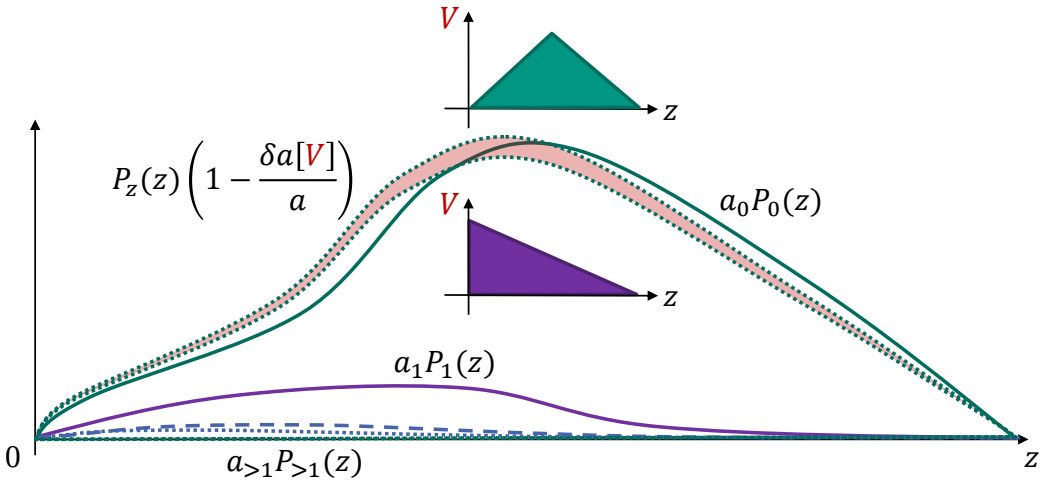

Figure 3.24.: Generalised weights for measures of variances: The presence of higher scattering orders (purple and blue) moves the sensitive region of general measures of variances $\sigma_z^2[V]$ to the back (dotted green) compared to the case of only zero scattering multiplicity $\sigma_0^2[V]$ (solid green). Also, the total amplitude of the quadratic terms has a small potential shape dependence (coloured area). For the sketched typical weights, this manifests in a dependence of the variance contribution on the potential antisymmetry. However, as shown in chapter 5 the contributions of $i > 1$ can be neglected for typical KATRIN conditions due to the intrinsic width of the energy loss function.

Normalisation and implementation: Since in continuous spectra $\Delta_{\bar{x}}[V]$ is not an observable, it depends on normalisation effects. For $\epsilon = 0$, $\exists\epsilon_i \neq 0$, $\Delta_{\bar{x}}$ is singular. In all observables like the left hand side of equation 3.140, which only depend on the product $\epsilon\Delta_{\bar{x}}$, those singularities caused by the above normalisation cancel. Still, the chosen representation and normalisation by the total susceptibility has practical applications when implementing the systematic uncertainty. In the simulation this can only be done by shifting spectra of different scattering multiplicity compared to the unscattered spectrum. However, there are infinitely many combinations of shifts which produce the same neutrino mass shift. Since ϵ is the summation over all susceptibilities, in this normalisation the correct neutrino mass shift is obtained when all spectra are shifted simultaneously by the value of $\Delta_{\bar{x}}[V]$. However, this is only a normalisation choice. The same shift can be obtained if the summation in equation 3.128 is normalised by a different value, for example one of the ϵ_i. In this case a different mean difference $\Delta_{\bar{x}'}[\ldots]$ is obtained, and when using its estimate, the correct neutrino mass shift is obtained by only shifting the spectrum of i scattering multiplicity in simulation. While in both cases the value of $\Delta_{\bar{x}}[V]$ or $\Delta_{\bar{x}'}[V]$ can be constrained by $\Delta_{10}[V]$ from the krypton measurement, it is not the value of the mean difference of the actual potential. If this is favoured, the $\Delta_{i0}[V]$ can be constrained individually from the krypton measurement. However, since the $\Delta_{i0}[V]$ are correlated, this leads to a more complicated analysis. Since the weights for higher scattering multiplicities are degenerated (cf. figure 3.13) and the differences of the $\Delta_{i0}[V]$ are expected to be small,

using the same shift of all mean differences and thus the above normalisation is preferred at the moment.

Normalisation and shape operators: When $\Delta_{\bar{x}}[V]$ is normalised by the standard deviation $\sigma_z[V]$, the shape operator $\hat{\rho}_{\bar{x},z}$ is obtained and the prefactor is the penalty for potentials that share its shape. This is discussed in section 3.6.1. Thus, this normalisation reveals the connection of neutrino mass shift to the potential shape. Also, since the standard deviation only vanishes in the trivial case of constant potentials, this formulation avoids singularities. However, there is no practical method to implement the shape operators in simulation, such that here still $\Delta_{\bar{x}}[V]$ needs to be used.

Constraints and scattering order: The operator $O_{\infty}^{(2)}[V]$ can be constrained by measuring any $(\Delta_{\bar{x}'}, \sigma_{z'})$, like (Δ_{10}, σ_0) from krypton-83m. In principle obtaining more estimates from different weights, like for example higher scattering orders, can improve these constraints. However, the gain is limited by the degeneracy of the weights for increasing scatterings (see figure 3.13) and the associated weight covariances of the krypton and tritium weights. In terms of potential modelling, more estimates would allow to construct plasma models with more parameters, but they also suffer from the same degeneracy. Consequently, obtaining estimates of higher scattering multiplicities from more complicated krypton-83m measurements is only of limited gain. Fortunately, the measurement of only Δ_{10} and σ_0 in krypton already reasonably constrains the neutrino mass shift, as shown in chapter 5.

The constraints already derived in section 3.3 work on $\Delta_{\bar{x}}[V]$ and $\sigma_z[V]$ separately. The ultimate goal is a constraint of the neutrino mass shift, i.e. of a combination of moments of the form equation 3.140, which is the topic of the next section.

3.5. Constraints for General Operators of Longitudinal Inhomogeneity

Estimates of $\Delta_{10}[V]$ and $\sigma_0[V]$ obtained in krypton-83m mode can be used to constrain their counterparts for tritium mode weights according to section 3.3. However, this approach is too conservative, since a given extremal solution for one of the operators is not an extremal solution of the other, such that both cannot be extremal simultaneously. The best possible approach for unknown potentials is to constrain equation 3.140 directly. However, since equation 3.140 is phenomenological and has no representation in the theoretical model of the tritium β spectrum, in sensitivity studies constrained values of $\Delta_{\bar{x}}[V]$ and $\sigma_z[V]$ have to be used. Here only the methods for the constraint of $O_{\infty}^{(2)}[V]$ are described, and an example is found in appendix A.3.

The derivative with regard to the vector of operating parameters $\boldsymbol{s}$ reads

$$\frac{\mathrm{d}O_{\infty}^{(2)}[V](\boldsymbol{s})}{\mathrm{d}\boldsymbol{s}} = \frac{\delta O^{(2)}[V]}{\delta V}\frac{\mathrm{d}V(\boldsymbol{s})}{\mathrm{d}\boldsymbol{s}} - \frac{\mathrm{d}(\epsilon(s)\Delta_{\bar{x}}[V](\boldsymbol{s}))}{\mathrm{d}\boldsymbol{s}} + \frac{\mathrm{d}(a(\boldsymbol{s})\sigma_z^2[V](\boldsymbol{s}))}{\mathrm{d}\boldsymbol{s}}\,. \tag{3.141}$$

The first term is the change of the potential with the operating conditions, the others are caused by the change of the weights. A priori the change of the potential with the operating conditions is unknown. Originally it was argued from plasma physics and simulation that the krypton mode potential at high temperature is an upper limit to the tritium mode potential at low temperature [KAT04b]. However, due to the unusual properties of the plasma at KATRIN, which are discussed in section 1.4.1, this is currently controversial. Without better knowledge the assumption $\frac{\mathrm{d}V}{\mathrm{d}\boldsymbol{s}} = 0$ is made here. If the krypton measurement gives an upper limit on the plasma inhomogeneity, this assumption is conservative for the change of $\sigma_z[V]$ between the modes. However, $\Delta_{\bar{x}}[V]$ depends also on the potential shape, such that the upper limit of the inhomogeneity is not sufficient to completely constrain its change with the potential. Future measurements will be performed at the same operating conditions, i.e. at the same potential, such that those problems will be avoided.

The terms from $\epsilon(\boldsymbol{s})$ and $a(\boldsymbol{s})$ do not contribute an uncertainty, since their function of the operating conditions is known from simulation. In all the following equations they are meant to be evaluated at tritium conditions, such that the relevant terms are

$$\frac{\mathrm{d}O_\infty^{(2)}[V](\boldsymbol{s})}{\mathrm{d}\boldsymbol{s}} \approx -\epsilon\frac{\mathrm{d}\Delta_{\bar{x}}[V](\boldsymbol{s})}{\mathrm{d}\boldsymbol{s}} + a\frac{\mathrm{d}\sigma_z^2[V](\boldsymbol{s})}{\mathrm{d}\boldsymbol{s}} \,. \tag{3.142}$$

The two relevant applications of this equation are seen in figure 3.25:

- Same conditions: Even if the estimates are obtained at the same operating conditions, the weights are different due to the different gas profiles of krypton and tritium. Thus, a difference $\Delta O_\infty^{(2)}[V]$ needs to be constrained.
- Extrapolation to different conditions: If the operating conditions are different and the potential is unknown, the only possibility is extrapolation under the assumption $\frac{\mathrm{d}V}{\mathrm{d}\boldsymbol{s}} = 0$. Thus, in linear extrapolation the derivative $\frac{\mathrm{d}O_\infty^{(2)}[V]}{\mathrm{d}\boldsymbol{s}}$ needs to be constrained.

Since by replacing $\frac{\mathrm{d}}{\mathrm{d}\boldsymbol{s}}$ with Δ both cases are formally equivalent, the notation $\mathrm{d}(\boldsymbol{s})$ is used in the following for both cases and the method of constrained Lagrangians is applied, which is shown in section 3.5.1. A second approach exists by expanding the derivatives of the operators in the original operators, which is shown in section 3.5.2.

3.5.1. Numerical Solution using Constrained Lagrangians

The operator $O_\infty^{(2)}[V]$ is given by the integral

$$O_\infty^{(2)}[V] = \int \frac{\mathrm{d}z}{L_{\mathrm{WGTS}}}(V - \langle V\rangle_z)\left[-\epsilon P_{\bar{x}} + (a - \delta a[V])(V - \langle V\rangle_z)P_z\right] \,. \tag{3.143}$$

Neglecting $\delta a[V]$ and the known terms from ϵ and a, the differential reads

$$\mathrm{d}O_\infty^{(2)}[V](\boldsymbol{s}) = \int \frac{\mathrm{d}z}{L_{\mathrm{WGTS}}}(V - \langle V\rangle_z)\left[-\epsilon\mathrm{d}P_{\bar{x}}(\boldsymbol{s}) + a(V - \langle V\rangle_z)\mathrm{d}P_z(\boldsymbol{s})\right] \,, \tag{3.144}$$

i.e. the change of the operator is only given by the change of the weights. Thus, given the measurement of $\Delta_{10}[V]$ and $\sigma_0^2[V]$ at krypton-83m conditions, the constrained Lagrangian

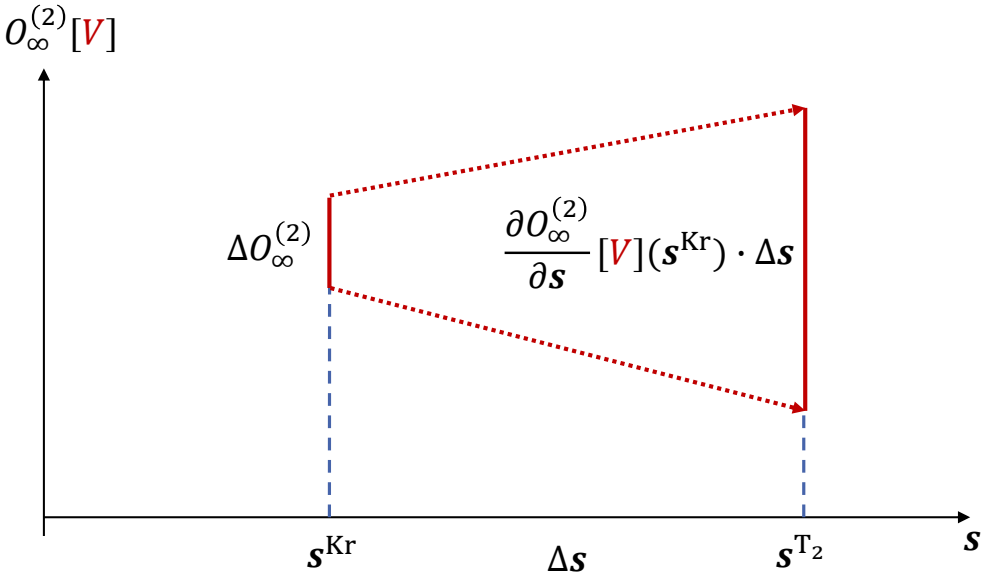

Figure 3.25.: Extrapolating varying operating conditions: Already at equal operating conditions $\boldsymbol{s}$ the prediction of $O_\infty^{(2)}[V]$ from krypton measurements has an uncertainty $\Delta O_\infty^{(2)}[V]$ due to the different gas profiles of krypton and tritium. For different operating conditions $\Delta\boldsymbol{s}$ the krypton prediction has to be extrapolated. The linear extrapolation is inside the trapezoid. The boundaries are calculated using constrained Lagrangians.

reads

$$\mathcal{L} = \mathrm{d}O_\infty^{(2)} + \lambda_\Delta \Delta_{10} + \lambda_\sigma \sigma_0^2 \,. \tag{3.145}$$

Stationary solutions are found by demanding the derivative with regard to V to vanish, leading to

$$V - \langle V \rangle_z = -\frac{1}{2} \frac{\lambda_\Delta (P_1 - P_0) - \epsilon \mathrm{d}P_{\bar{x}}(\boldsymbol{s}) - 2\lambda_\sigma \Delta_{z0} P_0}{a \mathrm{d}P_z(\boldsymbol{s}) + \lambda_\sigma P_0} \,. \tag{3.146}$$

$(\lambda_\sigma, \lambda_\Delta)$ are determined by demanding $\sigma_0^2[V]$ and $\Delta_{10}[V]$ to be the measured values, giving two coupled integral equations. While there are no trivial solutions, in simulation $(\sigma_0^2[V], \Delta_{10}[V], \mathrm{d}O_\infty^{(2)}[V])$ can be calculated in dependence of $(\lambda_\sigma, \lambda_\Delta)$ and subsequently the extrema of $\mathrm{d}O_\infty^{(2)}[V]$ can be found in dependence of $(\sigma_0^2[V], \Delta_{10}[V])$. Multiplying the extremal change with $\Delta\boldsymbol{s}$ gives the maximum uncertainties on $O_\infty^{(2)}[V]$ in linear extrapolation.

3.5.2. Expansions of Weight Derivatives in Weights

The following discussion only applies to the case of extrapolation between operating conditions, i.e. when the derivative of $O_\infty^{(2)}[V]$ with respect to operating parameters is needed. The idea is to replace the derivatives of $\Delta_{\bar{x}}[V]$ and $\sigma_z[V]$ in equation 3.142 with an expansion of known operators. As visible in equation 3.144, if the change of the potential is neglected, these derivatives always translate to derivatives of the weights $\frac{\mathrm{d}P_{\bar{x}}}{\mathrm{d}s}(z)$, $\frac{\mathrm{d}P_z}{\mathrm{d}s}(z)$.

Due to the derivative with regard to the operating parameters, both of these functions are normalised to 0, regardless of their original normalisation. Thus, an ansatz like [9]

$$s\frac{\mathrm{d}P_y}{\mathrm{d}s} = \sum_i c_i(s)(P_{i+1} - P_i)\,, \qquad c_i(s) \leq \mathcal{O}(1)\,, \tag{3.147}$$

can be made, with expansion coefficients $c_i(s)$ and the weights of the krypton measurement $P_i(z)$. Since the weights do not form a basis of L^2, this can only be an approximation. Also, since only $\Delta_{10}[V]$ and $\sigma_0[V]$ are known from krypton, higher order terms in this expansion again lead to non-measurable quantities.

In practice, it turns out that this ansatz works reasonably well for derivatives with regard to column density, and not so well for derivatives with regard to temperature. However, those are one order of magnitude smaller, such that the column density is the main concern. Also, using only one term of the expansion already leads to good results, such that the derivatives of the standard operators can be written with expressions like

$$s\frac{\mathrm{d}\Delta_{\bar{x}}[V]}{\mathrm{d}s} \approx c_0(s)\Delta_{10}[V] - c_1(s)\Delta_{21}[V]\,, \tag{3.148}$$

$$s\frac{\mathrm{d}\sigma_z^2[V]}{\mathrm{d}s} \approx c_0(s)\Delta_{10}[V^2]\,, \tag{3.149}$$

$$= c_0(s)(\sigma_1^2[V] - \sigma_0^2[V])\,. \tag{3.150}$$

Plugging those expressions into equation 3.142, the derivative of $O_\infty^{(2)}[V]$ reads

$$s\frac{\mathrm{d}O_\infty^{(2)}[V]}{\mathrm{d}s} \approx -\epsilon\left(c_0(s)\Delta_{10}[V] - c_1(s)\Delta_{21}[V]\right) + ac_0(s)(\sigma_1^2[V] - \sigma_0^2[V])\,. \tag{3.151}$$

If this ansatz works, it has a benefit over the extremal solutions: Namely, that the first term is known from the krypton measurement. Thus, the mean of $O_\infty^{(2)}[V]$ can be extrapolated by the predicted value, and only the two other terms contribute an uncertainty. An example application is found in appendix A.3.

3.6. Operators of Longitudinal Inhomogeneity and Potential Shape

In section 3.4.1 the following expression for general operators of longitudinal inhomogeneity in the presence of scattering was derived:

$$O_\infty^{(2)}[V] = -\epsilon\Delta_{\bar{x}}[V] + (a - \delta a[V])\,\sigma_z^2[V]\,.$$

It depends on a generalised mean difference $\Delta_{\bar{x}}[V]$ and a generalised variance $\sigma_z^2[V]$. From the discussion in section 3.2.1 it should be understood that both are not independent, but correlated by their shape operator

$$\hat{\rho}_{\bar{x},z}[\ldots] = \frac{1}{\kappa_{\bar{x},z}}\frac{\Delta_{\bar{x}}}{\sigma_z}[\ldots]\,,$$

[9] Alternatively also an ansatz in $P_i - P_0$ can be used.

which is bounded

$$-1 \leq \hat{\rho}_{\bar{x},z}[V] \leq 1 \quad \forall V \in L^2 \,.$$

The shape operator can be used for the alternative representation

$$O_{\infty}^{(2)}[V] = -\sigma_z[V] \left(2\epsilon_\rho \hat{\rho}_{\bar{x},z}[V] - (a - \delta a[V])\, \sigma_z[V]\right) \,, \tag{3.152}$$

where the *shape energy*

$$\epsilon_\rho \equiv -\frac{1}{2}\frac{\partial^2 O}{\partial \sigma_z \partial \hat{\rho}_{\bar{x},z}} \,, \tag{3.153}$$

$$= \frac{1}{2}\epsilon \kappa_{\bar{x},z} \geq 0 \tag{3.154}$$

has been defined. It represents the penalty term with regard to the worst possible potential shape. The case $\epsilon_\rho = 0$ only occurs for $\epsilon_i = 0\ \forall i$, i.e. if there is no scattering. A vanishing total susceptibility $\epsilon = 0$ alone is not sufficient, since then $\kappa_{\bar{x},z}$ is singular and the product finite. Thus, if there is scattering, there are always potential shapes (given by $\hat{\rho}_{\bar{x},z}$ and those which are correlated to it), which lead to a penalty. The inverse is not true, i.e. not every potential shape is penalised.

Since σ_z and $\hat{\rho}_{\bar{x},z}$ are uncorrelated, they can be treated as independent variables and their functional dependence on V can be omitted. Thus, in the case where $\delta a[V]$ is negligible, $O_{\infty}^{(2)}$ is fully determined by the measurement of two bounded scalars, allowing for simple curve sketching. As discussed in the following, this is the case for the neutrino mass shift.

3.6.1. Neutrino Mass Shift and Antisymmetry

As it is shown in chapter 5, for the neutrino mass shift higher scattering order variances are negligible:

$$P_z \approx P_0 \,,\ a \approx -2 \,,\ \delta a[V] \approx 0 \,. \tag{3.155}$$

For the shape operator of the tritium β spectrum an abbreviated notation like in the case of krypton is used:

$$P_\rho \equiv \frac{1}{\epsilon}\sum_i \epsilon_i (P_i - P_0) \,, \tag{3.156}$$

$$\hat{\rho}[\ldots] \equiv \hat{\rho}_{\rho,0}[\ldots] \,, \tag{3.157}$$

$$= \frac{1}{\kappa_{\rho,0}}\frac{\Delta_\rho}{\sigma_0}[\ldots] \,. \tag{3.158}$$

In chapter 5 it is shown that $\hat{\rho}$ is again a measure of potential antisymmetry for typical KATRIN conditions and it is thus called the *antisymmetry operator* [10].

[10] In contrast to the operator defined for krypton in equation 3.36 at least 2x scattering is relevant at typical KATRIN conditions in the tritium β measurements, such that the formal definitions are different. Thus, the detailed shapes of the krypton and tritium antisymmetry operators differ slightly, but this is also the case for the weights of the usual potential moments. All operators are only well defined, if their conditions (krypton or tritium, operating parameters) are specified.

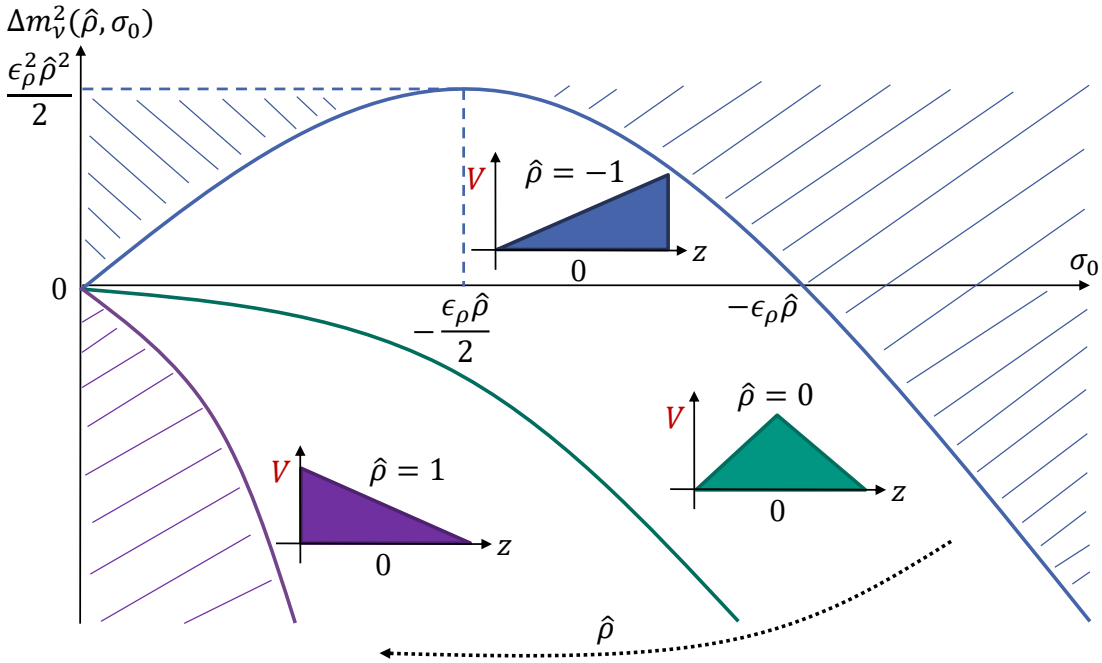

Figure 3.26.: Neutrino mass shift and potential antisymmetry: For shapes of potential with vanishing antisymmetry $\hat{\rho} = 0$, the neutrino mass shift has the known negative parabolic shape as function of the standard deviation σ_0 (green). For $\hat{\rho} > 0$ (purple), the negative neutrino mass shift increases faster than a parabolic form for small σ_0 and asymptotically parabolically for σ_0 larger than $\hat{\rho}\epsilon_\rho$. For $\hat{\rho} < 0$ (blue), the shift has a positive region and a maximum.

Using $\hat{\rho}$, the equation for the shift of the squared neutrino mass reads

$$\Delta m_\nu^2(\hat{\rho}, \sigma_0) = -2\sigma_0 \Big(\underbrace{\epsilon_\rho \hat{\rho}}_{\text{shape}} + \underbrace{\sigma_0}_{\text{variance}} \Big) . \tag{3.159}$$

The curve sketching is shown in figure 3.26 and discussed in the following.

Upper, lower and absolute limits: The upper and lower limits are found at the extremal values of $\hat{\rho}$

$$1 \xleftarrow{\hat{\rho}} -1$$

$$-2\sigma_0(\sigma_0 + \epsilon_\rho) \leq \Delta m_\nu^2(\hat{\rho}, \sigma_0) \leq -2\sigma_0(\sigma_0 - \epsilon_\rho) . \tag{3.160}$$

Using the triangle inequality it follows that the absolute value of the shift is limited by

$$|\Delta m_\nu^2(\hat{\rho}, \sigma_0)| \leq 2\sigma_0(\sigma_0 + \epsilon_\rho) . \tag{3.161}$$

These limits are those of extremal antisymmetry. For the high temperature potential simulation of figure 1.19, which has an antisymmetry of $\hat{\rho} = 0.88$, these limits might be appropriate. However, currently the true value of antisymmetry is unknown: The plasma simulations use simplified models and the experimental verification by the krypton-83m measurement suffers from systematics, as discussed in chapter 6.

Shift regimes: Along the line of increasing σ_0 the asymptotic cases of linear and parabolic regime are

$$\begin{aligned} 0 &\xrightarrow{\qquad\qquad\qquad\qquad\qquad\qquad \sigma_0 \qquad\qquad\qquad\qquad\qquad\qquad} \infty \\ -2\sigma_0\epsilon_\rho\hat{\rho} &\xleftarrow{\sigma_0 \ll \epsilon_\rho|\hat{\rho}|} \Delta m_\nu^2(\hat{\rho}, \sigma_0) \xrightarrow{\epsilon_\rho|\hat{\rho}| \ll \sigma_0} -2\sigma_0^2 \,. \end{aligned} \tag{3.162}$$

The shift of the squared neutrino mass strictly depends on the product $\epsilon_\rho\hat{\rho}$. Thus, for large enough σ_0 the shape energy is negligible, while for small σ_0 shape changes are dominant. For typical KATRIN conditions the shape energy ϵ_ρ is of the order of some hundred millielectronvolts such that σ_0 of the order of some ten millielectronvolts leads to shape dependent effects.

Zero crossing: The zero crossing is at

$$\Delta m_\nu^2(\hat{\rho}, \sigma_{0,\text{zero}}) = 0 \,, \tag{3.163}$$

$$\Leftrightarrow \sigma_{0,\text{zero}} = 0 \quad \text{or} \quad \sigma_{0,\text{zero}}(\hat{\rho}) = -\epsilon_\rho\hat{\rho} \,,\ \hat{\rho} < 0 \,. \tag{3.164}$$

While the first case is equivalent to the potential being constant, in the second case a non-constant potential leads to a vanishing shift of the neutrino mass.

Maximum shift: The $\sigma_{0,\text{max}}$ of the shift maximum is found by demanding the derivative to vanish

$$\begin{aligned} \left.\frac{\partial \Delta m_\nu^2(\hat{\rho}, \sigma_0)}{\partial \sigma_0}\right|_{\sigma_{0,\text{max}}} &= -4\sigma_{0,\text{max}} - 2\epsilon_\rho\hat{\rho} = 0 \,, \\ \Rightarrow \sigma_{0,\text{max}}(\hat{\rho}) &= -\frac{\epsilon_\rho\hat{\rho}}{2} \,,\ \hat{\rho} < 0 \,. \end{aligned} \tag{3.165}$$

Consequently, the shift of the squared neutrino mass at the maximum is

$$\Delta m_\nu^2(\hat{\rho}, \sigma_{0,\text{max}}) = 2\sigma_{0,\text{max}}^2(\hat{\rho}) = \frac{\epsilon_\rho^2\hat{\rho}^2}{2} \,,\ \hat{\rho} < 0 \,. \tag{3.166}$$

3.7. Conclusion

The preceding discussion of the neutrino mass shift concludes this chapter. In the presence of inelastic scattering its dependence on the source potential was shown to be fundamentally different than previously believed. The resulting consequences and complications for the krypton-83m and tritium measurement are manifold; one additional parameter has to be measured in krypton-83m, and not only do the observables depend on the potential, but also on the scattering probabilities and the measurement time distribution. These two new dependencies led to the introduction of one new energy scale and correlation coefficients between krypton-83m and tritium potential estimates. They are calculated for typical

KATRIN conditions in chapter 5. As has been shown by variational calculus the correlation coefficients are used for the translation of the potential estimates from the krypton to the tritium measurement. However, since the change of the potential for different conditions is not known, this translation still has to rely on plasma simulations or different operating conditions have to be avoided entirely. Due to the possible size of the newly introduced potential shape related neutrino mass shift this was chosen for future measurements: Different operating conditions for the krypton-83m and tritium measurement are avoided, such that remaining uncertainties stem only from the krypton-83m measurement itself and from the different gas profiles of the species.

This chapter established the connection of the krypton-83m potential observables to symmetries of the potential. Based on that, in the following chapter 4 it is discussed how krypton-83m potential observables can be used to construct potential models.

4. Plasma Potential Models from Krypton-83m Observables

In this chapter it is discussed how a given set of estimates from a krypton-83m measurement can be used to construct plasma potential models $V(z)$ for KATRIN. The elaborations laid out in chapter 2 and chapter 3 are an essential foundation for the discussions carried out here.

For a given rear wall voltage the estimates obtainable in the krypton-83m measurement are the Gaussian line broadening, the energy loss shift and the line position shift:

$$(U_{\mathrm{RW}}, \sigma_{\mathrm{g}}, \Delta\epsilon_{\mathrm{Eloss}}, \Delta E_{\mathrm{Mean}}) \ .$$

In this chapter it is assumed that the measured estimates can be translated to the potential moments established in section 3.1, which requires understanding of systematics and plasma fluctuations. The obtained moments are the zero scattering weighted standard deviation, the mean difference of one and zero scattering and the zero scattering weighted mean of the potential:

$$(U_{\mathrm{RW}}, \sigma_0[V], \Delta_{10}[V], \langle V\rangle_0) \ .$$

Equivalent formulations using the single-scattering weighted mean or the antisymmetry defined in section 3.2.1 are given by

$$(U_{\mathrm{RW}}, \sigma_0[V], \langle V\rangle_1 , \langle V\rangle_0)$$

and

$$(U_{\mathrm{RW}}, \sigma_0, \hat{\rho}, \langle V\rangle_0) \ .$$

The rigorous validation of a given potential model using these estimates has been described in section 3.3.1. The inverse problem of constructing a model from a given set of observables with certain model assumptions is the topic of this chapter.

The necessary symmetries that any model needs to incorporate to describe the krypton-83m observations are discussed in section 4.1. This allows to assess the efficiency of arbitrary models and gives an understanding how their parameters relate to the observables.

The implementation of models using linear combinations of z-dependent functions is discussed in section 4.2. The natural example of such models are polynomials with coefficients which are determined from the measurement.

4.1. Potential Symmetries and Antisymmetry Models

Parametrisations of potential models using the antisymmetry reveal the relation of the observables to the symmetries of the potential. Let $V_{\text{test}}(z)$ be an ansatz for the potential. The natural normalisation is to measure the potential relative to its zero weighted mean in units of its zero weighted standard deviation, giving the potential shape

$$\frac{1}{\kappa_{\bar{x},0}}\frac{P_{\bar{x}}}{P_0} \equiv \frac{1}{\sigma_0[V_{\text{test}}]}\left(V_{\text{test}} - \langle V_{\text{test}}\rangle_0\right) \ . \tag{4.1}$$

$\kappa_{\bar{x},0} = \sigma_0\left[\frac{P_{\bar{x}}}{P_0}\right]$ is the weight standard deviation defined in section 3.2.2. $P_0(z)$ is the zero scattering weight and $P_{\bar{x}}(z)$ is a weight normalised to zero, which is defined by this equation. The left side is a formalised way of writing the above normalisation in terms of weights: Its zero weighted mean vanishes and its zero weighted standard deviation is one. In section 3.3.1 it was identified that given such a potential shape, the following parametrisation of potential leads to the measured observables:

$$V - \langle V\rangle_0 = \sigma_0\left[\left(\hat{\rho} - \rho_{\bar{x}\overline{10},0}\frac{\sqrt{1-\hat{\rho}^2}}{\sqrt{1-\rho^2_{\bar{x}\overline{10},0}}}\right)\frac{P_1 - P_0}{P_0}\frac{1}{\kappa_{\overline{10},0}} + \frac{\sqrt{1-\hat{\rho}^2}}{\sqrt{1-\rho^2_{\bar{x}\overline{10},0}}}\underbrace{\frac{P_{\bar{x}}}{P_0}\frac{1}{\kappa_{\bar{x},0}}}_{\propto V_{\text{test}} - \langle V_{\text{test}}\rangle_0}\right] . \tag{4.2}$$

$\rho_{\bar{x}\overline{10},0}$ is the weight correlation discussed in section 3.2.2. With the exception of the marked V_{test} term, this model is completely determined by the observables. Choosing V_{test} such that the correlation vanishes

$$\rho_{\bar{x}\overline{10},0} \propto \text{Cov}_0\left[\frac{P_{\bar{x}}}{P_0}, \frac{P_1 - P_0}{P_0}\right] \overset{3.40}{=} \Delta_{10}\left[\frac{P_{\bar{x}}}{P_0}\right] \propto \Delta_{10}\left[V_{\text{test}}\right] \overset{!}{=} 0 \tag{4.3}$$

reveals the underlying symmetries. It follows:

$$V(z) = \underbrace{\sigma_0\left[\underbrace{\hat{\rho}\frac{P_1 - P_0}{P_0}(z)\frac{1}{\kappa_{\overline{10},0}}}_{\text{Antisymmmetry}} + \underbrace{\sqrt{1-\hat{\rho}^2}\frac{P_{\bar{x}}}{P_0}(z)\frac{1}{\kappa_{\bar{x},0}}}_{\text{Symmetry}}\right]}_{\text{Inhomogeneity}} + \underbrace{\langle V\rangle_0}_{\text{Mean}} \ . \tag{4.4}$$

Thus, for a potential model to be able to describe any given set of krypton-83m observables it needs an antisymmetric, a symmetric and a constant component [1], which is depicted in figures 4.1 and 4.2. The test potential V_{test}, which is not predicted by the data, defines the symmetrical component of the potential.

Due to the quadratic addition of the inhomogeneity components, the antisymmetric shape is approached slowly, as sketched in figure 4.3. Also, the term symmetry component

[1] The mentioned symmetries hold for the usual operating conditions. In general they are defined by the shape $\frac{P_1 - P_0}{P_0}$ and by the condition $\Delta_{10}\left[\frac{P_{\bar{x}}}{P_0}\right] = 0$.

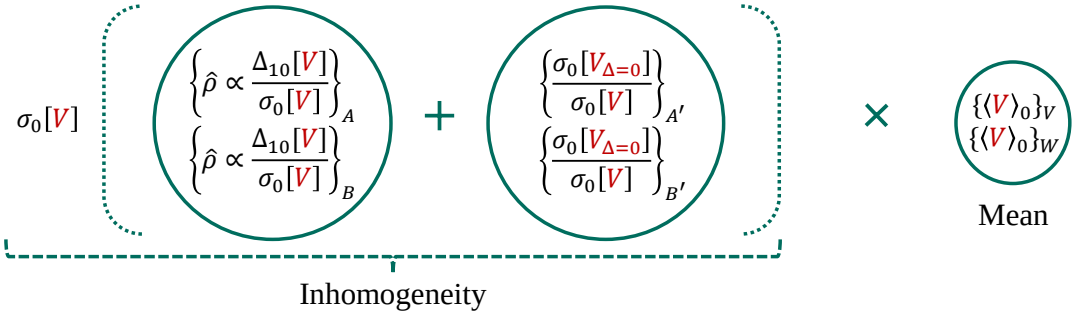

Figure 4.1.: Composition of the image of the KATRIN krypton-83m measurement: There are the three observables $(\sigma_0[V], \Delta_{10}[V], \langle V\rangle_0)$. A measure of the mean potential is given by $\langle V\rangle_0$. Since $\sigma_0[V]$ is non-zero for non-constant potentials, it can be used as an overall measure of inhomogeneity magnitude. Consequently, the total measured inhomogeneity $\sigma_0[V]$ is composed of inhomogeneities, which are manifest in both $\Delta_{10}[V]$ and $\sigma_0[V]$ and inhomogeneities, which are only manifest in $\sigma_0[V_{\Delta=0}]$. Thus, the potential shapes are divided into those with vanishing and non-vanishing expectation value of $\Delta_{10}[...]$.

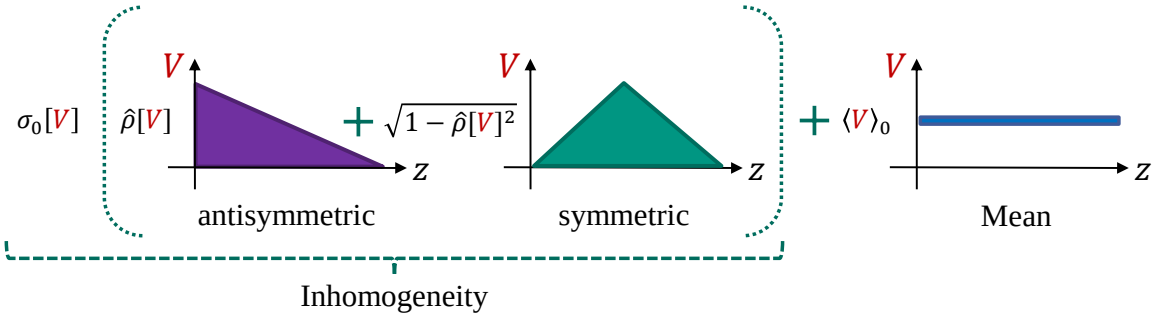

Figure 4.2.: Composition of the domain of the KATRIN krypton-83m measurement: The potential component which produces non-vanishing values of $\hat{\rho}$ typically is approximately antisymmetrical to the injection point, which is an exactly defined symmetry given by the weight functions $P_i(z)$. In contrast, the symmetry of the potential components which have vanishing expectation value of $\Delta_{10}[...]$ is only defined as being not antisymmetric, and the depicted symmetrical shape is only one simple possibility. Provided an ansatz for this component, the total potential can be modelled as being composed of both components plus its constant mean. The amplitudes of the inhomogeneity components add in quadrature.

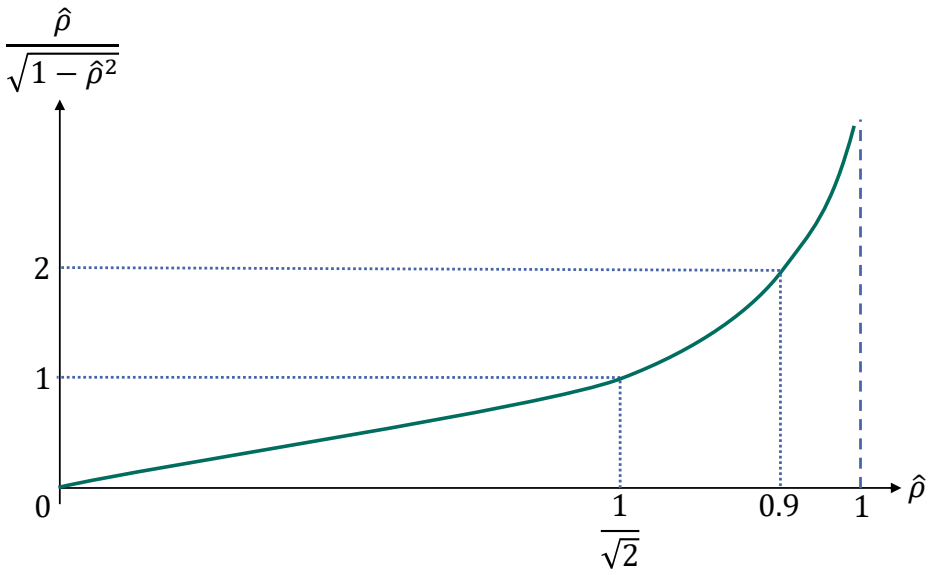

Figure 4.3.: Antisymmetry amplitude: The ratio of the amplitudes of the antisymmetry and the symmetry component are equal for an antisymmetry $\hat{\rho} \approx 0.7$. Due to the quadratic scaling, even for $\hat{\rho} \approx 0.9$ the antisymmetric component is only twice as large as the symmetric component. A factor 10 is reached for $\hat{\rho} \approx 0.995$.

should be used with some caution, since rigorously it is only given by the absence of antisymmetry ($\hat{\rho} = 0$). Since $\hat{\rho}[V] \propto \Delta_{10}[V]$, the defining condition for the potentials of the symmetry component is the vanishing mean difference. Thus, while for $\hat{\rho} = \pm 1$ the potential shape has the approximate triangular shape sketched in figure 4.2, it does not need to have the simple symmetrical shape for $\hat{\rho} = 0$.

Shape of the symmetry component: The potential shape of the symmetry component is defined by equation 4.1 and optionally equation 4.3. The defining characteristic of equation 4.1 is that the zero weighted mean of the supplied potential vanishes, and that it is normalised to its zero weighted standard deviation. If both is already put into the implementation of equation 4.2, any potential can be used.

Equation 4.3 is the optional condition for potentials in the kernel of the mean difference $\Delta_{10}[...]$. Solving for these potentials is a homogeneous Fredholm problem of first kind [Waz11] and the general solutions are non-trivial. Also, the subset of the kernel which can be expanded in weights

$$\Delta_{10}\left[\frac{\sum_k a_k (P_k - 1)}{P_1 - P_0}\right] = 0 \tag{4.5}$$

leads to non-physical solutions, since those expansions have non-regularised poles for $P_0(z) = P_1(z)$.

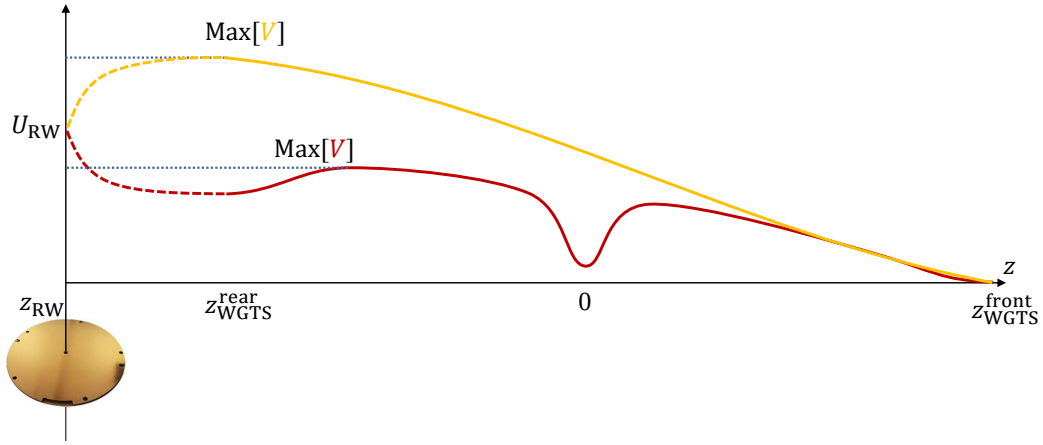

Figure 4.4.: Peak-to-peak value and maximum derivative: For a given $(\sigma_0, \hat{\rho})$, different maximum derivatives of the potential result in different peak-to-peak values. The linear connection (orange) with the smallest maximum derivative leads to a larger peak-to-peak value than if a structure is added (here in the center, red). In one case the maximum in the central WGTS is larger than the rear wall voltage, in the other smaller.

Simple solutions without the need for regularisation can be found from polynomial expansions. The simplest ansatz, which uses only two terms, is

$$V_{\Delta=0}(z) = a\left(\frac{\Delta_{10}[z^m]}{\Delta_{10}[z^n]}z^n - z^m\right), \quad a \in \mathbb{R}, \quad m, n \in \mathbb{N}. \tag{4.6}$$

The coefficients $\Delta_{10}[z^m]$ are discussed together with polynomial expansions in section 4.2. In practice implementations of the full equation 4.2 with arbitrary V_{test} can be used, such that the vanishing correlation (condition 4.3) is not required. However, in this work always models like equation 4.4 were used, since they lead to simpler propagations of uncertainties and directly show the symmetries of their components.

Symmetry component and peak-to-peak value: The symmetry component is independent from the measured $(\sigma_0, \hat{\rho})$. Nevertheless, in some cases it can be constrained from the applied rear wall voltage and the measured potential mean $(U_{\mathrm{RW}}, \langle V \rangle_0)$. The reasoning is as following: As discussed in section 3.3.3, the maximum derivative of the potential affects the obtained peak-to-peak value $\mathrm{PP}[V]$ for a given standard deviation $\sigma_0[V]$. Thus, the more structure the symmetry component has, the smaller is the resulting peak-to-peak value for a given set of observables. This is sketched in figure 4.4. For some rear wall regimes this allows to make a statement on the necessary structure, for example, if for large rear wall voltages the externally applied electric field dominates over the internal plasma processes. Due to energy conservation, in this case the maximum potential needs to be smaller than the rear wall voltage. Increasing the structure decreases the peak-to-peak value and consequently the maximum, while the other observables, especially the given σ_0, remain unchanged.

While the quantitative relation of the structure of the potential to the peak-to-peak value depends on the symmetry component, an approximate relation is sketched in the following. For upper constraints of the peak-to-peak value from the rear wall voltage it holds

$$\begin{aligned} \mathrm{PP}[V] &= \mathrm{Max}[V] - \mathrm{Min}[V] \,, && (4.7)\\ &= O(2)\ (\mathrm{Max}[V] - \langle V \rangle_0) \,, && (4.8)\\ &\overset{!}{=} O(2)\ (U_{\mathrm{RW}} - \langle V \rangle_0) \,. && (4.9) \end{aligned}$$

The equation is expanded to lower constraints, if the absolute value is taken. The true factor $O(2)$ of the distance of the mean $\langle V \rangle_0$ to the boundaries depends on the actual potential and the weight P_0.

Using the mean value theorem 3.99 leads to

$$\mathrm{Max}\left[\left|\frac{\mathrm{d}V}{\mathrm{d}z}\right|\right] \overset{!}{\geq} \frac{O(2)\ |U_{\mathrm{RW}} - \langle V \rangle_0|}{L_{\mathrm{WGTS}}} \,. \tag{4.10}$$

Thus, the difference of the rear wall voltage to the measured mean sets a lower bound to the necessary derivative of the potential. Since the antisymmetry component is approximately linear, it does not contribute large derivatives and increasing the derivative can only be done by adding structure to the symmetry component. As a consequence, if the peak-to-peak value of the potential model is larger than expected, for example from energy conservation, the structure of the symmetry component needs to be increased.

Due to the unknown factor $O(2)$ the above relation only serves to show the principle. This factor also needs to consider the distance from rear wall to central WGTS, which was neglected here.

Connection to the rear wall: Since the density of signal electrons in the $\approx$ 3 m long region between rear wall and WGTS is negligibly small, observables of the spectrum do not contain information of the potential shape in this region. As a consequence, including the rear wall voltage into the potential modelling is model dependent and any structure that is restricted to this region requires non-measurable parameters. This is sketched in figure 4.5.

Assuming no structure results in a linear connection potential

$$V_{\mathrm{Connect}}(z) = \frac{z^{\mathrm{rear}}_{\mathrm{WGTS}} - z}{z^{\mathrm{rear}}_{\mathrm{WGTS}} - z_{\mathrm{RW}}} \left(V_{\mathrm{RW}} - V(z^{\mathrm{rear}}_{\mathrm{WGTS}})\right) + V(z^{\mathrm{rear}}_{\mathrm{WGTS}}) \,, \tag{4.11}$$

where $z^{\mathrm{rear}}_{\mathrm{WGTS}}$ is the position of the end of the rear part of the WGTS and z_{RW} is the position of the rear wall.

The linear connection is only for illustrative purposes, since it is known that a plasma sheath decouples the rear wall from the WGTS for some voltage regimes. Thus, at least one parameter λ_s is required which defines the sheath width. Models using such parameters λ_k can fit the data, when the corresponding connection shape extends into the WGTS, such that the parameters are correlated with the observables. Otherwise only upper limits

$$\lambda_k < z^{\mathrm{rear}}_{\mathrm{WGTS}} - z_{\mathrm{RW}} \tag{4.12}$$

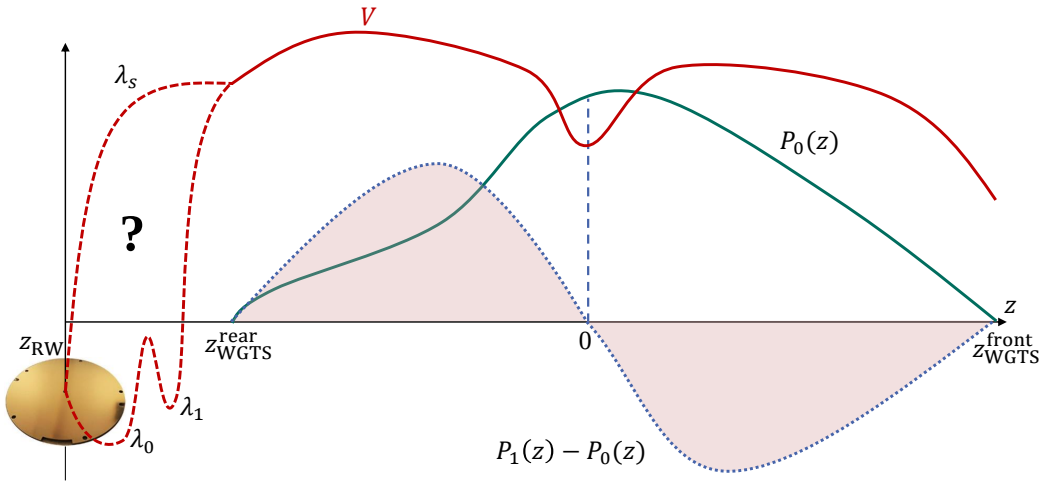

Figure 4.5.: Rear wall connection potential: Due to the vanishing weights P_0, P_1 between the rear wall and the WGTS, the spectrum does not contain any information on the potential V in this ≈ 3 m long region. It is known that a plasma sheath decouples the rear wall from the WGTS for some rear wall voltage regimes. This can be modelled as an exponential decoupling with sheath width λ_s, which is non-measurable if $\lambda_s \ll z^{rear}_{WGTS} - z_{RW}$. Any more physical effects, resulting in more complicated shapes, require more non-measurable parameters λ_k.

can be obtained from the data. However, in practice these conditions are problematic, since they lead to constraints of λ_k only for very a small portion of the krypton data (i.e. only when a strong external electric field is applied). Thus, in this work only the linear connection is shown.

Summary: The previous discussion allows to rigorously predict the effect of the three observables on the modelling:

- $\boldsymbol{\sigma_0}$: Serves as magnitude of the potential inhomogeneity.
- $\boldsymbol{\hat{\rho}}$: Gives the antisymmetry of the potential.
- $\boldsymbol{\langle V \rangle_0}$: Is the mean potential.

The only input to the model is the symmetry component. When including a physical principle like energy conservation, in some cases its structure can be constrained:

- $\boldsymbol{U_{RW} - \langle V \rangle_0}$: Is a lower limit for the necessary derivative of the symmetry component for some rear wall voltage regimes.

The results of the application of this model on KNM2 krypton data is found in section 6.4.

4.2. Linear Models and Polynomial Expansions

In the following the implementation of linear models is discussed. They are defined by

$$V(z) = \vec{c}\vec{f}(z)\,, \tag{4.13}$$

with a vector of N unknown, scalar, erroneous coefficients $\vec{c}$ and N functions

$$f_n : \{z \in [z_{\mathrm{RW}}, z_{\mathrm{WGTS,front}}]\} \to \mathbb{R}\,, \quad n < N\,. \tag{4.14}$$

They form the ansatz for the potential model. In the following for functions in $\vec{f}$ the notation f, g, h and for coefficients in $\vec{c}$ the notation a, b, c is used. Together with N boundary conditions $\vec{V}$ (for example $\langle V\rangle_0$ and $\langle V\rangle_1$, or the direct potential measurement V_{RW}) this gives a system of N linear equations

$$\vec{V} = \begin{pmatrix} \langle V\rangle_0 \\ \langle V\rangle_1 \\ V_{RW} \\ \vdots \end{pmatrix} = \begin{pmatrix} \langle f\rangle_0 & \langle g\rangle_0 & \langle h\rangle_0 & \cdots \\ \langle f\rangle_1 & \langle g\rangle_1 & \langle h\rangle_1 & \cdots \\ f(z_{RW}) & g(z_{RW}) & h(z_{RW}) & \cdots \\ \vdots & \vdots & \vdots & \ddots \end{pmatrix} \begin{pmatrix} a \\ b \\ c \\ \vdots \end{pmatrix} \equiv A\vec{c}\,, \tag{4.15}$$

which can be solved by matrix inversion. The matrix A and its inverse do not depend on the boundary conditions (i.e. the set of observables) and are specific to each model. The determination of the coefficients $\vec{c}$ from the provided observables then only requires the matrix multiplication

$$\vec{c} = A^{-1}\vec{V}\,. \tag{4.16}$$

Since only the three listed boundary conditions are known, the modelling is restricted to $N = 3$. The variance $\sigma_0^2[V]$ cannot be used in this linear ansatz.

The potential model can be used in two ways:

- Using equation 4.16 for a given set of observables. The use case is the krypton measurement.
- Using equation 4.15, if the coefficients $\vec{c}$ (i.e. the potential $V(z)$) are known. One use case is to study the translation from potential moments obtained in krypton measurements to tritium measurements on test models.

Naturally, the measurable moments of the model should be calculated. For the calculation of the variances $\sigma_i^2[V]$ two further matrices are needed. Using the outer product $\otimes$, the squared mean matrix

$$\left\langle \vec{f} \otimes \vec{f} \right\rangle_i = \begin{pmatrix} \langle ff\rangle_i & \langle fg\rangle_i & \langle fh\rangle_i & \cdots \\ \langle gf\rangle_i & \langle gg\rangle_i & \langle gh\rangle_i & \cdots \\ \langle hf\rangle_i & \langle hg\rangle_i & \langle hh\rangle_i & \cdots \\ \vdots & \vdots & \vdots & \ddots \end{pmatrix} \tag{4.17}$$

and the mean squared matrix

$$\left\langle \vec{f} \right\rangle_i \otimes \left\langle \vec{f} \right\rangle_i = \begin{pmatrix} \langle f\rangle_i \langle f\rangle_i & \langle f\rangle_i \langle g\rangle_i & \langle f\rangle_i \langle h\rangle_i & \cdots \\ \langle g\rangle_i \langle f\rangle_i & \langle g\rangle_i \langle g\rangle_i & \langle g\rangle_i \langle h\rangle_i & \cdots \\ \langle h\rangle_i \langle f\rangle_i & \langle h\rangle_i \langle g\rangle_i & \langle h\rangle_i \langle h\rangle_i & \cdots \\ \vdots & \vdots & \vdots & \ddots \end{pmatrix} \tag{4.18}$$

Table 4.1.: **Plasma antisymmetry for power functions.**
Odd orders of z^k show large absolute antisymmetry. The negative signs indicate that the antisymmetry shape decreases from rear to front. The linear shape is almost similar to the reflected antisymmetry shape, i.e. the amplitude of other components is smaller by a factor of seven. The values are calculated for KNM2 krypton operating conditions of $\rho d = 30$ %, $T = 100$ K, $\kappa_{\overline{10},0} = 0.69$.

	Exponent k					
Estimate ↓	0	1	2	3	4	5
$-\Delta_{10}[z^k]$	0	1.66	0.435	19.65	7.17	300.65
$\sigma_0[z^k]$	0	2.445	6.341	34.891	126.78	646.81
$-\hat{\rho}[z^k]$	-	0.98	0.10	0.82	0.08	0.67

are obtained. The calculation of the central variance $\sigma_i^2[V] = \langle V^2 \rangle_i - \langle V \rangle_i^2$ can thus be performed simply from precalculated matrices:

$$\sigma_i^2[V] = \vec{c}\left(\left\langle \vec{f} \otimes \vec{f} \right\rangle_i - \left\langle \vec{f} \right\rangle_i \otimes \left\langle \vec{f} \right\rangle_i\right)\vec{c}\,. \tag{4.19}$$

The propagated uncertainties $\sigma(\langle V \rangle_i)$ and $\sigma(\sigma_i^2[V])$ from the uncertainties $\sigma(\vec{c})$ of the $\vec{c}$ are obtained using the first derivative of equations 4.15 and 4.19, leading to the Jacobi matrix

$$\begin{pmatrix} \sigma(\langle V \rangle_i) \\ \sigma(\sigma_i^2[V]) \end{pmatrix} = \begin{pmatrix} \left\langle \vec{f} \right\rangle_i^T \\ 2\left(\left(\left\langle \vec{f} \otimes \vec{f} \right\rangle_i - \left\langle \vec{f} \right\rangle_i \otimes \left\langle \vec{f} \right\rangle_i\right)\vec{c}\right)^T \end{pmatrix} \sigma(\vec{c})\,. \tag{4.20}$$

Calculations for scattering multiplicities $i > 1$ and higher moments of the starting potential distributions are possible, but both lead to quantities not measurable in krypton.

Polynomial models: A common use case of linear models is the ansatz of a Taylor series

$$V(z) = \sum v_k \left(\frac{z}{\mathrm{m}}\right)^k \tag{4.21}$$

with coefficients v_k. Coincidentally, the symmetry of power functions around zero approximately fits to the symmetry of the antisymmetry operator. Thus, even orders (which are axially symmetric with regard to the coordinate origin) are suppressed in $\Delta_{10}[V]$, which can be seen in table 4.1. As a consequence, polynomial expansions need to have at least one even and one odd term, to reasonably cover the range of obtainable observables.

The solutions of general expansions with mixed coefficients can be obtained by the following matrices:

$$\sigma_0^2[V] = \begin{pmatrix} v_0 & v_1 & v_2 & v_3 & \cdots \end{pmatrix} \begin{pmatrix} 0 & 0 & 0 & 0 & \cdots \\ 0 & 5.978 & 1.721 & 76.03 & \cdots \\ 0 & 1.721 & 40.22 & 31.82 & \cdots \\ 0 & 76.03 & 31.82 & 1217 & \cdots \\ \vdots & \vdots & \vdots & \vdots & \ddots \end{pmatrix} \begin{pmatrix} v_0 \\ v_1 \\ v_2 \\ v_3 \\ \vdots \end{pmatrix}, \tag{4.22}$$

$$\sigma_1^2[V] = \begin{pmatrix} v_0 & v_1 & v_2 & v_3 & \cdots \end{pmatrix} \begin{pmatrix} 0 & 0 & 0 & 0 & \cdots \\ 0 & 3.868 & -8.404 & 48.79 & \cdots \\ 0 & -8.404 & 38.16 & -156.2 & \cdots \\ 0 & 48.79 & -156.2 & 854.1 & \cdots \\ \vdots & \vdots & \vdots & \vdots & \ddots \end{pmatrix} \begin{pmatrix} v_0 \\ v_1 \\ v_2 \\ v_3 \\ \vdots \end{pmatrix}, \tag{4.23}$$

$$\Delta_{10}[V] = \begin{pmatrix} 0 & -1.66 & -0.435 & -19.65 & \cdots \end{pmatrix} \begin{pmatrix} v_0 \\ v_1 \\ v_2 \\ v_3 \\ \vdots \end{pmatrix}. \tag{4.24}$$

They hold for KNM2 krypton operating conditions of $\rho d = 30\ \%,\ T = 100\ \mathrm{K}$.

By calculating the eigenvalues, it is easily shown that both $\sigma_0^2(kl)$ and $\sigma_1^2(kl)$ are positive definite and that $\sigma_0[V]$ and $\sigma_1[V]$ increase upon including higher orders of the potential v_k. As discussed, this does not hold for $\Delta_{10}[V]$. Specifically, there are infinitely many potential shapes for which $\Delta_{10}[V] \equiv 0$ holds. The coefficients are obtained from equation 4.24. Evidently, since all the entries in 4.24 have the same sign, this requires non-monotonous potentials. If for example only up to second order is used, one obtains

$$V_{\mathrm{sym}}(z) \propto 3.815 \left(\frac{z}{\mathrm{m}}\right)^2 - \frac{z}{\mathrm{m}} \tag{4.25}$$

for which $\Delta_{10}\left[V_{\mathrm{sym}}\right] = 0$ holds. It is used in section 6.3.1 as symmetrical component for the potential modelling of KNM2 krypton data.

Since every ansatz of linearly formulated potentials is model dependent, no further applications are shown in this work and the antisymmetry parametrisation is preferred. Nevertheless, during the work on this thesis many examples of polynomial models were calculated from KNM1 and KNM2 krypton data. For a given set of observables these models always showed the symmetries expected from the measured antisymmetry. Also, these models were used to check the theory developed here: They were put into full z-dependent toy spectra with a sliced source model (described in section 1.2.2) and their effect on krypton and tritium observables was fitted. In all tested cases the results were in agreement with the equations derived in this work. Thus, the fits to the krypton line spectra recover the moments $(\sigma_0[V], \langle V\rangle_1, \langle V\rangle_0)$ of the input potential. An ansatz for the resulting neutrino mass and endpoint shift was derived in section 3.4.3 in the form of expansions in potential moments. Calculating the coefficients of these expansions for typical KATRIN conditions is the topic of the next chapter.

5. Systematic Uncertainties of Tritium Observables due to Plasma Potential Moments

In this chapter the relations of the systematic shifts of the squared neutrino mass $\Delta m_\nu^2[V]$ and the endpoint $\Delta E_0[V]$ to the starting potential V are calculated for typical KATRIN measurement conditions. Here only the relevant coefficients and potential shapes of the theory which was derived in chapter 3 are calculated. Thus, the detailed elaboration in chapter 3 or the summary chapter 2 are an essential foundation for the discussions carried out here.

The developed theory uses a convolution of the krypton or tritium spectra with Starting Potential Distributions (SPD). Due to the longitudinal sensitivity on the source potential by inelastic scattering (discussed in section 1.4.2) this has to be carried out separately for each scattering multiplicity i. The relevant quantities for the characterisation of plasma potential systematics are the moments (equation 3.1) of the SPD_i obtained. Up to second order these are the means $\langle V \rangle_i$, the mean differences $\Delta_{i0}[V]$ and the standard deviations $\sigma_i[V]$. All source potential related quantities are weighted with the normalised longitudinal electron distributions (referenced as *scattering weights* in the following) $P_i(z)$ of the source, which are different for krypton and tritium. As a consequence, also the moments are different. Indices marking this difference are omitted here for brevity, but the difference should always be kept in mind.

As shown in chapter 3 the general equations for the systematic shifts of the squared neutrino mass and endpoint of the tritium β spectrum are of the form

$$\Delta m_\nu^2[V] = -\sum_{i>0} \epsilon_i \Delta_{i0}[V] - 2\sigma_0^2[V] + \sum_{i>0} a_i^\sigma \sigma_i^2[V] \,, \tag{5.1}$$

$$\Delta E_0[V] = -\langle V \rangle_0 - \sum_{i>0} a_i \Delta_{i0}[V] \,. \tag{5.2}$$

The goal of the first section 5.1 is the determination of the susceptibilities ϵ_i, a_i^σ and a_i. Their determination allows to reduce the above equations to the relevant terms at given measurement conditions.

As visible in this ansatz, in the tritium spectrum the scattering contributions are mixed and the susceptibilities specify the individual contributions. In section 3.4.3 it was shown

that the mixing of the Δ_{i0} can be condensed into a weight

$$P_\rho \equiv \frac{1}{\epsilon}\sum_i \epsilon_i (P_i - P_0)\,, \quad \epsilon = \left|\sum_i \epsilon_i\right| \,. \tag{5.3}$$

P_ρ is the weight of the mean difference $\Delta_\rho[V] = \langle V P_\rho \rangle$, which absorbs all scattering contributions and is the relevant quantity for the description of the neutrino mass shift. It was also shown that in an even more fundamental description the *antisymmetry operator*

$$\hat{\rho}[...] \equiv \frac{1}{\kappa_{\rho,0}} \frac{\Delta_\rho[...]}{\sigma_0[...]} \tag{5.4}$$

replaces $\Delta_\rho[...]$. It is a correlation operator, i.e. $|\hat{\rho}[V]| \leq 1$. The extrema of $\hat{\rho}[...]$ are produced by the *antisymmetry shape* $\frac{P_\rho}{P_0}(z)$, which is the potential shape that leads to the extremal neutrino mass shift. As shown in section 5.2, it is antisymmetrical for typical KATRIN measurement conditions. $\kappa_{\rho,0}$ is the standard deviation of the antisymmetry shape. Analogous definitions hold for $P_{\rho_a}, \Delta_{\rho_a}$ and $\hat{\rho}_a$ derived from the susceptibilities of the endpoint a_i.

Accordingly, section 5.2 is dedicated to the study of the antisymmetry shape and the standard deviations and correlations of different scattering weights for typical KATRIN measurement conditions.

The standard deviations and correlations of the scattering weights are relevant to calculate how the krypton-83m estimates $(\Delta_{10}[V], \sigma_0[V])$ constrain $(\Delta_\rho[V], \sigma_0[V])$ and thus the neutrino mass shift under tritium conditions. The corresponding relations were derived in chapter 3. In section 5.3 the resulting scaling factors and uncertainties are calculated for typical KATRIN measurement conditions.

The studies are based on the key conditions of the KNM1-3a measurements, shown in table 5.1. The different source conditions of the KNM1 and KNM2 tritium and krypton measurements are expected to result in a different plasma potential. This leads to an uncertainty in the prediction of the associated systematics, which can only be specified by assuming a potential model for extrapolation. This is not the topic of this work. The uncertainty was erased in KNM3a by choosing the same source conditions for both measurements. Still, the uncertainty due to the different scattering weights for the different gas species remains, which is calculated in this chapter. While the column density in krypton mode up to KNM3 was restricted to below 40 %, the column density in tritium mode can be varied freely up to the nominal amount [1]. To fit also to future campaigns, in the studies the column density in the tritium measurement is varied. All plots are produced using the SSC&KaFit software framework (cf. section 1.2.2) and the gas model it contains.

[1] Column density here always refers to the value of tritium. The krypton column density is irrelevant due to the low density limit discussed in section 1.3.1.

Table 5.1.: **KNM1-3 measurement conditions.**
While in KNM1 and KNM2 tritium column density ρd and temperature T of the krypton and tritium measurement were different, in KNM3a equal source conditions were chosen to avoid plasma differences. This is also referred to as *high temperature* or *equal source mode* in the following.

Campaign	ρd in % of nominal		T in K	
	T_2	Kr	T_2	Kr
KNM1	22	30	29	100
KNM2	84	30	29	100
KNM3a	40	40	80	80

5.1. Susceptibilities of Tritium Observables to Scattering Moments

In this section the susceptibilities of m_ν^2 and E_0 with regard to the starting potential moments $\Delta_{i0}[V]$ and $\sigma_i[V]$ for i scattering multiplicity are calculated. They are given by the partial derivatives

$$\epsilon_i = -\frac{\partial \Delta m_\nu^2}{\partial \Delta_{i0}} \,,\; a_i^\sigma = \frac{\partial \Delta m_\nu^2}{\partial \sigma_i^2} \,,\; a_i = -\frac{\partial E_0}{\partial \Delta_{i0}} \,. \tag{5.5}$$

As discussed in section 1.2.2, modifications of the differential spectra by source or transmission properties of KATRIN are considered in the response function $R(E, qU)$ (figure 1.11). E is the electron energy and qU the retarding energy of the spectrometer. Consequently, plasma potential systematics are also considered by a modification of the response function. The effect of the potential moments on the beta spectrum is equivalent to convolutions with a Gaussian $G(\Delta_{i0}, \sigma_i)$ for each scattering multiplicity (as derived in appendix A.1)

$$R(E, qU) = \int_{\epsilon=0}^{E-qU} \mathcal{T}(E-\epsilon, qU) \sum_{i=0}^{\infty} \langle p_i \rangle \, f_i(\epsilon) * G(\Delta_{i0}, \sigma_i) \mathrm{d}\epsilon \,. \tag{5.6}$$

Here $\mathcal{T}(E-\epsilon, qU)$ is the transmission function. The $\langle p_i \rangle$ are the average scattering probabilities and $f_i(\epsilon)$ is the i times convoluted energy loss function

$$f_i(\epsilon) = \delta(\epsilon) * \underbrace{f_1(\epsilon) * \ldots * f_1(\epsilon)}_{i\text{–times}} \,. \tag{5.7}$$

$f_1(\epsilon)$ is shown in figure 5.1. The $\langle p_i \rangle$ are plotted in figure 5.2 in dependence of the tritium column density.

Notably, an inhomogeneous plasma potential is only one possibility to arrive at non-vanishing moments of these Gaussian convolutions and for example uncertainties in the energy loss model or other spectrum contributions, which are shifted in energy compared to expectation, lead to similar effects.

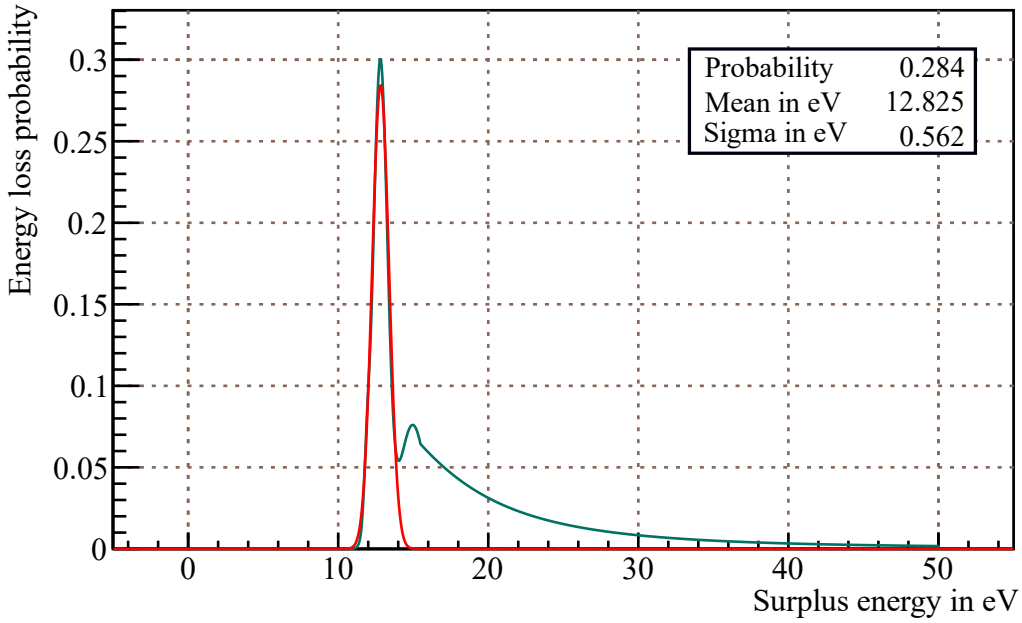

Figure 5.1.: Energy loss function $f_1(\epsilon)$: The width of the excitation peak, here fitted with a Gaussian (red), is already so large that additional variance due to plasma effects can be neglected. The function was measured by KATRIN during KNM2 [KATep].

The studies shown in the following use the shift method (see section 1.2.1) on toy data of the respective KNMx campaigns: the Δ_{i0} and σ_i^2 are varied in Asimov data and the resulting shifts of the tritium spectrum observables are fitted. The measurement time distribution (i.e. the distribution of the measurement time over the set points of the retarding energies) of KNM2 was used. For the study of the analysis interval dependence the respective retarding energies were excluded accordingly.

Susceptibilities to variances σ_i^2: For changes of the $\sigma_{i>0}$ on the order of 100 mV shifts of not more than a few millielectronvolt for m_ν and less than a millielectronvolt for E_0 were found. It can be concluded that those susceptibilities are negligible for typical KATRIN conditions:

$$a_i^\sigma = \frac{\partial \Delta m_\nu^2}{\partial \sigma_i^2} \approx 0 \text{ for } i > 0 \,. \tag{5.8}$$

The vanishing relevance of additional variances of the scattered spectra is explained by the intrinsic width of the energy loss function $f_1(\epsilon)$. The excitation peak has a width of 562 meV so that an additional width of 100 meV added in quadrature is in practice negligible. Including the ionisation tail or higher scattering order convolutions leads to even broader $f_i(\epsilon)$ and to less effect of additional variances.

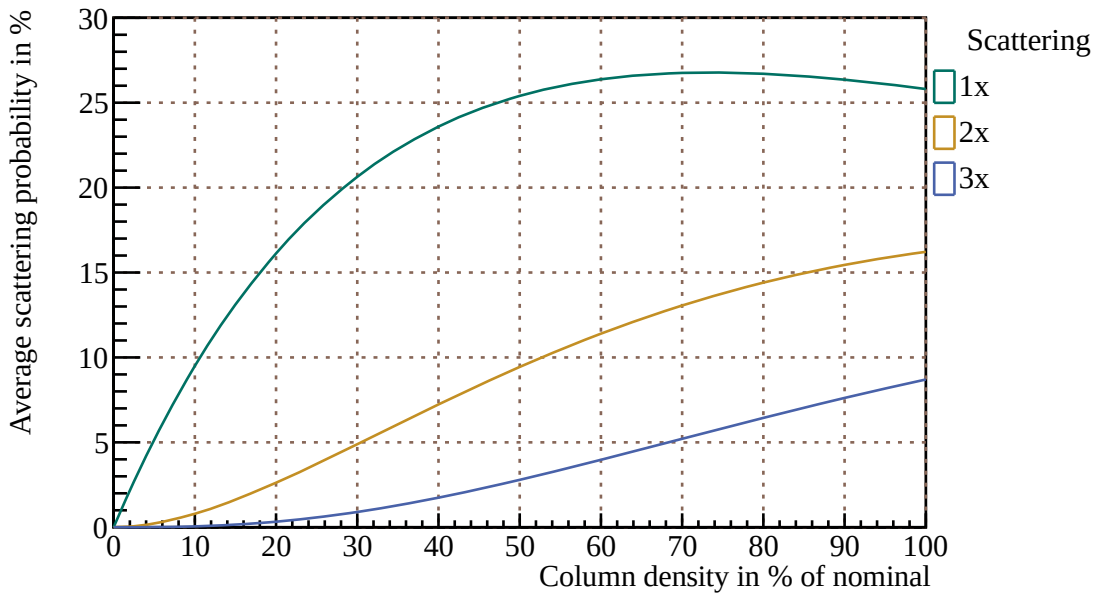

Figure 5.2.: Average scattering probabilities vs. column density: The scattering probabilities increase with increasing column density. Above 80 % of nominal column density the probability of single scattering decreases in favour of the probabilities of higher scattering multiplicity. The temperature is 29 K.

Susceptibilities to Mean Differences Δ_{i0}

When the higher variances are neglected, the neutrino mass and endpoint shift equations can be reformulated using the antisymmetry shape (equation 5.3 ff.). As discussed in section 3.4.3, hereby the summation over $\epsilon_i \Delta_{i0}$ is replaced by a product of the total susceptibility ϵ and Δ_ρ (analogously for the endpoint):

$$\Delta m_\nu^2[V] = -\epsilon \Delta_\rho[V] - 2\sigma_0^2[V] \,, \tag{5.9}$$

$$\Delta E_0[V] = -\langle V \rangle_0 - a \Delta_{\rho_a}[V] \,. \tag{5.10}$$

Notably, the antisymmetry shapes (and the corresponding mean differences Δ_ρ and Δ_{ρ_a}) for the neutrino mass and endpoint are in general different, since in general their contributing susceptibilities ϵ_i and a_i are different. Whether or not this is relevant can be investigated by studying the ratios of the susceptibilities: If they differ by more than a constant scaling, then the antisymmetry shapes are different.

The total susceptibilities ϵ and a are obtained by simultaneously shifting all Δ_{i0} in the Gaussian convolution (equation 5.6) by the same value. They are shown together with their components ϵ_i and a_i in figures 5.3, 5.4, 5.5, and 5.6 in dependence of column density, background rate and lower analysis interval.

Ratio of the susceptibilities: While the susceptibilities for neutrino mass and endpoint look very similar, their ratio is in general not constant. Also, for analysis intervals smaller

than 90 eV the ratio is larger for higher scattering multiplicities. Thus, the neutrino mass is more susceptible to shifts of higher scattering multiplicity than the endpoint. The non-constant ratio also remains when normalising it to the summation of the susceptibilities. As a consequence, generally $\Delta_\rho[V]$ and $\Delta_{\rho_a}[V]$ are different, i.e. different potential shapes lead to extremal neutrino mass and endpoint shifts. However, for the 40 eV range the contributions of $i > 1$ and the column density dependence of the ratio are small. In this case also the difference of the antisymmetry shapes can be neglected and in the following only the neutrino mass case Δ_ρ is considered. However, if a detailed analysis of the starting potential induced endpoint shift is the goal, especially for larger analysis intervals, then these differences are relevant.

Dependence on background rate and temperature: No sizeable difference between the source temperatures of 29 K and 80 K has been found. Below a background rate of $\approx$ 50 mcps the susceptibilities are greatly reduced.

Dependence on scattering contribution: The expectation that higher scattering contributions lead to larger susceptibilities is partially fulfilled; the susceptibilities increase with column density, as do the scattering probabilities (figure 5.2). However, the detailed scaling of the susceptibilities and scattering probabilities with the column density is different. Also, the dependence on the analysis interval is non-trivial: For intervals larger than 40 eV the total and 1x scattering susceptibilities start to decrease and in the region above 80 eV there is a zero crossing. Why this happens is not understood conclusively. However, vanishing total susceptibility should not be mistaken with vanishing neutrino mass or endpoint shift, as discussed in section 3.4.4 and in the following.

Normalisation and implementation: Neglecting the variance term, the expression of the shift of the squared neutrino mass (equation 5.9) is given by a product of the mean difference $\Delta_\rho[V]$ and the susceptibility ϵ. The susceptibility defines, which mean differences need to be shifted in the simulation. If the total susceptibility is used, all Δ_{i0} have to be shifted by the same amount $\Delta_\rho[V]$. However, this depends on the normalisation of P_ρ (equation 5.3). If it was normalised to one of the ϵ_i instead of ϵ, resulting in a different operator $\Delta_{\rho'}[...]$, in equation 5.9 the susceptibility ϵ_i would appear as prefactor. To obtain the same shift of the neutrino mass, in this case only Δ_{i0} needs to be shifted, but by the different value $\Delta_{\rho'}[V]$.

Consequently, by choosing which Δ_{i0} are shifted, the analysts decide which values $\Delta_\rho[V]$ or $\Delta_{\rho'}[V]$ are needed. In all cases those values are constrained by the krypton $\Delta_{10}[V]$ and the shifts are in general not the expectation values $\Delta_{i0}[V]$ of the actual potential.

As visible in the first term of equation 5.1

$$\begin{aligned}\Delta m_\nu^2[V]\big|_{\sigma_i=0} &= -\sum_{i>0} \epsilon_i \Delta_{i0}[V] \,, \\ &\overset{\Delta_{i0}[V]=\Delta[V]}{=} -\Delta[V] \underbrace{\sum_{i>0} \epsilon_i}_{\propto\epsilon} \,,\end{aligned}$$

if all mean differences actually have the same value $\Delta[V]$, they can be drawn in front of the sum. Thus, only in this case this term vanishes for $\epsilon = 0$. However, if the mean differences are different, the multiplication of ϵ with Δ_ρ then singular leads to a finite shift. Such singularities are avoided when $\Delta_\rho[...]$ is normalised to a susceptibility that does not vanish for the respective conditions. Consequently, for analysis intervals larger than 80 eV a shift of Δ_{20} should be chosen.

Conclusion: For the usual analysis interval of 40 eV the susceptibilities of neutrino mass and endpoint to mean differences are by coincidence the largest. Depending on the column density, the endpoint shift is not only determined by the mean potential $\langle V \rangle_0$, but has large contributions of $\Delta_{\rho_a}[V]$: up to 17 % for nominal column density, $\approx$ 6 % in KNM1, $\approx$ 15 % in KNM2 and $\approx$ 9 % in KNM3a. The contributions of $\Delta_\rho[V]$ to the shift of the squared neutrino mass are large, too. Due to the correlation of $\Delta_\rho[V]$ and $\sigma_0[V]$ they are easier to quantify when using the shape energy instead of the susceptibility. This discussion is carried out in the next section.

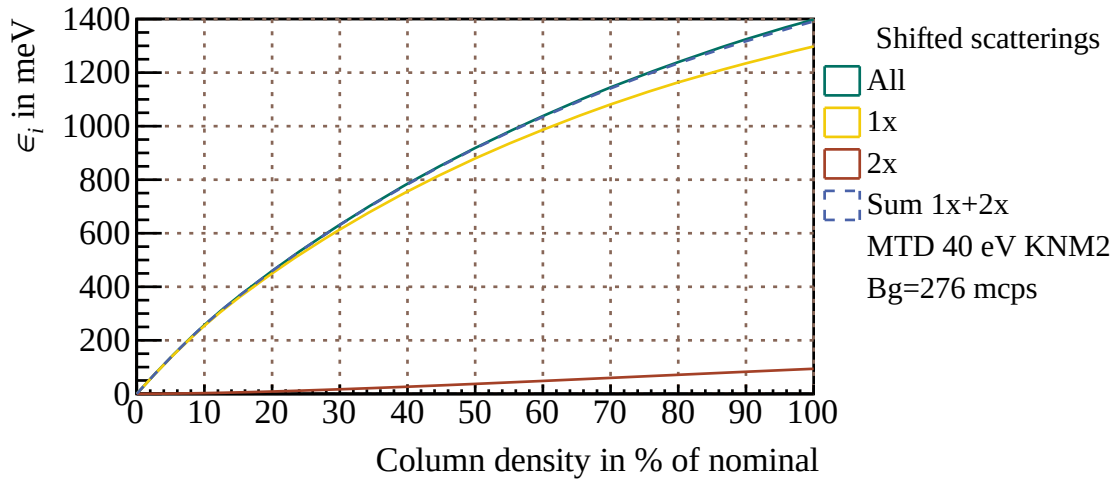

(a) Neutrino mass

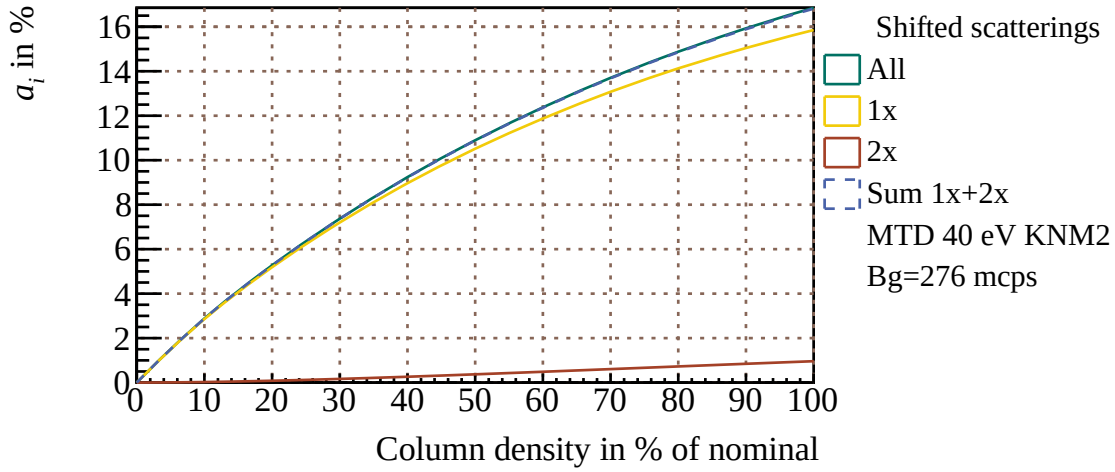

(b) Endpoint

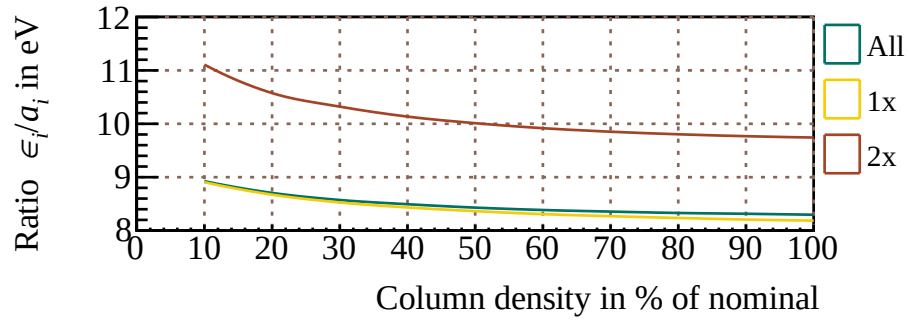

(c) Ratio

Figure 5.3.: Mean difference susceptibility vs. column density: As expected the susceptibilities strongly depend on the column density. Since the summation of the 1x and 2x susceptibilities are in practice identical to the total susceptibility, higher scattering orders are negligible. The ratios show a column density dependence, such that the antisymmetry shapes for endpoint and neutrino mass are not the same.

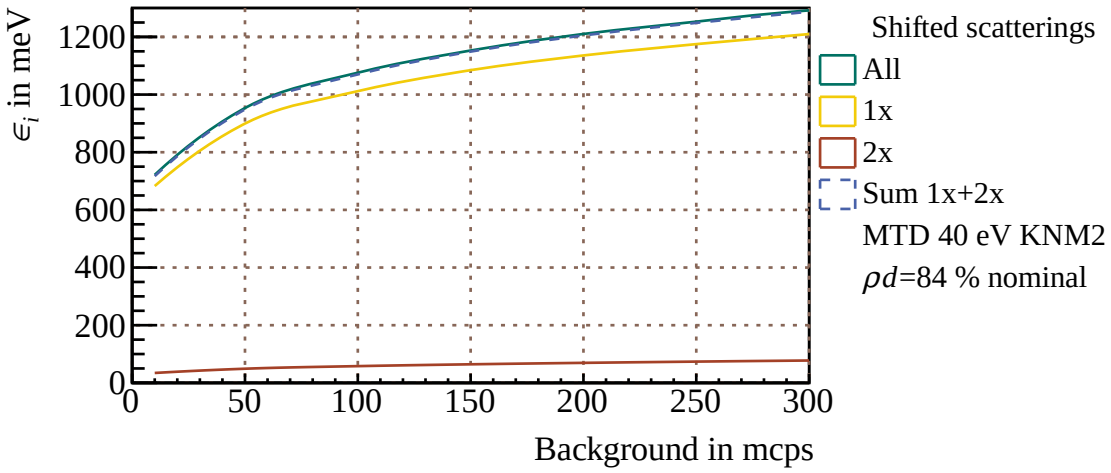

(a) Neutrino mass

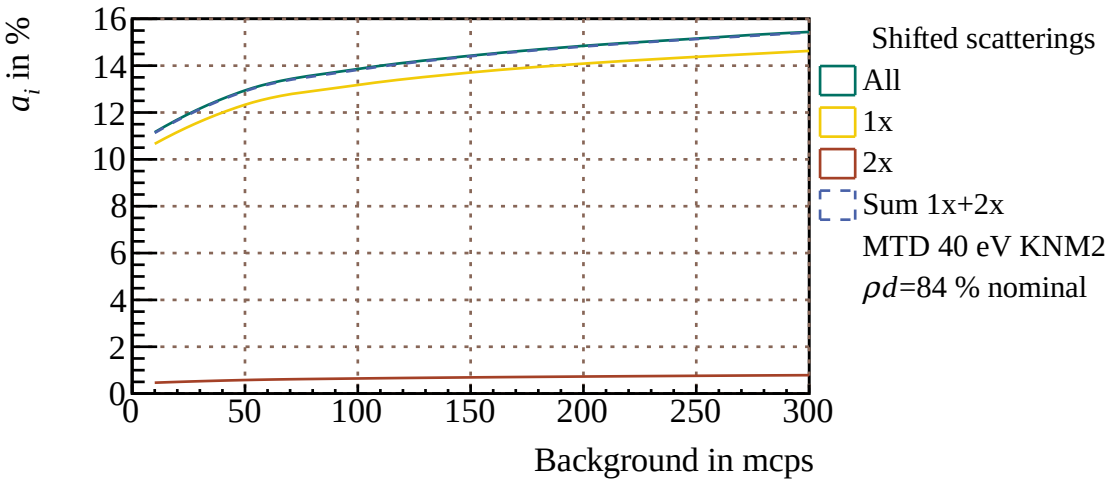

(b) Endpoint

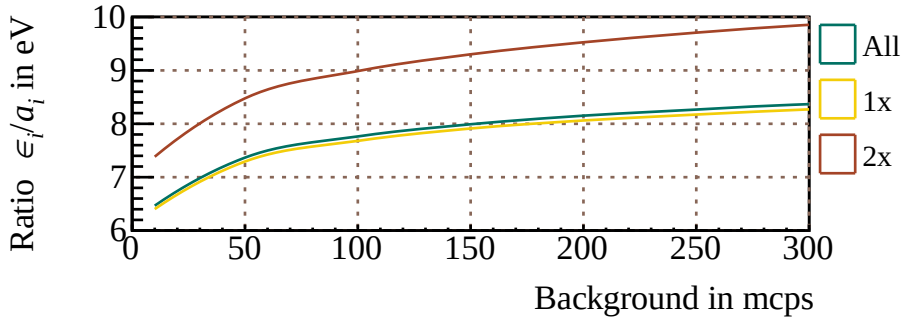

(c) Ratio

Figure 5.4.: Mean difference susceptibility vs. background: The susceptibilities to scattering moments increase with the background rate. Thus, the values obtained for Bg = 276 mcps are an upper limit for KNM2, which had a lower background in its last period 3. Reducing the background below ≈ 50 mcps would be strongly beneficial with regard to plasma potential systematics.

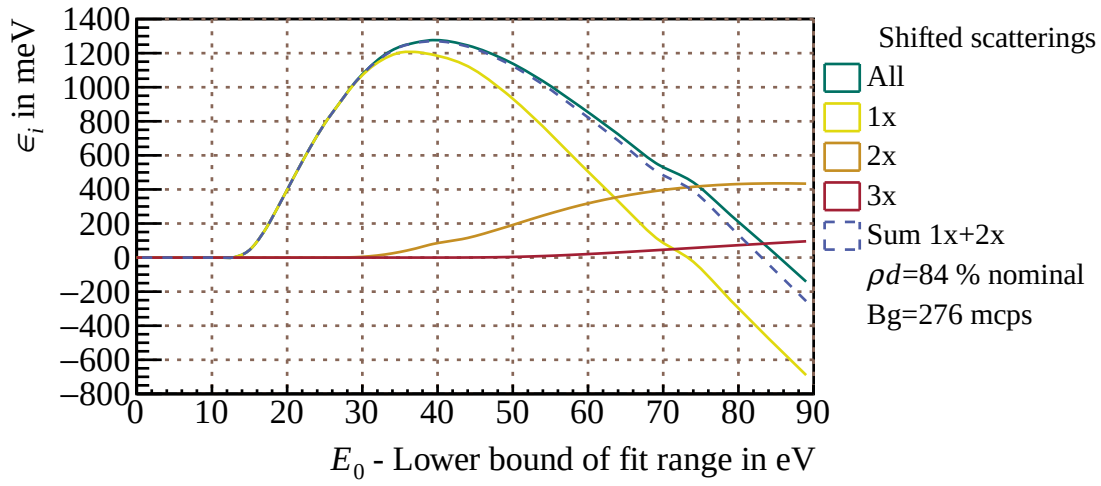

(a) Neutrino mass

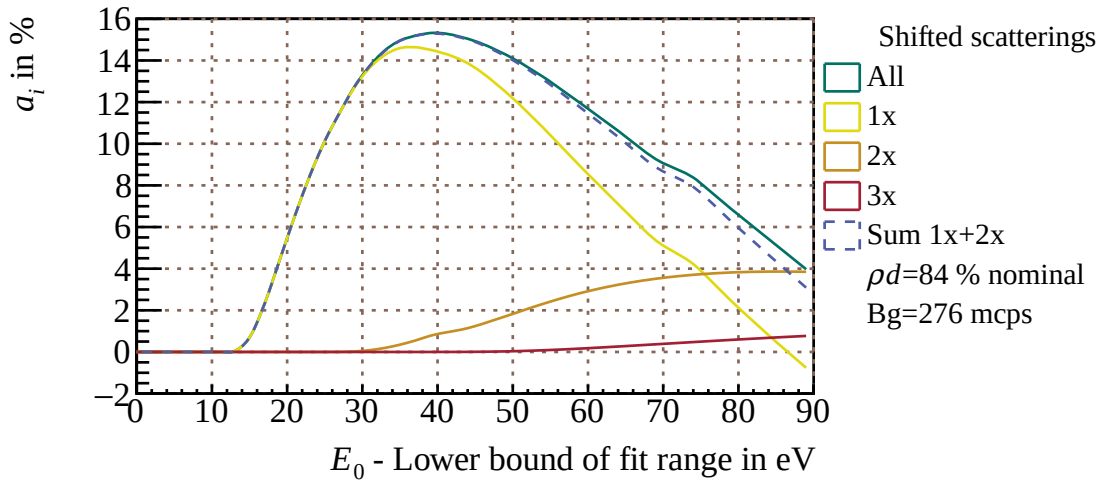

(b) Endpoint

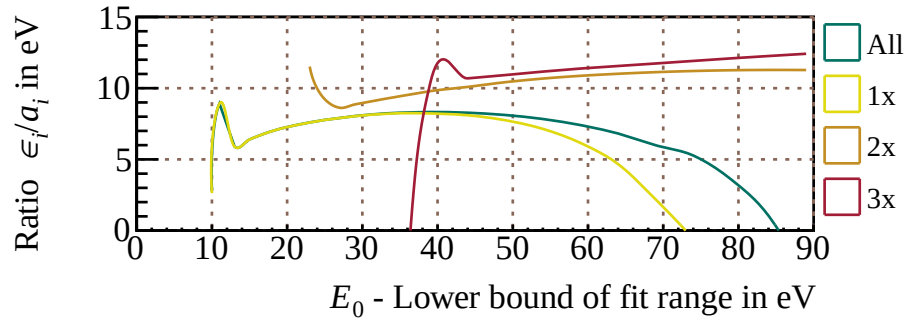

(c) Ratio

Figure 5.5.: Mean difference susceptibility vs. lower analysis interval: Increasing scattering multiplicities are only relevant if the analysis interval is large enough. In the standard 40 eV range the first two orders are sufficient. In the 90 eV range also 3x scattering has to be considered. Notably, the 40 eV range is accidentally the most susceptible, while above the shifts decrease. As discussed in the text, the zeros of the total susceptibilities do not imply vanishing endpoint or neutrino mass shift.

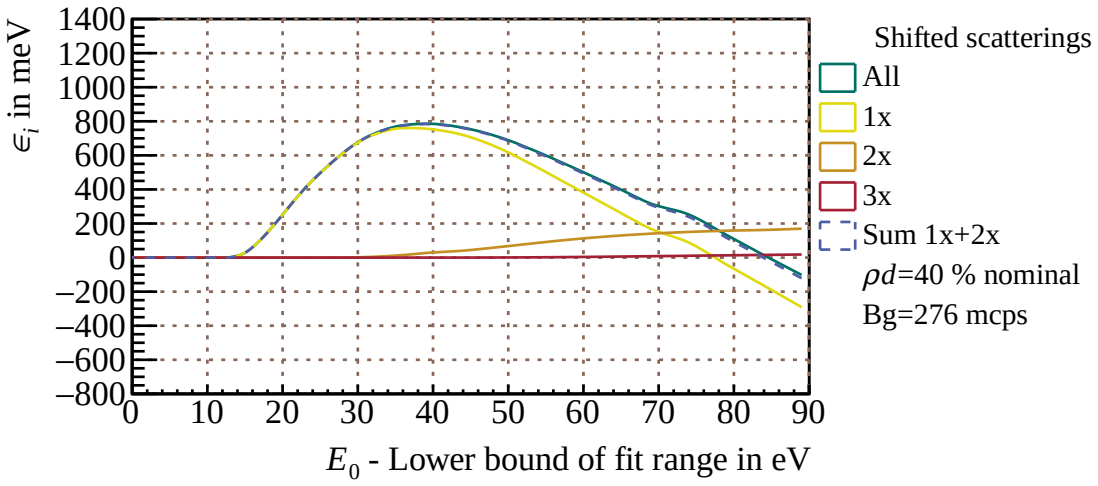

(a) Neutrino mass

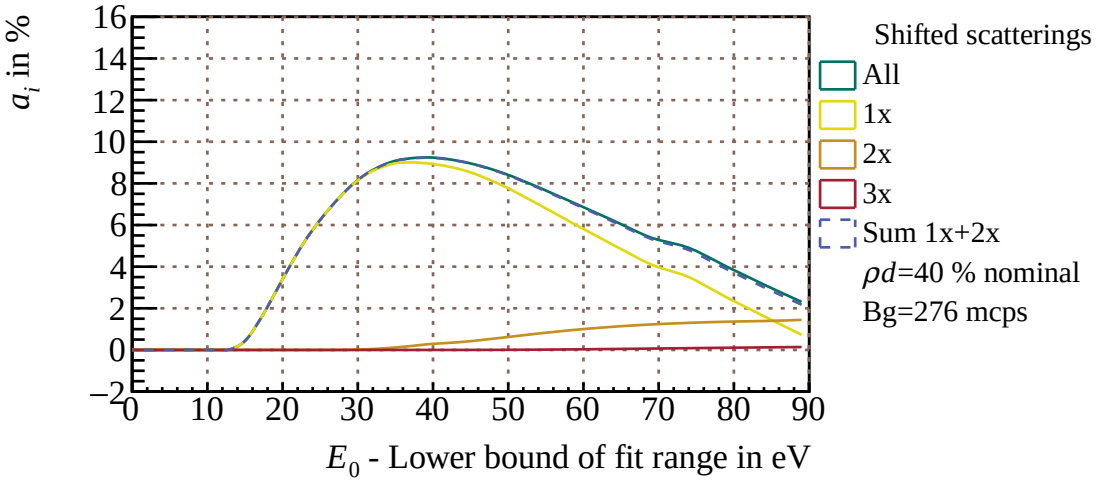

(b) Endpoint

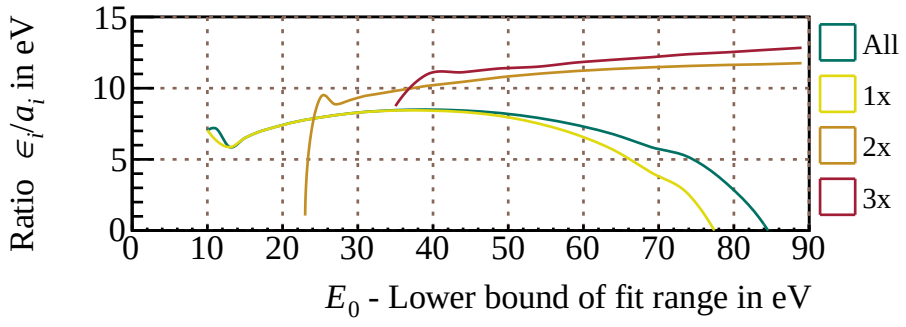

(c) Ratio

Figure 5.6.: Mean difference susceptibility vs. lower analysis interval, high temperature mode: Comparing to figure 5.5, the susceptibilities in first approximation scale with the column density. However, the zero crossings are slightly shifted, such that the scaling with column density is non-trivial in detail. As in figure 5.5, the ratios strongly vary, implying differences of the antisymmetry shapes of endpoint and neutrino mass.

5.2. Weights, Operator Constraints and Extremal Shapes

In this section the normalised longitudinal electron distributions $P_i(z)$ (also called *scattering weights*) for i scattering multiplicity and the derived antisymmetry shape $\frac{P_\rho}{P_0}(z)$ (equation 5.3 ff.) are studied. From their shapes follow the constraints of the plasma potential observables of the krypton-83m and tritium measurement and the extremal potential shapes leading to those constraints.

The theory was derived in section 3.3: there it was shown how standard deviations $\kappa_{\bar{x},z}$ of the normalised weights $P_{\bar{x}}, P_z$ can be used to constrain observables [2], typically resulting in inequalities. Related to these constraints are potential shapes, which produce the extremal effects. In this section only the inequalities and the shapes are shown.

Index rules: The following rules simplify the understanding of the derived equations:

- For all constraints a standard deviation σ_z needs to be measured; its weight gives the index after the comma.
- The weights before the comma are given by the involved $\Delta_{\bar{x}}$; weight correlations $\rho_{\rho\overline{10},0}$ appear if krypton constrains tritium. Standard deviations $\kappa_{\bar{x},z}$ appear, if a $\Delta_{\bar{x}}$ is constrained by a σ_z.

The pure scattering weights $P_i(z)$ of tritium are shown in figure 5.7, a comparison between krypton and tritium weights at equal source conditions is seen in figure 5.8.

Constraints can be obtained for the peak-to-peak value of the potential in the central WGTS PP[V] and for the mean differences $\Delta_{\bar{x}}[V]$, including the relevant mean difference for the tritium measurement $\Delta_\rho[V]$. However, as discussed in section 5.1, the latter is normalisation dependent. If instead the antisymmetry operator $\hat{\rho}$ defined in equation 5.4 is used for the parametrisation of the shift of the squared neutrino mass, then one obtains

$$\Delta m_\nu^2(\hat{\rho}, \sigma_0) = -2\sigma_0\Big(\underbrace{\epsilon_\rho \hat{\rho}}_{\text{shape}} + \underbrace{\sigma_0}_{\text{variance}}\Big) \tag{5.11}$$

as discussed in detail in section 3.6.1. The resulting prefactor is the *shape energy*

$$\epsilon_\rho = \frac{1}{2}\epsilon\kappa_{\rho,0} \geq 0\ . \tag{5.12}$$

Since $|\hat{\rho}| \leq 1$, it quantifies the extremal value of the above shape term, which is realised by the antisymmetry shape.

Mean differences: The weight standard deviations $\kappa_{\bar{x},z}$ constrain the size of $\Delta_{\bar{x}}$ via the shape operator $\hat{\rho}_{\bar{x},z}$, if σ_z is known:

$$|\Delta_{\bar{x}}[V]| = |\hat{\rho}_{\bar{x},z}[V]|\kappa_{\bar{x},z}\sigma_z[V] \leq \kappa_{\bar{x},z}\sigma_z[V]\ . \tag{5.13}$$

[2] Negated indices were introduced to specify the normalisation $\langle 1\rangle_{\bar{x}} = \langle P_{\bar{x}}\rangle = 0$, while for regular indices $\langle 1\rangle_z = \langle P_z\rangle = 1$ holds. Negated indices always appear in the context of mean differences $\Delta_{\bar{x}}$, while regular indices appear for variances σ_z. These operators and their weights are used to generalise from pure scattering weights P_i to mixed scattering contributions, which is relevant in the tritium β spectrum.

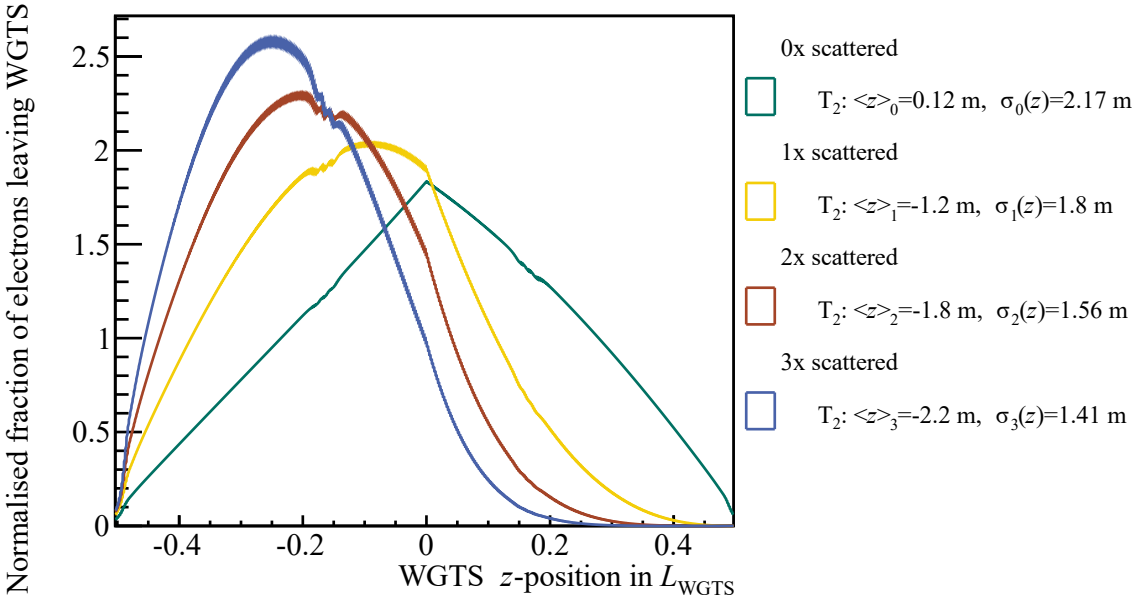

(a) ρd = 10 %

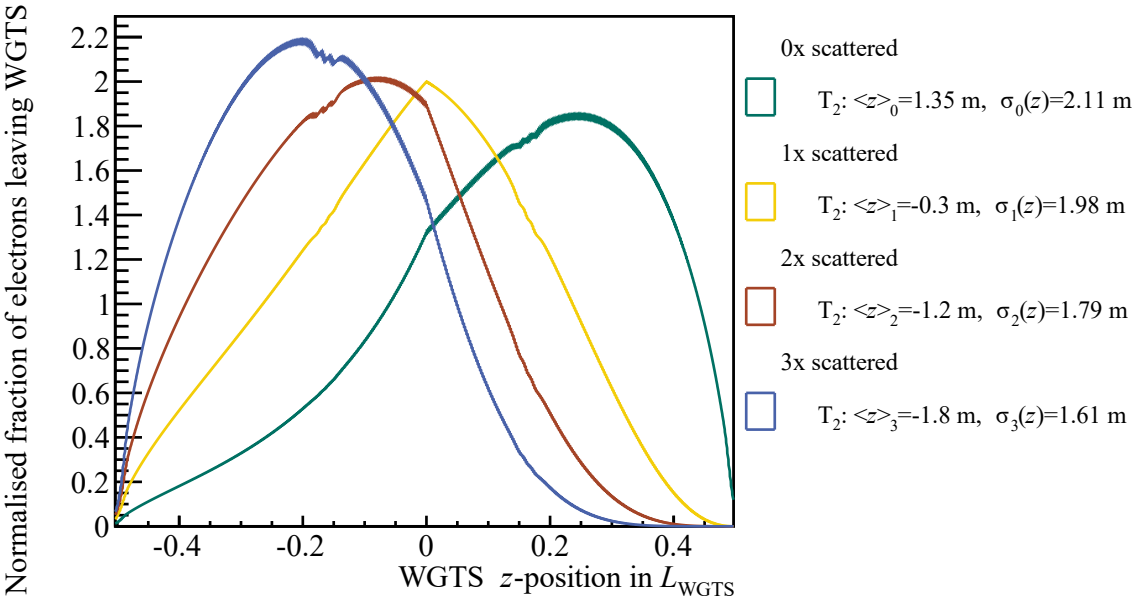

(b) ρd = 100 %

Figure 5.7.: Normalised electron distributions, tritium: For small column densities (a) the scattering probabilities are small and P_0 is essentially given by the gas profile. $P_{>1}$ show degeneracy, which decreases with increasing column density (b). The ripples visible in all source profiles at around ±20 % L_{WGTS} are due to variations in the pitch angle. They are caused by inhomogeneities of the magnetic field in the pump ports. Shown is the central WGTS with a length of ≈ 10 m.

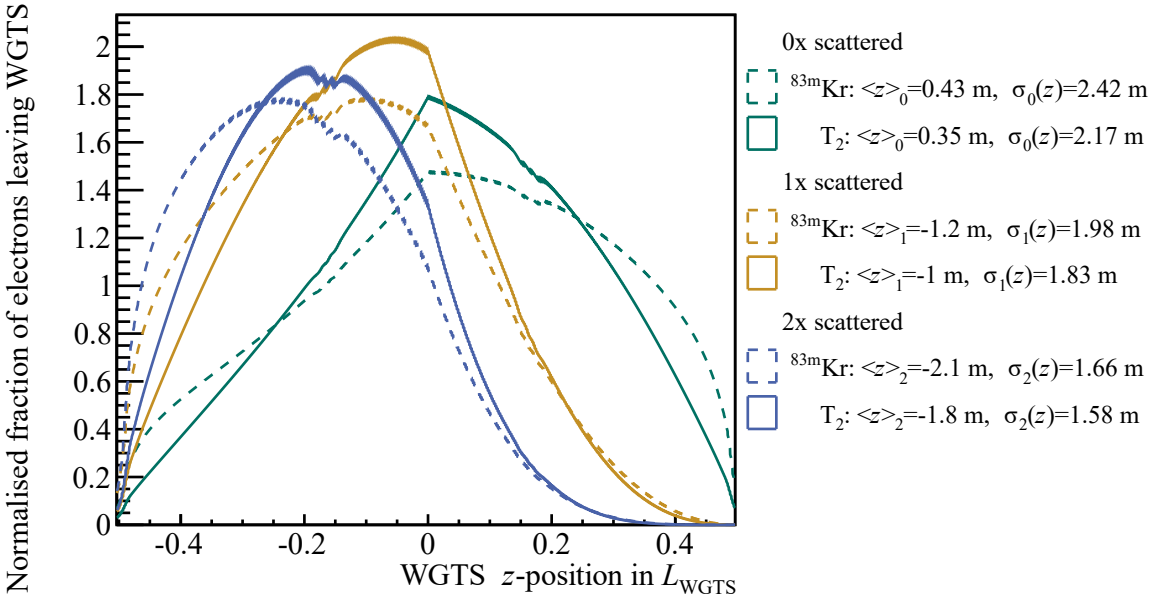

Figure 5.8.: Normalised electron distributions in high temperature mode: Even at same source conditions the weights of the krypton and tritium spectrum are different. This is related to the higher mass of krypton, which, compared to tritium, leads to accumulation at the WGTS ends.

They are shown in figure 5.9. The constraints of the Δ_{i0} only depend on the scattering weights, thus mainly on the column density and due to changes of the gas viscosity in principle on the temperature. However, as shown in section 5.1, the temperature dependence is negligible. In tritium, the constraint of Δ_ρ (defined by the summation over the Δ_{i0}, weighted with the susceptibilities) additionally depends on the susceptibilities and thus on the MTD, background and chosen normalisation of the summation. Due to the normalisation dependence, the detailed numbers should be discussed in terms of shape energy, as done below.

For krypton the relevant operators are Δ_{10}, σ_0 and the unweighted σ (in the range of the central WGTS). Considering the tritium column density in the krypton measurements of 30 – 40 % of nominal, it follows from figure 5.9 that the P_0 weighted and unweighted standard deviations need to be at least $\approx 0.66^{-1} \approx 1.5$ times larger than Δ_{10}. If that does not hold, the krypton measurement suffers from systematics.

The shapes leading to the maximum of the respective antisymmetry operator (i.e $\hat{\rho} = +1$) are shown in figure 5.10. For the shown analysis range of 40 eV the tritium Δ_ρ is dominated by Δ_{10}, leading to the typical antisymmetrical shape also observed in krypton. Thus, for given σ_0, this potential shape produces the largest neutrino mass and endpoint shift shape term, and the largest energy loss shift in krypton.

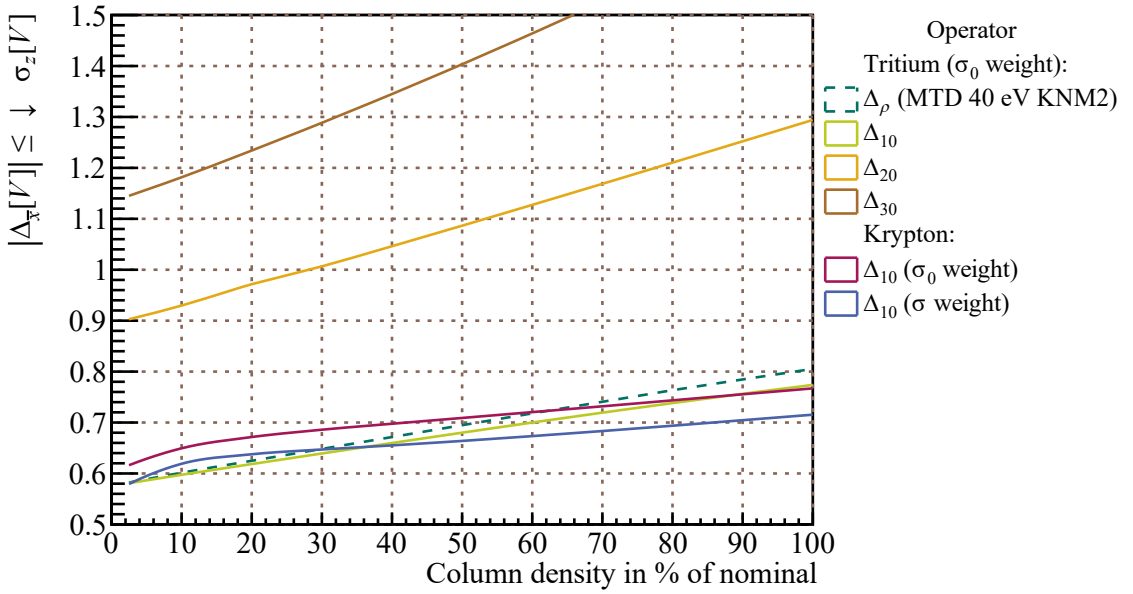

Figure 5.9.: Weight standard deviations and operator constraints: The operators are constrained by the weight standard deviations $\kappa_{\bar{x},z} = \sigma_z \left[\frac{P_{\bar{x}}}{P_z}\right]$ displayed on the y-axis. Here they are shown for all relevant $\Delta_{\bar{x}}$ and σ_z. Increasing scattering multiplicity or column density leads to larger departure of $P_{\bar{x}}$ from a constant behaviour.

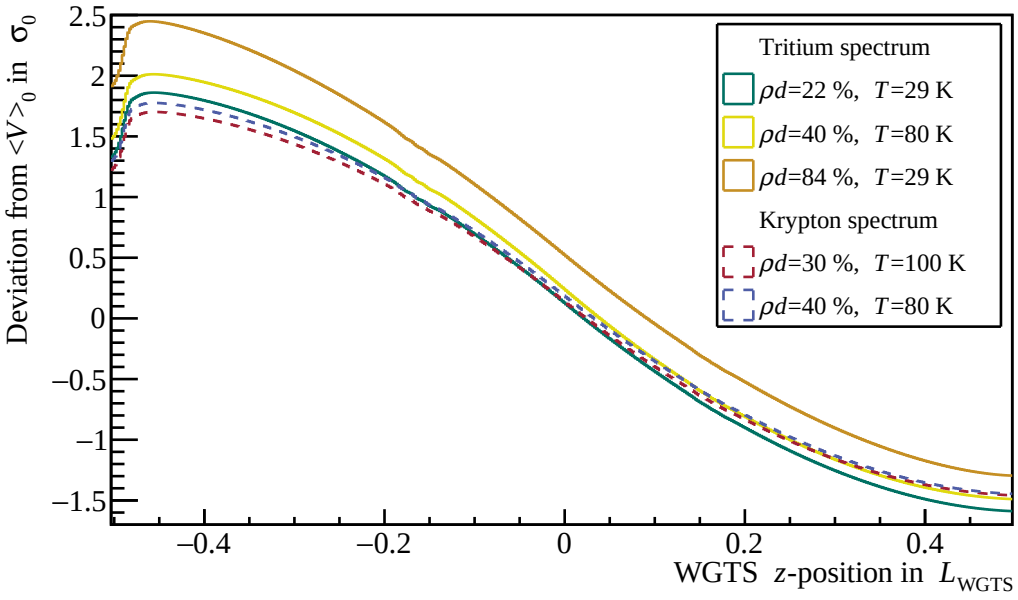

Figure 5.10.: Antisymmetry shapes: In all shown conditions the plotted weights $\frac{1}{\kappa_{\rho,0}}\frac{P_\rho}{P_0}$ (tritium) or $\frac{1}{\kappa_{\overline{10},0}}\frac{P_1-P_0}{P_0}$ (krypton) are approximately antisymmetrical. These shapes maximise the respective antisymmetry operators (i.e. $\hat{\rho} = +1$).

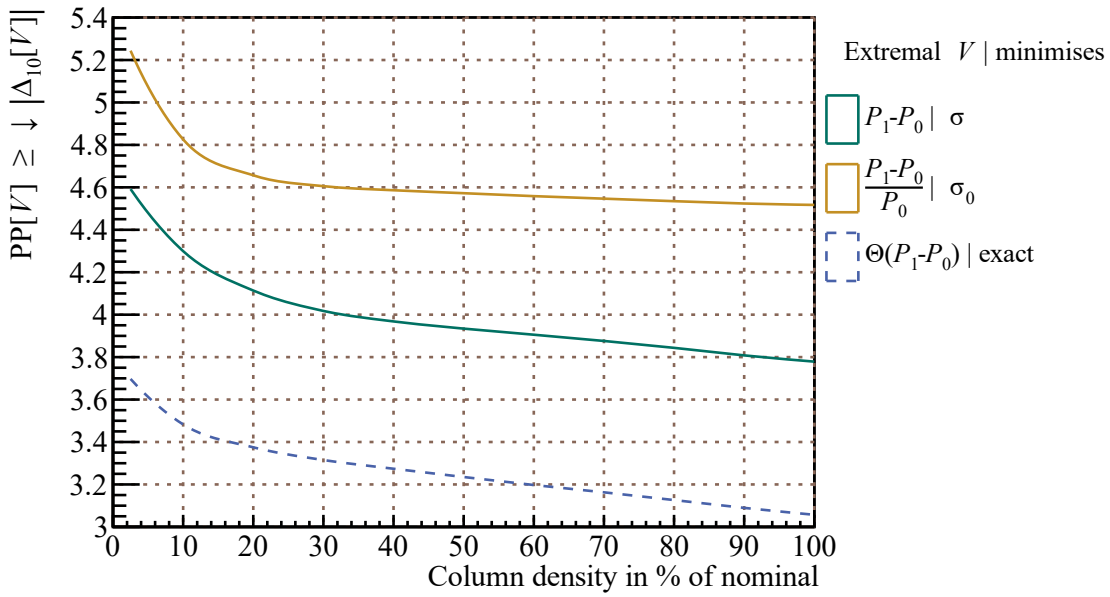

Figure 5.11.: Peak-to-peak value constraints: The measurement of Δ_{10} sets a lower limit to the peak-to-peak value of the potential. The exact solution is not differentiable. Approximate physical solutions are chosen to minimise σ_0 or σ (i.e. to be as constant as possible) for a given Δ_{10}. The values are given for krypton.

Peak-to-peak value: The peak-to-peak values of the shapes shown in figure 5.10 are also approximate constraints for general potentials

$$\mathrm{PP}[V] \gtrsim \frac{\mathrm{PP}\left[\frac{P_{\bar{x}}}{P_z}\right]}{\kappa_{\bar{x},z}} |\Delta_{\bar{x}}[V]| \,. \tag{5.14}$$

The constraints are shown in figure 5.11 for krypton $\Delta_{10}[V]$. As discussed in section 3.3.3 the exact solution is the potential $V \propto \Theta(P_1 - P_0)$, which is non-physical. However, all constraints are of the same order and it can be concluded that the peak-to-peak value of the potential in the central WGTS is at least ≈ 4 times larger than Δ_{10}.

Shape energy: The shape energy is visualised in figure 5.12. It increases with column density and is in the range of several 100 meV. Thus, the neutrino mass shift is not only determined by the standard deviation σ_0, but the shape energy needs to be considered: it is ≈ 550 meV for nominal column density, ≈ 150 meV in KNM1, ≈ 500 meV in KNM2 and ≈ 250 meV in KNM3a. Comparing to a standard deviation of $\sigma_0 \approx 50$ mV, this gives sizeable contributions even for a small antisymmetry of $|\hat{\rho}| = 0.1$. If a KNM2-like column density and the above potential estimates are assumed, the following shift of the squared neutrino mass is obtained:

$$\Delta m_\nu^2(\sigma_0 \approx 50\ \mathrm{mV}, \hat{\rho} \approx 0.1) \approx -2 \cdot 50\ (\underbrace{0.1 \cdot 500}_{\text{shape}} + \underbrace{50}_{\text{variance}})\ \mathrm{meV}^2 = -0.01\ \mathrm{eV}^2 \,. \tag{5.15}$$

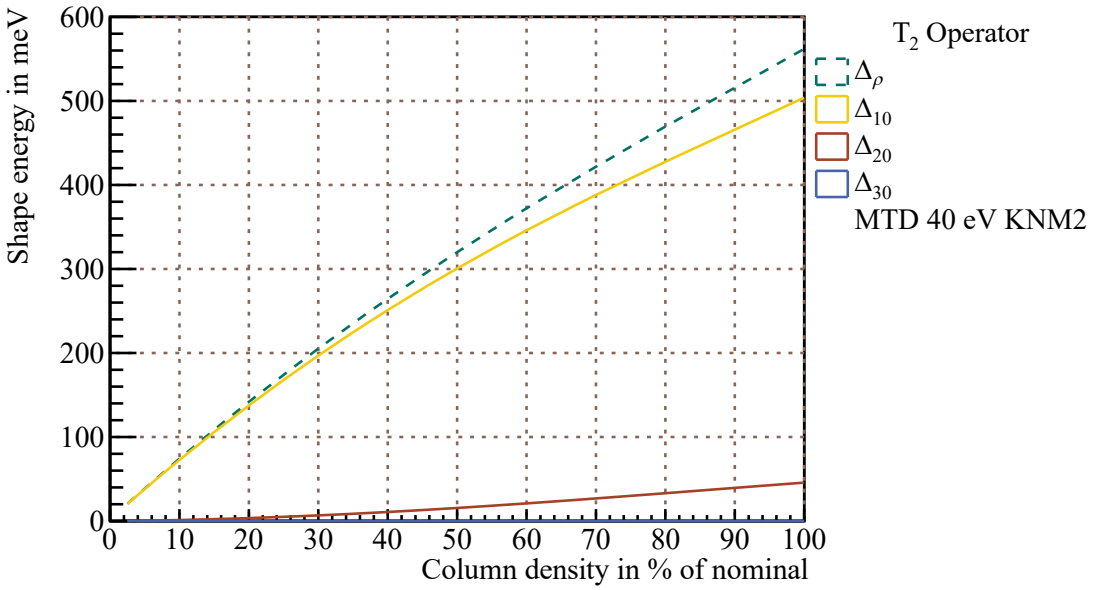

Figure 5.12.: Shape energy vs. column density: The shape energy ϵ_ρ causes a shift of the squared neutrino mass of $-2\sigma_0\epsilon_\rho\hat{\rho}$. Thus, the shape energy dominates compared to the usual variance term $-2\sigma_0^2$, if $\hat{\rho}\epsilon_\rho \gg \sigma_0$. For the expected range of $O(\sigma_0) = 50$ mV the contributions are of the same order already for potentials with small antisymmetry $O(\hat{\rho}) = 0.1$.

This shift is twice as large as the budget for energy scale systematics in the design report [KAT04b]. Notably, the antisymmetry is not necessarily small: the krypton plasma simulation shown in figure 1.19 has an antisymmetry of $\hat{\rho} = 0.88$, leading to a five times larger absolute value of the shift of the squared neutrino mass. Thus, the precise determination of both σ_0 and $\hat{\rho} \sim \Delta_\rho$ is necessary, since the obtained estimates can be used in the tritium model to correct for the systematic.

The connection of the shape energy term of the neutrino mass shift to the formulation using the total susceptibility is

$$\epsilon\Delta_\rho = 2\sigma_0\hat{\rho}\epsilon_\rho \ . \tag{5.16}$$

For given σ_0 and $\hat{\rho}$ this allows to calculate Δ_ρ directly from the shape energy. As obvious here, Δ_ρ depends on the susceptibility ϵ used to normalise it: If ϵ vanishes, Δ_ρ must be singular, since both sides of the equation must be finite. Notably, σ_0, $\hat{\rho}$ and ϵ_ρ do not depend on normalisations and are never singular, such that the right side is the more physical formulation. Moreover, the shape energy vanishes only for vanishing scattering. Since $\hat{\rho}$ can in practice not be implemented in simulations, still Δ_ρ needs to be used for actual systematic studies, as done in section 5.1.

Since the components of the shape energy are derived from covariances

$$\epsilon_{\rho,i} = \frac{1}{2}\epsilon_i\kappa_{\overline{i0},0} \ , \tag{5.17}$$

their summation follows the usual square rules

$$\epsilon_\rho^2 = \sum_i \epsilon_{\rho,i}^2 + 2\sum_{i<j} \epsilon_{\rho,i}\epsilon_{\rho,j}\rho_{\overline{i0}\ \overline{j0},0} \,. \tag{5.18}$$

$\rho_{\overline{i0}\ \overline{j0},0}$ are the weight correlations defined in section 3.2.2. Thus, the shape energy is smaller than the summation of the absolute values of its components:

$$\epsilon_\rho \leq \sum_i \left|\epsilon_{\rho,i}\right| \,. \tag{5.19}$$

The equality only holds for full correlation. Consequently, constraining $\hat{\rho}$ or Δ_ρ with estimates from the krypton measurement gives the best possible constraint on the neutrino mass shift. These constraints are obtained from weight correlations between krypton and tritium weights, which is discussed in the next section.

5.3. Scaling between Krypton and Tritium Plasma Moments

In this section it is quantified how the estimates $(\Delta_{10}[V], \sigma_0[V])^{\mathrm{Kr}}$ or $(\hat{\rho}, \sigma_0)^{\mathrm{Kr}}$ from krypton mode constrain $(\Delta_\rho[V], \sigma_0[V])^{\mathrm{T_2}}$ of the tritium spectrum and thus the neutrino mass shift. The indices for the gas species are omitted in the following. Tritium observables are always on the left side and krypton observables on the right side of the equations.

The total derivative of $\Delta_{\bar{x}}[V]$ and $\sigma_y^2[V]$ consists of a component which is related to the change of the weights and a component which is related to the change of the potential:

$$\mathrm{d}\Delta_{\bar{x}}[V] = \int_z \frac{\mathrm{d}z}{L_{\mathrm{WGTS}}} \Big[\underbrace{\mathrm{d}P_{\bar{x}}(z)V(z)}_{\text{weight uncertainty}} + \underbrace{P_{\bar{x}}(z)\mathrm{d}V(z)}_{\text{potential uncertainty}} \Big] , \tag{5.20}$$

$$\mathrm{d}\sigma_x^2[V] = \int_z \frac{\mathrm{d}z}{L_{\mathrm{WGTS}}} \Big[\underbrace{\mathrm{d}P_x(z)\,(V(z) - \langle V\rangle_x)^2}_{\text{weight uncertainty}} + 2\underbrace{P_x(z)\,(\mathrm{d}V(z) - \mathrm{d}\,\langle V\rangle_x)\,(V(z) - \langle V\rangle_x)}_{\text{potential uncertainty}} \Big] . \tag{5.21}$$

This section is only concerned with scaling uncertainties, arising from differences in weights. Uncertainties due to possible differences in the plasma potential have to be determined separately and are not the topic of this thesis.

Constraint of tritium $\Delta_{\bar{x}}$: The general equation for constraints of $\Delta_{\bar{x}}$ has been derived in section 3.3.1. For the specific case here it reads

$$\Delta_{\bar{x}}(\sigma_0, \hat{\rho} \sim \Delta_{10}) \overset{\mathrm{T_2}\leftrightarrow\mathrm{Kr}}{=} \Delta_{10} \underbrace{\frac{\kappa_{\bar{x},0}}{\kappa_{\overline{10},0}}\rho_{\bar{x}\overline{10},0}}_{\text{scaling factor}} \pm \underbrace{\sigma_0\kappa_{\bar{x},0}\sqrt{1-\rho^2_{\bar{x}\overline{10},0}}}_{\text{scaling uncertainty}} \sqrt{1-\hat{\rho}^2} \,. \tag{5.22}$$

Thus, the scaling factors are used to correct the measured Δ_{10} from krypton in the translation to tritium. The scaling uncertainties are used to calculate the additional uncertainty

on the resulting value. Weight standard deviations $\kappa_{\bar{x},0}$ and correlation $\rho_{\bar{x}\overline{10},0}$ are shown in figures A.19 and A.20 of appendix A.9 for different operating conditions and tritium operators. The weighting indicated with the index 0 always uses the krypton P_0. The resulting scaling factors and scaling uncertainties are shown in figures 5.13 and 5.14 as function of the column density of the tritium measurement.

The scaling factor of the relevant Δ_ρ is between 80 % and 100 %. Thus, estimates of tritium Δ_ρ have the tendency to be smaller than Δ_{10} in krypton. This follows from the fact that the standard deviation $\kappa_{\overline{10},0}$ in krypton is larger than $\kappa_{\rho,0}$ in tritium. The standard deviations quantify the variance of $P_1 - P_0$ in krypton or P_ρ in tritium, and due to the accumulation of the krypton at the ends of the WGTS, the krypton weights differ more strongly.

The scaling uncertainty of the relevant Δ_ρ is generally between 10 % and 30 % of σ_0. The main dependence is on the column density difference of the tritium and krypton modes. Thus, even at the same column density the scaling uncertainty is never below 10 % of σ_0. For the krypton plasma simulation shown in figure 1.19 the antisymmetry is $\hat{\rho} = 0.88$, giving $\sqrt{1-\hat{\rho}^2} = 0.47$. Thus, if the simulation is correct, the scaling uncertainty is only half as large. Notably, for $|\hat{\rho}| = 1$ the uncertainty vanishes, since the potential is exactly known.

Constraint of tritium σ_x^2: Constraints of variances $\sigma_x^2(\sigma_0^2, \hat{\rho}^2)$ for given krypton σ_0^2 and $\hat{\rho}^2$ cannot be formulated analytically. The numerical solution is found in appendix A.2. Only in the limits of $\hat{\rho} = 0$ and $\hat{\rho}^2 = 1$ analytical equations can be given. In the latter case the potential is exactly known and the ratio of σ_x and σ_0 is calculated from equation A.71 in the appendix. In the case of $\hat{\rho} = 0$, the following constraint was derived in section 3.3.2:

$$\sigma_x^2(\sigma_0^2) \overset{\mathrm{T_2 \leftrightarrow Kr}}{=} \sigma_0^2 \underbrace{+\sigma_0^2 \left(\mathrm{Max}\left[\frac{P_x(z)}{P_0(z)}\right] - 1 \right) - \sigma_0^2 \left(1 - \mathrm{Min}\left[\frac{P_x(z)}{P_0(z)}\right] \right)}_{\text{scaling uncertainty}} . \tag{5.23}$$

Thus, the scaling uncertainty is used to calculate the uncertainty on σ_0^2 in tritium, which is caused by the weight difference to the σ_0^2 in krypton. As discussed in the derivation, the maximum uncertainty assumes localised inhomogeneity at a specific z. If it can be assumed that the inhomogeneity is distributed over the whole WGTS length, this uncertainty vanishes. If it is known, that the inhomogeneity is concentrated in a specific region, only the extrema of the weight ratio in this region need to be considered.

The weight ratio $\frac{P_0^{\mathrm{T_2}}}{P_0^{\mathrm{Kr}}}$ is shown in figure 5.15 for different operating conditions. The resulting weight uncertainties are shown in figure 5.16.

The lower bounds are only relevant if the mean value of σ_0 is used in the tritium analysis. In the case where only upper limits are used, upper bounds are sufficient. They are generally between 110 % and 120 % of krypton σ_0, mainly depending on the column density difference of the tritium and krypton mode.

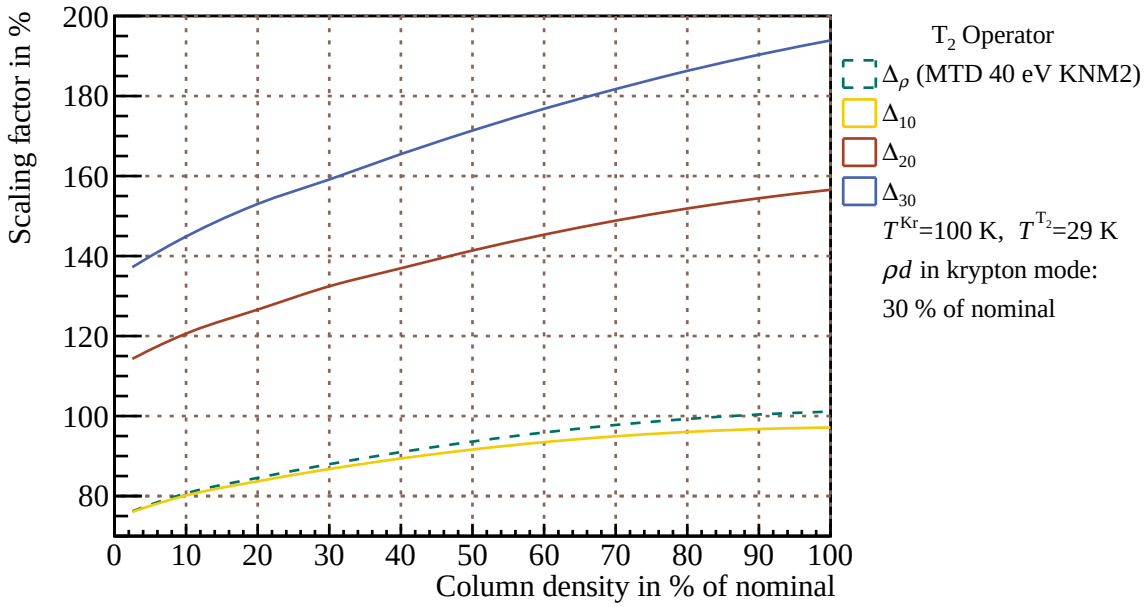

(a) KNM2 ρd = 30 % → 84 % like scaling

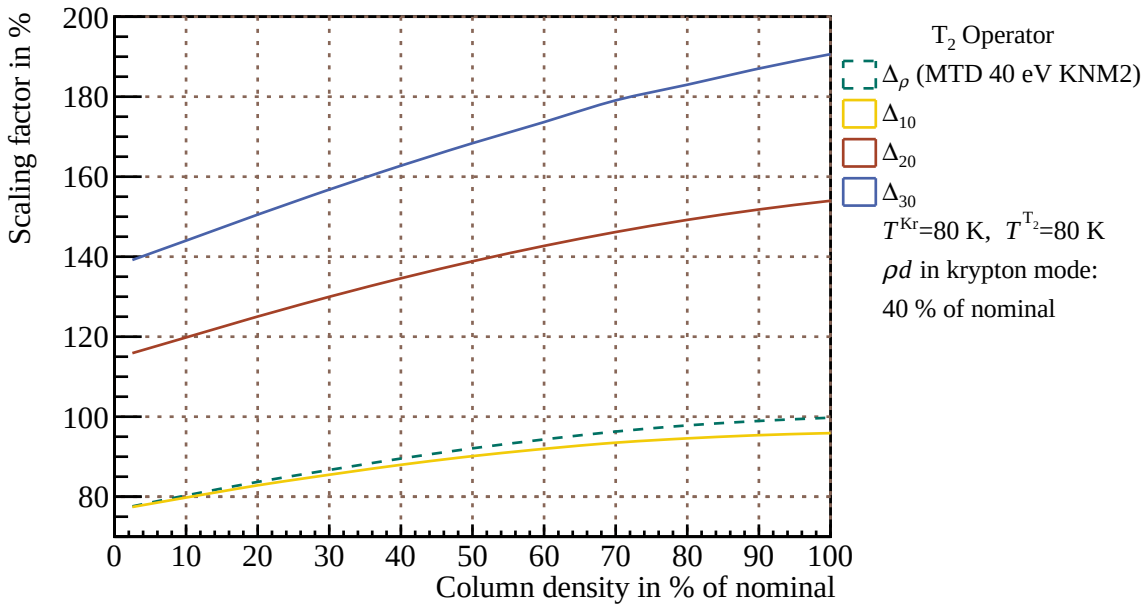

(b) KNM3 equal source mode like scaling

Figure 5.13.: Scaling factors, mean differences: In KNM2 (a) the column density of the tritium measurement was 84 % of nominal, resulting in a scaling factor of ≈ 100 % for Δ_ρ. In KNM3a (b) the column densities in both measurements were 40 % of nominal, resulting in a scaling factor of ≈ 90 % for Δ_ρ. Due to the demixing of the gas species, a measurement under the same conditions does not mean that no scaling is necessary.

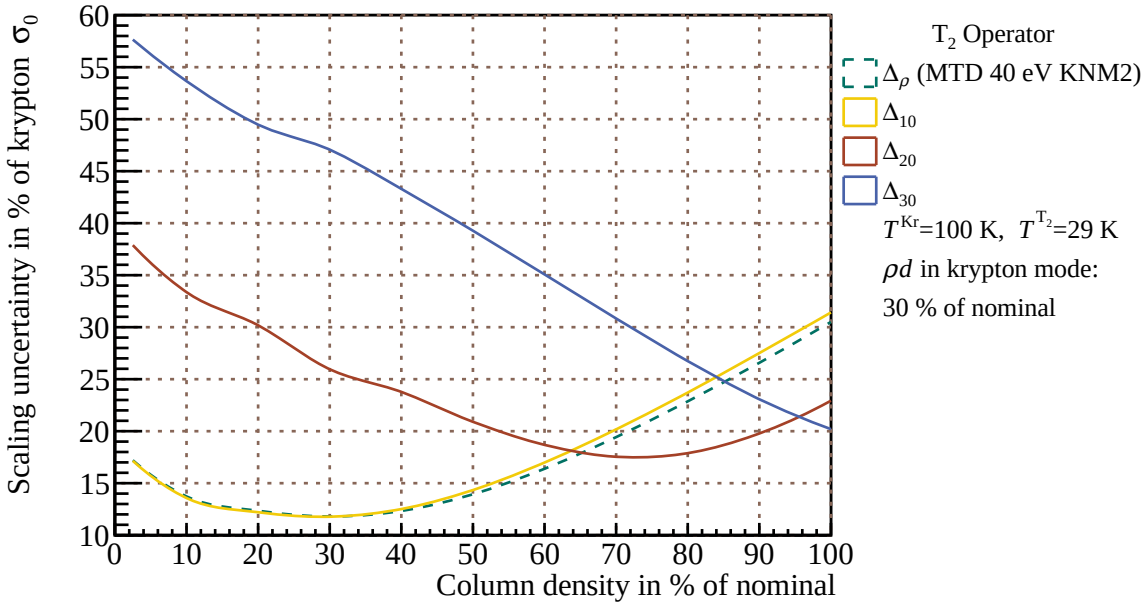

(a) KNM2 ρd = 30 % → 84 % like scaling

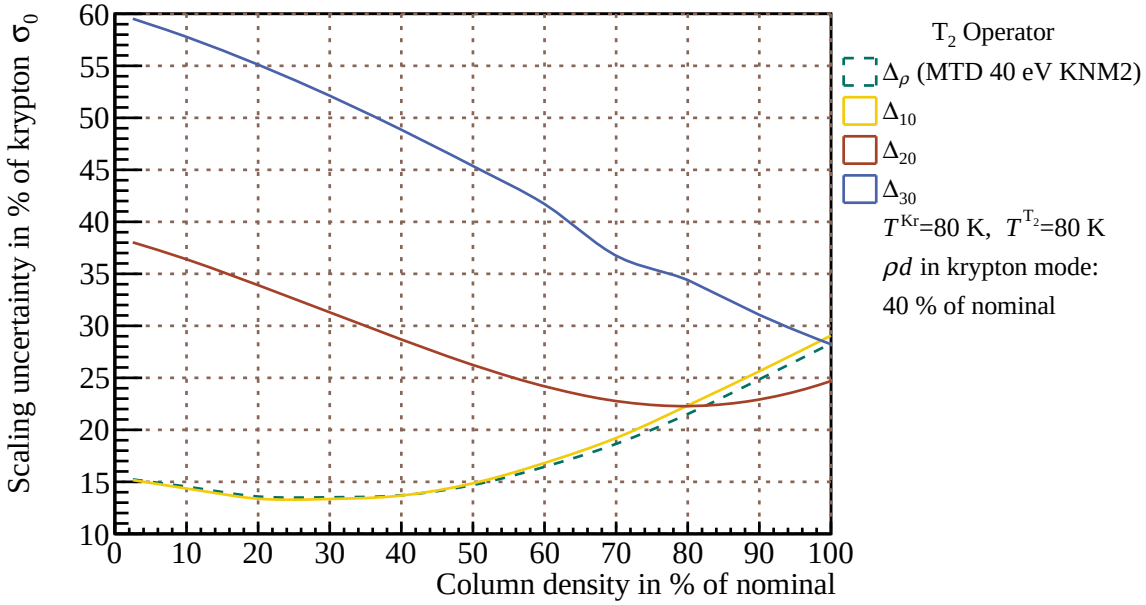

(b) KNM3 equal source mode like scaling

Figure 5.14.: Scaling uncertainties, mean differences: Differences in the krypton and tritium gas profiles contribute an uncertainty on the tritium plasma observables. For KNM2 (a) both column density and temperature of the krypton and tritium measurement were different, resulting in a scaling uncertainty of $\Delta_{\max}\left(\Delta_\rho\right) = 0.24\sigma_0$, mainly due to the different column densities. In KNM3 (b) both measurements were taken at the same conditions. Still, the uncertainty is $\Delta_{\max}\left(\Delta_\rho\right) = 0.13\sigma_0$, due to the demixing of the gas species.

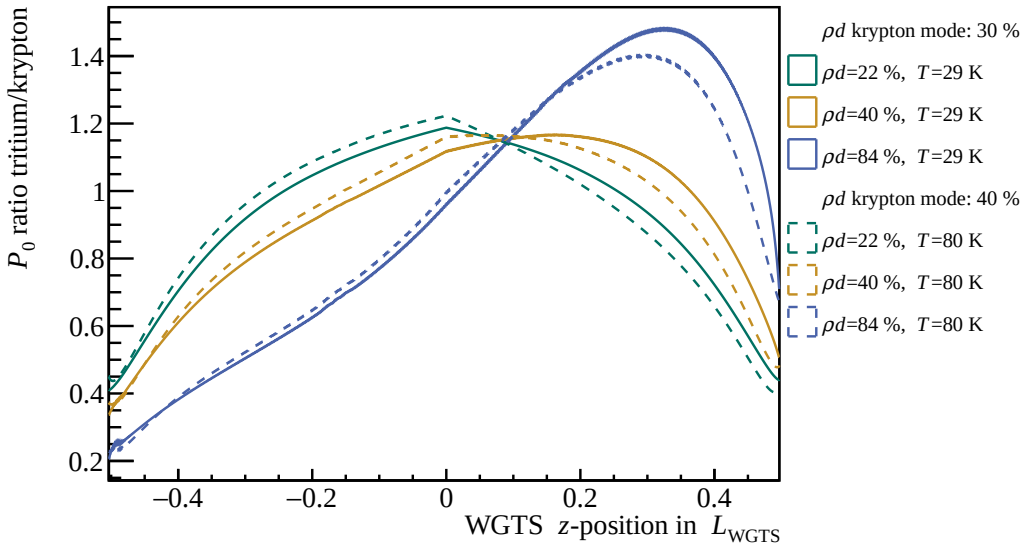

Figure 5.15.: Ratio of tritium to krypton zero weights: The extrema of the shown ratio of $P_0^{\mathrm{T_2}}$ and P_0^{Kr} constrain the ratio of tritium and krypton σ_0^2. Since krypton accumulates at the WGTS ends, the ratios are larger than one in the center and smaller than one at the ends for comparable tritium column density in the krypton and tritium measurement. For large column density extrapolation (blue) the maximum is shifted to the front.

Analysis methods: The best way of analysis depends on whether a usable estimate of Δ_{10} exists or not. There are two systematics which can prohibit the use of the measured value from krypton for neutrino mass analysis:

- Krypton systematics: The estimate of Δ_{10} can suffer from too large systematics of the krypton measurement. A main systematics driver at the moment is the uncertainty of the energy loss function for the energies used in the krypton measurement.
- Potential uncertainty: Significant changes of the shape of the potential between the operating modes can make the scaling impossible.

Currently both problems are relevant for the KNM2 analysis, and while the potential scaling was removed in KNM3a and KNM4 by choosing the same conditions of the measurements, still the systematic on Δ_{10} is present. Thus, at the moment the systematics are too large to use Δ_{10}. However, in the future this systematic will be removed by measuring the correct energy loss function. It follows:

- **Δ_{10} not available:** In this case the shape component of the neutrino mass shift is constrained directly by the shape energy, which assumes the worst possible potential shape. It can be either positive or negative, so only a symmetric constraint around zero can be constructed. For systematic studies the maximum $|\Delta_\rho|$ is needed and not the shape energy, which is obtained by equation 5.16 for $|\hat{\rho}| = 1$ or equivalently equation 5.13.

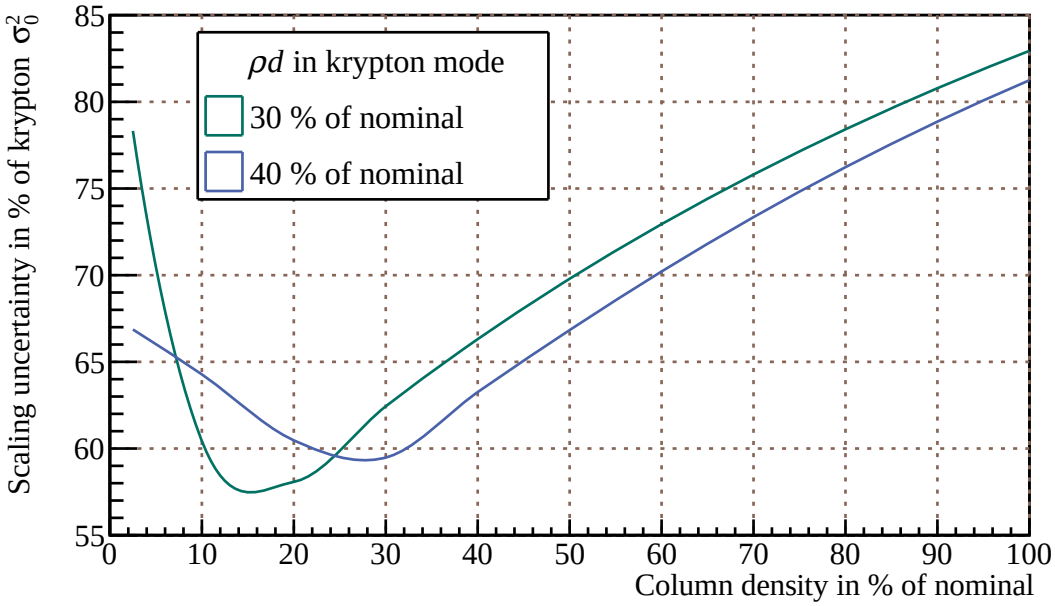

(a) Lower bound

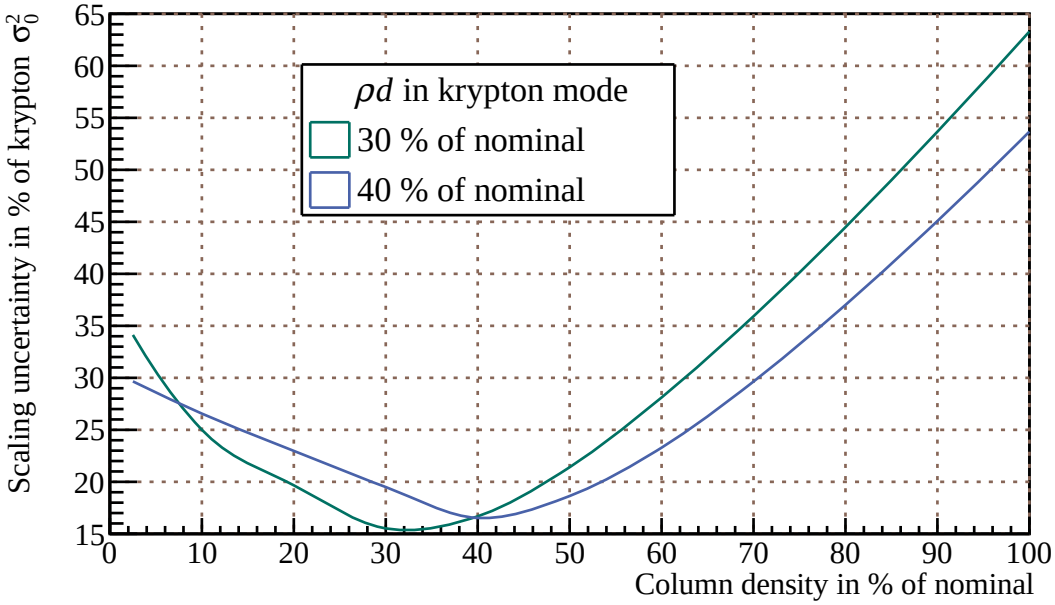

(b) Upper bound

Figure 5.16.: Scaling uncertainties, variances: The lower (a) and upper (b) bound are obtained by finding the minima and maxima of curves like the ones shown in figure 5.15 for different column densities in tritium mode. Since only the P_0 are relevant, this only depends on the column density difference of the measurements and not on the MTD. Prior to KNM4, the temperature limited the maximum column density in krypton mode to 30 % of nominal for 29 K and 40 % of nominal for 80 K and was chosen accordingly.

- **Usable Δ_{10}:** In this case the mean neutrino mass shift can be predicted and the uncertainty on the shift can be calculated as described. Depending on the size of the shift, the calculated Δ_ρ can be used in the tritium model to correct for the systematic shift.

In both cases the measurement of σ_0 in krypton and a reasonable potential scaling to tritium conditions is unavoidable. In general the potential scaling is correlated with the weight scaling. However, as long as σ_0 is not strongly dominated by localised inhomogeneities, it could be argued that small shape changes do not affect the estimate. This allows to treat it as a measure of potential magnitude only, and to decorrelate the two scalings. Which kind of inhomogeneity currently dominates the measurement data is not conclusively understood and can possibly only be determined in combination with plasma simulations. The neglect of the correlation and the quadratic addition of the uncertainties associated with the two scalings is conservative, so that the approach presented here is in any case useful for understanding the weight scaling.

In all cases uncertainties related to weight scaling are maximum uncertainties, i.e. the estimates stem from a uniform distribution bounded by the uncertainties. While it was shown that these distributions can in some cases also be approximated with Gaussians, uniform distributions were implemented by all groups performing the ongoing KNM2 analysis.

Scaling with the Lower Analysis Interval

The previous discussions were limited to the scaling of the plasma estimates with column density, which is relevant for the analyses performed so far in KNM1 and KNM2. However, in both cases the tritium spectrum was recorded over a larger energy interval than the one currently used for the spectrum fit. As visible in the analysis interval dependence of the susceptibilities in figure 5.5, increasing the interval reduces the overall sensitivity to scattering effects, such that using that data might be beneficial with regard to source potential systematics. Thus, in the following it is studied, how the analysis interval affects the predicted neutrino mass shift.

The analysis interval dependence cannot be studied using Δ_ρ, since it is singular for vanishing total susceptibility $\epsilon = 0$ [3]. Instead, the shape energy and the shift of the squared neutrino mass and its uncertainty are calculated directly. The latter two are obtained by multiplying equation 5.22 with $-\epsilon$, resulting in the shape energy term

$$\Delta m_\nu^2(\sigma_0, \hat{\rho} \sim \Delta_{10})\big|_{\sigma_0=0} \overset{\mathrm{T_2}\leftrightarrow\mathrm{Kr}}{=} \underbrace{-2\Delta_{10}\frac{r_\kappa \epsilon_\rho}{\kappa_{\overline{10},0}}\rho_{\rho\overline{10},0}}_{\text{prediction}} \pm \underbrace{2\sigma_0 r_\kappa \epsilon_\rho \sqrt{1-\rho^2_{\rho\overline{10},0}}\sqrt{1-\hat{\rho}^2}}_{\text{uncertainty}} . \tag{5.24}$$

Thus, the prediction is determined by the shape energy ϵ_ρ, the correlation $\rho_{\rho\overline{10},0}$ of P_ρ in tritium to $P_1 - P_0$ in krypton and the krypton weight standard deviation $\kappa_{\overline{10},0}$. The

[3] Thus, if future analyses use larger spectral fit intervals, the shift of $\Delta_{\bar{x}}$ cannot be modelled as simultaneous shift of all scattering moments, which is the current standard implementation. Instead it could be modelled by only shifting Δ_{20}, since ϵ_2 does not vanish.

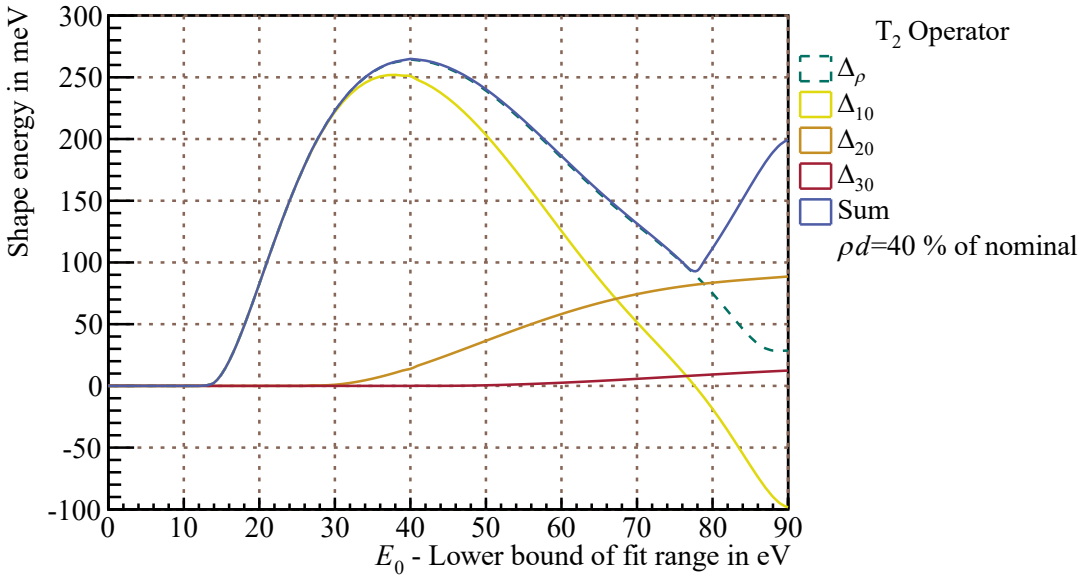

Figure 5.17.: Shape energy vs. lower analysis interval: For the 40 eV analysis interval, the penalty due to unknown potential shapes is maximal, while it is reduced by a factor of ≈ 5, when going to a 90 eV interval. Notably, in contrast to the total susceptibility the shape energy does never vanish, if scattering is present.

latter two are weighted with P_0 from krypton. $r_\kappa \approx 0.94$ is the ratio of $\kappa_{\rho,0}$ weighted with krypton P_0 divided by the value weighted with tritium P_0, shown in figure A.23 in the appendix. While r_κ also has a small contribution, the analysis interval dependence is mostly given by the shape energy ϵ_ρ and the correlation $\rho_{\rho\overline{10},0}$.

The shape energy, the predicted shift of the squared neutrino mass and the uncertainty on this prediction are shown in figures 5.17 and 5.18. There are no qualitative differences between the individual KNMx phases and only KNM3a is shown here. Equivalent investigations for KNM2 conditions are found in appendix A.9.

Discussion: As visible, the shape energy decreases strongly above the analysis interval of 40 eV to a minimum at 90 eV. Accordingly, also the predicted neutrino mass shift decreases strongly and vanishes for 90 eV. However, this is not related to a vanishing shape energy, but to a vanishing correlation of tritium and krypton operators, shown in figure 5.19. Thus, while the predicted mean for an analysis interval of 90 eV vanishes, the uncertainty of the prediction increases, indicating that lowest uncertainty is a trade-off between low shape energy and high correlation. With regard to plasma systematics, the minimum is the optimal interval for tritium measurements, if the krypton estimate of Δ_{10} is known. As long as it is not known, the interval of minimum shape energy should be used. However, such considerations also need to take into account other systematic effects which scale with the analysis interval and were not investigated here.

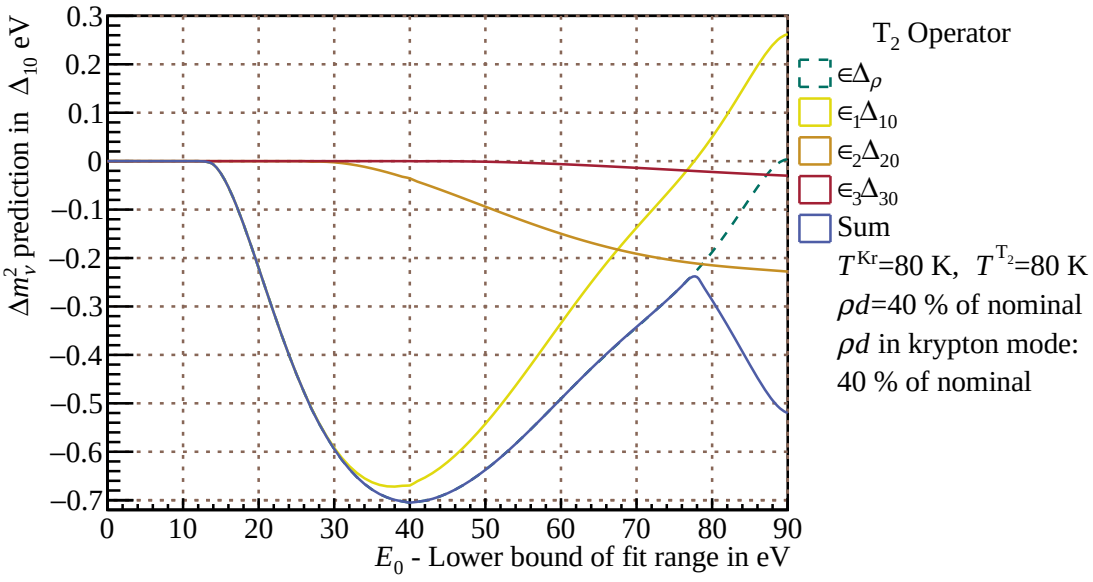

(a) Prediction

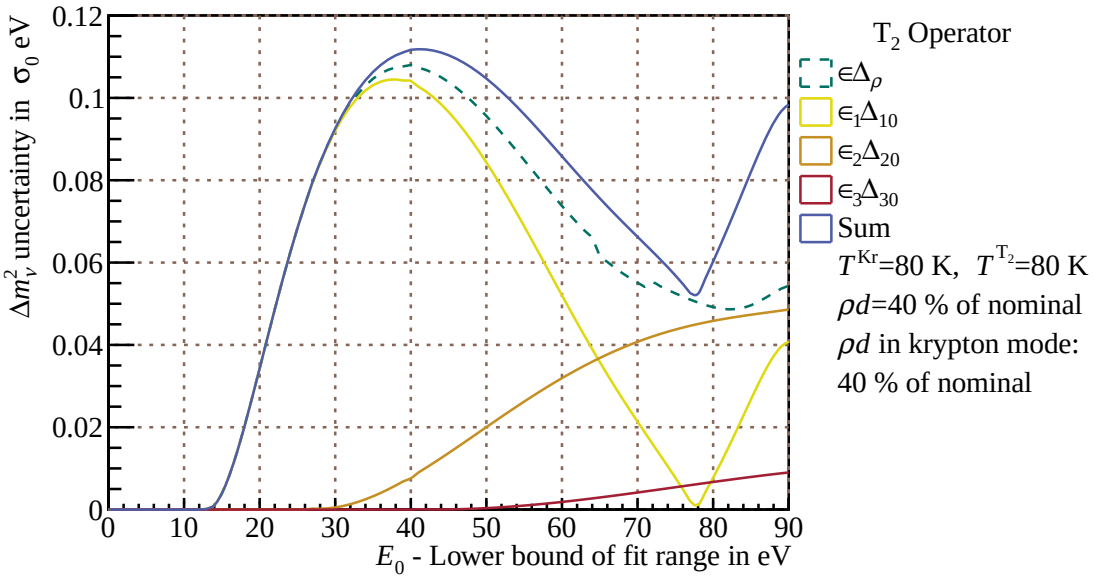

(b) Uncertainty

Figure 5.18.: Neutrino mass shift from mean difference vs. lower analysis interval: The mean value of the prediction of the shift of the squared neutrino mass (a) for given krypton Δ_{10} is closest to zero around 90 eV. This is not related to a vanishing shape energy, but to the vanishing correlation of tritium and krypton weights at this interval, which is visible in an increased uncertainty of the prediction (b). The minimum of the uncertainty in the range of 80 eV is a trade-off between small shape energy and high correlation of krypton to tritium operators. For smaller intervals the shape energy increases, for larger intervals the correlation decreases.

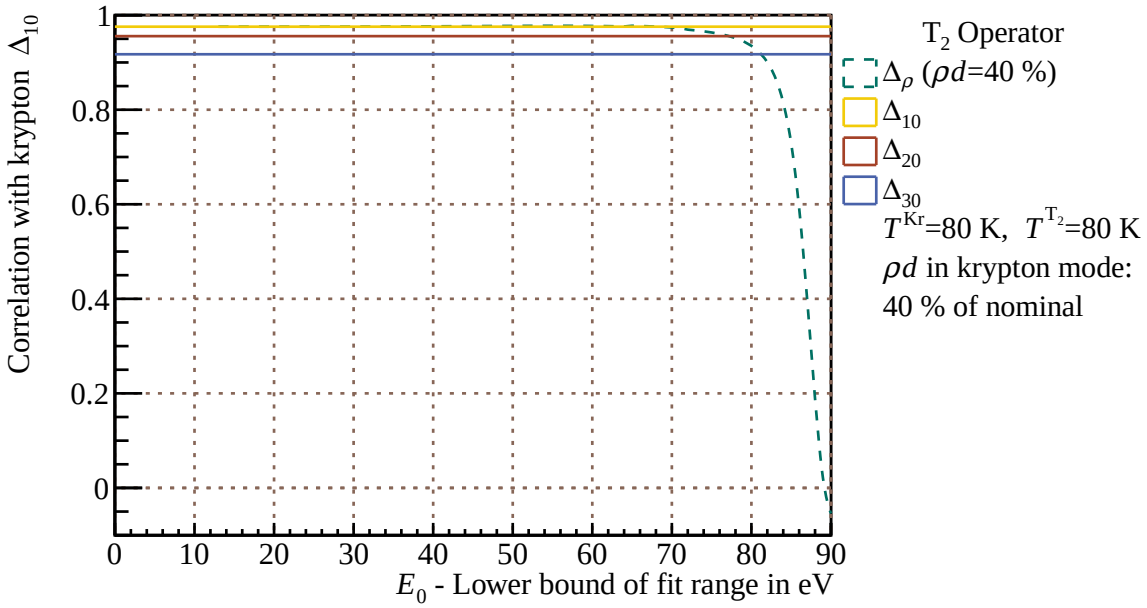

Figure 5.19.: Correlations of tritium and krypton weights vs. lower analysis interval: In general the measurement of the krypton Δ_{10} shows high correlations to the tritium $\Delta_{\bar{x}}$. At around 80 eV the tritium antisymmetry shape changes, as shown in figure 5.20, which leads to decreasing correlation.

The individual scattering contributions show the constraints for the actual $\Delta_{i0}[V]$ of the potential: As discussed in section 5.1, constraining $\Delta_\rho[V]$ assumes that all mean differences have the same value. Since this way only one quantity needs to be considered, the analysis is considerably simplified. As discussed in section 5.2, using $\Delta_\rho[V]$ or the total shape energy already includes all correlations and gives the best possible constraints. In contrast, if instead the $\Delta_{i0}[V]$ are constrained directly, their values are those of the actual potential, as predicted by the krypton-83m measurement. However, their correlations need to be considered, since the sum of the absolute values of the contributions shown in figures 5.17 and 5.18 overestimates the systematics. The only reason to still use the actual values of the potential $\Delta_{i0}[V]$ is correlations to non-plasma potential systematics, which can in principle lead to different results in both approaches. However, in the standard 40 eV interval the differences in the approaches are small.

The drastic change of the correlation (figure 5.19) also indicates a strong change of the antisymmmetry shape, which is shown in figure 5.20. In the range of 85 eV analysis interval the antisymmmetry shape no longer lives up to its name, as it acquires a significant symmetrical component. This explains the vanishing correlation of krypton $\Delta_{10}[V]$ and tritium $\Delta_\rho[V]$ for this interval. It should be recalled that the antisymmetry shape is the potential shape which produces the extremal neutrino mass shift shape term. Thus, if the potential shape is known, tuning the analysis interval accordingly allows to minimise the shape systematic. From this a hypothetical test experiment for the theory developed in this thesis can be constructed: As shown in section 6.3, the krypton-83m measurements prove

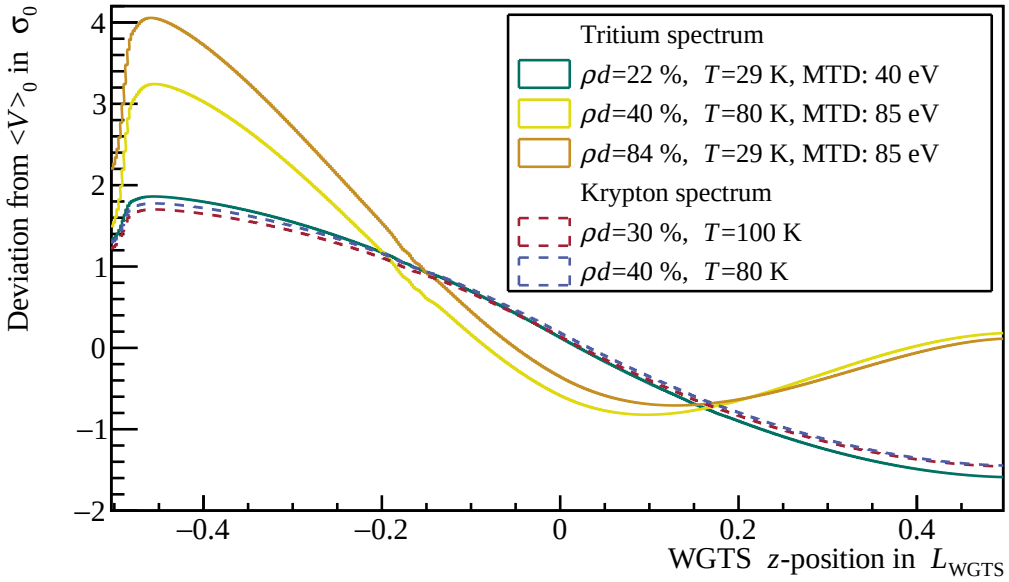

Figure 5.20.: Antisymmetry shapes vs. lower analysis interval: Increasing the analysis interval has a significant influence on the antisymmetry shape, since it adds contributions from Δ_{i0} of higher scattering multiplicity.

that applying a strong positive rear wall voltage U_{RW} leads to an antisymmetrical potential. This is the only known possibility to produce a potential which can be reasonably well determined directly by the experiment. Thus, it is the only configuration which allows to construct test cases for the theoretical description of plasma potential systematics. If tritium measurements are performed in this configuration, the absolute neutrino mass systematic is largest for an analysis interval of 40 eV and smaller for 90 eV. The use of $\sigma_0 \approx 500$ mV, which is motivated by the value measured at a rear-wall set point of $U_{\mathrm{RW}} = +5$ V in krypton-83m, leads to a shift of the squared neutrino mass of

$$\Delta m_\nu^2(\sigma_0 = 500\ \mathrm{mV}, \hat{\rho} \approx 1)^{40\ \mathrm{eV}} \approx -2 \cdot 500\ (1 \cdot 500 + \quad 500 \quad)\ \mathrm{meV}^2 = -1.0\ \mathrm{eV}^2\,, \tag{5.25}$$

$$\Delta m_\nu^2(\sigma_0 = 500\ \mathrm{mV}, \hat{\rho} \approx 0)^{90\ \mathrm{eV}} \approx -2 \cdot 500\ (\underbrace{0 \cdot 100}_{\text{shape}} + \underbrace{\quad 500 \quad}_{\text{variance}})\ \mathrm{meV}^2 = -0.5\ \mathrm{eV}^2\,. \tag{5.26}$$

A measurement at 84 % nominal column density like KNM2 was assumed and the corresponding shape energies were taken from figure A.22 in the appendix. Thus, while this effect is detectable by KATRIN, it would require several weeks of measurement time (comparable to the neutrino mass scans of KNM2) in this configuration, which is not realistic. If instead the endpoint was used for the same kind of analysis, the measurement time could likely be reduced to a few days only. Such considerations are relevant, since currently the plasma potential systematics dominates the KNM2 systematics budget and the precise understanding of experimental observables and theory is important. In addition, the dependence of the plasma potential systematics on the analysis interval is relevant for the measurements of more massive keV sterile neutrinos at KATRIN, which necessarily use larger intervals.

5.4. Conclusion

In this chapter the systematic effect of the plasma potential on the tritium neutrino mass measurement has been studied. This included the calculation of the susceptibilities to scattering effects and the relevant scattering weights and their correlations to their krypton counterparts.

Shape energies: As a result, the quantitative equation for the shift of the squared neutrino mass in dependence of the plasma observables was given:

$$\Delta m_\nu^2(\hat{\rho}, \sigma_0) = -2\sigma_0 (\underbrace{\hat{\rho}\epsilon_\rho}_{\text{shape}} + \underbrace{\sigma_0}_{\text{variance}}). \tag{5.27}$$

The neutrino mass shift is fully determined by the zero weighted standard deviation $\sigma_0[V]$ and the antisymmetry $\hat{\rho}[V]$ of the potential V. All experimental conditions are condensed into the shape energy ϵ_ρ, which is approximately 500 meV for the example of the KNM2 measurement. It mainly depends on the column density and the analysis interval of the spectral fit. Both dependences were studied in detail: while ϵ_ρ increases monotonously (approximately linearly) with the column density, the analysis interval dependence shows a minimum at around 90 eV. Thus, neglecting other systematic influences, adjusting the interval of analysis accordingly reduces the shape energy by a factor of five.

Related to the antisymmetry $\hat{\rho}$ is the mean difference $\Delta_\rho[V]$, where

$$\hat{\rho}[V] = 1.3 \frac{\Delta_\rho[V]}{\sigma_0[V]} \tag{5.28}$$

holds for KNM2 tritium conditions. Although $\hat{\rho}[V]$ fully specifies the shape term, $\Delta_\rho[V]$ is needed to implement the systematics in the tritium model by shifting all scattered spectra compared to the unscattered spectrum by its value.

Weight scaling from the krypton to the tritium measurement: All estimates of the plasma potential depend on the measurement conditions, since they are weighted with the longitudinal distribution of the signal electrons. The resulting necessary translation of the plasma potential estimates $(\hat{\rho}[V] \sim \Delta_{10}[V], \sigma_0[V])^{\mathrm{Kr}}$ determined in krypton-83m measurements to tritium estimates $(\hat{\rho}[V] \sim \Delta_\rho[V], \sigma_0[V])^{\mathrm{T_2}}$ was investigated in detail. Changes of the potential for different experimental conditions are expected, but were not quantified, and their impact on the scaling of the potential moments was neglected. In a conservative approach, which neglects the correlation of these two scalings, the resulting uncertainties of the potential moments can be added in quadrature.

It was shown that the translation $\Delta_{10}[V] \rightarrow \Delta_\rho[V]$ has an uncertainty of at least 10 % of $\sigma_0[V]$, even if both measurements are performed at the exact same conditions. This is related to differences in the gas profiles of krypton and tritium. For differences in the column density of the measurements, the uncertainty increases accordingly. Apart from the uncertainty, the mean value of $\Delta_{10}[V]$ also needs to be scaled in the translation,

where the factors range from 0.8 (same conditions) to 1 (KNM2 like scaling). Here, the differences in the gas profiles mean that the krypton values are smaller, even under exactly the same conditions, which is compensated when the column density is higher in the tritium measurement.

The scaling of $\sigma_0[V]$ depends on the inhomogeneity localisation. If nothing about its localisation is known and the tritium column density in the tritium and krypton measurement is the same, the upper bound of the tritium $\sigma_0[V]$ is given by ≈ 1.15 times the value measured in krypton-83m.

Weight standard deviations and correlations: All factors printed in this conclusion are related to standard deviations $\kappa_{\bar{x},z}$ or correlations $\rho_{\bar{x}\bar{y},z}$ of the involved weights. Here, they are rounded and given for KNM2-like conditions. Apart from these conditions they also depend on the parameters they constrain. The following rules for the indices simplify the understanding:

- For all constraints a standard deviation σ_z needs to be measured; its weight gives the index after the comma.
- The weights before the comma are given by the involved $\Delta_{\bar{x}}$; weight correlations $\rho_{\rho\overline{10},0}$ appear if krypton constrains tritium. Standard deviations $\kappa_{\bar{x},z}$ appear, if a $\Delta_{\bar{x}}$ is constrained by a σ_z.

For example, the factor in equation 5.28 is given by an inverse standard deviation $\kappa^{-1}_{\bar{x},z}$. In the printed case, both Δ_ρ and σ_0 are the tritium quantities and the factor is $\kappa^{-1}_{\rho,0} \approx 1.3$. For the relation of krypton Δ_{10} and σ_0 in KNM2 conditions the factor is $\kappa^{-1}_{\overline{10},0} \approx 1.5$, but here weighted with krypton P_0. If the tritium Δ_ρ should be constrained from the krypton σ_0, the factor is $\kappa^{-1}_{\rho,0} \approx 1.35$, also weighted with krypton P_0.

If the parameters are used in the tritium model to compensate for the plasma potential systematics, such details are relevant. Thus, while the developed theory needs many indices to specify the respective weightings, all are necessary for the variety of different use cases.

In a final step, the plasma observables are obtained in a krypton measurement and the resulting neutrino mass systematic is calculated. This is the topic of the next chapter.

Outlook: The weight profiles, antisymmetry shapes and scaling results depend on the validity of the gas model. Parameters like boundary conditions, viscosity or temperature profile can have few-percent effects. While these changes are unproblematic for the KNM1-3 measurements, for full KATRIN the gas model needs to be validated by measurement, which is currently in preparation. Also, influences of small quantities of gas residing in other parts than the central WGTS (for example in the differential pumping section) might be considered.

6. Krypton-83m Measurements in KNM1 and KNM2

In this chapter the systematics related to inhomogeneities of the plasma potential V in the KNM1 and KNM2 tritium measurement are discussed. All methodology necessary to describe the systematic shifts due to potential inhomogeneities has been derived in the previous chapters. It has been shown that they can be constrained by the potential moments $(\Delta_{10}[V], \sigma_0[V])$, which are obtained in krypton-83m measurements. The data analysis leading to those estimates in the KNM1 and KNM2 measurement campaigns is described in the following.

In section 6.1 methodology and data analysis of the KNM1 and KNM2 krypton measurements are described. For the determination of the broadening $\sigma_0[V]$ a precise estimate of the intrinsic Lorentzian line width is needed. Section 6.2 discusses available values for the L_3 line along with the value obtained from the KNM1 krypton only measurement.

In section 6.3, the results of the krypton plus tritium measurements are shown. It is also shown how the operator constraints derived in the previous chapters can be applied to krypton measurements to find physically allowed regions of $(\Delta_{10}[V], \sigma_0[V])$. Finally, in section 6.4 the obtained plasma estimates are scaled to tritium conditions and the expected systematics are calculated.

6.1. Methodology and Data Analysis

The KNM1 and KNM2 krypton campaigns were conduced after corresponding tritium campaigns to access the systematics resulting from plasma inhomogeneities in the WGTS. Both campaigns used approximately 30 % of the nominal column density of molecular tritium with an admixture of mesomeric krypton. The tritium column density was the maximum possible in ^{83m}Kr mode of the source. In both campaigns the rear wall voltage was varied in an interval between −5 and +5 volts to access different plasma regimes. In KNM1 also a krypton-83m only measurement was conducted to determine the intrinsic line parameters of the L_3-32 transition. While the KNM1 krypton campaign was the first campaign to use a krypton tritium mixture, it was not the first krypton campaign at KATRIN:

- **July 17:** The first ever gaseous source measurement at KATRIN was the krypton-83m measurement from July 2017. Besides the focus on the properties of the krypton-83m conversion electron spectrum, including also the measurement of the line parameters

of the L_3-32 transition [Sle+19], the energy scale linearity and the influence of different analysing plane magnetic fields were studied [Sei19].

- **STS3a:** The July 2017 krypton measurements were followed by the STS3a krypton measurements in October 2018, which for the first time used a mixture of krypton and a hydrogen isotopologue, here non-active molecular deuterium. This allowed to show that scattered electrons form a distinct step in the recorded L_3-32 spectra. Furthermore it could be proven that this step can indeed be shifted by a source potential. By applying ultra-violet radiation to the rear wall, electrons were created, which allowed to create a plasma without the usual charge creation by β electrons. The plasma could be influenced by different rear wall voltages, thereby producing the eloss shift, as predicted in this work. Furthermore, in STS3a yet another measurement of the intrinsic line parameters of the L_3-32 transition was performed. It was also observed that the functioning of deuterium as a carrier gas leads to a rate of the 32 keV transition of around 0.5 Mcps, which is a factor of $\propto 10$ increase compared to the krypton only measurement. These rates are also typical for the KNM1-3 measurements.

Already the STS3a measurement campaign employed basically the same model to fit electron energy spectra from krypton plus hydrogen mixtures or pure krypton spectra, as the later KNM1&2 measurements. Also, it showed many of the challenges which gaseous krypton measurements at KATRIN need to overcome. The model, the systematics and analysis strategies to mitigate them are described in the following sections.

6.1.1. Krypton Model and Observables

As described in section 1.3.2 the modelling of the integrated krypton rates consists of a gas model and a model of the differential spectrum. For the two use cases of reference measurements with pure krypton and mixtures of carrier gas and krypton, the model needs slight adjustments.

Krypton reference measurements: Here a constant spatial krypton distribution in the WGTS is assumed, which is expected for the low pressure regime without carrier gas. The spectral modelling usually consists of two Lorentzian lines for L_3 and L_3^{S3}, which are characterised by their individual width Γ, position ΔE and intensity I. In addition a constant background Bg is fitted, leading to seven free parameters. The relative position and relative intensity of the shake line were constrained with literature values from [Sei19]. Otherwise the fits showed difficulties, presumably due to a too small analysis interval. The uncertainties of the constraints on relative position and intensity were doubled compared to the literature, to avoid too strong bias.

Krypton plasma measurements: The fit of the plasma measurement uses the relative shake line intensity and position and both Lorentzians of L_3 and L_3^{S3} as fixed input. Additionally a Gaussian with variance σ_g^2 is convolved with the spectrum, leading to the Voigt profile described in section 1.3.2. Also, the gas model now needs to include the distribution of the

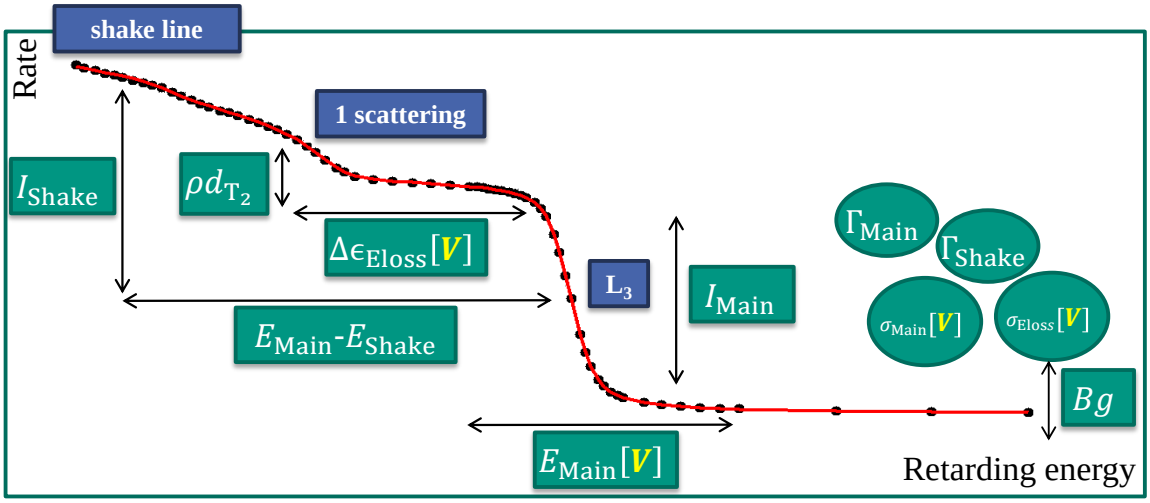

Figure 6.1.: Krypton fit: Shown are the parameters characterising the integrated krypton spectrum in the usually fit region. The shake parameters were fixed in the plasma measurements, while the scattered electrons and their parameters do not appear in reference measurements. $\sigma_{\mathrm{Main}} = \sigma_{\mathrm{Eloss}} \equiv \sigma_{\mathrm{g}}$ has been assumed in all fits, which is justified as shown in chapter 5. The scheme does not include a parameter for the background slope, which was not fitted in KNM2. Still, it needs to be considered as discussed below.

carrier gas and krypton in the source, which are calculated as described in section 1.3.2. Since the column density of the carrier gas is usually not well enough known, it is fitted from the ratio of the scattered and unscattered $\mathrm{L_3}$ lines. Here the scattering cross section $\sigma_{\mathrm{inel}} = 2.435 \cdot 10^{-22}\ \mathrm{m}^2$ [Lev19] for 30.4 keV electrons is used. The fit result of the column density also depends on the gas model and slicing, as discussed in appendix A.4. Lastly, the energy loss shift $\Delta\epsilon_{\mathrm{Eloss}}$ of the energy loss function figure 1.10 is fitted. This fit suffers from two systematic effects: Firstly, the correct energy loss function for 30.4 keV electrons and $T = 100$ K is not known, and secondly the transmission function change by scattering [Gro15] (in the following called *detailed transmission*) could not be used, since it increases the calculation time by several orders of magnitude. The influence of these systematics is discussed in section 6.3.1. In total the six parameters $(Bg, \rho d, \Delta\epsilon_{\mathrm{Eloss}}, \sigma_{\mathrm{g}}^2, \Delta E_{\mathrm{main}}, I)$ are fitted.

In both cases the magnetic and electric fields in the analysing plane are taken from FPD pixel dependent simulations, adjusted for the corresponding field settings. These simulations use particle tracking and the measured position of the hardware components [Hac17] to determine the mapping of the flux tube in the source to the point of energy spectroscopy in the analysing plane [Def17]. Thus, the field values are affected by uncertainties of those measurements and simulations, which is apparent by the misalignment discussed below. The modelling of the krypton-83m spectrum also includes energy losses due to synchrotron radiation and an additional broadening due to the Doppler effect, which is calculated for the respective temperatures.

Figure 6.1 shows an overview over all parameters.

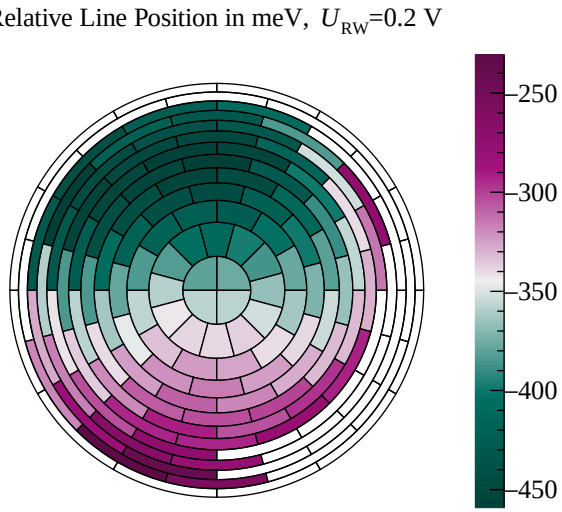

Figure 6.2.: Line position pixel map: As visible, the line positions are not uniformly distributed over the detector, but show about 200 meV differences in a dipole like structure. The shown rear wall voltage shows the smallest radial variance. The values are relative to the mean line position of the KNM1 reference measurement.

Calculation of uncertainties: The fits were always performed using ROOT::*Minuit* and *Minos* statistical uncertainty estimation [Ant+09]. In some cases the latter did not work and only the *Minuit* uncertainty was available, which usually is underestimated. In these cases the average *Minos* uncertainty from the working fits was used. The uncertainty does not strongly depend on the individual fit, since all fits have roughly the same statistics. No systematic uncertainties were included in the fits, but the influence of certain parameters or analyses were tested separately, as found in appendix A.4. Nevertheless, due to the drifts and radial effects discussed below, the distributions of the observables can still show overdispersion compared to the statistical uncertainty. This systematic uncertainty on the average usually dominates the total uncertainty. It was calculated by quadratic subtraction of the expected statistical width from the total width of the distributions. When necessary, Gaussian uncertainty propagation was used, as described in appendix A.5.

6.1.2. Alignment and Pixel-Wise Analysis

Figure 6.2 shows that the measured line positions are not equally distributed over the whole detector, but show an azimuthal dipole pattern, which is thought to have two possible origins:

- **Misalignment:** Radial or azimuthal misalignment of the flux tube through analysing plane and detector causes an offset of the parabolic minimum of the simulated spectrometer potential with the actual measurement. This would lead to the observed dipole structure and was already studied on krypton July 17 data, where usually a few

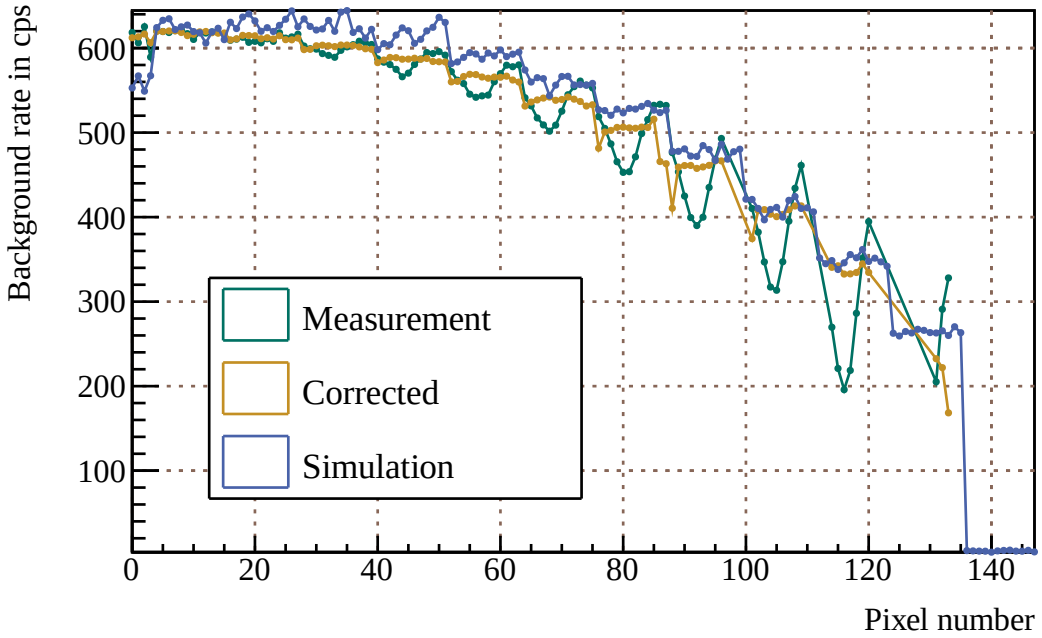

Figure 6.3.: Background fit and simulation: The shown background fit is from a run at $U_{\mathrm{RW}} = 200$ mV, however it does not strongly dependent on the voltage, as shown in [Ost20]. The correction was applied as described in [Ost20] and in the text. The simulation was carried out using particle tracking [Wei20]. As seen, the overall agreement is quite good. Thus, the non-adiabatic transmission of the krypton background can be predicted and the method can be used to determine the magnetic field alignment in the respective field setting. The simulation was scaled to fit the first ring of the measurement.

millimetres shift of the flux with regard to the ≈ 10 cm diameter detector [Ams+15] was found. However, the misalignment does not only depend on the positions of the magnets and detector, but also on the magnetic field setting. This is why any correction needs to be valid for the conditions of the respective measurement campaign. Furthermore, for a radially inhomogeneous plasma potential the effect could also be caused by a misalignment of rear wall and detector, leading to the danger of correcting actual plasma effects.

- **Azimuthal plasma potential:** A purely physical cause are azimuthal dependencies of the plasma potential. A priori those are not distinguishable from misalignment effects, when only considering the line position.

To disentangle both effects, a method has been developed in cooperation with Raphael Ostertag in [Ost20], which determines alignment not from the energy scale, but the background rate. Thus, while the former assumes a radially and azimuthally homogeneous energy scale of the source, which cannot be generally expected, this method assumes a radially and azimuthally homogeneous source strength, which is expected from simulation. The background rate in krypton reveals misalignment of the analysing plane magnetic

Table 6.1.: **List of excluded pixels.**
The listed pixels were excluded from the analysis of the respective campaigns to avoid shadowing and detector effects. They differ only in the pixels 99 and 113. The former was shadowed by the Forward Beam Monitor FBM [Ell19] in KNM1, which was moved to a new monitoring position in KNM2. The latter was excluded in KNM2, since it showed a small rate reduction due to shadowing. This was possibly caused by the slightly modified magnetic field setting compared to KNM1.

KNM1	97, 98, 99, 100, 110, 111, 112, 121, 122, 123, 124, 125, 126, 127, 128, 129, 130, 134, 135, 136, 137, 138, 139, 140, 141, 142, 143, 144, 145, 146, 147
KNM2	97, 98, 100, 110, 111, 112, 113, 121, 122, 123, 124, 125, 126, 127, 128, 129, 130, 134, 135, 136, 137, 138, 139, 140, 141, 142, 143, 144, 145, 146, 147

field and the detector due to the following reasoning: For measurements at L_3-32 the background is caused by electrons of the higher lines, which have on the order of 1500 eV surplus energy compared to the spectrometer potential. Energy loss, drift and storage effects of these electrons due to non-adiabatic transport increases with the radius of their trajectory in the spectrometer. This leads to a loss of background rate towards larger radii, visible in figure 6.3 along with a comparison to particle tracking simulations. Misalignments of the magnetic flux of analysing plane and detector lead to the observed wave pattern, since different pixels in a pixel ring observe a different radius of the analysing plane. From that the misalignment can be deduced, as shown in [Ost20]. In general the values are different to those found on the line position, indicating at least two different effects. Distinguishing those is the topic of ongoing studies on KNM3 data. Also, more simulation and measurement efforts using the electron gun are planned to overcome the issue. However, so far no satisfactory correction is available and in order to minimise systematic effects, all analyses are performed pixel by pixel. Thus, the pixel-wise fits of observable O are averaged using the uncertainty $\sigma(O)$ weighted average

$$\bar{O} = \frac{\sum \frac{O_i}{\sigma^2(O_i)}}{\sum \frac{1}{\sigma^2(O_i)}}, \quad \sigma^2(\bar{O}) = \frac{1}{\sum \frac{1}{\sigma^2(O_i)}}, \tag{6.1}$$

where the sum goes over the included pixels. Averages of Γ and σ_g were calculated on the squared values, since they are Gaussian distributed, as shown in appendix A.6.

Pixel exclusions: Due to collisions of the flux tube in the transport section some of the outer pixels show significantly reduced luminosity. These pixels were excluded from the analysis. A second criterion was the minimisation of detector effects like strongly deviating energy resolution. The list of excluded pixels is found in table 6.1. In both campaigns 117 out of the 148 pixels were used.

Pixel combinations: Usually the pixels are grouped to *rings*, giving 12 rings (labelled 1-12) with 12 pixels each and the bullseye with 4 pixels (labelled 0). To further reduce statistical

uncertainties and to produce clearer plots, the rings are often grouped to four *pseudo rings* or *combined rings*, consisting of three adjacent rings each, starting from the bullseye. By this grouping ring 12 is left over, however it is completely excluded anyway.

6.1.3. Transmission Properties and Background Slope

As discussed, the background at the L_3-32 line is created by electrons from higher energetic lines. Figure 6.4 shows the respective normalised rate contributions and their derivatives. The color coding indicates whether the lines are above or below L_3-32 line. As visible, the main background contributions stem from higher energetic M lines. However, as visible in the derivatives, their contribution is constant in the relevant analysis range. The background from the lower energetic L_2-32 and L_3^{S3} lines, however, creates a contribution that is not constant in the analysis interval. This leads to a systematic if a constant background model is assumed. The line for σ_g indicates when the additional broadening due to an unaccounted background slope exceeds 20 meV. Positive slopes produce negative broadenings and vice versa. Consequently, for contributions from L_2-32 and L_3^{S3} the additional broadening is positive, since slopes from lower energetic lines are negative. All other observables are also significantly affected by a slope. From these plots it follows that the L_2-32 and L_3^{S3} lines need to be included in the model.

Non-adiabaticity: However, the previous discussion assumes that the non-adiabaticity of the M electrons with $\approx$ 1500 eV surplus energy does not affect the rate contribution in the analysis interval. As it was shown in KNM3 krypton measurements this is not the case, since an orders of magnitude higher background slope was found than predicted here [Böt20; Gup20]. It was also shown in particle tracking simulations that this can indeed stem from non-adiabatic effects of the M lines. Thus, while still at least the L_3^{S3} line should be included in the model to avoid an additional curvature of the background, a background slope needs to be considered as well. In KNM3 it was measured by increasing the analysis interval to $\approx$ 150 eV above the L_3 line. It was shown that the slope correlates with the magnetic field setting and that it is stable, if the setting is fixed. Thus, the slopes measured in KNM3 were used in the present KNM1 and KNM2 analysis, which did not have the increased analysis interval to fit it. The L_2-32 line was included in none of the models, such that its contribution is absorbed in the fitted slopes. Since the slope increases to outer radii, including it removes radial structures in all observables. This was also observed in KNM3 and is expected from simulation. Still, it is believed that the transmission properties of high surplus energy electrons are not understood to a level where the effect becomes negligible.

6.1.4. Time Dependencies of Rate and Energy

All observables suffer from time dependencies, which are caused either by drifting rates or drifts of the energy scale.

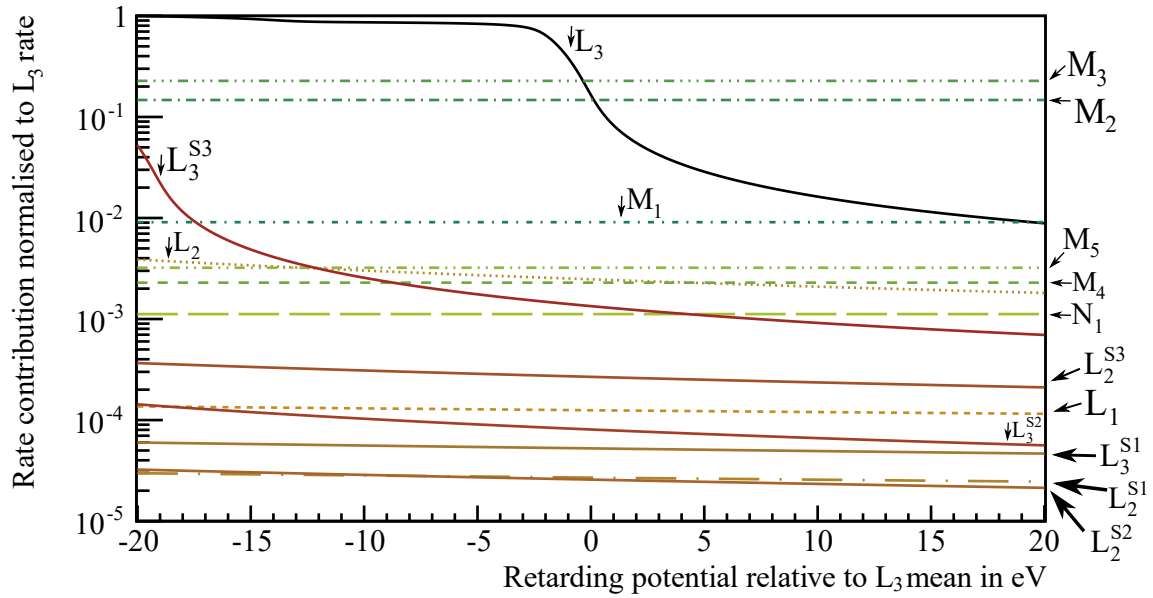

(a) Rate

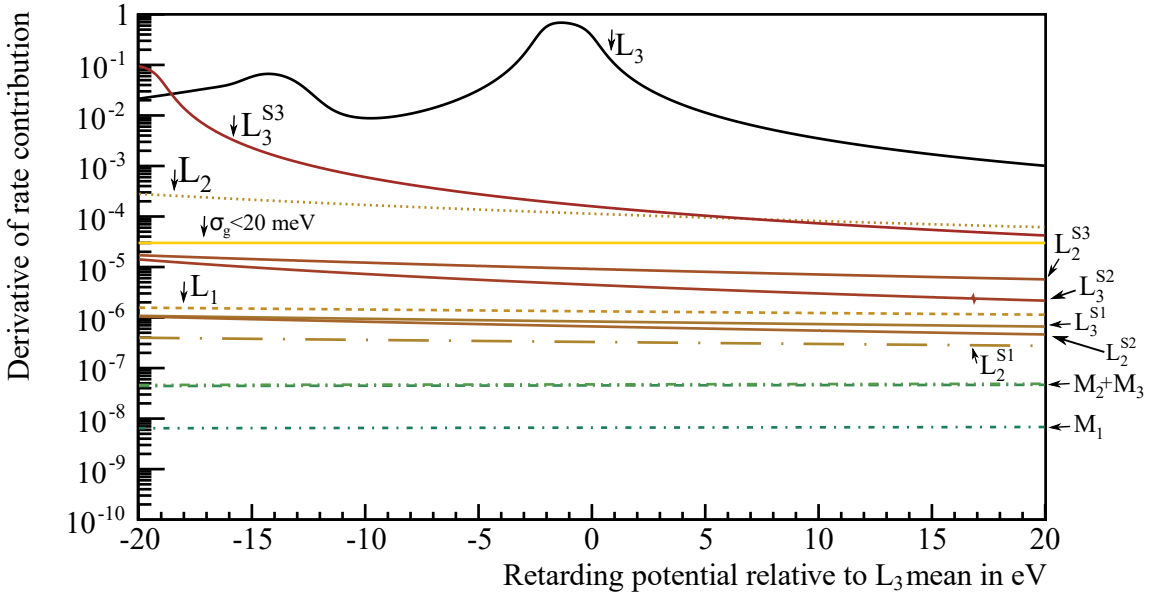

(b) Derivative

Figure 6.4.: Background contributions: Green colors indicate that the line is above L_3, red colors indicate that it is below. As visible in the normalised rate the constant background component is dominated by the higher energetic M lines. In contrast, the background slope is dominated by lower energetic L_2 and L_3^{S3} lines. However, this assumes adiabatic transport of the higher energetic electrons, which is not the case.

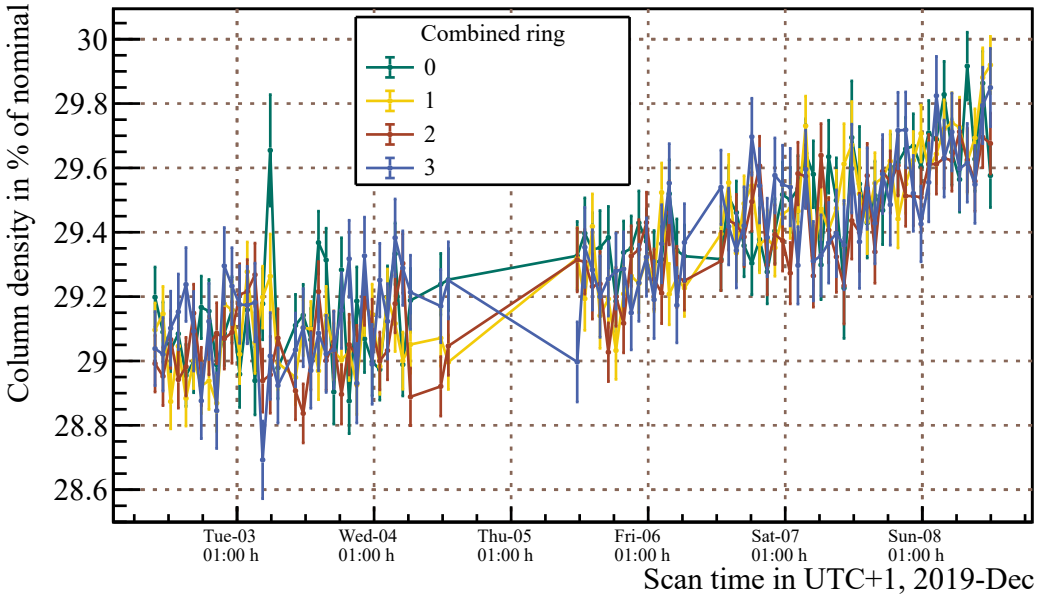

Figure 6.5.: Column density in KNM2: As visible, in the 6 days of KNM2 measurement the fitted tritium column density increased by about 1 %. Only if the background slope is included, like in this plot, no radial structure is observed as expected.

Rate drift in reference measurements: A strongly increasing rate of $0.7\frac{\text{kcps}}{\text{h}}$, corresponding to $\approx 1\,\%$ per scan, is observed in the KNM1 krypton only measurement, and a comparable number is found also in the STS3a reference measurement. It has been shown in [Mar20] that this is related to accumulating dirt (mainly air and hydrocarbons), which is outgassing from the pumps and acts as a carrier gas. Since the gas composition prior to KNM4 could not be cleaned in $^{83\text{m}}$Kr mode this dirt accumulates over time, thus increasing the krypton rate. In KNM3 part of the problem was solved by letting the dirt accumulate a few days before injecting krypton. For the KNM2 reference measurements the data from the initial measurement days was excluded when upwards and downwards scans showed significant differences in the observables.

Rate drift in plasma measurements: A small rate decrease can also be observed in the krypton plus tritium measurements. It has been shown in [Ost20] that its half-life time (79.92 ± 0.40) d is largely explained by the decay of the krypton-83m producing rubidium with a half-life time of 86.2 d. As apparent from the numbers, a small extra reduction has to exist to explain the still significant difference.

Column density drift: As visible in figure 6.5, in the plasma measurements also the tritium column density shows a drift, since it can only roughly be stabilised in $^{83\text{m}}$Kr mode. For KNM2 this drift was on the order of 1 % of nominal over the six measurement days. This drift contributes to the change of the krypton rate, due to the tritium acting as carrier

gas. However, the different time dependencies of rubidium decay, column density drift and other, unknown processes are hard to disentangle. The drifting column density also contributes to a change of the plasma and surface properties, which are discussed below.

All rate drifts in the plasma measurements are small enough that no significant difference of up and down scans is produced in the observables for the usual run times of $\propto 40$ min. Thus, no rate correction was applied.

Absolute energy scale drifts: Energy scale drifts can appear due to drifts of the spectrometer or the source potential. Many different measures are applied to access the stability of both potentials:

- **Spectrometer:** The different components of the spectrometer potential are calibrated via different methods, including the krypton-83m nuclear standard of the monitor spectrometer and Josephson normals [Res19]. In total it is concluded that a possible drift is smaller than 1 ppm over half a year, which is negligible for KNM2 krypton.
- **Rear wall current** [Fri20]**:** The rear wall can be used comparable to a Langmuir probe [Che03]. Thus, the IU-curve of rear wall or DPS dipole current I vs. rear wall voltage U is measured, and characteristic points are studied. An established method to access the stability of the energy scale is to study the zero crossing of the total WGTS current over time. It is given by the sum of the rear wall and DPS current. In the case where they do not compensate a third loss channel has to exist, which most likely are radial currents to the beam tube walls. They are not measurable with the current hardware. A homogeneous plasma potential both in radial and longitudinal direction is expected to result in minimum radial currents and thus a vanishing total WGTS current.
- **PRO-KATRIN** [Fri20]**:** In *Plasma Rear Wall Optimisation* the tritium rate is measured at a fixed retarding energy several hundred eV below the endpoint. Rate changes can be converted to energy scale changes using the slope of the tritium spectrum. This allows to perform fast scans of the energy scale for different rear wall voltages without the necessity to perform a full spectrum measurement. This method is also usually used to find the optimum rear wall voltage set point for the tritium measurement by demanding the minimum measured radial energy slope. PRO-KATRIN has the benefit that it can be performed in the same conditions as the tritium measurement.
- **Krypton:** In krypton measurements energy scale drifts are directly visible in the measured line position.

Figure 6.6 shows the line positions of KNM2 over the rear wall voltage. Both in PRO-KATRIN and krypton measurements also characteristics of these spectra like the rear wall voltage of minimal radial inhomogeneity or the start of good coupling can be studied. While the average krypton line position in KNM2 shows a change of approximately $-23\ \frac{\mathrm{meV}}{\mathrm{d}}$ [Ost20] if it is fitted linearly over the whole measurement campaign, the spectral measures like the start of good coupling are much more stable. Also, as shown in [Ost20], there

Table 6.2.: **Line parameters of L_3-32.**
Results without citation are unpublished from own analyses (STS3a and KNM1) or internal documents (KNM3). The listed systematics apply to the widths, however all the positions from KATRIN also include shifts due to the unknown mean *Beam Tube Work Function* (BTWF) or substrate work function in case of the *Condensed Krypton Source* (CKrS).

Source	Width Γ in eV	Position in eV	assumed unaccounted systematics
Literature [Vén+18]	1.19(24)	30472.2(5)	unknown
July 17 [Sei19]	$1.163^{+0.015}_{-0.016}$	30472.642(5)	uniform analysis, *Bg* slope, BTWF
STS3a	≈ 1.15	≈ 30472.68	unstable rate, *Bg* slope, BTWF
KNM1	1.062 ± 0.019	30472.200 ± 0.001	*Bg* slope, BTWF
KNM1 $N_{2,3}$ [Ost20]	1.011 ± 0.028	–	unknown
CKrS [Ful20]	1.0606(21)(150)	30473.7336(9)(880)	unknown
KNM3	≈ 1.06	≈ 30472.04	BTWF

are several drift regimes of the line position and an overall increase of the energy loss shift in the coupling region. The different drift regimes are separated by other calibration measurements, which presumably change surface properties of the WGTS or rear wall. Thus, it cannot be distinguished whether the drifts are caused by the changing column density, or the calibration measurements, or by shifting surface properties without any external change. The drift of surface properties can be caused by the absorption of particles, such that every time the system is changed, drifts may occur until they saturate. Notably, also in the tritium measurement, where the column density is much more stable, sometimes endpoint drifts can be seen. Thus, a final conclusion on cause and size of a possible energy scale drift could not be drawn.

It should also be mentioned that the change of the energy loss shift only appears in the coupling region. The rear wall voltage of +5 V measured at the beginning and the end of the campaign gives the same value, both for σ_0 and Δ_{10}. In contrast, the line position shows a difference of 100 meV. Thus, the strong external electric field at this large rear wall voltage leads to a reproducible potential shape in the WGTS.

6.2. Krypton-83m Spectrum Observables from Reference Measurements

In the following the krypton reference measurements are studied. They are used to obtain the intrinsic line parameters, most importantly the Lorentzian line width. A precise estimate is needed since the plasma inhomogeneity, observed as broadening of the line, is measured compared to the intrinsic width.

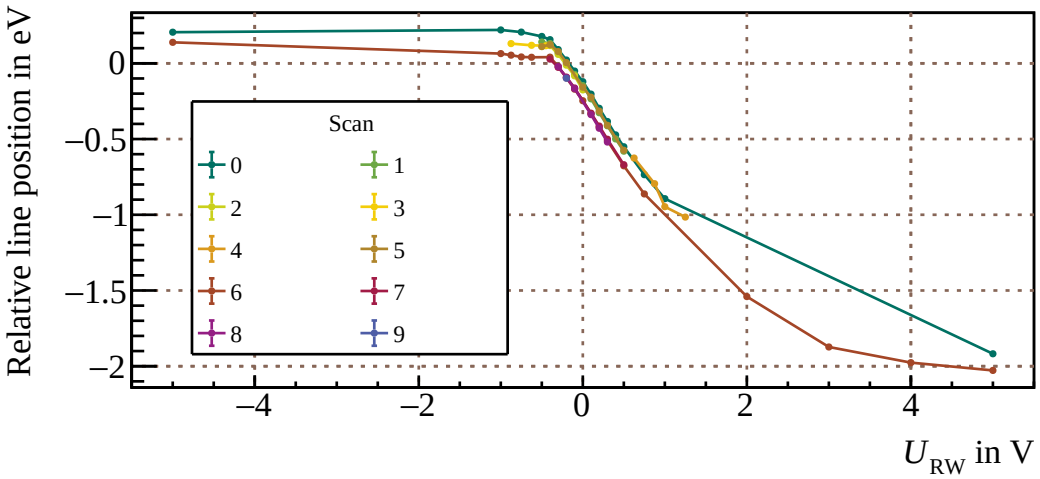

(a) KNM2 scans, uniform

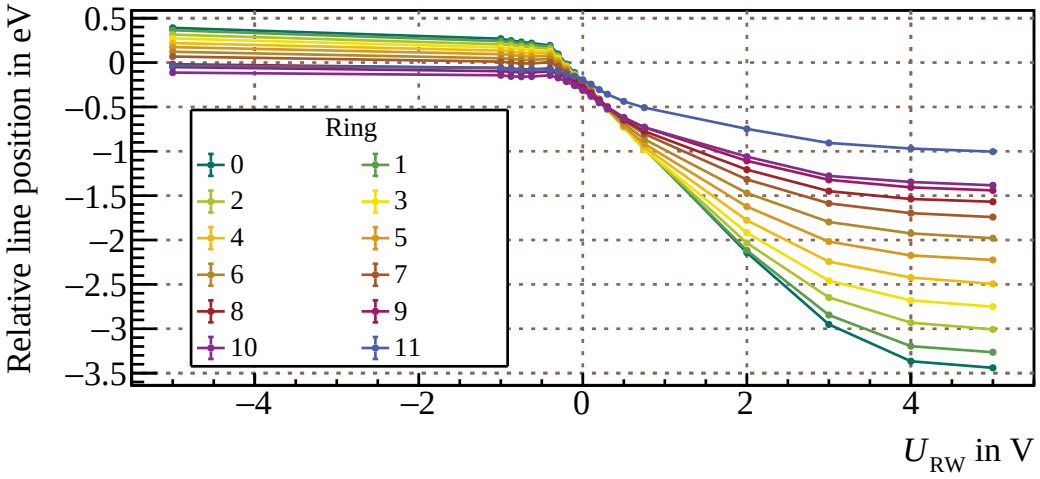

(b) Scan 6, ring wise

Figure 6.6.: Line positions in KNM2: A linearly coupled region from approximately −0.5 V to +1 V is surrounded by less coupled regions. More negative voltages only lead to small changes of all observables, while for more positive voltages increased inhomogeneity is observed in (σ_0, Δ_{10}). The different scans (a) show an overall drift of the line position compared to each other. The rear wall voltage of minimal inhomogeneity is visible in (b) as the line crossing, and a detailed analysis in [Ost20] shows that it is relatively stable over the runs at $U_{\mathrm{RW}} \approx 160$ meV. The values are relative to the KNM1 reference measurement position of 30472.2 eV. Statistical uncertainties are included, but not visible on this scale.

Measurements of the intrinsic line parameters from KATRIN have up to now been taken in July17, STS3a, KNM1 and KNM3. Table 6.2 lists the measured values of the L_3 line width and position and the assumed systematics on the width. Changes of absolute line positions or intensities are expected due to different source conditions. While the L_3 line position from the KNM1 reference measurement is used as a reference value for the KNM2 plasma measurement, it should not be understood as the intrinsic line position. Also, shifts compared to it are composed of work function and plasma changes. As discussed above, the work function of the source depends on the history of gas exposure, such that it may vary from campaign to campaign.

However, as visible, also the line width Γ shows significant decrease over the measurement campaigns, which must be caused by systematics unaccounted. The KNM1 L_3 width, determined with the $N_{2,3}$ method, and the *Condensed Krypton Source* (CKrS, see section 1.1 and [Ful20]) value both apply a correction in the analysis. The $N_{2,3}$ method uses the vanishing intrinsic width of the $N_{2,3}$ doublet: additional Gaussian systematics σ_g^2 are extracted from the doublet fit and included into the fit of the L_3 line. Some of the ongoing KNM3 analyses use the same procedure, but without reproducing the small value of KNM1 $N_{2,3}$. Despite this value, the latest KATRIN results of KNM1, CKrS and KNM3 are all in agreement, but disagree with previous results. However, they are affected by different systematics, which is apparent from the following example of the KNM1 analysis.

The Lorentzian width measured in KNM1 is shown in figure 6.7. The line width shows a significant radial dependence. It is known that the, here neglected, background slope makes the inner values larger, which suggests that the true value from this measurement is of the order of 10 meV smaller. However, in this case it is not in agreement with the values recorded from CKrS or in KNM3, which do not suffer from these particular systematics. On the other hand, the CKrS value is the only value which does not suffer from possible inhomogeneities of the work function of the beam tube, since it is not measured using the extended gaseous source, but a point source.

Thus, while the KNM3, CKrS and KNM1 measurements hint to a true Lorentzian with a width of roughly 1.06 eV, the remaining differences are not understood. The problem is obvious in some of the plasma measurements, since in some of the measurements a significant portion of the obtained Gaussian variances is negative, hinting to a too large Lorentzian. If the Lorentzian used in the fits of the plasma measurements is larger than the actual line width this is compensated by a negative Gaussian variance. Nevertheless, for the plasma fits shown in section 6.3, the CKrS value was used since it has the least known systematics, while being in reasonable agreement with the other values.

The connection between Gaussian and Lorentzian can be quantified. In the following it is shown that for the purpose of plasma systematics determination from the L_3 line, obtaining a meV precise result of the Lorentzian is necessary.

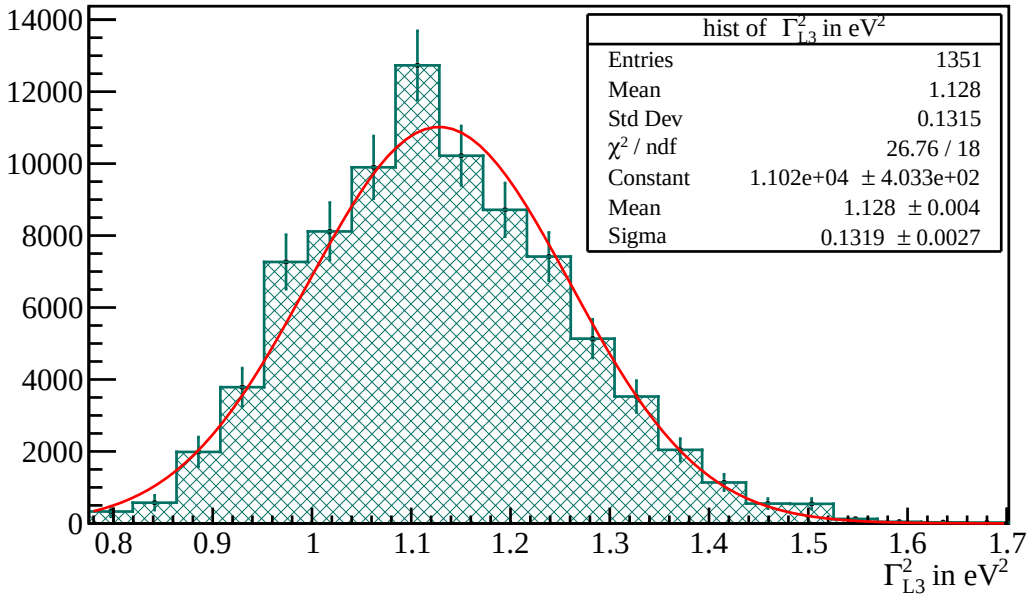

(a) Histogram

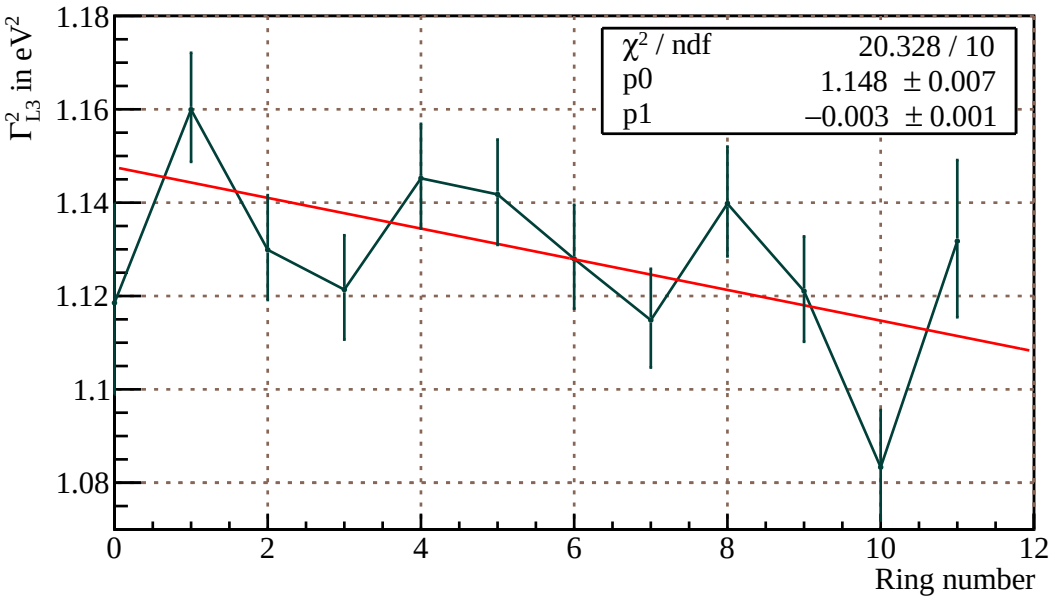

(b) Ring dependence

Figure 6.7.: KNM1 reference measurement of the L_3 line width: The histogram shows all included KNM1 krypton reference runs. The uncertainty of the mean is quoted as statistical uncertainty. However, the histogram shows some overdispersion due to radial systematics, as visible in (b). Subtracting the statistical width from the total width in quadrature gives $\sigma_{\mathrm{syst}}(\Gamma^2) = 0.04\ \mathrm{eV}^2$.

6.2.1. Connection between Gaussian and Lorentzian Distribution

The *full width of half maximum* f_{Voigt} of the Voigt profile for given Lorentzian Γ and Gaussian σ is [OL02]

$$f_{\text{Voigt}} = 0.5346\Gamma + \sqrt{0.2166\Gamma^2 + 8\ln(2)\sigma^2}\,. \tag{6.2}$$

From that it can be deduced how uncertainties of Γ translate to σ or vice versa, if the total width f_{Voigt} does not change:

$$\begin{aligned}
f_{\text{Voigt}} &= a\Gamma + \sqrt{b\Gamma^2 + 8\ln(2)\sigma^2}\,, \\
\Rightarrow (f_{\text{Voigt}} - a\Gamma)^2 &= f_{\text{Voigt}}^2 - 2a\Gamma f_{\text{Voigt}} + a^2\Gamma^2 = b\Gamma^2 + 8\ln(2)\sigma^2\,, \\
\overset{\mathrm{d}f_{\text{Voigt}}=0}{\Rightarrow} \quad -2a\mathrm{d}\Gamma f_{\text{Voigt}} + a^2\mathrm{d}\Gamma^2 &= b\mathrm{d}\Gamma^2 + 8\ln(2)\mathrm{d}\sigma^2\,, \\
\Leftrightarrow \mathrm{d}\sigma^2 &= \frac{1}{8\ln(2)}\left[-2a\mathrm{d}\Gamma f_{\text{Voigt}} + 2\Gamma\mathrm{d}\Gamma(a^2 - b)\right]\,, \\
&= (-0.1928 f_{\text{Voigt}} + 0.025\Gamma)\mathrm{d}\Gamma\,.
\end{aligned}$$

In the KATRIN use case at L_3 line $\sigma \ll \Gamma$ holds, leading to $f_{\text{Voigt}} \approx \Gamma$, and thus

$$\mathrm{d}\sigma^2 = -0.168\Gamma\mathrm{d}\Gamma\,, \tag{6.3}$$

$$= -0.084\mathrm{d}\Gamma^2\,. \tag{6.4}$$

For $\sigma \approx 0$ and $\Gamma = 1.0606$ eV this gives

$$\frac{\mathrm{d}\sigma}{\text{meV}} \approx -13.35\sqrt{\frac{\mathrm{d}\Gamma}{\text{meV}}}\,. \tag{6.5}$$

Thus, for an aimed sensitivity on σ below 20 meV, a trueness on Γ of 3 meV is necessary.

This only holds for $\mathrm{d}f_{\text{Voigt}} = 0$. In the fit, parameters like the measurement time distribution and line shape distortions by systematics or potentials affect the true relation. Thus, these equations should only be understood as rough estimates giving the magnitude. Foremost they show that there is no one-to-one connection, but that small changes in the Lorentzian lead to large changes in the Gaussian. The best approach is to fit the data sets for different Lorentzians, which takes lots of computation time. For the requirements of this work the approximation is sufficient.

If equation 6.2 is solved for σ^2, it can be treated as a function of $\Gamma_{\text{corr}} = \Gamma + \Delta\Gamma^{\text{ref}}$ with the previously calculated, fixed f_{Voigt} and a shift $\Delta\Gamma^{\text{ref}}$

$$\sigma^2(\Gamma_{\text{corr}}) = \frac{(f_{\text{Voigt}} - 0.5346\Gamma_{\text{corr}})^2 - 0.2166\Gamma_{\text{corr}}^2}{8\ln(2)}\,. \tag{6.6}$$

This allows to determine the necessary $\Delta\Gamma^{\text{ref}}$ for conditions on σ, for example for $\sigma \overset{!}{\geq} 0$. Also, it allows the propagation of the measured uncertainty of Γ to σ.

6.3. Plasma Observables from Plasma Measurements

In the following the estimates (σ_g, Δ_{10})[1] from KNM1 and KNM2 plasma measurements are shown. Further plots of the fitted data are found in appendix A.6.

The measured broadenings are shown in figure 6.8 [2]. The uncertainties include the statistical uncertainty of the measurement and the propagated uncertainty of Γ using equation 6.6. Since the latter dominates, they are correlated over all rear wall voltages.

Both campaigns show a similar structure, but a significant shift in absolute values for the coupled region. While differences in plasma properties cannot be excluded, they are not expected to this amount. A likely explanation is additional systematics in one of the campaigns. Notably, the hardware and magnetic field setting was adjusted by adding new aircoils in between KNM1 and KNM2. Thus, the applied background slope correction might be wrong for KNM1: while the correction removes all radial dependent structures in KNM2, for KNM1 the picture is not as clear. However, also the statistical uncertainties of KNM1 were larger, since much less data was taken. Lastly, in between KNM1 and KNM2 the rear wall hardware was adjusted, leading to an overall shift of the applied voltage in the few 10 mV range.

If no additional systematics existed, a correction of the Lorentzian $\Delta\Gamma^{\text{ref}} \approx -80$ meV would be necessary to make the measured broadenings in KNM1 positive. While this cannot be excluded it is not backed up by the reference measurements listed in table 6.2 and by the results of the KNM2 measurement. Thus, in the following no correction to the Lorentzian is applied and a focus is put on the KNM2 measurement.

6.3.1. Correction of the Mean Difference from Potential Antisymmetry

Due to uncertainties of the energy loss function at 30 keV and the disregard of detailed transmission, which is a modification of the transmission function caused by secondary effects resulting from inelastic scattering, the measured values of Δ_{10} suffer from systematics. Thus, a correction is applied using

$$\Delta_{10}(\Delta_{10}^{\text{Ref}})[V] = \Delta_{10}(0)[V] - \Delta_{10}^{\text{Ref}}\,, \tag{6.7}$$

which eliminates all linear systematics. This is driven by the assumption that the wrong energy loss function used to fit the data linearly shifts the mean fit value. This is expected if Δ_{10} is measured relative to the total mean energy loss. This assumption is discussed below in some more detail.

[1] σ_g is used here instead of σ_0, since it may contain an additional broadening from fluctuations.

[2] Here and in the following 500 mV bins for the rear wall voltages in the coupling region are used for clearer plots of KNM2 data. Many different voltages were measured without significant dependencies on rear wall voltage. Also, the rings are shifted in rear wall voltage compared to each others for better visibility.

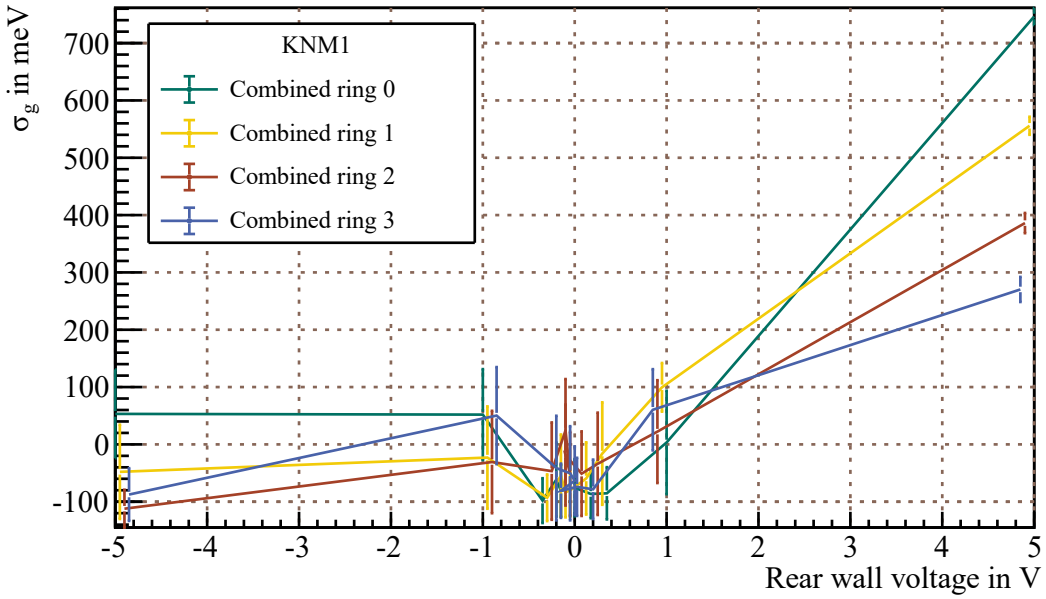

(a) KNM1

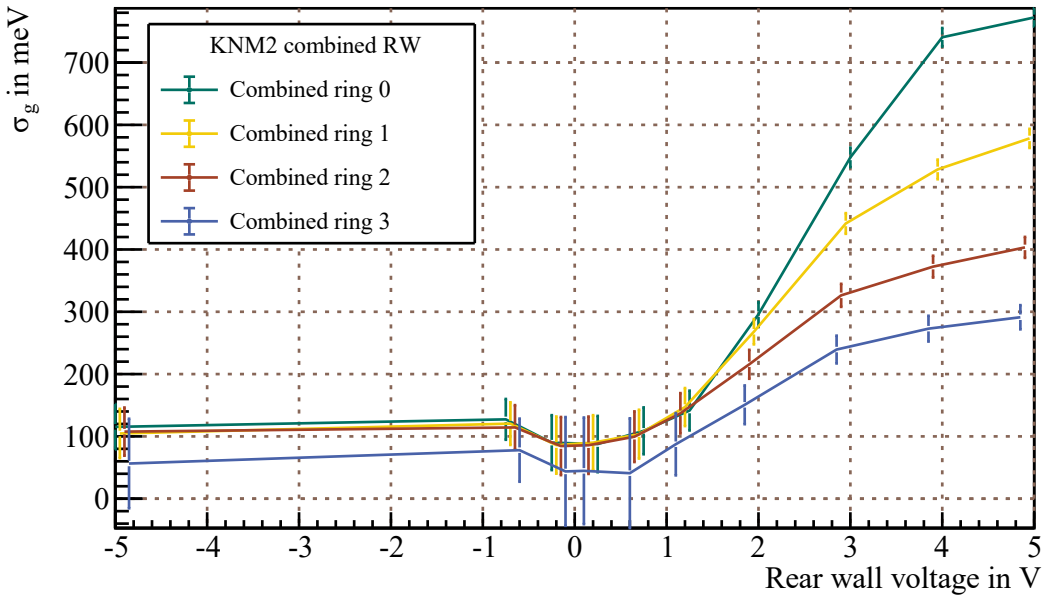

(b) KNM2

Figure 6.8.: Gaussian broadening in KNM1&2 krypton measurements: Both show comparable structure with small broadening in the coupling region and increasing broadening for large positive rear wall voltages. Both use the same Lorentzian of $\Gamma = 1.0606(21)(150)$ eV. However, while most of the values in the coupling region in KNM1 are negative, all are positive for KNM2. The uncertainties are dominated by the propagated uncertainty of Γ. The values for different rings are shifted in rear wall voltage for better visibility.

To account for the uncertainties of the measured parameters $(\sigma_0^2, \Delta_{10})$ the following χ^2 function is constructed for the correction:

$$\chi^2(\Delta_{10}^{\mathrm{Ref}}, \Delta\Gamma_{\mathrm{L_3}}^{\mathrm{Ref}}) = \sum_{\substack{U_{\mathrm{RW}},\\ \mathrm{Combined}\\ \mathrm{rings}}} \left[\left(\frac{\hat{\rho}^2(\Delta_{10}^{\mathrm{Ref}}) - 1}{\sigma(\hat{\rho}^2)} \right)^2 \Theta(\hat{\rho}^2 - 1) + \left(\frac{\sigma_0^2(\Delta\Gamma_{\mathrm{L_3}}^{\mathrm{Ref}})}{\sigma(\sigma_0^2)} \right)^2 \Theta(-\sigma_0^2) \right] . \quad (6.8)$$

Thus, only when the squared measured antisymmetry $\hat{\rho}^2$ [3] is unphysical or the Gaussian broadening is negative, the uncertainty weighted difference is added. Here $\sigma_{\mathrm{g}} = \sigma_0$ is assumed, which is the most conservative case. Since additional components of σ_{g} like fluctuations do not affect Δ_{10}, they would make the absolute value of the antisymmetry smaller, thus leading to tighter constraints.

χ^2 profiles: The two-dimensional profiles of the χ^2 for KNM1 and KNM2 are shown in figure 6.9. As visible, the Lorentzian correction is not bounded to negative values, since larger values of σ_0 lead to smaller antisymmetry. A priori, both results are in an unphysical region. For KNM1 this can only be solved for seemingly unreasonably high corrections of the Lorentzian.

For the given Lorentzian, the KNM2 data can be shifted to a physical region with [4]

$$\Delta_{10}^{\mathrm{Ref}} = (98 \pm 52)\ \mathrm{mV} . \quad (6.9)$$

This symmetrical shift with regard to the uncertainties is chosen for the following results, but in principle all corrections in this interval have the same possibility. As visible, the 0 σ contour [5] has a parabolic minimum, which would lead to tighter constraints for a larger Lorentzian, i.e for smaller measured broadenings. Thus, the uncertainty of the correction is proportional to the measured values of σ_0. In principle it is possible to fully constrain $\Delta_{10}^{\mathrm{Ref}}$ by σ_0 for plasmas with vanishing inhomogeneity. However, including the statistical uncertainties leads to broad, basically flat minima, such that this would also require significantly more statistics.

Also, the Δ_{10} results of KNM1 show an overall 60 mV shift compared to KNM2, which is not understood. Due to the neglect of the detailed transmission function the correction could depend on the column density, but the latter was rather comparable in the KNM1 and KNM2 krypton measurements. A second influence are the different energy loss functions of impurities in the source, which is studied in [Rodep]. Since the existence of impurities was not considered in the analysis, this also leads to a mismodelling of the energy loss function. If KNM1 and KNM2 krypton had a different concentration of impurities, this might contribute to the observed difference. Notably, increasing impurities could lead to the observed drift of the energy loss shift in KNM2. If that was the case, the different

[3] For the calculation of the antisymmetry all pixel estimates were averaged first. Details are found in appendix A.7.

[4] Not binning the rear wall voltages leads to $O(1)$ mV differences.

[5] Since the χ^2 function is constructed from inequalities, the 0 σ contour restricts the unconstrained region. This is in contrast to usual χ^2 functions, where it is the point of the minimum.

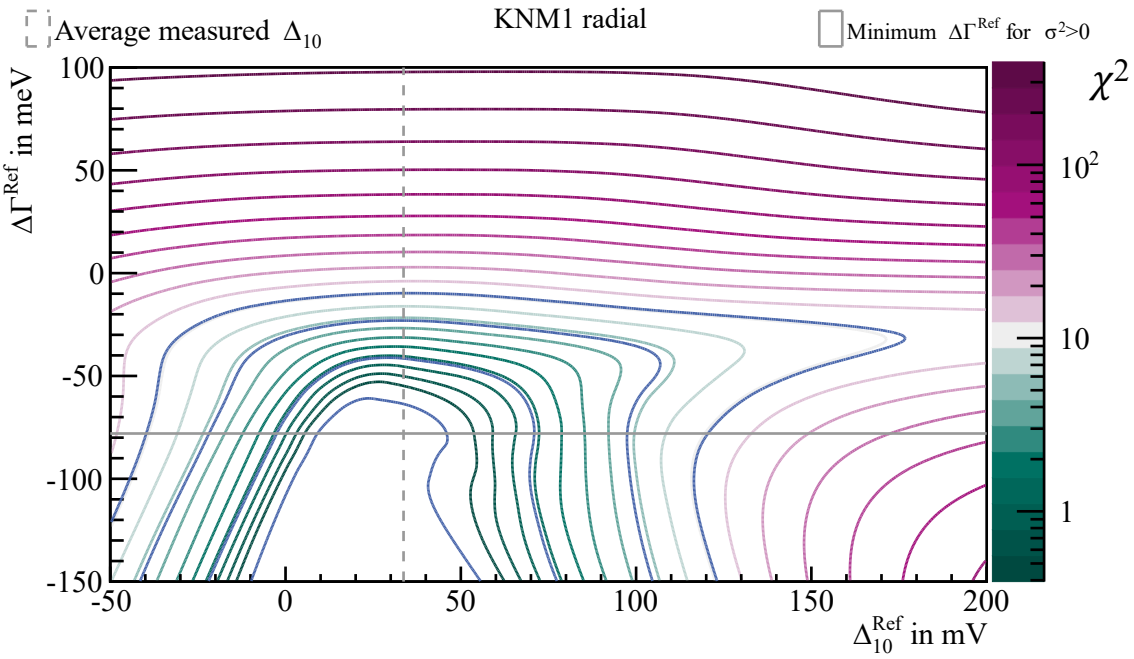

(a) KNM1

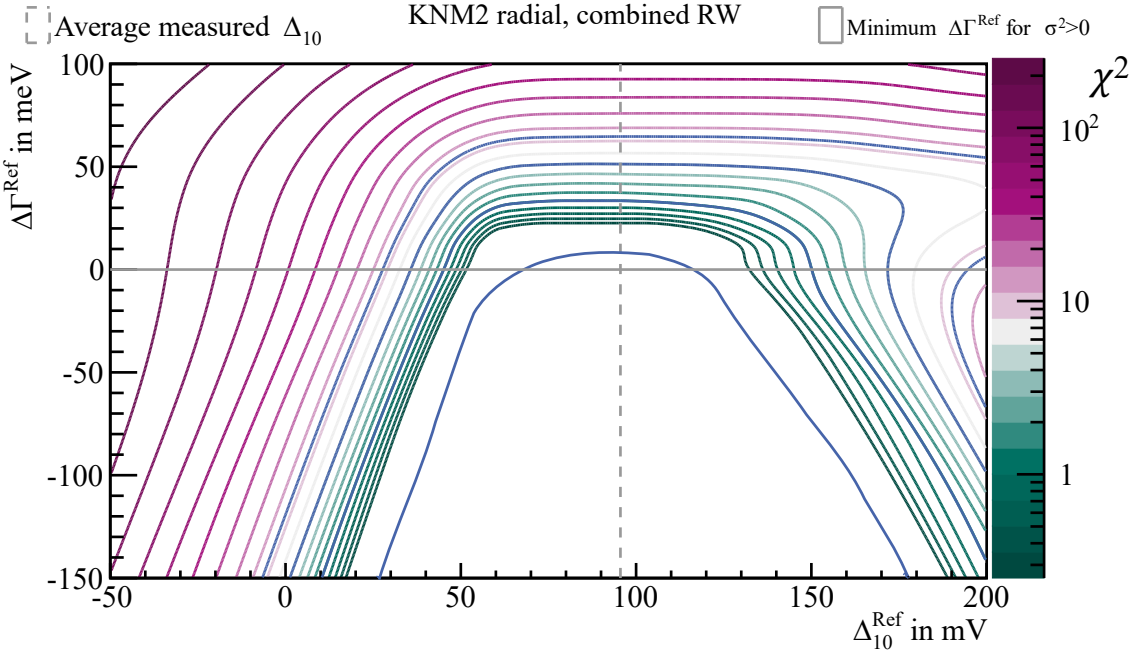

(b) KNM2

Figure 6.9.: Reference value exclusion plot: The x-axis is a linear correction of all measured energy loss shifts, the y-axis translates to a correction of the measured broadenings. The blue lines are the 0,1,2 and 3 σ contours. Thus, the region within the innermost blue line is unconstrained. While in KNM2 no correction needs to be applied to the Lorentzian, the necessary correction in KNM1 is at least -40 meV (1 σ contour). Also, it is visible that the mean differences measured in both campaigns show a shift of around 60 mV. Thus, a correction which brings both in agreement within the 1 σ contour is around 60 mV, which would lead to strong antisymmetry with opposite sign in both campaigns.

duration of the campaigns would be relevant: Since the KNM1 krypton campaign was three times shorter than the KNM2 krypton campaign, the overall increase of Δ_{10} would be smaller, leading to a smaller average in KNM1. However, the fact that the eloss shift of the $U_{\mathrm{RW}} = +5$ V measurement in KNM2 does not change over time speaks against this hypothesis: While the applied external field leads to a reproducible potential shape, it does not affect the gas composition and thus the mismodelling of the energy loss function. Thus, if caused by the latter, the increase of Δ_{10} should also be visible for large inhomogeneity, i.e. it should be consistent over all rear wall voltages. This is also not observed in KNM1, where the drift of Δ_{10} is either smaller than in KNM2, or even negative.

Mean difference: Figure 6.10 shows Δ_{10} over the rear wall voltage with and without correction. The chosen symmetrical correction shifts the values of Δ_{10} in the coupling region to ≈ 0, at the expense of increased uncertainties. The thereby obtained systematic error band is independent from the choice of correction, since an asymmetrical correction only shifts the mean values inside the band.

Antisymmetry and physical interpretation: Figure 6.11 shows the antisymmetry over the rear wall voltage with and without correction. Without correction most of the values are unphysical. With the symmetrical correction the potential has small antisymmetry in the coupling region. The large antisymmetry for large positive rear wall voltages only depends weakly on the correction, since here the data is dominated by the inhomogeneity. This region is an excellent test case for the theory developed in this work. The antisymmetry is expected, since a large positive rear wall voltage blocks positive ions from escaping the WGTS at the rear wall. Since they also cannot move against the gas flux away from the injection point, the ions in the rear part of the WGTS are trapped in longitudinal direction. They only escape if a large enough positive space charge forms, which drifts them out radially. This is in contrast to the ions in the front part, which can in all cases be extracted in the DPS dipole electrodes. Thus, at positive rear wall voltages a positive space charge is expected in the rear side of the WGTS, which overall produces an antisymmetrical potential as measured.

Peak-to-peak value: Figure 6.12 shows the allowed range of the peak-to-peak value of the potential in the central WGTS over the rear wall voltage. The uncertainty band was calculated as discussed in section 3.3.3 from σ_0 and the corrected Δ_{10}. The lower constraint uses a factor of 4 between peak-to-peak value and Δ_{10}, as derived in section 5.2. For the upper limit it is assumed that the potential inhomogeneity is not strongly localised, leading to $\sigma_0 \approx \sigma$ and a factor of 3.46 between the peak-to-peak value and σ_0. As discussed in section 3.3.3, the upper limit is obtained by a linear potential. The more structure the potential has, the smaller the peak-to-peak value for a given σ_0. Consequently, the structure of the potential increases, when going from top to bottom in the uncertainty band. The width of the band is only given by the different possible potential shapes and the uncertainties of σ_0 and Δ_{10} were neglected.

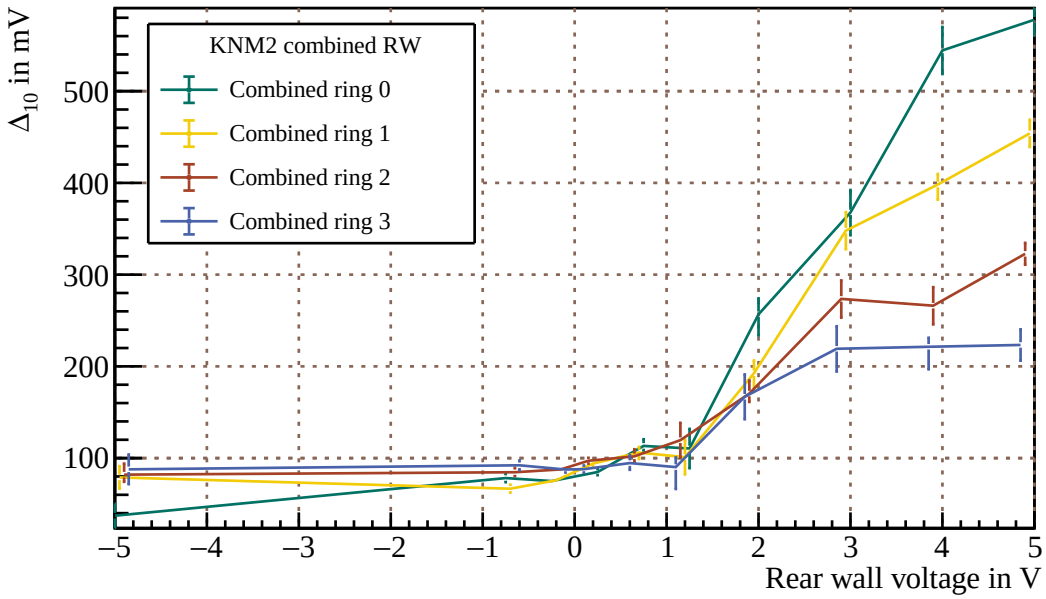

(a) Uncorrected

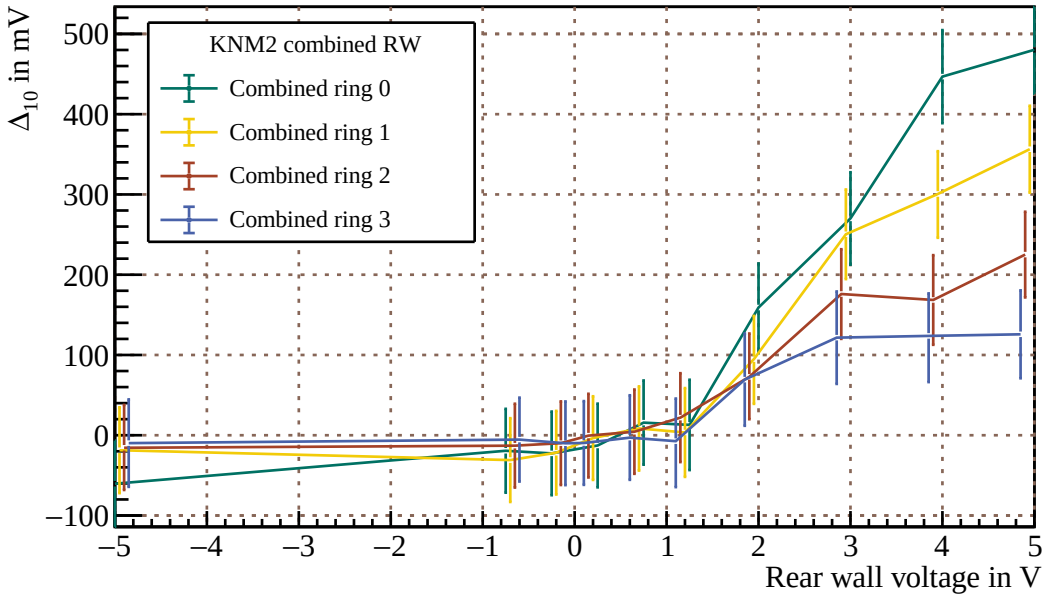

(b) Symmetrical correction

Figure 6.10.: Mean difference in KNM2 krypton measurement: The values increase for large positive rear wall voltages. The radial structure indicates a dependence on the coupling strength. The measured values (a) have an unknown offset. The symmetrical correction (b) shifts the values to the center of the unconstrained χ^2 function (figure 6.9), leading to vanishing mean difference for small rear wall voltages. The increased uncertainties are caused by the width of this unconstrained region.

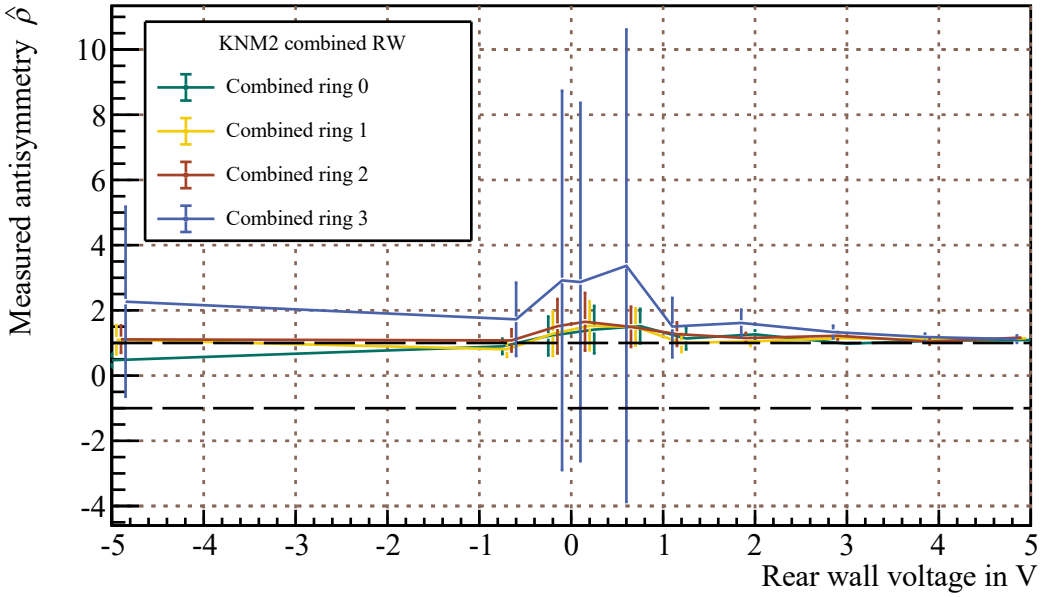

(a) Uncorrected

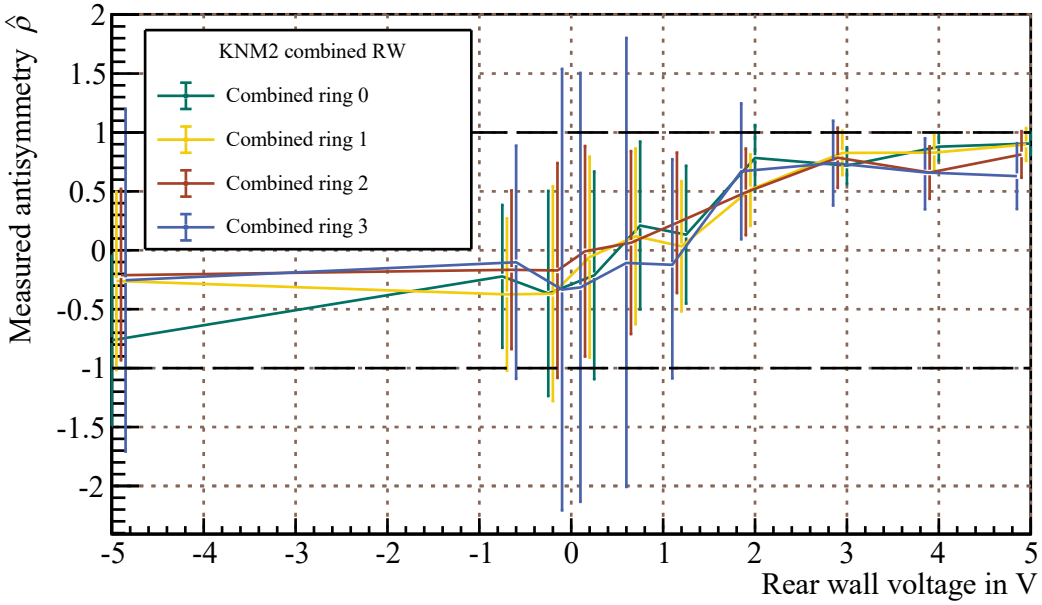

(b) Symmetrical correction

Figure 6.11.: Antisymmetry in KNM2 krypton measurement: Without correction (a) most of the values are not in the allowed range. Convergent behaviour for large positive rear wall voltages is observed, since here the data is dominated by inhomogeneity, not by systematics. Thus, the constraining region is the coupling region. After correction (b) all values are in the allowed range. The large uncertainties are caused by the unconstrained region of the χ^2 function (figure 6.9). The large antisymmetry for large positive voltages remains.

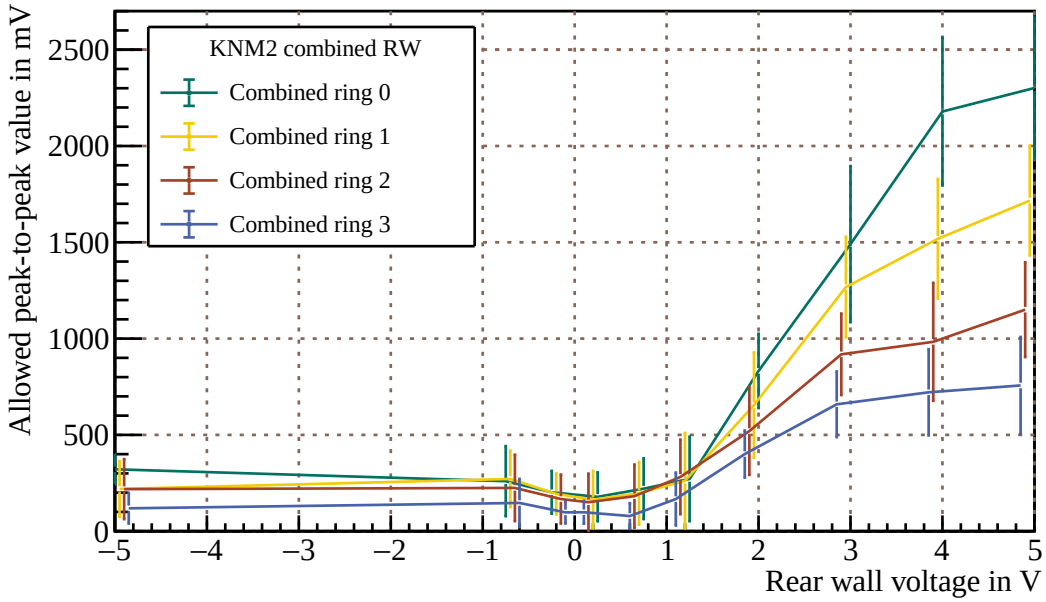

Figure 6.12.: Allowed peak-to-peak value over rear wall voltage in KNM2: The uncertainties mark an uncertainty band of equal possibility. Vertical translation implies a shape change, while for constant relative position on the band only the magnitude of the potential changes.

Change for large voltages: Due to energy conservation the change of the rear wall voltage should be an upper limit to the change of the observables. However, for the innermost rings, the change of Δ_{10} and σ_0 is approximately a factor of 2.5 between 2 V and 4 V rear wall voltage. Thus, the derivative is $\approx 1.25 > 1$. Still, for the peak-to-peak value a derivative less than 1 is possible in the uncertainty band, as it should be expected. As discussed above, this is associated with a shape change, which is illustrated in the following with two potential models.

Antisymmetry model for KNM2 data: The application of the antisymmetry model discussed in section 4.1 is shown in figures 6.13 and 6.14. The two models are used to illustrate the decrease of the peak-to-peak value with the increase of structure. For the symmetric component of the first model two half ellipses were used, as described in [Mac16]. The ratio of the semi-minor axis front to rear was fixed to 1.024, which produces a shape with vanishing Δ_{10} for the column density of 30 %. The second model uses an approximately parabolic symmetric component of

$$V_{\mathrm{sym}}(z) \propto 3.815 \left(\frac{z}{\mathrm{m}}\right)^2 - \frac{z}{\mathrm{m}}\,, \tag{6.10}$$

which also has vanishing Δ_{10}, as shown in section 4.2. The uncertainties are propagated from $(\langle V\rangle_0\,, \sigma_0, \Delta_{10})$. Only the statistical uncertainty is considered for the mean potential $\langle V\rangle_0 = -(E_{\mathrm{L_3}}^{\mathrm{plasma}} - E_{\mathrm{L_3}}^{\mathrm{ref}})$. Thus, there could be a constant shift of the mean potentials for

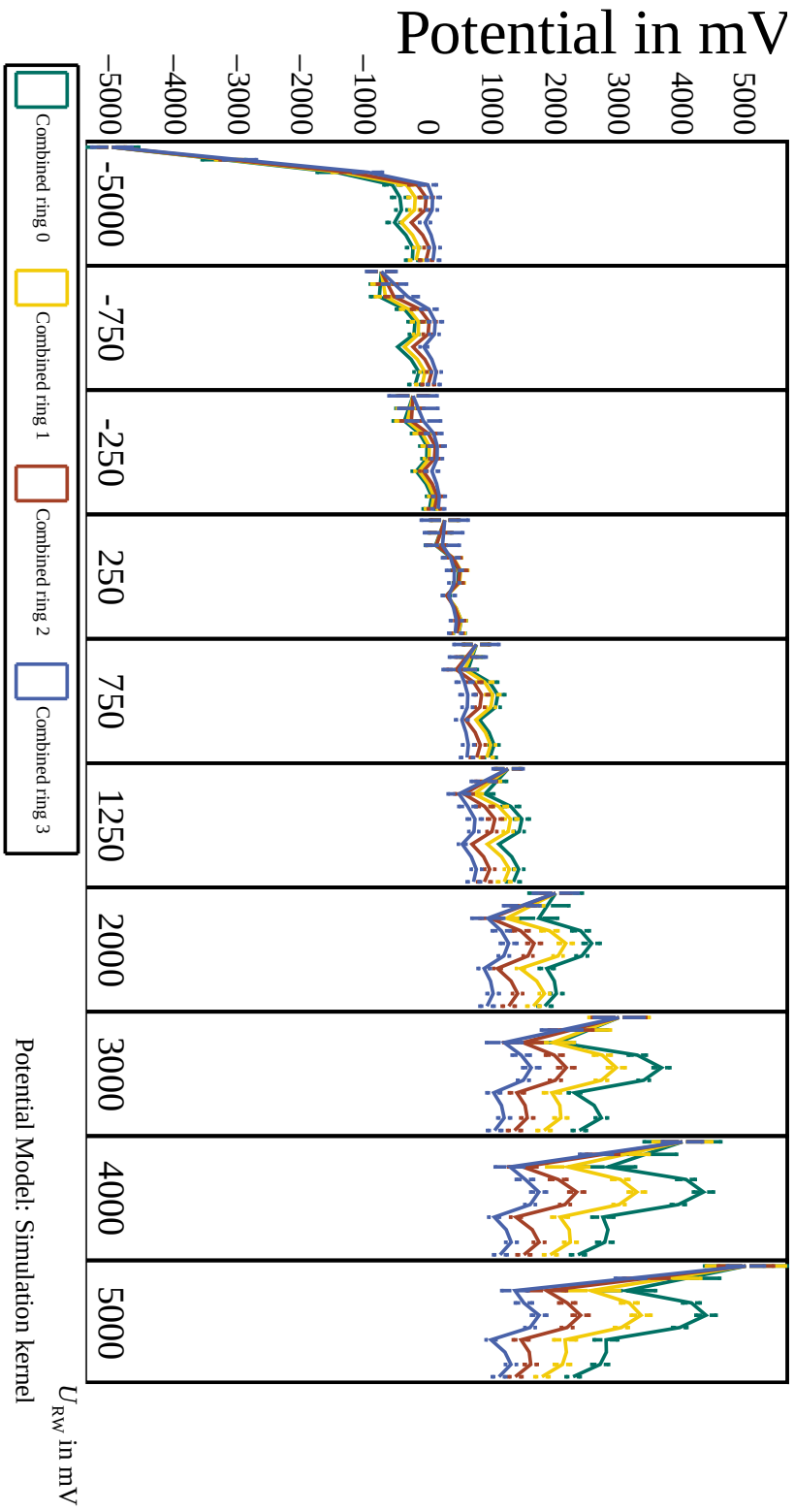

Figure 6.13.: Potential over rear wall voltage in KNM2, simulation kernel: The symmetric component of the potential is constructed from two half ellipses, which resemble the plasma simulations. The potential is most homogeneous in the 250 mV bin. A version without bins is found in appendix A.10. A linear connection between rear wall and rear of the WGTS is used, which is not physically motivated. The gap between the rear wall potential and the maximum in the WGTS for positive voltages is not expected, but likely caused by this modelling.

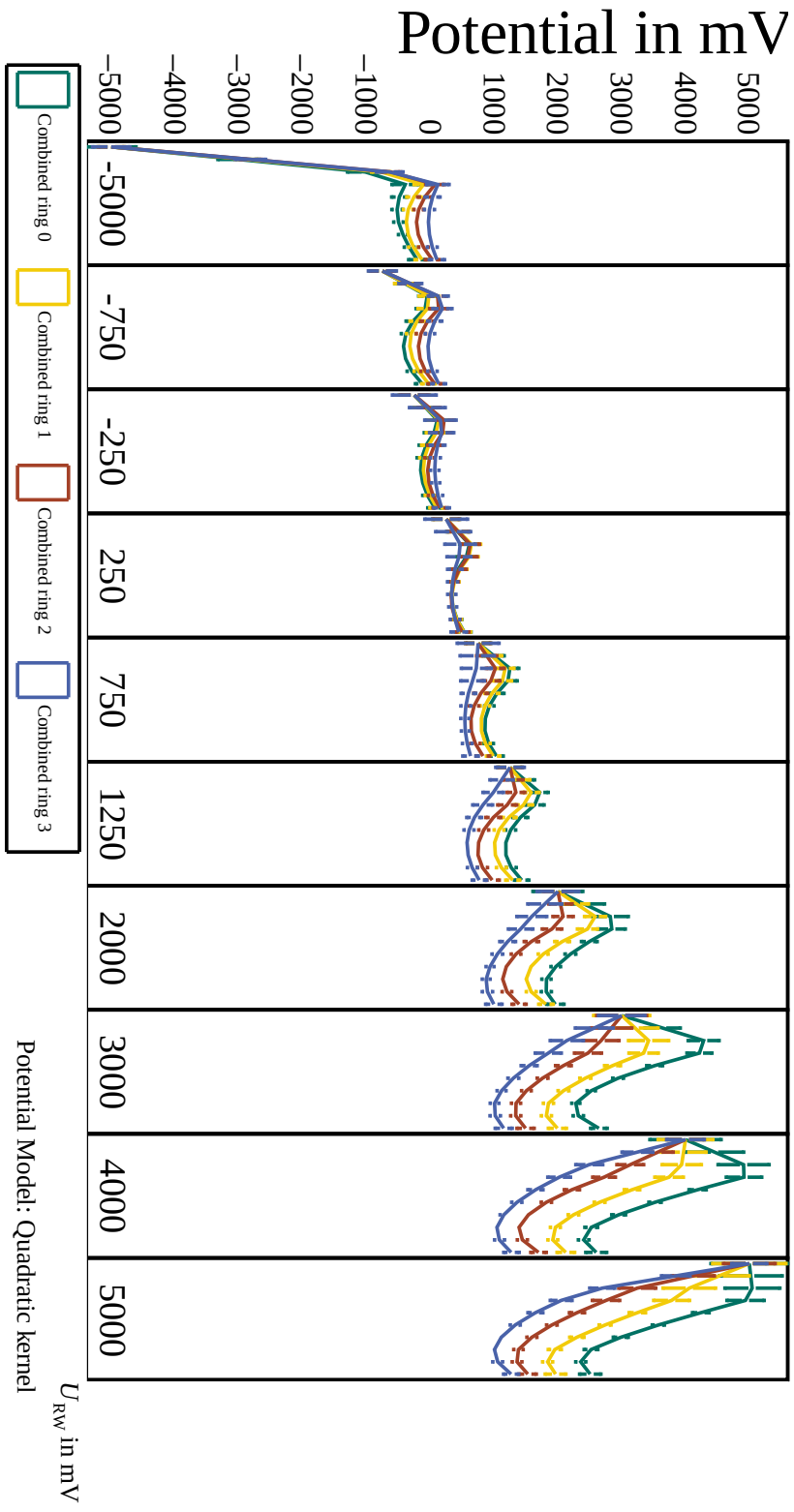

Figure 6.14.: Potential over rear wall voltage in KNM2, quadratic kernel: Here the symmetric component is approximately parabolic. As visible, there are large differences for large voltages to the previous ansatz. Here it is not possible to bridge the gap from rear wall and the maximum monotonously for the inner rings, while the outer rings do already connect. As explained in the text this is related to the smaller structure of the symmetric component. The version without bins is shown in appendix A.11.

all rear wall voltages, caused by differences of the mean potential in the reference and the plasma measurement.

As visible, due to the kink at the injection point in the centre of the source, the first ansatz resembles the plasma simulation. As discussed above, this excess of structure compared to the parabolic ansatz leads to smaller peak-to-peak values for the given observables, which is apparent at large voltages. Thus, in order to still make a monotonous connection from rear wall to the rear end of the WGTS for increasing voltages, increasing structure is needed. Presumably, the gap to the rear wall in the first ansatz could be made smaller, if the central gap was increased. A monotonous connection to the rear wall at large positive voltages is expected from plasma simulations [Kuc16]. Also, since the current measured at the rear wall saturates for large voltages [Fri20], it is expected that the electrons reach the rear wall and get drained. This would be prevented by a large potential drop between end of WGTS and rear wall. It is concluded that the potential likely has the central non-monotonous feature as predicted by the plasma potential simulation and that the application of large positive voltages leads to an asymmetrical amplification of this structure due to the accumulation of positive ions in the rear part (discussed above).

MTD and rear wall voltage dependence of $\Delta_{10}^{\mathrm{Ref}}$: As discussed in chapter 5, the fit of Δ_{10} is implemented as shift of the energy loss function $f_1(\epsilon)$. This makes two assumptions: First, that the plasma effect only leads to a shift of the measured energy loss and no change of the distribution. While this is an approximation, it is valid due to the intrinsic width of the energy loss function, which is much larger than possible plasma broadenings. The second assumption is that the correct function is known for the respective measurement conditions. If both assumptions hold, then the shifted function describes the data with good agreement. However, the second assumption does not hold, since the energy loss function used in the analysis stems from a measurement at $\approx$ 18 keV electron energy and a gas temperature of $\approx$ 29 K, while the krypton measurement uses $\approx$ 30 keV electrons and a temperature of $\approx$ 100 K. Both can lead to a change of the energy loss function, such that it does not fit the scattered krypton spectrum at L_3 even without plasma.

Using this wrong model leads to systematics on the fitted Δ_{10}. In minimisation its value is chosen such that the shifted wrong $f_1(\epsilon)$ produces the minimum χ^2 on the data set, which due to the wrong model depends on the total spectrum shape in the scattering region. Thus, Δ_{10} is not only affected by the real plasma induced Δ_{10}, but also by the measurement time distribution and the column density.

While in detail the χ^2 minimum depends on each of the measured bins of the total spectrum, as a perturbation it is most likely that it is mainly given by the mean of the function fitting to the mean of the data. Still the mean energy loss measured in the data depends on the analysis interval.

The mean energy loss as predicted from the $\approx$ 18 keV energy loss function is plotted in figure 6.15 over the surplus energy. The latter is cut by the lower analysis interval, which is usually $\approx$ 22 eV below the line mean. As visible, the slope of the mean energy loss in this region with a change of the analysis interval is around $m_{\bar{\epsilon}_{\mathrm{Eloss}}} = 508\ \frac{\mathrm{meV}}{\mathrm{eV}}$. While this is a large value, it is always considered in the model. Only the difference to the true value of

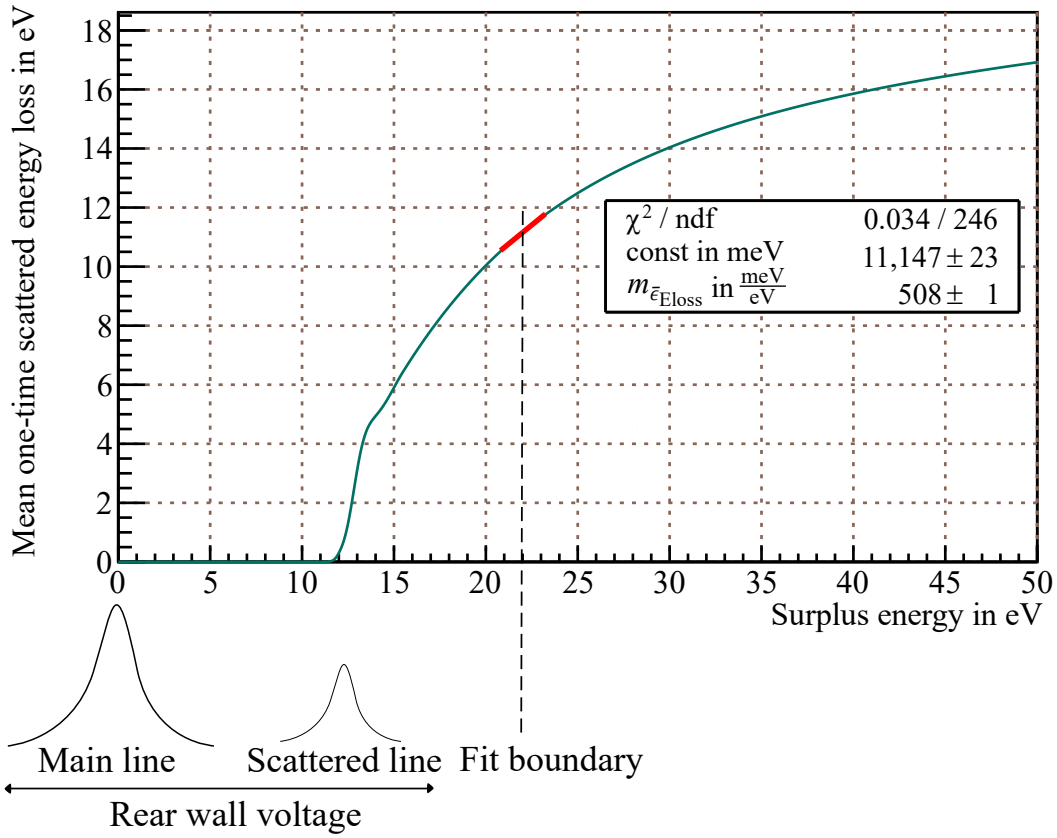

Figure 6.15.: Analysis interval dependence of the measurement of the mean difference: It is assumed that the fitted energy loss Δ_{10} is measured compared to the mean expected energy loss in the data. If the change of the latter with the analysis interval is wrongly predicted, since a wrong energy loss function is used, this leads to a systematic. This systematic has a dependence on the rear wall voltage, since the MTD is fixed to the retarding energy and thus is independent from the rear wall voltage. On the contrary, the zero point of the energy loss function is given by the line position, which shifts by the rear wall voltage with some coupling factor.

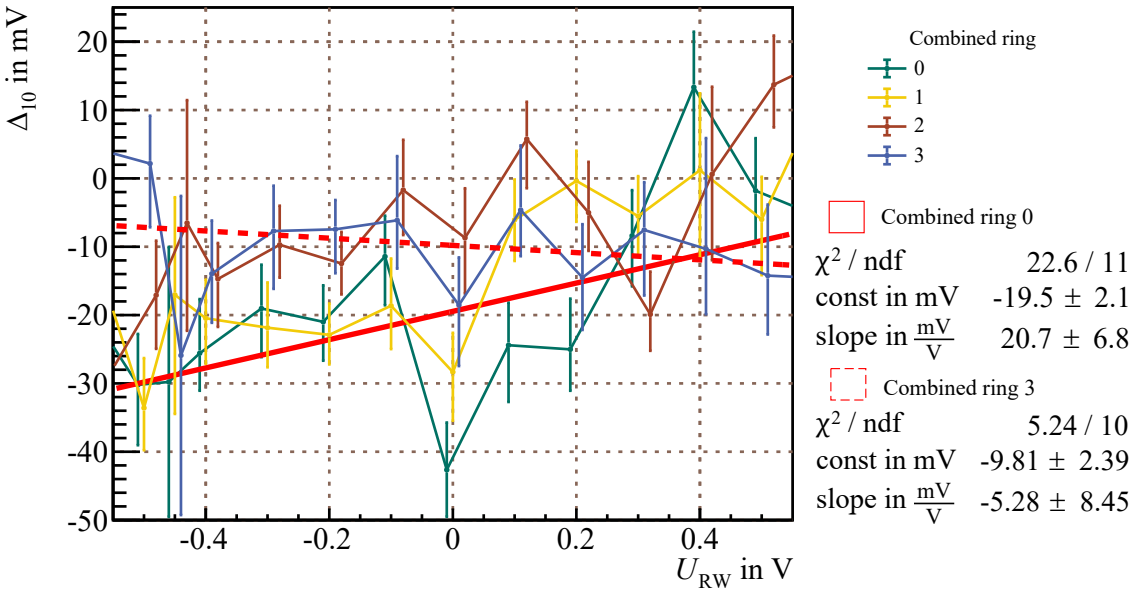

Figure 6.16.: Rear wall voltage dependence of the mean difference: As visible, the inner rings show a slope with the rear wall voltage, which vanishes for the outer rings. Due to the dependence on the coupling this would be expected both from systematics and from physical effects.

the true function leads to a systematic beyond the already considered constant shift Δ_{10}^{ref}. This systematic adds a dependence on the lower analysis interval like

$$\Delta(\Delta_{10}^{\text{Ref}})(\Delta qU_{\text{lower}}) = \Delta qU_{\text{lower}} \Delta m_{\bar{\epsilon}_{\text{Eloss}}} , \tag{6.11}$$

where ΔqU_{lower} is the difference to the lower analysis interval at which Δ_{10}^{Ref} was determined.

While the uncertainty on the predicted slope is not known, the determination of Δ_{10} should always use the same MTD to minimise the effect. However, since the MTD is fixed compared to the retarding energy, it does not depend on the rear wall voltage. The onset of the energy loss function, on the other hand, depends on the line position, which depends on the rear wall voltage. Thus, in principle the MTD would need to be adjusted for each rear wall voltage to avoid the effect completely, however this would also require that it is precisely known in advance what the actual coupling factor of the line position to the rear wall is. Also, since the coupling is radially dependent, a perfect solution is not possible.

A small dependence of Δ_{10} on the rear wall voltage was actually observed in KNM2. Figure 6.16 shows the corrected Δ_{10} measurement without rear wall bins. The uncertainties are statistical only, for better visibility. The outer rings show no dependence, while the inner rings have a slope. For the fitted innermost ring it is 20.7 $\frac{mV}{V}$. The radial dependence is expected due to the dependence on coupling, regardless of whether the slope is physical, or whether it stems from the described systematic. If it is due to this systematic, the

measurement allows to constrain the relative difference

$$\frac{\Delta m_{\bar{\epsilon}_{\mathrm{Eloss}}}}{m_{\bar{\epsilon}_{\mathrm{Eloss}}}} = \frac{\Delta(\Delta_{10})}{\Delta U_{\mathrm{RW}}} \frac{1}{m_{\bar{\epsilon}_{\mathrm{Eloss}}}} \leq (4 \pm 1)\ \% \,. \tag{6.12}$$

Regardless of the underlying effect, the slope is comparably small. If for example the 60 mV difference of Δ_{10} found between KNM1&2 krypton was to be attributed to this shift, this would require differences of the lower analysis interval or rear wall settings in the 3 V range. However, the change of the rear wall voltage is usually on the 100 mV scale, while the MTD was not changed at all.

Column density dependence of $\Delta_{10}^{\mathrm{Ref}}$: Since the detailed transmission function is not used the transmission function might depend on the amount of scattering. It is currently under investigation how large this dependence could be and if it could lead to sizeable effects. However, the column density difference between the KNM1&2 krypton campaigns was small, such that this cannot explain the observed difference of the Δ_{10} of the campaigns.

Usefulness of the Δ_{10} measurement: While the correction and obtained antisymmetry allows to proof the underlying theory and to obtain physical values of Δ_{10}, the resulting uncertainties in the coupling region are large. As discussed, they are proportional to the measured broadening in the coupling region and the overall statistical uncertainties. This holds only due to the small (radial) structure of the data in the coupling region: the less structure, the easier Δ_{10} can be shifted to 0. If no radial structure is present, the single measurement value Δ_{10} is fully correlated with its correction $\Delta_{10}^{\mathrm{ref}}$ and the total value can have any value allowed by $|\Delta_{10}| \leq \kappa_{\overline{10},0}\sigma_0$. Thus, in the case of vanishing (radial) structure like here and given the systematic uncertainties of Δ_{10}, the measurement of Δ_{10} does not lead to useful values in the coupling region. Instead, the neutrino mass shift or the value of Δ_{10} can be directly derived only from σ_0, which is done in the next section.

6.4. Systematics of the KNM1 and KNM2 Tritium Measurements

Finally, the systematic shift of the neutrino mass caused by the plasma potential in KNM1 and KNM2 is derived. As discussed in the previous section, the obtained measurement of Δ_{10} is not beneficial in the coupling region. Thus, only σ_{g} and the maximum shape energy is used. It is assumed that σ_{g} is caused only by σ_0.

For the inner rings in the coupling region it is given by

$$\sigma_0^{\mathrm{Kr}} = (90 \pm 30)\ \mathrm{meV} \tag{6.13}$$

for krypton conditions. The large uncertainty is caused by the uncertainty of the Lorentzian reference, which is the dominating systematic. Due to the large uncertainties of the analysis σ_0 is only used as upper limit with a mean of 0 in the tritium β-spectrum model. Adding

the uncertainty of 30 meV to the mean using Gaussian propagation for the squared value leads to

$$\sigma(\sigma_0)^{\mathrm{Kr}} \approx 116 \text{ meV} . \tag{6.14}$$

As discussed in section 5.3 additional uncertainties due to the possibility of different plasma potentials and differences in the scattering weights between tritium and krypton conditions arise. The former is not known, and disregarded here. The translation between the weights is shape dependent and different shapes produce the extremal changes of σ_0 and Δ_{10}. This leads to a correlation of the parameters, even if σ_0 and $\hat{\rho}$ are used. In the following the correlation is neglected and the extremal values of both are calculated independently, which overestimates the effect. However, the independent estimates are needed for systematic studies.

As discussed in section 5.3, the maximum of the neutrino mass shift variance term is obtained by multiplying the above result with a factor of 1.1 (KNM1) or 1.2 (KNM2). This leads to

$$\textbf{Maximum variance}: \quad \sigma(\sigma_0)^{\mathrm{KNM1}} \approx 128 \text{ meV} , \quad \sigma(\sigma_0)^{\mathrm{KNM2}} \approx 140 \text{ meV} . \tag{6.15}$$

The values are realised by a maximally localised inhomogeneity, which in turn has vanishing antisymmetry, as shown in section 3.3.2.

The maximum Δ_ρ are calculated directly from krypton σ_0 using the krypton weighted $\kappa_\rho = 0.6$ (KNM1) and $\kappa_\rho = 0.72$ (KNM2), which are found in figure A.19 in the appendix. Multiplying equation 6.14 with those values gives

$$\left|\Delta_\rho^{\mathrm{KNM1}}\right| \leq 70 \text{ meV} , \quad \left|\Delta_\rho^{\mathrm{KNM2}}\right| \leq 84 \text{ meV} . \tag{6.16}$$

Thus, while the standard deviations of equation 6.15 are the maximum allowed, the maximum antisymmetry would be produced by smaller values, which are calculated using the tritium weighted $\kappa_\rho = 0.63$ (KNM1) and $\kappa_\rho = 0.78$ (KNM2) from figure 5.9 and the given Δ_ρ

$$\textbf{Maximum shape energy}: \quad \sigma(\sigma_0)^{\mathrm{KNM1}} \approx 111 \text{ meV} , \quad \sigma(\sigma_0)^{\mathrm{KNM2}} \approx 108 \text{ meV} . \tag{6.17}$$

For σ_0 larger than those values σ_0 and $\hat{\rho}$ are correlated, i.e. for larger values the shape energy needs to decrease, and for the values of equation 6.15 it needs to vanish.

Using the above maximum standard deviations and the shape energy from figure 5.12 to calculate the absolute shifts of the squared neutrino mass leads to [6]

$$|\Delta m_\nu^2[V]|^{\mathrm{KNM1}} < 2 \left(111 \cdot 160 + 128 \cdot 128 \right) \text{meV}^2 = 0.07 \text{ eV}^2 , \tag{6.18}$$

$$|\Delta m_\nu^2[V]|^{\mathrm{KNM2}} < 2 \left(\underbrace{108 \cdot 490}_{\text{shape}} + \underbrace{140 \cdot 140}_{\text{variance}} \right) \text{meV}^2 = 0.15 \text{ eV}^2 . \tag{6.19}$$

[6] In addition to using this perturbative equation the shifts were also modelled on Asimov data by including different potentials with the moments measured in KNM1&2 krypton. The results are in agreement.

Due to the correlation these shifts are overestimated. Using only the maximum shape energy values, which are the largest simultaneously allowed for both terms, gives

$$|\Delta m_\nu^2[V]|^{\mathrm{KNM1}} \lesssim 2 \cdot 111 \; (\; 160 \; + \; 111 \;) \; \mathrm{meV}^2 = 0.06 \; \mathrm{eV}^2 \,, \tag{6.20}$$

$$|\Delta m_\nu^2[V]|^{\mathrm{KNM2}} \lesssim 2 \cdot 108 \; (\underbrace{\; 490 \;}_{\text{shape}} + \underbrace{\; 108 \;}_{\text{variance}}) \; \mathrm{meV}^2 = 0.13 \; \mathrm{eV}^2 \,. \tag{6.21}$$

Obviously the differences are minor. Thus, also the benefit of constraining the neutrino mass shift directly including the correlations, as discussed in section 3.5, is small. For the currently performed analysis of the KNM2 results σ_0 is directly constrained from the krypton measurement. The analysis is based on the larger KNM3 krypton dataset. It also includes an uncertainty due to the difference of the potential in the measurements, which is obtained by extrapolation between measurement conditions.

6.5. Conclusion

In this chapter the analysis of the KNM1 and KNM2 krypton measurements was described. The KNM1 krypton data showed non-understood systematics, which presumably are at least partly related to an insufficient background model. Thus, the KNM1 krypton data was not used further. However, the KNM2 krypton measurements showed consistent results. Its estimates of potential inhomogeneity were used to predict the respective neutrino mass shifts in the KNM1 and KNM2 tritium measurement. Furthermore, it was shown that the theory developed in this thesis, which relates the krypton observables to symmetries of the potential is fully applicable to the gaseous krypton measurements. If a strong positive voltage is applied to the rear wall, a negative longitudinal gradient of the potential through the source is expected. Since it dominates all other inhomogeneities and depends only on the precisely applied voltage, it should be reproducible. It was shown that the krypton measurements fully support these expectations. Moreover, it could be argued that in this case the potential shape is not smoothly linear decreasing, but that it likely has the central structure which is predicted by plasma simulations. While this was made plausible using two model-dependent simulations, the basic argument can already be made completely model independently only on the peak-to-peak value of the potential. In summary, it was shown that the theory developed in this work fully relates the krypton observables to the potential symmetries, that it gives a complete description of the gaseous krypton measurements at KATRIN and that it consequently should serve as the basis of the future measurements.

The analysis also revealed several challenges: Using only KNM1 and KNM2 krypton data, the impact of plasma potential inhomogeneities on KATRIN neutrino mass measurement systematics is huge. The systematic budget of full KATRIN of $\sigma_{\mathrm{sys,tot}}(m_\nu^2) \lesssim 0.017 \; \mathrm{eV}^2$ [KAT04b] is already exceeded by each of the plasma systematics of the first two campaigns. In KNM1 it is a factor of 3.5 times larger, in KNM2 a factor of 7.6. These large systematics are mainly caused by the unknown energy loss shift $\Delta_{10}[V]$, which was newly introduced in this work. While due to systematics of the krypton measurement its measured value can

currently not be used, it was shown that it can nevertheless be constrained from the measured potential variance $\sigma_0^2[V]$. However, the latter also suffers from large uncertainties, stemming from difficulties in the determination of the intrinsic L_3 line width Γ.

Despite these, currently still large, uncertainties, the plasma related shift of the squared neutrino mass of KNM1 is insignificant compared to the KNM1 budget of $\sigma_{\mathrm{sys,KNM1}}(m_\nu^2) = 0.32\ \mathrm{eV}^2$ [Ake+19], when added in quadrature. Thus, its disregard in the published analysis is justified.

However, for full KATRIN this will not be possible and already in KNM2 the plasma systematics is a dominating contributor of the systematic budget. To overcome the described challenges and to reduce the influence of plasma systematics, the KNM3 measurement campaign was dedicated to the study of the plasma potential and the krypton measurements were hugely expanded. This included extended measurements using L_3 and the $N_{2,3}$ doublet. Also, different column densities and temperatures were used to understand their influence on the plasma potential. Notably, the large systematic obtained in the analysis of this thesis would be already significantly reduced, if the measured mean of the plasma potential variance $\sigma_0^2[V]$ was used in the modelling of the β spectrum. Only its uncertainty needs to lead to a systematic of the measurement of the neutrino mass. While the determination of the plasma systematics in KNM1 followed the approach shown here (where only an upper limit was calculated), in KNM2 the measured mean will be considered in the modelling.

The systematic strongly depends on the size and knowledge of the total broadening σ_g. Ongoing analysis of the $N_{2,3}$ doublet on KNM3 data suggests that it is considerably smaller ($\sigma_\mathrm{g} \approx 50$ meV) [Gup20; Böt20] than the presented analysis shows. However, at the present stage still considerable tension to L_3 data exists, indicating, that both measurements suffer from different systematics. Nevertheless, using the $N_{2,3}$ doublet, in part the difficulties in the determination of the intrinsic L_3 line width Γ have already been solved.

Outlook: In the future an estimate of $\Delta_{10}[V]$ needs to be obtained, since the shape energy dominates the plasma potential systematics of the neutrino mass measurement. The present analysis shows that this measurement is possible and that the theory of the spectral effect of the plasma systematics is well understood. However, the determination of the correct energy loss function is vital to minimise the uncertainties. This problem is currently tackled from two sides: The change of the energy loss function with energy is calculated in theory and a new electron gun is under construction, which will be capable of producing quasi mono-energetic electrons at energies of ≈ 30 keV. This will allow to measure the energy loss function at these energies.

7. Runtime Schedules and Time Dependent Perturbations

In this chapter the systematics resulting from time dependent perturbations of operating parameters are discussed. The systematics depend on the interplay between the time scale T or frequency $f = \frac{1}{T}$ (angular frequency $\omega = 2\pi f$) of the perturbations and the runtime schedule, i.e. the time ordering of the retarding energy $qU(t)$. The observables of interest are the neutrino mass m_ν, the endpoint E_0 (tritium spectrum), the Gaussian broadening σ_g and the line position E_Main [1] (krypton spectrum). In both spectra also the nuisance parameters intensity and background and the χ^2 are affected.

In section 7.1 the relevant time scales of the runtime schedule and the corresponding regimes of systematic shifts are discussed along with general definitions. Furthermore correlation analysis of the schedules both in time and frequency domain is described, which allows to classify their frequency response independently of the spectrum and thus to generalise the findings to other than the studied schedules.

In section 7.2 the chosen semi-analytical implementation is described.

In section 7.3 the results are discussed based on the KNM2 tritium and krypton measurements for the example of energy scale perturbations.

7.1. Runtime Schedules in Time and Frequency Domain

The distribution of the total measurement time to the different retarding energies is determined by the *Measurement Time Distribution*, short MTD. The MTDs used in KNM2 krypton and tritium measurements are found in figures 7.1 and 7.2. The tritium MTD is optimised to yield the best sensitivity on the neutrino mass for a given total measurement time [Kle14]. Constant uncertainties of model parameters can be considered in the optimisation, but since no time dependent effects are considered, the timewise ordering of retarding energies does not affect the projected sensitivity. In this work the systematics resulting from non-constant parameters are discussed for different classes of runtime schedules.

[1] Systematics on the eloss shift $\Delta\epsilon_\mathrm{Eloss}$ have not been investigated. It is assumed that the magnitude of the systematics can already be determined from the used observables.

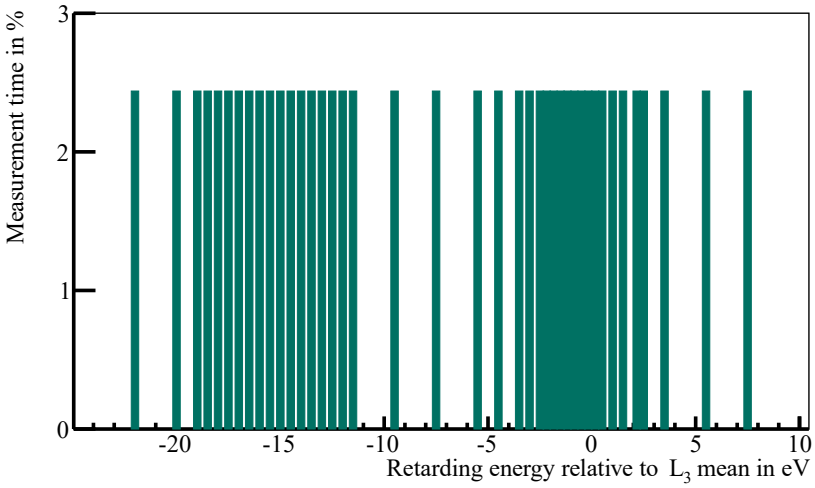

Figure 7.1.: KNM2 krypton measurement time distribution: As in most krypton measurements at KATRIN a flat MTD was used for KNM2 krypton. The regions with more dense points are at the expected line mean of L_3 and the line of one-time scattered electrons. For the studies performed in this chapter a stripped-down MTD without the scattered electrons is used, which already allows to determine the magnitude of systematics related to time dependent effects.

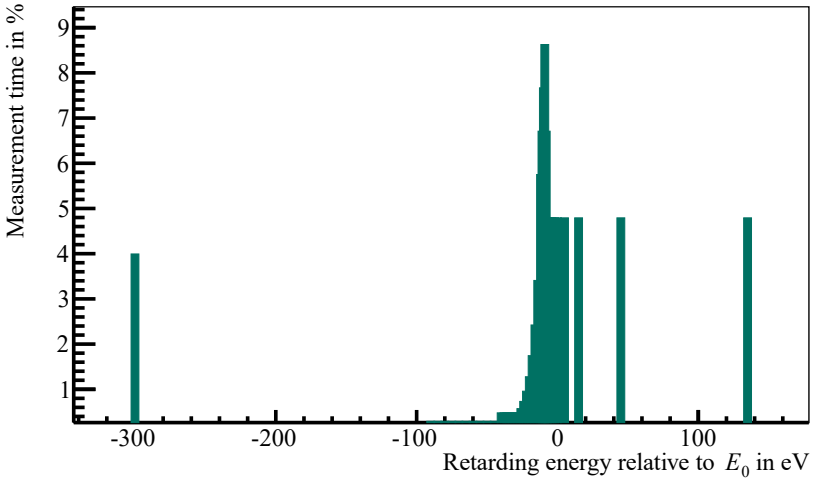

Figure 7.2.: KNM2 tritium measurement time distribution: The typical MTD for tritium measurements has a peak some eV below the endpoint with most m_ν sensitivity. The region above the endpoint serves to fit the background, the region below the endpoint determines the signal and the endpoint itself. One point several hundred eV below the endpoint is used for studies of systematics like radial energy dependencies. For the studies performed in this chapter the MTD is restricted to the 40 eV interval below the endpoint, which is the interval usually used for neutrino mass analysis.

7.1.1. Relevant Time Scales and Perturbation Regimes

In the following different time scales and their corresponding distributions are described, which occur based on how the runtime schedules are constructed from the total projected measurement time T_{tot}. The time scales are the moments of these distributions and they are used to identify the frequency regimes of the time dependent effects which produce qualitatively different systematic shifts of the observables for a given runtime schedule. With regard to the runtime schedules the focus lies on order versus randomisation, which is expected to be the cause of differences in systematics caused by time dependent effects.

Subrun time duration: Most data taking at KATRIN is performed at piecewise constant retarding energy $qU(t)$, in contrast to, for example, continuous ramping measurements [2]. A measurement at a fixed retarding energy is called *subrun* and the runtime schedule is fully described by the time ordered set of the N_{subrun} subruns. From this set the frequency distribution $N(t_{\text{subrun}})$ of each subrun duration t_{subrun} can be constructed, which has the time scale

$$T_{\text{subrun}} = \frac{T_{\text{tot}}}{N_{\text{subrun}}} \tag{7.1}$$

as its first moment. The existence of this time scale is unavoidable, since it is a measure of *time duration* spend in a measurement. Only the higher moments can lead to large or no dispersion of the distribution, or the time scale itself can be raised or lowered.

Subrun duration versus returns: The total projected time $t_{\text{MTD}}(qU)$ spent in each bin of the MTD in general is a summation over $n(qU)$ subruns of duration $t_{\text{subrun},i}(qU)$, $i \in \{1, ..., n(qU)\}$, where $n(qU)$ is the *number of returns* to the subrun. Using the mean subrun time

$$\langle t_{\text{subrun}} \rangle (qU) \equiv \frac{1}{n(qU)} \sum_{i}^{n(qU)} t_{\text{subrun},i}(qU) \,, \tag{7.2}$$

this reads

$$t_{\text{MTD}}(qU) = \langle t_{\text{subrun}} \rangle (qU) n(qU) \,. \tag{7.3}$$

The $t_{\text{subrun},i}(qU)$ can be taken from a probability distribution $p_{qU}(t_{\text{subrun}})$ [3], whose higher moments add to the dispersion of $N(t_{\text{subrun}})$. In this case equation 7.3 is approximate and convergence to the projected MTD on the scale $t_{\text{MTD}}(qU)$ is only achieved, if the number of returns $n(qU)$ is large or likewise the average subrun duration $\langle t_{\text{subrun}} \rangle (qU)$ is small.

Using the average $\langle n \rangle_{qU}$ of the returns over the N_{MTD} bins of the MTD, the total number of subruns can be expressed as

$$N_{\text{subrun}} = \sum_{qU}^{N_{\text{MTD}}} n(qU) = \langle n \rangle_{qU} N_{\text{MTD}} \,. \tag{7.4}$$

[2] Even here the extracted data is taken from periods which are small compared to the ramping speed, such that the retarding energy is assumed to be constant.

[3] In this case in this work the duration of a subrun was drawn from the distribution until the total time was larger than $t_{\text{MTD}}(qU)$, leading to varying n in each subrun.

From that it follows for the subrun time scale (i.e. the first moment of the subrun duration frequency distribution $N(t_{\text{subrun}})$) [4]

$$T_{\text{subrun}} = \frac{1}{N_{\text{subrun}}} \sum_{qU}^{N_{\text{MTD}}} \sum_{i}^{n(qU)} t_{\text{subrun},i}(qU) \,, \tag{7.5}$$

$$= \frac{1}{\langle n \rangle_{qU} N_{\text{MTD}}} \sum_{qU}^{N_{\text{MTD}}} \langle t_{\text{subrun}} \rangle (qU) n(qU) \,, \tag{7.6}$$

$$= \frac{\langle \langle t_{\text{subrun}} \rangle (qU) n(qU) \rangle_{qU}}{\langle n \rangle_{qU}} \,, \tag{7.7}$$

$$= \frac{T_{\text{tot}}}{N_{\text{MTD}} \langle n \rangle_{qU}} \,. \tag{7.8}$$

The last step assumes exact convergence of the MTD of the generated runtime schedule to the input MTD. Expectedly, T_{subrun} scales anti-proportional to the average number of returns $\langle n \rangle_{qU}$.

Run time scale: The specification of $p_{qU}(t_{\text{subrun}})$ can be used to construct an unordered set of subruns. Regarding the time ordering, the division is between schedules using some ordering criterion on the subruns, or randomisation. In both cases the average $\langle n \rangle_{qU}$ returns to the subruns imply a time scale

$$T_{\text{run}} \equiv \frac{T_{\text{tot}}}{\langle n \rangle_{qU}} \,, \tag{7.9}$$

$$= N_{\text{MTD}} T_{\text{subrun}} \,. \tag{7.10}$$

The name *run* comes from the special case of monotonous ordering of the subruns with increasing/decreasing qU, with constant subrun duration $t_{\text{subrun},i} = \frac{t_{\text{MTD}}(qU)}{n}$ for each return, and with n independent from the retarding energy [5]. In this case the schedule is comprised of $\frac{n}{2}$ exact copies of up and down runs, which are usually called *scan*s.

While the time scale T_{run} has the same definition for both the ordered and randomised case, its interpretation is fundamentally different:

- Highly ordered schedules: In this case the inverse of T_{run} is the return frequency to a self-similar measurement, i.e. run or corresponding structure.
- Fully randomised schedules: In this case the inverse of T_{run} is the centre of a non-self-similar noise regime of the frequency response of the schedule.

To study the frequency response of the schedule to perturbations and thus these two regimes and their non-trivial transition independently from the measured spectrum, the proper way of analysis is correlation and Fourier analysis, which is discussed in section 7.1.2.

[4] Subtleties regarding these equations arise due to the dead time discussed in one of the following paragraphs.
[5] If n depends on qU, the probability of a subrun appearing in one of these ramps can be taken to be proportional to $n(qU)$.

It is expected that these analyses and the actual simulations show different regimes of the systematic shifts of the observables according to the found time scales.

Perturbation regimes: Depending on the size of the perturbation period T compared to T_{subrun} and T_{tot} the following regimes are expected [6]:

- $T \ll T_{\text{subrun}}$, averaging: In this case time dependencies are averaged. Perturbations can be considered by convolution of their distribution with the spectrum. In leading order only mean μ and variance σ^2 of these distributions are considered.

  In the case of energy scale perturbations the following leading order shifts are expected [7]:

$$\Delta m_\nu^2 = -2\sigma^2 \,, \qquad \Delta E_0 = \mu \,, \tag{7.11}$$

$$\Delta \sigma_{\text{g}}^2 = \sigma^2 \,, \qquad \Delta E_{\text{Main}} = \mu \,. \tag{7.12}$$

- $T \gg T_{\text{tot}}$, drifts and constant shifts: In this case the perturbation is either a drift, or even constant on the time scale of the measurement. Energy drifts lead to proportional shifts of E_0 and E_{Main}, and shifts of m_ν and σ_{g} due to correlations to the former.
- $T_{\text{subrun}} \leq T \leq T_{\text{tot}}$, non-trivial regime: This case results in systematics of the observables, which depend on the magnitude of ordering in the runtime schedule. Highly ordered schedules lead to resonant systematics, randomised schedules lead to noise.

Dead time: The ramping of the retarding energy between two set points $qU_0 \rightarrow qU_1$ needs the *dead time* $t_{\text{dead}}(qU_1, qU_0)$ and the counts recorded in this time are not included in the analysed data.

Accordingly, the total time is given by the measured time T_{meas} and the total dead time T_{dead} through

$$T_{\text{tot}} = T_{\text{meas}} + T_{\text{dead}} \,. \tag{7.13}$$

To avoid inconsistencies and to predict the correct regimes also the run time T_{run} and subrun time T_{subrun} have to contain the dead time, which is accomplished by adding the dead time following a subrun to the subrun time. Thus, by dividing equation 7.13 by the number of subruns N_{subrun}

$$T_{\text{subrun}} = \langle t_{\text{subrun}} \rangle + \langle t_{\text{dead}} \rangle \tag{7.14}$$

is obtained, where $\langle t_{\text{dead}} \rangle$ is the average dead time per subrun.

[6] This holds if the total data set is analysed in one stacked fit, i.e. if all recorded spectra are added before fitting. Also, constant phase velocity of the perturbation is assumed. Implications of non-predictable phase and different stacking methods are discussed in sections 7.3.4 and 7.3.5.

[7] The perturbations used in the following will usually be defined such that $\mu = 0$.

Schedule efficiency: The schedule efficiency ϵ_{eff}, i.e. the measured vs. the total time, is given by

$$\epsilon_{\text{eff}} \equiv \frac{T_{\text{meas}}}{T_{\text{tot}}} = 1 - \frac{T_{\text{dead}}}{T_{\text{tot}}} , \tag{7.15}$$

or equivalently

$$\epsilon_{\text{eff}} = \frac{\langle t_{\text{subrun}} \rangle}{T_{\text{subrun}}} = 1 - \frac{\langle t_{\text{dead}} \rangle}{T_{\text{subrun}}} . \tag{7.16}$$

7.1.2. Correlation Analysis of the Runtime Schedule

In the following correlation and Fourier analysis of the schedules is described, which allows to classify the schedules independently from their individual properties and to understand the simulated shifts in terms of spectral analysis.

Regions of interest: To study correlations of the Runtime Schedules, *Regions Of Interest* (ROIs) of the MTD are defined, which provide the sensitivity to the observables [8].

Only considering intervals between retarding energies qU_0 and qU_1 results in the definition

$$\text{ROI}_o = [qU_0, qU_1) \tag{7.17}$$

for the observable o. This allows to define a Boolean function $s_o(t)$ [9], specifying whether at a given time o is measured or not, i.e.

$$s_o(t) = 1 , \text{ if } qU(t) \in \text{ROI}_o , \text{ else } 0 . \tag{7.18}$$

Autocorrelation function: The *autocorrelation functions* are defined as [Kri15]

$$\text{Corr}_{oo}(\tau) \propto \int_0^T s_o(t) s_o(t+\tau) \mathrm{d}t , \tag{7.19}$$

specifying the similarity of the schedule $qU(0)$ to the τ-shifted schedule $qU(\tau)$ with regard to the measurement of o. It is bounded between 0 and 1, meaning no or full similarity of the measurement. It allows for the visualisation of the schedule over all time scales:

- T_{subrun}: The autocorrelation drops from the initial full similarity to the percentage of measurement time spend in the respective ROI.
- T_{run}: The autocorrelation shows order (peaks) versus randomisation (flat) of the schedule.
- T_{tot}: The autocorrelation linearly drops to 0 (logarithmically in the representation over $\log(\tau)$).

[8] Due to correlations of the observables the detailed choice is to some extent arbitrary, however the resulting analysis of the schedules' correlation does not strongly depend on it. The usage of ROIs is necessary to construct non-trivial autocorrelations, as defined in the following.

[9] In a more general approach without strict ROIs $s_o(t)$ is a continuous function between 0 and 1 specifying the sensitivity to a given observable at a given retarding potential, i.e. at a given moment in time.

These regimes are simplified, since for non-Gaussian subrun duration distributions the higher moments of the distribution are relevant and the autocorrelation function might show more structure especially on the subrun time scale (more than one drop or peaks). Also, the time scale were derived from the total frequency distributions of the subruns which disregards the ROIs, while actually the frequency distributions and thus the time scales are different for the observables. In the plots in the results section only the global time scales without ROIs are given, but the above qualitative understanding easily allows to relate the respective time scales in the autocorrelation functions to the given subrun duration distributions of the observables.

Spectral density: In the frequency domain the analogous quantity to the autocorrelation function is the *spectral density*. It is the squared absolute value of the Fourier transformation of the autocorrelation function [10] [SH08]

$$S_{oo}(\omega) = \left| \int_0^\infty \mathrm{Corr}_{oo}(\tau) e^{i\omega\tau} \mathrm{d}\tau \right|^2 . \tag{7.20}$$

The spectral density allows to predict the response of the schedule to frequencies f:

- *peaks* indicate resonant frequencies, leading to resonant shifts of the observables.
- *linear* portions of slope $-n$ in double logarithmic representation indicate $\frac{1}{f^n}$ noise components, leading to chaotic shifts of the observables, but of predictable envelope:
  - *White noise* ($n = 0$) has a constant envelope and is produced in randomised schedules.
  - *Brown noise* ($n = 2$) leads to an envelope decreasing with frequency and is globally expected due to the limited total measurement time and the overall linear decrease of the autocorrelation function.

Discrete calculations: For the case of boolean $s_o(t)$ they can be interpreted as a set of time intervals and the integrand in the calculation of the autocorrelation function (equation 7.19) is found by calculating intersections as shown in figure 7.3. The integral can be replaced by a summation over the resulting time intervals $I_i \in s_o(t) \cap s_o(t+\tau)$

$$\mathrm{Corr}_{oo}(\tau) \propto \sum_{I_i} s_o(t) \cap s_o(t+\tau) , \tag{7.21}$$

allowing for fast calculations.

Using the convolution theorem the spectral density can be calculated as

$$S_{oo}(0) \propto \frac{1}{4\pi^2} \left[\sum_{[t_0,t_1) \in s_o(0)} (t_1 - t_0) \right]^2 \tag{7.22}$$

[10] For finite schedules with total measurement time T_{tot} the autocorrelation function is always 0 for $\tau > T_{\mathrm{tot}}$, which cuts the upper integration limit.

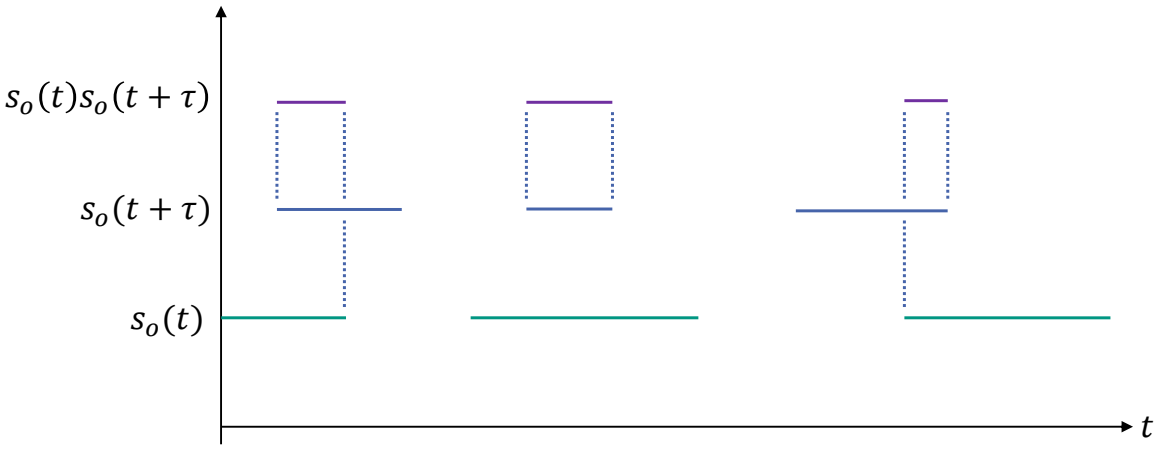

Figure 7.3.: Integrand of the autocorrelation function: For boolean $s_o(t)$ the integrand can be calculated by finding the overlap in time between $s_o(t)$ and $s_o(t+\tau)$.

and

$$S_{oo}(\omega) \overset{\omega\neq 0}{\propto} \frac{1}{(\omega\pi)^2}\left[\sum_{[t_0,t_1)\in s_o(0)} \cos\left(\frac{\omega}{2}(t_0+t_1)\right)\sin\left(\frac{\omega}{2}(t_1-t_0)\right)\right]^2 \tag{7.23}$$

$$+\frac{1}{(\omega\pi)^2}\left[\sum_{[t_0,t_1)\in s_o(0)} \sin\left(\frac{\omega}{2}(t_0+t_1)\right)\cos\left(\frac{\omega}{2}(t_1-t_0)\right)\right]^2 . \tag{7.24}$$

The following normalisations are used in this work:

$$\mathrm{Corr}_{oo}(0) = 1\,, \tag{7.25}$$

$$S_{m_\nu m_\nu}(0) = S_{\sigma_g\sigma_g}(0) = 1\,, \tag{7.26}$$

$$S_{E_0E_0}(0) = S_{E_{\mathrm{Main}}E_{\mathrm{Main}}}(0) = 10^{-7}\,. \tag{7.27}$$

The spectral densities of E_0 and E_{Main} have been shifted with regard to those of m_ν and σ_g for better visibility in the plots.

Bandwidth and structure: Since the time is limited by the total measurement time T_{tot}, the minimum structure size of the spectral density is on the order of $\frac{1}{T_{\mathrm{tot}}}$.

7.2. Semi-Analytical Implementation

Time dependent perturbations $\Delta\boldsymbol{x}(t)$ of the set of operating parameters $\boldsymbol{x}(t)$ can be separated from their mean values $\bar{\boldsymbol{x}}$ by

$$\boldsymbol{x}(t) = \bar{\boldsymbol{x}} + \Delta\boldsymbol{x}(t)\,. \tag{7.28}$$

The implemented shapes of the perturbations $\Delta\boldsymbol{x}(t)$ are discussed in section 7.2.2.

For a given subrun with starting time t_0 and end time t_1 at operating parameters $\boldsymbol{x}$, the observed counts N are given by

$$N(\boldsymbol{x}) = \int_{t_0}^{t_1} \frac{\mathrm{d}t}{\Delta T} \dot{N}\left(\boldsymbol{x}(t)\right) \Delta T \,, \tag{7.29}$$

where $\Delta T = t_1 - t_0$ is the measurement time of the subrun. Due to the Nyquist–Shannon sampling theorem the minimum number of sampling points for a direct numerical calculation scales with the frequency of the perturbation, such that direct calculations can only be carried out for small frequencies [11]. Calculations in all frequency regimes can be carried out using the method explained in the following.

7.2.1. Time Dependent Spectrum Calculations

In the following only the perturbation of one of the operating parameter x is considered [12]. If Δx_{max} is the maximum perturbation amplitude, the following expansion around the mean holds:

$$\begin{aligned} N(\boldsymbol{x}) &= \int_{t_0}^{t_1} \frac{\mathrm{d}t}{\Delta T} \dot{N}\left(\boldsymbol{x}(t)\right) \Delta T \,, \\ &= \Delta T \dot{N}(\bar{\boldsymbol{x}}) \sum_{n=0}^{\infty} \frac{1}{n!} \left.\frac{\mathrm{d}^n \dot{N}}{\mathrm{d}x^n}\right|_{\bar{\boldsymbol{x}}} \frac{\Delta x_{\mathrm{max}}^n}{\dot{N}(\bar{\boldsymbol{x}})} I_n \,, \\ &= \Delta T \dot{N}(\bar{\boldsymbol{x}}) \left(1 + \left.\frac{\mathrm{d}\dot{N}}{\mathrm{d}x}\right|_{\bar{\boldsymbol{x}}} \frac{\Delta x_{\mathrm{max}}}{\dot{N}(\bar{\boldsymbol{x}})} I_1 + \frac{1}{2} \left.\frac{\mathrm{d}^2 \dot{N}}{\mathrm{d}x^2}\right|_{\bar{\boldsymbol{x}}} \frac{\Delta x_{\mathrm{max}}^2}{\dot{N}(\bar{\boldsymbol{x}})} I_2 + \ldots\right) \,, \end{aligned} \tag{7.30}$$

with

$$I_n(t_0, t_1) = \int_{t_0}^{t_1} \frac{\mathrm{d}t}{\Delta T} \left(\frac{\Delta x(t)}{\Delta x_{\mathrm{max}}}\right)^n \,. \tag{7.31}$$

This expansion allows to separate the calculation of the time dependence I_n from the spectrum calculations $\frac{\mathrm{d}^n \dot{N}}{\mathrm{d}x^n}$. This is extremely beneficial if simple parametrisations for the I_n exist, for example if $\Delta x(t)$ is known analytically. In this case the calculation time for the I_n is independent of the perturbation time scale and can be carried out for all scales.

Derivatives: If other time and retarding potential derivatives are negligible the derivatives $\left.\frac{\mathrm{d}^n \dot{N}}{\mathrm{d}x^n}\right|_{\bar{\boldsymbol{x}}}$ do only need to be calculated once for each MTD bin.

The number of necessary terms n can be calculated by comparing the remainder terms to the Poisson uncertainty with demanded accuracy ϵ, leading to

$$\frac{1}{n!} \left|\left.\frac{\mathrm{d}^n \dot{N}}{\mathrm{d}x^n}\right|_{\bar{\boldsymbol{x}}}\right| \Delta x_{\mathrm{max}}^n T_{\mathrm{tot}} < \epsilon \sqrt{\dot{N}(\bar{\boldsymbol{x}}) T_{\mathrm{tot}}} \,, \tag{7.32}$$

[11] The time scale where full numerical calculations become unfeasible is in the regime of seconds, which is the relevant regime for non-trivial effects to occur.

[12] The general case can be implemented using the same method as described here, but needs to consider tensor formalism to store the necessary (mixed) derivatives and integrals.

where T_{tot} is the total measurement time. $\epsilon = 0.01$ has been used for all calculations, such that the uncertainty from the Taylor approximation on the counts in each bin of the MTD is 100 times smaller than the Poissonian uncertainty. The maximum allowed number of derivatives was limited to 7 and in all checked cases using 1 or 2 derivatives less than calculated by equation 7.32 did not affect the results.

The derivatives of the spectrum with regard to the energy E were calculated numerically using the noise-robust differentiator [Hol15]

$$\frac{\mathrm{d}\dot{N}(E)}{\mathrm{d}E} = \frac{2(\dot{N}(E+h) - \dot{N}(E-h)) + \dot{N}(E+2h) - \dot{N}(E-2h)}{8h} \,. \tag{7.33}$$

Higher derivatives were calculated by subsequent application of equation 7.33. Calculating the step size h following

$$h = 5 \text{ meV} + 0.04|E_0 - qU| \text{ (Tritium)} \,, \tag{7.34}$$

$$h = 80 \text{ meV} + 0.08|E_{\text{Main}} - qU| \text{ (Krypton)} \,, \tag{7.35}$$

yielded the best found results in terms of smoothness of the derivatives.

7.2.2. Perturbation Shapes

Different shapes of periodic fluctuations have been implemented. To cover the general case of single time scale perturbations a wide frequency spectrum between $10^{-10}\,\text{Hz} < f < 1\,\text{Hz}$ ($1\,\text{s} < T \lessapprox 300\,\text{y}$) is considered, which is 100 times larger than the maximum total data taking time of $\propto 3$ years and ten times smaller than realistic minimum subrun times of $\propto 10$ seconds. In this way all regimes are considered by using periodic functions and non-periodic drifts do not need to be implemented separately, since they are obtained in the regime $T \gtrsim T_{\text{tot}}$.

Sinusoidal shape: This analytical shape is used to calculate the systematics caused by a single frequency perturbation

$$\Delta x_{\text{sine}}(t) = \Delta x_{\text{max}} \sin(\omega(t - T_0) + \phi_0) \,. \tag{7.36}$$

The time integrals read

$$I_n(t_0, t_1) = \left(\frac{1}{2}\right)^n \frac{1}{\omega \Delta T} \sum_i^n \binom{n}{i} \begin{cases} n = 2i \,, & \omega \Delta T \,, \\ n \neq 2i \,, & \frac{1}{n-2i} \sin((n-2i)(\omega(t-T_0) - \frac{\pi}{2} + \phi_0))\Big|_{t_0}^{t_1} \end{cases} \,. \tag{7.37}$$

Periodic continuation: This shape is used to calculate the response to perturbations composed of discrete frequencies. Using the phase

$$\phi(t) = \frac{\omega(t - T_0) + \phi_0}{2\pi} \,, \tag{7.38}$$

the perturbation can be defined by periodic continuation

$$x(t) = \Delta x_{\max} R\left(\phi(t) - \lfloor \phi(t) \rfloor\right) \,, \tag{7.39}$$

where $R(\phi)$ is an arbitrary function defined in the interval $[0, 1)$ and $\lfloor \cdot \rfloor$ is the floor function.

The integrals read

$$I_n = \frac{1}{n+1} \frac{2\pi}{\omega \Delta T} \left[R_n\left(\phi - \lfloor \phi \rfloor\right)\Big|_{\phi_0}^{\phi_1} + \operatorname{trunc}(\phi)\Big|_{\phi_0}^{\phi_1} R_n(\phi)\Big|_0^1 \right] \,, \tag{7.40}$$

with R_n being the nth antiderivative of R and trunc(.) the truncation function.

Sawtooth wave: The definition

$$R_n(\phi) = \frac{1}{2}(2\phi - 1)^{n+1} + \frac{1}{2} \tag{7.41}$$

results in a sawtooth perturbation

$$\Delta x_{\text{sawtooth}}(t) = \Delta x_{\max}(\phi(t) - \lfloor \phi(t) \rfloor) \,, \tag{7.42}$$

whose rich Fourier spectrum

$$\Delta x_{\text{sawtooth}}(t) \propto \sum (-1)^k \frac{\sin(2\pi k f t)}{k} \tag{7.43}$$

is used to probe the response of the schedule to composed frequencies.

RMS values: The *root mean square* values are

$$\sigma_{\text{RMS}}(\Delta x_{\text{sine}}) = \frac{\Delta x_{\max}}{\sqrt{2}} \,, \tag{7.44}$$

$$\sigma_{\text{RMS}}(\Delta x_{\text{sawtooth}}) = \frac{\Delta x_{\max}}{\sqrt{3}} \,. \tag{7.45}$$

Using equations 7.11 and 7.12, for energy scale perturbations of amplitude A in the averaging regime

$$\text{sine} : \sqrt{\Delta m_\nu^2} = -A \,, \qquad \sqrt{\Delta \sigma_{\text{g}}^2} = \frac{A}{\sqrt{2}} \,, \tag{7.46}$$

$$\text{sawtooth} : \sqrt{\Delta m_\nu^2} = -\sqrt{\frac{2}{3}} A \,, \quad \sqrt{\Delta \sigma_{\text{g}}^2} = \frac{A}{\sqrt{3}} \,, \tag{7.47}$$

are expected [13].

[13] To allow negative square roots, $\sqrt{\ldots} = \operatorname{sgn}(\ldots)\sqrt{|\ldots|}$ is used, where sgn(...) is the signum function.

7.3. Results and Discussion

In the following the results of the studies are discussed. Section 7.3.1 discusses input parameters that are used for the studies and the result figures, which are used to present the results. The systematic shifts caused by sinusoidal fluctuations of the energy scale in ordered and randomised schedules is discussed in section 7.3.2. In section 7.3.3 the response to sawtooth fluctuations is discussed. Due to the contained integer harmonics this allows to investigate the linear combination of systematics. In section 7.3.4 it is shown that the results on order vs. randomisation can be understood in terms of coherence or decoherence of fluctuation phase and subrun starting time.

On run time scale, the separation into coherent and decoherent measurements allows to analytically derive the scaling of the systematics with perturbation amplitude and schedule return number, which is shown in section 7.3.5. Finally, section 7.3.6 gives the combined statistical and systematic uncertainty for the KNM2 tritium measurement with regard to possible run time scale fluctuations.

The results were cross checked [14] with an independent code using both the Taylor expansion described in section 7.2 and full numeric evaluation on the time scales, where this is possible. The results of all methods and codes are in agreement. Studies were performed both on the tritium and the krypton spectrum leading to equivalent results.

7.3.1. Input Parameters and Result Figures

In the following the premises for the studies as well as the figures used to visualise them are described.

Simulated data and resolution: Asimov spectra (cf. section 1.2.1) were simulated for $N = 10^4$ sinusoidal fluctuations with frequencies between $f_{\text{min}} = 10^{-10}$ Hz and $f_{\text{max}} = 1$ Hz. The frequencies were uniformly distributed on a logarithmic frequency scale according to

$$f_n = \frac{f_{\text{max}}}{r^n}\,,\quad r \equiv \left(\frac{f_{\text{max}}}{f_{\text{min}}}\right)^{\frac{1}{N-1}}\,,\quad n \in \{0, ..., N-1\}\,, \tag{7.48}$$

where $r \approx 1.0023$ for the given values.

This leads to constant relative time and frequency resolutions

$$R_f \equiv \frac{f_n - f_{n+1}}{f_n} = \frac{r-1}{r} \approx 2.3 \cdot 10^{-3}\,, \tag{7.49}$$

$$R_t \equiv \frac{\frac{1}{f_{n+1}} - \frac{1}{f_n}}{\frac{1}{f_n}} = r - 1 \approx 2.3 \cdot 10^{-3}\,. \tag{7.50}$$

Thus, the detection of structures of a width smaller than $R_f f_n$ in frequency domain is suppressed in the following studies. The smallest possible width is given by $\frac{1}{T_{\text{tot}}}$, such

[14] Many thanks to Ferenc Glück.

that structures caused by this scale are suppressed on run time scale, if $T_{\text{run}} < R_t T_{\text{tot}}$ and likewise on subrun time scale. As a consequence, especially on subrun time scale not all features might be visible in the following plots. To detect all structures on scale $\frac{1}{T_{\text{tot}}}$ over the whole frequency range, the number of points needs to be increased by four orders of magnitude which was unfeasible, since for the chosen N the calculation time was already in the range of one hour.

Fit: The fit of each spectrum was performed using ROOT::*Minuit* and the standard four parameter analysis, with fit parameters (m_ν^2, E_0, background, signal) in case of tritium and (σ_{g}^2, E_{Main}, background, signal) in case of krypton.

Campaigns considered: The following studies are modelled after the KNM2 krypton and tritium measurements.

Count rate: The rate of the spectra was modelled to fit to the measurements by using 84 % of nominal column density for KNM2 tritium and 190 kcps rate on the L_3 plateau for KNM2 krypton. The rate is relevant for the normalised χ^2 since shifts of the observables are detectable, if the χ^2 significantly differs from 0.

Result figures: Figures of the kind of 7.6 and 7.7 are exemplary for the visualisations of the tested schedules and the results in all studies. The left side 7.6 shows the schedule and the subrun duration histogram in time domain, in the inset of the schedule the autocorrelation function is shown. The right side 7.7 shows the fit results (the square root is taken for Δm_ν^2 and $\Delta\sigma_{\text{g}}^2$) over the fluctuation frequency together with the χ^2 and the spectral density of the schedule in frequency domain. This allows to relate patterns in the fit results directly to patterns in the spectral density.

Perturbations of operating parameters considered: Only perturbations of the energy scale

$$x(t) = E(t) = \bar{E} + \epsilon(t) \tag{7.51}$$

were considered, which can be caused by fluctuations of the retarding energy or the starting energy. It is conceivable that derivatives of the spectrum to other operating parameters produce less severe effects than derivatives of the energy scale.

Region of interest and MTDs: The KNM2 measurement MTDs for krypton and tritium were used. For tritium the lower bound of the MTD was restricted to 40 eV below the endpoint, which is the usual analysis interval. In krypton only 10 eV below the line mean was included, such that scattering effects were not considered.

The sensitive regions of peak-like MTDs are described in [Kle14]. Accordingly, the ROIs where picked to be

$$\mathrm{ROI}_{m_\nu} = [-20, 0)\ \mathrm{eV}\,, \tag{7.52}$$
$$\mathrm{ROI}_{E_0} = [-40, -20)\ \mathrm{eV}\,, \tag{7.53}$$

for the KNM2 tritium schedule.

Due to the flat MTD the definitions used for krypton are arbitrary and both ROIs are equivalent.

$$\mathrm{ROI}_{\sigma_g} = [-7, 1)\ \mathrm{eV}\,, \tag{7.54}$$
$$\mathrm{ROI}_{E_{\mathrm{Main}}} = [-4, -1)\ \mathrm{eV}\,, \tag{7.55}$$

were used.

Total measurement time and number of returns: The total measurement time T_{tot} of the KNM2 tritium golden run list was 33 days, consisting of 361 runs.

For the krypton measurements 20 runs were used, each with a run time of roughly half an hour, leading to a total measurement time of 8 hours. This approximates the measurements taken at a rear wall voltage of $U_{\mathrm{RW}} = 200$ mV. Other rear wall voltages were measured less often, but the total time was usually on the scale of some hours.

Dead time: The performance of the high voltage system in the KNM2 measurements was considered. The dead times only depended on the difference $\Delta qU = qU_1 - qU_0$ and can be modelled as second order polynomial [Rod20]

$$\frac{t_{\mathrm{dead}}(\Delta qU)}{\mathrm{s}} = a + b\frac{\Delta qU}{\mathrm{eV}} + c\left(\frac{\Delta qU}{\mathrm{eV}}\right)^2\,, \tag{7.56}$$

with

$$\mathrm{KNM2, T_2}: a = 32.27 \pm 0.936\,,\ b = -0.045 \pm 0.012\,,\ c = 0.00042 \pm 0.00011\,, \tag{7.57}$$
$$\mathrm{KNM2, Kr}: a = 19.10 \pm 0.711\,,\ b = -0.805 \pm 0.191\,,\ c = 0.5135 \pm 0.1176\,. \tag{7.58}$$

The means and uncertainties were used as mean and standard deviation of Gaussians, such that the dead time calculation obeys randomness, which mimics the true performance.

Fluctuation amplitude: The amplitude of the sine is fixed to 50 meV for the following results, which is the requirement from the KATRIN design report [KAT04b]. The scaling of the shifts with the amplitude is discussed in section 7.3.5.

7.3.2. Systematics for Sinusoidal Perturbations in Ordered and Randomised Schedules

The following pages show four different scenarios both for tritium and krypton, focusing on the effects of ramping vs. randomisation. The presented results include increasing randomness, as shown in figure 7.4:

- Ramping back and forth, subrun duration distribution from MTD (as used in the measurement),
- Random order, subrun duration distribution from MTD,
- Randomised subrun duration distribution, ramping back and forth,
- Randomised subrun duration distribution, random order.

Ramping: The ramp schedules show that resonant shifts of the observables occur at the time scale of scans and its harmonics. A zoom on the resonance at scan time in figure 7.7 is shown in figure 7.5. It shows that the first moment description of $T_{\text{scan}} = 2T_{\text{run}}$ perfectly predicts the resonances, despite the random dead time and non-trivial subrun duration distribution.

Randomisation: In the randomised schedules random noise appears over the whole non-trivial frequency regime. While the detailed features are different, the appearance of noise instead of peaks does not depend on whether the subrun length distribution or the return order is randomised. To access the noise amplitude, the standard deviations of 1000 shifts (one order of magnitude in frequency) centred around the run time scale are calculated.

Shift in the averaging regime: Overall the shifts observed in the averaging regime agree with the expectation equation 7.46. However, in detail the shift near $f = 1$ Hz consistently shows fluctuations towards some meV smaller values than the leading order prediction, both for krypton and tritium.

Mean shift on run time scale: On run time scale the observables also show a non-vanishing mean shift. For the endpoint and line position it is on the sub millivolt level for the tested amplitudes and presumably a result of higher order effects.

For the neutrino mass and Gaussian broadening in the ordered case it is approximately given by the expectation of the averaging regime. In the randomised case it is on this order, but there are larger discrepancies.

Total time scale shifts: In both cases for fluctuations on the time scale of the total duration of the measurement a wave pattern is observed. As visible in the shifts of E_0 and E_{Main} this is directly linked to the average energy shift of the fluctuation in the schedule. Given the fluctuation period T, the average vanishes for integer multiples $T_{\text{tot}} = nT$.

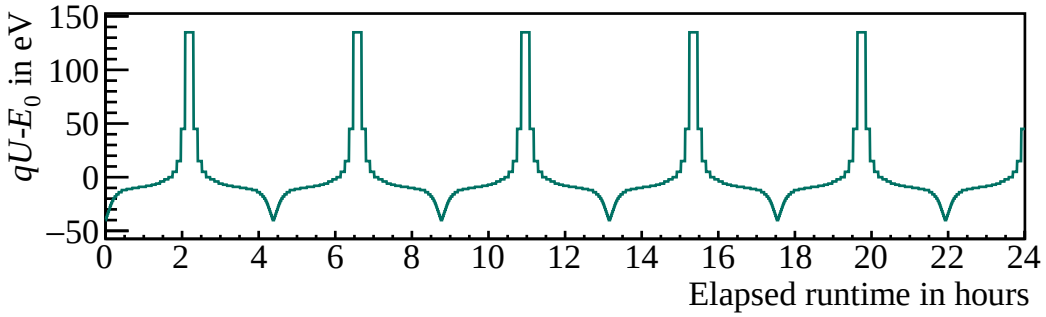

(a) Ramping, subrun duration distribution from MTD

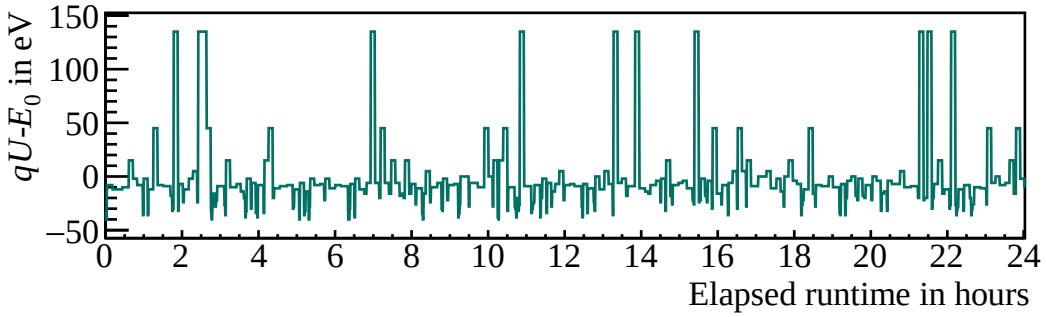

(b) Random order, subrun duration distribution from MTD

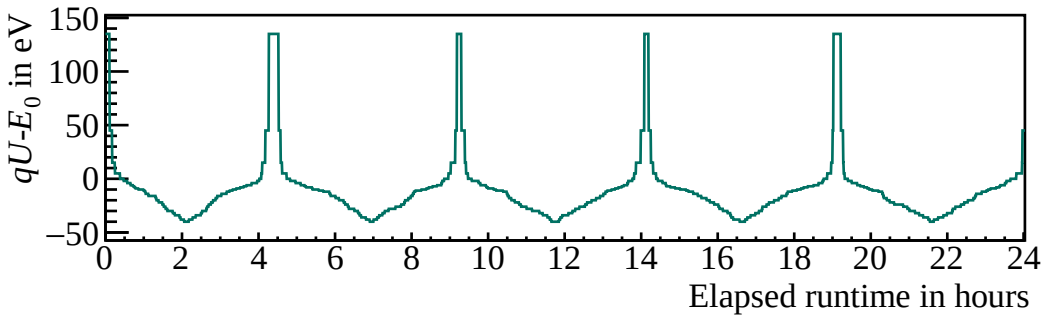

(c) Randomised subrun duration distribution, ramping

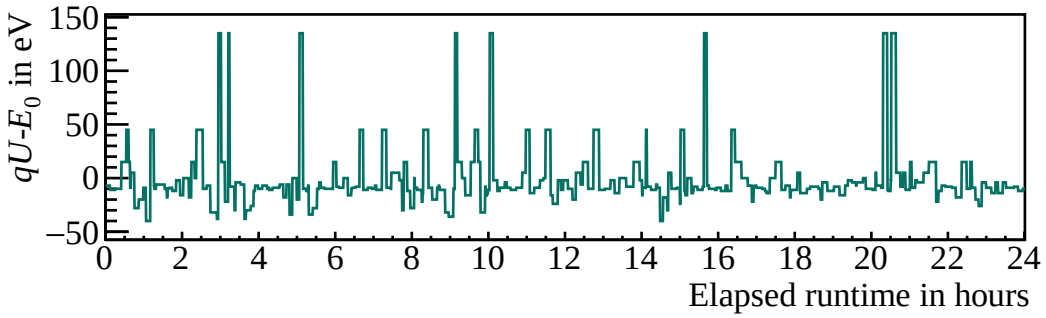

(d) Randomised subrun duration distribution, random order

Figure 7.4.: Retarding energy over time for different schedules: in (a) the subruns are ordered and their duration is picked according to the MTD and the run number. (b) is obtained by randomising the subrun order from (a). In (c) the subruns are ordered and their duration is randomised. (d) is obtained by randomising the subrun order from (c).

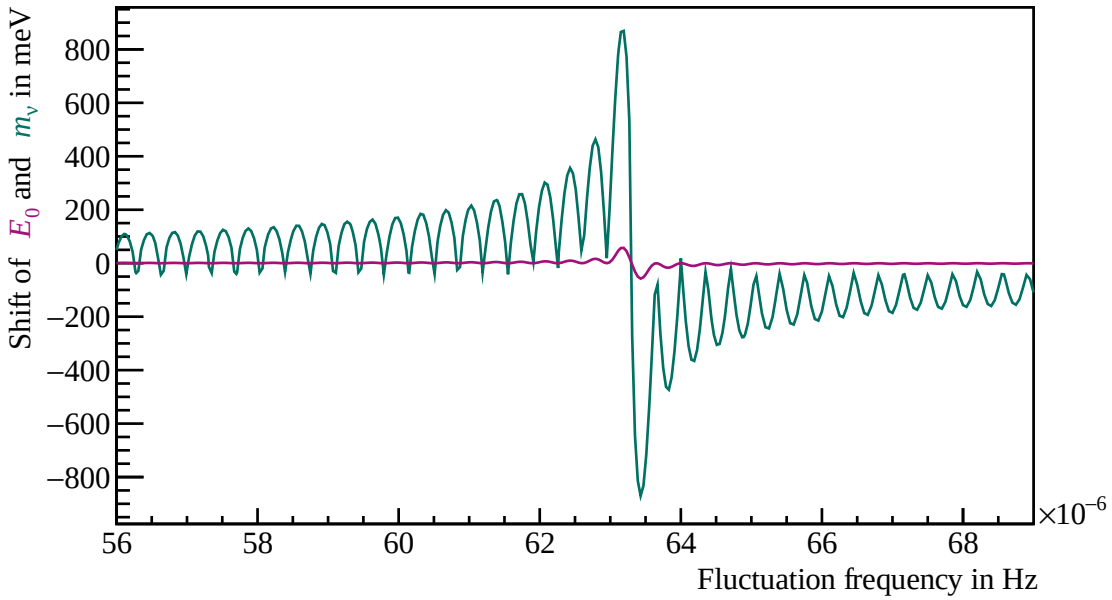

Figure 7.5.: Zoom on scan time resonance in ordered schedule: The scan time of the simulated ramp schedule was $T_{\text{scan}} = 15796$ s, leading to the fundamental resonance frequency $\frac{1}{T_{\text{scan}}} = 63.3 \cdot 10^{-6}$ Hz, which perfectly fits the simulation. The width of the shown periodic structure is exactly given by $\frac{1}{T_{\text{tot}}}$.

Krypton versus tritium: The simulations show equivalent results for krypton and tritium. In the case of krypton, however, it is likely that systematics of this size would be detected in a raised normalised χ^2, which is only rarely possible in the case of tritium. To test the available krypton data for run time scale fluctuations a stacked fit of the available runs has to be performed [15]. The significantly raised χ^2 in the stacked uniform approach of this simulation might not be detectable in pixel or ring fits, which have a factor of $n_{\text{pixels}} \approx 117$ or $n_{\text{rings}} \approx 12$ fewer counts.

[15] The usual analysis performed for krypton does not use stacking of the pixel or ring wise results to uniform fits. Also, all runs are analysed separately.

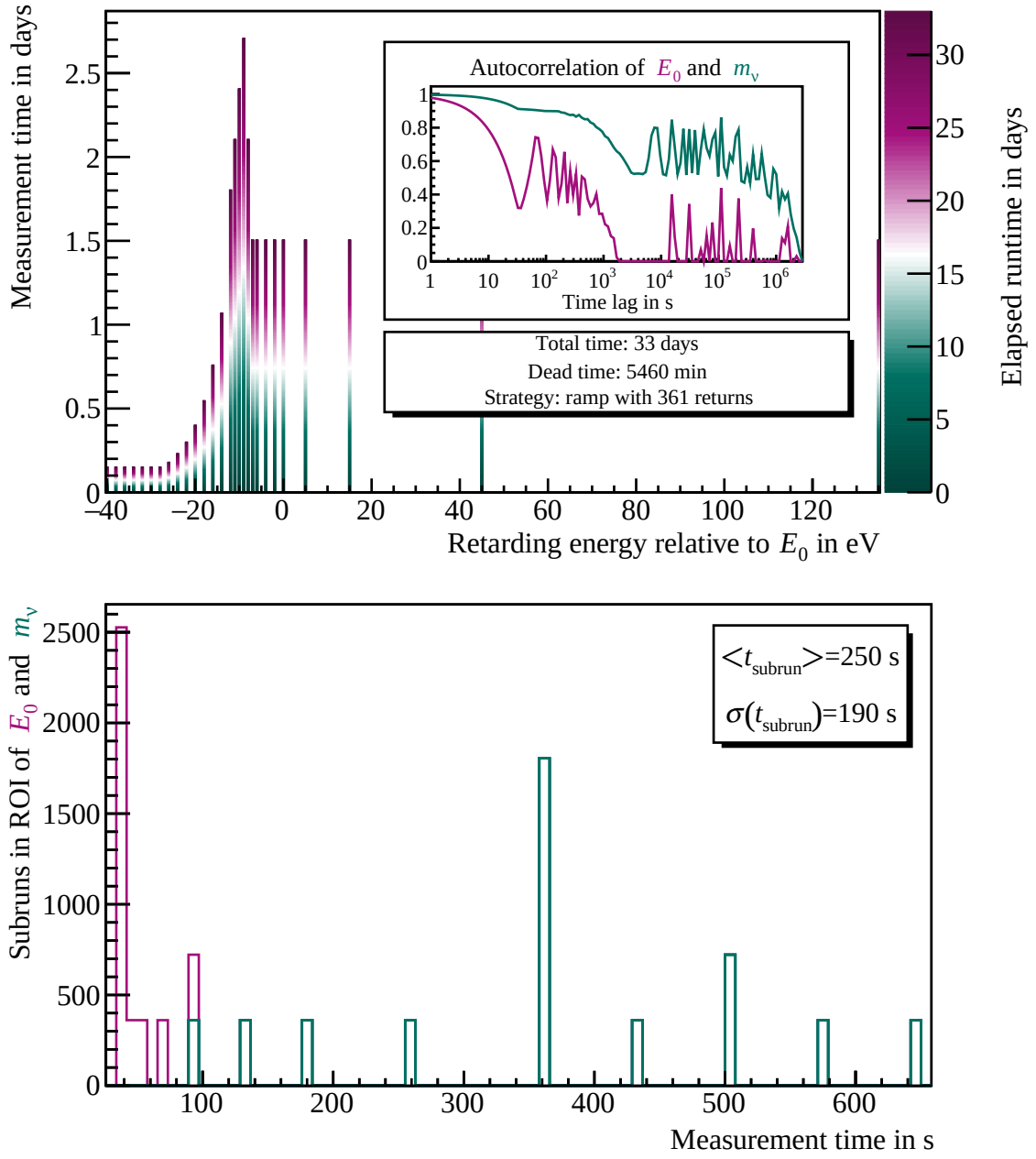

Figure 7.6.: KNM2 tritium schedule, ramping: The plotted scenario approximates the performed measurement in KNM2. 361 runs are in the golden runlist, and the measurement was performed in up and down ramps. The mean measured set time of the high voltage is included. The ramps are visible in the autocorrelation function.

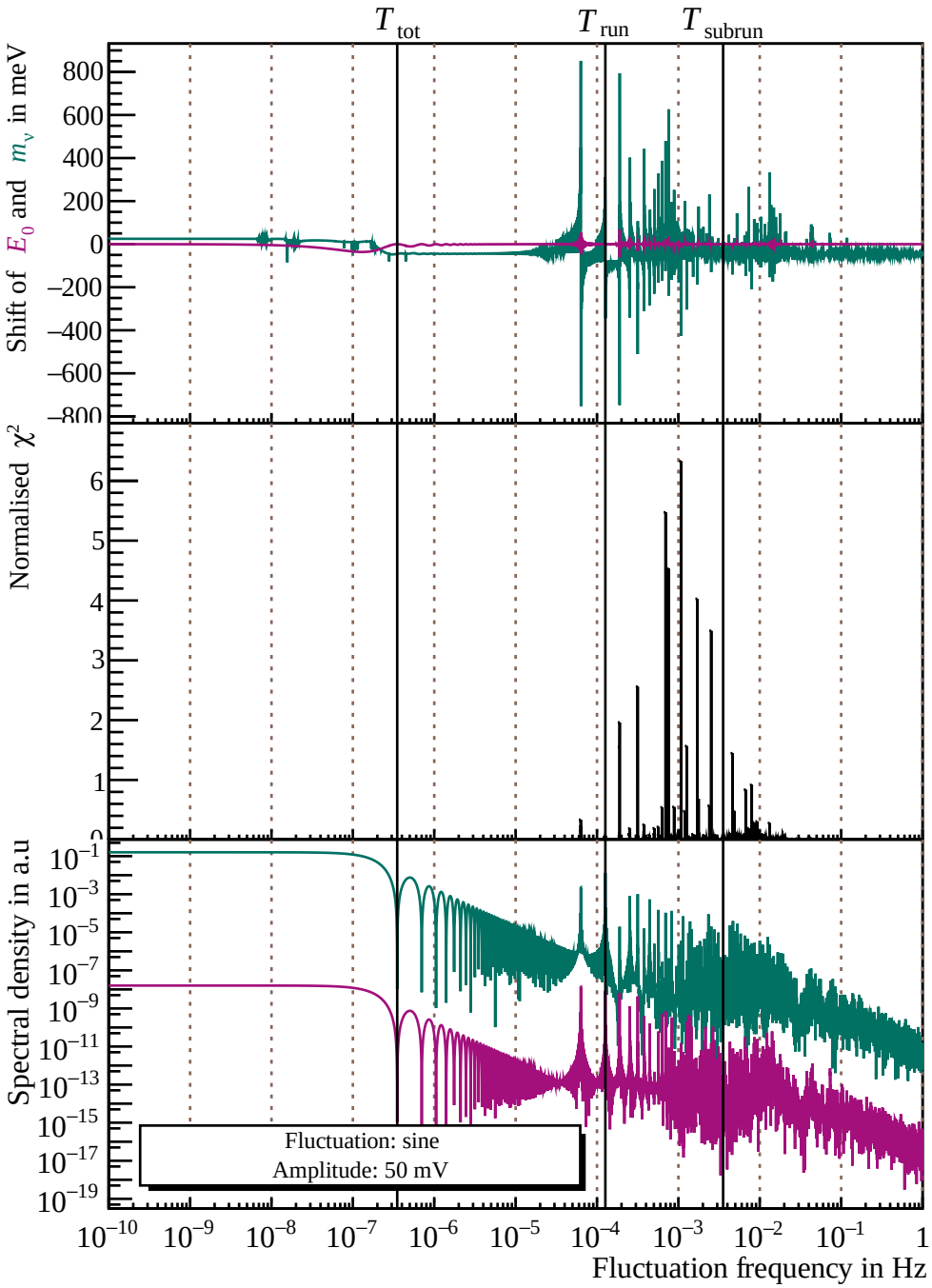

Figure 7.7.: KNM2 tritium systematics, ramping: In the non-trivial regime peaks in the several 100 meV range appear in the neutrino mass shift, which are mostly not detectable in a raised normalised χ^2. The peaks are related to peaks in the spectral density, appearing above the frequency $\frac{1}{2T_{\text{run}}}$ corresponding to one scan.

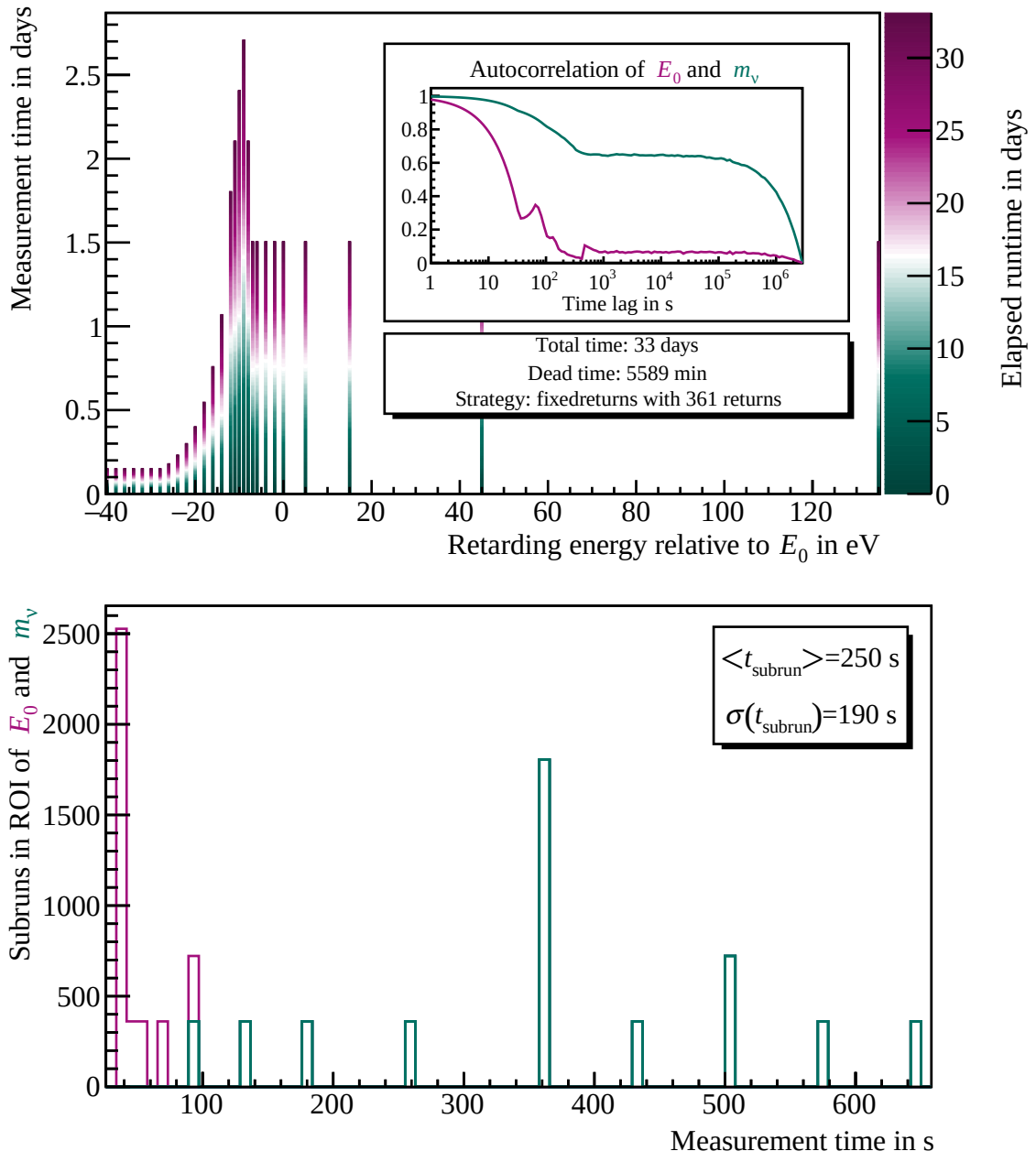

Figure 7.8.: KNM2 tritium schedule, random order: In this scenario the ordering of the retarding energies is randomly distributed, resulting in a slightly raised dead time due to high voltage setting. The structure in the autocorrelation function mostly disappears.

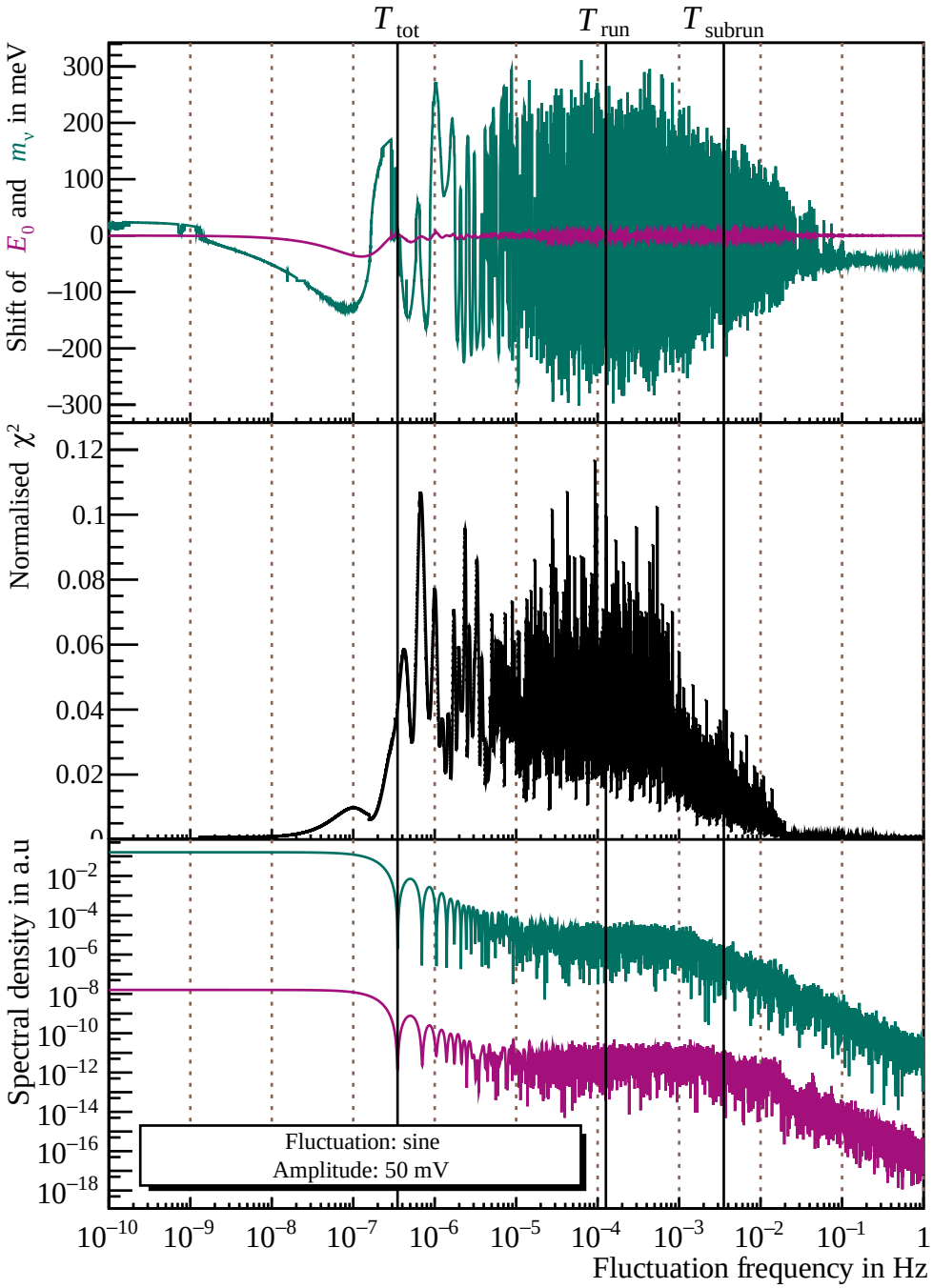

Figure 7.9.: KNM2 tritium systematics, random order: The peaks visible in the ramp measurements get smeared over a broad range of frequencies. The systematics are in no case detectable in the normalised χ^2. The standard deviations on run time scale are $\sqrt{\sigma(m_\nu^2)} \approx 164$ meV and $\sigma(E_0) \approx 2.3$ meV.

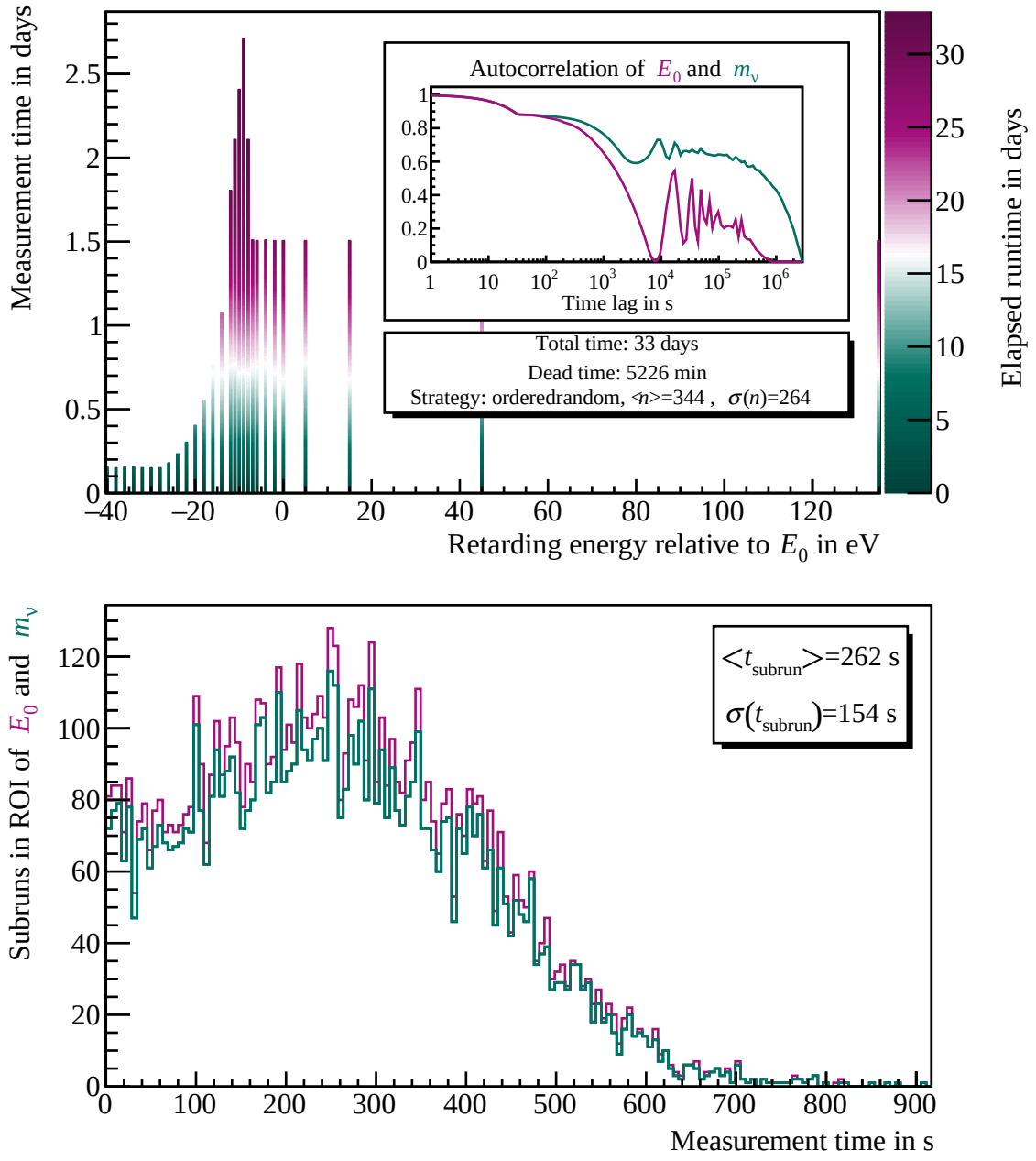

Figure 7.10.: KNM2 tritium schedule, ramping, randomised subrun duration: In this scenario the subrun duration is randomly picked from a Gaussian with comparable moments as before, while the ordering still obeys an up and down ramping pattern. However, since each of the small bins near -40 eV only makes up $\approx$ 5 h each, they get filled already after $\frac{5\text{ h}}{\langle t_{\text{subrun}}\rangle\langle n\rangle} \approx 20$ % of the total runtime.

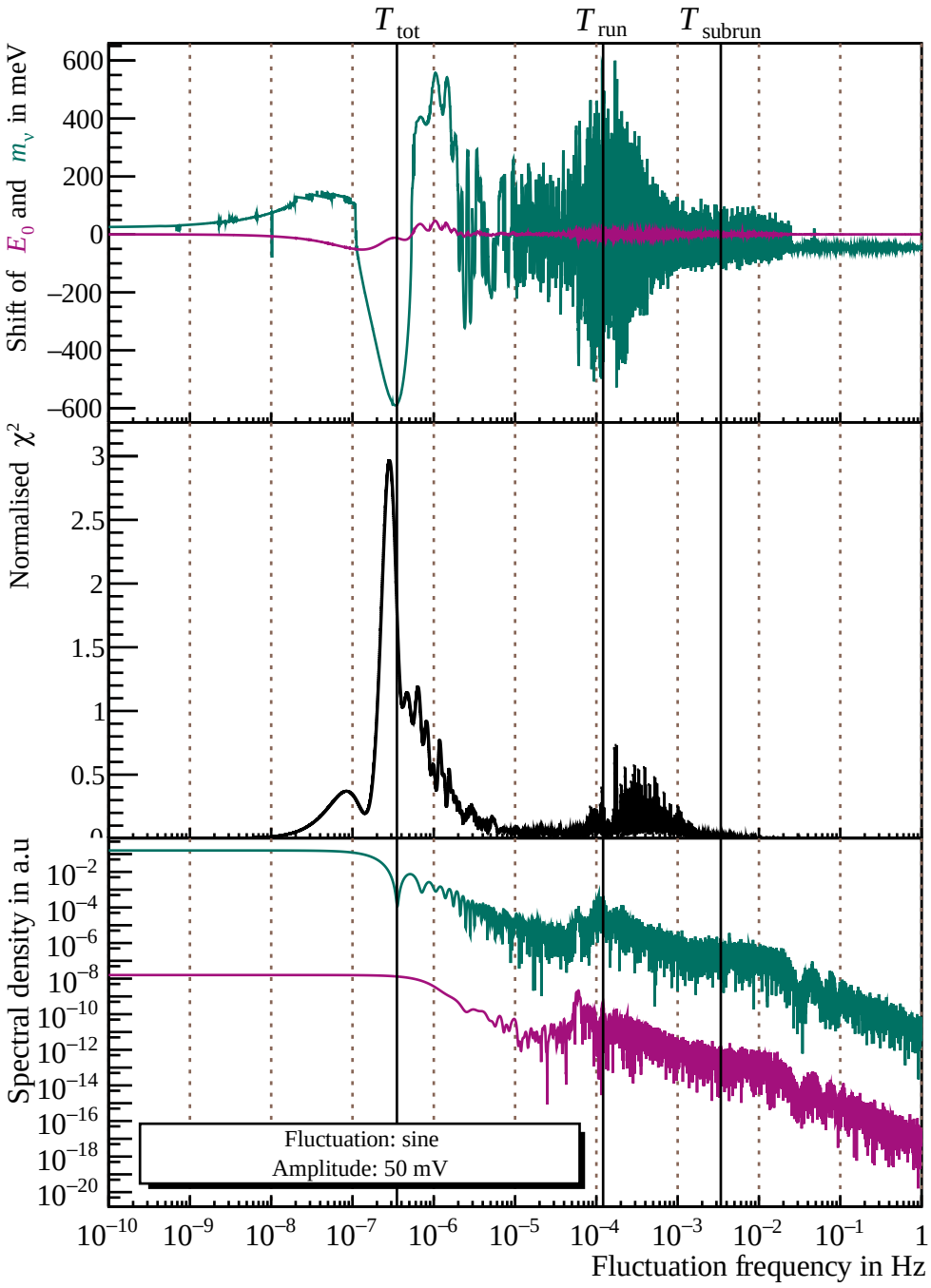

Figure 7.11.: KNM2 tritium systematics, ramping, randomised subrun duration: On run times scale increased noise can be observed, which is related to an excess of the spectral density in this region, caused by the ramping. Outside this region the noise is lower in amplitude. The standard deviations on run time scale are $\sqrt{\sigma(m_\nu^2)} \approx 287$ meV and $\sigma(E_0) \approx 8.0$ meV.

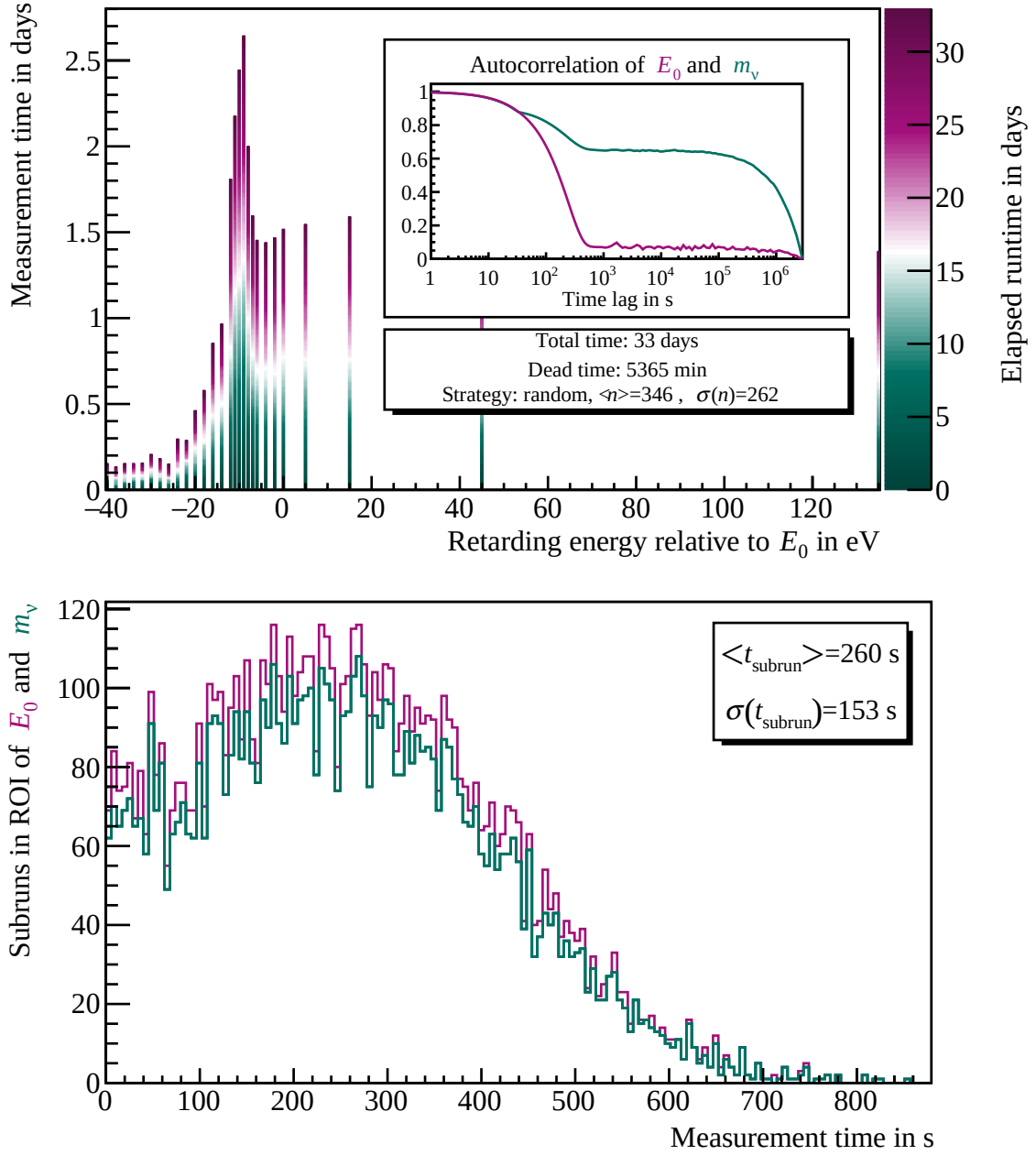

Figure 7.12.: KNM2 tritium schedule, random order, randomised subrun duration: In this scenario the duration of the subruns is randomly picked as before, and additionally the subrun order is randomised. The randomisation of the subrun duration is clearly visible in the frequency distribution, but other than removing some structures, the autocorrelation functions are very comparable to the ones without subrun duration randomisation.

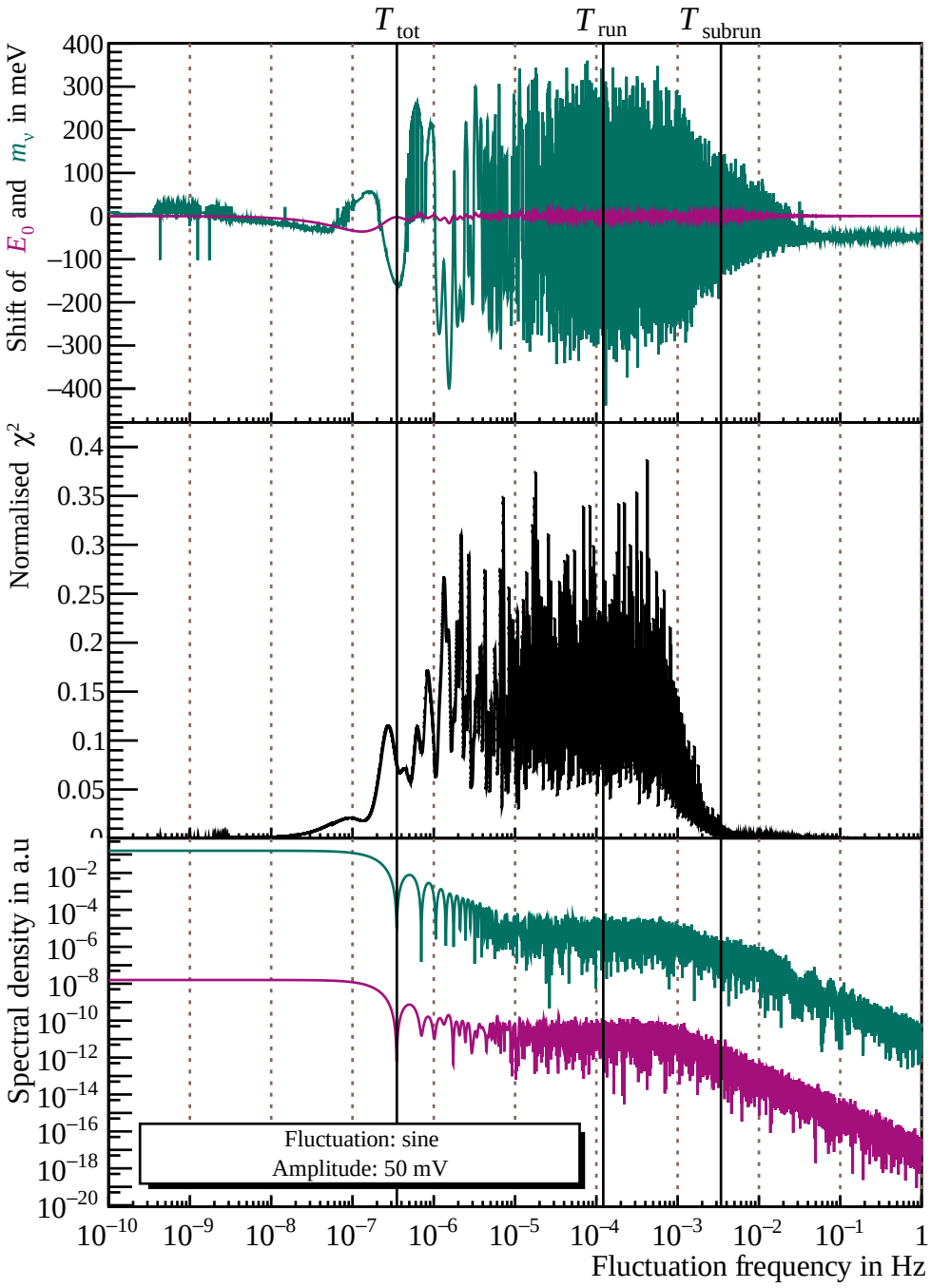

Figure 7.13.: KNM2 tritium systematics, random order, randomised subrun duration: Compared to only randomising the order of the subruns, also using a random subrun duration distribution only has minor effects on the spectral density, the systematic shifts and the χ^2. The standard deviations on run time scale are $\sqrt{\sigma(m_\nu^2)} \approx 209$ meV and $\sigma(E_0) \approx 4.0$ meV.

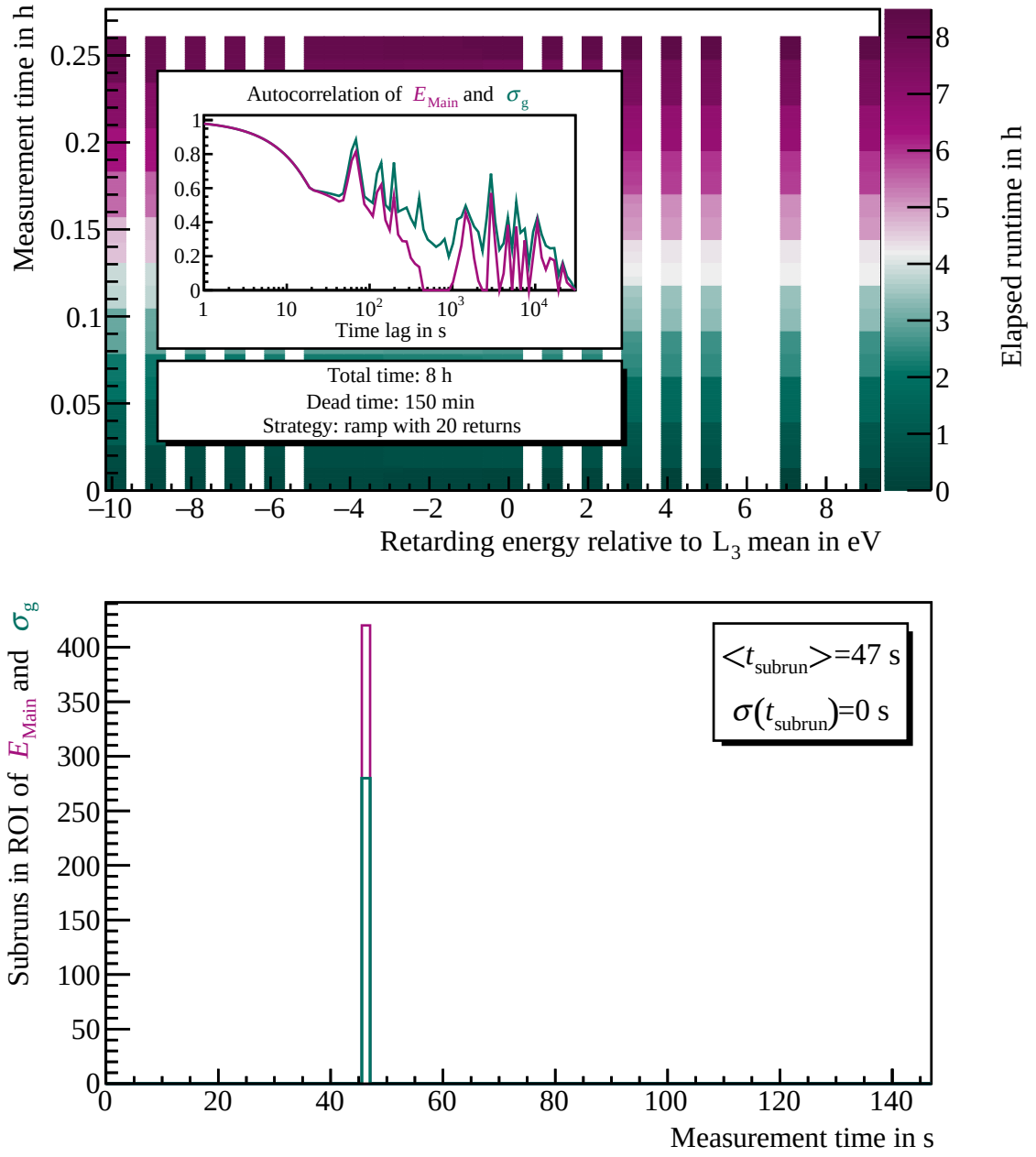

Figure 7.14.: KNM2 krypton schedule, ramping: The plotted scenario approximates the performed measurement in KNM2 at $U_{\mathrm{RW}} = 200$ mV. On the order of 20 runs were taken, and the measurement was performed in up and down ramps. The mean measured set time of the high voltage is included.

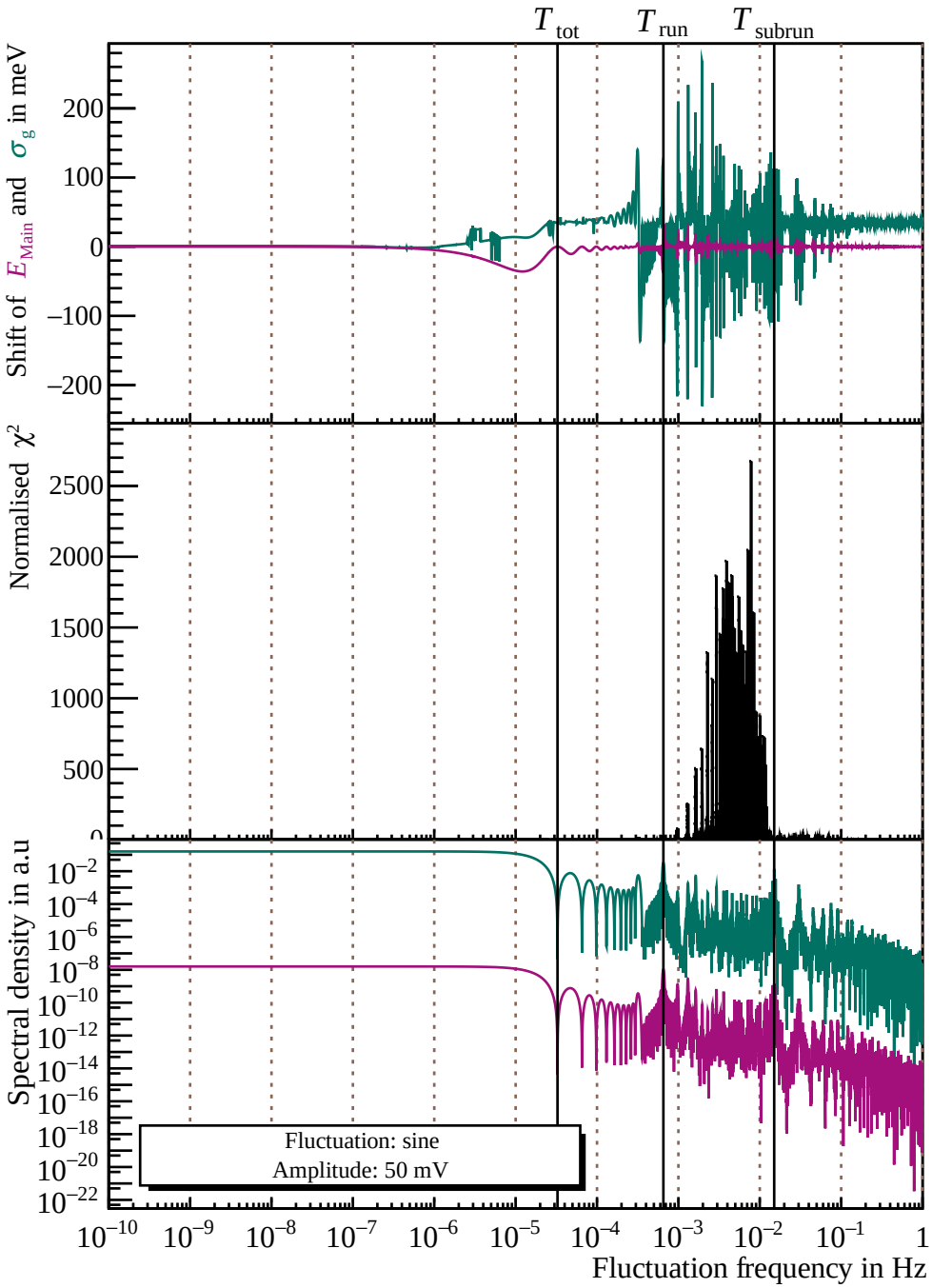

Figure 7.15.: KNM2 krypton systematics, ramping: In the non-trivial regime peaks in the few 100 meV range appear in the line broadening. In contrast to tritium, they will be detectable in a raised normalised χ^2. The peaks are related to peaks in the spectral density, appearing above the frequency $\frac{1}{2T_{run}}$ corresponding to one scan.

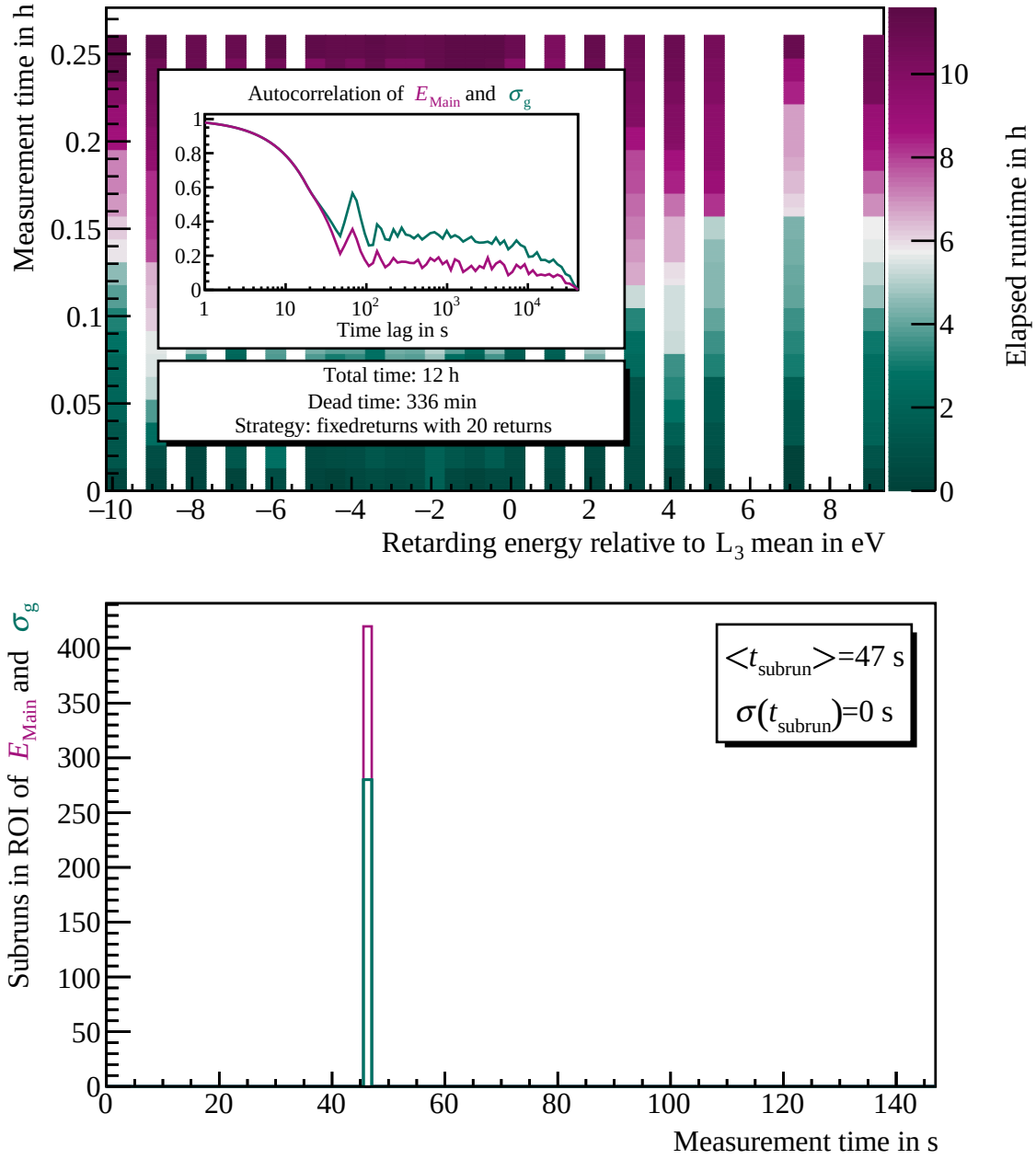

Figure 7.16.: KNM2 krypton schedule, random order: In this scenario the ordering of the retarding energies is randomly distributed, resulting in more than double the dead time due to high voltage setting.

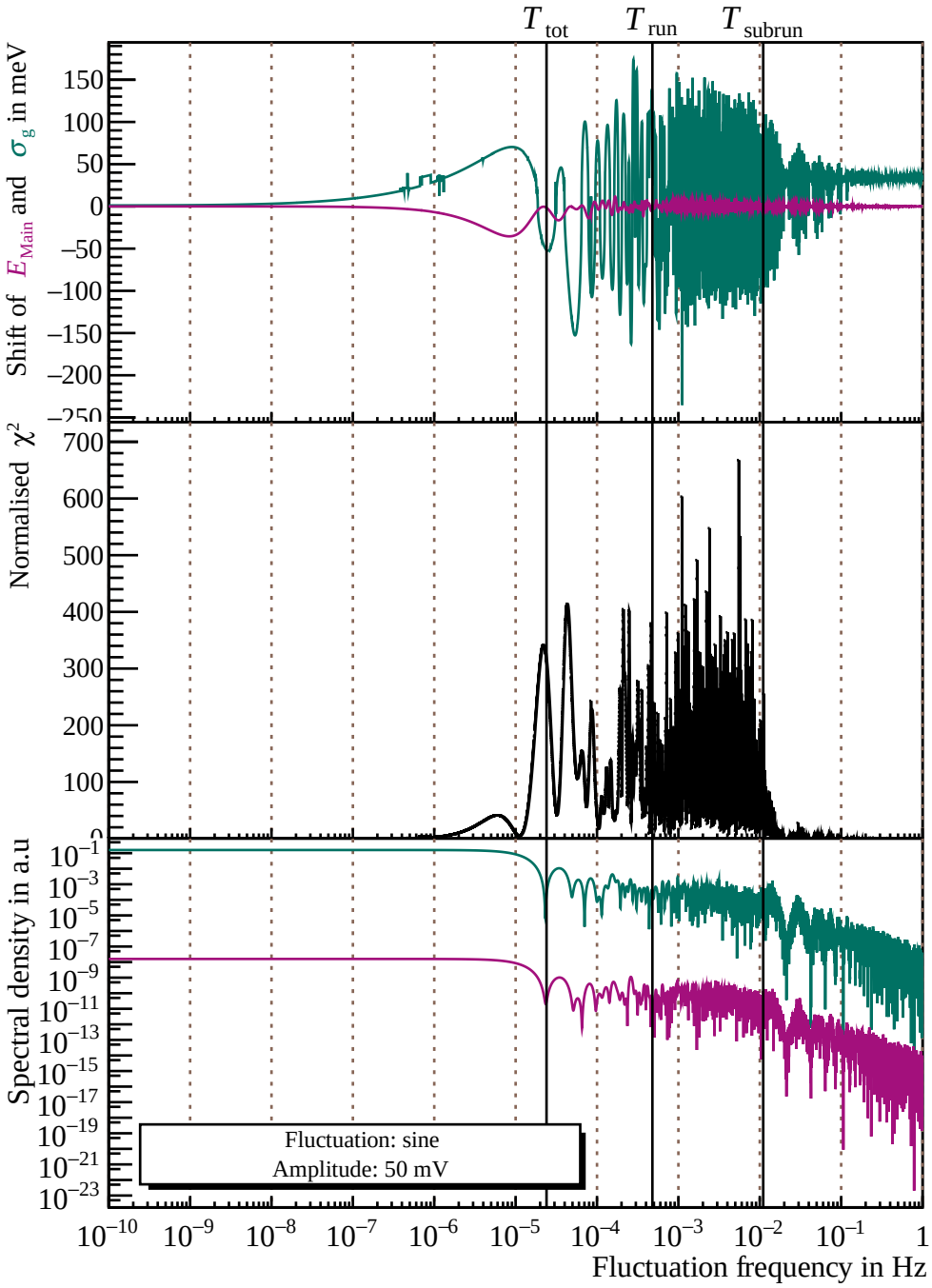

Figure 7.17.: KNM2 krypton systematics, random order: The peaks visible in the ramp measurements get smeared over a broad range of frequencies. Again, in contrast to the tritium β spectrum the systematics are most likely detectable in the normalised χ^2. The standard deviations on run time scale are $\sqrt{\sigma(\sigma_{\text{g}}^2)} \approx 99$ meV and $\sigma(E_{\text{Main}}) \approx 3.7$ meV, which is too large compared to the requirement of 20 meV precision.

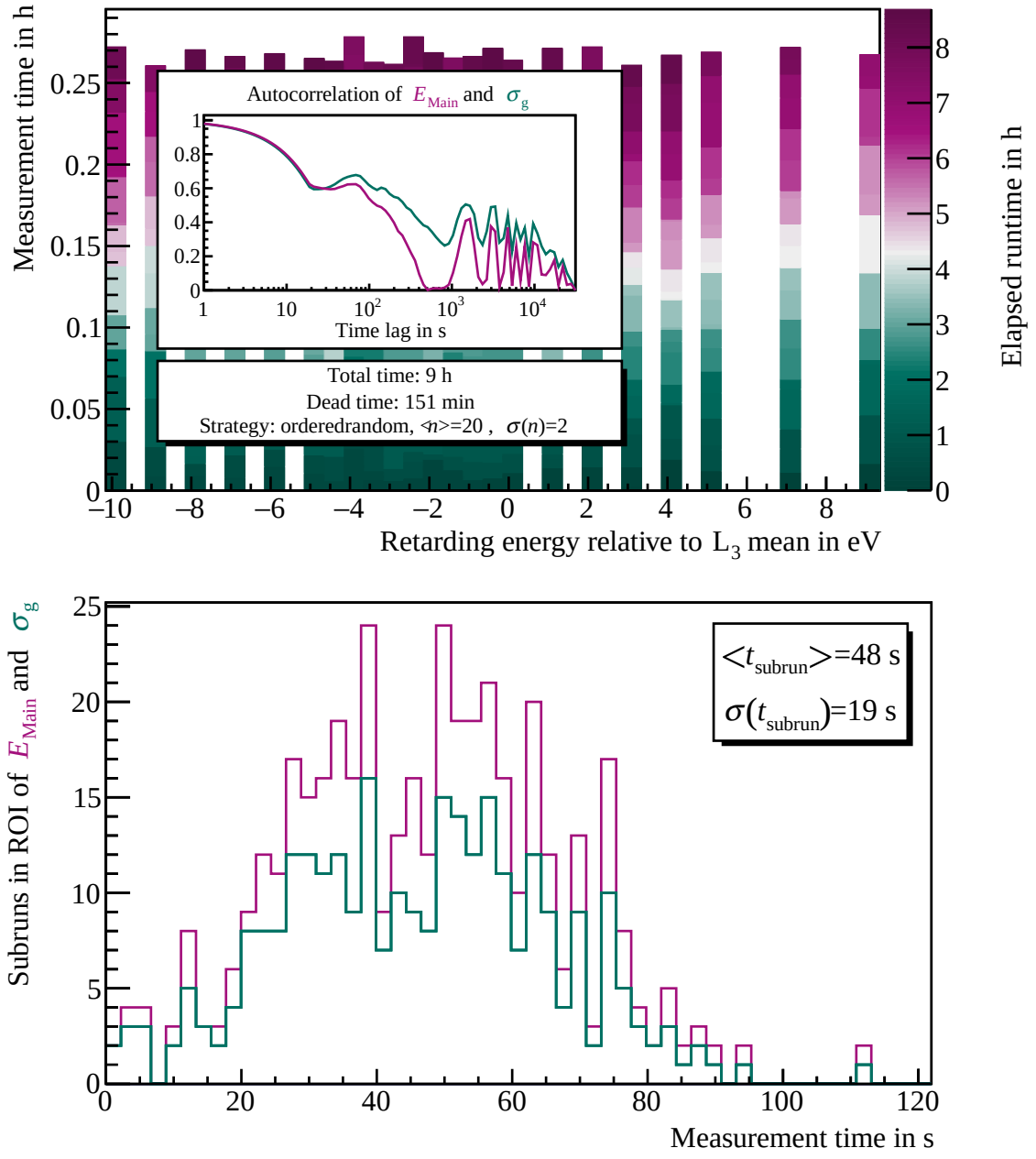

Figure 7.18.: KNM2 krypton schedule, ramping, randomised subrun duration: In this scenario the subrun duration is randomly picked from a Gaussian with comparable moments as before, while the ordering still obeys an up and down ramping pattern.

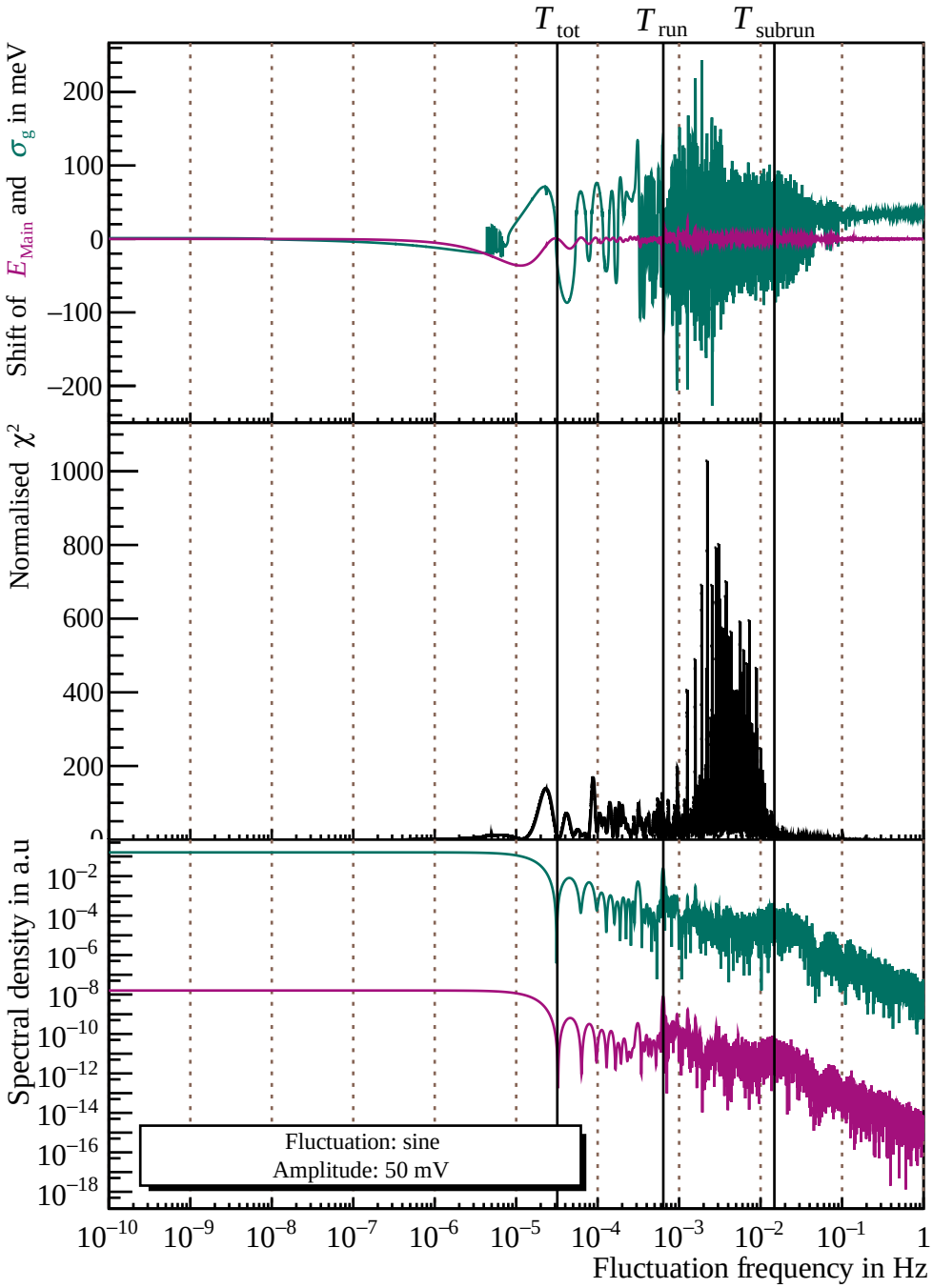

Figure 7.19.: KNM2 krypton systematics, ramping, randomised subrun duration: Between run and subrun times scales increased noise can be observed, which is related to fluctuations of the spectral density in this region, caused by the ramping. Outside this region the noise is lower in amplitude. The standard deviations on run time scale are $\sqrt{\sigma(\sigma_g^2)} \approx 103$ meV and $\sigma(E_{Main}) \approx 6.3$ meV.

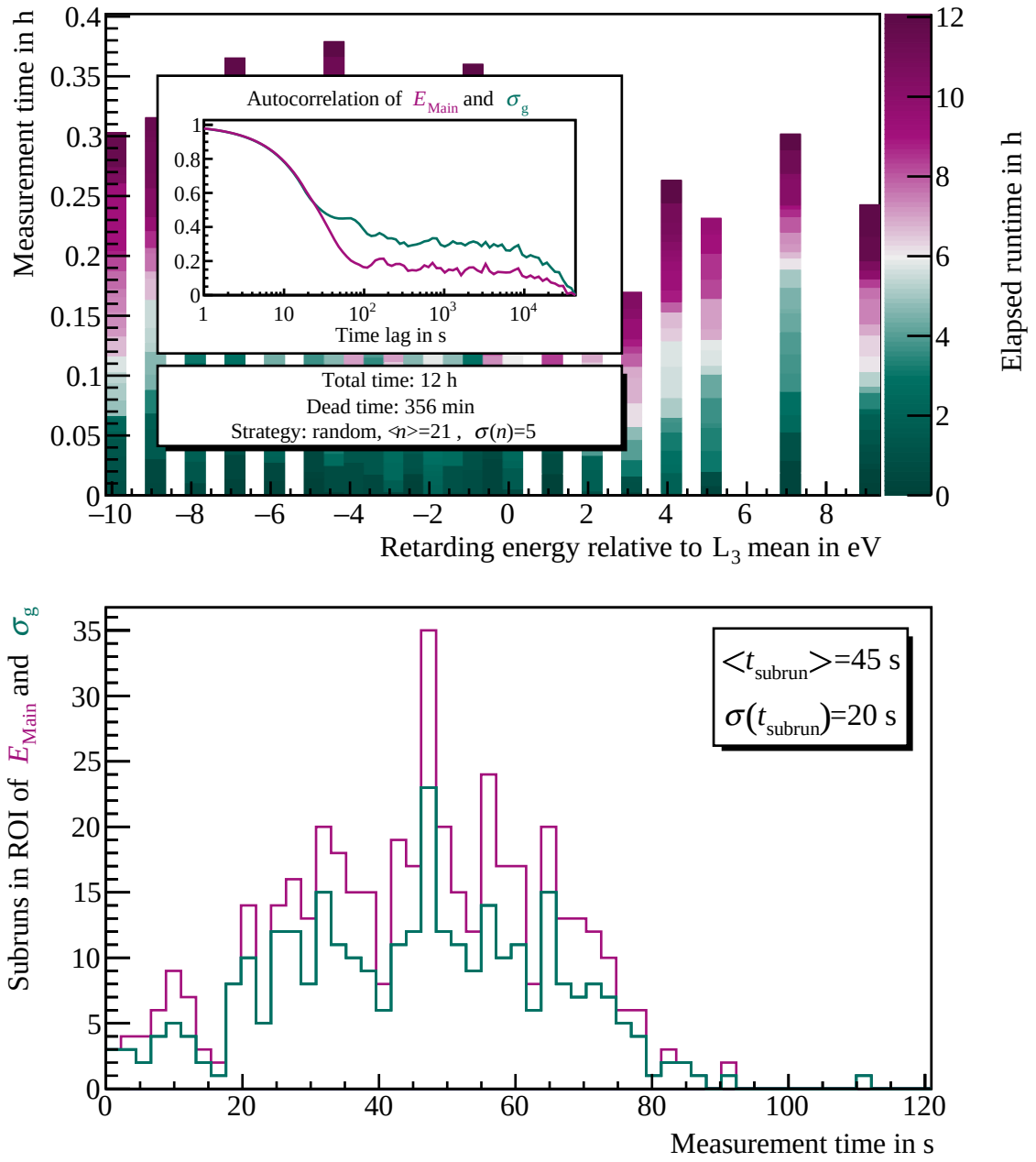

Figure 7.20.: KNM2 krypton schedule, random order, randomised subrun duration: In this scenario the duration of the subruns is randomly picked as before, and additionally the subrun order is randomised. The randomisation of the subrun duration is visible in the subrun duration distribution, but other than removing some structures, the autocorrelation functions are very comparable to the ones without subrun duration randomisation. Convergence to the MTD was not achieved due to the small total time.

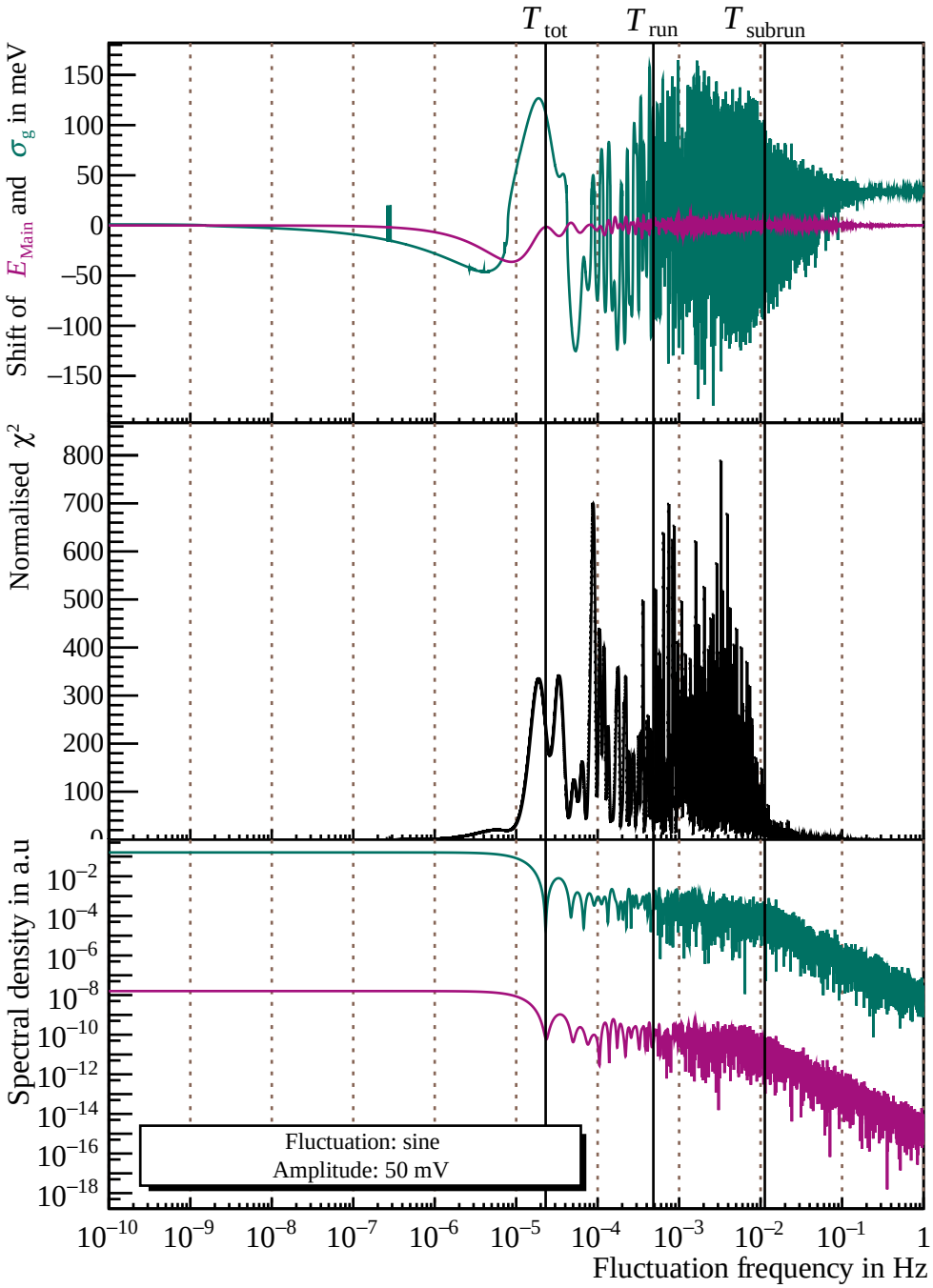

Figure 7.21.: KNM2 krypton systematics, random order, randomised subrun duration: Compared to only randomising the order of the subruns, also using a random subrun duration distribution only has minor effects on the spectral density, the systematic shifts and the χ^2. The standard deviations on run time scale are $\sqrt{\sigma(\sigma_{\text{g}}^2)} \approx 94$ meV and $\sigma(E_{\text{Main}}) \approx 4.3$ meV.

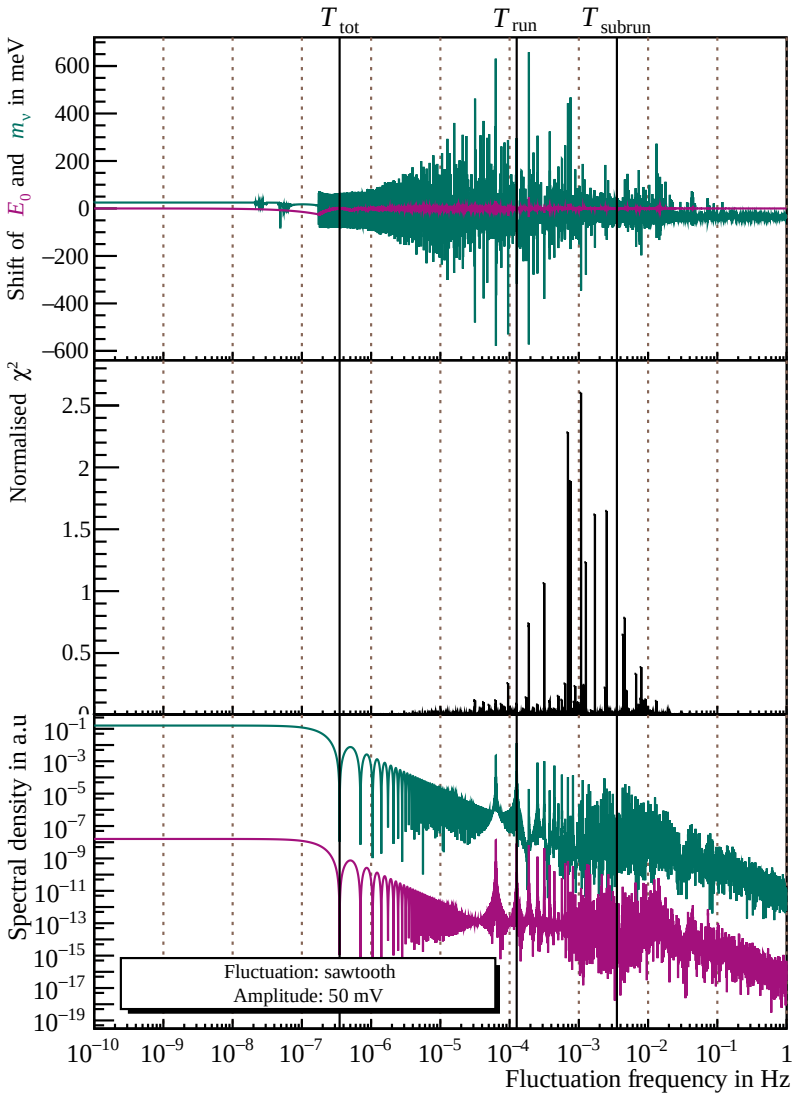

Figure 7.22.: Sawtooth perturbation, ramping: The envelope of the shift of the neutrino mass shows the scaling expected for linear combination of frequencies.

7.3.3. Systematics from Composed Perturbations

In the previous section only a single sinusoidal perturbation of the energy scale was considered. To assess the response to perturbations with a richer Fourier spectrum a sawtooth perturbation is used, which contains all integer harmonics of frequency $f_k = kf$ with power $\frac{1}{k} \propto \frac{1}{f_k}$.

Linear combination: Figures 7.22 and 7.23 show the resulting shifts. In the ramp schedule the envelope of the neutrino mass shifts decays from T_{scan} to T_{tot} with

$$\sqrt{\Delta m_\nu^2(\omega)} = \sqrt{\Delta m_\nu^2(\omega_0)} \sqrt{\frac{\omega}{\omega_0}} \,. \tag{7.59}$$

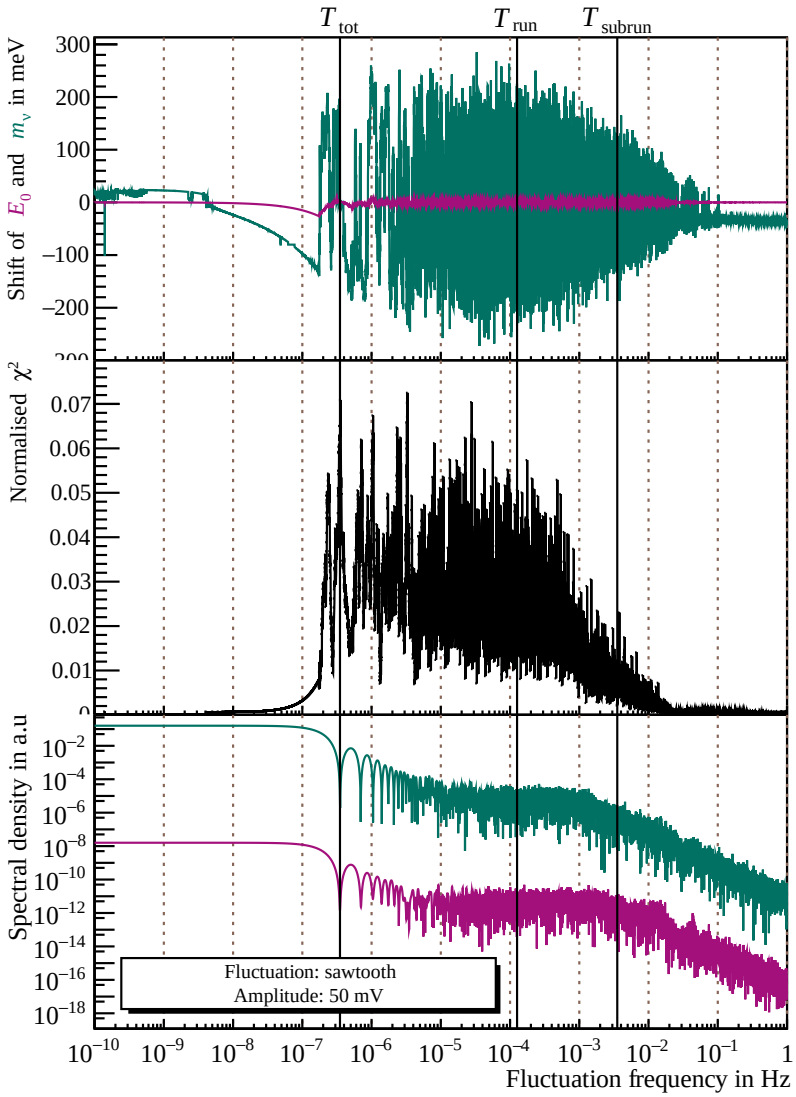

Figure 7.23.: Sawtooth perturbation, random order: In all tested randomised schedules the most prominent effect of using a sawtooth compared to a sinusoidal is visible in the reduction of standard deviations on run time scale, here $\sqrt{\sigma(m_\nu^2)} \approx 141$ meV and $\sigma(E_0) \approx 1.7$ meV.

This is expected, since in this frequency range the harmonics with power $\frac{1}{f_k}$ scatter on the resonance at the scan time, visible in the spectral density. Thus, the observed shift is a summation of the components of the perturbation.

Systematic amplitude: Compared to the sinusoidal, both the amplitude of the resonances and the standard deviations of the noise of m_ν^2 and E_0 are scaled by a factor of $\approx \sqrt{\frac{2}{3}}$, which is the ratio of the respective RMS values of the perturbations.

7.3.4. Effect of Run Time Scale (De-)Coherence on the Systematics

The simulations presented in the previous two sections show non-trivial shifts (either resonances or noise) of the observables on run time scale and damping of those shifts on subrun time scale. The included fluctuations leading to these shifts had a constant phase velocity over the whole simulated time. This section aims to show that on run time scale there is equivalence between

$$\begin{aligned} \text{resonance} &\Leftrightarrow \text{coherence}\,, \\ \text{noise} &\Leftrightarrow \text{decoherence}\,. \end{aligned}$$

From that it is possible to derive the scaling with the fluctuation amplitude and the number of returns of both the noise observed in decoherent measurements and the resonances observed in coherent measurements. Also, rather than only meaning constant phase velocity of the fluctuation, the term *(de-)coherence* should be understood as quantification of the interplay between the fluctuation phase and the subrun starting times, leading to the following distributions.

Phase distributions: Figure 7.24 shows the normalised [16] distributions of the starting phases of the fluctuation for the subruns in the ROIs of the neutrino mass and endpoint for different schedules. The following can be observed:

- Order on a given time scale is related to a structure in these distributions and to resonant shifts of the observables, i.e. coherence equals resonance.
- The absence of structure does not imply no shifts, i.e. coherence is not a prerequisite for the noise appearing on run time scale. On this scale it rather holds that decoherence equals noise.

For these distributions it is only relevant whether the fluctuation is in phase with the subrun starting times, or not. Thus, on run time scale random phase fluctuations and ramping is equivalent to fluctuations with constant phase velocity and random order, and both is called *decoherent* on run time scale. For the studies performed in this chapter only periodic fluctuations $x(t)$ were considered, where decoherence is solely given by the schedule. For signals $x(t)$ with non-predictable phase the proper measure to access the coherence of schedule and perturbation is the *coherence function.*

Coherence function: The coherence function is given by [SH08]

$$\gamma^2_{ox}(\omega) = \frac{|S_{ox}(\omega)|^2}{S_{oo}(\omega)S_{xx}(\omega)}\,, \tag{7.60}$$

where S_{oo} is the spectral density of the measurement $s_o(t)$ of observable o of the schedule, S_{xx} is the spectral density of the perturbation time signal $x(t)$ and S_{ox} is the cross-spectral

[16] To reduce the overlap in the plots, the endpoint distribution was scaled down by a factor of 0.7 compared to the neutrino mass distribution.

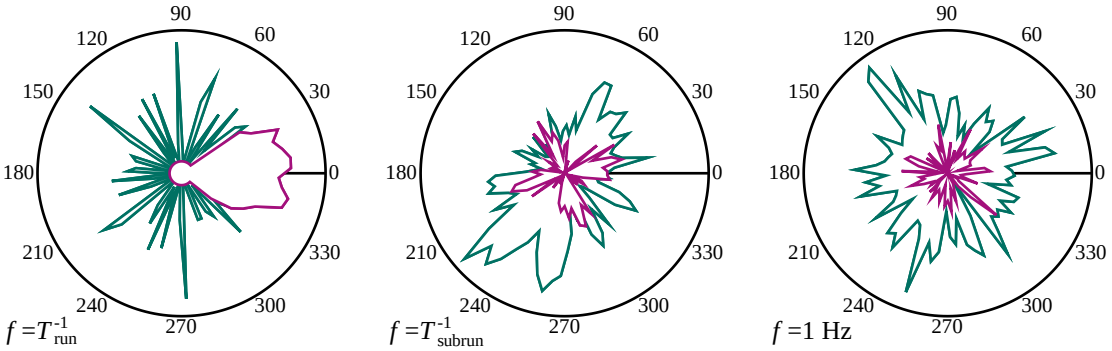

(a) Ramping

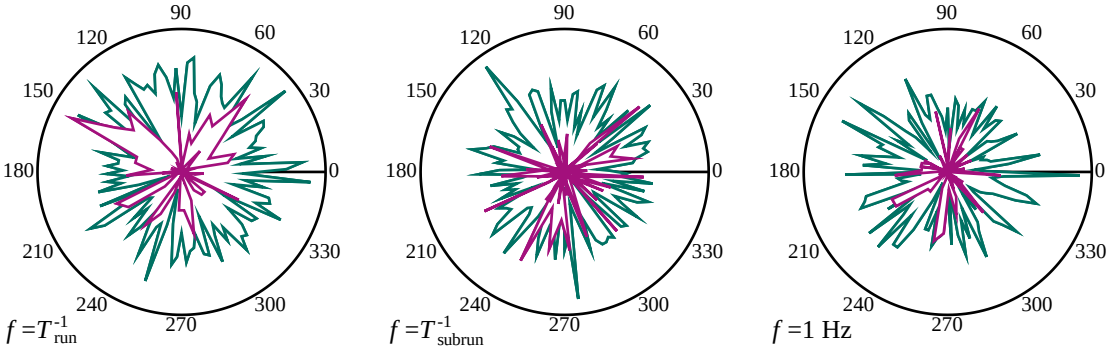

(b) Ramping, random subrun duration

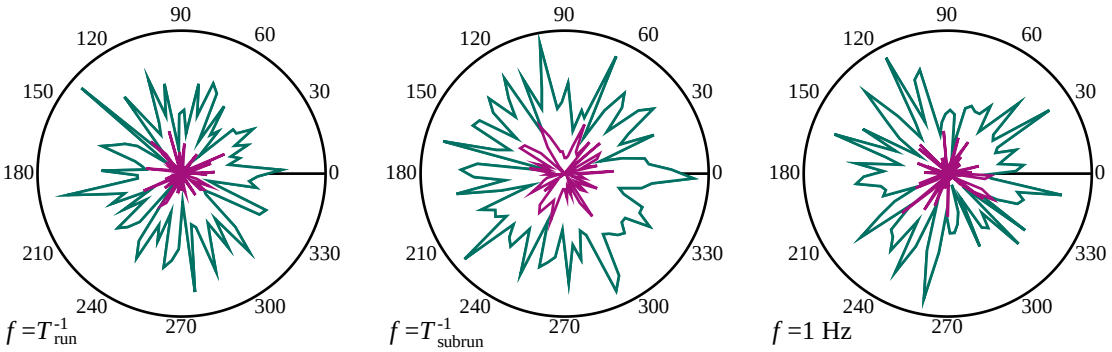

(c) Random order

Figure 7.24.: Perturbation coherence for different schedules: Shown are the normalised starting phase distributions for the subruns in the ROI of the neutrino mass (green) and endpoint (purple). The input fluctuation had a constant phase velocity over the whole simulated time. Structures for the frequency given by the inverse run time scale are visible for the ordered schedules (a) and (b), in case of (a) also for the inverse subrun time scale. Non of the schedules shows coherence for frequencies much larger than the inverse subrun time scale. Randomised subrun order (c) doesn't show any coherence.

density, which is the Fourier transform of the cross-correlation between $x(t)$ and $s_o(t)$. The coherence function is normalised

$$0 \leq \gamma_{ox}^2 \leq 1 \,, \tag{7.61}$$

such that values close to one indicate coherence.

In the following the scaling of the amplitudes of resonances and noise is derived based on completely coherent and completely decoherent measurements.

7.3.5. Scaling of the Systematics with Perturbation Amplitude and Schedule Returns

The non-trivial shifts of the observables appear around run time scale. Fluctuations on this scale imply predictable phase at least on the order of $T_{\text{run}} \gg T_{\text{subrun}}$, with the essential conclusion that run time scale fluctuations are constant on the subrun time scale. In this case extremal cases are given by coherent measurements, where a given subrun always observes the same fluctuation phase, and decoherent measurements, where the observed phase is random. As discussed, these cases lead to resonances or noise in the observables. In the following the relative count rate deviation caused by fluctuations on run time scale at retarding energy qU

$$r_{\text{run}}^{\text{res}}(qU) \equiv \frac{\Delta N}{N}(qU) \,, \quad r_{\text{run}}^{\text{noise}}(qU) \equiv \frac{\sigma(N)}{N}(qU) \,, \tag{7.62}$$

is calculated for both cases. The calculation is restricted to energy scale perturbations $\epsilon(t)$ with amplitude A and RMS value $\sigma_{\text{RMS}}(\epsilon)$.

Coherent measurements: In this case the energy shift $|\epsilon(qU)| \leq A$ of the subrun i only depends on the retarding energy. This leads to the deviation of the counts

$$\Delta N_i(qU) = [\dot{N}(qU + \epsilon(qU)) - \dot{N}(qU)]\Delta T_i \,, \tag{7.63}$$

$$\approx \frac{\mathrm{d}\dot{N}}{\mathrm{d}E}(qU)\Delta T_i \epsilon(qU) \,, \tag{7.64}$$

where leading order expansion was used in the last step and ΔT_i is the measurement time of the subrun. Summing over all subruns at retarding energy qU leads to

$$\Delta N(qU) = \sum \Delta N_i(qU) \,, \tag{7.65}$$

$$= \frac{\mathrm{d}\dot{N}}{\mathrm{d}E}(qU) t_{\text{MTD}}(qU) \epsilon(qU) \,. \tag{7.66}$$

Finally, normalising by the undisturbed counts gives

$$r_{\text{run}}^{\text{res}}(qU) = \frac{1}{\dot{N}(qU)} \frac{\mathrm{d}\dot{N}}{\mathrm{d}E}(qU) \epsilon(qU) \,, \tag{7.67}$$

$$\propto A \,. \tag{7.68}$$

Decoherent measurements: In this case the energy shift $|\epsilon_i| \leq A$ of the subrun i is randomly sampled from a probability distribution $P_{\text{run}}(\epsilon)$, independent from the retarding energy. More general also a noise distribution P_{noise} can be included, such that the total distribution for the ϵ_i is given by the convolution

$$P(\epsilon) = \left(P_{\text{run}} * P_{\text{noise}}\right)(\epsilon) \,. \tag{7.69}$$

It is assumed that the mean of $P(\epsilon)$ vanishes. The standard deviation is given by $\sigma(\epsilon)$, which is proportional to the amplitude A for small noise components.

The count deviation ΔN_i is obtained as

$$\Delta N_i = [\dot{N}(qU + \epsilon_i) - \dot{N}(qU)]\Delta T_i \,, \tag{7.70}$$

$$\approx \frac{\mathrm{d}\dot{N}}{\mathrm{d}E}(qU)\Delta T_i \epsilon_i \,, \tag{7.71}$$

where leading order expansion was used in the last step and ΔT_i is the measurement time of the subrun.

The variance $\sigma^2_{\text{run}}(N)(qU)$ after summation of ΔN_i over all $n(qU)$ returns to the subrun is obtained using the central limit theorem

$$\sigma^2_{\text{run}}(N)(qU) = n(qU)\sigma^2\left(\frac{\mathrm{d}\dot{N}}{\mathrm{d}E}(qU)\Delta T\epsilon\right) \,, \tag{7.72}$$

$$\approx \left(\frac{\mathrm{d}\dot{N}}{\mathrm{d}E}\right)^2 (qU)\left\langle t_{\text{subrun}}\right\rangle^2 (qU) n(qU)\sigma^2(\epsilon) \,. \tag{7.73}$$

Here the individual subrun times ΔT_i were approximated with their mean $\left\langle t_{\text{subrun}}\right\rangle(qU)$. Dividing by the undisturbed counts leads to the relative deviation

$$r^{\text{noise}}_{\text{run}}(qU) = \frac{\sigma_{\text{run}}(N)}{N}(qU) \,, \tag{7.74}$$

$$\approx \frac{1}{\left(\dot{N} n \left\langle t_{\text{subrun}}\right\rangle\right)(qU)} \frac{\mathrm{d}\dot{N}}{\mathrm{d}E}(qU)\sqrt{n(qU)}\left\langle t_{\text{subrun}}\right\rangle(qU)\sigma(\epsilon) \,, \tag{7.75}$$

$$= \frac{1}{\dot{N}(qU)} \frac{\mathrm{d}\dot{N}}{\mathrm{d}E}(qU) \frac{\sigma(\epsilon)}{\sqrt{n(qU)}} \,, \tag{7.76}$$

$$\propto \frac{A}{\sqrt{n(qU)}} \,. \tag{7.77}$$

Comparison to the χ^2: From the expression of the χ^2 (equation 1.17) the following scalings $\delta \in \{\sigma, \Delta\}$ (uncertainties σ or shifts Δ) of the observables and the normalised χ^2 with the relative deviations of the counts are evident

$$\delta(m_\nu^2) \propto \delta(\sigma_{\text{g}}^2) \propto \delta(E_0) \propto \delta(E_{\text{Main}}) \propto \sqrt{\left\langle r^2\right\rangle_{qU}} \,, \tag{7.78}$$

$$\chi^2 \propto \left\langle r^2\right\rangle_{qU} \,. \tag{7.79}$$

If all phases of the perturbation are present in the MTD, the averages of the squared rate deviations 7.67 and 7.76 over all retarding energies lead to proportionalities to the RMS value of the perturbation. Here correlations between the spectral parts and the energy perturbation (coherent) or the return number (decoherent) over the retarding energies qU were neglected [17]

$$\left\langle \left(\frac{1}{\dot{N}} \frac{\mathrm{d}\dot{N}}{\mathrm{d}E} \right)^2 f^2 \right\rangle_{qU} \approx \left\langle \left(\frac{1}{\dot{N}} \frac{\mathrm{d}\dot{N}}{\mathrm{d}E} \right)^2 \right\rangle_{qU} \left\langle f^2 \right\rangle_{qU} . \tag{7.80}$$

If the count deviations from the fluctuations on run time scale are dominant [18], this leads to the following prediction of the scalings

Resonances

$$\begin{aligned} \Delta m_\nu^2 \propto \Delta\sigma_\mathrm{g}^2 \propto \Delta E_0 \propto \Delta E_\mathrm{Main} \propto \sigma_\mathrm{RMS}(\epsilon) , \\ \chi^2 \propto \sigma_\mathrm{RMS}^2(\epsilon) , \end{aligned} \tag{7.81}$$

Noise

$$\begin{aligned} \sigma(m_\nu^2) \propto \sigma(\sigma_\mathrm{g}^2) \propto \sigma(E_0) \propto \sigma(E_\mathrm{Main}) \propto \frac{\sigma_\mathrm{RMS}(\epsilon)}{\sqrt{\langle n \rangle_{qU}}} , \\ \chi^2 \propto \frac{\sigma_\mathrm{RMS}^2(\epsilon)}{\langle n \rangle_{qU}} , \end{aligned} \tag{7.82}$$

Averaging

$$\begin{aligned} \Delta m_\nu^2 \propto \Delta\sigma_\mathrm{g}^2 \propto \sigma_\mathrm{RMS}^2(\epsilon) , \\ \Delta E_0 \approx \Delta E_\mathrm{Main} \approx \chi^2 \approx 0 . \end{aligned}$$

The averaging regime was included for comparison. All scalings were tested in simulation, showing good agreement. The discussion can be found in appendix A.8.

The linear scaling with the amplitude or RMS value is in contrast to the averaging regime, from which the usual limits on energy scale fluctuations in the systematic budget are derived. As a consequence, the systematic shifts in the noise and resonance regime disappear more slowly with decreasing RMS value than in the averaging regime. Given the size of the systematic shifts, especially in the resonance regime, this means that tighter limits have to be set for the RMS value on run time scale than for the RMS value on time scales larger than the subrun time scale.

Example of noise on run time scale: To show that noise is truly related to decoherence on run time scale, the KNM2 tritium ramping schedule of figure 7.6 used in the measurement was taken, and constant energy shifts ϵ_i for each subrun were randomly picked from a sinusoidal like

$$\phi_i = \text{random} \in [0, 2\pi) , \tag{7.83}$$

$$\epsilon_i = 50\ \text{meV} \sin(\phi_i) , \tag{7.84}$$

[17] This should be treated with caution, however it agrees with with the simulations in the used ramp schedule (see section 7.3.3) and is exact for constant return number, which is the most realistic case.

[18] Since no Poisson uncertainty and other systematics were included, this is the case in the simulations shown in this chapter.

which is independent from ordering and frequency. The comparison to the frequency dependent case of randomised subrun order is shown in figure 7.25. Both show equal standard deviations of the fitted neutrino masses and endpoints.

7.3.6. Combined Statistical and Systematic Uncertainty

Finally, the combined uncertainty from statistical uncertainty and uncertainty due to run time scale perturbations is calculated.

RMS value of the KNM2 high voltage measurement: The RMS value of the KNM2 high voltage measurement is [Rod20]

$$\sigma_{\mathrm{RMS}}(\mathrm{HV}) = 11\ \mathrm{mV}\,, \tag{7.85}$$

which is roughly a factor of five better than the design report requirement on energy scale fluctuations $\sigma(\epsilon) < 60$ meV [KAT04b].

RMS value of the KNM2 source potential: The total width of the zero scattered starting potential distribution measured in KNM2 krypton is analysed in chapter 6. It includes both longitudinal inhomogeneities and temporal instabilities. Thus, the obtained value of equation 6.15 is an upper limit on the RMS value for fluctuations on run time scale

$$\sigma_{\mathrm{RMS}}[V] < 140\ \mathrm{mV}\,. \tag{7.86}$$

This value is overly conservative, since it assumes that it is only caused by fluctuations, and that the longitudinal inhomogeneity vanishes.

RMS value of energy scale perturbations: The overall RMS value is obtained by quadratic addition of both components

$$\sigma_{\mathrm{RMS}}(\epsilon) < 140\ \mathrm{meV}\,. \tag{7.87}$$

Since the relevant RMS value for this systematic needs to be taken from a band-limited signal around the run time scale, which certainly has significantly less spectral contribution, the systematic on the neutrino mass calculated with the above values is an overly conservative upper limit on the total systematics. Also, since the source potential completely dominates, while its analysis suffers from significant uncertainties, in the following both values are treated separately.

KNM2 systematic shifts and uncertainties: The systematic shifts (assumed coherence) and uncertainties (assumed decoherence) due to run time scale energy fluctuations were taken from the ordered and random order schedules figures 7.6 and 7.8. The coherent case leads

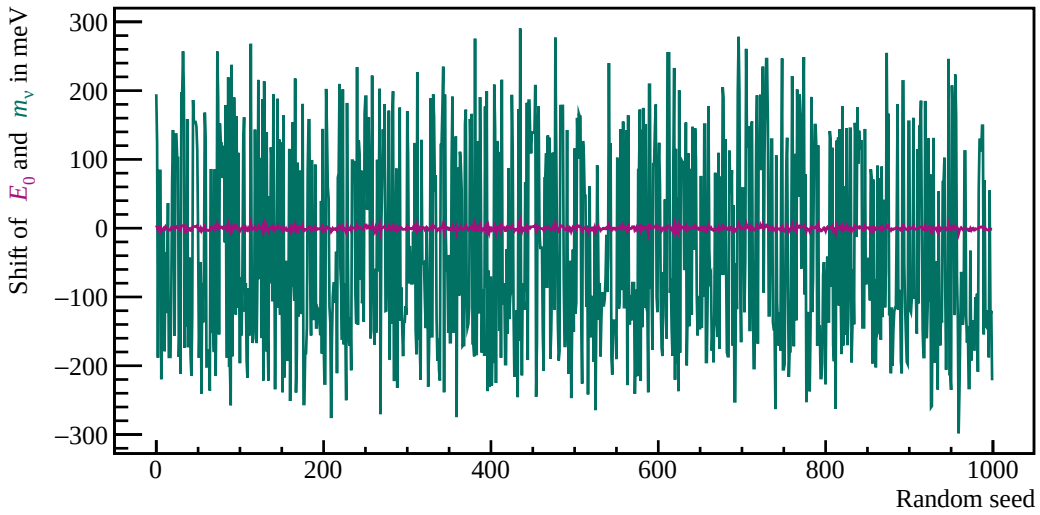

(a) Random distribution

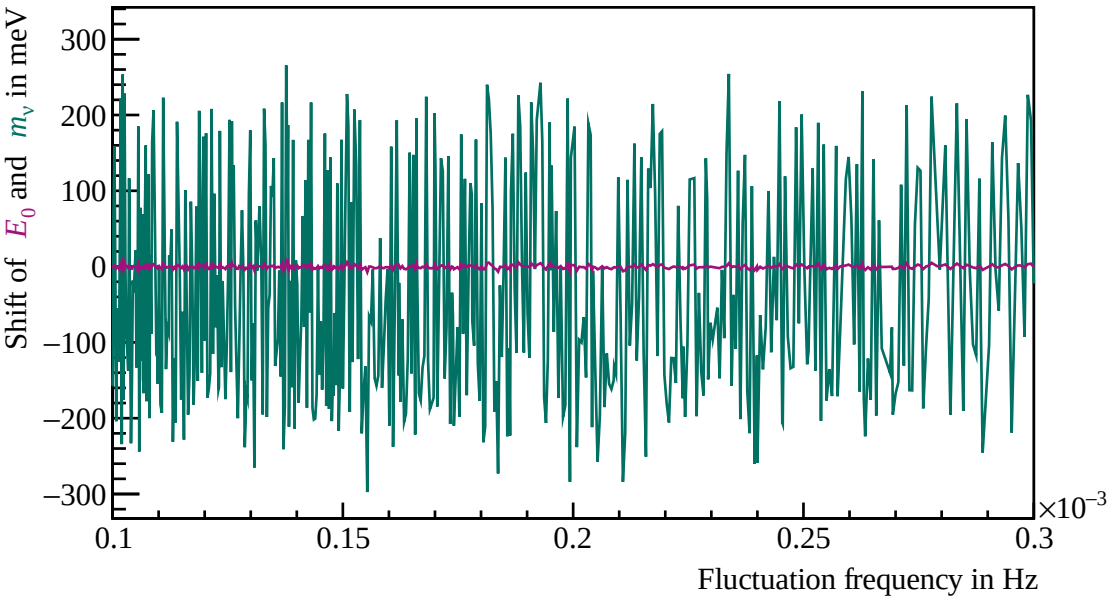

(b) Time dependent fluctuation, random subrun order

Figure 7.25.: Random distribution vs. frequency dependence: For (a) a constant energy shift of each subrun was picked from a sinusoidal of random phase and 50 meV amplitude. The standard deviations are $\sqrt{\sigma(m_\nu^2)} \approx 164$ meV, $\sigma(E_0) \approx 2.3$ meV. (b) is a zoom in on the run time scale of figure 7.9, i.e. the shifts are obtained by including a sinusoidal fluctuation of 50 meV amplitude with constant phase velocity and random subrun order. The standard deviations are identical $\sqrt{\sigma(m_\nu^2)} \approx 164$ meV, $\sigma(E_0) \approx 2.3$ meV.

to

$$\mathrm{Max}\left[\Delta m_\nu^2\right] \approx 20.8\ \sigma_{\mathrm{RMS}}(\epsilon)\ \mathrm{eV}\,, \tag{7.88}$$

$$\overset{\mathrm{HV}}{\ll} 0.229\ \mathrm{eV}^2\,, \tag{7.89}$$

$$\overset{V}{\ll} 2.912\ \mathrm{eV}^2\,. \tag{7.90}$$

Especially the second value is devastatingly large. However, the coherent case assumes that a perturbation of the energy scale of constant phase velocity with frequency $\frac{1}{2T_{\mathrm{run}}}$ exists with an accuracy of the order $\frac{1}{T_{\mathrm{tot}}}$. While also harmonics of this frequency lead to shifts of the above order, this case seems very unlikely.

Thus, in the following only the decoherent case is considered. This leads to

$$\sigma_{\mathrm{syst}}(m_\nu^2) \approx 14.5 \frac{\sigma_{\mathrm{RMS}}(\epsilon)}{\sqrt{\langle n\rangle_{qU}}}\ \mathrm{eV}\,, \tag{7.91}$$

$$\overset{n=361}{=} 0.76\ \sigma_{\mathrm{RMS}}(\epsilon)\ \mathrm{eV}\,, \tag{7.92}$$

$$\overset{\mathrm{HV}}{\ll} 8.4 \cdot 10^{-3}\ \mathrm{eV}^2\,, \tag{7.93}$$

$$\overset{V}{\ll} 0.106\ \mathrm{eV}^2\,. \tag{7.94}$$

Whether the values are significant is investigated below by comparing them to the statistical uncertainty of KNM2. Notably, if σ_{RMS} is taken to be the 60 meV requirement from the design report, the systematic uncertainty is $4.6 \cdot 10^{-2}$ eV^2, which is nine times larger than the $5 \cdot 10^{-3}$ eV^2 planned for full KATRIN [KAT04b]. Thus, for run time scale fluctuations more stringent limits need to be imposed.

Scaling of the total uncertainty with time scales: Due to the scaling of the noise in decoherent measurements with the return number, decreasing the subrun length while keeping the measurement time constant reduces the noise. On the other hand it increases the dead time and thus the statistical uncertainty. It is expected that the mean dead time per subrun does not depend on the subrun time scale or on the subrun ordering [19].

From the included dead time distribution defined in equation 7.57, the following mean dead time per subrun is expected

$$\langle t_{\mathrm{dead}}\rangle = T_{\mathrm{subrun}} - \langle t_{\mathrm{subrun}}\rangle \overset{\mathrm{KNM2}}{=} 32\ \mathrm{s}\,. \tag{7.95}$$

The efficiency thus is

$$\epsilon_{\mathrm{eff}} = \frac{\langle t_{\mathrm{subrun}}\rangle}{\langle t_{\mathrm{dead}}\rangle + \langle t_{\mathrm{subrun}}\rangle} \overset{\mathrm{KNM2}}{=} 0.89\,. \tag{7.96}$$

at $\langle t_{\mathrm{subrun}}\rangle = 250$ s.

[19] A study was performed where the subrun length was varied between 10 and 250 seconds, and the measurement time without dead time was kept constant. The study was performed for ordered and random order schedules, plots can be found in appendix A.8. These expectations are met.

The statistical uncertainty scales anti-proportionally to the square root of the measurement time

$$\sigma_{\mathrm{stat}}(m_\nu^2) \overset{\mathrm{KNM2}}{=} 0.3\ \mathrm{eV}^2 \propto \frac{1}{\sqrt{\epsilon_{\mathrm{eff}} T_{\mathrm{tot}}}} . \tag{7.97}$$

From equation 7.8 it follows for the scaling of the systematic uncertainty from run time scale fluctuations:

$$\sigma_{\mathrm{syst}}(m_\nu^2) \propto \frac{1}{\sqrt{\epsilon_{\mathrm{eff}} T_{\mathrm{tot}}}} \sqrt{\langle t_{\mathrm{subrun}} \rangle N_{\mathrm{MTD}}} . \tag{7.98}$$

Combining both and using the obtained values from simulation leads to

$$\sigma_{\mathrm{tot}}(m_\nu^2) = \sqrt{\sigma_{\mathrm{stat}}^2(m_\nu^2) + \sigma_{\mathrm{syst}}^2(m_\nu^2)} , \tag{7.99}$$

$$= \frac{1}{\sqrt{\epsilon_{\mathrm{eff}} T_{\mathrm{tot}}}} \sqrt{A^2 + B^2 \sigma_{\mathrm{RMS}}^2(\epsilon) \langle t_{\mathrm{subrun}} \rangle N_{\mathrm{MTD}}} , \tag{7.100}$$

$$= \sqrt{\frac{229014\ \mathrm{s} + 5879\ \sigma_{\mathrm{RMS}}^2(\epsilon)/\mathrm{eV}^2 \langle t_{\mathrm{subrun}} \rangle}{\epsilon_{\mathrm{eff}} T_{\mathrm{tot}}}}\ \mathrm{eV}^2 , \tag{7.101}$$

$$\overset{\mathrm{KNM2}}{=} \sqrt{0.09 + 0.58\ \sigma_{\mathrm{RMS}}^2(\epsilon)/\mathrm{eV}^2}\ \mathrm{eV}^2 , \tag{7.102}$$

$$\overset{\mathrm{HV}}{\ll} \sqrt{0.09 + 7.0 \cdot 10^{-5}}\ \mathrm{eV}^2 , \tag{7.103}$$

$$\overset{V}{\ll} \sqrt{0.09 + 0.01}\ \mathrm{eV}^2 . \tag{7.104}$$

It can be concluded that in KNM2 tritium decoherent run time scale fluctuations from the high voltage are completely negligible compared to the statistical uncertainty. Given that the RMS value is largely overestimated, this likely also holds for the source potential fluctuations on run time scale. Moreover, the ratio of the uncertainties

$$\frac{\sigma_{\mathrm{syst}}}{\sigma_{\mathrm{stat}}} \approx 2.5 \cdot 10^{-3} \frac{\sigma_{\mathrm{RMS}}(\epsilon)}{\mathrm{meV}} \tag{7.105}$$

will stay approximately constant if more runs are added with comparable run time schedules. Thus, only for an RMS value of 400 meV the uncertainties become equally large. This most likely allows to neglect systematic contributions from run time scale energy fluctuations also in the full KATRIN measurement.

7.4. Conclusion

In this chapter the sensitivity of different run time schedules to time dependent perturbations of the energy scale was investigated. The appropriate methods of analysis were described and consequently a set of simulation tools were implemented in the KATRIN simulation framework. They allow to easily assess the resulting systematic and statistical uncertainties also for other than the used KNM2 schedules.

The scaling of the simulation results with perturbation amplitude and return number could fully be understood in an analytical calculation. Different forms of systematic shifts were

identified, which occur for coherence or decoherence between schedule and perturbation phase. Together with the usual averaging case, three systematic regimes are possible (ordered by typical magnitude):

- Coherency on run time scale: Large systematic shifts, produced by the frequency of inverse scan time and its harmonics.
- Decoherency on run time scale: Medium Gaussian uncertainty, produced by a broad frequency range around inverse run time scale.
- Negligible RMS value on run time scale: Small systematic shift from the usual averaging regime.

Assessing the contributions of the regimes requires the knowledge of the power spectra of both the source and the spectrometer potential. Only overly conservative upper limits on the total RMS values of both power spectra could be inferred from the KNM2 krypton and KNM2 high voltage measurement. Even so, it turned out that the systematics of the decoherent case is negligible compared to the statistical uncertainty. Also, due to the known scalings, it is likely that this is also the case for the full KATRIN measurement. However, the shown reduction of the systematic shifts in the noise regime with the number of runs is only valid, if the obtained spectra are added and analysed in a stacked fit.

Outlook: The limits are overly conservative. Experimental limits on run time RMS values can be obtained from krypton-83m measurements in two ways:

- Overdispersion of the χ^2 distributions: In the usual analysis of individual runs, run time scale fluctuations lead to overdispersion of the χ^2 distributions. Usually, some small overdispersion was observed in KNM2, but also other systematic influences are possible.
- Change of the Gaussian variance by stacking: When comparing stacked and non-stacked analysis, a change of the measured Gaussian variance is a hint of the existence of run time scale perturbations. Due to time dependencies of the rate and tritium column density, this kind of analysis requires a multi-parameter fit model, which exceeded the scope of this work.

Also, the coherent case could not be fully excluded. Due to the necessary fine tuning of the perturbation frequency and the necessary constant phase velocity of the perturbation, its existence seems unlikely. In addition, more fine tuning would be needed to explain the magnitude of the Gaussian variance obtained in the KNM2 krypton measurement by coherent run time scale perturbations, instead of the more likely longitudinal inhomogeneities and plasma fluctuations of $>$ Hz frequencies.

With regard to future data acquisition, randomised runtime schedules would reliably avoid the large systematic shift of the neutrino mass resulting from fluctuations of the energy scale in the resonant regime and, given a stacked analysis of the obtained spectra, would lead to negligible systematics due to run time scale fluctuations.

8. Conclusions and Outlook

The existence of neutrino flavour oscillations proves indisputably that neutrinos have mass. The non-vanishing mass of neutrinos has a fundamental influence on the understanding of the physics of elementary particles, which requires the extension of the otherwise overwhelmingly successful Standard Model of elementary particle physics. Thus, neutrino physics is at the forefront of current physical questions and contributes to the understanding of physics from the smallest to the largest scales. With respect to the formation of the universe, this includes, for example, fundamental topics such as the search for dark matter or the origin of the asymmetry of matter and antimatter, which is at present not understood. Three complementary approaches are currently established to determine the size of the neutrino mass, including observational cosmology and the search for neutrinoless double beta decay. In both of these approaches, underlying assumptions need to be made - in the first case, the observations are interpreted in the framework of the Λ Cold Dark Matter standard cosmological model; in the second case, the neutrino has to be assumed of Majorana rather than Dirac type. By contrast, the only direct laboratory method that can determine the neutrino mass without additional theoretical assumptions is the measurement of the kinematics of weak decays involving neutrinos, such as beta decay or electron capture.

The latest beta decay experiment is the KArlsruhe TRItium Neutrino (KATRIN) experiment. It holds the currently strongest laboratory-based kinematic limit on the neutrino mass of $m_\nu < 1.1\,\mathrm{eV}$ (90 % C. L.) from its first published KNM1 campaign. In the tritium β decay spectrum a non-vanishing neutrino mass leads to a tiny imprint just below the kinematic endpoint of 18.6 keV. By precise spectroscopy of the β electrons in this region KATRIN aims to push the sensitivity on m_ν down to 200 meV (90 % C. L.) over the course of an overall 5-year data-taking campaign, which requires precise understanding and, wherever possible, mitigation of the systematic uncertainties. One of the most important systematics results from the calibration of the difference between the potentials of the spectrometer and the tritium source. This quantity must be monitored with an accuracy of the order of 10 mV. Such a precise calibration is at the limit of what is technically feasible and a chain of several interlinking calibration methods is employed to precisely determine both the high voltage of the spectrometer and the source potential. Since KATRIN uses an extended-volume source of gaseous tritium a calibration standard with which the spatially inhomogeneous source potential can be determined must also be gaseous under feasible measurement conditions. Mesomeric krypton-83m meets this requirement and its quasi mono-energetic conversion lines are used at KATRIN for calibration purposes.

In principle, shape distortions of the $^{83\mathrm{m}}$Kr conversion electron spectrum can be used to determine systematics affecting the difference of the spectrometer and source potential. In

the thesis at hand the influence of the spatially inhomogeneous source potential on the krypton-83m spectrum is investigated thoroughly. The findings were applied in several krypton-83m measurement phases in order to quantify the systematics of the neutrino mass measurement campaigns KNM1 and KNM2 carried out at KATRIN in 2019. It was shown that the previous modelling of the shape distortion of the tritium β spectrum caused by a spatially inhomogeneous source potential was incomplete and the necessary extensions were comprehensively described.

In addition to the investigation of systematics that result from the spatial inhomogeneities of the source potential, krypton-83m can also be used to investigate temporal fluctuations that can occur in both the source and the spectrometer potential. Both cases lead to a broadening of the krypton lines, which in leading order can be modelled with a Gaussian of width σ_g. In the commonly used, simplest description the resulting systematic shift of the squared neutrino mass for any potential inhomogeneity with standard deviation or RMS value σ is

$$\Delta m_\nu^2 = -2\sigma^2 \ . \tag{8.1}$$

This description assumes that the effect of the systematic on the β spectrum is also that of a broadening. However, as shown in the thesis at hand, for the situations described in the following this rule is not applicable since equation 8.1 is incomplete.

Temporal fluctuations: Measurements at KATRIN usually consist of repeated recordings of electron energy spectra, with one individual scan of the spectrum typically taking about 2-3 hours. Individual scan steps at a given retardation voltage setting have a duration between tens of seconds to several minutes. Non-broadening like shape distortions of the total spectrum can appear for perturbations of the energy of the individual bins. One extremal case are resonant perturbations, where each bin always observes the same energy offset. The other extreme are random perturbations, where the energy offset of each bin is random, mimicking statistical fluctuations. Both occurs for fluctuation frequencies on the time scale of the recording time of one spectrum. In this case, the resulting neutrino mass shifts do not follow equation 8.1, which is usually used to impose limits on the allowable RMS value of the fluctuation. For the resonant case, much tighter limits need to be used, however it only appears at fine tuned perturbation frequencies of tiny width. The random case was constrained by upper limits of the fluctuation RMS value in KNM2, which were taken from measurements of the spectrometer potential and from krypton-83m measurements. Given these limits, it could be shown that this systematic is negligible compared to the statistical uncertainty in KNM2. Since both random fluctuations and the statistical uncertainty decrease equally with the total measurement time, this systematic is likely also negligible for the full KATRIN measurement.

Source potential systematics: In case of systematics caused by inhomogeneities of the longitudinally extended source potential $V(z)$, the description was refined in two points: Firstly, it was shown that moments of the source potential have to be weighted with the longitudinal electron distributions $P_i(z)$. The index i indicates the multiplicity of inelastic scattering of the electrons on the gas molecules in the source. The dependence on the

scattering multiplicity is essential due to the following reasoning: The larger the portion of the gas column an electron needs to traverse to reach the detector, the more likely it is to undergo inelastic scattering on the gas molecules on the way. As a consequence, electrons of distinct scattering multiplicities on average stem from different spatial domains of the source, such that they observe different source potentials. With regard to the standard deviation of the potential, that of the unscattered electrons $\sigma_0[V]$ is relevant for the neutrino mass shift. While its value is different from the unweighted case, the effect on the spectra still is that of a broadening and the neutrino mass shift is calculated following equation 8.1.

In contrast, it was shown that in addition to $\sigma_0[V]$ a second measure of inhomogeneity $\hat{\rho}[V]$, $|\hat{\rho}[V]| \leq 1$, needs to be considered. It quantifies by how much the potential of the rear part of the 10 m long gaseous source differs from that of the front part, i.e it quantifies the prevalence of an antisymmetric potential shape in relation to the gas injection point in the centre of the source. Antisymmetric potentials ($\hat{\rho} = \pm 1$) produce shape distortions in all electron spectra of the gaseous source, which cannot be described by a broadening due to the following reasoning: Since upon inelastic scattering the electrons lose at least ≈ 13 eV of energy, electrons of different scattering multiplicities appear at different energies in the electron spectrum. Thus, on average different energies in the electron spectrum are affected by different spatial regions of the potential. For measurement conditions like the ones used in the KNM1 and KNM2 measurements, mainly one-time scattered and unscattered electrons are relevant, and the difference of their spatial distributions is characterised by an antisymmetric shape with regard to the gas injection point. As a consequence, potentials with that symmetry produce non-broadening shape distortions of the electron spectra.

As shown in this thesis, the resulting equation for the shift of the squared neutrino mass reads

$$\Delta m_\nu^2(\hat{\rho}, \sigma_0) = -2\sigma_0(\epsilon_\rho \hat{\rho} + \sigma_0)\,, \tag{8.2}$$

now consisting of a shape term in addition to the known broadening term. The shape energy ϵ_ρ depends on the contribution of the scattering multiplicities to the recorded β spectrum, i.e. on the respective measurement conditions. It was shown, that equation 8.2 fully specifies the neutrino mass shift caused by the extended source potential up to second order in the potential. For antisymmetric potentials the shape term strongly dominates the systematics at KNM2-like measurement conditions. For the source potential expected from simulations, which has a considerable antisymmetry of $\hat{\rho} = 0.88$, the resulting neutrino mass shift is 30 times larger than the one following from equation 8.1.

Krypton-83m measurements at KATRIN: Thus, the precise determination of both $\hat{\rho}[V]$ and $\sigma_0[V]$ from krypton-83m measurements is required to correct for the potential induced systematic in the theoretical model of the β spectrum. In the quasi mono-energetic krypton-83m conversion electron spectrum the one-time scattered electrons are visible as a line ≈ 13 eV below the unscattered electrons and the shape distortion due to antisymmetric potentials changes the distance separating the two lines. The potential induced change of the distance is given by the difference $\Delta_{10}[V]$ of the mean potential for one-time scattered

$\langle V \rangle_1$ and unscattered electrons $\langle V \rangle_0$. The spectral broadening of the line of unscattered electrons is given by $\sigma_0[V]$. From first-principle calculations it was shown that

$$\hat{\rho}[V] = \frac{1}{\kappa_{\overline{10},0}} \frac{\Delta_{10}[V]}{\sigma_0[V]} \tag{8.3}$$

with $\kappa_{\overline{10},0} \approx 0.7$ for KNM2 krypton measurement conditions, which rigorously connects the spectrum distortion $\Delta_{10}[V]$ with the potential antisymmetry $\hat{\rho}[V]$ and spectral broadening $\sigma_0[V]$. The change in the distance of the krypton lines of one-time and unscattered electrons divided by the spectral broadening of the krypton line of unscattered electrons accurately predicts the antisymmetry of the potential. In particular, this ratio cannot assume arbitrary values and the maximum change in the distance between the lines for a given broadening is given by antisymmetric potentials.

While with the measurement of $\Delta_{10}[V] \sim \hat{\rho}[V]$ and $\sigma_0[V]$ in krypton-83m the neutrino mass systematic can be constrained, it was shown that the translation to the β spectrum is subjected to some subtleties: Since the gas distributions of tritium and krypton in the source are known to show small differences, the distribution of the krypton-83m and tritium β signal electrons is different. As a consequence, the potential estimates for both gas species are different even at equal measurement conditions, which leads to uncertainties and scalings of the estimates in the translation from the krypton to the tritium spectrum. Those were rigorously quantified in the context of this work. The unavoidable uncertainty on $\Delta_{10}[V]$ is at least 10 % of $\sigma_0[V]$, even if the measurements are taken at the exact same source conditions. Given that $\Delta_{10}[V]$ needs to be determined with mV accuracy for full KATRIN, such uncertainties are indeed relevant.

All the more important it is to precisely understand the relation of krypton-83m observables to the source potential. This connection was fully established in this thesis. As discussed, the estimates of inhomogeneity $\sigma_0[V]$ and $\hat{\rho}[V]$ are the overall inhomogeneity magnitude and the antisymmetry of the potential. The additionally obtained line shift of the unscattered line is the mean potential $\langle V \rangle_0$. The remaining part of the potential, which is not predicted by the three observables of the krypton-83m measurement, is its symmetrical component with regard to the gas injection point. Inversely, source potentials obtained from simulations can rigorously be tested against the krypton-83m estimates. This exceeds a mere matching of the estimates of the simulation and the measurement, which alone would not allow to determine the possibility, that the simulation is the measured potential. However, since $\hat{\rho}[V]$ is linked to an exact defined symmetry of the potential, the more antisymmetric the potential is, the smaller is the space of potentials which can lead to the measured observables and the better is the possibility of the krypton-83m measurement to confirm the potential. For $\hat{\rho}[V] = \pm 1$ the potential is exactly known.

These principles were applied on the data of the KNM2 krypton measurement. The analysis and interpretation of the data are fully compatible with the predictions of the model developed in this thesis. When a strong positive bias voltage is applied to the rear wall of the extended source, the krypton-83m measurement indicates a strongly antisymmetric potential, i.e. the voltage drops over the length of the source. Moreover, from the difference of the applied voltage to the measured mean potential it could be deduced that a non-monotoneous feature of the potential needs to exist to ensure energy

conservation. Such a feature is predicted at the central gas injection point by the potential simulations. These conclusions were drawn without relying on any model dependencies and use only first-principle calculations and the krypton-83m observables. Importantly, the rear wall bias regime of strongly positive voltages is ideal to test the theoretical description, since the artificially induced inhomogeneity dominates over systematics of the krypton-83m measurement. In summary, the theoretical description of the effect of the source potential on the electron spectra provided by this work is exhaustive and was well tested in measurement.

However, due to the induced inhomogeneity, strong rear wall biases are not used for the neutrino mass measurements. For small bias voltages, it was shown that the gaseous krypton-83m measurement suffers from considerable systematics. Firstly, the intrinsic Lorentzian line width Γ of the used L_3-32 transition could not be determined with sufficient accuracy, leading to a systematic on $\sigma_0[V]$. The determination of Γ using the extended KATRIN source suffers from a systematic due to residual inhomogeneities of the work function of the source tube. Secondly, the intrinsic position of the scattered electron line in the krypton-83m spectrum is not known with sufficient accuracy, leading to a systematic on $\Delta_{10}[V]$. For tritium measurements, the energy loss function, which characterises the energy loss of electrons upon single scattering was experimentally determined by KATRIN. However, since the krypton measurement is performed at considerably higher energies than the tritium measurement (30.5 keV compared to 18.6 keV), it cannot be assumed that the measured function can be transferred to the higher energy range without further validation.

Thus, Γ was taken from a measurement of the condensed krypton-83m calibration source at KATRIN, which is point-like and does not suffer from source tube work function systematics. Its statistical uncertainty, however, is larger than that of the gaseous measurement and the thereby reached sensitivity on $\sigma_0[V]$ is not sufficient for full KATRIN.

The measured value of $\Delta_{10}[V]$ was discarded and the shape term of the neutrino mass shift was constrained by its extremal values $\hat{\rho}[V] = \pm 1$. While this leads to a large shift, the systematic contribution from the source potential in the KNM1 measurement was shown to be negligible with regard to the total systematic budget. The main reason is the small tritium column density of this measurement and thus the small shape energy $\epsilon_\rho \approx 160$ meV. The column density critically influences the shape energy, since it determines the amount of scattering in the source. As a consequence, for KNM2 and future measurements, which use a larger tritium column density, the corresponding shape term ($\epsilon_\rho \approx 490$ meV for KNM2) and the resulting systematic is much larger. With the estimates from the KNM2 krypton measurement, a systematic neutrino mass shift was found, which dominates the KNM2 systematic budget.

Outlook: The findings obtained and predictions made in this work have resulted in considerable collaborative efforts to improve the current and future measurements of KATRIN. The three main consequences are explained in more detail in the following:

- The systematics of the krypton-83m measurement need to be reduced. By the time of writing of this thesis the KNM3 krypton measurement campaign had already been

concluded. Due to the findings and predictions made in this work, this particular krypton measurement campaign was considerably extended compared to previous ones and specifically dedicated to the study of source potential systematics. The problem of the insufficiently known intrinsic width of the krypton-83m L_3-32 transition was tackled using a measurement of the $N_{2,3}$-32 transition: Since its intrinsic width is very small, it can be neglected compared to the source potential inhomogeneity. In principle this eliminates the systematic uncertainty on $\sigma_0[V]$. However, currently it is still under investigation, whether the approximation as mono-energetic transition is completely justified. Also, due to the very small branching ratio of the $N_{2,3}$-32 lines in relation to the L_3-32 line, in the future more of those measurements are planned, to reach the required sensitivity.

To reduce the systematic uncertainty on $\Delta_{10}[V]$ a new measurement of the energy loss function at krypton-83m energies needs to be performed. This requires a more advanced set-up and hardware improvements of the electron gun used for this measurement, which needs to be rated up to voltages of 35 keV, thus surpassing the current limitation at around 21 keV. As a consequence of the findings in this thesis the construction of the improved electron source is pursued within the collaboration with a high priority.

- The krypton-83m calibration measurement and the tritium neutrino mass measurement must be performed under the same source conditions to avoid systematic uncertainties due to scaling. Prior to the KNM4 measurement campaign, however, the processing of the different gases in the source required different working temperatures and tritium column densities in both modes. Considerable collaborative efforts have been made to implement and establish a new source mode in KNM4 that ensures that the tritium β and krypton-83m spectra can be recorded under exactly the same source conditions. However, due to hardware limitations, this new mode comes at the cost of a significant reduction in the amount of krypton-83m gas reaching the source tube, resulting in two orders of magnitude loss of activity.
- To partially compensate for the inevitable loss of krypton-83m gas in the new source mode, a stronger krypton-83m generator is required to generate the amount of krypton-83m needed for continued high-statistics measurements. This new generator is currently under construction and will deliver a krypton-83m activity up to five times larger than the one used so far. This increased source strength will also benefit the precision measurement of the weak $N_{2,3}$-32 lines.

When these improvements of the krypton-83m and tritium β measurements are successfully completed, further studies will be necessary to achieve the required accuracy on the estimates $\sigma_0[V]$ and $\Delta_{10}[V]$, including studies of the stability of these estimates for repeated krypton-83m measurements. Also, currently new simulations are being developed to calculate the source potential with refined models. Testing these simulations with krypton-83m measurements is an essential step towards a consistent picture of the source potential systematic. Applying all these measures will pave the way for KATRIN to achieve its planned sensitivity in determining the neutrino mass and to contribute to answering some of the most important contemporary physical questions.

A. Appendix

A.1. Convolution of Starting Potential Distributions

Here it is shown that the modelling of the source potential $V(z)$ can be absorbed in modifications of the i-times convoluted energy loss functions for i-fold scattering. To shorten the notation the integral operator $\mathrm{d}\mathcal{F}$ (acting to the right) is used in the following, absorbing all constants and integrals which are not of interest. The starting point is equation 1.20, giving the count rate $\dot{N}$ at a given retarding energy qU

$$\dot{N}(qU) = \sum_{k}^{\text{slices}} \epsilon_{\text{det}} \frac{\Omega_k}{4\pi} \int_{-\infty}^{\infty} N_k \left(\frac{\mathrm{d}\dot{N}}{\mathrm{d}E}\right) R(E + qV_k, qU)\, \mathrm{d}E\,, \tag{A.1}$$

$$= \underbrace{\epsilon_{\text{det}} \int_{-\infty}^{\infty} \mathrm{d}E \left(\frac{\mathrm{d}\dot{N}}{\mathrm{d}E}\right)}_{\equiv \mathrm{d}\mathcal{F}} \int_z \frac{\mathrm{d}z}{L_{\text{WGTS}}} \frac{\Omega(z)}{4\pi} N(z) R(E + qV(z), qU)\,. \tag{A.2}$$

Here ϵ_{det} is the detector efficiency, Ω the acceptance angle, N the number of gas atoms, $\left(\frac{\mathrm{d}\dot{N}}{\mathrm{d}E}\right)$ the differential spectrum, E the electron energy and $R(E, qU)$ the response function. In the second line the discrete calculation over slices was replaced with an integral along the WGTS of length L_{WGTS}. Plugging in the definition of the response function yields

$$\dot{N}(qU) = \mathrm{d}\mathcal{F} \int_z \frac{\mathrm{d}z}{L_{\text{WGTS}}} \frac{\Omega(z)}{4\pi} N(z) \int_{\epsilon=0}^{E+qV(z)-qU} \mathrm{d}\epsilon \mathcal{T}(E + qV(z) - \epsilon, qU) \sum_{i=0}^{\infty} p_i(z) f_i(\epsilon)\,. \tag{A.3}$$

$\mathcal{T}(E, qU)$ is the transmission function, the $p_i(z)$ are the scattering probabilities and $f_i(\epsilon)$ is the i-times convoluted energy loss function. Then the substitution $\epsilon \longrightarrow \epsilon - qV(z)$ moves the dependence on the electric potential to the energy loss function

$$\dot{N}(qU) = \mathrm{d}\mathcal{F} \int_z \frac{\mathrm{d}z}{L_{\text{WGTS}}} \frac{\Omega(z)}{4\pi} N(z) \int_{\epsilon=0}^{E-qU} \mathrm{d}\epsilon \mathcal{T}(E - \epsilon, qU) \sum_{i=0}^{\infty} p_i(z) f_i(\epsilon - qV(z))\,, \tag{A.4}$$

$$= \underbrace{\mathrm{d}\mathcal{F} \int_{\epsilon=0}^{E-qU} \mathrm{d}\epsilon \mathcal{T}(E - \epsilon, qU)}_{\equiv \mathrm{d}\mathcal{F}(qU)} \sum_{i=0}^{\infty} \int_z \frac{\mathrm{d}z}{L_{\text{WGTS}}} \underbrace{\frac{\Omega(z)}{4\pi} N(z) p_i(z)}_{\equiv P_i(z) \cdot \text{Norm}_i} f_i(\epsilon - qV(z))\,. \tag{A.5}$$

Thus, normalised weight functions

$$P_i(z) = \frac{1}{\text{Norm}_i} \frac{\Omega(z)}{4\pi} N(z) p_i(z) \tag{A.6}$$

were defined, which are the distributions of the signal electrons for i scattering. The normalisations, which are the amount of signal electrons for i scattering, read

$$\mathrm{Norm}_i = \int \frac{\mathrm{d}z}{L_{\mathrm{WGTS}}} \frac{\Omega(z)}{4\pi} N(z) p_i(z) \,. \tag{A.7}$$

Lastly, using the delta distribution $\delta(\eta)$, the z-integration is absorbed in a convolution (symbolised by the operator $*$) with the *Starting Potential Distribution* (SPD_i) for each scattering

$$\dot{N}(qU) = \mathrm{d}\mathcal{F}(qU) \sum_{i=0}^{\infty} \mathrm{Norm}_i \int_z \frac{\mathrm{d}z}{L_{\mathrm{WGTS}}} f_i(\epsilon - qV(z)) P_i(z) \,, \tag{A.8}$$

$$= \mathrm{d}\mathcal{F}(qU) \sum_{i=0}^{\infty} \mathrm{Norm}_i \int_z \frac{\mathrm{d}z}{L_{\mathrm{WGTS}}} \int_{-\infty}^{\infty} \mathrm{d}\eta f_i(\epsilon - \eta) P_i(z) \delta(\eta - qV(z)) \,, \tag{A.9}$$

$$= \mathrm{d}\mathcal{F}(qU) \sum_{i=0}^{\infty} \mathrm{Norm}_i f_i(\epsilon) * \mathrm{SPD}_i \,, \tag{A.10}$$

with [1]

$$\mathrm{SPD}_i(\eta) = \int \frac{\mathrm{d}z}{L_{\mathrm{WGTS}}} \delta(\eta - qV(z)) P_i(z) \,. \tag{A.11}$$

One important implication is that there are different SPD_i for each scattering. Thus, even to first order in the potential magnitude different means $\langle V \rangle_i$ of the potential need to be considered, if electrons of i scattering multiplicity are measured. In practice the full SPD_i cannot be obtained and need to be approximated. Using only up to their second moments leads to Gaussians $G(\langle V \rangle_i, \sigma_i[V])$ or $G(\Delta_{i0}[V], \sigma_i[V])$ (depending on the treatment of $\langle V \rangle_0$), where $\sigma_i[V]$ is the standard deviation of the SPD_i and $\Delta_{i0}[V] = \langle V \rangle_i - \langle V \rangle_0$.

A.2. Quadratic Operator Constraints using Variational Calculus

Here the general constraint of a variance σ_x^2 by a measured variance σ_z^2 and mean difference $\Delta_{\bar{y}}$ is calculated. The statement of the problem is given in section 3.3.2.

Stationary solutions of the Lagrangian 3.47 are found by

$$\begin{aligned}
\frac{\mathrm{d}\mathcal{L}_\sigma}{\mathrm{d}V} &= 2(V - \langle V \rangle_x) P_x + 2\lambda_\sigma (V - \langle V \rangle_z) P_z + \lambda_\Delta P_{\bar{y}} \,, \\
&= 2V(P_x + \lambda_\sigma P_z) - 2(\Delta_{xz}[V] + \langle V \rangle_z) P_x - 2\lambda_\sigma \langle V \rangle_z P_z + \lambda_\Delta P_{\bar{y}} \,, \\
&= 2(V - \langle V \rangle_z)(P_x + \lambda_\sigma P_z) - 2\Delta_{xz}[V] P_x + \lambda_\Delta P_{\bar{y}} \,, \\
&= 0 \,, \\
\Rightarrow V - \langle V \rangle_z &= \Delta_{xz}[V] \frac{P_x}{P_x + \lambda_\sigma P_z} - \frac{\lambda_\Delta}{2} \frac{P_{\bar{y}}}{P_x + \lambda_\sigma P_z} \,.
\end{aligned} \tag{A.12}$$

In the following the different cases of vanishing λ_σ or λ_Δ are considered separately.

[1] The so defined distributions are energy distributions. The corresponding potential distributions are trivially obtained by scaling the x-axis with $1/q$.

No measurement ($\lambda_\sigma = \lambda_\Delta = 0$): The solution reads

$$V = \langle V \rangle_x \ , \tag{A.13}$$

which is the definition of a constant potential. Thus, constant potentials minimise quadratic operators.

Measured only $\Delta_{\bar{y}}$ ($\lambda_\sigma = 0, \lambda_\Delta \neq 0$): The solution reads

$$V - \langle V \rangle_x = -\frac{\lambda_\Delta}{2} \frac{P_{\bar{y}}}{P_x} \ . \tag{A.14}$$

λ_Δ is determined from the known $\Delta_{\bar{y}}[V]$

$$\Delta_{\bar{y}}[V - \langle V \rangle_x] = -\frac{\lambda_\Delta}{2} \Delta_{\bar{y}} \left[\frac{P_{\bar{y}}}{P_x} \right] \ , \tag{A.15}$$

$$\overset{3.39}{=} -\frac{\lambda_\Delta}{2} \kappa^2_{\bar{y},x} \ , \tag{A.16}$$

$$\Rightarrow \lambda_\Delta = -2 \frac{\Delta_{\bar{y}}[V]}{\kappa^2_{\bar{y},x}} \ , \tag{A.17}$$

$$\Rightarrow V - \langle V \rangle_x = \frac{\Delta_{\bar{y}}[V]}{\kappa^2_{\bar{y},x}} \frac{P_{\bar{y}}}{P_x} \ . \tag{A.18}$$

Due to their different normalisations it also follows that $P_x \neq P_{\bar{y}}$, leading to a finite value of $\kappa^2_{\bar{y},x}$. Calculating the expectation value of $\sigma_x[\ldots]$ leads to

$$\sigma_x[V] = \frac{|\Delta_{\bar{y}}[V]|}{\kappa_{\bar{y},x}} \ . \tag{A.19}$$

As before, this gives the minimum $\sigma_x[V]$ in case $\Delta_{\bar{y}}[V]$ has been measured.

Measured only σ_z ($\lambda_\sigma \neq 0, \lambda_\Delta = 0$): The solution reads

$$V - \langle V \rangle_z = \Delta_{xz}[V] \frac{P_x}{P_x + \lambda_\sigma P_z} \ . \tag{A.20}$$

λ_σ is determined by demanding consistency with the expectation values of $\langle \ldots \rangle_z$ and $\Delta_{xz}[\ldots]$:

$$0 = \langle V \rangle_z - \langle V \rangle_z = \Delta_{xz}[V] \left\langle \frac{P_x}{P_x + \lambda_\sigma P_z} \right\rangle_z \ , \tag{A.21}$$

$$\Rightarrow \Delta_{xz}[V] = 0 \quad \text{or} \quad \left\langle \frac{P_x}{P_x + \lambda_\sigma P_z} \right\rangle_z = 0 \ . \tag{A.22}$$

Plugging the first case $\Delta_{xz}[V] = 0$ into equation A.20 leads to the trivial constant solution $V = \langle V \rangle_z$, i.e. $\sigma_x[V] = \sigma_z[V] = 0$.

The second case is an integral equation for the determination of λ_σ. Using $\langle P_x \rangle_z = \langle P_x P_z \rangle$ it follows:

$$0 = \left\langle \frac{P_x}{P_x + \lambda_\sigma P_z} \right\rangle_z , \tag{A.23}$$

$$= \frac{1}{\lambda_\sigma} \left\langle \frac{\lambda_\sigma P_z}{P_x + \lambda_\sigma P_z} \right\rangle_x , \tag{A.24}$$

$$= \frac{1}{\lambda_\sigma} \left(1 - \left\langle \frac{P_x}{P_x + \lambda_\sigma P_z} \right\rangle_x \right) , \tag{A.25}$$

$$\Leftrightarrow \left\langle \frac{P_x}{P_x + \lambda_\sigma P_z} \right\rangle_x = 1 . \tag{A.26}$$

In the 3 line the enumerator was expanded to match the denominator, which will be a useful trick also in the following. Subtracting the original condition equation A.23 from this new condition gives

$$\Rightarrow \Delta_{xz} \left[\frac{P_x}{P_x + \lambda_\sigma P_z} \right] = 1 . \tag{A.27}$$

Thus, the consistency with the expectation value of $\Delta_{xz}[...]$ of the extremal solution equation A.20

$$\Delta_{xz}[V - \langle V \rangle_z] = \Delta_{xz}[V] \Delta_{xz} \left[\frac{P_x}{P_x + \lambda_\sigma P_z} \right] , \tag{A.28}$$

$$\Rightarrow \Delta_{xz}[V] = 0 \quad \text{or} \quad \Delta_{xz} \left[\frac{P_x}{P_x + \lambda_\sigma P_z} \right] = 1 , \tag{A.29}$$

is automatically fulfilled and equation A.23 is the only necessary condition for non-trivial solutions. Also, it can be shown that the inverse implication

$$\Delta_{xz} \left[\frac{P_x}{P_x + \lambda_\sigma P_z} \right] = 1 \Rightarrow \left\langle \frac{P_x}{P_x + \lambda_\sigma P_z} \right\rangle_z = 0 \tag{A.30}$$

is in general only valid for $\lambda_\sigma \neq -1$. Indeed, $\left\langle \frac{P_x}{P_x - P_z} \right\rangle_z \neq 0$ was found for the tested weights, although $\Delta_{xz} \left[\frac{P_x}{P_x - P_z} \right] = 1$ trivially holds. Thus, equation A.23 is the necessary condition and equation A.27 alone is not sufficient.

The expectation value of the measured $\sigma_z[...]$ reads

$$\sigma_z[V - \langle V \rangle_z] = |\Delta_{xz}[V]| \sigma_z \left[\frac{P_x}{P_x + \lambda_\sigma P_z} \right] , \tag{A.31}$$

$$\Rightarrow V - \langle V \rangle_z = \mathrm{sgn}(\Delta_{xz}[V]) \sigma_z[V] \frac{P_x}{P_x + \lambda_\sigma P_z} / \sigma_z \left[\frac{P_x}{P_x + \lambda_\sigma P_z} \right] , \tag{A.32}$$

$$\Rightarrow V - \langle V \rangle_z = \pm \sigma_z[V] \frac{P_x}{P_x + \lambda_\sigma P_z} / \sigma_z \left[\frac{P_x}{P_x + \lambda_\sigma P_z} \right] . \tag{A.33}$$

The expectation value of $\sigma_x[...]$ is

$$\sigma_x[V - \langle V\rangle_z] = \sigma_z[V]\frac{\sigma_x\left[\frac{P_x}{P_x+\lambda_\sigma P_z}\right]}{\sigma_z\left[\frac{P_x}{P_x+\lambda_\sigma P_z}\right]}\,. \tag{A.34}$$

Using the necessary condition equation A.23 this can be further simplified. First, the relations obtained in the derivation of equation A.26 should be collected again. It holds:

$$\left\langle \frac{P_n}{P_x+\lambda_\sigma P_z}\right\rangle_m = \delta_{nm}\left(\delta_{nx}+\delta_{nz}\frac{1}{\lambda_\sigma}\right)\,,\quad n,m\in\{x,z\}\,, \tag{A.35}$$

or written out:

$$\left\langle \frac{P_xP_z}{P_x+\lambda_\sigma P_z}\right\rangle = \left\langle \frac{P_x}{P_x+\lambda_\sigma P_z}\right\rangle_z = \left\langle \frac{P_z}{P_x+\lambda_\sigma P_z}\right\rangle_x = 0\,, \tag{A.36}$$

$$\left\langle \frac{P_x^2}{P_x+\lambda_\sigma P_z}\right\rangle = \left\langle \frac{P_x}{P_x+\lambda_\sigma P_z}\right\rangle_x = \lambda_\sigma\left\langle \frac{P_z}{P_x+\lambda_\sigma P_z}\right\rangle_z = \lambda_\sigma\left\langle \frac{P_z^2}{P_x+\lambda_\sigma P_z}\right\rangle = 1\,. \tag{A.37}$$

Using that it follows

$$\begin{aligned}
\sigma_x^2\left[\frac{P_x}{P_x+\lambda_\sigma P_z}\right] &\overset{A.37}{=} \left\langle \frac{P_x^2}{(P_x+\lambda_\sigma P_z)^2}\right\rangle_x - 1\,, && \text{(A.38)}\\
&= -\left\langle \frac{2\lambda_\sigma P_zP_x+\lambda_\sigma^2P_z^2}{(P_x+\lambda_\sigma P_z)^2}\right\rangle_x\,, && \text{(A.39)}\\
&= -\left\langle \frac{2\lambda_\sigma P_zP_x+\lambda_\sigma P_z(\lambda_\sigma P_z+P_x-P_x)}{(P_x+\lambda_\sigma P_z)^2}\right\rangle_x\,, && \text{(A.40)}\\
&= -\left\langle \frac{\lambda_\sigma P_zP_x}{(P_x+\lambda_\sigma P_z)^2}\right\rangle_x - \left\langle \frac{\lambda_\sigma P_z(P_x+\lambda_\sigma P_z)}{(P_x+\lambda_\sigma P_z)^2}\right\rangle_x\,, && \text{(A.41)}\\
&\overset{A.36}{=} -\lambda_\sigma\sigma_z^2\left[\frac{P_x}{P_x+\lambda_\sigma P_z}\right] - \lambda_\sigma\left\langle \frac{P_z}{P_x+\lambda_\sigma P_z}\right\rangle_x\,, && \text{(A.42)}\\
&\overset{A.36}{=} -\lambda_\sigma\sigma_z^2\left[\frac{P_x}{P_x+\lambda_\sigma P_z}\right]\,. && \text{(A.43)}
\end{aligned}$$

Finally, this leads to the solutions

$$\sigma_x[V] = \sigma_z[V]\sqrt{-\lambda_\sigma}\,,\quad \left\langle \frac{P_x}{P_x+\lambda_\sigma P_z}\right\rangle_z = 0\,, \tag{A.44}$$

which are discussed in the following:

- The simplicity of the solutions is already apparent from the Lagrangian 3.47, from which
$$\frac{\mathrm{d}\sigma_x^2[V]}{\mathrm{d}V} = -\lambda_\sigma\frac{\mathrm{d}\sigma_0^2[V]}{\mathrm{d}V} \tag{A.45}$$
follows for $\lambda_\Delta = 0$. Thus, $\sigma_x^2[V]$ and $\sigma_0^2[V]$ vary proportionally with potential magnitude.

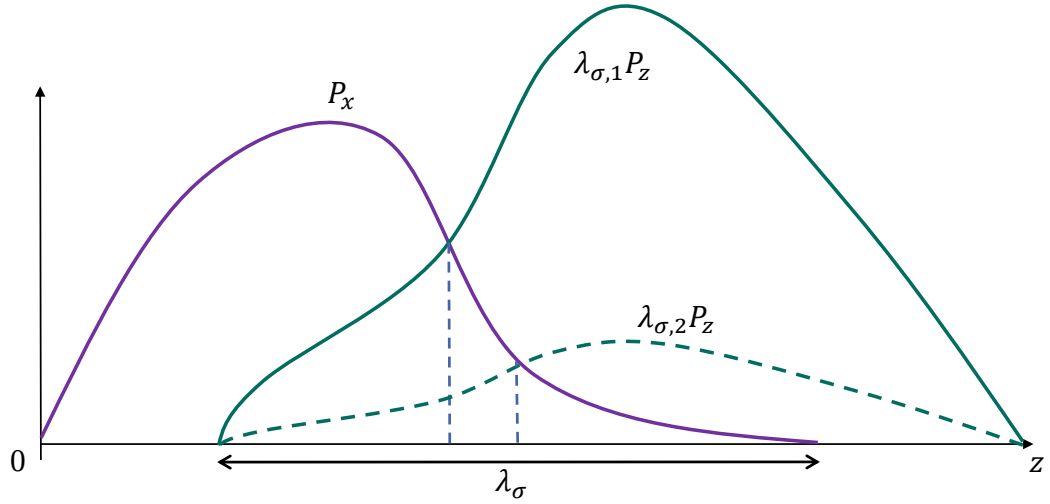

Figure A.1.: Intersection of scaled weights: Scaling P_z with λ_σ leads to an intersection with P_x at z_0 in the interval of z, where both weights are not vanishing.

- In the asymptotic cases of $\lambda_\sigma \to \pm\infty$ it follows that $\left\langle \frac{P_x}{P_x+\lambda_\sigma P_z} \right\rangle_z \to \frac{1}{\lambda_\sigma} \neq 0$. Also, since the weights are positive, solutions are limited to an interval I of negative λ_σ.
- Due the normalisation of P_x and P_z to 1 they need to intersect. Thus, $P_x(z_0) = P_z(z_0)$ holds for at least one z_0, such that $P_x + \lambda_\sigma P_z$ has roots for $\lambda_\sigma < 0$. They are at

$$\frac{P_x}{P_z}(z_0) = -\lambda_\sigma \,. \tag{A.46}$$

  Thus, the potential has a pole at $z_0(\lambda_\sigma)$. I is trivially obtained by finding the maximum and minimum of $\frac{P_x}{P_z}(z)$. As visible in figure A.1, changing λ_σ in this interval shifts the pole exactly to all z_0, where P_x and P_z are not vanishing.
- $\left\langle \frac{P_x}{P_x+\lambda_\sigma P_z} \right\rangle_z = 0$ can only hold, if the argument is not strictly positive or negative. This happens only for $\lambda_\sigma \in I$.

Thus, for potentials with strongly localised inhomogeneity at z_0 equation A.44 can be reformulated to

$$\frac{\sigma_x^2[V]}{\sigma_z^2[V]} = \frac{P_x}{P_z}(z_0) \,, \tag{A.47}$$

which is the result from the main text.

Measured both σ_z and $\Delta_{\bar{y}}$ ($\lambda_\sigma \neq 0, \lambda_\Delta \neq 0$): The solution reads

$$V - \langle V \rangle_z = \Delta_{xz}[V] \frac{P_x}{P_x + \lambda_\sigma P_z} - \frac{\lambda_\Delta}{2} \frac{P_{\bar{y}}}{P_x + \lambda_\sigma P_z} \,. \tag{A.48}$$

The function $\lambda_\Delta(\lambda_\sigma)$ can be determined by demanding consistency with the expectation values of $\langle\ldots\rangle_z$ and $\Delta_{xz}[\ldots]$:

$$0 = \langle V\rangle_z - \langle V\rangle_z = \Delta_{xz}[V]\left\langle\frac{P_x}{P_x+\lambda_\sigma P_z}\right\rangle_z - \frac{\lambda_\Delta}{2}\left\langle\frac{P_{\bar{y}}}{P_x+\lambda_\sigma P_z}\right\rangle_z , \tag{A.49}$$

$$\Rightarrow \Delta_{xz}[V]\left\langle\frac{P_x}{P_x+\lambda_\sigma P_z}\right\rangle_z = \frac{\lambda_\Delta}{2}\left\langle\frac{P_{\bar{y}}}{P_x+\lambda_\sigma P_z}\right\rangle_z . \tag{A.50}$$

$$\Delta_{xz}[V-\langle V\rangle_z] = \Delta_{xz}[V]\Delta_{xz}\left[\frac{P_x}{P_x+\lambda_\sigma P_z}\right] - \frac{\lambda_\Delta}{2}\Delta_{xz}\left[\frac{P_{\bar{y}}}{P_x+\lambda_\sigma P_z}\right] , \tag{A.51}$$

$$\Rightarrow \Delta_{xz}[V]\left(\Delta_{xz}\left[\frac{P_x}{P_x+\lambda_\sigma P_z}\right]-1\right) = \frac{\lambda_\Delta}{2}\Delta_{xz}\left[\frac{P_{\bar{y}}}{P_x+\lambda_\sigma P_z}\right] . \tag{A.52}$$

Again it can be shown, that from the condition on $\langle\ldots\rangle_z$ the condition on $\Delta_{xz}[\ldots]$ follows and that for $\lambda_\sigma \neq -1$ both conditions are equivalent. By solving for $\frac{\lambda_\Delta}{2}$ they can be used to rewrite the solution equation A.48 as

$$V - \langle V\rangle_z = \Delta_{xz}[V]\left(\frac{P_x}{P_x+\lambda_\sigma P_z} - r(\lambda_\sigma)\frac{P_{\bar{y}}}{P_x+\lambda_\sigma P_z}\right) . \tag{A.53}$$

Here

$$r(\lambda_\sigma) \equiv \frac{\left\langle\frac{P_x}{P_x+\lambda_\sigma P_z}\right\rangle_z}{\left\langle\frac{P_{\bar{y}}}{P_x+\lambda_\sigma P_z}\right\rangle_z} = \frac{\Delta_{xz}\left[\frac{P_x}{P_x+\lambda_\sigma P_z}\right]-1}{\Delta_{xz}\left[\frac{P_{\bar{y}}}{P_x+\lambda_\sigma P_z}\right]} \tag{A.54}$$

has been defined [2].

For brevity of notation, the following expectation values of weights as function of λ_σ are defined:

$$\mu_{nm} \equiv \left\langle\frac{P_n}{P_x+\lambda_\sigma P_z}\right\rangle_m = \left\langle\frac{P_nP_m}{P_x+\lambda_\sigma P_z}\right\rangle , \quad n,m \in \{x,\bar{y},z\} , \tag{A.55}$$

$$\mu_{nm} = \mu_{mn} , \tag{A.56}$$

$$\mu_{xn} = \langle P_n\rangle - \lambda_\sigma\mu_{zn} , \tag{A.57}$$

$$\Sigma_k^{nm} \equiv \mathrm{Cov}_k\left[\frac{P_n}{P_x+\lambda_\sigma P_z},\frac{P_m}{P_x+\lambda_\sigma P_z}\right] = \left\langle\frac{P_nP_mP_k}{(P_x+\lambda_\sigma P_z)^2}\right\rangle - \mu_{nk}\mu_{mk} , \tag{A.58}$$

$$\Sigma_k^{nm} = \Sigma_k^{mn} , \tag{A.59}$$

$$\Sigma_k^{xx} = \lambda_\sigma^2\Sigma_k^{zz} , \tag{A.60}$$

$$\Sigma_k^{nx} = -\lambda_\sigma\Sigma_k^{nz} , \tag{A.61}$$

$$\Sigma_x^{nm} = -\lambda_\sigma\Sigma_z^{nm} + \mu_{nm} - \mu_{nx}\mu_{mx} - \lambda_\sigma\mu_{nz}\mu_{mz} , \tag{A.62}$$

[2] The $\langle\ldots\rangle_z$ condition avoids problematic expressions of the form $\frac{0}{0}$ at $\lambda_\sigma = -1$. However, due the existence of poles in practice the $\Delta_{xz}[\ldots]$ condition might lead to more stable results, if simple numerical integration algorithms are used.

i.e. one change $x \rightarrow z$ in an upper index requires a factor $-\lambda_\sigma$. This can be proven by expanding the enumerator and by using binomial formulas.

The expectation value $\Delta_{xz}[V]$ is determined from the measured $\Delta_{\bar{y}}[V]$

$$\Delta_{\bar{y}}[V - \langle V \rangle_z] = \Delta_{xz}[V]\Delta_{\bar{y}}\left[\frac{P_x}{P_x + \lambda_\sigma P_z} - r\frac{\bar{y}}{P_x + \lambda_\sigma P_z}\right], \tag{A.63}$$

$$= \Delta_{xz}[V](\mu_{\bar{y}x} - r\mu_{\bar{y}\bar{y}}) . \tag{A.64}$$

$$\Rightarrow \Delta_{xz}[V] = \Delta_{\bar{y}}[V]\frac{1}{\mu_{\bar{y}x} - r\mu_{\bar{y}\bar{y}}} \equiv \Delta_{\bar{y}}[V]r' . \tag{A.65}$$

The expectation value $\sigma_k^2[V]$ is given by

$$\sigma_k^2[V - \langle V \rangle_z] = \Delta_{\bar{y}}^2[V]r'^2\left(\Sigma_k^{xx} + r^2\Sigma_k^{\bar{y}\bar{y}} - 2r\Sigma_k^{x\bar{y}}\right) . \tag{A.66}$$

Thus, the ratio of the standard deviations is given by

$$\frac{\sigma_x[V]}{\sigma_z[V]} = \sqrt{\frac{\Sigma_x^{xx} + r^2\Sigma_x^{\bar{y}\bar{y}} - 2r\Sigma_x^{x\bar{y}}}{\Sigma_z^{xx} + r^2\Sigma_z^{\bar{y}\bar{y}} - 2r\Sigma_z^{x\bar{y}}}}, \tag{A.67}$$

and the absolute value of the shape operator reads

$$|\hat{\rho}_{\bar{y},z}[V]| = \frac{1}{\kappa_{\bar{y},z}}\frac{|\Delta_{\bar{y}}[V]|}{\sigma_z[V]}, \tag{A.68}$$

$$= \frac{1}{\kappa_{\bar{y},z}|r'|}\frac{1}{\sqrt{\Sigma_z^{xx} + r^2\Sigma_z^{\bar{y}\bar{y}} - 2r\Sigma_z^{x\bar{y}}}} . \tag{A.69}$$

The last two equations can be calculated in dependence of λ_σ, implicitly defining an exclusion area $\frac{\sigma_x}{\sigma_z}(|\hat{\rho}_{\bar{y},z}|)$.

Expectation value for $\hat{\rho}_{\bar{y},z} = \pm 1$: As shown in section 3.3 in this case the full potential is given by

$$V - \langle V \rangle_z = \pm\frac{\sigma_z}{\kappa_{\bar{y},z}}\frac{P_{\bar{y}}}{P_z}, \tag{A.70}$$

with the weight standard deviation $\kappa_{\bar{y},z}$. The ratio of the standard deviations is thus given by

$$\frac{\sigma_x[V]}{\sigma_z[V]} = \frac{\sigma_x\left[\frac{P_{\bar{y}}}{P_z}\right]}{\sigma_z\left[\frac{P_{\bar{y}}}{P_z}\right]} . \tag{A.71}$$

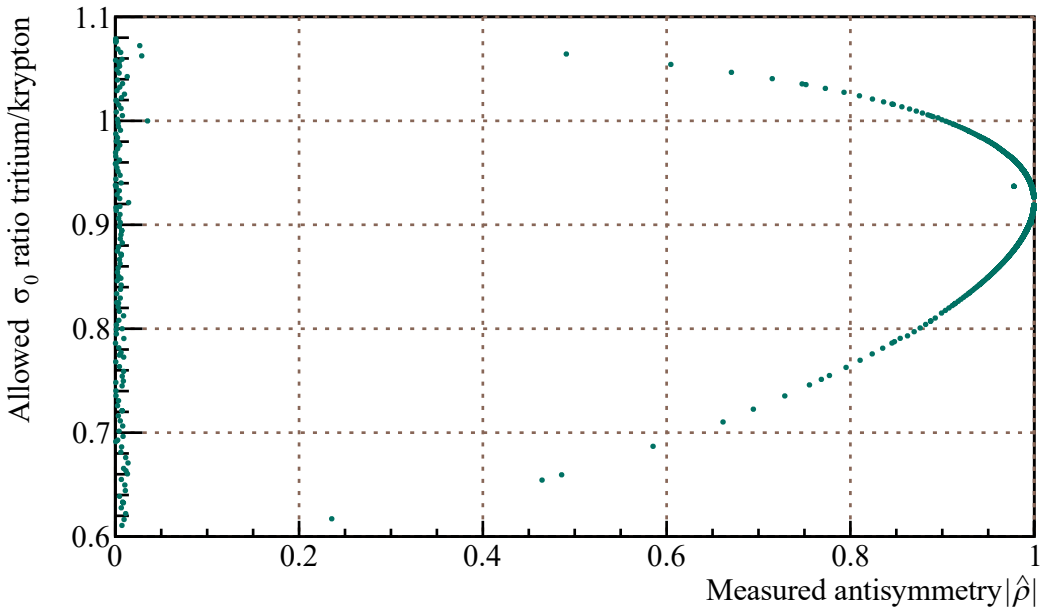

Figure A.2.: Constraint of tritium σ_0 for given krypton observables: In the limit of vanishing antisymmetry the extremal solutions are poles at z_0, and the constraint is given by the square root of the ratio of the P_0 at z_0. In this region instabilities occur due to the numerical integration over the pole in the potential. For maximum antisymmetry the exact potential is known, and the constraint gives a ratio as predicted in the text. The simulation used 40 % tritium column density for both krypton and tritium mode.

Example for σ_0 of tritium constrained from krypton: The resulting constraint is plotted in figure A.2. It is given by equations A.67 and A.69, which are calculated numerically. Each marker corresponds to one λ_σ. The allowed ratios are inside the ellipse. As discussed in the main text and visualised in figure 3.17 the constraint of σ_x strongly depends on the localisation of the inhomogeneity. For small antisymmetry the inhomogeneity can be localised in a pole at z_0, such that the ratio of the variances is the ratio of the weights at z_0. For large antisymmetry the potential shape is exactly known. This produces the overall approximately elliptic contour.

A.3. Uncertainty on the Predicted Shift of the Squared Neutrino Mass from Column Density Uncertainty

As discussed in section 3.5, differences in operating parameters between the krypton and tritium measurement translate into an uncertainty of the prediction of the shift of the squared neutrino mass for given krypton estimates $(\hat{\rho}, \sigma_0)$. Two methods were shown, one by calculating the extremal derivatives of the predicted shift of the squared neutrino mass, the other by expanding the derivative of the squared neutrino mass in the known operators.

Figure A.3 shows the derivative of the neutrino mass shift prediction with respect to the tritium column density, calculated with both methods. Here, the tritium column density in the krypton measurement was taken to be 45 % of the nominal value and the uncertainty of the neutrino mass shift prediction is obtained when the values are multiplied with the relative uncertainty of the column density determination or the relative column density difference to the tritium measurement. Thus, for usual column density uncertainties of 1 %, uncertainties on the prediction of the shift of the squared neutrino mass of $\propto 10^{-3}$ eV^2 are obtained, which increase accordingly for actual column density differences of the measurements.

Since both methods agree well, one can use the approximate weight expansion to further reduce the uncertainties. In this example, the following expansion was found

$$\rho d \frac{\mathrm{d}P_0}{\mathrm{d}\rho d}\bigg|_{\rho d=45\ \%}(z) \approx -0.44(P_1 - P_0)(z)\,, \quad \rho d\ \frac{\mathrm{d}P_1}{\mathrm{d}\rho d}\bigg|_{\rho d=45\ \%}(z) \approx -0.56(P_2 - P_1)(z)\,. \tag{A.72}$$

This allows to write the derivative of the shift of the squared neutrino mass as

$$\rho d \frac{\mathrm{d}\Delta m_\nu^2[V]}{\mathrm{d}\rho d}\bigg|_{\rho d=45\ \%} = 0.86(\sigma_1^2[V] - \sigma_0^2[V]) - 980\ \mathrm{meV}\Delta_{10}[V] + 487\ \mathrm{meV}\Delta_{21}[V]\,. \tag{A.73}$$

Thus, the derivative has a component $\propto \Delta_{10}[V]$, which is known from the measurement and the uncertainty of the extrapolation stems only from the other two terms. The known term can be used to extrapolate the mean $\Delta m_\nu^2[V](\rho d)$ and only the unknown terms are left, to calculate its uncertainty $\Delta_{\rho d}(\Delta m_\nu^2[V](\rho d))$. Compared to the extremal solution, this reduces the uncertainty from column density extrapolation by approximately a factor of 2 in this example.

The linear extrapolation using only the first derivative was tested with known potentials, and in all tested cases it was sufficient, even for column density changes above 10 % of nominal.

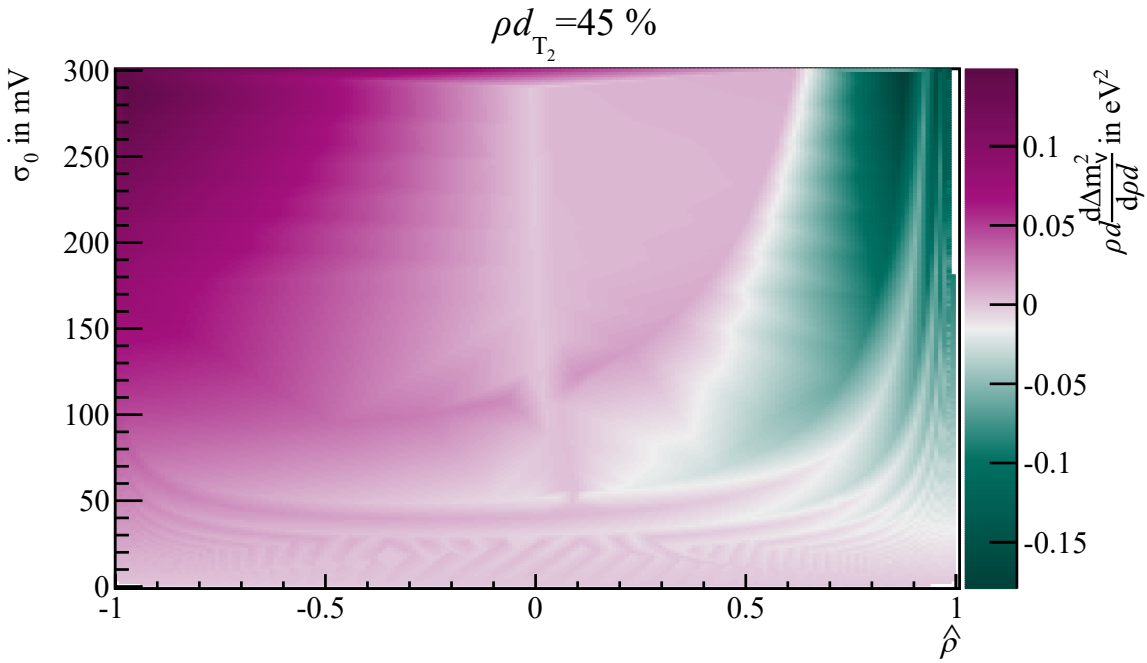

(a) Exact stationary solutions

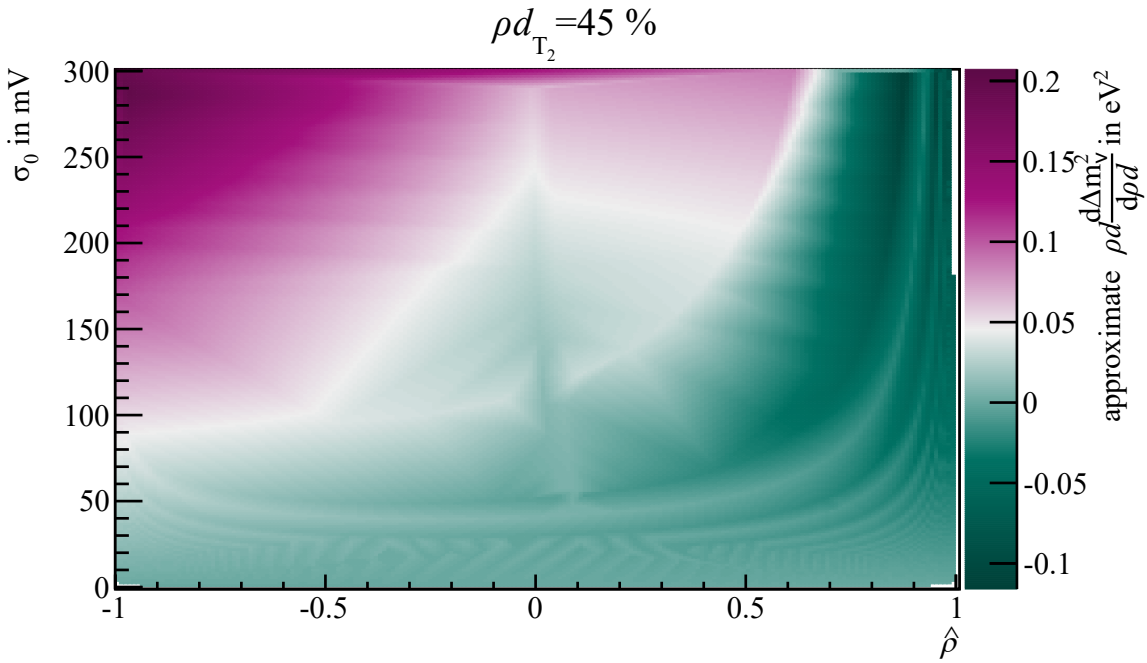

(b) Approximate expansion of weights

Figure A.3.: Column density uncertainty of neutrino mass shift prediction: For a given set of krypton estimates $(\hat{\rho}, \sigma_0)$, the plots show the change of the predicted shift of the squared neutrino mass with tritium column density ρd. When multiplied with the relative column density uncertainty, the uncertainty of the predicted shift of the squared neutrino mass is obtained. The stationary solution (a) and the approximate weight expansion (b) largely agree. Both show non-trivial topology and oscillatory patterns. Since they differ slightly in the extrema, the color scales are not the same.

A.4. Performed Studies on Krypton Data

Many analysis methods were tried on the fitted data, some of which are described in the following.

Pile-up correction: Pile-up correction has been applied to all krypton plasma fits. In krypton reference runs, where the total rate is approximately 10 times smaller than in plasma runs, the correction does not make a significant difference.

Fit tolerance dependence: Fit tolerances in the range from 0.5 to 0.05 were tried, which showed almost exactly the same estimates.

Fitting only energies above 30462 eV (unscattered electrons): When only fitting the unscattered L_3-32 line, within uncertainties the same results are obtained as when fitting the total spectrum. This has been tested for total Lorentzian fit, Gaussian broadening fit and the line position.

Remove KNM1 runs where the tritium the column density drifted strongly: In KNM1 the column density drifted strongly for run numbers smaller than 52680. Removing them only affects the measurements at the rear wall voltages of -150 mV and 175 mV. The general shape of the estimates over the rear wall voltage is conserved and the overall changes are small.

Krypton in DPS1F$_2$: The krypton generator is connected to a DPS1F$_2$ pump port. Thus, krypton cannot flow in opposite direction of the gas stream coming from the central WGTS, such that it reaches the injection chamber only after being circled once. This gave reason to believe that there might be some significant over density $N_{\mathrm{DPS2F_2}}$ of krypton inside the DPS1F$_2$ compared to the modelling with 0 density in the SSC gas profile. This would lead to an increased number of unscattered electrons and thus look like a smaller tritium column density in a fit. This was tested on KNM1 krypton data by fixing the tritium column density to 27 % of the its nominal value as expected from the BIXS rate and fitting a constant density inside DPS1F$_2$ ($z_{\mathrm{DPS1F_2}} = 6.58931$ m, $L_{\mathrm{DPS1F_2}}/2 = 0.1273$ m compared to injection point). Run 5276 was used in a uniform fit with 100 slices, the result being $\frac{N_{\mathrm{DPS2F_2}}}{N_{\mathrm{Injection}}} = 0 \pm 7 \cdot 10^{-3}$. However, this result did not include a background slope yet and should be repeated on newer data. If it is true, it can be concluded that there is no significant amount of unscattered krypton-83m electrons not predicted by the SSC gas profile.

Effect of source slicing on the fitted column density: To obtain correct values for the column density from the krypton fit, the WGTS model needs to be sliced. 100 slices were used. For a non-sliced model the difference of the krypton and tritium gas profiles cannot be considered. Since, compared to the tritium the krypton accumulates at the WGTS ends, the

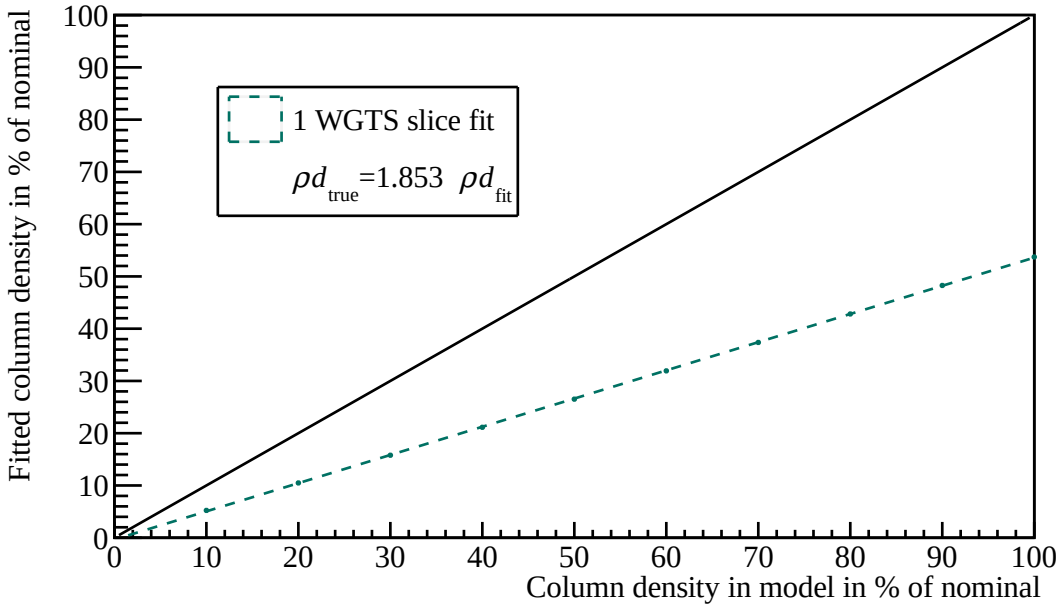

Figure A.4.: Fitted tritium column density for 1 WGTS slice in comparison to true value: If only 1 slice is used in the fit, the correct value of the column density is obtained by $\rho d_{\text{true}} = 1.853 \rho d_{\text{fit}}$.

fraction of unscattered to one-time scattered electrons is larger in krypton, which without slicing is misinterpreted by a too small tritium column density. As shown in figure A.4 on Asimov data, for a non-sliced fit the true column density is approximately 1.853 times the fitted one. This does not have a sizeable effect ($\lesssim$ 1 mV) on the plasma estimators, which was found in simulations using 100 compared to 1 slice. Thus, in principle, if the column density is not of interest, no slicing needs to be used, which speeds up the calculations significantly. The same reasoning holds for other parameters specifying the intensity, i.e. the fitted conversion coefficient, which is only correct for more than $\approx$ 10 slices.

A.5. Uncertainty Propagation

The following square root and square transformations were used regularly. Gaussian propagation and direct transformation are equal for the calculated condition. Thus, for larger means the Gaussian propagation and for smaller means the direct transformation of the uncertainties is used.

Square root transformation:

$$x^2 \rightarrow x\,, \tag{A.74}$$

i.e. x^2 is the free variable, given are mean x^2 and uncertainty $\sigma(x^2)$. $\sigma(x)$ should be calculated. The transformation function is $f(...) = \sqrt{...}$:

$$\frac{\partial\sqrt{x^2}}{\partial x^2} = \frac{1}{2\sqrt{x^2}}\,, \tag{A.75}$$

$$= \frac{1}{2|x|}\,, \tag{A.76}$$

$$\Rightarrow \sigma(|x|) = \frac{1}{2|x|}\sigma(x^2)\,. \tag{A.77}$$

For small mean compared to uncertainty:

$$\frac{1}{2|x|}\sigma(x^2) \overset{!}{>} \sqrt{\sigma(x^2)}\,, \tag{A.78}$$

$$\Leftrightarrow \frac{1}{4x^2}\sigma^2(x^2) > \sigma(x^2)\,, \tag{A.79}$$

$$\Leftrightarrow \sigma(x^2) > 4x^2\,. \tag{A.80}$$

Square transformation:

$$x \rightarrow x^2\,, \tag{A.81}$$

i.e. x is the free variable, given are mean x and uncertainty $\sigma(x)$. $\sigma(x^2)$ should be calculated. The transformation function is $f(...) = (...)^2$:

$$\frac{\partial x^2}{\partial x} = 2x\,, \tag{A.82}$$

$$\Rightarrow \sigma(x^2) = 2x\sigma(x)\,. \tag{A.83}$$

For small mean compared to uncertainty:

$$2x\sigma(x) \overset{!}{>} \sigma^2(x)\,, \tag{A.84}$$

$$\Leftrightarrow \sigma(x) > 2x\,. \tag{A.85}$$

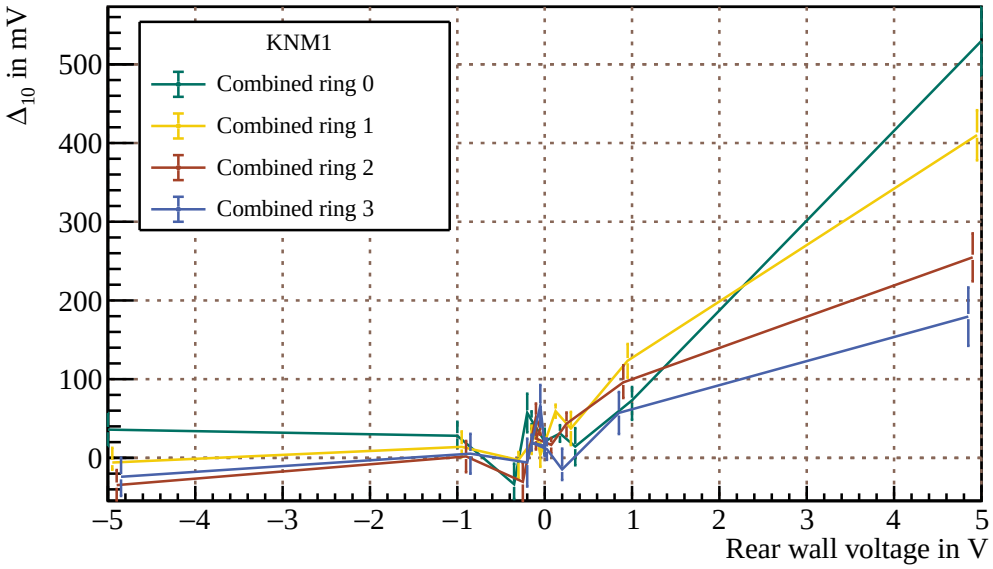

Figure A.5.: Measured mean difference in KNM1 krypton: The curves resemble the measurement of KNM2 but are shifted by roughly 60 mV. For 1 eV and 5 eV rear wall voltage the shift reduces to ≈ 30 mV. Since at large voltages the measurement is dominated by the external field and not by systematics, a vanishing/reducing shift in this region is a hint for real physical effect. An overall constant shift would be likely caused by an analysis error.

A.6. Plots of the KNM1 and KNM2 Krypton Results

In this section plots of the KNM1 and KNM2 krypton measurement are shown. Figure A.5 shows the measured mean differences in KNM1. The overall spectrum is comparable to KNM2, however the absolute values are shifted by roughly 60 mV.

The following histograms are shown:

- Figure A.6: χ^2 distributions of the fits.
- Figure A.7: Histograms of the measured tritium column density.
- Figure A.8: Histograms of the measured variances σ_g^2.
- Figure A.9: Histograms of the measured mean differences Δ_{10}.

All obey the expected overall Gaussian (or χ^2) distributions. Since the histograms also include strongly positive rear wall voltages, which leads to shifts of the estimates, they can obey non-Gaussian structure. However, most of the data was taken in the coupling region, such that the mean of the fitted Gauss peak to very good degree reflects the measured mean for small rear wall voltages. Significant differences exist for the plasma inhomogeneity estimates of the two campaigns, the reason of which is not understood entirely.

Figures A.10 and A.11 show the z-dependent potentials, deduced from the KNM2 measurement, without bins of the rear wall voltages.

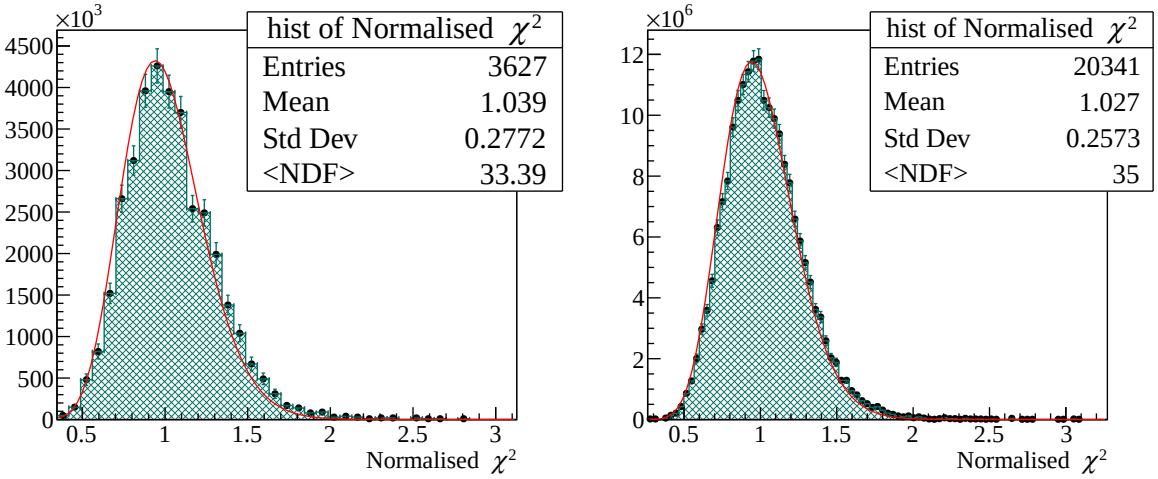

(a) KNM1 (b) KNM2

Figure A.6.: χ^2 distributions of the fits: As visible both distributions show good agreement with the expectation, i.e. the model described most of the data without obvious errors. The small amount of higher values is caused by the fits at large positive rear wall voltages. In KNM1 the number of subruns in up and down scans differed by 1, such that the average number of degrees of freedom is not integer.

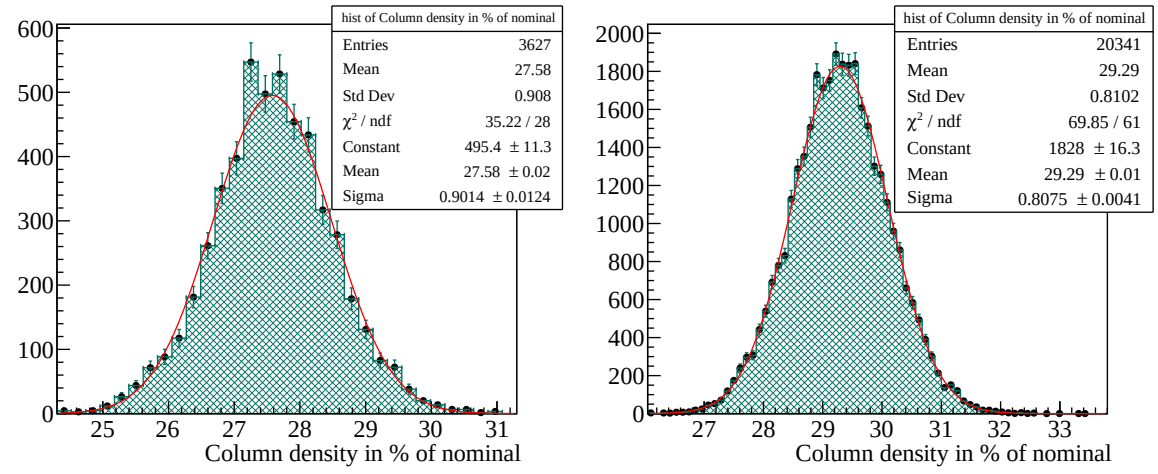

(a) KNM1 (b) KNM2

Figure A.7.: Histograms of the measured tritium column density: The column density is fitted from the ratio of one-time scattered to unscattered electrons. Both campaigns show a column density of roughly 30 % of nominal, which was the maximum possible in the respective campaigns. The fitted column density values were compared to the BIXS and FBM values and agree within uncertainties.

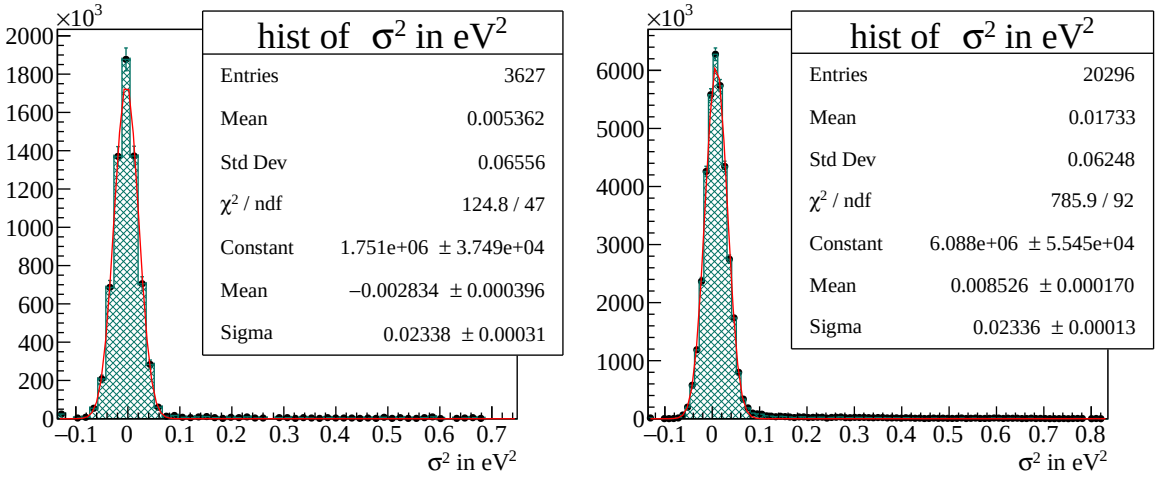

(a) KNM1 (b) KNM2

Figure A.8.: Histograms of the measured variances: The KNM1 results are significantly more negative than the KNM2 results. The reason is not understood. The used intrinsic Lorentzian $\Gamma = 1.0606(21)(150)$ eV is taken from the CKrS measurement.

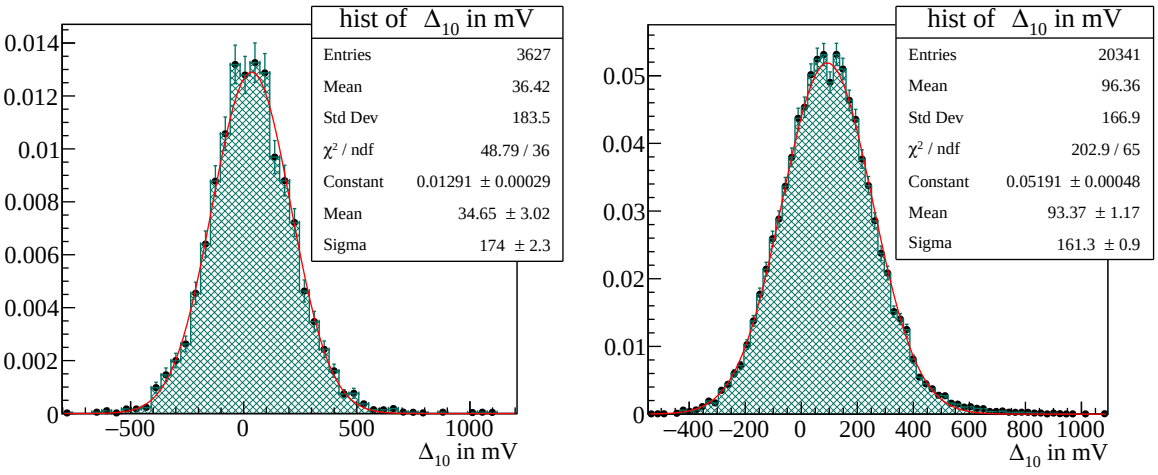

(a) KNM1 (b) KNM2

Figure A.9.: Histograms of the measured mean differences: The results are shifted compared to each others by approximately 60 mV. The values are not corrected for the wrong energy loss function and neglected detailed transmission.

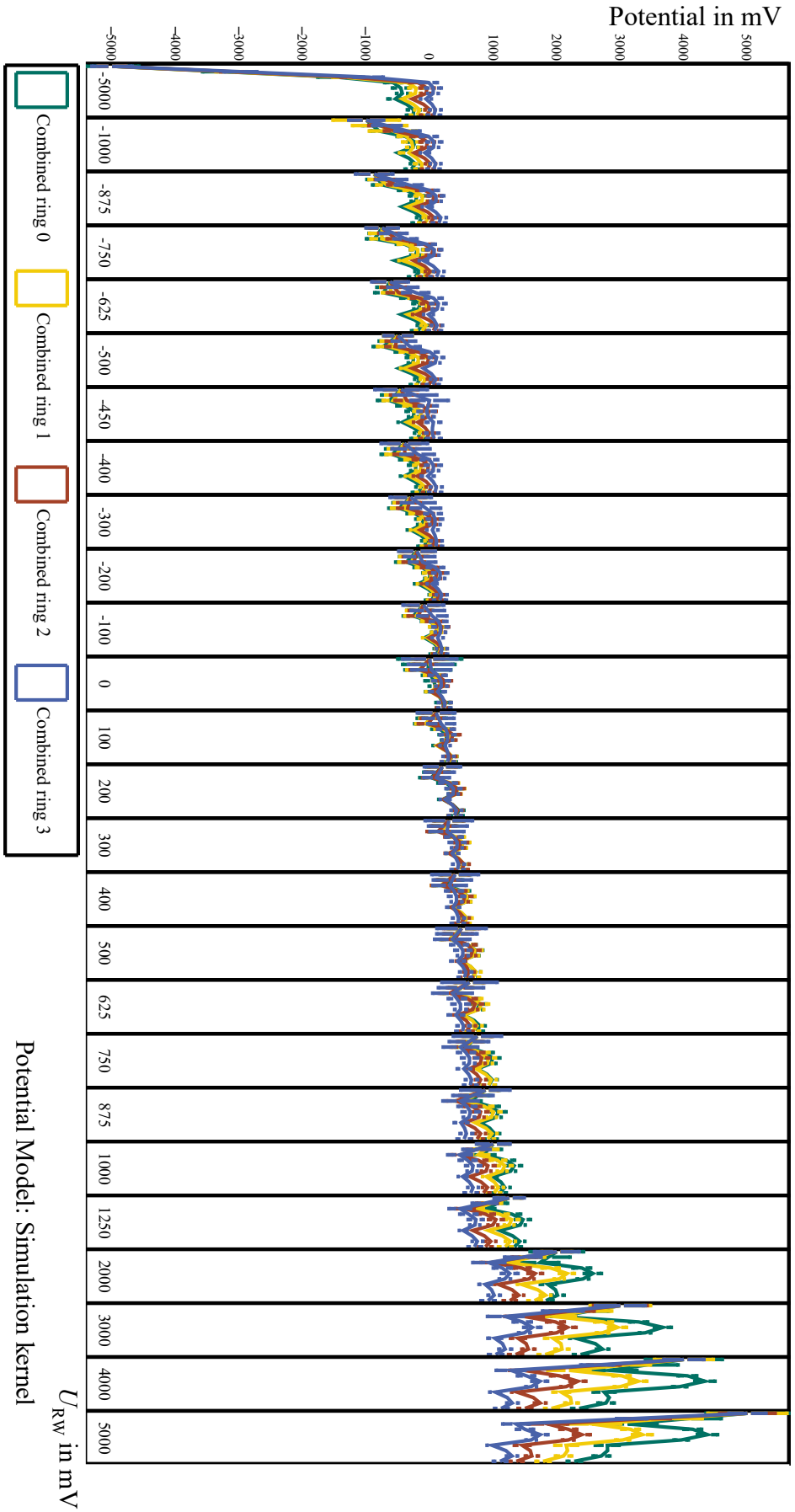

Figure A.10.: Potential over rear wall voltage in KNM2, no bins, simulation kernel.

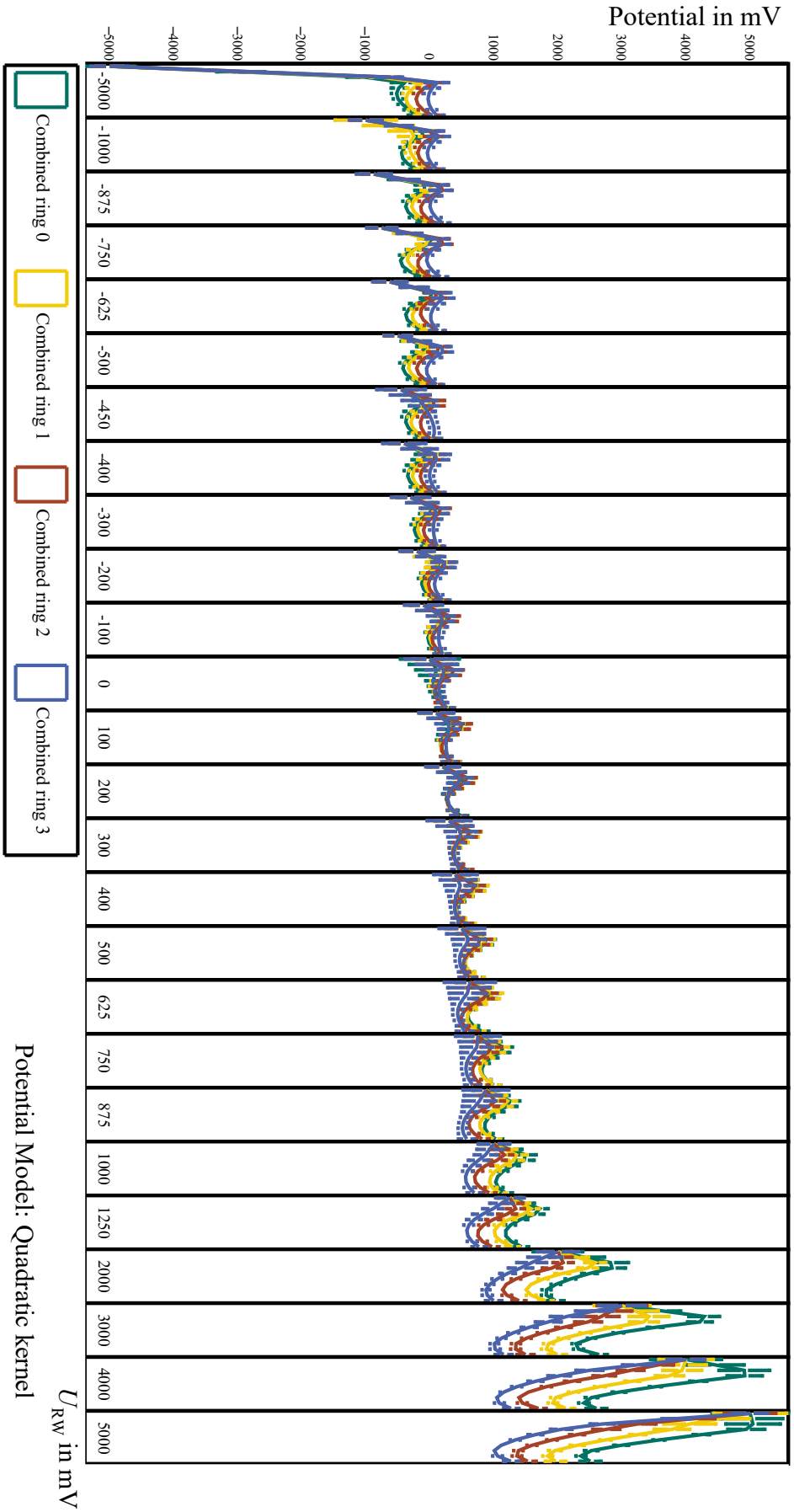

Figure A.11.: Potential over rear wall voltage in KNM2, no bins, quadratic kernel.

A.7. Calculation of the Antisymmetry Estimates for Parameters with Uncertainty

Since the measured estimates have uncertainties, the uncertainty calculation of the antisymmetry estimates has to include the covariance term

$$\sigma^2_{\mathrm{Cov}}\left(\hat{\rho}[V]\kappa_{\overline{10},0}\right) = -\frac{\Delta_{10}}{\sigma_{\mathrm{g}}^4}\mathrm{Cov}(\Delta_{10}, \sigma_{\mathrm{g}}^2)\ . \tag{A.86}$$

However, since the absolute correlation of Δ_{10} and σ_{g} is < 0.2 in average over the whole data set for all rear wall voltages and thus negligible, this does not significantly change the results.

Nevertheless, the estimates of the antisymmetry depend on whether the pixel results for the standard deviation and the eloss function shift are averaged first to combined rings and after that the antisymmetry is calculated, or if it is done the other way around. However, this is not the case for large positive rear wall voltages, i.e. when the estimates themselves are not systematics dominated. To model this effect, it is assumed that the estimate consists of the true value, a random systematic uncertainty, which scales with the reciprocal sample size or cancels due to symmetry (like statistical uncertainty or the alignment) and a constant systematic uncertainty (like the wrong reference values)

$$\mathrm{Estimate} = \mathrm{True} + \mathrm{Random} + \mathrm{Const}\ .$$

If the averages are taken first, the random component can be neglected and the resulting antisymmetry reads

$$\begin{aligned}\overline{\hat{\rho}[V]}\kappa_{\overline{10},0} &= \frac{\Delta_{10}[V] + \Delta_{\mathrm{Const}} + n^{-1}_{\mathrm{Samples}}\sum_k^{\mathrm{samples}}\Delta_{\mathrm{Random},k}}{\sigma_0[V] + \sigma_{\mathrm{Const}} + n^{-1}_{\mathrm{Samples}}\sum_k^{\mathrm{samples}}\sigma_{\mathrm{Random},k}}\ ,\\ &\approx \frac{\Delta_{10}[V] + \Delta_{\mathrm{Const}}}{\sigma_0[V] + \sigma_{\mathrm{Const}}}\ .\end{aligned} \tag{A.87}$$

The other way around the resulting equation is

$$\overline{\hat{\rho}[V]}\kappa_{\overline{10},0} = \frac{1}{n_{\mathrm{Samples}}}\sum_k^{\mathrm{samples}}\frac{\Delta_{10}[V] + \Delta_{\mathrm{Const}} + \Delta_{\mathrm{Random},k}}{\sigma_0[V] + \sigma_{\mathrm{Const}} + \sigma_{\mathrm{Random},k}}\ . \tag{A.88}$$

Since the distribution of the ratio of random variables is not necessarily a Gaussian [Hin69], the resulting mean is not necessarily the same as in equation A.87. Averaging first will minimise the uncertainties and thus problems due to misunderstood distributions will be avoided. Also, if the true values dominate the fluctuating components (i.e. for large positive rear wall voltages), both approaches give the same result.

The equations are only approximated, since in practice the uncertainty weighted average is used.

A.8. Scaling of Run Time Scale Shifts

The expectations for the scaling of the shifts of the observables caused by energy fluctuations on run time scale are described in section 7.3.5. In this section the scaling with fluctuation amplitude A and mean number of returns $\langle n \rangle_{qU}$ is simulated to test the expectations. The shifts of the observables o were fitted using [3]

$$\Delta o = \text{Scale} \cdot \left(\frac{A}{\text{meV}} \right)^{\text{Power}} \quad \text{or} \quad \Delta o = \text{Scale} \cdot \left(\langle n \rangle_{\text{qU}} \right)^{\text{Power}} . \tag{A.89}$$

Scaling of the Shifts with the Perturbation Amplitude

Figures A.13 and A.14 show the scaling of ramping and random order schedules with the perturbation amplitude.

All fits of endpoint, neutrino mass and χ^2 match the expected scalings both in tritium and krypton. An exemplary fit of the ramping case in tritium is shown in figure A.12.

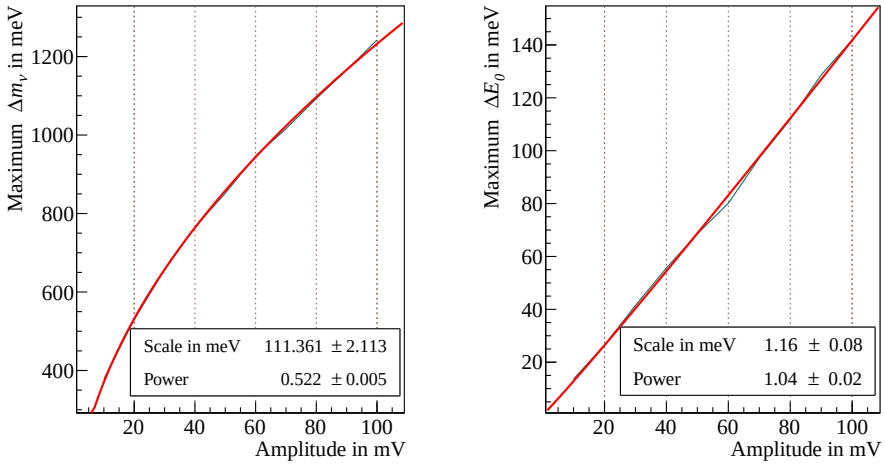

(a) (b)

Figure A.12.: Maximum shift of (a) neutrino mass and (b) endpoint with the amplitude of a sinusoidal fluctuation of the energy scale for a ramping schedule.

In section 7.3.3 it has been confirmed, that instead of the amplitude also the RMS value can be used, which is more specific since it depends also on the perturbation shape.

[3] When using transformations of the observables, such that the scalings are linear, a first order polynomial yields fit results with better χ^2. However, showing the results for endpoint and neutrino mass on the same linear energy scale is preferred here.

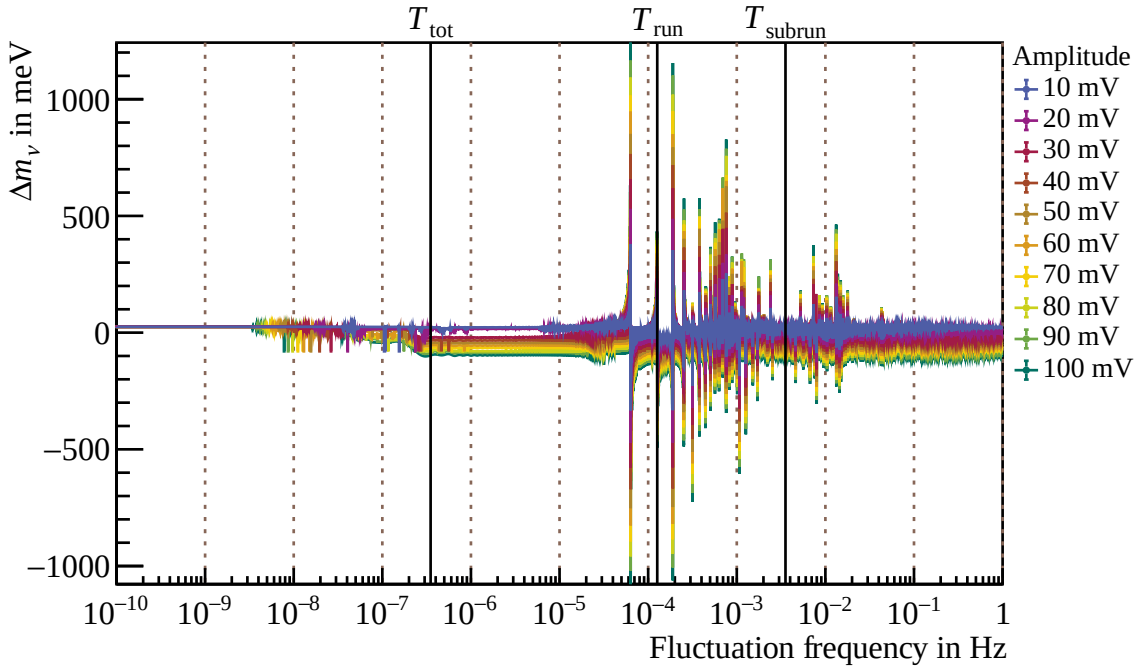

Figure A.13.: Ramping, amplitude scaling: The shown study uses the KNM2 ramping schedule from figure 7.6, but equivalent results have been found for krypton and for all other schedules. The magnitude of the largest peak scales with the square root of the fluctuation amplitude.

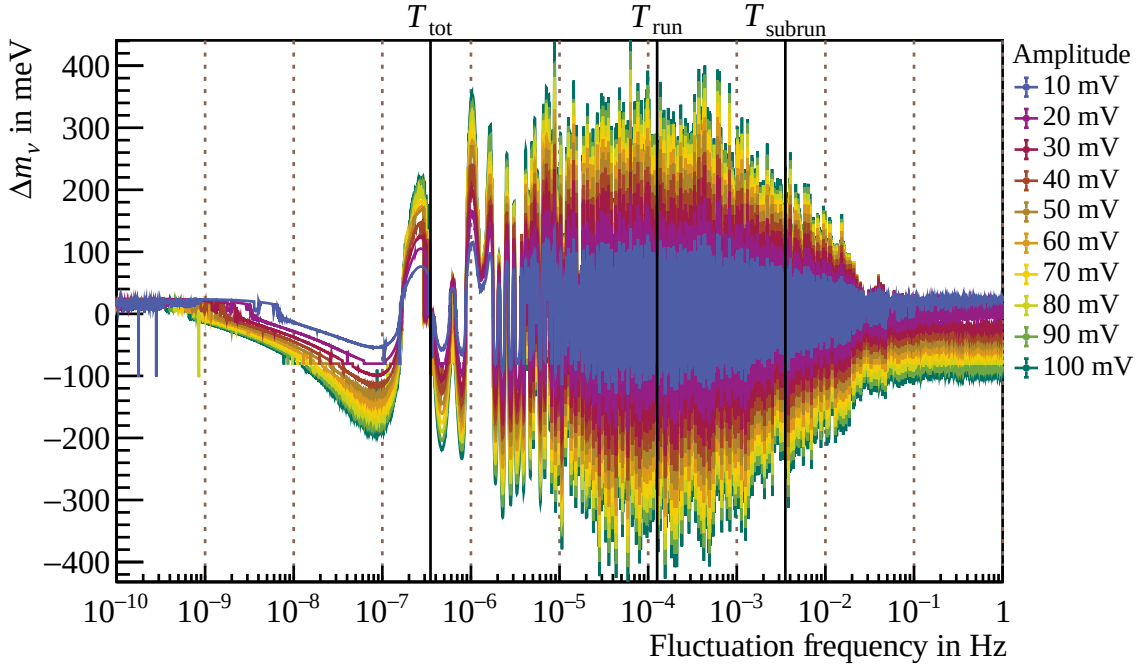

Figure A.14.: Random order, amplitude scaling: The shown study uses the random schedule from figure 7.8, but equivalent results have been found for krypton and for all other schedules. The magnitude of the envelope scales with the square root of the fluctuation amplitude.

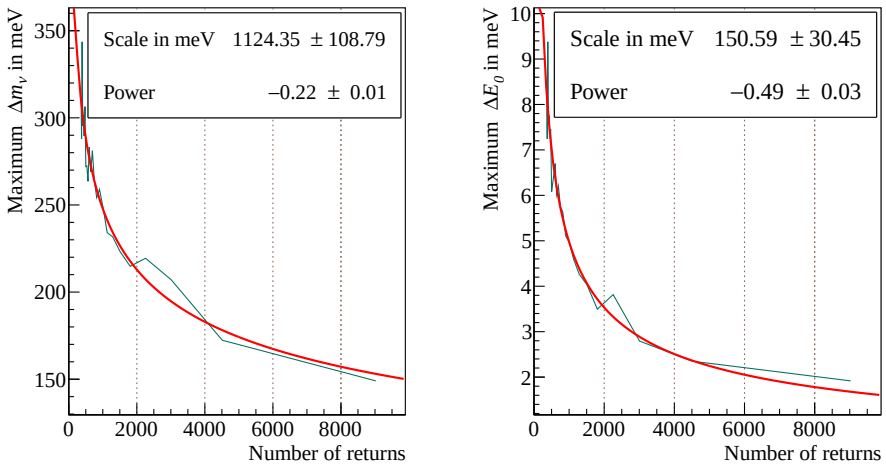

(a) (b)

Figure A.15.: Maximum shift of (a) neutrino mass and (b) endpoint with the number of returns for a schedule with random order. Using the standard deviation on run time scale instead of the maximum leads to the same scaling.

Scaling of the Shifts with the Subrun Duration

Figures A.16 and A.17 show the scaling of ramping and random order schedules with the mean subrun duration, which is anti-proportional to the return number. For the randomised case the expected scalings are found, as shown in figure A.15.

Due to the limited resolution of the simulation, the scaling for the ordered schedules is harder to investigate. As discussed in section 7.3.1 the resolution is only good enough to see all structures starting from $\frac{1}{T_{\text{tot}}}$ to three orders of magnitude above in frequency. Since the width of the peaks is proportional to $\frac{1}{T_{\text{tot}}}$ which depends on the varied return number, this causes a systematic in the simulation. In accordance with the expectation the power of the return number tended towards zero with increasing frequency resolution. In any case it is expected that no coherent fluctuations exist on run time scale, and that the randomised case is more realistic.

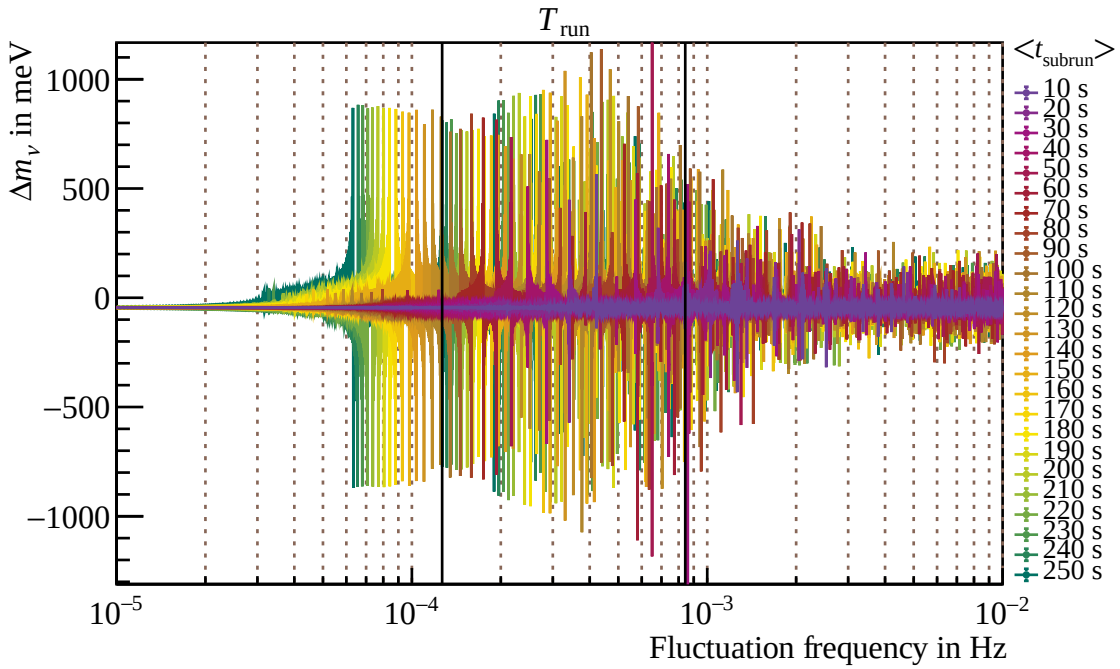

Figure A.16.: Ramping, scaling with subrun duration: Ramps where performed according to the KNM2 MTD and plain total measurement time. The number of returns was varied, leading to the shown $\langle t_{\text{subrun}} \rangle$. The range of the resulting run time scale is given by the vertical lines. Due to the increased dead time for small mean subrun duration, the total time varies between 33 and 124 days. The frequency range was decreased to increase the resolution.

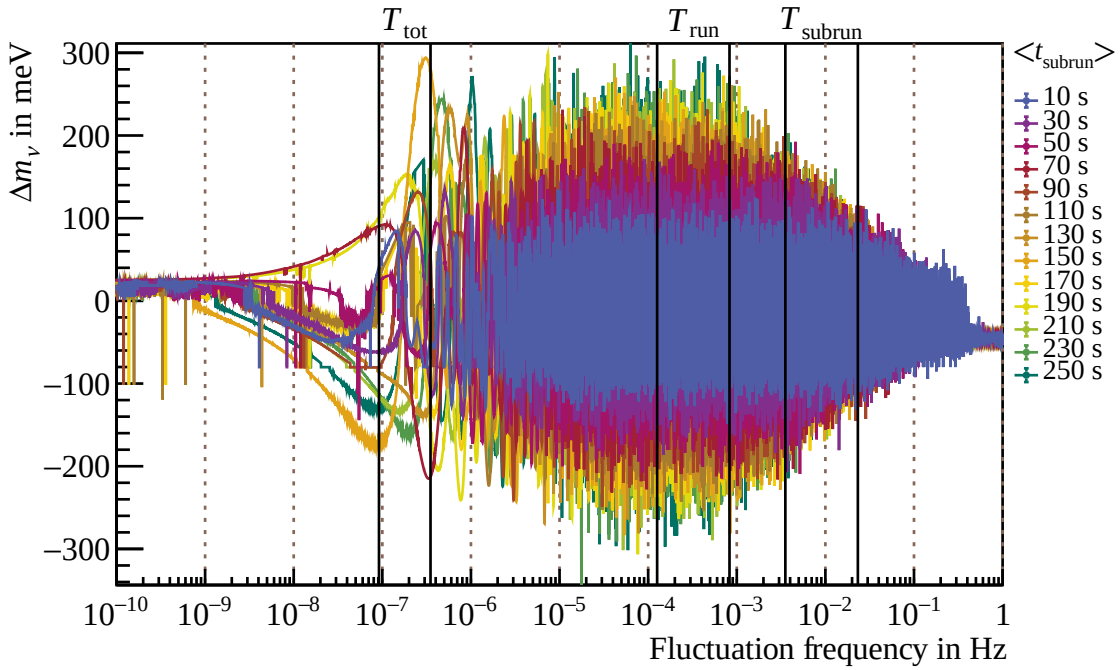

Figure A.17.: Random order, scaling with subrun duration: Same subrun duration distribution as in the above plot, but the order of the subruns is randomised. As in the ramping case, the dead time increases when decreasing $\langle t_{\text{subrun}} \rangle$, here by approximately a factor of 3.8 in the plotted range.

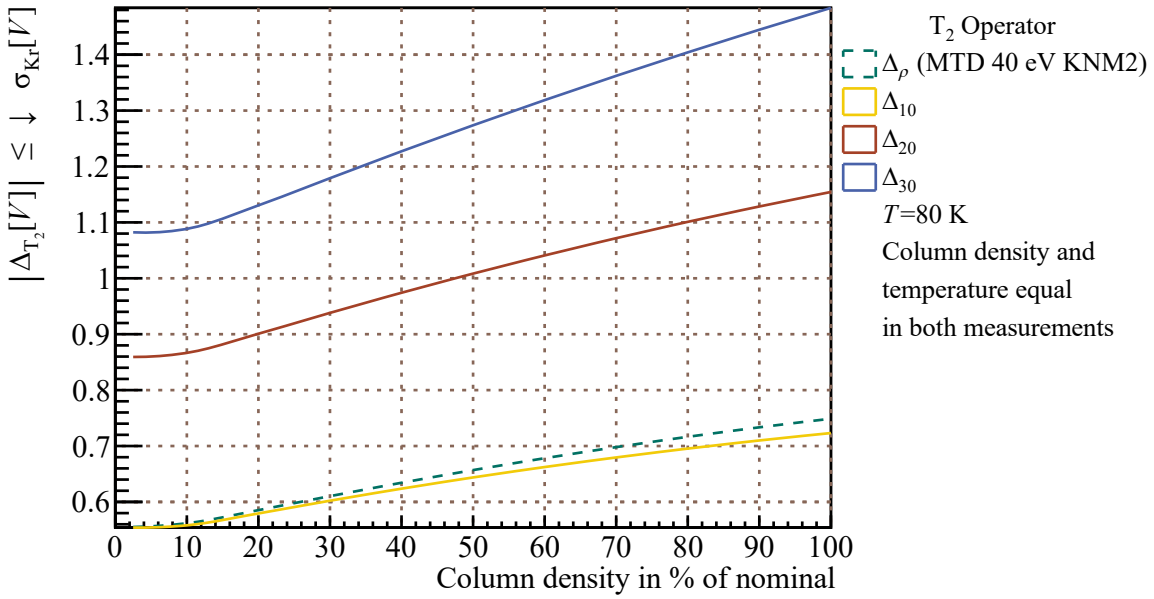

Figure A.18.: Tritium weight standard deviation, krypton weighted, equal column density: Here the source conditions are equal in both modes, which is the plan for the future measurements. The above factors can be used to constrain the $\Delta_{\bar{x}}$ of tritium directly from the krypton σ_0.

A.9. Weight Standard Deviations and Correlations

The following pages show weight standard deviations and correlations supplementary to the ones shown in chapter 5. The following is shown:

- Figure A.18: Tritium weight standard deviations, krypton weighted. The source conditions are equal in both the krypton and tritium measurement, as planned for future measurements.
- Figure A.19: Tritium weight standard deviations, krypton weighted. The essential difference to figure A.18 is the tritium column density in the krypton measurement, which is either 30 % or 40 % of nominal (like in the measurements of KNM2 and KNM3a).
- Figure A.20: Correlations of tritium and krypton mean differences.
- Figure A.21: Neutrino mass shift from mean difference vs. lower analysis interval, KNM2.
- Figure A.22: Shape energy vs. lower analysis interval, KNM2.
- Figure A.23: Ratio of krypton and tritium weighted standard deviations of weights.

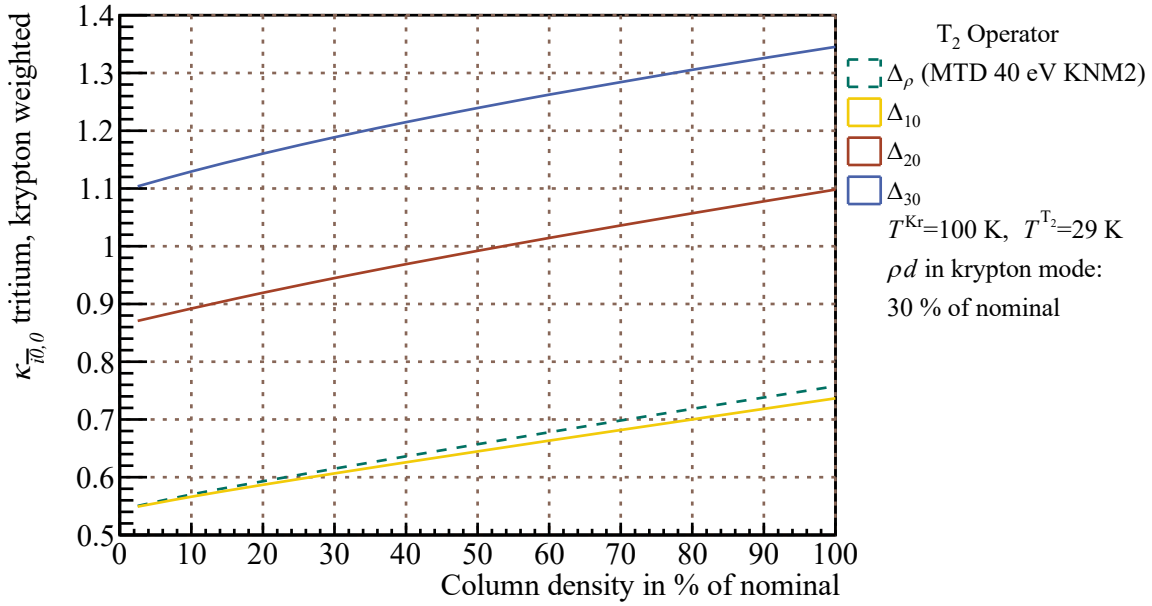

(a) KNM2 ρd = 30 % → 84 % constraints

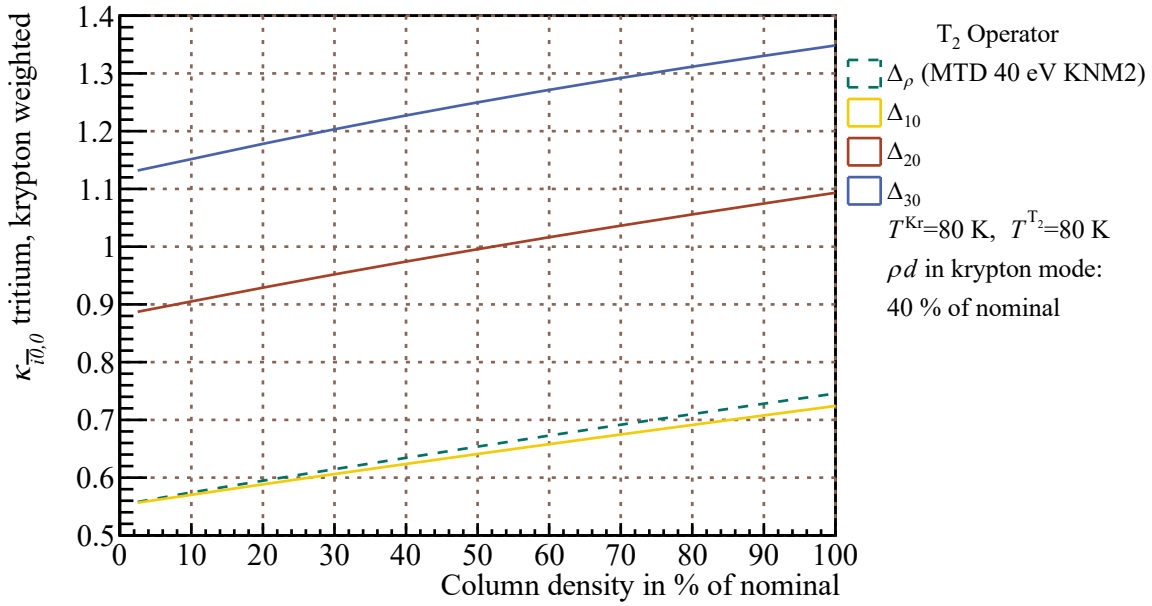

(b) KNM3 equal source mode constraints

Figure A.19.: Tritium weight standard deviation, krypton weighted: There is no practical difference of the standard deviations for the different conditions, since the temperature dependence has been found to be negligible and the change of krypton P_0 from 30 % to 40 % column density is small. The above $\kappa_{\tilde{x},0}$ can be used to constrain $\Delta_{\tilde{x}}$ of tritium directly from the krypton σ_0.

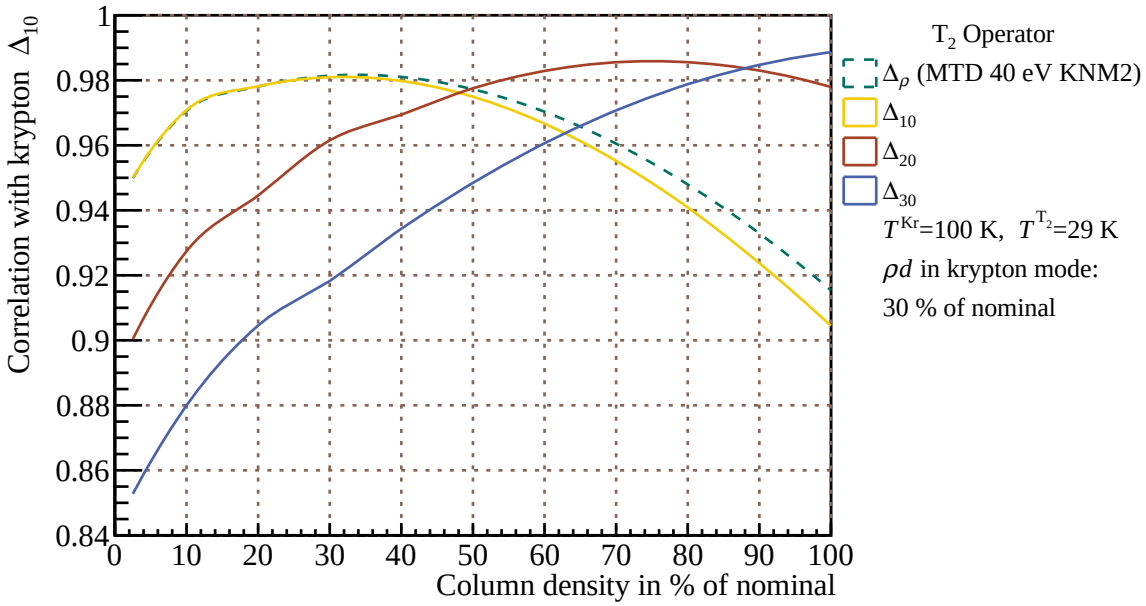

(a) KNM2 ρd = 30 % → 84 % correlations

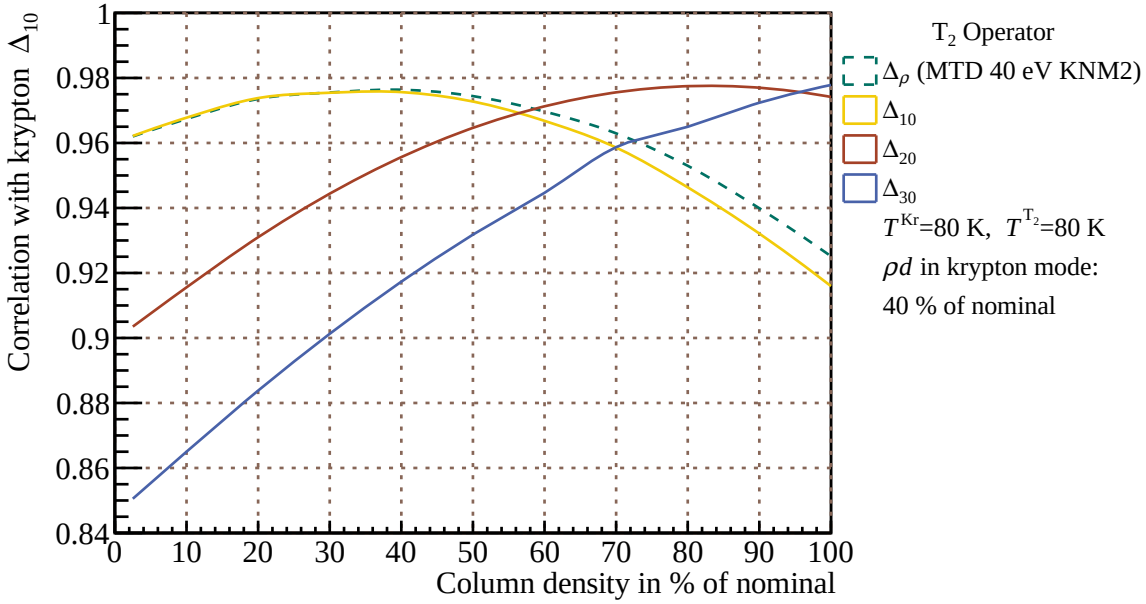

(b) KNM3 equal source mode correlations

Figure A.20.: Correlations of tritium and krypton mean differences: The correlations of the measurement of Δ_{10} in krypton and Δ_ρ in tritium are highest, when the column density difference between the measurements is small. However, when the higher Δ_{i0} are relevant in the tritium measurement (i.e. for large analysis intervals of the MTD), which affects Δ_ρ, this does not hold.

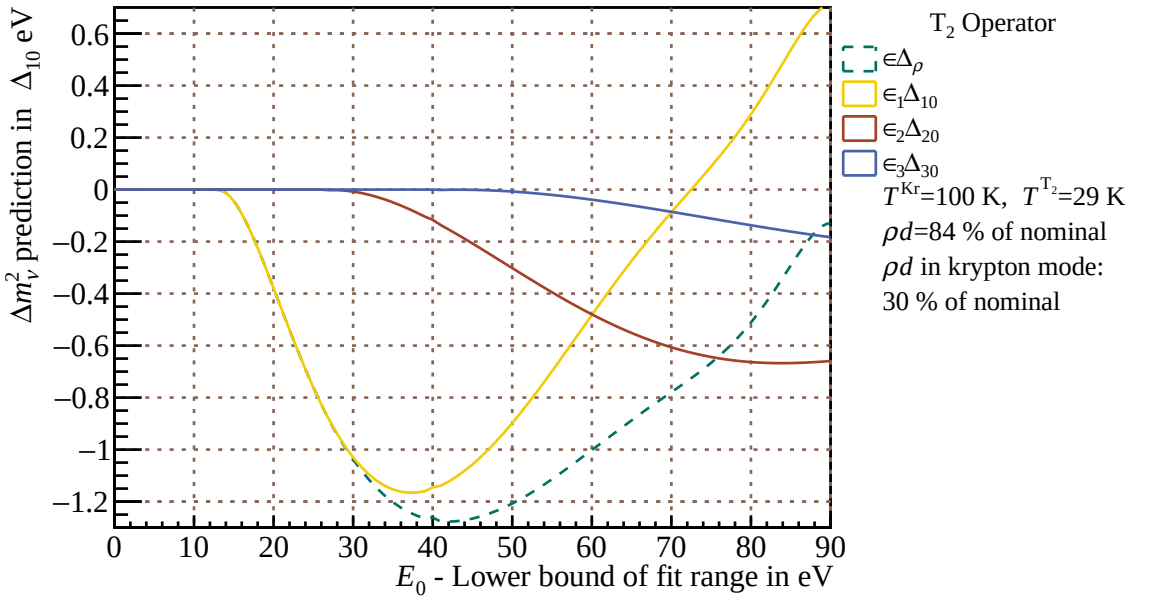

(a) Prediction

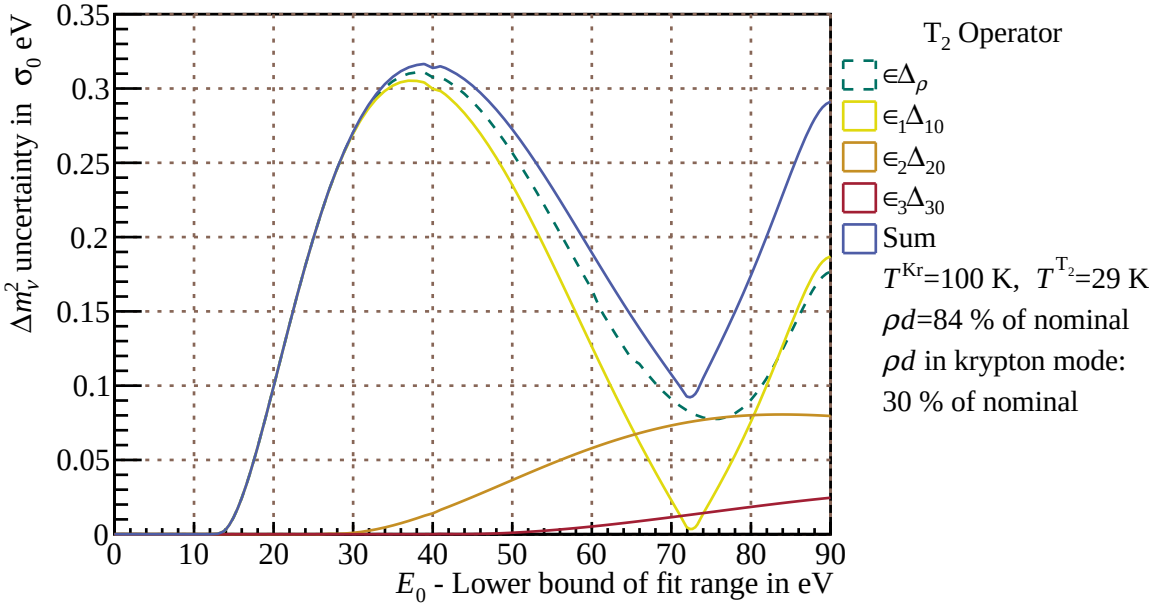

(b) Uncertainty

Figure A.21.: Neutrino mass shift from mean difference vs. lower analysis interval, KNM2: The neutrino mass shift prediction (a) and uncertainty of the prediction (b) is qualitatively similar to that of the high temperature mode, shown in the main text.

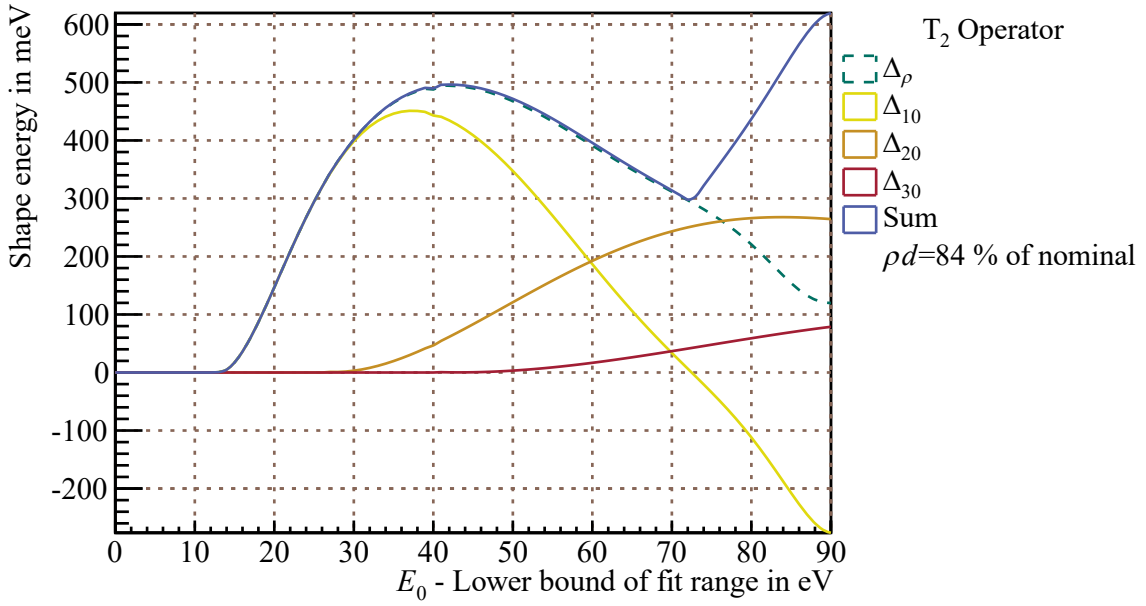

Figure A.22.: Shape energy vs. lower analysis interval, KNM2: Compared to figure 5.17 for ρd = 40 % of nominal, here the shape energy is scaled with the higher column density of KNM2. Other than that its dependence on the analysis interval is very similar.

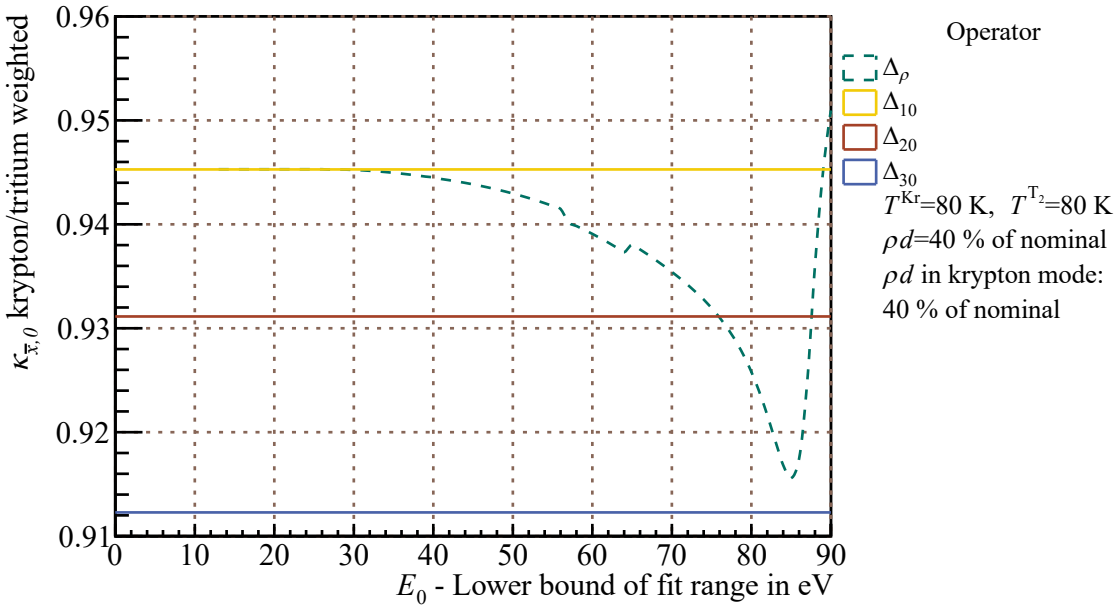

Figure A.23.: Ratio of krypton and tritium weighted standard deviations of weights: The shape energy is defined for tritium σ_0. If it is to be calculated from krypton σ_0, it has to be scaled with the above ratio.

Bibliography

[Abd+94] J. N. Abdurashitov et al. “Results from SAGE (The Russian-American gallium solar neutrino experiment)”. In: *Physics Letters B* 328.1 (1994), pp. 234–248. ISSN: 0370-2693.

[Ake+19] M. Aker et al. “Improved upper limit on the neutrino mass from a direct kinematic method by KATRIN”. In: *Physical review letters* 123.22 (2019), p. 221802.

[Ams+15] J. F. Amsbaugh et al. “Focal-plane detector system for the KATRIN experiment”. In: *Nuclear Instruments and Methods in Physics Research Section A: Accelerators, Spectrometers, Detectors and Associated Equipment* 778 (2015), pp. 40–60. ISSN: 0168-9002.

[Ant+09] I. Antcheva et al. “ROOT—A C++ framework for petabyte data storage, statistical analysis and visualization”. In: *Computer Physics Communications* 180.12 (2009), pp. 2499–2512.

[Are+18] M. Arenz et al. “First transmission of electrons and ions through the KATRIN beamline”. In: *Journal of Instrumentation* 13.04 (2018), P04020.

[Ase+11] V. N. Aseev et al. “Upper limit on the electron antineutrino mass from the Troitsk experiment”. In: *Phys. Rev. D* 84 (11 Dec. 2011), p. 112003. DOI: 10.1103/PhysRevD.84.112003. URL: https://link.aps.org/doi/10.1103/PhysRevD.84.112003.

[Ase+12] V. N. Aseev et al. “Measurement of the electron antineutrino mass in tritium beta decay in the Troitsk nu-mass experiment”. In: *Physics of Atomic Nuclei* 75.4 (2012), pp. 464–478. URL: http://link.springer.com/content/pdf/10.1134%2FS1063778812030027.pdf.

[Bab14] M. Babutzka. “Design and development for the Rearsection of the KATRIN experiment”. PhD thesis. Karlsruher Institut für Technologie (KIT), 2014.

[BB67] J. A. Bearden and A. F. Burr. “Reevaluation of X-ray atomic energy levels”. In: *Reviews of Modern Physics* 39.1 (1967), p. 125. URL: http://journals.aps.org/rmp/pdf/10.1103/RevModPhys.39.125.

[Beh17] J. Behrens. “Design and Commissioning of a Monoenergetic Photoelectron Source and Active Background Reduction by Magnetic Pulse at the KATRIN Experiment”. PhD thesis. Westfälische Wilhelms-Universität Münster (WWU), 2017.

[Bel+08] A. I. Belesev et al. “Investigation of space-charge effects in gaseous tritium as a source of distortions of the beta spectrum observed in the Troitsk neutrino-mass experiment”. In: *Physics of atomic nuclei* 71.3 (2008), pp. 427–436. URL: http://link.springer.com/content/pdf/10.1134%2FS1063778808030046.pdf.

[Bon03] J. Bonn. *WG(Kr-T)S exploring systematics with ^{83m}Kr in the WGTS*. Internal presentation. KATRIN 6.TB, Mainz, July 8, 2003.

[Bor11] B. Bornschein. "Between Fusion and Cosmology-The Future of the Tritium Laboratory Karlsruhe". In: *Fusion Science and Technology* 60.3 (2011), pp. 1088–1091.

[Böt20] M. Böttcher. "Analysis of krypton conversion electron lines of the gaseous krypton-tritium source of KATRIN". MA thesis. Westfälische Wilhelms-Universität Münster (WWU), 2020.

[BW36] G. Breit and E. Wigner. "Capture of Slow Neutrons". In: *Phys. Rev.* 49.7 (Apr. 1936), pp. 519–531. URL: http://link.aps.org/doi/10.1103/PhysRev.49.519.

[Cal+06] A. Caló et al. "The Kr valence photoelectron satellite lines in the photon energy region below the 3d threshold". In: *Journal of Physics B: Atomic, Molecular and Optical Physics* 39.20 (2006), p. 4169.

[CH20] S. R. Choudhury and S. Hannestad. "Updated results on neutrino mass and mass hierarchy from cosmology with Planck 2018 likelihoods". In: *Journal of Cosmology and Astroparticle Physics* 2020.07 (2020), p. 037.

[Che03] F. F. Chen. "Langmuir probe diagnostics". In: *IEEE-ICOPS Meeting, Jeju, Korea*. Vol. 2. 6. 2003.

[CN73] T. A. Carlson and C. W. Nestor Jr. "Calculation of electron shake-off probabilities as the result of X-ray photoionization of the rare gases". In: *Physical Review A* 8.6 (1973), pp. 2887–.

[Cow+11] G. Cowan et al. "Asymptotic formulae for likelihood-based tests of new physics". In: *The European Physical Journal C* 71.2 (2011), pp. 1–19.

[Cow+56] C. L. Cowan et al. "Detection of the free Neutrino: a Confirmation". In: *Science, vol. 124, no. 3212, pp. 103-104* (1956).

[Def17] M. Deffert. "Simulation of global beamline alignment of the KATRIN experiment". In: *Verhandlungen der Deutschen Physikalischen Gesellschaft* (2017).

[Des+03] R. D. Deslattes et al. "X-ray transition energies: new approach to a comprehensive evaluation". In: *Rev. Mod. Phys.* 75.1 (Jan. 2003), pp. 35–99. URL: http://link.aps.org/doi/10.1103/RevModPhys.75.35.

[Din+05] A. Dinklage et al. *Plasma physics: confinement, transport and collective effects*. Vol. 670. Springer Science & Business Media, 2005.

[DP91] D. Dubois and H. Prade. "Fuzzy sets in approximate reasoning, Part 1: Inference with possibility distributions". In: *Fuzzy sets and systems* 40.1 (1991), pp. 143–202.

[DS90] D. J. Decman and W. Stoeffl. "Atomic electron binding energies of multiply charged krypton ions by internal-conversion-electron spectroscopy". In: *Phys. Rev. Lett.* 64.23 (June 1990), pp. 2767–2770. URL: http://link.aps.org/doi/10.1103/PhysRevLett.64.2767.

[Eic+08] F. Eichelhardt et al. "First tritium results of the KATRIN test experiment TRAP". In: *Fusion Science and Technology* 54.2 (2008), pp. 615–618.

[Ell19] E. Ellinger. "Development and investigation of the Forward Beam Monitor for the KATRIN experiment". PhD thesis. Universität Wuppertal, Fakultät für Mathematik und Naturwissenschaften, 2019.

[Eri+87] B. Eriksson et al. “The high energy excited shake-up electron spectra of krypton”. In: *Le Journal de Physique Colloques* 48.C9 (1987), p. 531.

[Fis14] S. Fischer. “Commissioning of the KATRIN Raman system of durability studies of optical coatings in glove box and tritium atmospheres”. PhD thesis. Karlsruher Institut für Technologie (KIT), 2014.

[FP12] J. A. Formaggio and the Project 8 Collaboration. “Measuring Neutrino Masses Using Radio-Frequency Techniques”. In: *Journal of Physics: Conference Series* 375.4 (2012), pp. 042005–. ISSN: 1742-6596. URL: http://stacks.iop.org/1742-6596/375/i=4/a=042005.

[Fri20] F. Friedel. “Ion and plasma systematics during the first KATRIN neutrino mass measurements”. PhD thesis. Karlsruher Institut für Technologie (KIT), 2020.

[Fuk+01] S. Fukuda et al. “Constraints on neutrino oscillations using 1258 days of Super-Kamiokande solar neutrino data”. In: *Physical Review Letters* 86.25 (2001).

[Ful20] A. Fulst. “A Novel Quasi-Differential Method for MAC-E Filters and Determination and Control of the Electric Potentials of the KATRIN Experiment with a Stabilized Condensed Krypton Source and a UV llumination System”. PhD thesis. Westfälische Wilhelms-Universität Münster (WWU), 2020.

[Gal12] P. Gallagher. *Introduction to plasma physics*. Lecture slides. 2012. URL: https://www.tcd.ie/Physics/people/Peter.Gallagher/lectures/PlasmaPhysics/Lecture1n2_basic_properties.pdf.

[Gro+08] S. Grohmann et al. “Cryogenic design of the KATRIN source cryostat”. In: *AIP Conference Proceedings*. Vol. 985. 1. American Institute of Physics. 2008, pp. 1277–1284.

[Gro15] S. Groh. “Modeling of the response function and measurement of transmission properties of the KATRIN experiment”. PhD thesis. Karlsruher Institut für Technologie (KIT), 2015.

[Gup20] V. Gupta. “Calibration and Monitoring of the Energy Scale in the KATRIN experiment”. MA thesis. Max-Planck-Institute of physics, Munic, 2020.

[Hac17] M. T. Hackenjos. “KATRIN" First Light"-Commissioning and Modelling of the Beamline”. PhD thesis. Karlsruher Institut für Technologie (KIT), 2017.

[Ham+99] W. Hampel et al. “GALLEX solar neutrino observations: Results for GALLEX IV”. In: *Physics Letters B* 447.1 (1999), pp. 127–133. ISSN: 0370-2693.

[Har15] F. Harms. “Characterization and Minimization of Background Processes in the KATRIN Main Spectrometer”. PhD thesis. Karlsruher Institut für Technologie (KIT), 2015.

[Hei15] F. Heizmann. “Optimization of a KATRIN source analysis tool and investigations of the potential to constrain the relic neutrino background”. MA thesis. Karlsruher Institut für Technologie (KIT), 2015.

[Hin69] D. V. Hinkley. “On the ratio of two correlated normal random variables”. In: *Biometrika* 56.3 (Dec. 1969), pp. 635–639. ISSN: 0006-3444. DOI: 10.1093/biomet/56.3.635. eprint: https://academic.oup.com/biomet/article-pdf/56/3/635/636493/56-3-635.pdf. URL: https://doi.org/10.1093/biomet/56.3.635.

[Hol15] P. Holoborodko. *Smooth noise-robust differentiators*. Last checked: 26.06.2020. Aug. 2015. URL: http://www.holoborodko.com/pavel/numerical-methods/numerical-derivative/smooth-low-noise-differentiators/#noiserobust_2.

[Höt12] M. Hötzel. "Simulation and analysis of source-related effects for KATRIN". PhD thesis. Karlsruher Institut für Technologie (KIT), 2012.

[Jam04] F. James. *The interpretation of errors*. Cern, 2004.

[Jan15] A. Jansen. "The Cryogenic Pumping Section of the KATRIN Experiment-Design Studies and Experiments for the Commissioning". PhD thesis. Karlsruher Institut für Technologie (KIT), 2015.

[KAT04a] KATRIN. *WGTS charging*. KATRIN internal document. 2004. URL: https://fuzzy.fzk.de/bscw/bscw.cgi/78568?op=preview&back_url=1005311%3fclient_size%3d1463x979.

[KAT04b] Collaboration KATRIN. "KATRIN design report 2004". In: *FZKA report* 7090 (2004). URL: http://inspirehep.net/record/680949/files/FZKA7090.pdf.

[KATep] Collaboration KATRIN. "Precision measurement and parametrization of the energy loss function of the KATRIN experiment". In: (in prep.).

[Kelep] J. Kellerer. "Plasma Simulations of the KATRIN Tritium Source". PhD thesis. Karlsruher Institut für Technologie (KIT), in prep.

[Ken49] M. G. Kendall. "On the reconciliation of theories of probability". In: *Biometrika* 36.1/2 (1949), pp. 101–116.

[Kik+96] A. Kikas et al. "High-resolution study of the correlation satellites in photoelectron spectra of the rare gases". In: *Journal of electron spectroscopy and related phenomena* 77.3 (1996), pp. 241–266.

[Kle+19] M. Kleesiek et al. "β-decay spectrum, response function and statistical model for neutrino mass measurements with the KATRIN experiment". In: *The European Physical Journal C* 79.3 (Mar. 2019). ISSN: 1434-6052. DOI: 10.1140/epjc/s10052-019-6686-7. URL: http://dx.doi.org/10.1140/epjc/s10052-019-6686-7.

[Kle14] M. Kleesiek. "A Data-Analysis and Sensitivity-Optimization Framework for the KATRIN Experiment". PhD thesis. Karlsruher Institut für Technologie (KIT), 2014. URL: http://digbib.ubka.uni-karlsruhe.de/volltexte/documents/3232293.

[Kle19] M. Klein. "Tritium ions in KATRIN: blocking, removal and detection". PhD thesis. Karlsruher Institut für Technologie (KIT), 2019.

[Kra+05] Ch. Kraus et al. "Final results from phase II of the Mainz neutrino mass searchin tritium {\ beta} decay". In: *The European Physical Journal C-Particles and Fields* 40.4 (2005), pp. 447–468. URL: https://link.springer.com/content/pdf/10.1140%2Fepjc%2Fs2005-02139-7.pdf.

[Kri15] V. Krishnan. *Probability and random processes*. John Wiley & Sons, 2015.

[KS10] D. Kalempa and F. Sharipov. *Separation phenomenon in the Windowless Gaseous Tritium Source of KATRIN experiment. Ternary mixtures*. Tech. rep. Tech. rep., Depto de Fısica, UFPR, 2010. URL: http://fisica.ufpr.br/sharipov/KATRIN/report5.pdf.

[Kuc16] L. Kuckert. “The Windowless Gaseous Tritium Source of KATRIN - Characterisation of gas dynamical and plasma properties”. PhD thesis. Karlsruher Institut für Technologie (KIT), 2016.

[Lab17] Ionospheric Radio Science Laboratory. *Sun and Solar Wind*. Lectures. Sept. 2017. URL: https://irsl.ss.ncu.edu.tw/media/course/106%E5%B9%B4%E7%AC%AC1%E5%AD%B8%E6%9C%9F%E4%B8%AD%E5%A4%AE%E5%A4%A7%E5%AD%B8%E9%AB%98%E7%AD%89%E5%A4%AA%E7%A9%BA%E7%A7%91%E5%AD%B8I/ASS_3.pdf.

[Lev19] F. Leven. “Analysis of Selected Models for Inelastic Electron-Scattering in the KATRIN Gaseous Tritium Source”. MA thesis. Karlsruher Institut für Technologie (KIT), 2019.

[LUX+14] D. S. LUX Collaboration Akerib et al. “First Results from the LUX Dark Matter Experiment at the Sanford Underground Research Facility”. In: *Phys. Rev. Lett.* 112.9 (Mar. 2014), pp. 091303–. URL: http://link.aps.org/doi/10.1103/PhysRevLett.112.091303.

[Mac16] M. Machatschek. “Simulation of the ^{83m}Kr Mode of the Tritium Source of the KATRIN Experiment”. MA thesis. Karlsruher Institut für Technologie (KIT), May 12, 2016.

[Mar20] A. Marsteller. “Characterization and Optimization of the KATRIN Tritium Source”. PhD thesis. Karlsruher Institut für Technologie (KIT), 2020.

[McC15] E. A. McCutchan. “Nuclear Data Sheets for A = 83”. In: *Nuclear Data Sheets* 125 (Mar. 2015), pp. 201–394. ISSN: 0090-3752. URL: http://www.sciencedirect.com/science/article/pii/S0090375215000034.

[Ni+19] K. Ni et al. “Searching for neutrino-less double beta decay of 136Xe with PandaX-II liquid xenon detector”. In: *Chinese Physics C* 43.11 (2019), p. 113001.

[OL02] J. J. Olivero and R. L. Longbothum. “Empirical fits to the Voigt line width: A brief review”. In: *Journal of Quantitative Spectroscopy and Radiative Transfer* (2002).

[Ost08] B. Ostrick. “Eine kondensierte ^{83m}Kr-Kalibrationsquelle für das KATRIN-Experiment”. PhD thesis. Westfälische Wilhelms-Universität Münster (WWU), 2008.

[Ost20] R. Ostertag. “Investigation of Plasma Effects in the KATRIN Source with ^{83m}Kr”. MA thesis. Karlsruher Institut für Technologie (KIT), June 2020.

[OW08] E. W. Otten and Ch. Weinheimer. “Neutrino mass limit from tritium β decay”. In: *Reports on Progress in Physics* 71.8 (2008), p. 086201. URL: http://iopscience.iop.org/article/10.1088/0034-4885/71/8/086201/pdf.

[Pau30] W. Pauli. “Offener Brief an die Gruppe der Radioaktiven bei der Gauvereins-Tagung zu Tübingen”. In: *datiert* 4 (1930), pp. 1316–1317.

[Pfe09] Vacuum GmbH Pfeiffer. *Vacuum Technology Know How*. Mar. 2009.

[Pic+92] A. Picard et al. “Precision measurement of the conversion electron spectrum of 83mKr with a solenoid retarding spectrometer”. In: *Zeitschrift für Physik A Hadrons and Nuclei* 342.1 (1992), pp. 71–78. ISSN: 0939-7922. URL: http://dx.doi.org/10.1007/BF01294491.

[Res19] O. Rest. “Precision high voltage at the KATRIN experiment and new methods for an absolute calibration at ppm-level forhigh-voltage dividers”. PhD thesis. Westfälische Wilhelms-Universität Münster (WWU), 2019.

[RK88] R. G. H. Robertson and D. A. Knapp. "Direct Measurements of Neutrino Mass". In: *Annu. Rev. Nucl. Part. Sci.* 38.1 (Dec. 1988), pp. 185–215. ISSN: 0163-8998. DOI: 10.1146/annurev.ns.38.120188.001153. URL: http://dx.doi.org/10.1146/annurev.ns.38.120188.001153.

[Rob+91] R. G. H. Robertson et al. "Limit on $\bar{\nu}_e$ mass from observation of the β decay of molecular tritium". In: *Phys. Rev. Lett.* 67.8 (Aug. 1991), pp. 957–960. URL: http://link.aps.org/doi/10.1103/PhysRevLett.67.957.

[Rod20] C. Rodenbeck. *Internal communication*. June 2020.

[Rodep] C. Rodenbeck. "Investigation of inelastic scattering of beta electrons in KATRIN's gaseous tritium source using time of flight methods to determine the neutrino mass". PhD thesis. Westfälische Wilhelms-Universität Münster (WWU), in prep.

[Röl15] M. Röllig. "Tritium analytics by beta induced X-ray spectrometry". PhD thesis. Karlsruher Institut für Technologie (KIT), 2015.

[Röt19] C. Röttele. "Tritium suppression factor of the KATRIN transport section". 51.03.01; LK 01. PhD thesis. Karlsruher Institut für Technologie (KIT), 2019. 140 pp. DOI: 10.5445/IR/1000096733.

[Sch16] K. Schönung. "Development of a Rear Wall for the KATRIN Rear Section and investigation of tritium compatibility of Rear Section components". PhD thesis. Karlsruher Institut für Technologie (KIT), 2016.

[SD95] W. Stoeffl and D. J. Decman. "Anomalous structure in the beta decay of gaseous molecular tritium". In: *Physical review letters* 75.18 (1995), p. 3237. URL: http://journals.aps.org/prl/pdf/10.1103/PhysRevLett.75.3237.

[Sei19] H. Seitz-Moskaliuk. "Characterisation of the KATRIN tritium source and evaluation of systematic effects". PhD thesis. Karlsruher Institut für Technologie (KIT), 2019.

[Sev79] K. D. Sevier. "Atomic electron binding energies". In: *Atomic Data and Nuclear Data Tables* 24.4 (1979), pp. 323–371. ISSN: 0092-640X. URL: http://www.sciencedirect.com/science/article/pii/0092640X79900123.

[SH08] K. Shin and J. Hammond. *Fundamentals of signal processing for sound and vibration engineers*. John Wiley & Sons, 2008.

[Sle+19] M. Slezák et al. "High-resolution spectroscopy of gaseous ^{83m}Kr conversion electrons with the KATRIN experiment". In: *arXiv preprint arXiv:1903.06452v2* (2019).

[Sle16] M. Slezák. "Monitoring of the energy scale in the KATRIN neutrino experiment". PhD thesis. Nuclear Physics Institute, Czech Academy of Sciences, 2016.

[SNO+02] SNO et al. "Direct Evidence for Neutrino Flavor Transformation from Neutral-Current Interactions in the Sudbury Neutrino Observatory". In: *Phys. Rev. Lett.* 89.1 (June 2002), pp. 011301–. URL: http://link.aps.org/doi/10.1103/PhysRevLett.89.011301.

[Suz95] Y. Suzuki. "Kamiokande solar neutrino results". In: *Nuclear Physics B-Proceedings Supplements* 38.1 (1995), pp. 54–59. ISSN: 0920-5632.

[Vén+14] D. Vénos et al. “Gaseous source of 83m Kr conversion electrons for the neutrino experiment KATRIN”. In: *Journal of Instrumentation* 9.12 (2014), P12010–. ISSN: 1748-0221. URL: http://stacks.iop.org/1748-0221/9/i=12/a=P12010.

[Vén+18] D. Vénos et al. “Properties of 83mKr conversion electrons and their use in the KATRIN experiment”. In: *Journal of Instrumentation* 13.02 (2018), T02012.

[War+91] D. L. Wark et al. “Correspondence of electron spectra from photoionization and nuclear internal conversion”. In: *Phys. Rev. Lett.* 67.17 (Oct. 1991), pp. 2291–2294. URL: http://link.aps.org/doi/10.1103/PhysRevLett.67.2291.

[Waz11] A.-M. Wazwaz. *Linear and nonlinear integral equations*. Vol. 639. Springer, 2011.

[Wei20] E. Weiss. “Non-adiabaticity simulation”. Internal KATRIN document. 2020.

[Wil+87] J. F. Wilkerson et al. “Limit on ν_e Mass from Free-Molecular-Tritium Beta Decay”. In: *Physical review letters* 58.20 (1987), p. 2023. URL: http://journals.aps.org/prl/pdf/10.1103/PhysRevLett.58.2023.

[Wil03] J. F. Wilkerson. *Physics motivation for using a Windowless Gaseous Kr Source*. Internal presentation. KATRIN 6. TB, Mainz, July 8, 2003.

[WW30] V. Weisskopf and E. Wigner. “Berechnung der natürlichen Linienbreite auf Grund der Diracschen Lichttheorie”. In: *Zeitschrift für Physik* 63.1-2 (1930), pp. 54–73. URL: http://link.springer.com/content/pdf/10.1007%2FBF01336768.pdf.

[Zac15] M. Zacher. “High Field Electrodes Design and an Angular Selective Photoelectron Source for the KATRIN Spectrometers”. PhD thesis. Westfälische Wilhelms-Universität Münster (WWU), 2015.

[Zub11] K. Zuber. *Neutrino physics*. CRC press, 2011.

Danksagung

An dieser Stelle möchte ich mich bei allen bedanken, die zum Gelingen dieser Arbeit beigetragen haben. Im Besonderen danken möchte ich:

- Prof. Dr. Kathrin Valerius, für ihren Einsatz mir ein selbstständiges und unabhängiges Arbeiten in der KATRIN Kollaboration zu ermöglichen.
- Prof. Dr. Ulrich Husemann, für die kurzfristige Übernahme des Korreferats, den kritischen Blick von außen und die absolut stress- und verzögerungsfreie Kommunikation.
- Prof. Dr. Guido Drexlin, für die Möglichkeit in der KATRIN Kollaboration zu arbeiten.
- Dr. Manuel Klein und Dr. Magnus Schlösser, für die umfassenden Korrekturen der Arbeit. Ihnen und Dr. Fabian Friedel außerdem stellvertretend für die konstruktive Arbeit im Plasmateam.
- Dr. Alexander Jansen, Dr. Thomas Thümmler und allen Organisatoren der Messkampagnen. Außerdem den Operateuren im Kontrollraum, insbesondere Caroline Rodenbeck, Dr. Rudolf Sack und Dr. Fabian Friedel, ohne die die STS3a und KNM1 Krypton Messkampagnen deutlich weniger reibungslos verlaufen wären. Raphael Ostertag für die selbstständige und zuverlässige Arbeit rund um die KNM2 Krypton Messkampagne.
- Dr. Wonqook Choi, für die effiziente und schnelle Erweiterung des Analysecodes und für viele fruchtbare Diskussionen.
- Dr. Hendrik Seitz-Moskaliuk, Fabian Block und Fabian Leven für die entspannte und konstruktive Atmosphäre im Büro. Dr. Hendrik Seitz-Moskaliuk außerdem für die Unterstützung in der Lehre.
- Klaus Mehret, für abwechslungsreiche Gespräche und die garantiert gute Laune danach.
- Vielen weiteren ungenannten Kolleginnen und Kollegen, für sachliche und spannende Diskussionen und für die gute Atmosphäre am Institut.

Weiterhin danke ich den vielen großartigen Mitwirkenden der Theatergruppen am KIT für die Möglichkeit gemeinsam auf diesem Niveau Kultur zu machen. Was wir zusammen auf die Beine gestellt haben, gehört zum Besten, was ich je gemacht habe.

Zum Schluss danke ich meiner Familie und meinen Freunden Clara, Johanna und Bert für ihre Unterstützung auch und gerade in den Zeiten, in denen es besonders schwierig war.